

# Polarized Line Formation in Turbulent and Scattering Media

A THESIS

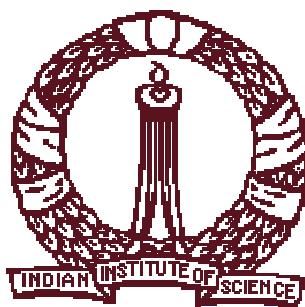
SUBMITTED FOR THE DEGREE OF

**Doctor of Philosophy**

IN THE FACULTY OF SCIENCE

by

**M. Sampurna**



Department of Physics  
Indian Institute of Science  
Bangalore – 560 012  
India

April 2008



# Declaration

I hereby declare that this thesis, submitted to the Physics Department, Indian Institute of Science, for the award of a Ph.D. degree, is a result of the investigations carried out by me at Indian Institute of Astrophysics, Bangalore, under the Joint Astronomy and Astrophysics Program, under the supervision of Professor K. N. Nagendra. The results presented herein have not been subject to scrutiny for the award of a degree, diploma, associateship or fellowship whatsoever, by any university or institute. Whenever the work described is based on the findings of other investigators, due acknowledgment has been made. Any unintentional omission is regretted.

Prof. K. N. Nagendra  
(Thesis Supervisor)  
Indian Institute of Astrophysics,  
2nd Block, Koramangala,  
Bangalore 560 034,  
India.

M. Sampoorna  
(Ph.D. Candidate)  
Department of Physics,  
Indian Institute of Science,  
Bangalore 560 012,  
India.

April 2008



– Dedicated to my Parents –



# Acknowledgments

I am deeply indebted to Prof. K. N. Nagendra, who was not only my thesis supervisor, but also a great source of inspiration. He introduced me to the Physics of “Hanle scattering”, when I conducted a summer project under his able guidance during the summer of 2002. Since then, his constant moral support and backing has been a big motivating factor for me to do research in the field of “theory and numerics of polarized radiation transfer”. I have greatly benefited from his deep knowledge in polarized line formation theory and numerical methods. Apart from the confidence shown in my work, he gave me the necessary freedom and encouragement to develop my own ideas. He always gave me a great deal of time for discussions, which were of immense help. I am grateful to him for bringing me in contact with Prof. Hélène Frisch and Prof. Jan Olof Stenflo who are pioneers in this field. I acknowledge him for making possible my visits to the Observatoire de la Côte d’Azur (OCA) at Nice, France; Instituto Ricerche Solari Locarno (IRSOL) at Locarno, Switzerland and Institute of Astronomy, ETH at Zurich, Switzerland. Besides the constant academic support, I will never forget his beautiful descriptions of the Nature; and our interesting and enlightening discussions on philosophy, music, history of mankind etc. He always took great care and interest in advising and guiding me on academic and various matters regarding the scientific profession.

I wish to thank Prof. Siraj Hasan, Director, Indian Institute of Astrophysics (IIA) and Prof. Vinod Krishan, Dean of faculty, IIA, for providing me with excellent research facilities and constant encouragement over the years. I am grateful to the former Directors of IIA Prof. J. H. Sastry and Prof. R. Cowsik for their support during the early years. I would also like to thank the Indian Institute of Science (IISc), Bangalore, for organizing the “Joint Astronomy and Astrophysics Program (JAAP)” under which I was selected to conduct research in Astrophysics. I am very grateful to Prof. Chanda J. Jog, convener of JAAP and my official guide at IISc, for her constant moral support, guidance and

encouragement in both academic as well as JAAP related matters. I particularly enjoyed her clear lectures on “statistical equilibrium equations and radiation transfer in interstellar medium” presented during the one year mandatory course work. I am thankful to Prof. Arnab Rai Choudhuri (former JAAP convener) for his encouragement. I particularly liked his interesting lectures on “Solar dynamo theory and magnetic fields” delivered at the Kodai Winter School held in Kodaikanal, India. I would like to thank Prof. H. L. Bhat for his encouragement.

I specially thank Prof. H el ene Frisch, for her joint guidance along with Prof. K. N. Nagendra, on part-I of the thesis (namely, stochastic polarized line formation), and for her comments and suggestions, which greatly helped me on part-II of the thesis. She organized three short term visits for me at the Observatoire de la C ote d’Azur, Nice, France (during 2004, 2005 and 2007). The work on turbulent Zeeman line formation was started in December 2003 during her visit to IIA, Bangalore, and continued here at IIA, and completed during the above said three visits, which resulted in 5 major papers in international Journals and 2 papers in Refereed conference proceedings. I have learned a lot from her deep knowledge in the analytic/ asymptotic techniques applied to polarized radiation transfer. Her constant encouragement to learn  $\mathcal{T}_Q^K$ ’s (the irreducible tensors for polarimetry) introduced by Egidio Landi Degl’Innocenti, has greatly helped me in my research. It will be certainly useful in the future works too. I would like to thank Prof. Uriel Frisch for supporting my first visit to Nice in 2004, and for interesting discussions on India, linguistics etc. during tea time. I will never forget the wonderful time spent walking along the sea shore with Prof. H el ene Frisch and the time spent at her home. My sincere thanks are due to Prof. Albert Bijaoui, Director, Laboratoire Cassiopee, for extending the research facilities during my visits. I also acknowledge the warm hospitality given to me by other staff members of OCA - the library staff, and particularly the secretaries who took care of all the official matters. A heart felt thanks are due to Dr. Genevi eve Amieux for expending time and effort in taking me in her very interesting great classic car to do site seeing in and around Nice. The beautiful Nice city, the drive along the coast line (from Nice to Antibes), boat drive to St. Tropez, the Mediterranean sea, the train journey from Nice to Ascona, Switzerland and back, and finally the Nice specialty cuisine ‘Socca’ are some of the wonderful experiences at Nice, which I fondly remember!

I am especially grateful to Prof. J. O. Stenflo for his joint guidance along with Prof. K. N. Nagendra, on part-II of the thesis (namely polarized line formation theory with partial redistribution in Hanle-Zeeman scattering). He invited me with my thesis supervisor to visit Institute of Astronomy, ETH, Zurich for a week in October 2004, during which



he and his wife Joyce were kind enough to organize my stay at their beautiful home at Würenlos in the outskirts of Zurich. It was a wonderful experience to go by train from his home to the Institute, and listen to the discussions of my thesis supervisor with him (I had shallow knowledge in scattering polarization at that time and hence could not participate much!). In the subsequent years this modest beginning developed into a very intense collaboration on the theory of partial redistribution for Hanle effect, which resulted in 3 major papers in ‘The Astrophysical Journal’. Prof. J. O. Stenflo has kindly provided me some of the figures presented in Chapter 1. I have learned a lot from his powerful intuition in Physics, and in particular the vastness and the clarity of his thinking on solar magnetic fields. I thank Dr. Dominique Fluri, Dr. Rene Holzreuter and Prof. Svetlana Berdyugina for taking us around the campus of the famous ETH, and it was inspiring for me to see those lecture halls where great physicists like Pauli, and Einstein attended, and taught the students. I am also grateful to them for very useful discussions on multi-level atom radiation transfer codes.

I thank all my family members for their constant moral support over the last 4.5 years of research career. I am particularly grateful to my parents L. Nagesh Bhat and Sathyavathi N. Bhat for the full freedom and undisturbed time they gave me during my entire career. I dedicate this thesis to them. I thank my sister Vasudhakka and her family for entertaining me on most of the weekends at their home. It was refreshing to play with her son Varun. I thank Mayakka, Kiranakka and my brother Santhosh for their helping hand.

I am extremely grateful to Mrs. S. Vimala Nagendra, for her motherly affection towards me. Her support during my visits to Nice and Locarno has been invaluable. She made me feel at home in a foreign land by taking care of me. I particularly admire her strong will-power, which is exemplary. I like her philosophical views and her kind advices to me. It is a pleasure to meet and talk to Mrs. Shamala (mother of Mrs. Vimala), Sumana and Aaditya (daughter and son of Dr. K. N. Nagendra).

I am grateful to Dr. Michele Bianda for his warm and kind invitation to visit IRSOL at Locarno, Switzerland. It is from him, that I learned how to do solar polarimetric observations. The great enthusiasm and interest with which he described to me the world’s best polarimeter, the ZIMPOL-II (Zurich IMaging POLarimeter), is still fresh on my mind. The first scattering polarization observation of the well known Ca I 4227 Å line was made at IRSOL by Wiehr several decades ago. It was inspiring for me to observe the same line in this historic place and with such a state-of-the-art polarimeter. During the first two visits (in 2004 and 2005) we could gather plenty of data on this line, which we plan to

reduce and model in the near future. The 2007 visit was memorable, as the 5th Solar Polarization Workshop was held at Ascona (half an hour journey from Locarno), followed by a few weeks stay at Locarno. Prof. Jan Olof Stenflo visited us during our stay at Locarno, and it was awe inspiring for me to discuss with him, and learn the art of reducing highly complex mathematical problems, using intelligent physical approximations. I also like to thank Dr. Renzo Ramelli for his help in observations. The stay in Locarno was made pleasant by Mrs. Anna Michele, and Dr. Michele Bianda who took us for site seeing in the beautiful southern Switzerland. I can not forget the tasty pizzas prepared by Mrs. Annaliese, and warm welcome of Mrs. Elena. It was particularly exciting to play with little Aline, Michele's daughter, who made us learn few words in Italian language. Time spent with Michele's mother at her home in Ascona is a memorable one. It is a pleasure to remember the time spent with Katya and Rafaele (wife and daughter of Renzo). I am grateful to Dr. Philippe Jetzer for financial support to visit Locarno.

I appreciate very much the help extended by Dr. Veronique Bommier in resolving the sign differences between the classically and quantum mechanically derived Hanle-Zeeman redistribution matrix. I also acknowledge the series of very enlightening e-mail correspondence on time reversal symmetry and her kind words for me.

I gratefully acknowledge the financial support by the Council of Scientific and Industrial Research (CSIR) through the award of Research Fellowship (Grant No. 9/890(01)/2004-EMR-I) for conducting research at IIA, Bangalore, India. I am very grateful to the Indo-French Sandwich Thesis Program of French Embassy in India, New Delhi, for financial support during my visit to OCA, Nice, France. In particular I acknowledge the kind help, encouragement, and support of Dr. Bruno ROUOT, Attaché for Science and Technology, French Embassy in India. I also would like to thank Mr. Ashok Charoth, and Dr. Vivek DHAM of French Embassy in India, for efficiently handling my Sandwich program related matters. I am grateful to the Laboratoire Cassiopée (CNRS), the PNST (CNRS) and the French Ministère de l'Éducation Nationale for financial support during visits to the OCA, Nice, France.

I sincerely thank Dr. Baba Varghese of IIA for his everlasting help and perfect solutions to problems in computer hardware/ software, graphics, and programming. I would like to thankfully acknowledge the constant and kind encouragement by Dr. K. E. Rangarajan, Dr. R. T. Gangadhara, and Dr. Sunetra Giridhar. Particularly I am grateful to Dr. K. E. Rangarajan and computer committee for acquiring the cluster machine named pleades, which greatly helped my computing needs. I gratefully acknowledge the chair and mem-

bers of Board of Graduate Studies (BGS), who took care of all the official support, and constantly encouraged me over the years. I am thankful to Dr. Jayant Murthy and Mr. J. S. Nathan for providing me the necessary computing facilities. I am very grateful to the IIA administrative staff for their support in official matters. Particularly I thank Mr. K. T. Rajan, and Mrs. Pramila for all the help over the years, at Director's secretariat. I would like to gratefully acknowledge the help from Mr. A. Narasihma Raju regarding my CSIR scholarship, my accommodation and office room related matters. I would also like to thank Mr. Dhananjaya and Mr. K. Shankar for their help in solving many day to day problems.

Mrs. A. Vagiswari and Dr. Christina Birdie are acknowledged gratefully for their kind help in extending the library facilities. I am grateful to all the library staff for their help. In particular, I thank Mr. B. S. Mohan, assistant librarian for his help in readily making available the required books and also in acquiring useful books for myself from CSIR contingency grant. I also thank Mr. P. N. Prabhakar for his help in scanning, photocopying and with the binding of the thesis copies. I thank Mr. Murali for his help in arranging the auditorium facility during my seminars. I thank the dispatch section for taking care of regular mails. I also thank the stores department for providing stationaries. I am thankful to the binding section for their help in neatly binding this thesis.

I appreciate the help provided by Mrs. Rukma, Mrs. Meena and all the administrative staff of Physics department, IISc. Particularly I thank Mrs. Rukma for answering all my questions concerning the transfer of fellowship, exams and finally regarding thesis submission and related matters.

My stay at IIA was made memorable by my student colleagues. I thank all of them. To name a few, Ambika, Nagaraju, and Anusha. I also like to thank my JAAP friends, Shashikant, Ekta, Abhay, and Siddarth for making my stay at IISc a pleasant one. Thanks to Piyali Chatterjee for providing the thesis template. My special thanks go to Padmalekha, my senior at IISc (as well as at Bangalore University), for her advice and help whenever I needed it. I thank Dr. Yee Yee Oo and Prof. G. Ramachandran for fruitful collaboration.

The inspiring lectures of Dr. A. R. Ushadevi, Dr. C. R. Ramaswamy, and Dr. Sharath Ananthamurthy at the Department of Physics, Bangalore University are still fresh in mind. It is from them that I learned quantum mechanics, nuclear physics and spectroscopy. I am grateful to them for teaching good physics with clarity. I particularly admire the deep dedication to Physics shown by Dr. A. R. Ushadevi, from whom I have learned to be always self-reliant. I thank my post-graduate friends Sreenath, Ramya, Sheela and Nataraj for

their company.

I am grateful to my teachers Ms. Chandrika of Vidya Vardhaka Sangha (VVS), for her help during a critical point in my carrier. It is she who encouraged me to do PhD in Astrophysics. It is from her that I came to know about various research institutes in Bangalore, and it is she who introduced me to my thesis supervisor. I would like to thank the great help from my teachers Mrs. Veena, Mrs. Lakshmi Narasu, Mrs. Rekha, Mrs. Anuradha, and Mrs. Gayathri, for building up strong foundations in Physics, Chemistry and Mathematics, through their wonderful teaching abilities. I also like to thank Mr. Prakash, Mrs. Soumitra, and Mrs. Saraswati for their wonderful lectures on English, Macbeth, and Meghadoota. I am thankful to my pre-university lecturers and VVS school teachers for their good teaching. I particularly thank Mrs. Leelavathi and Mr. Dwarakanath for encouraging and shaping my mind when I was still very young. I also thank my friends in BSc classes Mamatha, Roopa, and Shubha for their wonderful company and also my pre-university friends Jalaja, Smitha, and Nayana.

It is a pleasure to read the great work by S. Chandrasekhar on “Radiative Transfer”, from which I learned the physics of Rayleigh scattering. From the famous book by Dimitri Mihalas on “Stellar Atmospheres”, I learned the physics of partial redistribution and line radiative transfer. It is inspiring to work with the book by Jan Olof Stenflo on “Solar Magnetic Fields”, from which I learned the classical theory of scattering. I have greatly benefited from the big book by Landi Degl’Innocenti & Landolfi on “Polarization in Spectral Lines”, from which I learned the  $\mathcal{T}_Q^K$  technology and many other facts.

Finally I would like to thank each and every person who directly or indirectly helped me in pursuing my research work. My apologies to those whom I have left out, inadvertently, without proper acknowledgments.

Bangalore  
April 2008

M. Sampoorna

# List of Publications

This Thesis is based on the following publications

## In International Journals

1. Stochastic polarized line formation I. *Zeeman propagation matrix in a random magnetic field*, Frisch, H., **Sampoorna, M.**, & Nagendra, K. N. 2005, **A&A**, 442, 11-28
2. Stochastic polarized line formation II. *Zeeman line transfer in a random magnetic field*, Frisch, H., **Sampoorna, M.**, & Nagendra, K. N. 2006a, **A&A**, 453, 1095-1109
3. Generalized Voigt functions and their derivatives, **Sampoorna, M.**, Nagendra, K. N., & Frisch, H. 2007, **JQSRT**, 104, 71-85
4. Some aspects of polarized line formation in magneto-turbulent media, **Sampoorna, M.**, Frisch, H., & Nagendra, K. N. 2008, **New Astronomy**, 13, 233-243
5. Zeeman line formation in solar magnetic fields: *Studies with empirical probability distribution functions*, **Sampoorna, M.**, Nagendra, K. N., Frisch, H., & Stenflo, J. O. 2008, **A&A** (under review)
6. Hanle-Zeeman redistribution matrix I. *Classical theory expressions in the laboratory frame*, **Sampoorna, M.**, Nagendra, K. N., & Stenflo, J. O. 2007a, **ApJ**, 663, 625-642
7. Hanle-Zeeman redistribution matrix II. *Comparison of classical and quantum electrodynamic approaches*, **Sampoorna, M.**, Nagendra, K. N., & Stenflo, J. O. 2007b, **ApJ**,

8. Hanle-Zeeman redistribution matrix III. *Solution of the polarized line formation problem*, **Sampoorna, M.**, Nagendra, K. N., & Stenflo, J. O. 2008, **ApJ** (in press)
9. The Hanle effect with partial frequency redistribution. *Construction of frequency dependent polarization matrix and numerical solution by a PALI method*, **Sampoorna, M.**, Nagendra, K. N., & Frisch, H. 2008, **JQSRT** (under review)
10. Scattering polarization in the presence of magnetic and electric fields, Yee Yee Oo, **Sampoorna, M.**, Nagendra, K. N., Sharath Ananthamurthy, & Ramachandran, G. 2007, **JQSRT**, 108, 161-179 (arXiv:astro-ph/0702312)

## In Refereed Conference Proceedings

1. Polarized spectral line formation in turbulent magnetic fields: *The Zeeman and Hanle effects*, Frisch, H., **Sampoorna, M.**, & Nagendra, K. N. 2006b, in **ASP Conf. Ser.** 358, Solar Polarization 4, ed. R. Casini, & B. W. Lites, 126-131
2. Turbulent magnetic field averages for the Zeeman effect, Frisch, H., **Sampoorna, M.**, & Nagendra, K. N. 2007, **Mem. S. A. It.**, 78, 142-147
3. Theory of polarized scattering in the mixed Hanle-Zeeman regime, **Sampoorna, M.**, Nagendra, K. N., & Stenflo, J. O. 2008, in **ASP Conf. Ser.** ..., Solar Polarization 5, ed. S. V. Berdyugina, K. N. Nagendra, & R. Ramelli (Submitted)
4. Numerical methods in polarized line formation theory, Nagendra, K. N., & **Sampoorna, M.** 2008, in **ASP Conf. Ser.** ..., Solar Polarization 5, ed. S. V. Berdyugina, K. N. Nagendra, & R. Ramelli (Submitted)
5. Phase matrices for higher multipoles of scattering in external magnetic fields, Yee Yee Oo, Phyu Phyu San, **Sampoorna, M.**, Nagendra, K. N., & Ramachandran, G. 2008, in **ASP Conf. Ser.** ..., Solar Polarization 5, ed. S. V. Berdyugina, K. N. Nagendra, & R. Ramelli (Submitted)

# Abstract

This thesis is devoted to improve our knowledge on the theory of polarized line formation in a magneto-turbulent medium, and in a scattering dominated magnetized medium, where partial redistribution (PRD) effects become important. Thus the thesis consists of two parts. In the first part we carry out a detailed investigation on the effect of random magnetic fields on Zeeman line radiative transfer. In the second part we develop the theory of polarized line formation in the presence of arbitrary magnetic fields and with PRD. We present numerical methods of solution of the relevant transfer equation in both part-I and II.

In Chapter 1 we give a general introduction, that describes the basic physical concepts required in both parts of the thesis. Chapters 2 - 6 deal with the part-I, namely stochastic polarized Zeeman line formation. Chapters 7 - 10 deal with part-II, namely the theory and numerics of polarized line formation in scattering media. Chapter 11 is devoted to the future outlook on the problems described in part-I and II of the thesis. Appendices are devoted to additional mathematical details.

## **Part-I of the Thesis : Stochastic polarized line formation in magneto-turbulent media**

Magneto-convection on the Sun has a size spectrum that spans several orders of magnitudes and hence develops turbulent elements or eddies the sizes of which are much smaller than the spatial resolution of current spectro-polarimeters (about 0.2 arcsec or 150 km at the photospheric level). We were thus strongly motivated to consider the Zeeman effect in a medium where the magnetic field is random with characteristic scales of variation comparable to the radiative transfer characteristic scales.

In Chapter 2, we consider the micro-turbulent limit and study the mean Zeeman absorption matrix in detail. The micro-turbulent limit refers to the case when the scales of fluctuations of the random field are much smaller than the photon mean free paths associated to the line formation. The ‘mean’ absorption and anomalous dispersion coefficients are calculated for random fields with a non-zero mean value - isotropic or anisotropic Gaussian distributions that are azimuthally invariant about the direction of the mean field. The averaging method is described in detail, and fairly explicit expressions for the mean coefficients are established. A detailed numerical investigation of the mean coefficients illustrates two simple effects of the magnetic field fluctuations: (i) broadening of the  $\sigma$ -components by fluctuations of the field strength, leaving the  $\pi$ -components unchanged, and (ii) averaging over the angular dependence of the  $\pi$  and  $\sigma$  components. Angular averaging can modify the frequency profiles of the mean coefficients quite drastically, namely, the appearance of an unpolarized central component in the diagonal absorption coefficient, even when the mean field is in the direction of the line-of-sight.

For isotropic fluctuations, the mean coefficients can be expressed in terms of generalized Voigt and Faraday-Voigt functions, which are related to the derivatives of the Voigt and Faraday-Voigt functions. In Chapter 3, we study these functions in detail. Simple recurrence relations are established and used for the calculation of the functions themselves and of their partial derivatives. Asymptotic expansions are also derived.

In Chapter 4, we consider the Zeeman effect from a random magnetic field which has a finite correlation length (meso-turbulence) that can be varied from zero to infinity and thus made comparable to the photon mean free-path. The random vector magnetic field  $\mathbf{B}$  is modeled by a Kubo-Anderson process - a piecewise constant Markov process characterized by a correlation length and a probability distribution function (PDF) for the random values of the magnetic field. The micro- and macro-turbulent limits are recovered when the correlation length goes to zero or infinity respectively. Mean values and rms fluctuations around the mean values are calculated numerically for a random magnetic field with isotropic Gaussian fluctuations. The effects of a finite correlation length are discussed in detail. The rms fluctuations of the Stokes parameters are shown to be very sensitive to the correlation length of the magnetic field. It is suggested to use them as a diagnostic tools to determine the scale of unresolved features in the solar atmosphere.

In Chapter 5, using a statistical approach, we analyze the effects of random magnetic fields on Stokes line profiles. We consider the micro and macro-turbulent regimes, which provide bounds for more general random fields with finite scales of variations. The mean



Stokes parameters are obtained in the micro-turbulent regime, by first averaging the Zeeman absorption matrix  $\Phi$  over the PDF  $P(\mathbf{B})$  of the magnetic field and then solving the concerned radiative transfer equation. In the macro-turbulent regime, the mean solution is obtained by averaging the emergent solution over  $P(\mathbf{B})$ . In this chapter, we consider the same Gaussian PDFs that are used to construct  $\langle \Phi \rangle$  in Chapter 2.

Numerical simulations of magneto-convection and analysis of solar magnetograms provide the empirical PDF for the magnetic field line-of-sight component on the solar atmosphere. In Chapter 6, we explore the effects of different kinds of PDFs on Zeeman line formation. We again consider the limits of micro and macro-turbulence. The types of PDFs considered are: (a) Voigt function and stretched exponential type PDFs for fields with fixed direction but fluctuating strength. (b) Cylindrically symmetrical power law for the angular distribution of magnetic fields with given field strength. (c) Composite PDFs accounting for randomness in both strength and direction obtained by combining a Voigt function or a stretched exponential with an angular power law. The composite PDF proposed has an angular distribution peaked about the vertical direction for strong fields and is nearly isotropically distributed for weak fields, which could mimic solar surface random fields. We also describe how the averaging technique for a normal Zeeman triplet may be generalized to the more common case of anomalous Zeeman splitting patterns.

## **Part-II of the Thesis: Polarized line formation in scattering media- Theory and numerical methods**

Many of the strongest and most conspicuous lines in the Second Solar Spectrum are strong lines that are formed rather high, often in the chromosphere above the temperature minimum. From the standard, unpolarized and non-magnetic line-formation theory such lines are known to be formed under the conditions that are very far from local thermodynamic equilibrium. They are characterized by broad damping wings surrounding the line core. Doppler shifts in combination with collisions cause photons that are absorbed at a given frequency to be redistributed in frequency across the line profile in a complex way during the scattering process. Two idealized, limiting cases to describe this redistribution are “frequency coherence” and “complete redistribution” (CRD), but the general theory that properly combines these two limiting cases goes under the name “partial frequency redistribution” (PRD). Resonance lines which are usually strong can be properly modeled only when PRD is taken into account. To use these strong lines for magnetic field diagnostics we need a line scattering theory of PRD in the presence of magnetic fields of arbitrary

strength. In the second part of the thesis we develop such a theory and derive the polarized PRD matrices. These matrices are then used in the polarized line transfer equation to compute the emergent Stokes parameters.

Polarized scattering in spectral lines is governed by a  $4 \times 4$  matrix that describes how the Stokes vector is scattered in all directions and redistributed in frequency within the line. In Chapter 7, using a classical approach we develop the theory for this redistribution matrix in the presence of magnetic fields of arbitrary strength and direction, and for a  $J = 0 \rightarrow 1 \rightarrow 0$  transition. This case of arbitrary magnetic fields is called the Hanle-Zeeman regime, since it covers both the partially overlapping weak and strong-field regimes, in which the Hanle and Zeeman effects respectively dominate the scattering polarization. In this general regime the angle-frequency correlations that describe the so-called PRD are intimately coupled to the polarization properties. We also show how the classical theory can be extended to treat atomic and molecular scattering transitions for any combinations of  $J$  quantum numbers.

In Chapter 8, we show explicitly that for a  $J = 0 \rightarrow 1 \rightarrow 0$  scattering transition there exists an equivalence between the Hanle-Zeeman redistribution matrix that is derived through quantum electrodynamics (Bommier 1997b) and the one derived in Chapter 7 starting from the classical, time-dependent oscillator theory of Bommier & Stenflo (1999). This equivalence holds for all strengths and directions of the magnetic field. Several aspects of the Hanle-Zeeman redistribution matrix are illustrated, and explicit algebraic expressions are given, which are of practical use for the polarized line transfer computations.

In Chapter 9, we solve the polarized radiative transfer equation numerically, taking into account both the Zeeman absorption matrix and the Hanle-Zeeman redistribution matrix. We compute the line profiles for arbitrary field strengths, and scattering dominated line transitions. We use a perturbation method (see eg. Nagendra et al. 2002) to solve the Hanle-Zeeman line transfer problem. The limiting cases of weak field Hanle scattering and strong field Zeeman true absorption are retrieved. The intermediate regime, where both Zeeman absorption and scattering effects are important, is studied in some detail.

Numerical method used to solve the Hanle-Zeeman line transfer problem in Chapter 9 is computationally expensive. Hence it is necessary to develop fast iterative methods like PALI (Polarized Approximate Lambda Iteration). As a first step in this direction we develop such a method in Chapter 10 to solve the transfer problem with weak field Hanle scattering. We use a ‘redistribution matrix’ with coupling between frequency redistribution and polarization and no domain decomposition. Such a matrix is constructed by

angle-averaging the frequency dependent terms in the exact weak field Hanle redistribution matrix for a two-level atom with unpolarized ground level (that can be obtained by taking the weak field limit of the Hanle-Zeeman redistribution matrix). In the past, the PALI technique has been applied to redistribution matrices in which frequency redistribution is ‘decoupled’ from scattering polarization, the decoupling being achieved by an adequate decomposition of the frequency space into several domains. In this chapter, we examine the consequences of frequency space decomposition, and the resulting decoupling between the frequency redistribution and polarization, on the solution of the polarized transfer equation for the Stokes parameters.



# Contents

<b>Acknowledgments</b>	<b>i</b>
<b>List of Publications</b>	<b>vii</b>
<b>Abstract</b>	<b>ix</b>
<b>1. General introduction</b>	<b>1</b>
1.1 Sources of polarized radiation in astronomy . . . . .	1
1.2 Representation of polarized radiation . . . . .	2
1.2.1 Stokes vector formalism . . . . .	2
1.2.2 Coherency matrix formalism . . . . .	3
1.2.3 Mueller calculus . . . . .	4
1.3 Solar polarization and its diagnostic potential . . . . .	5
1.3.1 The Zeeman effect . . . . .	6
1.3.2 The resonance scattering . . . . .	9
1.3.3 The Hanle effect . . . . .	13
1.4 Turbulent magnetic fields in the solar atmosphere . . . . .	16
1.5 Historical background on stochastic Zeeman line formation theory . . . . .	18
1.6 Theory of light scattering on atoms . . . . .	19
1.6.1 Scalar redistribution functions . . . . .	20

1.6.2	Historical account of the polarized PRD theories . . . . .	21
1.7	Polarized line radiation transfer and numerical methods of solution . . . . .	23
1.7.1	Zeeman line radiation transfer . . . . .	24
1.7.2	NLTE polarized line radiation transfer . . . . .	27
1.8	Outline of the thesis . . . . .	32
1.8.1	Outline on part-I of the thesis . . . . .	32
1.8.2	Outline on part-II of the thesis . . . . .	33
<b>Part-I</b>	<b><u>Stochastic polarized line formation in magneto-turbulent media</u></b>	<b>35</b>
<b>2.</b>	<b>Zeeman absorption matrix in a random magnetic field</b>	<b>37</b>
2.1	Introduction . . . . .	37
2.2	The Zeeman absorption matrix . . . . .	40
2.2.1	Absorption and anomalous dispersion coefficients . . . . .	41
2.2.2	An alternative form for the absorption and dispersion coefficients . . . . .	43
2.2.3	Rotation of the reference frame . . . . .	44
2.2.4	The mean coefficients . . . . .	45
2.3	Fluctuations parallel to the mean field (1D turbulence) . . . . .	46
2.4	Isotropic fluctuations (3D turbulence) . . . . .	48
2.4.1	Exact and approximate expressions for the mean coefficients . . . . .	49
2.4.2	Profiles of the mean coefficients in the weak and strong mean field limits . . . . .	52
2.4.3	The general case of arbitrary mean fields - Numerical evaluations . . . . .	56
2.4.4	The mean coefficient $\langle \varphi_I \rangle$ . . . . .	57
2.4.5	Dependence on the Landé factor . . . . .	59
2.5	Fluctuations perpendicular to the mean field (2D turbulence) . . . . .	62

2.5.1	Exact and approximate expressions for the mean coefficients . . . . .	64
2.5.2	Profiles of the mean coefficients for 1D, 3D and 2D turbulence . . . . .	65
2.6	Summary and concluding remarks . . . . .	69
<b>3.</b>	<b>Generalized Voigt functions and their derivatives</b>	<b>75</b>
3.1	Introduction . . . . .	75
3.2	Generalized Voigt functions $H^{(n)}$ and $F^{(n)}$ . . . . .	76
3.2.1	Definitions and recurrence relations . . . . .	76
3.2.2	Some properties of the generalized Voigt functions . . . . .	78
3.2.3	Computational aspects of $H^n$ and $F^{(n)}$ functions . . . . .	83
3.3	Partial derivatives of generalized Voigt functions . . . . .	85
3.3.1	Recurrence relations . . . . .	87
3.3.2	Initialization of the recurrence relations . . . . .	88
3.3.3	Asymptotic behavior of the partial derivatives . . . . .	89
3.3.4	Computation of the partial derivatives of $H^{(n)}$ and $F^{(n)}$ . . . . .	90
3.4	Partial derivatives of $H^{(0)}$ and $F^{(0)}$ in terms of $H^{(n)}$ and $F^{(n)}$ . . . . .	93
3.5	Concluding remarks . . . . .	94
<b>4.</b>	<b>Zeeman line radiative transfer in a random magnetic field</b>	<b>97</b>
4.1	Introduction . . . . .	97
4.2	Analytical calculation of the mean Stokes parameters . . . . .	99
4.2.1	Expression for the emergent Stokes parameters . . . . .	99
4.2.2	The random magnetic field model . . . . .	100
4.2.3	The mean propagation operator . . . . .	101
4.2.4	Mean values of the emergent Stokes parameters . . . . .	104
4.2.5	The macro and micro-turbulent limits . . . . .	104

4.2.6	Emergent residual Stokes vector . . . . .	105
4.3	Numerical evaluation of the mean Stokes parameters . . . . .	107
4.3.1	Numerical results: Effects of a finite correlation length . . . . .	107
4.4	Second-order moments and dispersion of the Stokes parameters . . . . .	112
4.4.1	Transfer equation for the second-order moment of the Stokes vector	114
4.4.2	Averaging the second-order moments . . . . .	117
4.4.3	Numerical evaluation of the dispersion . . . . .	121
4.5	Various generalizations . . . . .	124
4.5.1	Exponential source function . . . . .	124
4.5.2	Arbitrary depth-dependence of source function and line strength . .	125
4.5.3	Depth-dependence of correlation length . . . . .	126
4.5.4	Arbitrary direction of propagation . . . . .	126
4.6	Summary and concluding remarks . . . . .	127
<b>5.</b>	<b>Unno-Rachkovsky solution for turbulent magnetic fields</b>	<b>131</b>
5.1	Introduction . . . . .	131
5.2	Micro-turbulence with isotropic Gaussian fluctuations . . . . .	133
5.2.1	Weak mean field (strong fluctuations) limit . . . . .	134
5.2.2	Strong mean field (weak fluctuations) limit: Longitudinal case . . .	136
5.2.3	Strong mean field (weak fluctuations) limit: Transverse case . . . .	139
5.3	Macro-turbulence with isotropic Gaussian fluctuations . . . . .	141
5.4	Micro and macro-turbulent profiles for arbitrary orientation of $\mathbf{B}_0$ . . . .	142
5.5	Anisotropic magnetic field distributions . . . . .	144
5.6	Summary and concluding remarks . . . . .	146
<b>6.</b>	<b>Studies with empirical probability distribution functions</b>	<b>149</b>



6.1	Introduction . . . . .	149
6.2	Magnetic field strength distribution: Voigt PDF . . . . .	151
6.2.1	Symmetric Voigt PDF . . . . .	152
6.2.2	Asymmetric Voigt PDF . . . . .	155
6.3	Magnetic field strength distribution: Stretched exponential PDF . . . . .	159
6.4	Magnetic field angular distribution: Power law PDF . . . . .	162
6.5	PDFs to represent the random vector magnetic fields . . . . .	166
6.5.1	Stretched exponential * Power law PDF . . . . .	167
6.5.2	Voigt * Power law PDF . . . . .	169
6.6	Turbulent line formation for anomalous Zeeman splitting . . . . .	170
6.7	Concluding remarks . . . . .	172
 <b>Part-II <u>Polarized line formation in scattering media: Theory and numerical methods</u></b>		<b>175</b>
 <b>7. Classical theory of Hanle-Zeeman redistribution matrix</b>		<b>177</b>
7.1	Introduction . . . . .	177
7.2	Coherency matrix . . . . .	180
7.2.1	Redistribution in the atomic frame . . . . .	181
7.2.2	Redistribution in the laboratory frame: Doppler effect . . . . .	183
7.3	Analytical form of the Hanle-Zeeman redistribution matrix . . . . .	186
7.4	A study of magnetic redistribution functions . . . . .	189
7.4.1	Dependence of the magnetic redistribution functions on scattering angle and incoming frequency . . . . .	189
7.4.2	Dependence of the magnetic redistribution functions on field strength	199
7.5	Extension to the general quantum mechanical scattering case . . . . .	205

7.6	Concluding remarks . . . . .	208
<b>8.</b>	<b>Equivalence of classical and quantum redistribution matrix</b>	<b>211</b>
8.1	Introduction . . . . .	211
8.2	Quantum electrodynamic redistribution matrix in the lab frame . . . . .	213
8.2.1	$\mathbf{R}^{\text{II}}$ type redistribution matrix in the lab frame . . . . .	214
8.2.2	$\mathbf{R}^{\text{III}}$ type redistribution matrix in the lab frame . . . . .	216
8.3	Equivalence of the classical and quantum expressions for $\mathbf{R}$ . . . . .	219
8.3.1	The type III redistribution . . . . .	221
8.3.2	The type II redistribution . . . . .	222
8.4	Numerical evidence for the equivalence of classical and quantum $\mathbf{R}$ . . . . .	223
8.5	Hanle-Zeeman scattering of an unpolarized incident flat spectrum . . . . .	226
8.6	Concluding remarks . . . . .	229
<b>9.</b>	<b>Solution of the Hanle-Zeeman line formation problem</b>	<b>231</b>
9.1	Introduction . . . . .	231
9.2	Governing equations of the Hanle-Zeeman scattering theory . . . . .	233
9.2.1	Formulation of the relevant radiative transfer equation . . . . .	233
9.2.2	The scattering part of the emission vector . . . . .	235
9.2.3	The non-scattering part of the emission vector . . . . .	235
9.2.4	The Hanle-Zeeman line transfer equation . . . . .	236
9.3	Numerical method of solution for the transfer equation . . . . .	237
9.3.1	Stage 1: Initializing $\mathcal{S}_{\text{scat}}(\tau, x, \mathbf{n})$ . . . . .	237
9.3.2	Stage 2: Full solution by perturbation . . . . .	238
9.3.3	Formal solution using DELOPAR . . . . .	238
9.3.4	The convergence criteria . . . . .	240

---

9.3.5	Computational details . . . . .	241
9.4	Results and discussions . . . . .	242
9.4.1	Scattering at optically thin slabs . . . . .	243
9.4.2	Convergence behavior of the perturbation method . . . . .	246
9.4.3	Hanle saturation of the line polarization . . . . .	247
9.4.4	Comparison of angle-dependent and angle-averaged solutions . . . . .	250
9.5	Concluding remarks . . . . .	252
<b>10.</b>	<b>A PALI method for Hanle effect with partial redistribution</b>	<b>253</b>
10.1	Introduction . . . . .	253
10.2	The weak field Hanle redistribution matrix . . . . .	256
10.3	Transfer equation for the real irreducible Stokes vector components . . . . .	257
10.4	The PALI7 iterative method . . . . .	259
10.4.1	The details of the iteration scheme . . . . .	259
10.4.2	Calculation of source vector corrections . . . . .	260
10.4.3	Angle-averaged magnetic redistribution functions . . . . .	260
10.5	Numerical results and tests of the PALI7 method . . . . .	263
10.5.1	Thin slab model . . . . .	264
10.5.2	Thick slab model . . . . .	266
10.5.3	Irradiated slab model . . . . .	268
10.6	The effect of elastic collisions on the Stokes profiles . . . . .	271
10.7	Concluding remarks . . . . .	273
<b>11.</b>	<b>Outlook: Future developments</b>	<b>277</b>
11.1	Stochastic atmospheres for solar polarimetric studies . . . . .	277
11.2	Matter-radiation interaction including partial redistribution effects . . . . .	278

Appendices	281
A. Some properties of Wigner rotation matrices $D_{mm'}^{(l)}$ and spherical harmonics $Y_{lm}$	281
B. Integration over Gaussian probability distribution functions	282
C. Modified spherical Bessel functions	284
D. Some properties of the transport operator	285
E. Zeeman absorption matrix in the magnetic reference frame	287
F. Unno-Rachkovsky solution for the deterministic fields	289
G. Auxiliary coefficients and phase matrices related to $\mathbf{R}$	291
H. Laboratory frame composite redistribution functions	294
I. Auxiliary coefficients and phase matrices related to $\mathbf{R}^{\text{III}}$	297
J. Hanle scattering matrix of Stenflo (1994) in terms of $\mathcal{T}_Q^K$	300
K. Transformation between magnetic and atmospheric frames	305
L. Elements of the magnetic kernel $\mathbf{N}^r(x, x', \mathbf{B})$	307
References	313

# Chapter 1

## General introduction

In the review article on “Theory of Polarization: What’s Next?”, Landi Degl’Innocenti (2003), points out three challenging fields which need theoretical improvements in the near future. These three fields of solar spectro-polarimetry are (a) basic matter-radiation interaction, (b) stochastic processes, (c) sophisticated modeling of the solar atmosphere. Under topic (a), there is an urgent need for developing a fully consistent formalism capable of handling the partial redistribution problem for polarized radiation transfer. Under topic (b), there is a need for a deeper investigation in to the problem of line formation in a stochastic medium. In this thesis we have attempted to advance our knowledge in both the above mentioned issues that are of great current interest.

### 1.1 Sources of polarized radiation in astronomy

The information about the physical conditions prevailing in the astrophysical objects like the Sun and stars is encoded in the radiation that we receive from them. The signatures of the different physical parameters are imprinted in subtle and non-linear ways on the profiles of the many spectral lines that make stellar spectra so richly structured. The information is contained not only in the intensity but also in the state of polarization of the radiation as a function of frequency. The full state of polarization can be completely specified by the four Stokes parameters  $I$ ,  $Q$ ,  $U$  and  $V$ , which will be defined in § 1.2.1.

In polarimetric observations the Stokes parameters are recorded with the best possible spectral and polarimetric precision and good spatial and temporal resolution. Spectro-polarimetry is the basic tool to record the polarized spectrum of the Sun or stars. From the observed spectra we can extract the entangled information and deduce the physical properties of the remote region, where the observed radiation originates. Therefore, it is

essential to understand in detail the properties of the polarized radiation, its formation processes and its interactions with matter. In this thesis we have attempted to advance a particular aspect of the interaction of polarized radiation with matter (in particular atoms).

Polarization is produced when the spatial symmetry is broken in the physical process that generates the radiation that we observe (see Stenflo 2002). Breaking of symmetry can be caused by macroscopic magnetic (Hanle and Zeeman effects) and electric (Stark effect) fields, by oblique reflection (eg. non-symmetrical components in a telescope), or by an anisotropic excitation process (radiative or collisional). Collisional excitation by directed particle beams may lead to the so-called impact polarization (eg. solar flares). Scattering at free electrons (Compton or Thomson scattering) makes the radiation linearly polarized (eg. solar coronal white-light). Scattering of anisotropically incident beams of radiation, by atoms and molecules also gives rise to linearly polarized light (Rayleigh or Resonance scattering). For an exhaustive list and detailed description of the various physical mechanisms that can generate polarized radiation, see Landi Degl’Innocenti (2002, see also Rybicki & Lightman 1979). In this thesis we mainly focus on the generation and transfer of polarized radiation, that is produced by a magnetic field, and by scattering of radiation on atoms (both in the presence and absence of magnetic field).

## 1.2 Representation of polarized radiation

Here we introduce the formalism and notation used in this thesis to describe the polarized radiation. The state of polarization of a radiation beam can be described using several different powerful tools, in particular the Jones vector, the coherency matrix, or the Stokes vector. The Jones formalism is however unable to describe a statistical ensemble of uncorrelated photons, which is needed to relate the theory to observations. The statistical properties of the radiation field can be described by the coherency matrix and Stokes vector formalisms, which are equivalent to each other. In § 1.2.1 we introduce the Stokes representation for the polarized light and in § 1.2.2 we introduce the coherency matrix formalism for the polarized light. In this thesis we use both the Stokes (in large part of the thesis) and coherency matrix (in Chapter 7) formalisms.

### 1.2.1 Stokes vector formalism

It is well known that for a proper parametric representation of the polarized radiation, four parameters should be specified which will give the intensity, the degree of polarization, the plane of polarization, and the ellipticity of the radiation. In Stokes formalism light is

represented by a four component vector

$$\mathbf{I} = (I Q U V)^T, \quad (1.1)$$

where  $I$  is the intensity,  $Q$  and  $U$  represent the degree and plane of linear polarization, and  $V$  is the circular polarization. Stokes parameters were formulated by Sir George Stokes in 1852 and introduced into astrophysics by the Nobel laureate Subrahmanyan Chandrasekhar in 1946. An excellent description of Stokes formalism is presented in Chandrasekhar (1950, see also Rybicki & Lightman 1979). Here we briefly recall few important equations.

Let us introduce a set of orthogonal basis vectors  $\mathbf{e}_1$  and  $\mathbf{e}_2$  in a plane perpendicular to the light beam. At any point in space the electric vector can be decomposed as

$$\mathbf{E} = \Re(E_1 \mathbf{e}_1 + E_2 \mathbf{e}_2), \quad (1.2)$$

where

$$E_k = E_{0k} e^{-i(\omega t - \phi_k)}, \quad k = 1, 2. \quad (1.3)$$

$\omega$  and  $\phi_k$  are the frequency and phase of the electromagnetic radiation. Clearly  $E_{0k}$  and  $\phi_k$  with  $k = 1, 2$  completely define the polarization state of the light beam. The Stokes parameters are defined as

$$\begin{aligned} I &= \langle E_{01}^2 + E_{02}^2 \rangle; & Q &= \langle E_{01}^2 - E_{02}^2 \rangle, \\ U &= \langle 2E_{01}E_{02} \cos(\phi_1 - \phi_2) \rangle; & V &= \langle 2E_{01}E_{02} \sin(\phi_1 - \phi_2) \rangle. \end{aligned} \quad (1.4)$$

In the above equations the angular brackets represent averaging over a statistical ensemble of uncorrelated photons (or wave packets). For a completely polarized beam of light the relation  $I^2 = Q^2 + U^2 + V^2$  holds, while the partially polarized light obeys the inequality  $I^2 \geq Q^2 + U^2 + V^2$ . In the case of unpolarized light  $Q = U = V = 0$ .

We use the standard convention for the sign of circular polarization  $V$  (see Rees 1987, Stenflo 1994), namely when the electric vector rotates clockwise in a fixed plane as seen by the observer, we speak of right-handed circular polarization ( $V > 0$ ), when the sense of rotation is counterclockwise we have left-handed circular polarization ( $V < 0$ ).

### 1.2.2 Coherency matrix formalism

Stokes formalism is best suited to describe the partially polarized light, which is due to the incoherent superposition of uncorrelated photons with different polarization states (since

they have been created by stochastically independent atomic processes). The same information is also contained in the coherency matrix formalism, which is the best representation of radiation in quantum field theory.

The  $2 \times 2$  coherency matrix  $\mathbf{D}$  of the radiation field is given by

$$\mathbf{D} = \langle \mathbf{J} \mathbf{J}^\dagger \rangle, \quad (1.5)$$

where the Jones vector  $\mathbf{J}$  is defined as

$$\mathbf{J} = \begin{pmatrix} E_1 \\ E_2 \end{pmatrix}, \quad (1.6)$$

and  $\mathbf{J}^\dagger$  denotes the adjoint of  $\mathbf{J}$  (transposition and complex conjugation of  $\mathbf{J}$ ). The angular brackets in Eq. (1.5) again represent the averaging over a statistical ensemble of uncorrelated photons.

The relation between the coherency matrix and the Stokes parameters is given by

$$\mathbf{D} = \frac{1}{2} \begin{pmatrix} I + Q & U + iV \\ U - iV & I - Q \end{pmatrix}. \quad (1.7)$$

### 1.2.3 Mueller calculus

A formalism that allows to calculate the effect of a medium such as a stellar atmosphere on the Stokes vector, goes under the name of Mueller calculus. For details of Mueller calculus in the astrophysical context see Stenflo (1994, also Stenflo 2002). Here we present only a few important equations.

Let us now consider a wave train that enters a medium as Jones vector  $\mathbf{J}'$  and exits it as  $\mathbf{J}$ . The relation between them can be described by the complex  $2 \times 2$  Jones matrix  $\mathbf{w}$ :

$$\mathbf{J} = \mathbf{w} \mathbf{J}'. \quad (1.8)$$

Then the coherency matrix transforms as

$$\mathbf{D} = \mathbf{w} \mathbf{D}' \mathbf{w}^\dagger. \quad (1.9)$$

The transformation of the incident Stokes vector  $\mathbf{I}'$  by a medium can be described by the  $4 \times 4$  Mueller matrix  $\mathbf{M}$ :

$$\mathbf{I} = \mathbf{M} \mathbf{I}'. \quad (1.10)$$



Using the relation between the Stokes parameters and the coherency matrix (Eq. (1.7)), we can express the Mueller matrix in terms of the Jones matrix  $\mathbf{w}$ , as

$$\mathbf{M} = \mathbf{T}\mathbf{W}\mathbf{T}^{-1}, \quad (1.11)$$

where the physical properties of the medium are contained in

$$\mathbf{W} = \mathbf{w} \otimes \mathbf{w}^* = \begin{pmatrix} w_{11}w_{11}^* & w_{11}w_{12}^* & w_{12}w_{11}^* & w_{12}w_{12}^* \\ w_{11}w_{21}^* & w_{11}w_{22}^* & w_{12}w_{21}^* & w_{12}w_{22}^* \\ w_{21}w_{11}^* & w_{21}w_{12}^* & w_{22}w_{11}^* & w_{22}w_{12}^* \\ w_{21}w_{21}^* & w_{21}w_{22}^* & w_{22}w_{21}^* & w_{22}w_{22}^* \end{pmatrix}. \quad (1.12)$$

The symbols  $\otimes$  and  $*$  denote tensor product and complex conjugation respectively.  $\mathbf{T}$  and  $\mathbf{T}^{-1}$  are purely mathematical transformation matrices without any physical contents, given by

$$\mathbf{T} = \begin{pmatrix} 1 & 0 & 0 & 1 \\ 1 & 0 & 0 & -1 \\ 0 & 1 & 1 & 0 \\ 0 & -i & i & 0 \end{pmatrix}; \quad \mathbf{T}^{-1} = \frac{1}{2} \begin{pmatrix} 1 & 1 & 0 & 0 \\ 0 & 0 & 1 & i \\ 0 & 0 & 1 & -i \\ 1 & -1 & 0 & 0 \end{pmatrix}. \quad (1.13)$$

Mueller calculus is an important tool in spectro-polarimetry, as it can be used to describe the effect of various optical components in a telescope, spectrograph etc. Mueller matrix is also used in radiative transfer equation for the Stokes vector (see § 1.7), both as the  $4 \times 4$  absorption matrix that describes the Zeeman effect (see § 1.3.1), and the scattering matrix that can include both coherent and incoherent scattering, partial frequency redistribution, and the Hanle effect (see § 1.3.3).

### 1.3 Solar polarization and its diagnostic potential

The Sun provides us with an unique astrophysics laboratory because we can spatially resolve its structures in relatively greater detail, when compared to other stars. This is because, the nearest stars are about a million times more distant than the Sun. Thus, we can study various physical processes occurring in different regions of the Sun. For this reason the Sun has often been referred to as the ‘‘Rosetta Star’’ of astrophysics. Once we understand the various physical processes occurring in the Sun, we can then apply the acquired knowledge to other astrophysical objects.

By the word ‘‘Solar Polarization’’ we mean the polarized spectrum of the Sun recorded in four Stokes parameters. Solar polarization is produced mainly by coherent scattering of

the anisotropic radiation field in the solar atmosphere and by the magnetic field (Zeeman and Hanle effects).

### 1.3.1 The Zeeman effect

Splitting of a spectral line in the presence of an external magnetic field is referred to as the Zeeman effect. The Zeeman effect was discovered by Zeeman (1897) in a laboratory in 1896. To explain the observed phenomenon, H. Lorentz quickly developed a classical theory. In 1902, Zeeman and Lorentz shared the Nobel prize in Physics for their discovery and understanding of the Zeeman effect.

According to the classical theory of Lorentz, an atom is viewed as a negative electric charge (an electron) oscillating at frequency  $\omega_0$  under the action of a positive restoring force (central Coulomb potential due to the nucleus). In other words an atom is represented by a classical oscillator. In the presence of an external magnetic field  $\mathbf{B}$  and an external, oscillating electric field  $\mathbf{E}'$ , the motion of this bound electron is described by the oscillator equation

$$\frac{d^2\mathbf{r}}{dt^2} + \frac{e}{m} \left( \frac{d\mathbf{r}}{dt} \times \mathbf{B} \right) + \gamma \frac{d\mathbf{r}}{dt} + \omega_0^2 \mathbf{r} = -\frac{e}{m} \mathbf{E}', \quad (1.14)$$

where  $\mathbf{r}$  is the relative position vector of the bound electron,  $\gamma$  is the damping constant,  $e$  and  $m$  are the charge and mass of the electron. To decouple the above equation, we introduce the spherical vectors  $\mathbf{e}_q$ , with  $q = 0, \pm 1$ , where

$$\mathbf{e}_0 = \mathbf{e}_z; \quad \mathbf{e}_{\pm} = \mp(\mathbf{e}_x \pm i\mathbf{e}_y)/\sqrt{2}. \quad (1.15)$$

$\mathbf{e}_{x,y,z}$  are Cartesian unit vectors with the  $Z$ -axis along the direction of the magnetic field. Thus the three decoupled component equation for  $r_q$  are

$$\frac{d^2 r_q}{dt^2} - (2qi\omega_L - \gamma) \frac{dr_q}{dt} + \omega_0^2 r_q = -\frac{e}{m} E'_q, \quad (1.16)$$

where  $\omega_L = eB/(2m)$  is the Larmor frequency. Solution of the oscillator equation (Eq. (1.14) or Eq. (1.16)), gives the trajectory of the bound electron in an external magnetic field. In Fig. 1.1 we show the precessional motion of the bound electron in a plane perpendicular to the direction of the magnetic field.

From Eq. (1.16), it is clear that we have three mutually independent oscillators with oscillation frequency of  $\omega_0 - q\omega_L$ . The oscillator with frequency  $\omega_0$  (referred to as  $\pi$ -component) oscillates along the field direction, thus representing linear polarization in this direction, while the oscillators which resonate at frequencies  $\omega_0 \pm \omega_L$  (referred to as  $\sigma$ -components) represent right and left circular polarization. These three types of oscillators

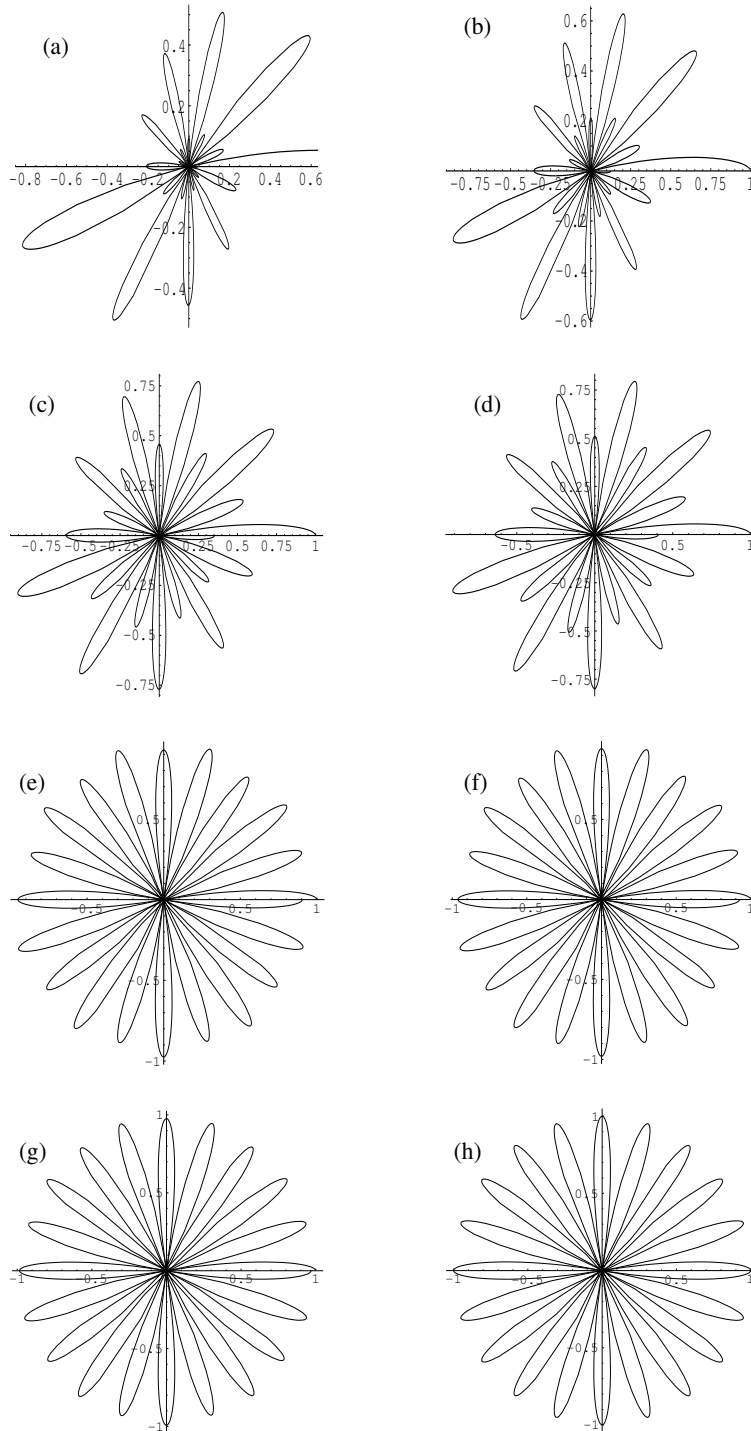


Figure 1.1: The damped rosette (precessional) motion of a bound electron in a plane transverse to the magnetic field. Panels (a) - (h) show the damped rosette for varying field strengths that are applied in the increasing order. When the field applied is weak we obtain a highly damped rosette as that shown in (a), (b), (c), and (d) (Hanle effect). As the field strength increases further, the rosette becomes more and more complete as shown in (e), (f), and (g) (saturated Hanle regime). A complete rosette as shown above in (h) is obtained when the field is strong, which corresponds to the case of Zeeman effect.

emit electromagnetic radiation like a dipole. The polarization properties of the radiation observed in a given direction is simply determined by the geometrical projection of the oscillating dipole vector on a plane perpendicular to the line-of-sight (LOS). Thus for a field directed along the LOS (longitudinal Zeeman effect) contribution from the  $\pi$ -component vanishes, while the  $\sigma$ -components are right and left circularly polarized. For the field oriented perpendicular to the LOS (transverse Zeeman effect) the  $\sigma$  and  $\pi$ -components are linearly polarized perpendicular and parallel to the field direction (assuming an emission line - situation is opposite for an absorption line). When the field has an arbitrary orientation the Zeeman line components are elliptically polarized. For an excellent description of classical electrodynamic theory of Zeeman effect see Collett (1993), and Stenflo (1994) for its application in Solar magnetic field diagnostics.

The classical theory described above holds good for the so-called normal Zeeman triplet (a  $J = 0 \rightarrow 1 \rightarrow 0$  transition). In this case we get one unshifted  $\pi$ -component and two  $\sigma$ -components symmetrically placed on either side of the  $\pi$ -component. However, in general an “anomalous” splitting pattern arises with several  $\pi$  and  $\sigma$ -components. The anomalous Zeeman effect can be explained using only the quantum mechanics (which takes into account the spin of the electron). According to quantum mechanics, an external magnetic field causes the atomic energy levels to split into different magnetic sublevels, and the emitted radiation gets polarized. This phenomenon is referred to as the Zeeman effect (see Fig. 1.2). The transition from such split levels gives rise to several components in place of an otherwise unsplit spectral line. The wavelength shift  $\Delta\lambda_B$  of the different components relative to the unsplit case is

$$\Delta\lambda_B = 4.67 \times 10^{-13} g \lambda^2 B, \quad (1.17)$$

where  $B$  is in Gauss units,  $\lambda$  is the line center wavelength at zero magnetic field in Å, and  $g$  is the Landé factor.

While the amount of wavelength shift is proportional to the field strength and the Landé factor of the line, the polarization and the relative strengths of the components are determined by the field orientation (as described above). Thus Zeeman effect will serve as a diagnostic tool to determine the stellar or solar magnetic fields. In fact it is through Zeeman effect measurements that Hale (1908) discovered the existence of the magnetic field in sunspots.

The overall spectral signatures due to the Zeeman effect, can be seen clearly in Stokes images as shown in the Fig. 1.3 for the Na I  $D_1$  and  $D_2$  lines. The transverse Zeeman

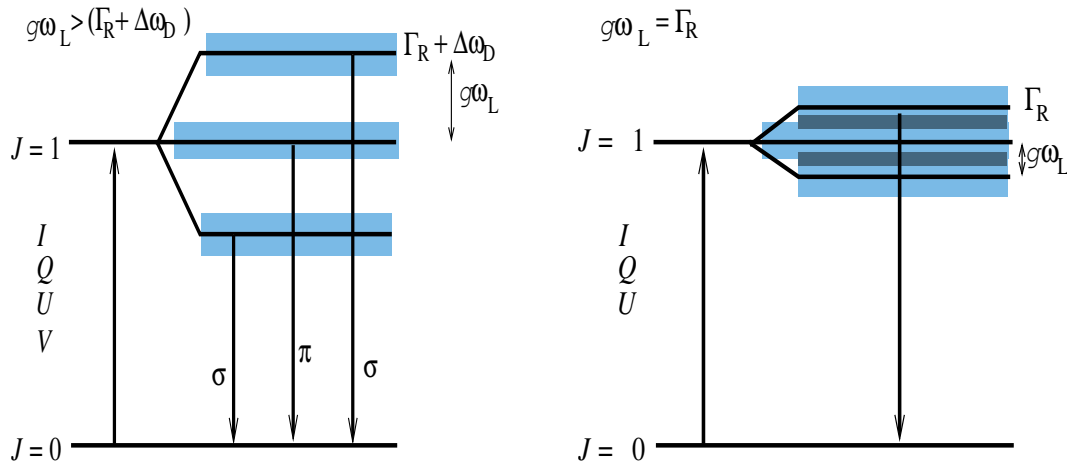


Figure 1.2: Level diagram for a  $J = 0 \rightarrow 1 \rightarrow 0$  transition in the presence of a strong (left panel) and weak (right panel) magnetic field.  $\Gamma_R$  and  $\Delta\omega_D$  are the radiative and Doppler width of the upper level. When the Zeeman splitting ( $g\omega_L$ ) is comparable or larger than the total width ( $\Gamma_R + \Delta\omega_D$ ) of the upper level, we are in the Zeeman regime. When Zeeman splitting is comparable to the radiative width ( $\Gamma_R$ ), the Zeeman sublevels superimpose and we have Hanle effect.

effect produces line profile signatures in Stokes  $Q$  and  $U$  that are nearly symmetric around the line-center. The longitudinal Zeeman effect produces line profile signatures in Stokes  $V$  that are nearly anti-symmetric around the line-center. Note that there is also a fairly strong signal from the transverse Zeeman effect in the Ni I line between the  $D_2$  and  $D_1$  lines of Na I.

The full Stokes polarimetry in  $I$ ,  $Q$ ,  $U$ ,  $V$  allows us in principle, to determine both the strength and orientation of the magnetic field vector. Zeeman effect observations in the photosphere reveal that only about 1% of the photospheric volume is filled with strong-fields of kiloGauss (kG) flux tubes (see Stenflo 2002). The remaining 99% of the photosphere is however fully magnetized with weak and mixed polarity (turbulent) fields. In the first part of the thesis we shall consider the effect of turbulent magnetic fields on the Zeeman line formation.

### 1.3.2 The resonance scattering

Line polarization can also be produced by radiative scattering, when the incident radiation has some degree of anisotropy. In contrast to polarization produced by the Zeeman effect, scattering polarization is formed even when the magnetic field is zero. The term resonance

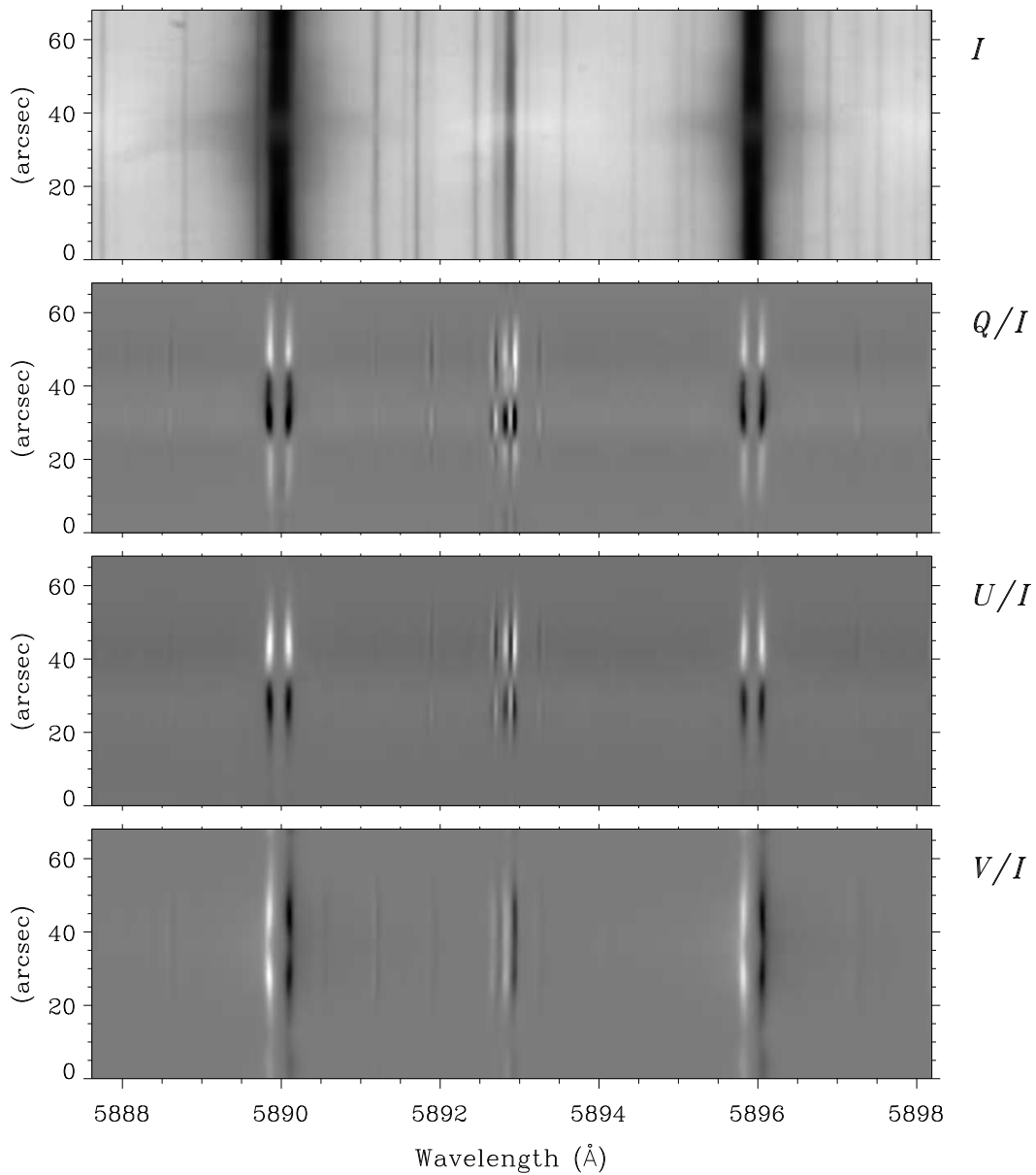


Figure 1.3: Example of the Stokes vector spectro-polarimetry showing the Zeeman-effect signatures in the four Stokes parameters. The two strong spectral lines at 5890 and 5896 Å are the Na I  $D_2$  and  $D_1$  resonance lines, which are formed in the lower chromosphere of the Sun. This illustration is taken from Stenflo et al. (2001).

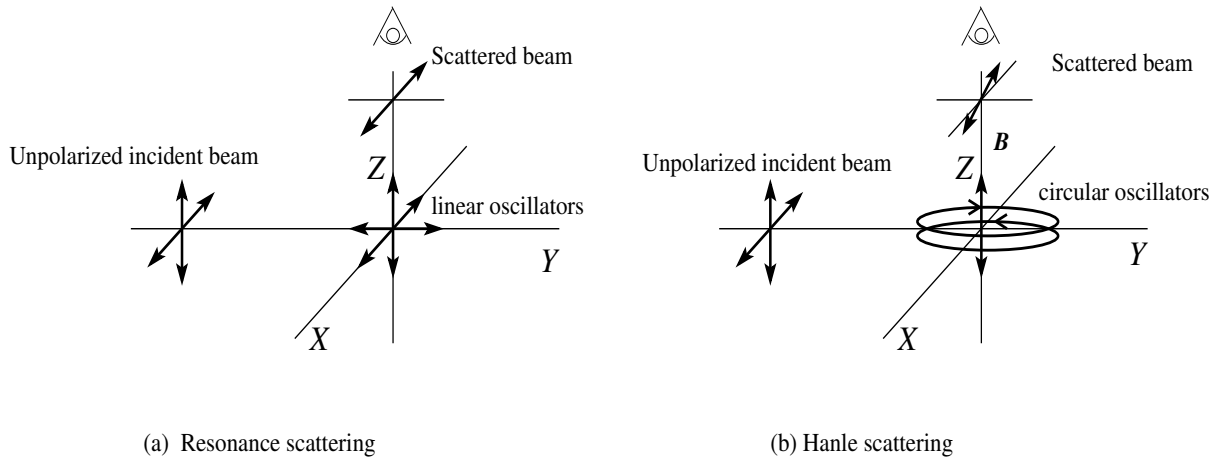


Figure 1.4: Classical description of a  $90^\circ$  scattering event (a) in the absence of magnetic field and (b) in the presence of a weak magnetic field parallel to the LOS. See § 1.3.2 for discussions.

scattering refers to the scattering on two bound levels of an atom (in particular when one of the levels involved is the ground state). The scattering polarization is formed exclusively by radiative excitation followed by spontaneous emission.

The formation of scattering polarization can be understood by using a classical harmonic oscillator model for the atom. Let us consider a simple scattering event that is illustrated in Fig. 1.4a. The beam incident along the  $Y$ -axis is unpolarized and is represented by two perpendicular uncorrelated electric field oscillations. In the absence of the magnetic field, the atom can be represented by three independent linear oscillators vibrating at angular frequency  $\omega_0$  along the axes of the reference system. Clearly only the  $X$  and  $Z$  oscillators are excited by the incident beam. These two oscillating dipoles radiate independently in all directions except along the axis of the dipole, and they decay radiatively with a damping constant  $\gamma$ . Thus the scattered radiation along the  $Z$ -axis is linearly polarized along the  $X$ -axis. It is interesting to note that, the same conclusion can be reached by considering the  $X$ -oscillator as resulting from the coherent superposition of two counter-rotating circular oscillators that are oscillating in phase with respect to each other at frequency  $\omega_0$  in the  $X$ - $Y$  plane.

The quantum analogue of above described classical harmonic oscillator model is a two-level atom having a lower level of angular momentum  $J = 0$  and an upper level of angular momentum  $J' = 1$ . The excitation of one of the classical oscillator is equivalent to excitation of one of the Zeeman sublevels of the upper level. In this analogy, the linear oscillator

corresponds to the sublevel  $M' = 0$ , while the circular oscillators correspond to the sublevels  $M' = \pm 1$ , respectively. When the field is zero, magnetic sublevels are degenerate and the atom can exist in a coherent superposition of these levels. Thus the photons emitted from  $M' = +1$  and  $M' = -1$  levels (by two different atoms) are highly coherent (i.e., identical in frequency and phase), and oppositely circularly polarized. These photons interfere to give 100% linearly polarized light (which explains the resonance scattering). Clearly the polarization produced is due to the population imbalances and quantum interferences among the Zeeman sublevels, which is sometimes referred to as ‘atomic polarization’ (see Trujillo Bueno 2001).

In the solar atmosphere the atomic polarization is caused mainly by the anisotropic illumination of the atom. This anisotropic radiative scattering (also referred to as coherent scattering) occurs in the photosphere due to the limb darkening in the solar atmosphere. Even with the presence of anisotropic radiation field, the emergent scattering polarization is zero at the solar disk center due to the axial symmetry around the LOS, which leads to mutual cancellation. The scattering polarization increases monotonically as we move towards the limb. The whole solar spectrum, both lines and continuum, is polarized by such scattering processes in the solar atmosphere. The continuum is polarized mainly by Thomson scattering at free electrons and by Rayleigh scattering at neutral hydrogen. The line is polarized due to resonance scattering.

The first systematic exploration of the linearly polarized spectrum formed by coherent scattering processes was done by Stenflo et al. (1983a, 1983b). But only with the advent of the CCD based polarimeter ZIMPOL (Povel et al. 1990, Povel 1995) was the polarimetric sensitivity enhanced enough to explore this scattering polarization in greater detail. The observations by Stenflo & Keller (1996, 1997) have revealed a highly structured linearly polarized spectrum. Since it looks very much different from the usual intensity spectrum, Ivanov (1991) named this linearly polarized spectrum of the sun as the “second solar spectrum”. A complete atlas of the “second solar spectrum” near the solar limb in the visible and near UV was recorded by Gandorfer (2000, 2002, 2005).

The word “coherent scattering processes” in the preceding paragraphs refer to the scattering events that are undisturbed by collisions regardless of the frequency redistribution (see § 1.6.1), since the phase coherence is preserved (see Stenflo 1994). However, in the traditional literature (Mihalas 1978), the term coherent scattering referred to frequency-coherent scattering, which is unphysical in the laboratory frame due to the Doppler redistribution, although in the atom’s rest frame it is perfectly physical.



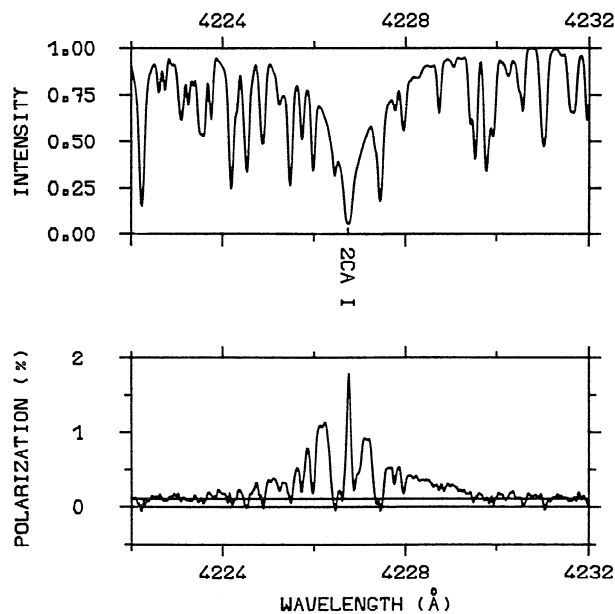


Figure 1.5: Intensity and Polarization profile of the Ca I 4227 Å line in a non-magnetic region on the solar atmosphere. This illustration is taken from Stenflo (1994).

An example of the “second solar spectrum” produced by coherent scattering processes is presented in Fig. 1.5. The Ca I 4227 Å line is the most strongly polarized line in the entire solar spectrum. Figure 1.5 shows the intensity and linear polarization profile of this line, obtained inside the south solar limb in a non-magnetic region (Stenflo et al. 1983a, Stenflo 1994, p. 99). This line is formed in the low chromosphere. The intensity spectrum shows a strong absorption line with many blends. The linear polarization spectrum shows a peak in the line core and two rather broad maxima in the line wings.

The linear polarization that is produced by coherent scattering processes is modified by the weak magnetic field and also by the elastic collisions. We discuss the modifications caused by a weak magnetic field in § 1.3.3, and that by elastic collisions in § 10.6.

### 1.3.3 The Hanle effect

Magnetic modification of the scattering polarization (or atomic polarization) in lines, is referred to as the Hanle effect. The Hanle effect when first observed in 1920s, was known as “magnetic depolarization of the resonance radiation”. The first correct interpretation of this phenomenon, related to the effect of a weak magnetic field on the linear polarization of the spectral line radiation scattered by a mercury vapor illuminated anisotropically, was provided by Wilhelm Hanle of Göttingen University (see Hanle 1923, 1924), and hence

the name Hanle effect. The observed influence of a weak magnetic field (of the order of 1 G) on the linear polarization corresponding to the zero magnetic field case, was a rotation of the plane of linear polarization (observed experimentally by Hanle himself) and a depolarization (clearly pointed out previously by Wood & Ellett 1923). This so-called Hanle effect played a fundamental role in the development of quantum mechanics, since it led to the introduction and clarification of the concept of coherent superposition of pure states (see Bohr 1924, Hanle 1924, 1925, Heisenberg 1925).

An introduction to the Hanle effect and the historical perspective can be found in the classical monograph of Mitchell & Zemansky (1934) and in the book edited by Moruzzi & Strumia (1991). Other books and articles related to this topic (and its application to solar magnetic field diagnostics) are the following: Stenflo (1994), Faurobert-Scholl (1996), Trujillo Bueno (1999, 2001), Stenflo (2002, 2003) and Landi Degl'Innocenti & Landolfi (2004). We shall now briefly describe the classical and quantum interpretations proposed by Hanle to understand the observed effect.

Let us again consider the scattering event illustrated in Fig. 1.4. We now apply an external magnetic field along the  $Z$ -axis. Thus we have to take into account the influence of the Lorentz force on the motion of the bound electron. As a result the atom cannot be interpreted as three independent linear oscillators (as we did in the non-magnetic case), but as a linear oscillator parallel to the magnetic field and two counter-rotating circular oscillators in the  $X$ - $Y$  plane oscillating at angular frequencies  $\omega_0 + \omega_L$  and  $\omega_0 - \omega_L$  (see Eq. (1.16)). The resulting trajectory of the electron in the  $X$ - $Y$  plane is given by (obtained by solving the Eq. (1.14) by setting the r.h.s. to zero)

$$\begin{aligned} x(t) &= e^{-\gamma t/2} \cos(\omega_L t) \cos(\omega_0 t), \\ y(t) &= e^{-\gamma t/2} \sin(\omega_L t) \cos(\omega_0 t). \end{aligned} \quad (1.18)$$

The bound electron thus describes in the  $X$ - $Y$  plane a complicated pattern called “rosette” pattern (see Fig. 1.1). The shape of the rosette is controlled by the ratio  $\omega_L/\gamma$ . We can have three cases:

- Case 1 ( $\omega_L \gg \gamma$ ) - when the field applied is strong, the bound electron precesses about the magnetic field several times before being affected by the damping. The bound electron thus describes a “daffodil” pattern shown in Figs. 1.1g, and 1.1h. In this case scattering polarization (along  $Z$ -axis) is zero. However in this regime polarization can be produced by Zeeman effect (see § 1.3.1).
- Case 2 ( $\omega_L \ll \gamma$ ) - when the field applied is very weak, the electron performs a highly damped oscillation and linearly polarized light is emitted (the case of resonance scattering,

see § 1.3.2).

- Case 3 ( $\omega_L \approx \gamma$ ) - when the field applied is weak, such that  $\omega_L \approx \gamma$ , then there can occur two competing processes. The applied field, forcing the electron to precess about the magnetic field and the radiation damping trying to suppress this motion. As a result the bound electron describes a rosette in the  $X$ - $Y$  plane (see Figs. 1.1a - 1.1f), and thus the polarization of the scattered radiation - which reflects the weighted average of the pattern - is reduced and rotated from the direction corresponding to the non-magnetic case. This is the well known Hanle effect.

Quantum mechanically, the magnetic field lifts the degeneracy of the magnetic sublevels. As long as the Zeeman sublevels overlap (see Fig. 1.2 right panel), the coherence among the Zeeman sublevels are reduced and dephased. In other words atomic polarization is modified by the magnetic field, and hence the resulting linear polarization is also modified. This phenomenon referred to as the Hanle effect is most sensitive if the Zeeman splitting is of the order of the natural line width ( $\Gamma_R$ , which is equivalent to the damping width  $\gamma$ ). Quantitatively, the field for which Hanle effect is sensitive is

$$8.79 \times 10^6 Bg \approx 1/t_{\text{life}}, \quad (1.19)$$

where  $t_{\text{life}}$  is the life time of the considered atomic level (see Trujillo Bueno 2001). On the other hand, the typical Zeeman effect is sensitive to fields for which level splitting is of the order of or larger than the total line width. Total line width is dominated by the Doppler broadening on the Sun and thus much larger than the natural width of the line. Therefore, the Zeeman effect can be used to diagnose magnetic fields of a few hundred Gauss to a few kG, while the Hanle effect is sensitive to weaker fields, typically between 1 and 100 G for upper level Hanle effect. A further difference is that the Hanle effect is mainly sensitive to the horizontal fields, whereas the Zeeman effect is more easily seen in the vertical fields because the longitudinal Zeeman effect gives stronger polarization signals than the transverse Zeeman effect. The Hanle and Zeeman effects are therefore highly complementary to each other and are used to diagnose the solar magnetic fields (see Stenflo 2001). Hanle effect has also been used to diagnose stellar magnetic fields (see Ignace et al. 1997, 1999, Ignace 2001).

The Hanle effect is illustrated in Fig. 1.6 which shows the intensity and polarization profiles of the Ca I 4227 Å line recorded near an active magnetic region (Stenflo 1982, Stenflo 1994, p. 100). Because of the rotation of the plane of polarization, most of the core peak now appears in  $U/I$  (which would be zero in the absence of magnetic field), whereas the  $Q/I$  core peak is suppressed (compare  $Q/I$  core peaks in Figs. 1.5 and 1.6).

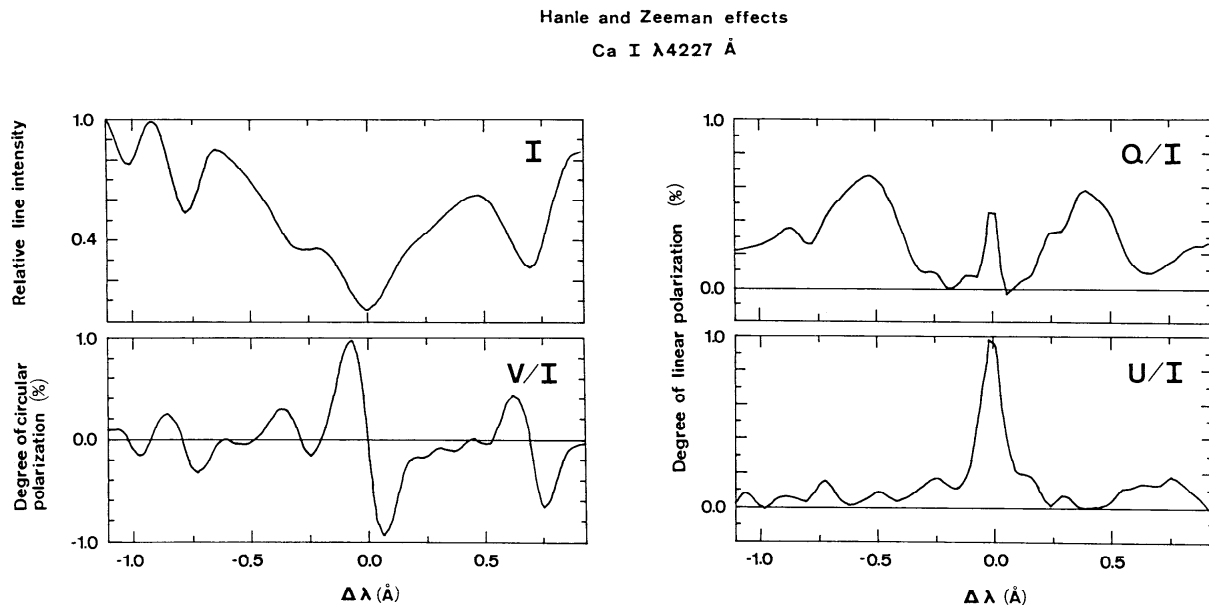


Figure 1.6: Intensity and Polarization profiles of the Ca I  $4227 \text{ \AA}$  line in a magnetic region on the solar atmosphere. This illustration is taken from Stenflo (1994)

The polarization in the wing is largely unaffected because Hanle effect is operative in the line core and not in the line wings (see Stenflo 1994, 1998). The anti-symmetric profile signatures in the  $V/I$  are due to the longitudinal Zeeman effect, which affects both the Ca I line core and the blend lines. The transverse Zeeman effect is too weak in this particular case to compete with the linear polarization caused by scattering (see Stenflo 1994).

Hanle effect refers to scattering in the presence of weak magnetic fields. In the second part of the thesis we consider the theory of atomic line scattering in the presence of magnetic fields of arbitrary strength.

## 1.4 Turbulent magnetic fields in the solar atmosphere

It is well known that the total flux seen in longitudinal magnetograms (which is a map of the circular polarization at a given wavelength in the wing of a spectral line), has its source in the kG fluxtubes with an average filling factor of less than 1% (see Stenflo 1994). These kG fields appear in magnetograms as intermittent flux patches outlining the boundaries of the giant velocity cells of the supergranulation. The cell interior referred to as internetwork regions occupies 99% of the photosphere, and wrongly appear as non-magnetic in routine magnetograms. However, 99% of the photosphere cannot be field-free due to the diffusion

processes and finite efficiency of field concentration (see Stenflo 1987). In fact the high-spatial-resolution magnetograms show a multitude of mixed magnetic polarities within the internetwork regions. These opposite polarity fields mixed on a small scale are apparently “invisible” and are referred to as “turbulent” or “hidden” fields. The presence of this hidden magnetic field in the quiet internetwork regions of the solar photosphere might have several important consequences for the overlying solar atmosphere, such as ubiquity of reconnecting current sheets and heating processes (see Trujillo Bueno 2005). Thus it is important to study the nature of this hidden magnetic field.

Turbulent magnetic fields that are hidden for a low-resolution longitudinal magnetograms, reveal their existence through the following three effects in the solar spectrum (see Stenflo 1982)

- magnetic line broadening,
- Hanle effect depolarization,
- transverse Zeeman effect.

For a review on the diagnostic potential of all the three effects listed above, see Stenflo (1989). We describe these three effects briefly below. One of the effects of a hidden tangled magnetic field is to broaden the spectral lines, although the average polarization effects may be zero. This magnetic broadening distinguishes itself from other broadening mechanisms by being correlated with the Landé factor of the lines used. Searching for such a correlation through a regression analysis involving about 400 Fe I lines, Stenflo & Lindegren (1977) could set an upper limit of 100 G to the strength of the possible turbulent fields.

The two principle observables for Hanle effect are rotation of the plane of linear polarization (generation of  $U/I$  signal) and depolarization (decrease in  $Q/I$  signal, see § 1.3.3). In a tangled magnetic field with random orientations of the field vectors, there is no preferred direction of rotation, but the depolarization due to the Hanle effect remains. Even if the mixed polarities cancel each other completely within the resolution element, the Hanle effect depolarization is never canceled out, as it has only one sign (decrement). This Hanle effect depolarization as a diagnostic tool to determine the turbulent field was first proposed by Stenflo (1982), who’s simplified application gave a lower limit of 10 G for the strength of the turbulent field. Even though this technique has a great promise for diagnosing the turbulent fields, the interpretation of the observations is very complicated as it relies on the comparison between the observed linear polarization and that calculated for the zero-field reference case. Applying a one-dimensional (1D) polarized radiation transfer approach to model the scattering polarization observed in Sr I 4607 Å line, Faurobert-Scholl (1993a), Faurobert-Scholl et al. (1995), and Faurobert et al. (2001) determined the strength of the

turbulent field to be between 20 and 10 G. Recently Trujillo Bueno et al. (2004, see also Trujillo Bueno 2005, Trujillo Bueno et al. 2006) have modeled the same line using a more realistic multi-level scattering polarization calculations in 3D models of the solar photosphere. They estimate a mean magnetic field between 60 and 130 G. All these authors assume a micro-turbulent magnetic field (see § 1.5) with isotropic angular distribution. A general theory of Hanle effect in random magnetic field with finite correlation length has been recently developed by Frisch (2006).

The transverse Zeeman effect as a diagnostic tool to determine the quiet Sun turbulent fields was first considered by Stenflo (1987). Over the last few years the observational and theoretical evidence for small-scale mixture of weak and strong fields in the quiet Sun has increased considerably (eg. Socas-Navarro & Sánchez Almeida 2003, Khomenko et al. 2003, Socas-Navarro & Lites 2004, Sánchez Almeida et al. 2003a, 2003b, Cattaneo 1999, Cattaneo et al. 2003, Vögler 2003, Stein & Nordlund 2006), so also the controversy about the true abundance of kG fields in the internetwork regions of the quiet Sun (eg. Domínguez Cerdeña et al. 2003a, 2003b, Lites & Socas-Navarro 2004, Sánchez Almeida et al. 2004, de Wijn et al. 2005, Khomenko et al. 2005). For recent reviews with contrasting viewpoints on the magnetism of the very quiet Sun, see Sánchez Almeida (2004) and Khomenko (2006).

In the part I of the thesis we approach the problem of turbulent magnetic fields purely from the theoretical view point. In particular we consider the effect of random magnetic fields with finite correlation lengths on the Zeeman line formation.

## **1.5 Historical background on stochastic Zeeman line formation theory**

It is well known that the turbulence causes the formation of eddies of many different length scales. The average eddy size is referred to as correlation length. A statistical theory of turbulence was first proposed by Kolmogorov (1941). Still, a complete description of turbulence remains one of the unsolved problems in Physics. For a detailed description of Kolmogorov 1941 theory and other developments in the theory of turbulence see the monograph by Frisch (1995).

The effect of turbulent velocity on spectral line formation was studied in detail in 1970's. See Frisch & Frisch (1975) and also Mihalas (1978) for a review on this topic. As a consequence of velocity turbulence, magnetic fields present in the stellar atmosphere also become

turbulent (frozen-in condition). The form of polarized transfer equation in the presence of a micro-turbulent (correlation length much smaller than the photon mean free path) magnetic field was first written by Stenflo (1971). The effect of micro-turbulent magnetic field on spectral lines formed in optically thin atmospheres were first considered by Dolginov & Pavlov (1972), and Domke & Pavlov (1979). We re-examine this micro-turbulent limit in detail in Chapter 2. In this limit the Zeeman absorption matrix is replaced by an average over various realization of the random magnetic field. To incorporate the effect of such micro-turbulent magnetic fields in realistic model atmosphere calculations, Sánchez Almeida et al. (1996) have developed MISMA (Micro Structured Magnetic Atmospheres) model.

The macro-turbulent limit, wherein the correlation length is much larger than the photon mean free path, was considered by Stenflo (1971, 1973, 1994) and Stenflo et al. (1984). In this limit averaging over different realization of the random field should be performed on the ‘emergent solutions’ of the transfer equation.

The general regime referred to as meso-turbulence leads to stochastic polarized radiative transfer equation (transfer equation with random coefficients). This regime has been considered by Landi Degl’Innocenti (1994, see also Landi Degl’Innocenti & Landolfi 2004), and more recently by Carroll & Staude (2003a, 2003b, 2005a, 2005b, 2006), and Carroll & Kopf (2007). We study this meso-turbulent regime in greater detail in Chapter 4.

## 1.6 Theory of light scattering on atoms

Radiation becomes polarized upon scattering even in the absence of magnetic fields. For example the polarization of the blue sky is due to the molecular Rayleigh scattering. On the Sun scattering processes contribute to the formation of both the continuous and line spectrum.

In a scattering event, the direction, frequency, and polarization of the scattered photon may change relative to that of the incident photon. A proper description of the angle, frequency and polarization correlation between the incident and scattered photon goes under the name of partial frequency redistribution (PRD). The effects of PRD are observable in the wings of strong resonance lines and to a lesser extent in the line core. For example two broad maxima in the wings of Ca I 4227 Å line (see  $Q/I$  panel in Figs. 1.5 and 1.6), are due to the PRD.

Partial frequency redistribution effects are described by a  $4 \times 4$  redistribution matrix

$\mathbf{R}(\nu, \mathbf{n}, \nu', \mathbf{n}')$  in the absence of the magnetic field and  $\mathbf{R}(\nu, \mathbf{n}, \nu', \mathbf{n}'; \mathbf{B})$  in the presence of the magnetic field.  $\mathbf{R}$  gives the joint probability of absorbing a photon with frequency  $\nu'$  and direction  $\mathbf{n}'$  and re-emitting a photon with frequency  $\nu$  and direction  $\mathbf{n}$ . Aim of a scattering theory is to determine this  $\mathbf{R}$  in the most general situation. For the scalar case (no polarization)  $\mathbf{R}$  becomes a redistribution function  $R(\nu, \mathbf{n}, \nu', \mathbf{n}')$ . Scalar frequency redistribution functions for two-level atoms, neglecting collisions were derived both in the atomic and laboratory frame by Hummer (1962). More general expressions for collisional frequency redistribution on resonance and subordinate lines were derived by Oxenius (1965), Heinzel (1981), Hubeny (1982), Hubeny et al. (1983a, 1983b), Hubeny & Cooper (1986), and Hubeny & Lites (1995). For an introduction to the scalar PRD functions see Mihalas (1978). For a classic review on PRD and its application to astrophysics see Hubeny (1985) and Frisch (1988). In the following section we briefly describe the scalar PRD functions.

### 1.6.1 Scalar redistribution functions

Here we discuss only the redistribution functions for frequency coherent (in the atomic frame) and frequency incoherent scattering. For other type of redistribution function we refer the reader to Mihalas (1978), and Heinzel (1981). Redistribution functions are first derived in the atomic frame. Doppler effects due to the thermal movements of the atoms are then incorporated by means of a convolution with a velocity distribution to obtain the laboratory (observers) frame redistribution functions. Following two assumptions are made, first that the atomic velocity is unchanged during the scattering process, second that the velocity distribution for the lower level of the transition is a Maxwellian. The former approximation is justified by the short duration of the scattering process. The latter approximation certainly holds for the resonance lines because the lower level of the transition can be considered as having an infinite life-time. For more detailed discussion on these assumptions and the possibility of relaxing these assumptions see Hubeny (1985), Landi Degl'Innocenti (1996) and Bommier (1999, 2003).

The scalar redistribution function in the atomic frame may be written as

$$R_0(\xi, \mathbf{n}, \xi', \mathbf{n}') = r(\xi, \xi')p(\mathbf{n}, \mathbf{n}'), \quad (1.20)$$

where the subscript “0” identifies the quantities in the atomic rest frame.  $\xi, \xi'$  are the frequencies of the scattered and incident photons in the atomic frame. The angular phase function  $p(\mathbf{n}, \mathbf{n}')$  describes the probability that the photon is scattered from solid angle  $d\mathbf{n}'$  in direction  $\mathbf{n}'$ , into solid angle  $d\mathbf{n}$  in direction  $\mathbf{n}$ .



### Frequency coherent scattering

Consider an atomic transition with an infinitely sharp lower level and a radiatively broadened upper level. In the atomic frame, the absorption of radiation with frequency  $\xi'$  will be followed by the re-emission at the same frequency, and the frequency redistribution function is given by

$$r_{\text{II}}(\xi, \xi') = \mathcal{L}(\xi')\delta(\xi - \xi'), \quad (1.21)$$

where  $\delta$  is the Dirac distribution and  $\mathcal{L}(\xi')$  is the rest frame absorption profile, which is a Lorentzian.

The convolution of  $r_{\text{II}}(\xi, \xi')$  with a Maxwellian distribution (to take care of the Doppler motion of the atoms) gives the laboratory frame redistribution function  $R_{\text{II}}(\nu, \mathbf{n}, \nu', \mathbf{n}')$ , where  $\nu$  and  $\nu'$  are the frequencies of the scattered and incident photons in the laboratory frame. The explicit form of  $R_{\text{II}}$  can be found for example in Mihalas (1978, see also Chapter 7 of this thesis).

### Frequency incoherent scattering

Consider again the same atomic transition. Now the upper level is broadened not only by the finite life time of the upper level but also due to elastic collisions with other atoms. We assume that the collisions are so frequent that all the excited electrons are randomly reshuffled over the substates of the upper state before emission occurs. Thus the incident and scattered photon frequencies are uncorrelated and the redistribution function in the atomic frame is given by

$$r_{\text{III}}(\xi, \xi') = \mathcal{L}(\xi')\mathcal{L}(\xi). \quad (1.22)$$

Since there is no correlation between the frequencies of the absorbed and emitted photons, the redistribution is referred to as complete frequency redistribution (CRD).

In the laboratory frame the resulting redistribution function is denoted by  $R_{\text{III}}(\nu, \mathbf{n}, \nu', \mathbf{n}')$ . See Mihalas (1978) for its explicit form (see also Chapter 7 in this thesis).

#### 1.6.2 Historical account of the polarized PRD theories

The determination of a self-consistent PRD redistribution matrix both in the presence and absence of magnetic field is a difficult theoretical problem. This problem has been approached using both the classical physics and quantum mechanics. A correct description of the scattering physics under the most general situation of course, requires a quantum

mechanical approach. However a major advantage of the classical approach is that it is physically transparent, and it gives us excellent guidance for an intuitive grasp of the physics. For a review on PRD of polarized radiation see Frisch (1996, see also Frisch et al. 2001). See Stenflo (1996) for a review on scattering physics both from the classical and quantum mechanical perspective.

In classical theory a scattering system is represented by a forced damped oscillator (see Eq. (1.14)). The classical theory of PRD was originally introduced by Zanstra (1941a,b). He addressed the issue of collisions on non-magnetic frequency redistribution in resonance lines. A modern approach to the classical oscillator theory was developed by Stenflo (1994, 1996, 1998), where he considered frequency coherent scattering in the presence of arbitrary strength magnetic fields. This classical framework was extended by Bommier & Stenflo (1999) to handle PRD effects in the presence of arbitrary field strengths and collisions. They showed that the stationary solutions of the harmonic oscillator corresponds to the frequency coherent terms and the transitory solutions to the frequency incoherent ones. They derived the redistribution matrix in the atomic frame.

In a quantum mechanical atomic system scattering can occur between different atomic states. When the quantum numbers of the initial and final states are the same, we speak of Rayleigh scattering, when they are different we have the more general case of Raman scattering. The special case of Rayleigh scattering when the frequency of the incident photon does not differ from the resonant frequency of the atomic transition by much more than the damping width is usually called resonant scattering. The corresponding special case of Raman scattering is called fluorescent scattering.

The first quantum mechanical calculation of the redistribution matrix for the resonance polarization, taking into account the effects of elastic collisions was performed by Omont et al. (1972, see also references cited therein). The effect of magnetic field is considered in Omont et al. (1973). This paper contains several interesting comments and remarks, in particular that the Hanle effect may act in the core of a line but not in its wings because of the very short life-time of the excited level for wing frequencies. For non-magnetic resonance polarization, based on the work of Omont et al. (1972), Domke & Hubeny (1988, see also Streater et al. 1988) derived a tractable analytical expression of the redistribution matrix. It contains frequency coherent and incoherent terms with branching ratios depending on the atomic model and various collision rates.

“Density matrix” is a fundamental concept in atomic physics. The first application of density matrix for the interpretation of the linear polarization observed in a solar promi-

nence was by Bommier (1977), Bommier & Sahal-Br  chot (1978), Landi Degl’Innocenti (1982). In a series of papers Landi Degl’Innocenti (1983a, 1983b, 1984) showed that the density matrix technique, combined with the formalism of the irreducible tensor components of radiation field offer an alternative and powerful approach. This theory can handle polarized scattering on multi-level atoms, but is restricted to CRD. Using this theory Landi Degl’Innocenti & Landi Degl’Innocenti (1988) derived the explicit analytic form of the Hanle phase matrix in the atmospheric reference frame ( $Z$ -axis along the normal to the atmosphere) for a two-level atom. A first attempt to include PRD in density matrix formalism was by Bommier (1996). To incorporate PRD into the density matrix approach, Landi Degl’Innocenti et al. (1997) developed a theory based on the formalism of metalevels to describe coherent scattering, which is valid in the absence of collisions only. The problem of PRD including collisions was re-analyzed by Bommier (1997a, 1997b, see also Bommier 1999, 2003) who could show that PRD appears automatically in the density matrix formalism when the perturbation expansion in the atom-radiation interaction is continued to all orders in a quantum electrodynamic (QED) theory. CRD corresponds to the dominant term in such an expansion.

In Chapter 7 of this thesis, starting from the classical approach of Bommier & Stenflo (1999), we derive the laboratory frame PRD redistribution matrix in the presence of arbitrary magnetic fields, and including collisions. The equivalence between the classical and QED approach of Bommier (1997b) will be established in Chapter 8.

## 1.7 Polarized line radiation transfer and numerical methods of solution

The basic theoretical tool for the quantitative analysis of Stokes spectral line observation is the polarized radiative transfer equation (which is the statement of conservation of energy for a ray of light passing through a medium). It describes how the Stokes vector spectrum that we observe is formed in the solar atmosphere in the presence or absence of magnetic field.

In this thesis we always assume that the solar or stellar atmosphere can be approximated by a plane-parallel, static slab with homogeneous layers. Further, we assume a two-level atom with unpolarized lower level. The polarized radiative transfer equation can then be written as

$$\mu \frac{\partial \mathbf{I}}{\partial s} = \mathbf{K} \mathbf{I} - \mathbf{j} = \mathbf{K}(\mathbf{I} - \mathbf{S}), \quad (1.23)$$

where the depth, frequency, and angle dependence of the variables has been omitted for brevity of notation. Here  $\mathbf{I}$  is the Stokes vector;  $s$  is the ray-path coordinate which varies inside the medium from 0 to  $\infty$ , with the surface at  $s = 0$ ;  $\mathbf{K}$  is the  $4 \times 4$  absorption matrix;  $\mathbf{j}$  is the total emission vector; and  $\mathbf{S}$  is the total source vector. As usual,  $\mu = \cos \vartheta$ , with  $\vartheta$  the angle made by the line-of-sight with the normal to the atmosphere.

The source vector describes the interaction of the radiation field with the plasma when the light propagates through the atmosphere. Thus the exact form of  $\mathbf{S}$  depends on the physical processes that are considered. Under local thermodynamic equilibrium (LTE), the source vector is given by unpolarized Planck function, which is determined exclusively by the local temperature. LTE is a good approximation in the lowest regions of the atmosphere (lower photosphere), where the collisions dominate. However in the outer layers of the atmosphere (upper photosphere, chromosphere), where the radiative scattering dominates, we have non-local coupling of the atmosphere over distances that are of the order of the photon mean free path. Thus non-local thermodynamic equilibrium (NLTE) prevails in such scattering dominated atmospheres. In this case the source vector becomes decoupled from the local temperature and instead is determined by the radiation field from non-local sources.

In § 1.7.1 we shall present historical developments in the theory of Zeeman line transfer (both under LTE and NLTE - incoherent scattering included through CRD like source function). Historical background on NLTE polarized line transfer both in the presence and absence of magnetic field will be considered in § 1.7.2.

### 1.7.1 Zeeman line radiation transfer

The polarized line transfer problem where in polarization signal can be produced only through the Zeeman effect is referred to as the Zeeman line transfer problem. The Zeeman line transfer equation is given by Eq. (1.23), with the  $4 \times 4$  absorption matrix of the form

$$\mathbf{K} = k_c \mathbf{E} + k_0 \mathbf{\Phi}, \quad (1.24)$$

where  $k_c$  and  $k_0$  are the continuum and line center opacity,  $\mathbf{E}$  is  $4 \times 4$  unit matrix and  $\mathbf{\Phi}$  is the Zeeman line absorption matrix. The explicit form of  $\mathbf{\Phi}$  will be presented in Chapter 2. The total emission vector is given by

$$\mathbf{j} = k_c S_c \mathbf{U} + k_0 S_L \mathbf{U}, \quad (1.25)$$

where  $\mathbf{U} = (1\ 0\ 0\ 0)^T$ ,  $S_c$  and  $S_L$  are the continuum and line source functions.

Under LTE, both  $S_c$  and  $S_L$  are given by Planck function. Zeeman line transfer problem under LTE for a normal Zeeman triplet was first formulated by Unno (1956) in a phenomenological way, and independently by Stepanov (1958a) using a more stringent classical derivation that implicitly also included the magneto-optical effects. Stepanov's approach was extended by Rachkovsky (1962a, 1962b), who provided a firm classical foundation for the problem, and later by Beckers (1969a, 1969b) to treat arbitrary Zeeman multiplet. A new classical derivation of the LTE transfer equation for normal Zeeman triplet has been performed by Jefferies et al. (1989). A similar approach is presented in Stenflo (1994). For a historical review on Zeeman line transfer see Stenflo (1971), Rees (1987). A quantum electrodynamical theory for the same problem was developed by Landi Degl'Innocenti & Landi Degl'Innocenti (1972).

Analytic solutions to the LTE Zeeman line transfer equation for a Milne-Eddington atmosphere (linear variation of source function with optical depth) and constant magnetic vector were given by Unno (1956), Rachkovsky (1962a, 1967). The numerical method of solution started with the work by Beckers (1969a, 1969b). Some of the numerical methods developed later are by Wittmann (1974), Landi Degl'Innocenti (1976), Martin & Wickramasinghe (1981), and Nagendra & Peraiyah (1985a, 1985b). For a detailed discussion on various numerical methods of solution see Landi Degl'Innocenti & Landolfi (2004). An excellent description of Zeeman line transfer can be found in Stenflo (1994), del Toro Iniesta (2003), and Landi Degl'Innocenti & Landolfi (2004).

The earliest attempts to include incoherent scattering in Zeeman line transfer theory was by Stepanov (1958b) and Rachkovsky (1963). For NLTE Zeeman line transfer problem, the continuum source function  $S_c$  is given by Planck function  $B_{\nu_0}$ , while the line source vector which now includes incoherent scattering is given by (see Stenflo 1994)

$$S_L = (1 - \epsilon)\bar{J}_{\text{pol}} + \epsilon B_{\nu_0}, \quad (1.26)$$

where  $\epsilon$  is the photon destruction probability per scattering, and

$$\bar{J}_{\text{pol}} = \frac{1}{4\pi} \int_{-\infty}^{+\infty} d\nu' \int d\mathbf{n}' (\varphi_{I'} I' + \varphi_{Q'} Q' + \varphi_{U'} U' + \varphi_{V'} V'), \quad (1.27)$$

where  $\varphi_{I,Q,U,V}$  are the elements of first column of Zeeman line absorption matrix  $\Phi$  (see Chapter 2), the 'prime' on the quantities indicates the incoming frequency  $\nu'$ .

The basic theory for the NLTE Zeeman line transfer has been developed by Domke & Staude (1973a), Dolginov & Pavlov (1973, 1974), Šidlichovský (1974), House & Steinitz

(1975), Landi Degl’Innocenti & Landi Degl’Innocenti (1975), Landi Degl’Innocenti et al. (1976), and Landi Degl’Innocenti et al. (1991b).

First numerical solution of the NLTE Zeeman line transfer problem was by Rees (1969), and later by Domke & Staude (1973a, 1973b), Auer et al. (1977), Stenholm & Stenflo (1978), and Rees et al. (1989). All these authors assumed ‘field-free approximation’, namely  $\bar{J}_{\text{pol}}$  was replaced by  $\bar{J}_{\text{unpol}} = (1/4\pi) \int_{-\infty}^{+\infty} d\nu' \int d\mathbf{n}' \phi_{\nu'} I'$ , where  $\phi_{\nu'}$  is the absorption profile function.  $\bar{J}_{\text{unpol}}$  is computed with a non-magnetic NLTE code and then simply apply a formal solution of the Stokes transfer equations accounting for Zeeman effect.

Trujillo Bueno & Landi Degl’Innocenti (1996) show that the field-free approximation cannot be safely used for a height dependent magnetic field. To handle such field gradients, they introduced polarization free (POF) approximation. In this approximation, one replaces  $\bar{J}_{\text{pol}}$  by  $\bar{J}_{\text{POF}} = (1/4\pi) \int_{-\infty}^{+\infty} d\nu' \int d\mathbf{n}' \varphi_I I'$ , which is obtained again by solving scalar NLTE transfer equation but with  $\phi_{\nu}$  replaced by  $\varphi_I$ . Other alternative methods to solve the same problem are those by Bommier & Landi Degl’Innocenti (1996), Takeda (1991). The POF approximation has been extended by Bruls & Trujillo Bueno (1996) to solve multi-level NLTE Zeeman line transfer problem.

Auer et al. (1977) used the vector version of the scalar Feautrier (1964) method to solve the NLTE Zeeman line transfer problem. Another exact method to solve the same problem again by a matrix method based on discrete space theory is presented in Nagendra & Peraiah (1985a, 1985b). These methods involve matrix manipulations and hence are slow. A much faster method was developed by Rees et al. (1989), which they called DELO (Diagonal Elements Lambda Operator) method. The DELO method can be used as a formal solver (for a given source vector) to solve the NLTE Zeeman line transfer problem. A highly accurate formal solver, which is a vector version of the scalar short-characteristic method of Kunasz & Auer (1988) has been developed by Trujillo Bueno (2003a). He also developed a more accurate version of DELO, which he calls as DELOPAR.

In the NLTE Zeeman line transfer formulation presented above only incoherent scattering (CRD) has been included. The way to include coherent scattering (PRD) in this formalism was first discussed by Stenflo (1994). In this thesis we will consider a numerical method of solution for this latter class of problem (see Chapter 9).

### 1.7.2 NLTE polarized line radiation transfer

NLTE polarized radiative transfer problem in the absence of magnetic field (resonance scattering) for monochromatic radiation was first formulated by Chandrasekhar (1950). He solved also this transfer problem exactly. The relevant scattering phase matrix was derived quantum mechanically by Hamilton (1947, see Chandrasekhar 1950 for a classical derivation of the same). Since then, problems of increasing degree of complexity have been formulated and solved.

In the literature, the polarized line transfer problem has been formulated using two different approaches, namely the ‘scattering approach’ and the ‘density matrix approach’. The scattering approach makes use of vector (polarized) differential and integral equations for polarized line transfer, which requires the explicit analytic form of the redistribution matrix. In this approach the radiative transfer equation plays a pivotal role. The density matrix approach is based on the formalism of quantum electrodynamics. In this formalism the atom is described by its density matrix, while the polarized radiation field by means of irreducible tensors. The transfer equations for the irreducible tensors are coupled to the statistical equilibrium equations for the density matrix elements. In this approach the central role is played by the statistical equilibrium equations. This formalism lends itself easily to multi-level atoms including lower-level atomic polarization. Frisch (1998, 1999) has shown that the two approaches are equivalent in the case of two-level atom with CRD. In this thesis we pursue the scattering formalism, which allows a somewhat straight forward implementation of PRD effects.

#### Density matrix approach

The theoretical formalism for density matrix approach was developed by Bommier & Sahal-Br  chot (1978), and Landi Degl’Innocenti (1982, 1983a, 1983b, 1984, 1985). In the first two papers mentioned above only statistical equilibrium equations were considered, while in other four papers a more general formalism capable of describing the physics of resonance polarization for a multi-level atom in an optically thick, magnetized, multi-dimensional medium was developed. Coupled system of equations resulting from this formalism for the Hanle effect was solved by Landi Degl’Innocenti et al. (1987) using a perturbation method. In this method the intensity of the radiation field is first calculated neglecting the polarization and the magnetic field; the elements of the density matrix are then derived by solving the statistical equilibrium equations and the resulting polarization of the radiation field is deduced. This method relies on the fact that the observed linear polarization rates

are small (a few % in solar prominences).

The above theoretical formalism was particularized to two-level atomic model neglecting lower-level polarization and stimulated emission by Landi Degl’Innocenti et al. (1990) for Hanle effect, Landi Degl’Innocenti et al. (1991a) for arbitrary field strength and Landi Degl’Innocenti et al. (1991b) for strong field (neglecting coherences between the Zeeman sublevels). An “integral equation method” to solve the Hanle line transfer problem based on the formalism of Landi Degl’Innocenti et al. (1990) was developed by Bommier et al. (1991). For a review on density matrix approach see Landi Degl’Innocenti (1996), Bommier (1996), and Landi Degl’Innocenti & Landolfi (2004).

Fast iterative methods based on operator splitting for the density matrix approach of Landi Degl’Innocenti have been developed by Trujillo Bueno and co-workers. Such iterative methods for resonance scattering in a two-level atom have been developed by Trujillo Bueno & Manso Sainz (1999) neglecting lower-level polarization, and by Trujillo Bueno & Landi Degl’Innocenti (1997) with lower-level polarization included. Trujillo Bueno & Manso Sainz (1999) generalize to the polarized case the Jacobi-based approximate  $\Lambda$ -iteration (ALI) method of Olson et al. (1986) and the iterative schemes based on Gauss-Seidel and successive overrelaxation (SOR) methods of Trujillo Bueno & Fabiani Bendicho (1995) developed for solving scalar NLTE problems. Trujillo Bueno (1999) has then generalized this iterative method to handle multi-level atom with lower-level polarization. The same iterative scheme has been extended to include Hanle effect in 1D, 2D, and 3D atmospheres by Manso Sainz & Trujillo Bueno (1999) for a two-level atom neglecting lower-level polarization and by Manso Sainz & Trujillo Bueno (2003, see also Manso Sainz 2002) for multi-level atom with both upper and lower-level polarization. They use the formal solver developed by Fabiani Bendicho & Trujillo Bueno (1999) to solve 3D Hanle line transfer problems. For a fine review on all these developments see Trujillo Bueno (1998, 2003a).

It is important to note that the theory and method of solution for density matrix approach discussed above is restricted to CRD only. The PRD effects has only been recently included in the formalism of density matrix for a two-level atom by Landi Degl’Innocenti et al. (1997) neglecting collisions and by Bommier (1997a, 1997b, see also Bommier 1999, 2003) including collisions.

## Scattering approach

The traditional scattering approach is presented in Mihalas (1978) for the unpolarized case, and in Stenflo (1994), Ivanov et al. (1997) for the polarized case.



In the scattering approach, the zero field NLTE theory of resonance line polarization was given by Stenflo (1976), which is in principle applicable to multi-level atom and multi-dimensional geometry. This theory was applied by Stenflo & Stenholm (1976) to calculate UV emission polarization in resonance lines of a two-level atom. They solved the transfer problem using Rybicki's core saturation method, treating the Stokes  $Q$  parameter as a perturbation. Rees (1978) solved the same problem using a polarized integral equation method. Both the above mentioned papers assumed CRD during scattering.

PRD effects were first taken into account by Dumont et al. (1977) who used a Feautrier method. However they considered only the case of pure Doppler redistribution in the line core. PRD calculations coupling the wings and the line core have been done by Rees & Saliba (1982), McKenna (1984a, 1984b, 1985), Saliba (1985, 1986), Faurobert (1987, 1988), and Nagendra (1986, 1988, 1989, 1994, 1995). Rees & Saliba (1982) and Saliba (1985, 1986) used a differential equation method such as the Feautrier method with Stokes  $Q$  treated as a perturbation. McKenna (1984a, 1984b, 1985) used the integral equation method, while Faurobert (1987, 1988) used non-perturbative Feautrier method. Nagendra (1986, 1988, 1989, 1994, 1995) used a non-perturbative discrete space method (DSM) to solve the resonance line transfer problem. All the above mentioned authors used plane-parallel atmosphere, except Nagendra, who used spherical atmosphere. For a review on analytic/ asymptotic methods in polarized line transfer see Ivanov (1991).

The paper by Rees & Saliba (1982) represents an important epoch in this field. They introduce the so called 'hybrid approximation', which assumes a full decoupling of the frequency redistribution and the polarization (represented through a angular phase matrix). In the absence of the magnetic field, the NLTE transfer equation is given by Eq. (1.23) with  $\mathbf{K} = [k_c + k_0\phi(x)]\mathbf{E}$ , where  $\phi(x)$  is the normalized absorption profile with  $x$  being non-dimensional frequency. The source vector is given by

$$\mathbf{S}(x, \mu) = \frac{k_0\phi(x)\mathbf{S}_L(x, \mu) + k_c B_{\nu_0}\mathbf{U}}{k_c + k_0\phi(x)}, \quad (1.28)$$

with the line source vector

$$\mathbf{S}_L(x, \mu) = \frac{1 - \epsilon}{\phi(x)} \int_{-\infty}^{+\infty} dx' \oint d\mathbf{n}' \mathbf{R}(x, \mathbf{n}, x', \mathbf{n}') \mathbf{I}(x', \mathbf{n}') + \epsilon B_{\nu_0}\mathbf{U}, \quad (1.29)$$

where  $\mathbf{U} = (1\ 0)^T$ , and  $\mathbf{I} = (I\ Q)^T$  (since the radiation field is axisymmetric  $U = V = 0$ ). According to the hybrid approximation of Rees & Saliba (1982),

$$\mathbf{R}(x, \mathbf{n}, x', \mathbf{n}') = R(x, \mathbf{n}, x', \mathbf{n}') \mathbf{P}_R(\mathbf{n}, \mathbf{n}'), \quad (1.30)$$

where  $\mathbf{P}_R(\mathbf{n}, \mathbf{n}')$  is the Rayleigh phase matrix (see Chandrasekhar 1950). For the redistribution function  $R(x, \mathbf{n}, x', \mathbf{n}')$  one uses  $R_{\text{II}}$  function of Hummer (1962) for resonance lines. To reduce the CPU requirements in radiative transfer calculations an assumption is normally made that the function  $R_{\text{II}}$  can be angle-averaged independent of  $\mathbf{P}_R(\mathbf{n}, \mathbf{n}')$ , so that we can write

$$\mathbf{R}(x, \mathbf{n}, x', \mathbf{n}') = R(x, x')\mathbf{P}_R(\mathbf{n}, \mathbf{n}'). \quad (1.31)$$

Under CRD approximation,  $R(x, x') = \phi(x)\phi(x')$  and for PRD  $R(x, x') = R_{\text{II}}(x, x')$ .

Angle-dependent redistribution function  $R(x, \mathbf{n}, x', \mathbf{n}')$  were used by Faurobert (1987, 1988) and Nagendra (1986, 1987, 1989), while other authors mentioned above used angle-averaged  $R_{\text{II}}(x, x')$  or CRD. The correct form of redistribution matrix for resonance line scattering including collisions was derived by Domke & Hubeny (1988) and Streater et al. (1988). The Domke-Hubeny redistribution matrix was used in line transfer computation by Nagendra (1994, 1995), who used the discrete space method for the solution.

A weak field NLTE theory of Hanle effect line polarization under scattering approach was first developed by Stenflo (1978). He derived the Hanle phase matrix in a reference frame where magnetic field is along the normal to the atmosphere. For arbitrary orientation of magnetic field the Hanle phase matrix is derived by Landi Degl'Innocenti & Landi Degl'Innocenti (1988). This phase matrix has been used for the first time by Faurobert-Scholl (1991) to solve the Hanle PRD line transfer problem. As a bold step, she introduced the following 1D-domain based Hanle redistribution matrix

$$\mathbf{R}(x, \mathbf{n}, x', \mathbf{n}') = R_{\text{II}}(x, x') \times \begin{cases} \mathbf{P}_H(\mathbf{n}, \mathbf{n}', \mathbf{B}) & \text{for } |x| < x_c, \\ \mathbf{P}_R(\mathbf{n}, \mathbf{n}') & \text{for } |x| > x_c, \end{cases} \quad (1.32)$$

based on the fact that Hanle effect is operative only in the core.  $\mathbf{P}_H(\mathbf{n}, \mathbf{n}', \mathbf{B})$  is the Hanle phase matrix,  $x_c$  is the cut-off frequency. Faurobert-Scholl (1991) used two methods to solve the Hanle line transfer problem, one is the non-perturbative Feautrier method and the other which treats polarization as a perturbation to the specific intensity (Rees 1978). The latter method uses the Fourier azimuthal expansion of the radiation field with respect to the azimuth angle  $\varphi$  of the direction of propagation. Such an expansion ‘reduces’ the non-axisymmetric ( $\varphi$ -dependent) problem to the axisymmetric one (only  $\mu$ -dependent). A correct form of Hanle redistribution matrix including collisions was given by Bommier (1997b). She derived these matrices by going to the weak field limit of her more general theory. She gave more sophisticated 2D-domain based PRD matrices, the so called “Approximation II” that uses angle-dependent frequency redistribution functions of Hummer,

and “Approximation III” that uses corresponding angle-averaged functions. Approximation III, but without collisions has been used by Faurobert-Scholl et al. (1999) to solve Hanle PRD problem using a perturbation method. Nagendra et al. (2002) have used both the Approximation II and III (also including collisions) to solve the Hanle PRD problem using a perturbation method. In the works mentioned above the Zeeman effect was neglected, by using a scalar absorption coefficient instead of an absorption matrix. In Chapter 9 of this thesis we solve an even more general “Hanle-Zeeman” PRD line transfer problem using a perturbation method, which takes into account both the ‘Zeeman absorption matrix’ and ‘Hanle-Zeeman redistribution matrix’ (that will be derived in Chapters 7 and 8).

The various numerical methods mentioned above are computationally expensive. Hence it is necessary to develop fast iterative methods. Novel iterative methods were developed for the scalar transfer problems in the 1970’s. One such method is called Approximate  $\Lambda$ -Iteration (ALI) method, which is based on the idea of operator perturbation. It was developed by Olson et al. (1986). One of the best reviews that describes the concept of ALI in scalar line transfer theory is that of Hubeny (2003, see also Hubeny 1992). Extension of ALI methods to include polarization under the scattering approach, was done in the following series of papers. Faurobert-Scholl et al. (1997) developed a PALI (Polarized ALI) method for resonance line scattering with CRD. The PRD effects were incorporated for the same problem by Paletou & Faurobert-Scholl (1997). PALI method for Hanle effect with CRD was developed by Nagendra et al. (1998). The 1D-domain based PRD for Hanle effect was then included by Nagendra et al. (1999, see also Nagendra et al. 2000). The 2D-domain based PRD (Approximation III of Bommier 1997b) was implemented in PALI method by Fluri et al. (2003b). For a fine review on the development of PALI methods see Nagendra (2003a). Current information on state-of-the-art numerical methods used in line radiative transfer can be found in the proceedings volumes “Stellar atmosphere modeling”, edited by Hubeny et al. (2003).

The “traditional” PALI methods are based on the azimuthal Fourier expansion of the radiation field  $\mathbf{I}$  with respect to the outgoing ray azimuth  $\varphi$ , and a double Fourier expansion of the redistribution matrix with respect to both outgoing and incoming ray azimuths  $\varphi$  and  $\varphi'$  respectively. Such an expansion allows to decompose the non-axisymmetric radiative transfer equation into a  $\varphi$ -independent form. The concept of Fourier azimuthal expansion was first introduced by Chandrasekhar (1950) for Rayleigh scattering problem. This was extended to Hanle scattering problem by Faurobert-Scholl (1991). A better way of expansion is presented in Nagendra et al. (1998). Recently Frisch (2007) has proposed a elegant method for the above said decomposition, using the irreducible ‘spherical tensors for

polarimetry' introduced by Landi Degl'Innocenti (1984, 1985). This new approach is used in Chapter 10 of the thesis to develop a PALI method for a non-domain based PRD theory of Hanle effect. A non-domain based PRD matrix is obtained there by performing an angle-average over the laboratory frame redistribution matrix derived under the Approximation I of Bommier (1997b).

## 1.8 Outline of the thesis

In this thesis we have attempted to improve our knowledge on two topics of current interest in the field of polarized line radiation transfer theory. The thesis consists of two parts. Chapters 2 to 6 constitute Part-I of the thesis. Part-I deals with a detailed investigation of the Zeeman line formation in a stochastic medium. Chapters 7 to 10 constitute Part-II of the thesis. In Part-II we develop the theory of line scattering with PRD in the presence of arbitrary strength magnetic fields, and also present numerical methods of solution.

### 1.8.1 Outline on part-I of the thesis

In Chapter 2 we revisit the micro-turbulent limit and study the mean Zeeman absorption matrix in detail. The micro-turbulent limit refers to the case when the scales of fluctuations of the random field are much smaller than the photon mean free paths associated to the line formation. Random magnetic field is characterized by isotropic (which we call 3D turbulence) or anisotropic (which we call 1D or 2D turbulence) Gaussian distributions. A detailed analytic as well as the numerical study of this limit is necessary for understanding the more complex problem of meso-turbulence (random magnetic field with finite correlation length). Some of the mathematical details on the special functions and on the method of averaging that are required in Chapter 2 are presented in Appendices A - C.

Chapter 3 is devoted to a detailed study of a new class of functions which we call generalized Voigt and Faraday-Voigt functions, that were first introduced by Dolginov & Pavlov (1972). They appear in the analytic expression for mean Zeeman absorption and dispersion coefficients, that are obtained when we consider isotropic fluctuations of the random field in Chapter 2. It is necessary to develop numerical algorithm for correct evaluation of these functions. Chapter 3 focuses on these aspects.

Observations and numerical simulations of magneto-convection show a highly variable solar magnetic field. To interpret these observations, there is a need to develop theory of polarized line formation in the presence of a random magnetic field with finite correlation

length (the so called meso-turbulent limit). Chapter 4 is devoted to the detailed study of this meso-turbulent limit. We model the random vector magnetic field by a Kubo-Anderson process (KAP). KAP is characterized by a correlation length and a probability distribution function (PDF) for the random values of the magnetic field. Some properties of the transport operator that is used in Chapter 4 are presented in Appendix D. In Appendix E we give the Zeeman absorption matrix in a frame where the mean magnetic field is along the polar  $Z$ -axis.

In Chapter 5 we undertake a detailed study on the effects of random magnetic fields on Stokes line profiles. For this purpose we restrict ourselves to micro and macro-turbulent regimes, which provide bounds for a more general meso-turbulent regime. In this chapter we continue to use Gaussian PDFs that were considered in Chapter 2. The solution of the transfer equation for the deterministic fields (Unno-Rachkovsky solution) are presented in Appendix F. They are useful for the interpretation of the results presented in Chapter 5.

Empirically determined PDFs from observations and numerical simulations of magneto-convection are used to compute mean Stokes profiles in Chapter 6. PDFs need to be actually determined from observations. So far PDFs corresponding ‘only to the field strength’ have been provided by observations (see eg. Stenflo & Holzreuter 2002, 2003a, 2003b). However there is an urgent need to determine from observations the PDFs not only for the field strength but also for the ‘field orientation’.

### 1.8.2 Outline on part-II of the thesis

The polarized spectrum of strong resonance lines like CaI 4227 Å could be modeled only when the PRD is taken into account in line scattering. Hence it is necessary to develop polarized PRD line formation theories in the presence of arbitrary strength magnetic fields. In Chapter 7, we develop the theory for the PRD redistribution matrix for a two-level atom ( $J = 0 \rightarrow 1 \rightarrow 0$  scattering transition) in the presence of magnetic fields of arbitrary strength and direction. We transform the atomic frame time-dependent classical oscillator theory of Bommier & Stenflo (1999) to the laboratory frame. It involves extensive calculations. We refer to the resulting redistribution matrix as the ‘Hanle-Zeeman redistribution matrix’, as it covers the entire field strength regime. The auxiliary coefficients and phase matrices entering the redistribution matrix are listed in Appendix G.

The equivalence between the Hanle-Zeeman redistribution matrix that we derive through quantum electrodynamic approach of Bommier (1997b) and the one we derived in Chapter 7 through the classical theory is established in Chapter 8. This ‘equivalence’ is proved

explicitly for a  $J = 0 \rightarrow 1 \rightarrow 0$  scattering transition both in the atomic as well as the laboratory frames. The various functions and phase matrices contained in type III redistribution matrix are presented in Appendices H and I. In Appendix J we describe the method to include the spherical tensors in to the Hanle scattering matrix of Stenflo (1994). This method is used in Chapter 8 to establish the equivalence between the classical and QED redistribution matrices. The frame transformation equations are presented in Appendix K.

In Chapter 9, we solve the polarized radiative transfer equation numerically, taking into account consistently and simultaneously both the Zeeman absorption matrix and the Hanle-Zeeman partial redistribution matrix in arbitrary fields. We apply a perturbation method (see eg. Nagendra et al. 2002) to solve this highly general Hanle-Zeeman line transfer equation. It represents the very first solution of this problem.

Apart from deriving the theoretical framework, the challenge for theorists is to develop ‘efficient algorithms’ to solve the polarized radiation transfer equation. The numerical method used in Chapter 9 is computationally expensive. Hence it is necessary to develop fast iterative methods based on operator perturbation. As a first step in this direction, we develop such a method in Chapter 10 in the particular case of ‘weak field limit’ of Hanle-Zeeman redistribution matrix. The elements of the weak field non-domain based partial redistribution matrix are listed in Appendix L.

Finally, open questions and the future developments in the theory of polarized line formation are discussed in Chapter 11. The ultimate goal of astrophysical scattering theory is to model the observations, and to understand the various physical processes occurring in the distant source. In our case, the idea behind developing such a sophisticated scattering theory is to model the Hanle effect signatures in the “second solar spectrum”.

## **Part-I**

**Stochastic polarized line formation in  
magneto-turbulent media**





## Chapter 2

# Zeeman absorption matrix in a random magnetic field<sup>1</sup>

### 2.1 Introduction

Observations of the solar magnetic field and numerical simulations of solar magnetohydrodynamical processes all converge to a magnetic field which is highly variable on all scales, certainly in the horizontal direction and probably also in the vertical one. Solving radiative transfer equations for polarized radiation in a random magnetic field, is thus an important but not a simple problem since one is faced with a transfer equation with stochastic coefficients (Landi Degl'Innocenti 2003, Landi Degl'Innocenti & Landolfi 2004, henceforth LL04). In principle the mean radiation field can be found by numerical averaging over a large number of realizations of the magnetic field and other relevant random physical parameters like velocity and temperature. A more appealing approach is to construct, with chosen magnetic field models, closed form equations or expressions for the mean Stokes parameters. Landi Degl'Innocenti (2003) has given a nice and comprehensive review of the few models that have been proposed.

The problem of obtaining mean Stokes parameters simplifies if one can single out fluctuations with scales much smaller than the photon mean free paths. The radiative transfer equation has the same form as in the deterministic case, except that the coefficients in the equation, in particular the absorption matrix, are replaced by averages over the distribution of the magnetic field vector and other relevant physical parameters. This micro-turbulent approximation is currently being used for diagnostic purposes in the frame work of the

---

<sup>1</sup>This chapter is based on the publication : Frisch, H., Sampoorna, M., & Nagendra, K. N. 2005, A&A, 442, 11-28

MISMA (Micro Structured Magnetic Atmospheres) hypothesis (Sánchez Almeida et al. 1996, Sánchez Almeida 1997, Sánchez Almeida & Lites 2000) and commonly observed features like Stokes  $V$  asymmetries and broad-band circular polarization could be correctly reproduced. In the MISMA modeling the mean Zeeman absorption matrix is actually a weighted sum of two or three absorption matrices, each corresponding to a different constituent of the atmosphere characterized by its physical parameters (filling factor, magnetic field strength and direction, velocity field, etc.).

The problem simplifies also when the scales of fluctuations are much larger than the photon mean free paths. The magnetic field can then be taken constant over the line forming region and the transfer equation for polarized radiation is the standard deterministic one. Mean Stokes parameters can be obtained by averaging its solution over the magnetic field distribution. For magnetic fields with a finite correlation length, i.e. comparable to photons mean free paths, the macro-turbulent and micro-turbulent limits are recovered when the correlation scales go to infinity or zero.

The micro-turbulent limit is certainly a rough approximation to describe the effects of a random magnetic field, but as the small scale limit of more general models, it is interesting to study somewhat systematically the effect of a random magnetic field on the Zeeman absorption matrix. This is the main purpose of this chapter. The problem has actually been addressed fairly early by Dolginov & Pavlov (1972, henceforth DP72) and by Domke & Pavlov (1979, henceforth DP79), with anisotropic Gaussian distributions of the magnetic field vector. These two papers have attracted very little attention, although they contain quite a few interesting results showing the drastic effects of isotropic or anisotropic magnetic field distributions with a non zero mean field. More simple distribution have been introduced for diagnostic purposes, in particular in relation with the Hanle effect. For example, following Stenflo (1982), a single-valued magnetic field with isotropic distribution is commonly used to infer turbulent magnetic fields from the linear polarization of Hanle sensitive lines (Stenflo 1994, Faurobert-Scholl 1996, and references therein). A somewhat more sophisticated model is worked out in detail in LL04 for the case of the Zeeman effect. The angular distribution is still isotropic, but the field strength has a Gaussian distribution with zero mean. The two models predict zero polarization for the Zeeman effect, since all the off diagonal elements of the absorption matrix are zero. Recently, measurements of the fractal dimensions of magnetic structures in high-resolution magnetograms (Stenflo & Holzreuter 2003a), and numerical simulations of magneto-convection (Cattaneo 1999, Cattaneo et al. 2003, Janßen et al. 2003) have suggested that distribution of the vertical component of the magnetic field strength could be described by Voigt or stretched

exponential functions respectively. Such distributions are now considered for diagnostic purposes (Socas-Navarro & Sánchez Almeida 2003, Trujillo Bueno et al. 2004). Actually not so much is known on the small scale distribution of the magnetic field vector and on the correlations between the magnetic field and velocity field fluctuations. For isotropic turbulence, symmetry arguments show that correlations are zero when the magnetic field is treated as a pseudo-vector (DP79).

Here we concentrate on the effects of Gaussian magnetic field fluctuations. We believe that a good understanding of the sole action of a random magnetic field is important before considering more complex situations with anisotropic random velocity fields and correlations between velocity field and magnetic field fluctuations, although they seem to be needed to explain circular polarization asymmetries. One can find in LL04 (Chapter 9) a simple example showing the effects of such correlations. So here we assume, as in DP79, that there is no correlation between the magnetic field and velocity field fluctuations and that the latter behave like thermal velocity field fluctuations. They can thus be incorporated in the line Doppler width. We assume that the medium is permeated by a mean magnetic field  $\mathbf{B}_0$  with anisotropic Gaussian fluctuations. We write the random field distribution function, also called probability distribution function (PDF), in the form

$$P(\mathbf{B})d\mathbf{B} = \frac{1}{(2\pi)^{3/2}\sigma_T^2\sigma_L} \exp\left[-\frac{B_T^2}{2\sigma_T^2}\right] \exp\left[-\frac{(B_L - B_0)^2}{2\sigma_L^2}\right] d^2B_T dB_L. \quad (2.1)$$

Here  $B_T$  and  $B_L$  are the components of the random field in the directions perpendicular and parallel to the mean field. The coefficient  $\sigma_L$  and  $\sigma_T$  are proportional to the root mean square (rms) fluctuations of the longitudinal and transverse components. With the above definition  $\langle(B_L - B_0)^2\rangle = \sigma_L^2$  and  $\langle B_T^2\rangle = 2\sigma_T^2$ . We will also consider the case of isotropic fluctuations with  $\sigma_T = \sigma_L = \sigma$ . In that case  $\langle(\mathbf{B} - \mathbf{B}_0)^2\rangle = 3\sigma^2$ . The distribution written in Eq. (2.1) is invariant under a rotation about the direction of the mean field and is normalized to unity. The choice of the factor 2 in the exponential is arbitrary. Changing it will modify the normalization constant and the relation between the rms fluctuations and the coefficients  $\sigma_T$  and  $\sigma_L$ .

The distribution written in Eq. (2.1) is the most general azimuthally symmetric Gaussian distribution. Here we consider three specific types of fluctuations : (i) longitudinal fluctuations in the direction of the mean field, also referred to as 1D fluctuations; they correspond to the case  $\sigma_T = 0$ . (ii) isotropic fluctuations, also referred to as 3D fluctuations; they correspond to  $\sigma_T = \sigma_L$ . (iii) fluctuations perpendicular to the mean field which we refer to as 2D fluctuations; they correspond to the case  $\sigma_L = 0$ . In cases (i) and (iii) the

fluctuations are anisotropic. They are isotropic by construction in case (ii). In case (i), only the magnitude of  $\mathbf{B}$  is random but in cases (ii) and (iii), both the magnitude and the direction of the magnetic field are random.

For these three types of distribution we give expressions, as explicit as possible, of the mean absorption and anomalous dispersion coefficients. Many of them can be found also in DP72 and DP79 where they are often stated with only a few hints at how they may be obtained. Here we give fairly detailed proofs. Some of them can be easily transposed to non-Gaussian distribution functions. Also we perform a much more extended numerical analysis of the mean coefficients and in particular carry out a detailed comparison of the frequency profiles produced by the longitudinal, perpendicular and isotropic distributions. This comparison is quite useful for building a physical insight into the averaging effects.

This chapter is organized as follows: In § 2.2 we establish a general expression for the calculation of the mean Zeeman absorption matrix which holds for any azimuthally invariant magnetic field vector distributions. In §§ 2.3, 2.4 and 2.5 we consider in detail the three specific distributions listed above. § 2.6 is devoted to a summary of the main results and contains also some comments on possible generalizations.

## 2.2 The Zeeman absorption matrix

We are interested in the calculation of

$$\langle \Phi \rangle = \int \Phi(\mathbf{B}) P(\mathbf{B}) d\mathbf{B}, \quad (2.2)$$

where  $\Phi$  is the absorption matrix in the transfer equation for polarized radiation. It depends on the strength of the magnetic field  $|\mathbf{B}| = B$  and on the angle between the line-of-sight (LOS) and the direction of the magnetic field. In the LOS reference frame shown in Fig. 2.1 where the  $Z$ -axis is toward the observer,  $\Phi$  depends on the polar and azimuthal angles  $\theta$  and  $\phi$  of the random magnetic field. In contrast, the magnetic field distribution introduced in Eq. (2.1) is defined with respect to the direction of the mean field  $\mathbf{B}_0$ . In terms of  $\Theta$  and  $\Psi$ , the polar and azimuthal angles of  $\mathbf{B}$  with respect to  $\mathbf{B}_0$ , the distribution function has the form

$$P(\mathbf{B})d\mathbf{B} = \frac{1}{(2\pi)^{3/2}\sigma_T^2\sigma_L} \exp\left[-\frac{B^2 \sin^2 \Theta}{2\sigma_T^2}\right] \exp\left[-\frac{(B \cos \Theta - B_0)^2}{2\sigma_L^2}\right] B^2 \sin \Theta dB d\Theta d\Psi. \quad (2.3)$$

To carry out the averaging process, one must either express  $P(\mathbf{B}) d\mathbf{B}$  in terms of  $\theta$  and  $\phi$  or the matrix  $\Phi$  in terms of  $\Theta$  and  $\Psi$ . The second option is actually simpler to work out. As

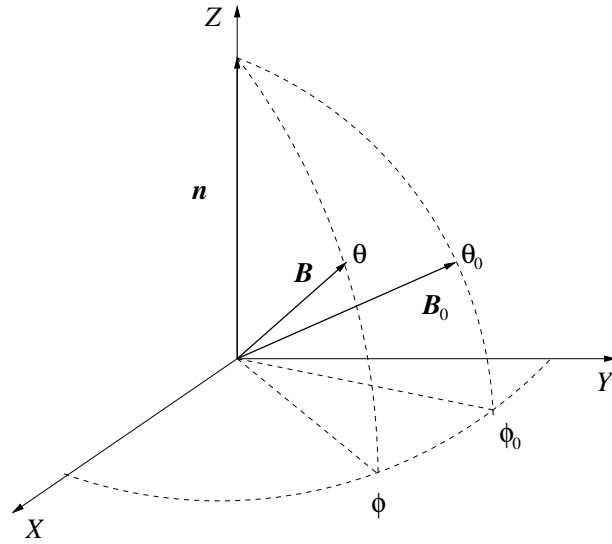


Figure 2.1: Definition of  $\theta$  and  $\phi$ , the polar and azimuthal angles of the random magnetic field vector  $\mathbf{B}$ , and of  $\theta_0$  and  $\phi_0$ , the corresponding angles for the mean magnetic field  $\mathbf{B}_0$ . The angles  $\theta$  and  $\theta_0$  are defined with respect to the LOS  $\mathbf{n}$ .

pointed out in DP79, the angular dependence of the elements of  $\Phi$  can be written in terms of the spherical harmonics  $Y_{lm}(\theta, \phi)$ . This comes out naturally when the radiation field is represented by means of the polarization matrix rather than with the Stokes parameters. The  $Y_{lm}$ , because they are tensors of rank  $l$ , obey well known transformation laws under a rotation of the reference frame. A rotation of the LOS reference frame to a new frame defined by the direction of the mean magnetic field will thus yield the elements of  $\Phi$  in terms of  $\Theta$  and  $\Psi$ . The averaging process can then be carried out fairly easily.

In § 2.2.1 we recall the standard expressions of the elements of the  $4 \times 4$  Zeeman absorption matrix in the Stokes parameters representation and in § 2.2.2 we give their expression in the polarization matrix representation. In § 2.2.3 we explain in detail the transformation of the  $Y_{lm}$  and in § 2.2.4 establish general expressions for the mean coefficients.

### 2.2.1 Absorption and anomalous dispersion coefficients

We consider for simplicity a normal Zeeman triplet but our results are easily generalized to the anomalous Zeeman effect (see §§ 2.6 and 6.6). For a normal Zeeman triplet, the line absorption matrix can be written as (Landi Degl'Innocenti 1976, Rees 1987, Stenflo 1994,

LL04)

$$\Phi = \begin{bmatrix} \varphi_I & \varphi_Q & \varphi_U & \varphi_V \\ \varphi_Q & \varphi_I & \chi_V & -\chi_U \\ \varphi_U & -\chi_V & \varphi_I & \chi_Q \\ \varphi_V & \chi_U & -\chi_Q & \varphi_I \end{bmatrix}. \quad (2.4)$$

The absorption coefficients,  $\varphi_{I,Q,U,V}$  and the anomalous dispersion coefficients  $\chi_{Q,U,V}$  may be written as

$$\begin{aligned} \varphi_I &= \frac{1}{2}\varphi_0 \sin^2 \theta + \frac{1}{4}(\varphi_{+1} + \varphi_{-1})(1 + \cos^2 \theta), \\ \varphi_Q &= \frac{1}{2} \left[ \varphi_0 - \frac{1}{2}(\varphi_{+1} + \varphi_{-1}) \right] \sin^2 \theta \cos 2\phi, \\ \varphi_U &= \frac{1}{2} \left[ \varphi_0 - \frac{1}{2}(\varphi_{+1} + \varphi_{-1}) \right] \sin^2 \theta \sin 2\phi, \\ \varphi_V &= \frac{1}{2}(\varphi_{+1} - \varphi_{-1}) \cos \theta, \\ \chi_Q &= \frac{1}{2} \left[ f_0 - \frac{1}{2}(f_{+1} + f_{-1}) \right] \sin^2 \theta \cos 2\phi, \\ \chi_U &= \frac{1}{2} \left[ f_0 - \frac{1}{2}(f_{+1} + f_{-1}) \right] \sin^2 \theta \sin 2\phi, \\ \chi_V &= \frac{1}{2}(f_{+1} - f_{-1}) \cos \theta. \end{aligned} \quad (2.5)$$

Here  $\varphi_q$  ( $q = 0, \pm 1$ ) are Voigt functions and  $f_q$  Faraday-Voigt functions defined below.

We introduce a Doppler width  $\Delta\nu_D$  and measure all the independent variables appearing in  $\varphi_q$  and  $f_q$  in Doppler width units. We thus write

$$\varphi_q(x, a, B) = H(x - q\Delta_Z B, a) = \frac{a}{\pi^{3/2}} \int_{-\infty}^{+\infty} \frac{e^{-u^2}}{(x - q\Delta_Z B - u)^2 + a^2} du, \quad (2.6)$$

and

$$f_q(x, a, B) = F(x - q\Delta_Z B, a) = \frac{1}{\pi^{3/2}} \int_{-\infty}^{+\infty} \frac{(x - q\Delta_Z B - u)e^{-u^2}}{(x - q\Delta_Z B - u)^2 + a^2} du, \quad (2.7)$$

where  $x = (\nu_0 - \nu)/\Delta\nu_D$  is the frequency measured from the line center, in units of  $\Delta\nu_D$ ,  $a$  the damping parameter and  $\Delta_Z B$  the Zeeman displacement by the random field with

$$\Delta_Z = g \frac{e}{4\pi m} \frac{1}{\Delta\nu_D}. \quad (2.8)$$

Here  $g$  is the Landé factor,  $m$  and  $e$ , the mass and charge of the electron.

We use here Voigt functions which are normalized to unity when integrated over the dimensionless frequency  $x$ , and the associated Faraday-Voigt functions (a factor  $1/\sqrt{\pi}$

is added to the usual definition of  $H$  and a factor  $2/\sqrt{\pi}$  to the usual definition of  $F$ ). With this definition the Voigt function is exactly the convolution product of a Lorentzian describing the natural width of the line and of a Gaussian. The latter can describe pure thermal Doppler broadening, or a combination of thermal and micro-turbulent velocity broadening, provided the velocity field has an isotropic Maxwellian distribution. What we call here the Doppler width and denote by  $\Delta\nu_D$  is actually the total broadening parameter, including the micro-turbulent velocity field. Thus, with standard notations,

$$\Delta\nu_D = \frac{\nu_0}{c} \left( v_{\text{th}}^2 + v_{\text{tv}}^2 \right)^{1/2}, \quad (2.9)$$

where  $\nu_0$  is the line center frequency,  $c$  the speed of light,  $v_{\text{th}} = (2kT/M)^{1/2}$  and  $v_{\text{tv}}$  are the rms thermal and turbulent velocities, respectively.

If the frequency  $x$  is measured in units of thermal Doppler width  $\Delta\nu_D = \nu_0 v_{\text{th}}/c$ , then  $\varphi_q(x, a)dx$  become  $\varphi_q(x/\gamma_v, a/\gamma_v)dx/\gamma_v$  with  $\gamma_v = (1 + v_{\text{tv}}^2/v_{\text{th}}^2)^{1/2}$ . The change of variables  $x/\gamma_v \rightarrow x$  and  $a/\gamma_v \rightarrow a$  and the definition of  $\Delta\nu_D$  as in Eq. (2.9) lead back to Eqs. (2.6) and (2.7).

### 2.2.2 An alternative form for the absorption and dispersion coefficients

For the calculation of the mean Zeeman absorption matrix, it is convenient to rewrite the elements as in DP79, namely in the form

$$\begin{aligned} \varphi_I &= A_0 - \frac{1}{3}A_2(3\cos^2\theta - 1); & \varphi_V &= A_1 \cos\theta, \\ \varphi_Q &= A_2 \sin^2\theta \cos 2\phi; & \varphi_U &= A_2 \sin^2\theta \sin 2\phi, \end{aligned} \quad (2.10)$$

with

$$\begin{aligned} A_0 &= \frac{1}{3} \sum_{q=-1}^{q=+1} \varphi_q(x, a, B), & q &= 0, \pm 1 \\ A_1 &= \frac{1}{2} \sum_{q=\pm 1} q \varphi_q(x, a, B), \\ A_2 &= \frac{1}{4} \sum_{q=-1}^{q=+1} (2 - 3q^2) \varphi_q(x, a, B), & q &= 0, \pm 1. \end{aligned} \quad (2.11)$$

The anomalous dispersion coefficients have similar expressions with the  $\varphi_q$  replaced by the  $f_q$ . It is straightforward to verify that the expressions given above are identical to those given in Eq. (2.5). We note here that they appear automatically when the polarized

radiation field is represented by the time averaged polarization tensor rather than by the Stokes vector (DP72, DP79, Dolginov et al. 1995).

The main interest of this formulation, in addition to the fact that the  $A_i$ , ( $i = 0, 1, 2$ ) depend only on the strength of the random magnetic field, is that the functions which contain the angular dependence can be expressed in terms of spherical harmonics  $Y_{l,m}(\theta, \phi)$  and Legendre polynomials  $P_l(\cos \theta)$  which obey simple transformation laws in a rotation of the reference frame.

In terms of these special functions,

$$\begin{aligned} \varphi_{\text{I}} &= A_0 - (2/3)A_2P_2(\cos \theta); & \varphi_{\text{V}} &= A_1P_1(\cos \theta), \\ \varphi_{\text{Q}} &= A_2\sqrt{(32\pi/15)}\Re[Y_{2,2}(\theta, \phi)]; & \varphi_{\text{U}} &= A_2\sqrt{(32\pi/15)}\Im[Y_{2,2}(\theta, \phi)]. \end{aligned} \quad (2.12)$$

The Legendre polynomials  $P_l(\cos \theta)$  are special cases of  $Y_{lm}(\theta, \phi)$ , corresponding to  $m = 0$  (see Appendix A).

### 2.2.3 Rotation of the reference frame

We now perform a rotation of the reference frame to obtain the absorption coefficients in a reference frame connected to the mean magnetic field where the averaging process is easily carried out. The initial reference frame is the  $(XYZ)$  frame, also referred as the LOS reference frame (see Fig. 2.1). We perform on this reference frame a rotation defined by the Euler angles  $\alpha = \phi_0$ ,  $\beta = \theta_0$  and  $\gamma = 0$ . This rotation is realized by performing a rotation by an angle  $\theta_0$  around the  $Y$ -axis and a rotation by an angle  $\phi_0$  around the initial  $Z$ -axis. Since the random field is invariant under a rotation about the direction of the mean field, we have taken  $\gamma = 0$ . Rotational transformations and Euler angles are described in many textbooks (Brink & Satchler 1968, Varshalovich et al. 1988, LL04).

The spherical harmonics  $Y_{lm}$  are irreducible tensors of rank  $l$ . They are particular cases of the Wigner  $D_{mm'}^{(l)}(\alpha, \beta, \gamma)$  functions corresponding to  $m = 0$  or  $m' = 0$  (see Appendix A). In a rotation of the reference frame, defined by the Euler angles  $\alpha, \beta, \gamma$ , they transform according to (Varshalovich et al. 1988, p. 141, Eq. 1)

$$Y_{lm}(\Theta, \Psi) = \sum_{m'} Y_{lm'}(\theta, \phi) D_{m'm}^{(l)}(\alpha, \beta, \gamma), \quad (2.13)$$

where  $\theta$  and  $\phi$  are the polar angles in the initial LOS coordinate system and  $\Theta$  and  $\Psi$  the polar angles in the final mean magnetic coordinate system. Thus  $\Theta$  and  $\Psi$  define the direction of the random field  $\mathbf{B}$  in the new reference frame.



Actually, we need the inverse transformation which will give us the  $Y_{lm}(\theta, \phi)$  in terms of the  $Y_{lm}(\Theta, \Psi)$ . The inverse transformation is (Varshalovich et al. 1988, p. 74, Eq. 13)

$$Y_{lm}(\theta, \phi) = \sum_{m'} Y_{lm'}(\Theta, \Psi) D_{m'm}^{(l)}(0, -\theta_0, -\phi_0). \quad (2.14)$$

The inverse transformation is obtained by performing the three elementary rotations in the reverse order and with the opposite rotation angles. Explicit expressions of the  $Y_{lm}$  and  $D_{m'm}^{(l)}$  are given in Appendix A.

To calculate the mean coefficients  $\langle \varphi_{I,Q,U,V} \rangle$  we have to integrate Eq. (2.12) over  $\Psi$ . Since the distribution function  $P(\mathbf{B})$  and the  $A_i$  ( $i = 0, 1, 2$ ), are independent of  $\Psi$  (see Eqs. (2.3) and (2.11)), only the  $Y_{lm}$  have to be integrated over  $\Psi$ . When Eq. (2.14) is integrated over  $\Psi$ , only the term with  $m' = 0$  will remain. For  $m' = 0$  the  $D_{m'm}^{(l)}$  reduce to  $Y_{lm}$  and the  $Y_{l0}$  to Legendre polynomials. Thus after integration, Eq. (2.14) reduces to

$$\frac{1}{2\pi} \int Y_{lm}(\theta, \phi) d\Psi = P_l(\cos \Theta) Y_{lm}(-\theta_0, -\phi_0). \quad (2.15)$$

We are now in the position to average Eq. (2.12).

#### 2.2.4 The mean coefficients

Using Eq. (2.15) with  $l = 2, m = 0$  for  $\varphi_I$ ,  $l = 1, m = 0$  for  $\varphi_V$  and  $l = 2, m = \pm 2$  for  $\varphi_Q$  and  $\varphi_U$ , we obtain the very compact expressions

$$\begin{aligned} \langle \varphi_I \rangle &= \bar{A}_0 - \frac{1}{3} \bar{A}_2 (3 \cos^2 \theta_0 - 1); & \langle \varphi_V \rangle &= \bar{A}_1 \cos \theta_0, \\ \langle \varphi_Q \rangle &= \bar{A}_2 \sin^2 \theta_0 \cos 2\phi_0; & \langle \varphi_U \rangle &= \langle \varphi_Q \rangle \tan 2\phi_0, \end{aligned} \quad (2.16)$$

where

$$\begin{aligned} \bar{A}_0 &= \langle A_0(x, a, B) \rangle, \\ \bar{A}_1 &= \langle A_1(x, a, B) \cos \Theta \rangle, \\ \bar{A}_2 &= \langle A_2(x, a, B) \frac{1}{2} (3 \cos^2 \Theta - 1) \rangle. \end{aligned} \quad (2.17)$$

The notation  $\langle \rangle$  represents an integration over  $\Theta$  and  $B$  weighted by the azimuthal average of the magnetic field distribution. This result is quite general and can be used for any random field distribution, provided it is invariant in rotations about the mean magnetic field direction. We have similar expressions for the  $\chi_{Q,U,V}$  with the  $\varphi_q$  replaced by the  $f_q$ . Since  $\langle \varphi_U \rangle$  is simply related to  $\langle \varphi_Q \rangle$ , (see Eq. (2.16)) we do not consider it in the following.

With the PDF considered here (see Eqs. (2.1) or (2.3)), the mean coefficients have the same symmetry properties as the non-random coefficients, namely  $\langle\varphi_I\rangle$  and  $\langle\varphi_Q\rangle$  are symmetric with respect to the line center  $x = 0$  (they are even functions of  $x$ ) and  $\langle\varphi_V\rangle$  is antisymmetric (odd function of  $x$ ). We stress also that the integrals of  $\langle\varphi_I\rangle$  and  $\langle\varphi_Q\rangle$  over frequency are not affected by turbulence. Hence if one consider only the integration over  $x \geq 0$ , the integral of  $\langle\varphi_Q\rangle$  is zero and the integral of  $\langle\varphi_I\rangle$  equal to 1/2.

### 2.3 Fluctuations parallel to the mean field (1D turbulence)

When fluctuations are along the direction of the mean field  $\mathbf{B}_0$ , the PDF for the random field can be written as

$$P_L(\mathbf{B}) d\mathbf{B} = \frac{1}{(2\pi)^{1/2}\sigma} \exp\left[-\frac{(B - B_0)^2}{2\sigma^2}\right] dB, \quad (2.18)$$

where  $B$  is the 1D random magnetic field which varies between  $-\infty$  and  $+\infty$  and  $\sigma = [(\langle(B - B_0)^2\rangle)]^{1/2} = [\langle B^2\rangle - B_0^2]^{1/2}$  is the square-root of the dispersion (or variance) around the mean field  $B_0$ , also known as the standard deviation or rms fluctuations. The factor 2 ensures that  $\sigma$  is exactly the rms fluctuation defined as above. This distribution is normalized to unity. It can be obtained from Eq. (2.1) by integrating over the transverse component of the magnetic field. To simplify the notation, we have set  $\sigma_L = \sigma$ . We note that the Gaussian tends to a Dirac distribution when  $\sigma \rightarrow 0$ . Thus for  $\sigma = 0$ , the magnetic field is non-random and equal to the mean field  $\mathbf{B}_0$ .

We introduce the new dimensionless variable  $y$  and the parameters  $y_0$  and  $\gamma_B$  defined by

$$y = \frac{B}{\sqrt{2}\sigma}; \quad y_0 = \frac{B_0}{\sqrt{2}\sigma}; \quad \gamma_B = \Delta_Z \sqrt{2}\sigma, \quad (2.19)$$

where the constant  $\Delta_Z$  is defined in Eq. (2.8). These dimensionless quantities will also be used in the case of isotropic and 2D turbulence. The variable  $y$  and the parameter  $y_0$  measure the random field and mean field in units of the standard deviation. The random Zeeman displacement is  $\Delta_Z B = y\gamma_B$  and the Zeeman shift by the mean field is  $\Delta_Z B_0 = y_0\gamma_B$ . The variable  $\gamma_B$  represents the rms fluctuations  $\sigma$  converted to Zeeman shift in Doppler width units. In these new variables,  $\varphi_q$  can be written as

$$\varphi_q(x, a, y) = \frac{a}{\pi^{3/2}} \int_{-\infty}^{+\infty} \frac{e^{-u^2}}{(x - q\gamma_B y - u)^2 + a^2} du, \quad (2.20)$$

and the distribution function becomes

$$P_L(\mathbf{B}) d\mathbf{B} = \frac{1}{\sqrt{\pi}} e^{-(y-y_0)^2} dy, \quad \text{for } -\infty \leq y \leq +\infty. \quad (2.21)$$

To calculate the mean absorption coefficients it suffices to take the average of the  $A_i$  over  $B$  in Eq. (2.11) since the random field is along the direction  $\theta_0, \phi_0$ . This procedure is equivalent to set  $\cos \Theta = 1$  in Eq. (2.17). The averaging over the magnetic field distribution amounts to the convolution product of a Voigt function with a Gaussian coming from the distribution of the magnetic field strength. The effect is similar to a broadening by a Gaussian turbulent velocity field, except that it does not affect the  $\varphi_0$  term (the  $\pi$ -component) since the latter does not depend on the strength of the magnetic field. One obtains (see Appendix B)

$$\begin{aligned}\bar{A}_0 &= \frac{1}{3} \sum_{q=-1}^{q=+1} \frac{1}{\gamma_q} H(\bar{x}_q, \bar{a}_q), \quad q = 0, \pm 1, \\ \bar{A}_1 &= \frac{1}{2} \sum_{q=\pm 1} q \frac{1}{\gamma_q} H(\bar{x}_q, \bar{a}_q), \\ \bar{A}_2 &= \frac{1}{4} \sum_{q=-1}^{q=+1} (2 - 3q^2) \frac{1}{\gamma_q} H(\bar{x}_q, \bar{a}_q), \quad q = 0, \pm 1,\end{aligned}\tag{2.22}$$

where  $H$  is the Voigt function introduced in Eq. (2.6),

$$\bar{x}_q = \frac{x - q\Delta_Z B_0}{\gamma_q}, \quad \bar{a}_q = \frac{a}{\gamma_q},\tag{2.23}$$

and

$$\gamma_q = \sqrt{1 + q^2 \gamma_B^2}; \quad q = 0, \pm 1.\tag{2.24}$$

We see that  $\gamma_1$  is a broadening parameter which combines the Doppler and magnetic field effects. Note that  $\gamma_0 = 1$ ,  $\bar{x}_0 = x$  and  $\bar{a}_0 = a$ . The  $\varphi_0$  term is not modified as already mentioned above. Note also that the functions  $H(\bar{x}_q, \bar{a}_q)/\gamma_q$  are normalized to unity (their integral over  $x$  is unity).

The broadening of the  $\sigma$ -components can be described in terms of a total Doppler width  $\Delta_C$  that combines the effects of thermal, velocity and magnetic field broadening. It can be written as

$$\Delta_C = \sqrt{\Delta\nu_D^2 + g^2 \left(\frac{e}{4\pi m}\right)^2 2\sigma^2},\tag{2.25}$$

where  $\Delta\nu_D$  is the Doppler width defined in Eq. (2.9).

When the Zeeman shift by the mean magnetic field  $\Delta_Z B_0$  is smaller than the combined Doppler and magnetic broadening ( $\Delta_Z B_0 \ll \gamma_1$ ), a situation referred to as the *weak field*

limit, as in DP72, one has, to the leading order

$$\begin{aligned}\bar{A}_0 &\simeq \frac{1}{3} \left[ H(x, a) + \frac{2}{\gamma_1} H\left(\frac{x}{\gamma_1}, \frac{a}{\gamma_1}\right) \right], \\ \bar{A}_1 &\simeq \frac{2\Delta_z B_0}{\gamma_1^3} \left[ x H\left(\frac{x}{\gamma_1}, \frac{a}{\gamma_1}\right) - a F\left(\frac{x}{\gamma_1}, \frac{a}{\gamma_1}\right) \right], \\ \bar{A}_2 &\simeq \frac{1}{2} \left[ H(x, a) - \frac{1}{\gamma_1} H\left(\frac{x}{\gamma_1}, \frac{a}{\gamma_1}\right) \right].\end{aligned}\quad (2.26)$$

When the mean field  $\mathbf{B}_0$  is zero, the circular polarization is zero but not the linear polarization unless the random field fluctuations are along the LOS ( $\theta_0 = 0^\circ$ ). The mean diagonal absorption coefficient is given by

$$\langle \varphi_I \rangle = \frac{1}{2} H(x, a) \sin^2 \theta_0 + \frac{1}{2\gamma_1} H\left(\frac{x}{\gamma_1}, \frac{a}{\gamma_1}\right) (1 + \cos^2 \theta_0). \quad (2.27)$$

To summarize, in the case of longitudinal fluctuations, the mean absorption coefficients have the same form as the original coefficients given in Eqs. (2.5) or (2.10) but the  $\sigma$ -components are broadened by the random magnetic field while the  $\pi$ -components are not affected. Mean coefficients for longitudinal fluctuations are shown in § 2.5.2 and compared to the mean coefficients for 2D and 3D turbulence.

## 2.4 Isotropic fluctuations (3D turbulence)

We now assume that the fluctuations of the magnetic field are isotropically distributed. This implies that  $\sigma_L = \sigma_T$  in Eq. (2.1). The PDF takes the form

$$P_1(\mathbf{B}) d\mathbf{B} = \frac{1}{(2\pi)^{3/2} \sigma^3} \exp\left[-\frac{(\mathbf{B} - \mathbf{B}_0)^2}{2\sigma^2}\right] B^2 \sin \Theta dB d\Theta d\Psi. \quad (2.28)$$

Here  $B$ , the strength of the magnetic field, varies from 0 to  $\infty$ . The rms fluctuations are  $[\langle (\mathbf{B} - \mathbf{B}_0)^2 \rangle]^{1/2} = [\langle B^2 \rangle - B_0^2]^{1/2} = \sqrt{3}\sigma$ . In terms of the dimensionless parameters introduced in Eq. (2.19), the distribution function becomes

$$P_1(\mathbf{B}) d\mathbf{B} = \frac{1}{\pi^{3/2}} e^{-(y_0^2 + y^2)} e^{2y_0 y \cos \Theta} y^2 dy \sin \Theta d\Theta d\Psi, \quad (2.29)$$

where  $y$  varies from 0 to  $\infty$ , the angle  $\Theta$  from 0 to  $\pi$  and  $\Psi$  from 0 to  $2\pi$ . The azimuthal average of this distribution is simply given by the r.h.s. of Eq. (2.29) without the  $d\Psi$ .

### 2.4.1 Exact and approximate expressions for the mean coefficients

We now calculate the  $\bar{A}_i$  defined in Eq. (2.17). Introducing the variable  $\mu = \cos \Theta$ , we can write

$$\bar{A}_i = \frac{2}{\sqrt{\pi}} \int_0^\infty e^{-(y_0^2+y^2)} A_i(x, a, \sqrt{2}\sigma y) y^2 \int_{-1}^{+1} e^{2y_0 y \mu} c_i(\mu) d\mu dy, \quad (2.30)$$

where

$$c_0(\mu) = 1, \quad c_1(\mu) = \mu, \quad c_2(\mu) = \frac{1}{2}(3\mu^2 - 1). \quad (2.31)$$

The integration over  $\mu$  can be carried out explicitly. Regrouping the exponential terms  $e^{-(y_0^2+y^2)}$  and  $e^{2y_0 y}$  and then taking advantage of the symmetries with respect to a change  $y$  into  $-y$ , one obtains

$$\bar{A}_0 = \frac{2}{3\sqrt{\pi}} \sum_{q=-1}^{q=+1} \frac{1}{2y_0} \int_{-\infty}^{+\infty} e^{-(y-y_0)^2} H(x - q\gamma_B y, a) y dy, \quad (2.32)$$

$$\bar{A}_1 = \frac{1}{\sqrt{\pi}} \sum_{q=\pm 1} q \frac{1}{2y_0} \int_{-\infty}^{+\infty} e^{-(y-y_0)^2} H(x - q\gamma_B y, a) \left( y - \frac{1}{2y_0} \right) dy, \quad (2.33)$$

$$\bar{A}_2 = \frac{1}{2\sqrt{\pi}} \sum_{q=-1}^{q=+1} (2 - 3q^2) \frac{1}{2y_0} \int_{-\infty}^{+\infty} e^{-(y-y_0)^2} H(x - q\gamma_B y, a) \left( y - \frac{3}{2y_0} + \frac{3}{4y_0^2 y} \right) dy. \quad (2.34)$$

These equations, which are of the convolution type, were first given in DP79. Note that  $y$  varies from  $-\infty$  to  $+\infty$ . For the anomalous dispersion coefficients we have similar relations where the Voigt functions  $H$  are replaced by the Faraday-Voigt functions  $F$ .

As shown in Appendix B, the  $\bar{A}_i$  can be expressed in terms of the generalized Voigt and Faraday-Voigt functions  $H^{(n)}$  and  $F^{(n)}$  defined by

$$H^{(n)}(x, a) = \frac{a}{\pi^{3/2}} \int_{-\infty}^{+\infty} \frac{u^n e^{-u^2}}{(x-u)^2 + a^2} du, \quad (2.35)$$

$$F^{(n)}(x, a) = \frac{1}{\pi^{3/2}} \int_{-\infty}^{+\infty} \frac{u^n (x-u) e^{-u^2}}{(x-u)^2 + a^2} du. \quad (2.36)$$

They were introduced in DP72 where the  $F^{(n)}$  are denoted  $G^{(n)}$  (in DP79 they are denoted  $Q^{(n)}$ ). For  $n = 0$ , one recovers the usual Voigt and Faraday-Voigt functions. The functions  $H^{(n)}$  and  $F^{(n)}$  are plotted in Fig. 2.2 for  $a = 0$ ,  $n = 0, 1, 2$ . They can be calculated with recurrence relations given in Chapter 3 which take particularly simple forms for  $a = 0$ . In particular

$$H^{(n)}(x, 0) = \frac{1}{\sqrt{\pi}} x^n e^{-x^2}. \quad (2.37)$$

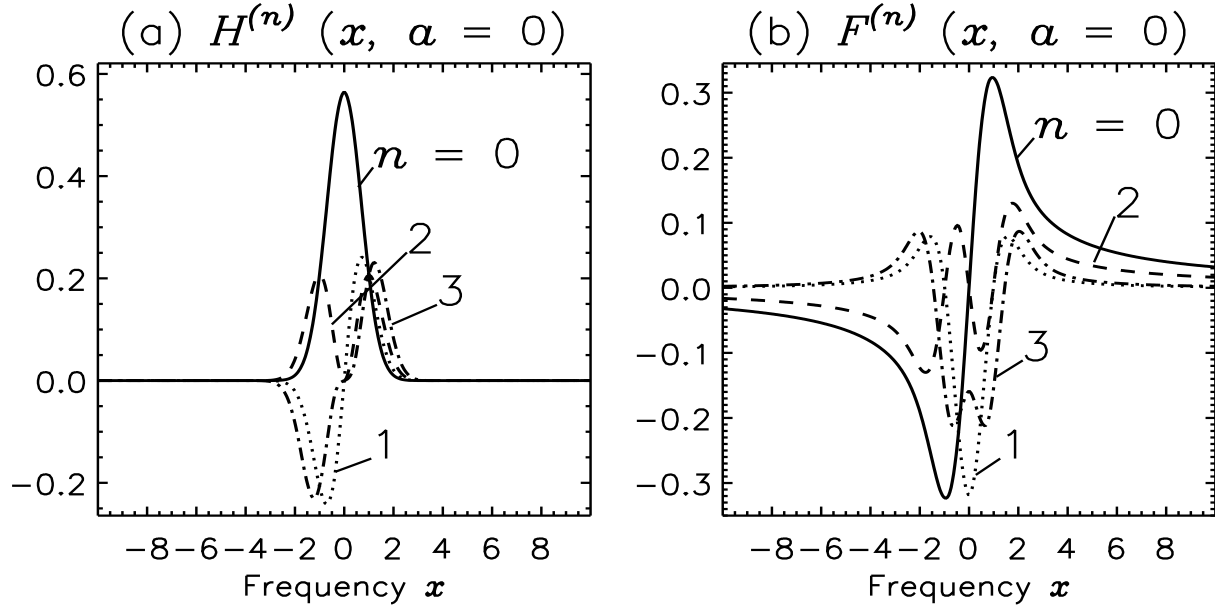


Figure 2.2: The  $H^{(n)}$  and  $F^{(n)}$  functions for several orders  $n$ . The damping parameter  $a = 0$ . The  $H^{(n)}$  are even functions when  $n$  is even and odd when  $n$  is odd. For the  $F^{(n)}$  it is the opposite.

We also note that the  $H^{(n)}$  and  $F^{(n)}$  functions are simply related to the derivatives of the Voigt and Faraday-Voigt functions (see Chapter 3).

The functions  $\bar{A}_0$  and  $\bar{A}_1$  have closed form (i.e. exact) expressions in terms of the  $H^{(n)}$  but not  $\bar{A}_2$  for which only approximate expressions can be given because of the term with  $1/y$  (see Eq. (2.34)). The exact expressions for  $\bar{A}_0$  and  $\bar{A}_1$  are

$$\bar{A}_0 = \frac{1}{3} \sum_{q=-1}^{q=+1} \frac{1}{\gamma_q} \left[ H^{(0)}(\bar{x}_q, \bar{a}_q) + q \frac{\gamma_B}{y_0 \gamma_q} H^{(1)}(\bar{x}_q, \bar{a}_q) \right], \quad (2.38)$$

$$\bar{A}_1 = \frac{1}{2} \sum_{q=\pm 1} q \frac{1}{\gamma_q} \left[ \left( 1 - \frac{1}{2y_0^2} \right) H^{(0)}(\bar{x}_q, \bar{a}_q) + q \frac{\gamma_B}{y_0 \gamma_q} H^{(1)}(\bar{x}_q, \bar{a}_q) \right], \quad (2.39)$$

where  $\bar{x}_q$  and  $\bar{a}_q$  have been defined in Eq. (2.23).

For  $\bar{A}_2$ , approximate expressions can be constructed in the limiting cases  $y_0 \gg 1$  and  $y_0 \ll 1$ , which we refer to respectively as the strong mean field and weak mean field limits for reasons explained now. We discuss these two cases separately.

### Strong mean field limit

When the mean field strength  $B_0$  is much larger than the rms fluctuations, i.e. when  $B_0 \gg \sqrt{2}\sigma$ , one has  $y_0 \gg 1$ . In this case the Zeeman shift  $\Delta_Z B_0$  by the mean magnetic field is much larger than the broadening  $\gamma_B = \Delta_Z \sqrt{2}\sigma$  by the random magnetic field fluctuations. We call this situation the *strong mean field* limit but it can also be viewed as a weak turbulence limit. When  $y_0 \gg 1$ , one can neglect the term  $3/4y_0^2y$  in Eq. (2.34) and thus obtain

$$\bar{A}_2^{\text{st}} \simeq \frac{1}{4} \sum_{q=-1}^{q=+1} \frac{1}{\gamma_q} (2 - 3q^2) \left[ \left(1 - \frac{3}{2y_0^2}\right) H^{(0)}(\bar{x}_q, \bar{a}_q) + q \frac{\gamma_B}{y_0 \gamma_q} H^{(1)}(\bar{x}_q, \bar{a}_q) \right], \quad (2.40)$$

where the superscript “st” stands for strong.

We remark here that if we keep  $\gamma_B$  finite but let  $y_0 \rightarrow \infty$ , we recover the longitudinal turbulence case discussed in the preceding section. This can be checked on Eqs. (2.38) to (2.40).

### Weak mean field limit

We now consider the case where  $y_0 \ll 1$ . This means that the Zeeman shift by the mean field satisfies  $\Delta_Z B_0 \ll \gamma_B$ . Since  $\gamma_B < \gamma_1$ , this condition automatically implies that the mean Zeeman shift is smaller than the combined Doppler and Zeeman broadening. Thus in this limit, which we refer to as *weak mean field limit*, the mean magnetic field is too weak for the  $\sigma$ -components to be resolved. The best method to obtain the mean absorption coefficients is to start from Eq. (2.30) and expand the exponentials  $\exp(-y_0^2)$  and  $\exp(2y_0y)$  in powers of  $y_0$ . Using the change of variables described in Appendix B with  $y_0 = 0$ , one obtains at the leading order,

$$\bar{A}_2^{\text{w}} \simeq y_0^2 \frac{1}{5} \left\{ H^{(0)}(x, a) - \frac{1}{\gamma_1^6} \left[ H^{(0)}\left(\frac{x}{\gamma_1}, \frac{a}{\gamma_1}\right) + 2\gamma_B^2 H^{(2)}\left(\frac{x}{\gamma_1}, \frac{a}{\gamma_1}\right) + \frac{4}{3}\gamma_B^4 H^{(4)}\left(\frac{x}{\gamma_1}, \frac{a}{\gamma_1}\right) \right] \right\}, \quad (2.41)$$

where the superscript “w” stands for weak. The important point is that  $\bar{A}_2^{\text{w}}$  is of order  $y_0^2$ . This point has already been made in DP72 and DP79 but the full expression was not given.

For the functions  $\bar{A}_0$  and  $\bar{A}_1$ , the expansion in powers of  $y_0$  yields

$$\bar{A}_0^{\text{w}} \simeq \frac{1}{3} \sum_{q=-1}^{q=+1} \frac{1}{\gamma_q^3} \left[ H^{(0)}\left(\frac{x}{\gamma_q}, \frac{a}{\gamma_q}\right) + 2q^2 \gamma_B^2 H^{(2)}\left(\frac{x}{\gamma_q}, \frac{a}{\gamma_q}\right) \right], \quad (2.42)$$

$$\bar{A}_1^w \simeq \frac{2y_0\gamma_B}{\gamma_1^4} \left[ H^{(1)} \left( \frac{x}{\gamma_1}, \frac{a}{\gamma_1} \right) + \frac{2}{3}\gamma_B^2 H^{(3)} \left( \frac{x}{\gamma_1}, \frac{a}{\gamma_1} \right) \right]. \quad (2.43)$$

Note that  $\bar{A}_1^w$  is proportional to  $y_0\gamma_B$ , i.e. to the shift  $\Delta_Z B_0$  by the mean magnetic field.

In this weak field limit the mean value of the absorption coefficient  $\varphi_I$  is simply given by  $\langle \varphi_I \rangle \simeq \bar{A}_0^w$  since the contribution from  $\bar{A}_2^w$ , which is of order  $y_0^2$ , can be neglected. Thus  $\langle \varphi_I \rangle$  is independent of the direction of the mean field. This property holds also when the mean field is constant. The proof given here is an alternative to the standard method which relies on a Taylor series expansion of the Voigt function (Jefferies et al. 1989, Stenflo 1994, LL04).

When the total broadening of the line is controlled by Doppler broadening, i.e. when  $\gamma_B = \Delta_Z \sqrt{2}\sigma \ll 1$ , one can set  $\gamma_1 = 1$ . Equations (2.42) and (2.43) lead to the standard results  $\varphi_I \simeq H(x, a)$  and  $\varphi_V \simeq 2\Delta_Z B_0 H^{(1)}(x, a) = -\Delta_Z B_0 \partial H^{(0)}(x, a) / \partial x$ .

### Zero mean field

When the mean magnetic field is zero, the angular averaging over  $\Theta$  and  $\Psi$  (or  $\theta$  and  $\phi$  in the original variables) becomes independent of the averaging over the magnitude of the magnetic field. Because of the isotropy assumption,  $\bar{A}_1 = \bar{A}_2 = 0$  and the polarization is zero, namely  $\langle \varphi_{Q,U,V} \rangle = 0$  and  $\langle \chi_{Q,U,V} \rangle = 0$ . The diagonal absorption coefficient is given by  $\langle \varphi_I \rangle = \bar{A}_0^w$  with  $\bar{A}_0^w$  equal to the r.h.s. of Eq. (2.42). One can verify that our result is identical to the last equation in § 9.25 of LL04. There  $\langle \varphi_I \rangle$  is written in terms of the second order derivative of the Voigt function.

### 2.4.2 Profiles of the mean coefficients in the weak and strong mean field limits

In Figs. 2.3 to 2.5 we show the effects of an isotropic distribution with a non-zero mean field on the absorption and anomalous dispersion coefficients  $\varphi_{I,Q,V}$  and  $\chi_{Q,V}$ . We discuss separately the weak and strong mean field limits. The results are presented for the damping parameter  $a = 0$ .

#### Weak mean field profiles

In the weak mean field limit,  $\langle \varphi_I \rangle = \bar{A}_0^w$ , up to terms of order  $y_0^2$ ,  $\langle \varphi_V \rangle = \bar{A}_1^w \cos \theta_0$ , up to terms of order  $y_0^3$ , and  $\langle \varphi_Q \rangle$  which is order of  $y_0^2$  can be neglected. As already mentioned above,  $\langle \varphi_I \rangle$  is independent of the mean field direction. We show in Fig. 2.3 the profiles of  $\langle \varphi_I \rangle$  and  $\langle \varphi_V \rangle$  for  $\theta_0 = 0^\circ$  calculated with  $\Delta_Z B_0 = 0.1$  and  $\gamma_B = 1, 2, 3$ . With



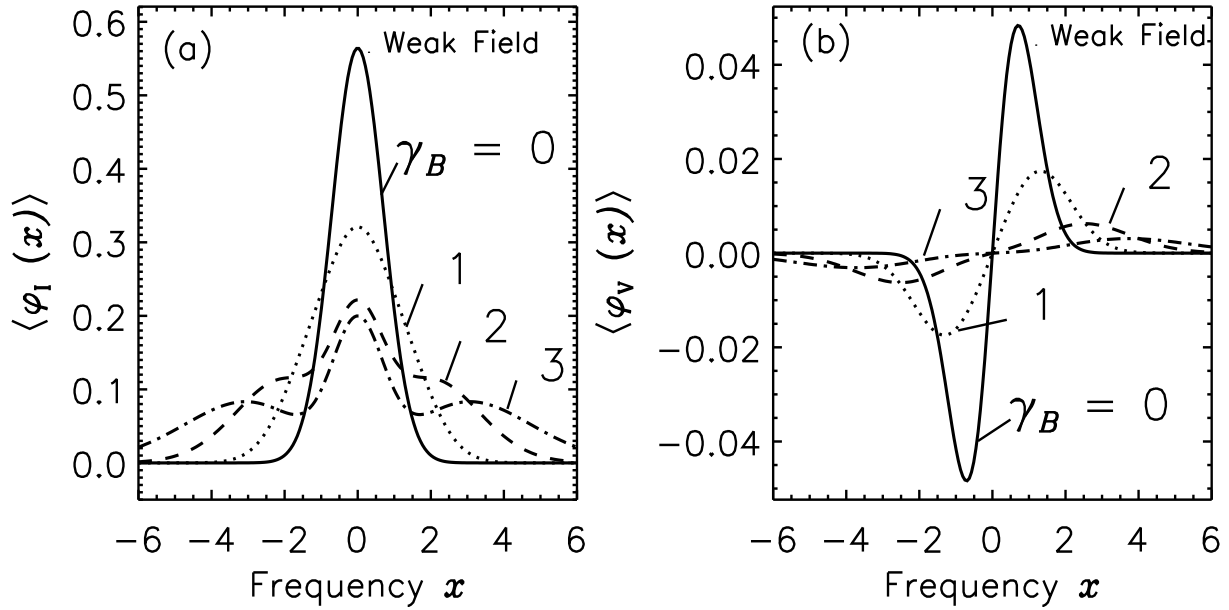


Figure 2.3: Weak mean field limit. Isotropic fluctuations. Absorption coefficients  $\langle \varphi_{I,V} \rangle$  for a longitudinal mean magnetic field are shown. Mean Zeeman shift  $\Delta_Z B_0 = 0.1$ ; Voigt parameter  $a = 0$ . The curve  $\gamma_B = 0$  corresponds to a constant magnetic field equal to  $B_0$ .

this choice of parameters, we satisfy the weak mean field condition since  $y_0 = \Delta_Z B_0 / \gamma_B$  stays smaller than unity. As can be observed in Fig. 2.3a the increase of  $\gamma_B$  produces two different effects on  $\langle \varphi_I \rangle$ . There is a global decrease in amplitude due to the factor  $1/\gamma_1^3$  in front of the square bracket in Eq. (2.42) and the appearance of two shoulders created by the increasing contribution of the term with  $H^{(2)}$ . They are clearly visible for  $\gamma_B = 3$ . The position and amplitude of these shoulders can be deduced from the behavior of  $H^{(2)}$ . Equation (2.37) shows that the  $H^{(n)}$  have maxima at  $x_{\max}^{(n)} = \pm \sqrt{n/2}$ . A rescaling of frequency by the factor  $\gamma_1$ , predicts that the position of these shoulders is around  $|x| \simeq \gamma_1$  and their amplitude around  $(\gamma_B^2 / \gamma_1^3)(4/3e\sqrt{\pi})$ , in agreement with the numerical results. These shoulders are a manifestation of the  $\sigma$ -components which appear with increasing probability when  $\gamma_B$ , i.e. the dispersion  $\sigma$  of the random magnetic field, increases.

### Strong mean field profiles

In this limit  $\langle \varphi_{I,Q,V} \rangle$  are given by Eq. (2.16) with  $\bar{A}_0, \bar{A}_1$  given by the exact expressions in Eqs. (2.38), (2.39) and  $\bar{A}_2$  given by the approximate relation (2.40). Thus errors that can be created by this approximation will all come from  $\bar{A}_2$  and affect only  $\langle \varphi_Q \rangle$  and to a lesser extent than  $\langle \varphi_I \rangle$ . For  $\langle \varphi_V \rangle$  we are using an exact expression. Figures 2.4 and 2.5 illustrate

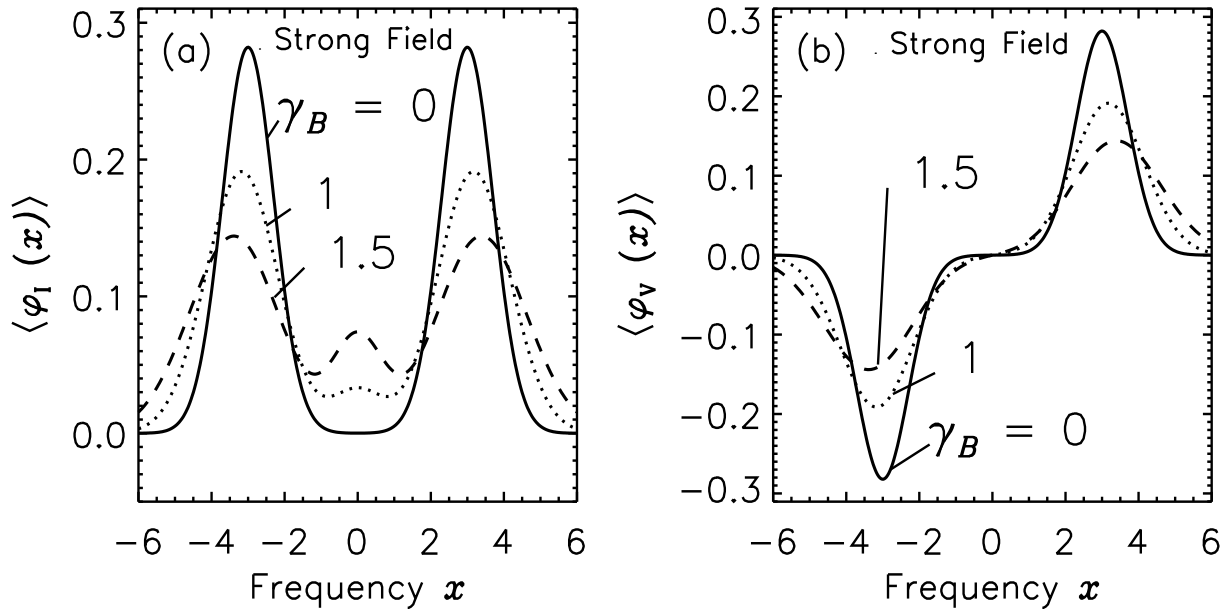


Figure 2.4: Strong mean field limit. Isotropic fluctuations. Absorption coefficients  $\langle \varphi_I \rangle$  and  $\langle \varphi_V \rangle$  for a longitudinal mean magnetic field ( $\theta_0 = 0^\circ$ ) are shown. Mean Zeeman shift  $\Delta_Z B_0 = 3$ ; Voigt parameter  $a = 0$ . The curve  $\gamma_B = 0$  corresponds to a constant magnetic field equal to  $B_0$ .

the variations of  $\langle \varphi_I \rangle$ ,  $\langle \varphi_Q \rangle$  and  $\langle \varphi_V \rangle$  with the parameter  $\gamma_B$ . To satisfy the strong field condition ( $y_0 = \Delta_Z B_0 / \gamma_B \gg 1$ ), we have chosen  $\Delta_Z B_0 = 3$  and kept  $\gamma_B$  smaller than 1.5. The variations of  $\langle \varphi_I \rangle$  are more easy to understand if we expand the sums over  $q$  in Eqs. (2.38) and (2.40). This gives

$$\begin{aligned}
\langle \varphi_I \rangle &\simeq \frac{1}{3} H(x, a) \left[ 1 - \frac{1}{2} (3 \cos^2 \theta_0 - 1) \left( 1 - \frac{3}{2y_0^2} \right) \right] + \frac{1}{3\gamma_1} [H(\bar{x}_{+1}, \bar{a}) + H(\bar{x}_{-1}, \bar{a})] \\
&\times \left[ 1 + \frac{1}{4} (3 \cos^2 \theta_0 - 1) \left( 1 - \frac{3}{2y_0^2} \right) \right] + \frac{1}{3} \frac{\gamma_B}{y_0 \gamma_1^2} [H^{(1)}(\bar{x}_{+1}, \bar{a}) - H^{(1)}(\bar{x}_{-1}, \bar{a})] \\
&\times \left[ 1 + \frac{1}{4} (3 \cos^2 \theta_0 - 1) \right]. \tag{2.44}
\end{aligned}$$

To simplify the notation we have used  $H^{(0)}(x, a) = H(x, a)$ ,  $\bar{a}_{\pm 1} = \bar{a}$  and  $\bar{a}_0 = a$ .

The term containing  $H(x, a)$  creates a central component even when the mean field is longitudinal ( $\theta_0 = 0^\circ$ ). The existence of this central component, which has no polarization counterpart, was pointed out in DP72. It is created by the averaging of the  $\pi$ -component opacity  $\varphi_0 \sin^2 \theta / 2$  over the isotropic random magnetic field distribution. When  $\theta_0 = 0^\circ$ , this central component behaves as  $H(x, a) / 2y_0^2$ . It becomes clearly visible when  $\gamma_B = 1.5$

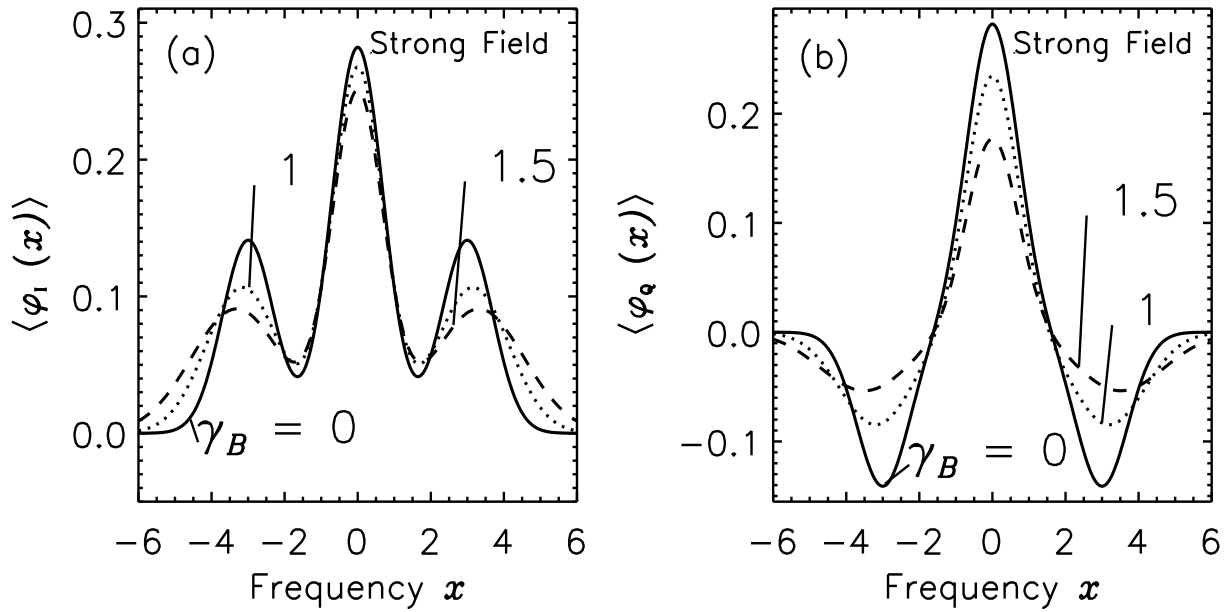


Figure 2.5: Strong mean field limit. Isotropic fluctuations. Mean values of  $\langle \varphi_I \rangle$  and  $\langle \varphi_Q \rangle$  for a transverse mean magnetic field ( $\theta_0 = 90^\circ$ ). Same parameters as in Fig. 2.4 ( $\Delta_Z B_0 = 3$ ;  $a = 0$ ).

(i.e.  $y_0 = 2$ ). In Fig. 2.4 it increases with  $\gamma_B$  because we are keeping the product  $y_0 \gamma_B = \Delta_Z B_0$  constant. When  $\theta_0 = 90^\circ$ , this component behaves as  $(1 - 1/2y_0^2)H(x, a)/2$ . As can be seen in Fig 2.5, it is not very sensitive to the value of  $\gamma_B$ .

The  $\sigma$ -components come mainly from the second term in Eq. (2.44). They vary like  $(1 - 1/2y_0^2)H(\bar{x}_{\pm 1}, \bar{a})/2\gamma_1$  for  $\theta_0 = 0^\circ$  and as  $(1 + 1/2y_0^2)H(\bar{x}_{\pm 1}, \bar{a})/4\gamma_1$  for  $\theta_0 = 90^\circ$ . Thus, an increase in  $\gamma_B$  produces a broadening of the components and a decrease in their peak value. There is also a shift away from line center more specifically due to the increase of the relative importance of the  $H^{(1)}$  terms with respect to the  $H$  terms.

The mean coefficients  $\langle \varphi_V \rangle$  and  $\langle \varphi_Q \rangle$  are given by  $\langle \varphi_V \rangle = \bar{A}_1 \cos \theta_0$  and  $\langle \varphi_Q \rangle \simeq \bar{A}_2^{\text{st}} \sin^2 \theta_0 \cos 2\phi_0$  with  $\bar{A}_1$  and  $\bar{A}_2^{\text{st}}$  given in Eqs. (2.39) and (2.40). The profiles shown in Figs. 2.4 and 2.5 are easy to understand. The dominant contributions come from the terms with  $H^{(0)}(\bar{x}_q, \bar{a}_q)$ ,  $q = 0, \pm 1$ . For  $\langle \varphi_V \rangle$ , the  $\sigma$ -components behave essentially as  $(1 - 1/2y_0^2)H^{(0)}(\bar{x}_{\pm 1}, \bar{a})/2\gamma_1$ , i.e as the  $\sigma$ -components of  $\langle \varphi_I \rangle$ . Hence their amplitude decreases and their width increases when  $\gamma_B$  increases. For  $\langle \varphi_Q \rangle$ , the  $\sigma$ -components behave as  $-(1 - 3/2y_0^2)H^{(0)}(\bar{x}_{\pm 1}, \bar{a})/4\gamma_1$  and the central component as  $(1 - 3/2y_0^2)H^{(0)}(x, a)/2$ , to be compared to  $(1 - 1/2y_0^2)H^{(0)}(x, a)/2$  for  $\langle \varphi_I \rangle$ . Hence as observed in Fig. 2.5, the central component of  $\langle \varphi_Q \rangle$  is more sensitive to the value of  $\gamma_B$  than the central component of  $\langle \varphi_I \rangle$ .

### 2.4.3 The general case of arbitrary mean fields - Numerical evaluations

We now discuss the behavior of the mean opacity coefficients when  $y_0 = B_0/\sqrt{2}\sigma$  is of order unity. For  $\bar{A}_0$  and  $\bar{A}_1$  we have exact expressions given in Eqs. (2.38) and (2.39) but there is nothing similar for  $\bar{A}_2$ . Roughly, the weak field limit is valid for  $y_0 < 0.1$  to  $0.2$  and the strong field limit for  $y_0 > 2$ . Hence for  $y_0$  of order unity, neither the weak nor the strong mean field approximation holds and  $\langle\varphi_I\rangle$  and  $\langle\varphi_Q\rangle$  must be calculated numerically. For the numerical calculations it is preferable to return to Eq. (2.30). The integration over  $\mu$  can be carried out explicitly. One obtains, for the mean absorption profile,

$$\begin{aligned} \langle\varphi_I(x, a)\rangle &= \frac{4}{3} \frac{1}{\sqrt{\pi}} e^{-y_0^2} \int_0^\infty e^{-y^2} y^2 \sqrt{\frac{\pi}{4y_0y}} \left\{ \left[ I_{1/2}(2y_0y) - \frac{1}{2} I_{5/2}(2y_0y) (3 \cos^2 \theta_0 - 1) \right] \right. \\ &\quad \times H(x, a) + \left[ I_{1/2}(2y_0y) + \frac{1}{4} I_{5/2}(2y_0y) (3 \cos^2 \theta_0 - 1) \right] \\ &\quad \left. \times [H(x - \gamma_B y, a) + H(x + \gamma_B y, a)] \right\} dy, \end{aligned} \quad (2.45)$$

for the mean linear polarization profile

$$\begin{aligned} \langle\varphi_Q(x, a)\rangle &= \sin^2 \theta_0 \cos 2\phi_0 \frac{2}{\sqrt{\pi}} e^{-y_0^2} \int_0^\infty e^{-y^2} y^2 \sqrt{\frac{\pi}{4y_0y}} I_{5/2}(2y_0y) \\ &\quad \times \left\{ H(x, a) - \frac{1}{2} [H(x - \gamma_B y, a) + H(x + \gamma_B y, a)] \right\} dy, \end{aligned} \quad (2.46)$$

and for the mean circular polarization,

$$\langle\varphi_V(x, a)\rangle = \cos \theta_0 \frac{4}{\sqrt{\pi}} e^{-y_0^2} \int_0^\infty e^{-y^2} y^2 \sqrt{\frac{\pi}{4y_0y}} I_{3/2}(2y_0y) \frac{1}{2} [H(x - \gamma_B y, a) - H(x + \gamma_B y, a)] dy. \quad (2.47)$$

The  $I_{l+\frac{1}{2}}$  are the modified spherical Bessel functions of fractional order (Abramowitz & Stegun 1964, p. 443). They have explicit expressions in terms of hyperbolic functions (see Appendix C). In  $\langle\varphi_I\rangle$  the terms with  $I_{1/2}$  come from  $\bar{A}_0$  and the terms with  $I_{5/2}$  from  $\bar{A}_2$ . These expressions are a bit bulky but clearly show the coefficients of the  $\pi$  and  $\sigma$ -components and how they differ from the coefficients in Eq. (2.5).

The integration over  $y$  is performed numerically using a Gauss-Legendre quadrature formula. The integrand varies essentially as  $e^{-y^2} e^{2y_0y}$ , with the factor  $e^{2y_0y}$  coming from the Bessel function. The maximum of the integrand is around  $y = y_0$ . With 10 to 30 points in the range  $[0, 2y_0]$  we can calculate the integrals with a very good accuracy (errors around  $10^{-6}$ ). The averaging process increases the overall frequency spread of the mean coefficients. A total band width  $x_{\max} \approx 4\Delta_Z B_0$  is adequate to represent the full profiles.

In the following sections we discuss the dependence of  $\langle\varphi_I\rangle$  on the strength of the mean field, on its rms fluctuations and on the damping parameter  $a$ . A full section is devoted to  $\langle\varphi_I\rangle$  which has the most complex behavior. Then we discuss the dependence of all the mean coefficients, including the anomalous dispersion coefficients, on the Landé factor for a given random magnetic field. All the calculations have been carried out with a damping parameter  $a = 0$ , except when we consider the dependence on  $a$ .

#### 2.4.4 The mean coefficient $\langle\varphi_I\rangle$

Equation (2.45) shows that  $\langle\varphi_I\rangle$  has a central component around  $x = 0$  which corresponds to the  $\pi$ -component. It is of the form  $H(x, a)$  times a factor which depends on  $y_0$  and on the orientation  $\theta_0$  of the mean magnetic field. When  $y_0$  is small, the Bessel functions can be replaced by their asymptotic expansions around the origin (see Appendix C) and the central component has the approximate expression

$$\langle\varphi_I\rangle_\pi \simeq e^{-y_0^2} \left[ \frac{1}{3} - \frac{y_0^2}{15} (3\cos^2\theta_0 - 1) \right] H(x, a). \quad (2.48)$$

For  $y_0 = 0$  and  $a = 0$  we recover the weak field limit  $\langle\varphi_I\rangle_\pi \simeq e^{-x^2}/3\sqrt{\pi}$ . The two other terms in Eq. (2.45) correspond to the two  $\sigma$ -components, averaged over the random magnetic field. They depend on  $y_0$  and  $\theta_0$  and also on  $\gamma_B = \Delta_Z\sqrt{2}\sigma$ .

#### Dependence on the mean magnetic field strength

We show  $\langle\varphi_I\rangle$  in Fig. 2.6 for different values of  $y_0$ . We keep  $\gamma_B = 1$ , hence  $\Delta_Z B_0 = y_0$ . We cover all the regimes of magnetic splitting from the weak field regime for  $y_0 < 0.1$  to the strong field regime for  $y_0 > 2$ . These two regimes have been discussed in §§ 2.4.1 and 2.4.2. For  $y_0 < 0.1$  there is a single central peak described by the  $H^{(0)}$  terms in Eq. (2.42). There is essentially no contribution from the term with  $H^{(2)}$ . For  $y_0 = 1$ , one is in the intermediate regime described by Eq. (2.45). There is still a single peak because the Zeeman shift  $\Delta_Z B_0 = 1$  is smaller than the broadening parameter  $\gamma_1 = \sqrt{2}$ . Once  $y_0 > 2$ , one enters in the strong field regime, with well separated  $\sigma$ -components at  $x = \pm\Delta_Z B_0 = \pm y_0$ , discussed in detail in § 2.4.2. When  $y_0 \rightarrow \infty$  while  $\gamma_B$  is kept finite, the isotropic distribution goes to the 1D distribution. In the longitudinal case ( $\theta_0 = 0^\circ$ ), the central component goes then to zero and the  $\sigma$ -components to  $H(\bar{x}_{\pm 1}, \bar{a})/2\gamma_1$ , while in the transverse case ( $\theta_0 = 90^\circ$ ), they go to  $H(x, a)/2$  and  $H(\bar{x}_{\pm 1}, \bar{a})/4\gamma_1$ , respectively.

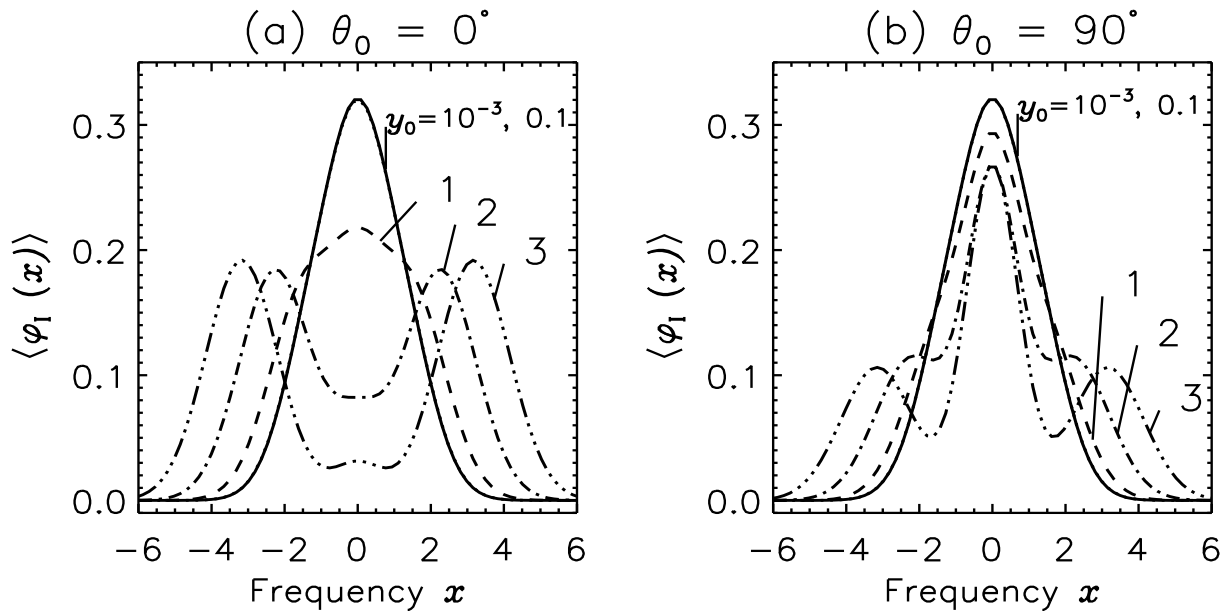


Figure 2.6: Dependence of  $\langle \varphi_I \rangle$  on the mean magnetic field strength measured by the parameter  $y_0$ . Isotropic fluctuations. The parameters used are :  $a = 0$ ,  $\gamma_B = 1$ . The curves for  $y_0 = 10^{-3}$  and  $0.1$  coincide. The panels (a) and (b) correspond to the longitudinal ( $\theta_0 = 0^\circ$ ) and transverse ( $\theta_0 = 90^\circ$ ) cases, respectively.

### Dependence on the magnetic field dispersion

Figure 2.7 shows  $\langle \varphi_I \rangle$  for a fairly strong mean magnetic splitting  $\Delta_Z B_0 = 2$  and several values of  $\gamma_B$  varying from 0 to 6. For  $\gamma_B = 0$  we are in the deterministic case with two well separated  $\sigma$ -components at  $x = \pm \Delta_Z B_0 = \pm 2$ . Their amplitudes are  $H(\Delta_Z B_0, a)/2$  and  $H(\Delta_Z B_0, a)/4$  for  $\theta_0 = 0^\circ$  and  $\theta_0 = 90^\circ$ , respectively. The  $\pi$ -component for  $\theta_0 = 90^\circ$  has an amplitude  $H(0, a)/2 = 1/2\sqrt{\pi}$  since  $a = 0$ . For  $\gamma_B = 1$ , we are still in the strong field regime ( $y_0 = 2$ ) with  $\sigma$ -components still roughly at  $x = \pm \Delta_Z B_0$  but the peaks have smaller amplitude because of the factor  $1/\gamma_1$  in Eq. (2.44). For  $\gamma_B = 3$ , one starts entering into the weak field regime which has been discussed in § 2.4.2 since the corresponding value of  $y_0$  is  $2/3$ .

### Dependence on the damping parameter

Figure 2.8 shows  $\langle \varphi_I \rangle$  for the longitudinal Zeeman effect. Panel (a) is devoted to the strong mean field regime (see also Fig. 2.4) and panel (b) to the weak field regime (see also Fig. 2.3). As long as  $a < 10^{-2}$ , there are no observable effects on the mean value of  $\varphi_I$ . The

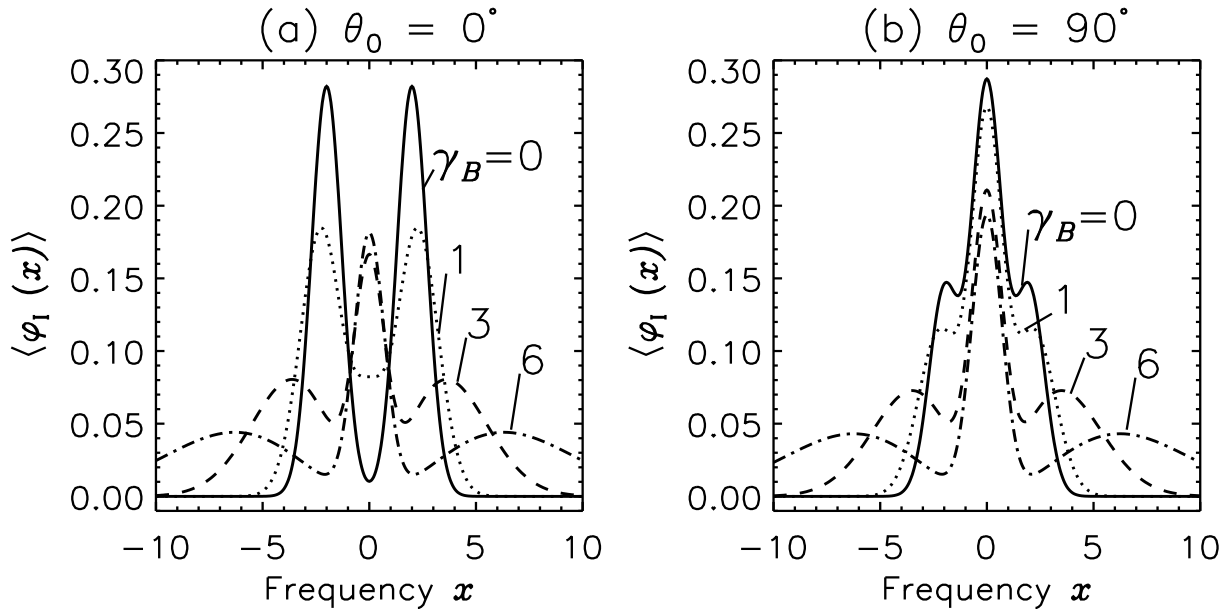


Figure 2.7: Dependence of  $\langle \varphi_I \rangle$  on the magnetic field dispersion measured by  $\gamma_B$ . Isotropic fluctuations. The parameters used are :  $a = 0$ ,  $\Delta_Z B_0 = 2$ . The panels (a) and (b) correspond to longitudinal ( $\theta_0 = 0^\circ$ ) and transverse ( $\theta_0 = 90^\circ$ ) cases respectively. Notice the saturation of the central  $\pi$ -component for  $\gamma_B > 3$ .

effects of the damping parameter on  $\langle \varphi_I \rangle$  become noticeable when  $a > 0.1$ . As expected, the peak value of the  $\pi$  and  $\sigma$ -components decrease and Lorentzian wings appear. When  $a > 0.5$ , the central component in the strong field case almost disappears. Thus for values of  $a \approx 10^{-3}$  to 0.1, the  $\pi$  and  $\sigma$ -components are insensitive to changes in  $a$  and the effects of turbulence discussed in this chapter for  $a = 0$  survive. In the solar case, this situation will hold except for very strong lines.

#### 2.4.5 Dependence on the Landé factor

We now consider the effect of a given random magnetic field on lines with different Zeeman sensitivities. We give  $\mathbf{B}_0$  and the dispersion  $\sigma$ , but let the Landé parameter  $g$  vary. Thus  $y_0 = B_0/\sqrt{2}\sigma$  is constant, but  $\gamma_B = \Delta_Z \sqrt{2}\sigma$  and  $\Delta_Z B_0 = y_0 \gamma_B$  are varying with  $g$  (see Eq. (2.8)). The mean coefficients have been calculated with  $y_0 = 1$  and  $\gamma_B = 1$  to 6. For this choice of  $y_0$  we are in an intermediate field regime and the mean coefficients are given by Eqs. (2.45), (2.46) and (2.47).

Figure 2.9 shows  $\langle \varphi_I \rangle$ . For  $\gamma_B = 1$  the Zeeman components are not resolved (the same curve is shown in Fig. 2.6a,  $y_0 = 1$ ). For  $\theta_0 = 0^\circ$ , the central peak is quite broad

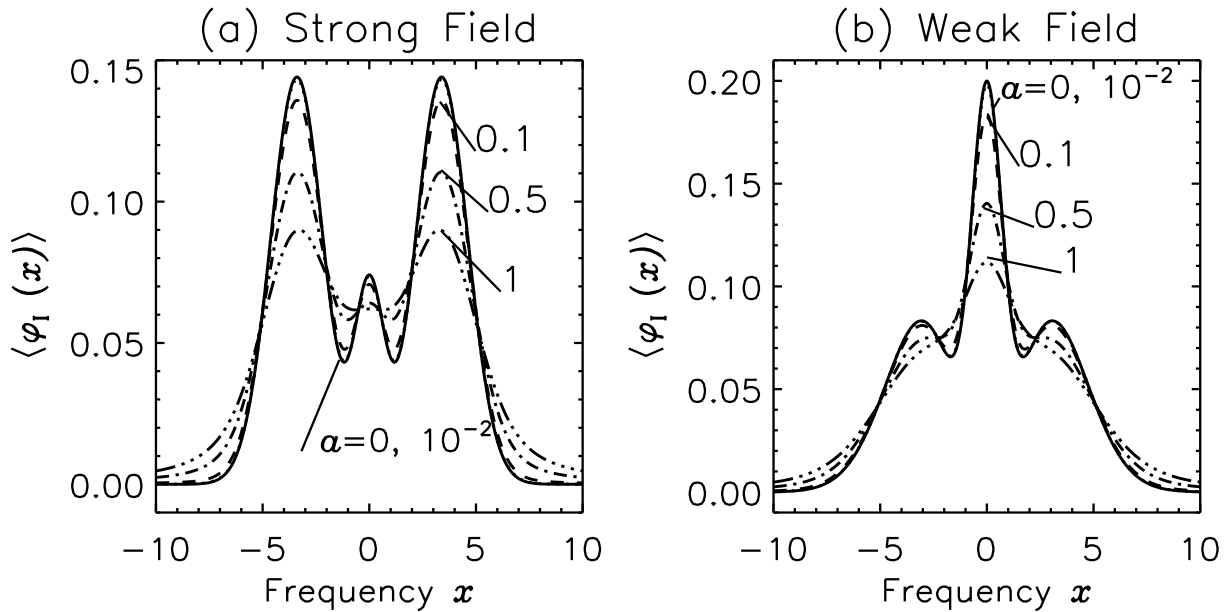


Figure 2.8: Dependence of  $\langle \varphi_1 \rangle$  on the damping parameter  $a$  in the  $\theta_0 = 0^\circ$  case. Isotropic fluctuations. Panel (a) shows the strong field case ( $\Delta_Z B_0 = 3$  and  $\gamma_B = 1.5$ ) and panel (b) the weak field case ( $\Delta_Z B_0 = 10^{-3}$  and  $\gamma_B = 3$ ). For large values of  $a$ , the  $\pi$  and  $\sigma$ -components decrease in strength.

(Full Width at Half Maximum FWHM=5) because of the superposition of the central  $\pi$ -component coming from the first term in Eq. (2.45) (responsible for the narrow tip) with the two  $\sigma$ -components given by the two other terms in the same equation. For  $\theta_0 = 90^\circ$ , the central peak is more narrow (FWHM = 3), because the contribution from the  $\sigma$ -components is smaller. As can be observed in Eq. (2.45), the coefficient of  $H(x \pm \gamma_B y, a)$  is  $(I_{1/2} + \frac{1}{2}I_{5/2})$  for  $\theta_0 = 0^\circ$  but only  $(I_{1/2} - \frac{1}{4}I_{5/2})$  for  $\theta_0 = 90^\circ$ . We recall that the modified Bessel functions are positive functions. When  $\gamma_B$  is large enough, the  $\pi$ -component is given by the first term in Eq. (2.45). It is independent of  $\gamma_B$  and its FWHM is around 2. Its amplitude is larger in the transverse than in the longitudinal case since the coefficients of  $H(x, a)$  in the integrand are respectively  $(I_{1/2} + \frac{1}{2}I_{5/2})$  and  $(I_{1/2} - I_{5/2})$ . If it were not for the isotropic distribution, there would be no  $\pi$ -component when  $\theta_0 = 0^\circ$ .

The  $\sigma$ -components have essentially the same behavior in the longitudinal and transverse case. The positions of the peaks depend little on  $\theta_0$  and can be deduced from the position of the maximum of the integrand in Eq. (2.45). Ignoring the shifted  $H$  functions, keeping only the Bessel function of order 1/2 and the positive exponential in the sinh function (see Eq. (C.1)), we find that the maximum is at  $y_{\max} \simeq (y_0 + \sqrt{y_0^2 + 2})/2$ . For  $y_0 = 1$ , we



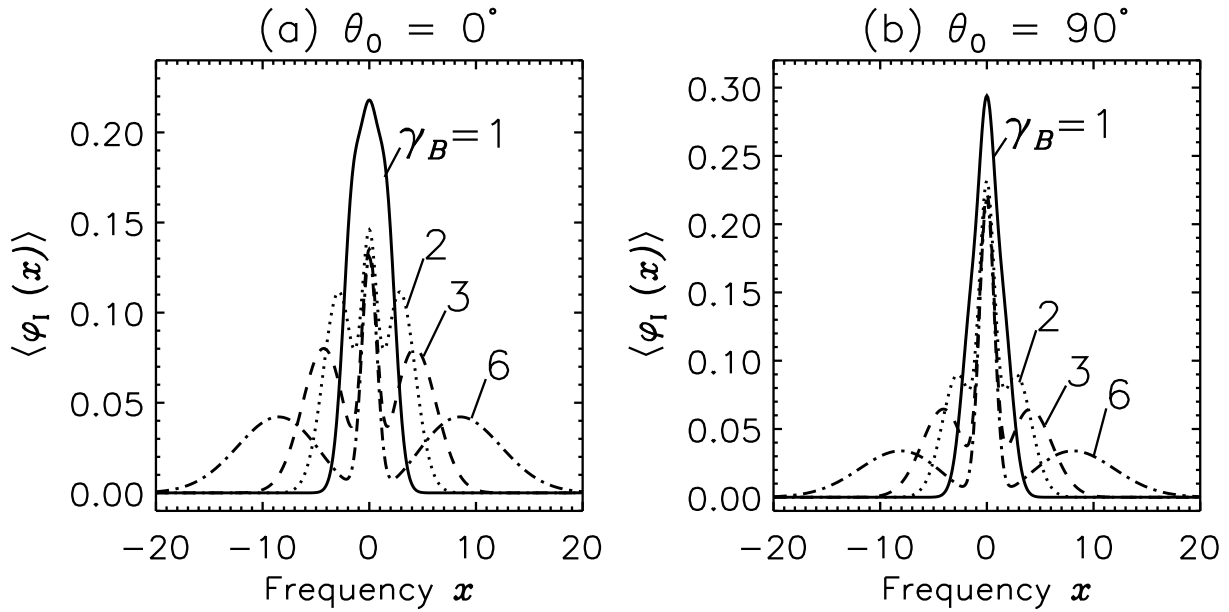


Figure 2.9: Dependence of  $\langle \varphi_I \rangle$  on the Zeeman sensitivity (the Landé  $g$  factor) introduced through the  $\gamma_B$  parameter (see the text for details) Isotropic fluctuations. The parameters used are  $a = 0$ , and  $y_0 = 1$ . Notice the saturation of the  $\pi$ -component at the line center. The panels (a) and (b) correspond to longitudinal ( $\theta_0 = 0^\circ$ ) and transverse ( $\theta_0 = 90^\circ$ ) cases respectively.

get  $x_{\max} \simeq y_{\max} \gamma_B \simeq 1.35 \gamma_B$  in fair agreement with the numerical results. The height of the peaks is somewhat larger in the longitudinal than in the transverse case, because the coefficients of the shifted  $H$  functions are larger in the first case, as pointed out above.

Figure 2.10 shows the mean absorption coefficient  $\langle \varphi_V \rangle$  divided by  $\cos \theta_0$  and  $\langle \varphi_Q \rangle$  divided by  $\sin^2 \theta_0 \cos 2\phi_0$  (see Eqs. (2.47) and (2.46)). The profile of  $\langle \varphi_V \rangle$  is quite standard. As with  $\langle \varphi_I \rangle$  the positions of the peaks increase linearly with the Landé factor  $g$  and are around  $1.35 \gamma_B$ . For  $\langle \varphi_Q \rangle$ , the central peak, given by term with  $H(x, a)$  is independent of  $\gamma_B$ , hence it goes to a constant value when the two  $\sigma$ -components are sufficiently far away from line center. This constant value will of course depend on  $y_0$ .

Finally, in Fig. 2.11 we have plotted the mean anomalous dispersion coefficients  $\langle \chi_Q \rangle$ , divided by  $\sin^2 \theta_0 \cos 2\phi_0$ , and  $\langle \chi_V \rangle$ , divided by  $\cos \theta_0$ . They are given by Eqs. (2.46) and (2.47) with the Voigt function  $H(x, a)$  replaced by the Faraday-Voigt function  $F(x, a)$ . The coefficient  $\langle \chi_Q \rangle$ , which has the same symmetry as  $\langle \varphi_V \rangle$ , keeps more or less the same shape as the Landé factor increases, except for a small broadening long ward of the peaks. This can be explained by considering Eq. (2.46). The overall shape is controlled by the first

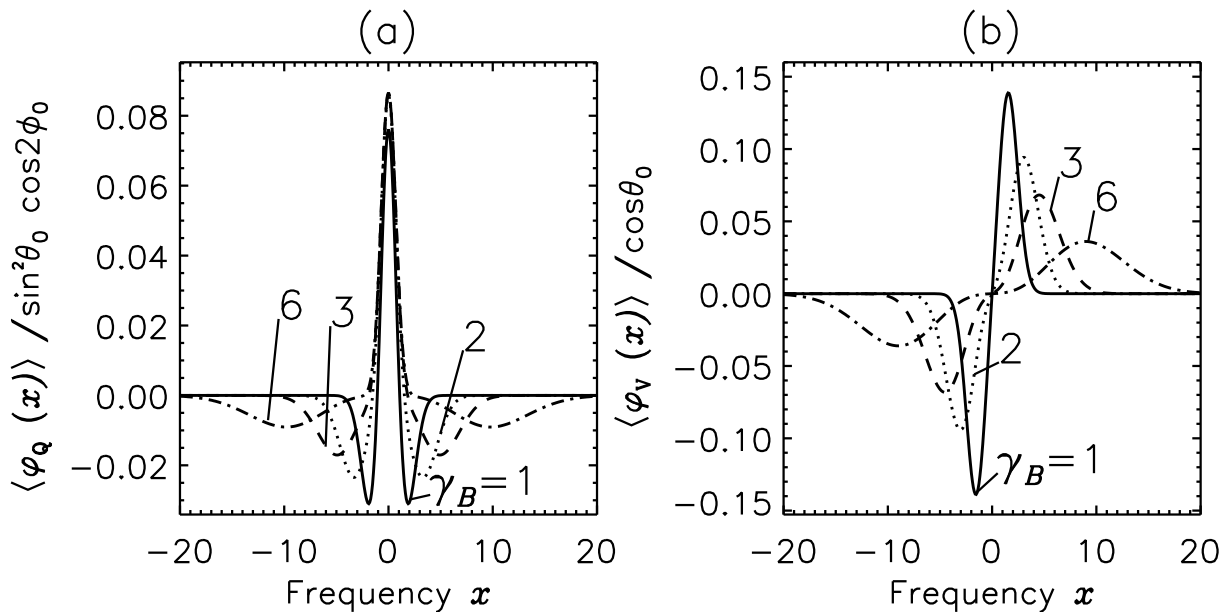


Figure 2.10: Same as Fig. 2.9, but for  $\langle \varphi_Q \rangle$  and  $\langle \varphi_V \rangle$ . The panels (a) and (b) correspond to  $\langle \varphi_Q \rangle / \sin^2 \theta_0 \cos 2\phi_0$  and  $\langle \varphi_V \rangle / \cos \theta_0$  respectively

term which is independent of  $\gamma_B$ . The two other terms are responsible for the broadening of the peaks but since they more or less compensate each other around  $x = 0$ , they do not affect the central part of the profile.

The coefficient  $\langle \chi_V \rangle$ , has the same symmetries as  $\langle \varphi_Q \rangle$  but the opposite sign. Because it involves the difference  $F(x - \gamma_B y, a) - F(x + \gamma_B y, a)$  (see Eq. (2.47)), it is very sensitive to the value of  $\gamma_B$  and hence to the Landé factor. For  $\gamma_B \geq 3$ , one clearly recognizes the shapes of two shifted Dawson integrals with opposite signs in Fig. 2.11b.

## 2.5 Fluctuations perpendicular to the mean field (2D turbulence)

We now assume that the fluctuations of the magnetic field are confined to a plane perpendicular to the direction of the mean field  $\mathbf{B}_0$ . Integrating over the longitudinal component in Eq. (2.1), we get the PDF

$$P_T(\mathbf{B}) d\mathbf{B} = \frac{1}{(2\pi) \sigma^2} \exp \left[ -\frac{B_T^2}{2\sigma^2} \right] B_T dB_T d\Psi, \quad (2.49)$$

where  $B_T$  is the amplitude of the magnetic field in the plane perpendicular to  $\mathbf{B}_0$  and  $\Psi$  its azimuthal angle in this plane. To simplify the notation we have set  $\sigma_T = \sigma$ . We recall

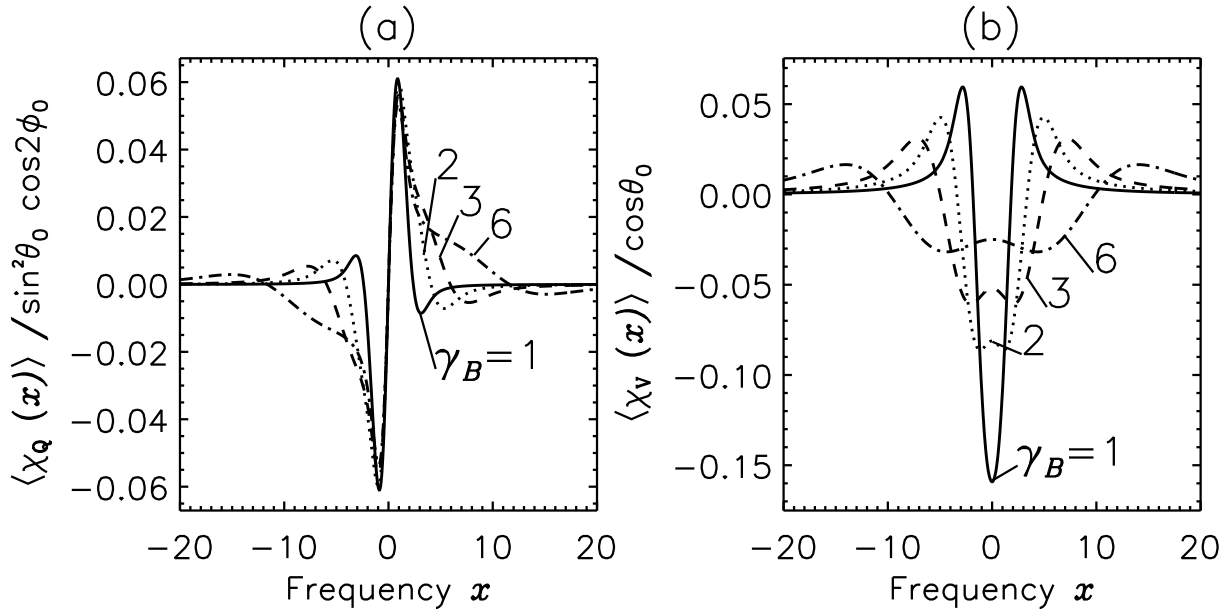


Figure 2.11: Dependence of magneto-optical coefficients  $\langle \chi_{Q,V} \rangle$  on the Landé factor. Same model as Fig. 2.9. Notice the similarity between  $\langle \chi_Q \rangle$  and  $\langle \varphi_V \rangle$  as well as  $\langle \chi_V \rangle$  and  $\langle \varphi_Q \rangle$ .

that  $\langle B_T^2 \rangle = 2\sigma^2$ . The random field  $\mathbf{B}$  is the sum of the mean field  $\mathbf{B}_0$  and the fluctuations  $\mathbf{B}_T$ . Its amplitude satisfies

$$B^2 = B_T^2 + B_0^2. \quad (2.50)$$

Using Eq. (2.50) and introducing the dimensionless variables defined in Eq. (2.19), we can rewrite the 2D distribution function as

$$P_T(\mathbf{B}) d\mathbf{B} = \frac{1}{\pi} e^{-(y^2 - y_0^2)} y dy d\Psi, \quad (2.51)$$

where  $y$  varies from  $y_0$  to  $+\infty$ . Equation (2.17) with  $\cos \Theta = B_0/B = y_0/y$  leads to

$$\bar{A}_0 = \frac{2}{3} \sum_{q=-1}^{q=+1} \int_{y_0}^{\infty} e^{-(y^2 - y_0^2)} H(x - q\gamma_B y, a) y dy, \quad (2.52)$$

$$\bar{A}_1 = y_0 \sum_{q=+1} q \int_{y_0}^{\infty} e^{-(y^2 - y_0^2)} H(x - q\gamma_B y, a) dy, \quad (2.53)$$

$$\bar{A}_2 = \frac{1}{4} \sum_{q=-1}^{q=+1} (2 - 3q^2) \int_{y_0}^{\infty} e^{-(y^2 - y_0^2)} H(x - q\gamma_B y, a) \left( 3\frac{y_0^2}{y^2} - 1 \right) y dy. \quad (2.54)$$

When  $y_0 \rightarrow 0$ , i.e. when the mean magnetic field is zero,  $\bar{A}_1 = 0$  and thus  $\langle \varphi_V \rangle$  is also zero. In contrast,  $\bar{A}_2$  and hence the mean linear polarization coefficients  $\langle \varphi_{Q,U} \rangle$  are not zero.

### 2.5.1 Exact and approximate expressions for the mean coefficients

As shown in DP79, closed form expressions of  $\bar{A}_0$  and  $\bar{A}_1$  can be obtained in terms of the error function when the damping parameter  $a = 0$ . For  $\bar{A}_2$  approximate expressions can be obtained for  $y_0 \gg 1$  and  $y_0 \ll 1$ . These different expressions are easily deduced from Eqs. (2.52) to (2.54). We give them below together with the weak mean field limits for  $\bar{A}_0$  and  $\bar{A}_1$ . They will be used to analyze the effects of 2D turbulence. Equations (2.52) and (2.53) lead to

$$\bar{A}_0 = \frac{1}{3} \left[ \frac{1}{\sqrt{\pi}} e^{-x^2} + \frac{1}{\gamma_1^2} \sum_{q=\pm 1} \frac{1}{\sqrt{\pi}} e^{-(x-q\Delta_Z B_0)^2} + 2x \frac{\gamma_B}{\gamma_1^2} \frac{1}{y_0} \bar{A}_1 \right], \quad (2.55)$$

with

$$\bar{A}_1 = y_0 \frac{1}{2\gamma_1} e^{y_0^2} e^{-x^2/\gamma_1^2} \sum_{q=\pm 1} q \operatorname{erfc} \left( y_0 \gamma_q - qx \frac{\gamma_B}{\gamma_q} \right), \quad (2.56)$$

where  $\operatorname{erfc}$  is the standard complementary error function (Abramowitz & Stegun 1964). If the  $\operatorname{erfc}$  function is approximated by a Gaussian, one can regroup the exponentials, and their product behaves as  $\exp[-(x - q\Delta_Z B_0)^2]$ , i.e. as a shifted Gaussian (we have used  $y_0 \gamma_B = \Delta_Z B_0$ ). Thus in contrast with 3D and 1D turbulence, there is little broadening of the  $\sigma$ -components by the turbulent magnetic field and the positions of the  $\sigma$ -components will be almost independent of  $\gamma_B$ .

When  $y_0 \gg 1$ , one has the approximation

$$\bar{A}_2^{\text{str}} \simeq \frac{e^{-x^2}}{2\sqrt{\pi}} \left( 1 - \frac{3}{2y_0^2} \right) - \frac{y_0}{4\gamma_1} e^{y_0^2} e^{-x^2/\gamma_1^2} \sum_{q=\pm 1} \operatorname{erfc} \left( y_0 \gamma_q - qx \frac{\gamma_B}{\gamma_q} \right). \quad (2.57)$$

The first term is obtained by an asymptotic expansion for large  $x$ , of the the integrand in Eq. (2.54) and the second one by assuming  $y \simeq y_0$  in the term  $(3y_0^2/y^2 - 1)y$ . The factor  $3/2y_0^2$  is not present in the expansion given in DP79. This factor is needed to explain the  $\pi$ -component observed in Fig. 2.15.

The combination of Eqs. (2.55) and (2.57) with Eq. (2.16), yields an expression of  $\langle \varphi_I \rangle$  for large values of  $y_0$ . It contains a term proportional to  $e^{-x^2}$ , which yields the central component, and terms which are exactly or approximately of the form  $e^{-(x-q\Delta_Z B_0)^2}$  which determine the  $\sigma$ -components.

In the weak mean field limit, i.e. when  $y_0 \ll 1$ , we have, to leading order,

$$\bar{A}_0^{\text{w}} \simeq \frac{1}{3} \left[ \frac{2 + \gamma_1^2}{\gamma_1^2} \frac{1}{\sqrt{\pi}} e^{-x^2} + 2x \frac{\gamma_B}{\gamma_1^3} e^{-x^2/\gamma_1^2} \operatorname{erf} \left( x \frac{\gamma_B}{\gamma_1} \right) \right], \quad (2.58)$$

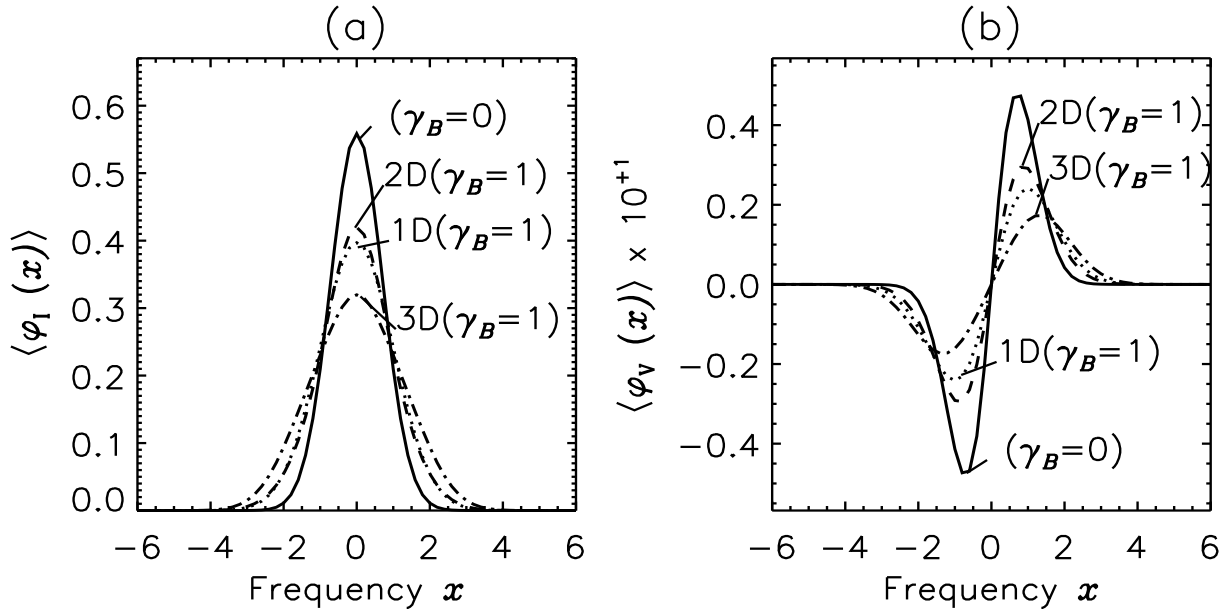


Figure 2.12: Dependence of  $\langle \varphi_I \rangle$  and  $\langle \varphi_V \rangle$  on the magnetic field distribution in the weak mean field limit for the longitudinal Zeeman effect ( $\theta_0 = 0^\circ$ ). The model parameters are  $a = 0$ ,  $\Delta_z B_0 = 0.1$  and  $\gamma_B = 1$  (hence  $y_0 = 0.1$ ). The curves with  $\gamma_B = 0$  correspond to a constant magnetic field equal to  $\mathbf{B}_0$ .

$$\bar{A}_1^w \simeq \frac{y_0}{\gamma_1} e^{-x^2/\gamma_1^2} \operatorname{erf} \left( x \frac{\gamma_B}{\gamma_1} \right), \quad (2.59)$$

$$\bar{A}_2^w \simeq -\frac{1}{4\gamma_1^2} \left[ \gamma_B^2 \frac{1}{\sqrt{\pi}} e^{-x^2} - x \frac{\gamma_B}{\gamma_1} e^{-x^2/\gamma_1^2} \operatorname{erf} \left( x \frac{\gamma_B}{\gamma_1} \right) \right]. \quad (2.60)$$

The corrections are  $\mathcal{O}(y_0^2)$  for  $\bar{A}_0$  and  $\bar{A}_2$  and  $\mathcal{O}(y_0^3)$  for  $\bar{A}_1$ . If the erf function is approximated by a Gaussian, its product with  $e^{-x^2/\gamma_1^2}$  yields  $e^{-x^2}$ . This implies that broadening by 2D turbulence will be weak.

When the mean field is zero,  $\bar{A}_1 = 0$  and  $\bar{A}_0$  and  $\bar{A}_2$  are given by the r.h.s. in Eqs. (2.58) and (2.60) which become exact results.

### 2.5.2 Profiles of the mean coefficients for 1D, 3D and 2D turbulence

We compare in Figs. 2.12 to 2.15, the mean absorption coefficients corresponding to 1D, 2D and 3D turbulence. Figure 2.12 corresponds to a weak mean field limit and the other figures to an intermediate regime, neither weak nor strong, with  $y_0 = 1$ . In each figure we also show the absorption coefficients corresponding to a non-random field equal to the mean field  $\mathbf{B}_0$ . It will be seen that the frequency profiles of the mean coefficients are very

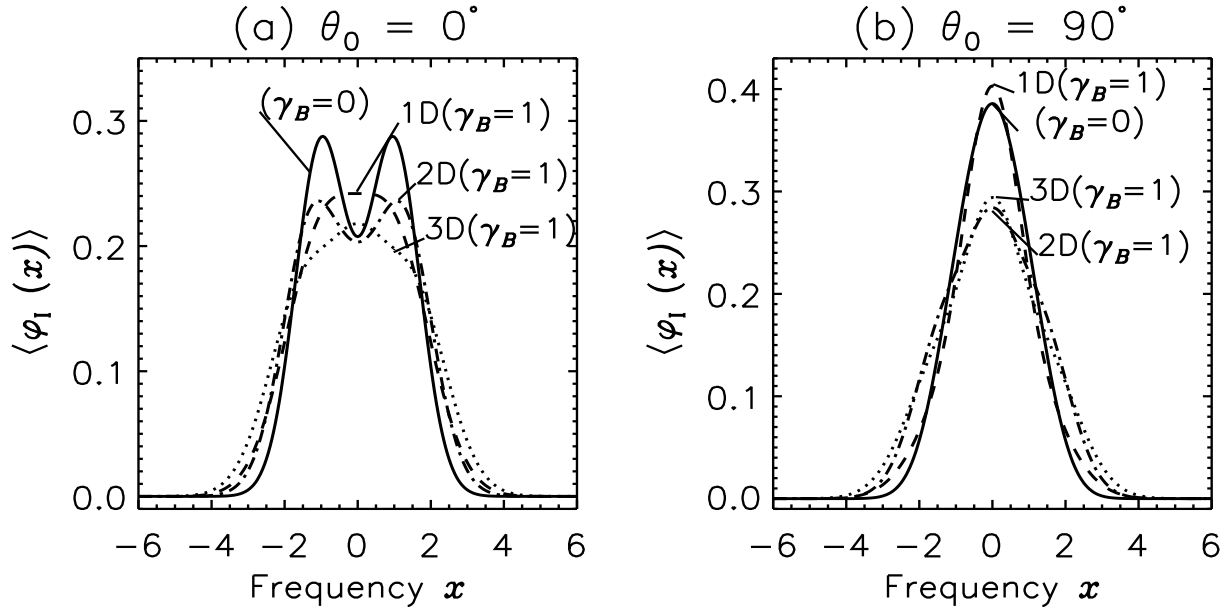


Figure 2.13: Dependence of  $\langle \varphi_1 \rangle$  on the magnetic field distribution. The model parameters are  $a = 0$ ,  $\Delta_Z B_0 = 1$ ,  $\gamma_B = 1$  (hence  $y_0 = 1$ ). The curves with  $\gamma_B = 0$  correspond to a constant magnetic field equal to  $\mathbf{B}_0$ . Panels (a) and (b) correspond to longitudinal ( $\theta_0 = 0^\circ$ ) and transverse ( $\theta_0 = 90^\circ$ ) cases, respectively.

sensitive to the nature of the turbulent fluctuations. However there are a few common features linked to the invariance of the frequency integrated mean coefficients (see § 2.2.4). In particular a broadening (narrowing) of the profile is associated to a decrease (increase) in the peak value.

In Fig. 2.12,  $y_0 = \Delta_Z B_0 / \gamma_B = 0.1$  is much smaller than the broadening parameter  $\gamma_1 = (1 + \gamma_B^2)^{1/2} = \sqrt{2}$ . Hence  $\langle \varphi_1 \rangle$  shows a single central peak. The random fluctuations produce a decrease in the peak value and an associated broadening. The decrease in peak value is the largest for 3D turbulence and the smallest for 2D turbulence. This can be explained with equations established in the previous sections.

For 1D fluctuations and  $\theta_0 = 0^\circ$ , we have (see Eq. (2.27)),

$$\langle \varphi_1 \rangle_{1D}^w \simeq \frac{1}{\gamma_1} H \left( \frac{x}{\gamma_1}, \frac{a}{\gamma_1} \right). \quad (2.61)$$

For 2D turbulence,

$$\langle \varphi_1 \rangle_{2D}^w \simeq \frac{2 + \gamma_B^2}{2\gamma_1^2} \frac{1}{\sqrt{\pi}} e^{-x^2}, \quad (2.62)$$

around the line center (see Eqs. (2.58) and (2.60)). For isotropic turbulence (see Eq. (2.42))

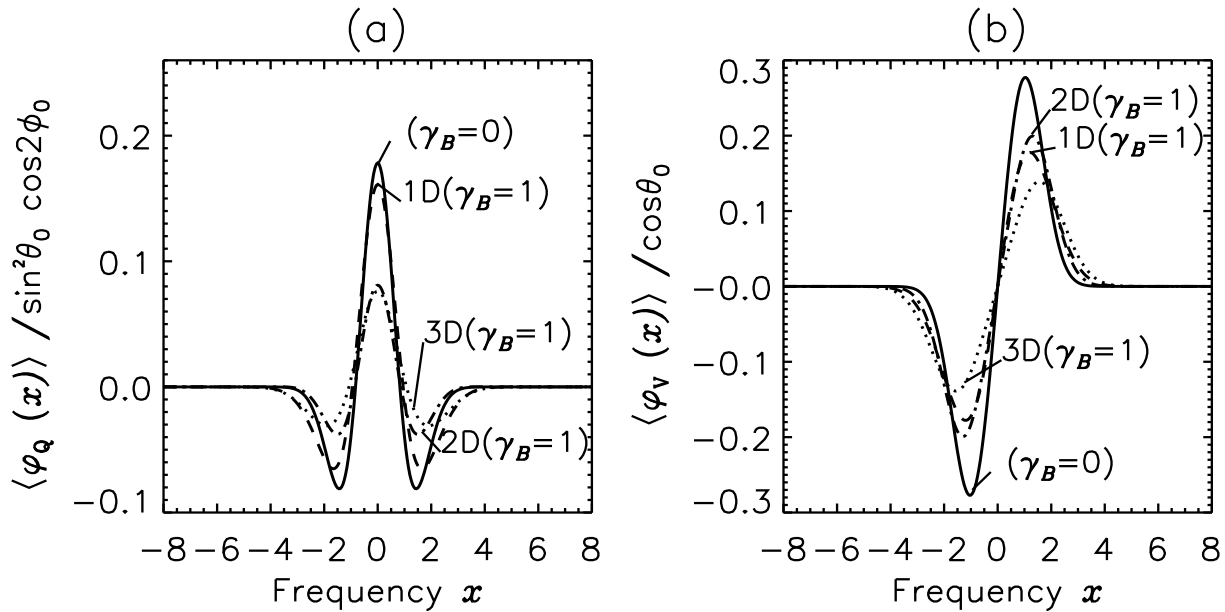


Figure 2.14: Dependence of  $\langle \varphi_Q \rangle$  and  $\langle \varphi_V \rangle$  on the magnetic field distribution. Same model parameters as in Fig. 2.13. Panels (a) and (b) correspond to transverse ( $\theta_0 = 90^\circ$ ) and longitudinal ( $\theta_0 = 0^\circ$ ) cases, respectively.

we can neglect the contribution of  $\bar{A}_2$ , which is  $\mathcal{O}(y_0^2)$ . Hence,  $\langle \varphi_I \rangle^w$  reduces to  $\bar{A}_0$ , and we have

$$\langle \varphi_I \rangle_{3D}^w \simeq \frac{1}{3} \left[ H^{(0)}(x, a) + \frac{2}{\gamma_1} H^{(0)} \left( \frac{x}{\gamma_1}, \frac{a}{\gamma_1} \right) + 4\gamma_B^2 H^{(2)} \left( \frac{x}{\gamma_1}, \frac{a}{\gamma_1} \right) \right]. \quad (2.63)$$

The contribution of the term with  $H^{(2)}$  is negligible when  $\gamma_B = 1$ , but becomes relevant when  $\gamma_B = 2$ , creating pseudo  $\sigma$ -components at  $|x| \simeq \gamma_1$  as in Fig. 2.3. One can verify that the above expressions correctly predict the profiles shown in Fig. 2.12.

For circular polarization,  $\langle \varphi_V \rangle = \bar{A}_1^w$ , with  $\bar{A}_1^w$  given in Eqs. (2.26), (2.43) and (2.59) for 1D, 3D and 2D turbulence, respectively. The peak value is the largest for 2D turbulence and the smallest for isotropic turbulence (see Fig. 2.12b), exactly as observed for  $\langle \varphi_I \rangle$ . The frequencies of the  $\langle \varphi_V \rangle$  peaks are at  $|x| = 1/\sqrt{2}$  for zero turbulence, around  $|x| \simeq \gamma_1/\sqrt{2} = 1$  for 1D turbulence and further away from line center for isotropic turbulence because of the contribution of the term with  $H^{(3)}$  (see the discussion in § 2.4.2). For 2D turbulence, numerical simulations show that the maxima are around  $|x| \simeq 1$  with not much dependence on the value of  $\gamma_B$ . This result is suggested in § 2.5.1.

We now discuss Figs. 2.13 and 2.14 where  $\Delta_Z B_0 = 1$  and  $\gamma_B = 1$ . In the non-random case, the two  $\sigma$ -components of the  $\varphi_I$  profile are partially separated when  $\theta_0 = 0^\circ$  but

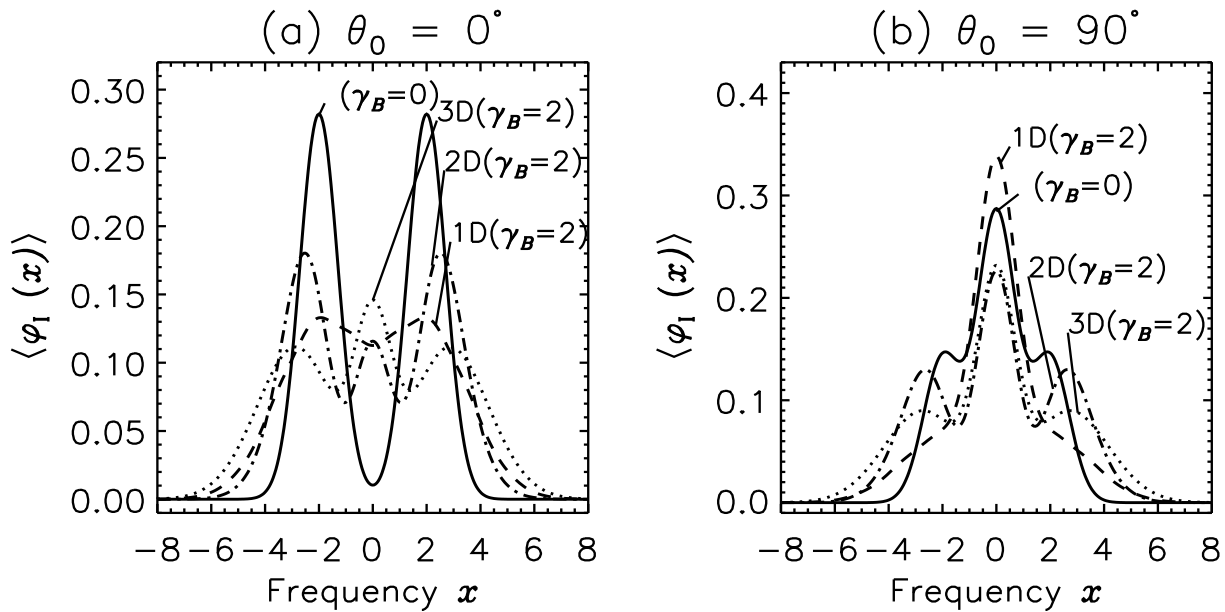


Figure 2.15: Dependence of  $\langle \varphi_1 \rangle$  on the magnetic field distribution. The model parameters are  $a = 0$ ,  $\Delta_Z B_0 = 2$ ,  $\gamma_B = 2$  (hence  $y_0 = 1$ ). The curves with  $\gamma_B = 0$  correspond to a constant magnetic field equal to  $\mathbf{B}_0$ . Panels (a) and (b) correspond to longitudinal ( $\theta_0 = 0^\circ$ ) and transverse ( $\theta_0 = 90^\circ$ ) cases, respectively.

form a single peak with the  $\pi$ -component when  $\theta_0 = 90^\circ$ . Panel (a) shows that the central frequencies are quite sensitive to the angular distribution of the random field. For 1D turbulence there is a strong broadening of the  $\sigma$ -components which fill up the depression at line center. For 2D turbulence, the  $\sigma$ -components are still well marked but have a smaller magnitude. As pointed out above, the broadening of the  $\sigma$ -components is small in the 2D case. For isotropic turbulence, there is also a single broad peak (the same profile is shown in Fig 2.9a). Fig. 2.13b corresponds to  $\theta_0 = 90^\circ$ . We note that 2D and 3D turbulence have essentially the same effects. The decrease in the central peak value comes from the angular averaging over  $\sin^2 \theta$ . In contrast, the profile is left almost unaffected in the 1D case because the main contribution to the central peak comes from the  $\pi$ -component which is insensitive to the fluctuations of the random field strength.

Figures 2.14a,b show  $\langle \varphi_Q \rangle$  and  $\langle \varphi_V \rangle$  respectively. We see that  $\langle \varphi_Q \rangle / \sin^2 \theta_0 \cos 2\varphi_0 = \bar{A}_2$  behaves in much the same way as  $\langle \varphi_1 \rangle$  for  $\theta_0 = 90^\circ$ . For 1D turbulence, the central peak is not significantly affected for the reason given above. The  $\sigma$ -components on the other hand suffer some broadening, which goes together with a decrease in its amplitude. For 2D and 3D turbulence there is a sharp drop in the central peak and also in the  $\sigma$ -components, but



the broadening with 2D turbulence is, as already pointed out, much smaller than with 3D turbulence. For  $\langle\varphi_V\rangle(=\bar{A}_1)$ , the fluctuations of the magnetic field produce a decrease in the peak value, a small shift away from line center and a broadening which has its largest value for 3D and its smallest value for 2D. The strongest effect is produced by isotropic fluctuations. The decrease in the peak value can be explained by the factor  $(1 - 1/2y_0^2)$  in Eq. (2.39).

When the rms fluctuations increase, i.e. when  $\gamma_B$  increases, the profiles  $\langle\varphi_Q\rangle$  and  $\langle\varphi_V\rangle$  keep essentially the same shape but the effects are amplified. All the peaks have a smaller value and for 2D and 3D turbulence the  $\sigma$ -components are moved away further from line center. One also observes a significant decrease in the slope of  $\langle\varphi_V\rangle$  at line center.

In Fig. 2.15 we still have  $y_0 = 1$ , (rms fluctuations equal to the mean field strength) but  $\Delta_Z B_0 = 2$  and  $\gamma_B = 2$ . Hence the  $\sigma$ -components are well separated as can be observed. Panel (a) of this figure clearly shows the central component created by the averaging of  $\pi$ -component over the random directions of the magnetic field for 2D and 3D turbulence. For 2D turbulence, the  $\sigma$ -components are significantly more intense and more narrow than for 3D turbulence. The central peak on the other hand is shallower. For 1D turbulence, there is no central component but a strong broadening of the  $\sigma$ -components. The decrease in the amplitude of the  $\sigma$ -components is controlled by the factor  $1/\gamma_1 \simeq 1/\sqrt{5} \simeq 0.44$  (see Eq. (2.22)). For the transverse case (panel (b)), the  $\sigma$ -components disappear for 1D turbulence because they are multiplied by  $1/\gamma_1$  but the central peak increases due to the contribution of the broadened  $\sigma$ -components. This increase of the central peak can also be understood in terms of the constancy of the frequency integral of  $\langle\varphi_I\rangle$ . For 2D and 3D turbulence, the  $\sigma$ -components are still well marked but they are somewhat shifted away from line center with the 3D components being broader and shallower than the 2D components. The decrease of central peak is due to the averaging over  $\varphi_0 \sin^2 \theta/2$  term.

## 2.6 Summary and concluding remarks

In this chapter we have examined the effects of a random magnetic field on the Zeeman line transfer absorption matrix. We have considered a fairly general case where the magnetic field has anisotropic but azimuthally invariant Gaussian fluctuations about a given mean magnetic field  $\mathbf{B}_0$  which can be set to zero. We have examined in detail three types of random fluctuations: (i) longitudinal fluctuations which take place along the direction of the mean field, referred to as 1D or longitudinal turbulence; (ii) fluctuations which are distributed isotropically around the direction of the mean field, referred to as isotropic or

3D turbulence; (iii) fluctuations isotropically distributed in a plane perpendicular to the mean field, referred to as 2D turbulence - the total random field (sum of the fluctuating part and of the mean field) does not lie in this plane unless the mean field is zero. In all three cases, the random field depends on two parameters, the mean field  $\mathbf{B}_0$  and the dispersion  $\sigma^2$  around the mean field (see Eqs. (2.18), (2.28), and (2.49)).

First we give a fairly compact and simple expression for the mean coefficients of the absorption matrix. It is valid for any random field invariant in a rotation around the mean field direction (Eq. (2.16)). This general expression is obtained by taking advantage of the fact that the angular dependence of the Zeeman matrix elements can be written in terms of the spherical harmonics  $Y_{lm}(\theta, \phi)$ , where  $\theta$  and  $\phi$  are the polar and azimuthal angles of the random field with respect to direction of the line-of-sight.

The random fluctuations of the magnetic field have two types of effects. The fluctuations of the magnetic field strength produce random Zeeman shifts which lead to a broadening of the  $\sigma$ -components. It is important to note that the  $\pi$ -component is not affected by this phenomenon. The second effect, which occurs only for 2D and 3D turbulence, is the averaging over the angular dependence of the coefficients which affects both  $\pi$  and  $\sigma$ -components. As a result, the frequency profiles of the mean coefficients can look quite different from the standard profiles created by a constant magnetic field. The physically relevant parameters for the analysis of the mean profiles are the dimensionless parameters  $y_0$  - which measures the strength of the mean magnetic field  $\mathbf{B}_0$  in units of the rms fluctuations  $\sigma$  - and  $\gamma_B$  the Zeeman shift by the rms fluctuations. The Zeeman shift by the mean magnetic field is  $\Delta_Z |\mathbf{B}_0| = y_0 \gamma_B$ . The broadening by the magnetic field strength fluctuations combined with the standard Doppler broadening (by thermal and/or micro-turbulent velocity fluctuations) is described by a parameter  $\gamma_1 = \sqrt{1 + \gamma_B^2}$ . There are two interesting limiting regimes. A *weak mean field* regime corresponding to  $\Delta_Z |\mathbf{B}_0| \ll \gamma_1$ , i.e. to a Zeeman shift by the mean magnetic field smaller than the combined Doppler and magnetic broadening. The other interesting limit, referred to as the *strong mean field* or *weak turbulence* regime, corresponds to  $y_0 \gg 1$ . In this limit, the  $\sigma$ -components stay well separated in spite of the random field fluctuations, provided  $\gamma_1$  stays smaller than  $y_0$ . We now briefly summarize the main effects for three types of fluctuations that we have considered.

For 1D turbulence, the direction of the random magnetic field remains constant and same as the direction  $(\theta_0, \phi_0)$  of the mean magnetic field. The only effect is a broadening and a decrease in amplitude by a factor  $\gamma_1$  of the  $\sigma$ -components (see § 2.3 and Figs. 2.12 to 2.15). For the transverse Zeeman effect ( $\theta_0 = 90^\circ$ ) and when  $y_0 \simeq 1$ , a consequence of

this broadening is that the central  $\pi$ -component can be enhanced by the magnetic field fluctuations while the  $\sigma$ -components almost entirely disappear (see Fig. 2.15). When the strength of the mean magnetic field is zero, the coefficient of circular polarization  $\langle\varphi_V\rangle$  (and  $\langle\chi_V\rangle$ ) are zero but not the mean linear polarization coefficients  $\langle\varphi_Q\rangle$  and  $\langle\varphi_U\rangle$ . Circular polarization is destroyed by fields of opposite directions but not linear polarization which has a quadratic dependence on the polar angle of the magnetic field.

For isotropic (3D) turbulence, the two effects namely, magnetic broadening of the  $\sigma$ -components and angular averaging are at work. The dependence of the absorption and anomalous dispersion coefficient profiles on the magnetic field parameters and on the Landé factor is discussed in detail in § 2.4. One striking effect in the case of the longitudinal Zeeman effect ( $\theta_0 = 0^\circ$ ) is the formation in  $\langle\varphi_I\rangle$  of a central component with no polarization counterpart created by the averaging of  $\varphi_0 \sin^2 \theta/2$ . This component is particularly noticeable when  $y_0 \simeq 1$  (see Figs. 2.9 and 2.15). The circular polarization coefficients  $\langle\varphi_V\rangle$  (and  $\langle\chi_V\rangle$ ) can be expressed in terms of generalized Voigt and Faraday-Voigt functions  $H^{(n)}$  and  $F^{(n)}$ . We study these functions in a greater detail in Chapter 3. The other mean coefficients can also be expressed in terms of these generalized functions but only in weak mean field and strong mean field regimes. When the mean magnetic field is zero, the random field  $\mathbf{B}$  is strictly isotropic (there is no preferred direction) and both circular  $\langle\varphi_V\rangle$  and linear  $\langle\varphi_Q\rangle$  and  $\langle\varphi_U\rangle$  polarization coefficients are zero. The same is true of course for the anomalous dispersion coefficients.

For 2D turbulence the mean profiles resemble the mean profiles for isotropic turbulence. One can observe in particular the formation of a non-polarized central component due to the averaging of  $\varphi_0 \sin^2 \theta/2$  over the directions of the random field, but in contrast to isotropic turbulence, there is very little broadening of the  $\sigma$ -components because the magnitude of the random field is more centered around the magnitude of the mean field. The  $\sigma$ -components are not only more narrow they are also stronger than with 1D or 3D turbulence (see the figures in § 2.5). When the mean magnetic field is zero, the mean circular polarization coefficient  $\langle\varphi_V\rangle$  is zero but not the linear coefficients  $\langle\varphi_Q\rangle$  and  $\langle\varphi_U\rangle$ . So even if the mean magnetic field is zero, anisotropic turbulence like 1D or 2D turbulence will produce linear polarization.

In this work we have considered for simplicity a normal Zeeman triplet. In the anomalous Zeeman splitting case, each elementary component  $\varphi_q$  ( $q = 0, \pm 1$ ) must be replaced

by a weighted average of the form

$$\bar{\varphi}_q = \sum_{M_u} S_q(M_l, M_u) H(x_q, a), \quad q = M_l - M_u, \quad (2.64)$$

where  $S_q$  is the strength of the transition between the lower and upper levels of magnetic quantum numbers  $M_l$  and  $M_u$  and  $x_q = x - (g_l M_l - g_u M_u) \Delta'_Z B$ , with  $B$  the strength of the random magnetic field (Stenflo 1994), and  $\Delta'_Z = e/(4\pi m \Delta \nu_D)$ . The absorption and anomalous dispersion coefficients can still be written as in Eqs. (2.10) and (2.11) with the  $\varphi_q$  replaced by  $\bar{\varphi}_q$  and the summation now over  $M_u$ . Similarly, the mean coefficients are given by Eq. (2.16) where the  $\bar{A}_i$  are now calculated with the  $\bar{\varphi}_q$ . The exact and approximate expressions given for 1D, 2D and 3D turbulence can thus be carried over to the anomalous Zeeman splitting.

In this chapter we have considered only Gaussian distributions but it is clear that the averaging method and the main effects that we have described will carry over to other types of distributions. Such effects as the broadening of the  $\sigma$ -components by random Zeeman shifts or the appearance of unpolarized central components due to angular averaging should persist. The assumption that the random fields are azimuthally symmetric plays an important role in the averaging method, but is a fairly realistic assumption for small scale fluctuations. As for correlations between magnetic and velocity fluctuations, they can certainly be incorporated in the averaging method without major difficulties.

For weak lines (optical depth small compared to unity), the opacity coefficients give a fair approximation to the observable Stokes parameters and a comparison between observations and mean coefficient profiles could provide informations on the statistical properties of the magnetic field. For example, the strength of the mean magnetic field could be obtained with the center-of-gravity method (see e.g. LL04, p. 640). This method is based on the measurements of the center of gravity wavelength  $x_{\pm}$ . For weak lines, they can be written as

$$x_{\pm} = \frac{\int (\langle \varphi_I \rangle \pm \langle \varphi_V \rangle) x dx}{\int (\langle \varphi_I \rangle \pm \langle \varphi_V \rangle) dx}, \quad (2.65)$$

where the frequency integration is extended to the full line profile. As  $\langle \varphi_V \rangle$  is antisymmetric with respect to line center,  $\langle \varphi_I \rangle$  symmetric and normalized to unity, Eq. (2.65) reduces to

$$x_{\pm} = \pm \int \langle \varphi_V \rangle x dx. \quad (2.66)$$

Using Eqs. (2.11), (2.16) and (2.17), one obtains

$$x_{\pm} = \pm \cos \theta_0 \Delta_Z \int B \cos \Theta P(\mathbf{B}) d\mathbf{B}, \quad (2.67)$$

where  $\Theta$  is the angle between the random field  $\mathbf{B}$  and the mean field  $\mathbf{B}_0$ . Hence  $B \cos \Theta$  is the longitudinal component of the random field. The integration over the magnetic field distribution given in Eq. (2.1) leads to

$$x_{\pm} = \pm \cos \theta_0 \Delta_Z B_0, \quad (2.68)$$

hence to a measure of the longitudinal component  $B_0 \cos \theta_0$  of the mean magnetic field.

A detailed analysis of Stokes profiles for lines with different Zeeman sensitivity (Landé factors) would be a way to evaluate the dispersion of the random fluctuations. The detection of an unpolarized central component in Stokes  $I$  would indicate strong variations in the direction of the magnetic field. However, specific observations at high resolution would be required to verify this fact, because a central unpolarized component may also be produced by a non-magnetic region within the resolution element.

For spectral lines with moderate to large optical depths, radiative transfer effects must be taken into account. The Unno-Rachkovsky solution shows very large differences in the observable Stokes parameters, depending on whether the magnetic field is random or not. This topic will be addressed in Chapters 4 and 5, where we consider line formation in a random magnetic field with a finite correlation length.



## Chapter 3

# Generalized Voigt functions and their derivatives<sup>1</sup>

### 3.1 Introduction

The Voigt function  $H(x, a) = H^{(0)}(x, a)$  is widely used to represent spectral line shapes in many fields of physics such as astrophysics, atmospheric spectroscopy, plasma physics etc., wherever measurements and theory of spectral line profiles are involved. The quantity  $x$  is the non-dimensional frequency and  $a$  is the damping parameter, both expressed in Doppler width units. In the presence of a magnetic field, the medium becomes anisotropic, causing differential absorption/refraction for different states of polarization. The absorption of radiation is described by the imaginary part of the complex refractive index of the medium. The real part describes the dispersive effects, also called magneto-optical effects, when the anisotropy is caused by the presence of a magnetic field. The dispersive or magneto-optical effects involve a line shape function called “anomalous dispersion function”  $F(x, a) = F^{(0)}(x, a)$  (also denoted by  $K(x, a)$ , or  $G(x, a)$ , or  $L(x, a)$  in literature). These functions  $H^{(0)}(x, a)$  and  $F^{(0)}(x, a)$  together have been traditionally employed in the theory of Zeeman line formation, which involves absorption and emission of photons between the Zeeman sub-states of an atom (see Chapter 2).

Magnetic fields met in astrophysics, say stellar atmospheres, will have in general random fluctuations and the line formation theory has to be extended to account for the randomness of the field. When the characteristic scale of the fluctuations is much smaller than the photon mean free path, randomness of the field can be taken into account by locally

---

<sup>1</sup>This chapter is based on the publication : Sampoorana, M., Nagendra, K. N. & Frisch, H. 2007, JQSRT, 104, 71-85

averaging (convolving) the Zeeman “absorption matrix” with a given vector magnetic field PDF (see LL04, Chapter 2 and references cited therein). In some cases the averaging process can be performed analytically, for example when the PDF of the magnetic field is an isotropic Gaussian. For isotropic fluctuations, the mean coefficients can be expressed in terms of new class of functions called generalized Voigt and Faraday-Voigt functions  $H^{(n)}(x, a)$  and  $F^{(n)}(x, a)$  introduced in Dolginov & Pavlov (1972, see also Chapter 2). They appeared first in the theory of the turbulent Zeeman effect, but may be of interest in other related fields. This has motivated us to study them in some detail. Hereafter, for convenience, we drop the arguments  $(x, a)$  on these functions.

Non-linear least square fitting algorithms require higher order partial derivatives of  $H^{(0)}$  and  $F^{(0)}$  in extracting physical parameters from the polarized spectral line data (see Stenflo 1994, del Toro Iniesta 2003, LL04). Rapid approximations to compute the derivatives of  $H^{(0)}$  and  $F^{(0)}$  have been developed by Heinzl (1978) and Wells (1999, see also references cited therein). In this chapter we discuss  $H^{(n)}$  and  $F^{(n)}$  for  $n \geq 1$ , and also their  $m^{\text{th}}$  order partial derivatives. They will be essential for the development of inversion techniques employing Zeeman line formation theory in turbulent media (DP72, DP79, Chapters 2, 4).

In § 3.2 we define  $H^{(n)}$  and  $F^{(n)}$  and introduce a new function  $W^{(n)}(z)$ , where  $z$  is complex. Starting from this function  $W^{(n)}(z)$  we derive recurrence relations for  $H^{(n)}$  and  $F^{(n)}$ . We show that  $F^{(n)}$  can be expressed in terms of the real Dawson’s function for the special case of  $a = 0$ . In this § 3.2, we also graphically present the  $H^{(n)}$  and  $F^{(n)}$  up to 7-th order, for different values of  $a$ , and discuss the properties of these functions as well as computational aspects. A method for obtaining simple recurrence relations for the partial derivatives of  $H^{(n)}$  and  $F^{(n)}$  with respect to  $x$  and  $a$  is presented in § 3.3, along with the computational details. In § 3.4, we show that partial derivatives of the conventional Voigt and Faraday-Voigt functions  $H^{(0)}$  and  $F^{(0)}$  can be expressed in terms of  $H^{(n)}$  and  $F^{(n)}$ .

## 3.2 Generalized Voigt functions $H^{(n)}$ and $F^{(n)}$

### 3.2.1 Definitions and recurrence relations

For the sake of clarity, we re-write the functional form of  $H^{(n)}$  and  $F^{(n)}$  presented in Eqs. (2.35) and (2.36) as

$$H^{(n)}(x, a) = \frac{a}{\pi^{3/2}} \int_{-\infty}^{+\infty} \frac{u^n e^{-u^2}}{(x-u)^2 + a^2} du, \quad (3.1)$$



$$F^{(n)}(x, a) = \frac{1}{\pi^{3/2}} \int_{-\infty}^{+\infty} \frac{u^n (x-u) e^{-u^2}}{(x-u)^2 + a^2} du. \quad (3.2)$$

We know that for  $n = 0$ , the usual  $H^{(0)}$  and  $F^{(0)}$  functions are the real and imaginary part of the function  $W^{(0)}(z)$ , known as the complex probability function or Faddeeva function (see for e.g. Abramowitz & Stegun 1964, Faddeeva & Teren'tev 1961, Humlíček 1982). In a similar way  $H^{(n)}$  and  $F^{(n)}$  are the real and imaginary parts of a complex valued function

$$W^{(n)}(z) = \frac{i}{\pi^{3/2}} \int_{-\infty}^{+\infty} \frac{u^n e^{-u^2}}{z-u} du, \quad \Im(z) > 0, \quad (3.3)$$

where  $z = x + ia$ , with  $x$  and  $a$  being real and  $a > 0$ . The function  $W^{(n)}$  is analytic in the upper half of the complex plane. It has a branch cut along the real axis. The limit  $a \rightarrow 0$  can be taken in the definitions of  $H^{(n)}(x, a)$  and  $F^{(n)}(x, a)$ . When  $a \rightarrow 0$ , the Lorentzian in Eq. (3.1) becomes a delta function and the integral can be calculated exactly. The  $H^{(n)}(x, 0)$  are modified Gaussian functions (see Eq. (3.8)). As for the  $F^{(n)}(x, 0)$  functions, they can be expressed in terms of the real Dawson function (see Eq. (3.11)).

The  $W^{(n)}$  satisfy a recurrence formula which in turn leads to simple recurrence relations for  $H^{(n)}$  and  $F^{(n)}$  and enable us to propose a method of calculation. In the numerator of Eq. (3.3), we can write  $u^n = u^{n-1}(u - z + z)$  and immediately obtain

$$W^{(n)}(z) = zW^{(n-1)}(z) - \frac{i}{\pi^{3/2}} \int_{-\infty}^{+\infty} u^{n-1} e^{-u^2} du, \quad n \geq 1. \quad (3.4)$$

Separating the real and imaginary parts, we find the two recurrence relations

$$H^{(n)}(x, a) = xH^{(n-1)}(x, a) - aF^{(n-1)}(x, a), \quad (3.5)$$

$$F^{(n)}(x, a) = xF^{(n-1)}(x, a) + aH^{(n-1)}(x, a) - \frac{1}{\pi} c^{(n-1)}, \quad (3.6)$$

where  $c^{(n-1)}$  is a constant which is zero when  $n$  is even. When  $n$  is odd, say  $n = 2k + 1$ , with  $k$  a positive integer, we have

$$c^{(2k)} = \frac{1}{\sqrt{\pi}} \int_{-\infty}^{+\infty} u^{2k} e^{-u^2} du = \frac{1.3 \dots (2k-1)}{2^k}. \quad (3.7)$$

The recurrence relations take very simple forms when the Voigt parameter  $a = 0$ . For  $H^{(n)}$ , we obtain from the recurrence relation, or directly from Eq. (3.1),

$$H^{(n)}(x, 0) = \frac{1}{\sqrt{\pi}} x^n e^{-x^2}. \quad (3.8)$$

For  $F^{(n)}$  we have two different expressions depending on the parity of  $n$ . For odd values of  $n$  ( $n = 2k + 1$ ),

$$F^{(2k+1)}(x, 0) = xF^{(2k)}(x, 0) - \frac{1}{\pi}c^{(2k)}, \quad (3.9)$$

and for even values of  $n$  ( $n = 2k$ ),

$$F^{(2k)}(x, 0) = xF^{(2k-1)}(x, 0). \quad (3.10)$$

$F^{(0)}(x, 0)$  can be simply expressed in terms of the real Dawson's function,  $D(x)$ , as shown in Heinzl (1978). The recurrence relations (3.9) and (3.10) yield higher order  $F^{(n)}(x, 0)$  ( $n \geq 1$ ). We list below first four  $F^{(n)}(x, 0)$  for convenience:

$$\begin{aligned} F^{(0)}(x, 0) &= \frac{2}{\pi}D(x); & F^{(1)}(x, 0) &= \frac{1}{\pi} \left[ -1 + 2xD(x) \right], \\ F^{(2)}(x, 0) &= \frac{x}{\pi} \left[ -1 + 2xD(x) \right]; & F^{(3)}(x, 0) &= \frac{1}{\pi} \left[ -\frac{1}{2} - x^2 + 2x^3D(x) \right], \end{aligned} \quad (3.11)$$

where the real Dawson's function is defined (see for example Abramowitz & Stegun 1964) as

$$D(x) = e^{-x^2} \int_0^x e^{t^2} dt = \frac{1}{2} \int_0^\infty e^{-t^2/4} \sin(xt) dt. \quad (3.12)$$

### 3.2.2 Some properties of the generalized Voigt functions

We have calculated the  $H^{(n)}$  and  $F^{(n)}$  with recurrence relations given above. They have to be initialized with the values of  $H^{(0)}$ ,  $F^{(0)}$ , and  $D(x)$ . For the calculations of the latter we have used the algorithm given in Matta & Reichel (1971, see also Chiarella & Reichel 1968). Recently an efficient algorithm has been proposed by Wells (1999). We have compared graphically the results presented in Wells (1999, see his Figs. 1, 2, 11 and 12) for  $H^{(0)}$ ,  $F^{(0)}$  and first partial derivative of  $H^{(0)}$ , with the results of the Matta & Reichel algorithm. We have found that the latter has a comparable accuracy and hence have retained it for its simplicity. Actually many algorithms are available for computation of  $H^{(0)}$  and  $F^{(0)}$ . They have been introduced for studies in atmospheric physics or astrophysics. Schreier (1992) has made a comparative study of some of them based on the accuracy and computational speed (see also Wells 1999). Unfortunately these studies do not include the algorithm of Matta & Reichel (1971) but they show for example, that algorithms by Humlíček (1982) and Wells (1999) provide a greater accuracy in the computation of  $H^{(0)}$  and  $F^{(0)}$  over a larger domain in  $x$  and  $a$  than that of Hui et al. (1978). In § 3.2.3 we give some details on the Matta & Reichel algorithm and discuss accuracy problems, but first we show the overall behavior of  $H^{(n)}$  and  $F^{(n)}$  around the line center. They are displayed in Figs. 3.1

and 3.2 respectively, for  $n = 0$  to 7 and several damping parameter values ( $a = 0, 0.1, 0.5, 1.0, 2.0$ ). For computing  $H^{(n)}(x, 0)$ , we use recurrence relation (3.5), although Eq. (3.8) can also be employed. Similarly, for computing  $F^{(0)}(x, 0)$ , the first one among the set of Eqs. (3.11) is used, and for  $n \geq 1$ , recurrence relation (3.6) is used.

We now discuss Fig. 3.1. The first obvious remark is that for even  $n$  the  $H^{(n)}$  are even functions of  $x$ , and for odd  $n$ , odd functions of  $x$ . For  $a = 0$ , we can easily find the position and amplitudes of the maxima. Differentiating Eq. (3.8) with respect to  $x$ , we get

$$x_{\max}^{(n)} = \pm \sqrt{n/2}, \quad (3.13)$$

and hence the value of  $H^{(n)}$  at  $x_{\max}$  is

$$|H^{(n)}(x_{\max}^{(n)}, 0)| = \frac{1}{\sqrt{\pi}} \left(\frac{n}{2}\right)^{n/2} e^{-n/2}. \quad (3.14)$$

We note that the absolute value of  $H^{(n)}$  at maxima decreases from  $n = 0$  to  $n = 2$ , but then increases for  $n > 2$  as  $\exp\{(n/2)[\ln(n/2) - 1]\}$ . When  $a \neq 0$ , we observe a broadening of the peaks and a decrease in their amplitude. For even  $n$ , the broadening of the individual peaks causes a superposition, resulting in profiles with a single peak at line center.

We now turn to Fig. 3.2. The definition of  $F^{(n)}$  shows immediately that the  $F^{(n)}$  are odd functions of  $x$  for even  $n$  and even functions of  $x$  for odd  $n$ . For  $a = 0$ , the recurrence relations (3.9) and (3.10), and the explicit expressions given in Eq. (3.11) allow one to understand the qualitative behavior of the  $F^{(n)}$ . The function  $F^{(0)}$  is an odd function of  $x$ , which is zero at  $x = 0$  and has two symmetric peaks around  $|x| = 1$  (the maximum of the Dawson's integral is at  $x = 0.924$  and has a value 0.541, Abramowitz & Stegun 1964, p. 298 or p. 319). To go from  $F^{(0)}$  to  $F^{(1)}$  there is multiplication by  $x$  which transforms the odd function into an even function. Further, a subtraction of the term  $1/\pi$  then yields the result shown in Fig. 3.2. To go from  $F^{(1)}$  to  $F^{(2)}$ , there is only a multiplication by  $x$ . The central dip in  $F^{(1)}$  gives rise to a sine-shaped curve around  $x = 0$  in  $F^{(2)}$  and the two maxima around  $|x| = 1$  get transformed into a maximum about  $x = +1$  and a minimum about  $x = -1$ . The sine-shaped curve around  $x = 0$  in  $F^{(2)}$  will lead to a w-shaped minimum around  $x = 0$  in  $F^{(3)}$ . For  $n \geq 4$ , we have similar patterns. All the  $F^{(n)}$  with odd values of  $n$  are similar to  $F^{(3)}$  and all the  $F^{(n)}$  with even values of  $n$  are similar to  $F^{(2)}$ . We observe a small shift of the extrema away from  $x = 0$ , when  $n$  increases together with an increase in the absolute values of extrema. The reason for this behavior, common to  $H^{(n)}$  and  $F^{(n)}$ , is given above (see discussion following Eq. (3.14)).

When the damping parameter is not zero, the curves keep the same shapes but we can

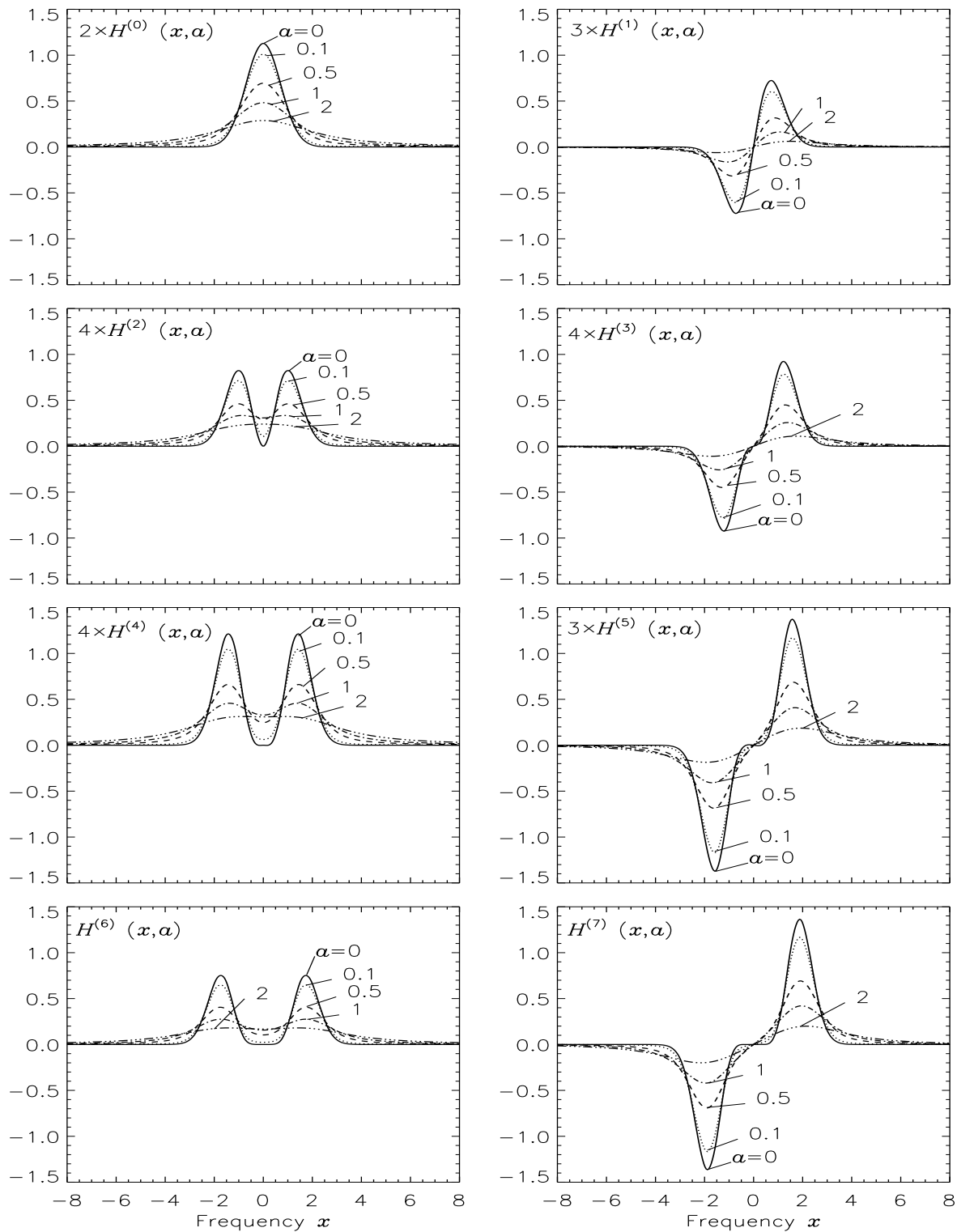


Figure 3.1:  $H^{(n)}$  functions for  $n = 0$  to  $7$ . Various line types refer to different values of the damping parameter  $\alpha$ . All the functions are expressed in same scale for the sake of comparison.  $H^{(n)}$  ( $n = 1, 3, 5, 7, \dots$ ) have positive and negative maxima, while  $H^{(n)}$  ( $n = 2, 4, 6, \dots$ ) are entirely positive valued functions.

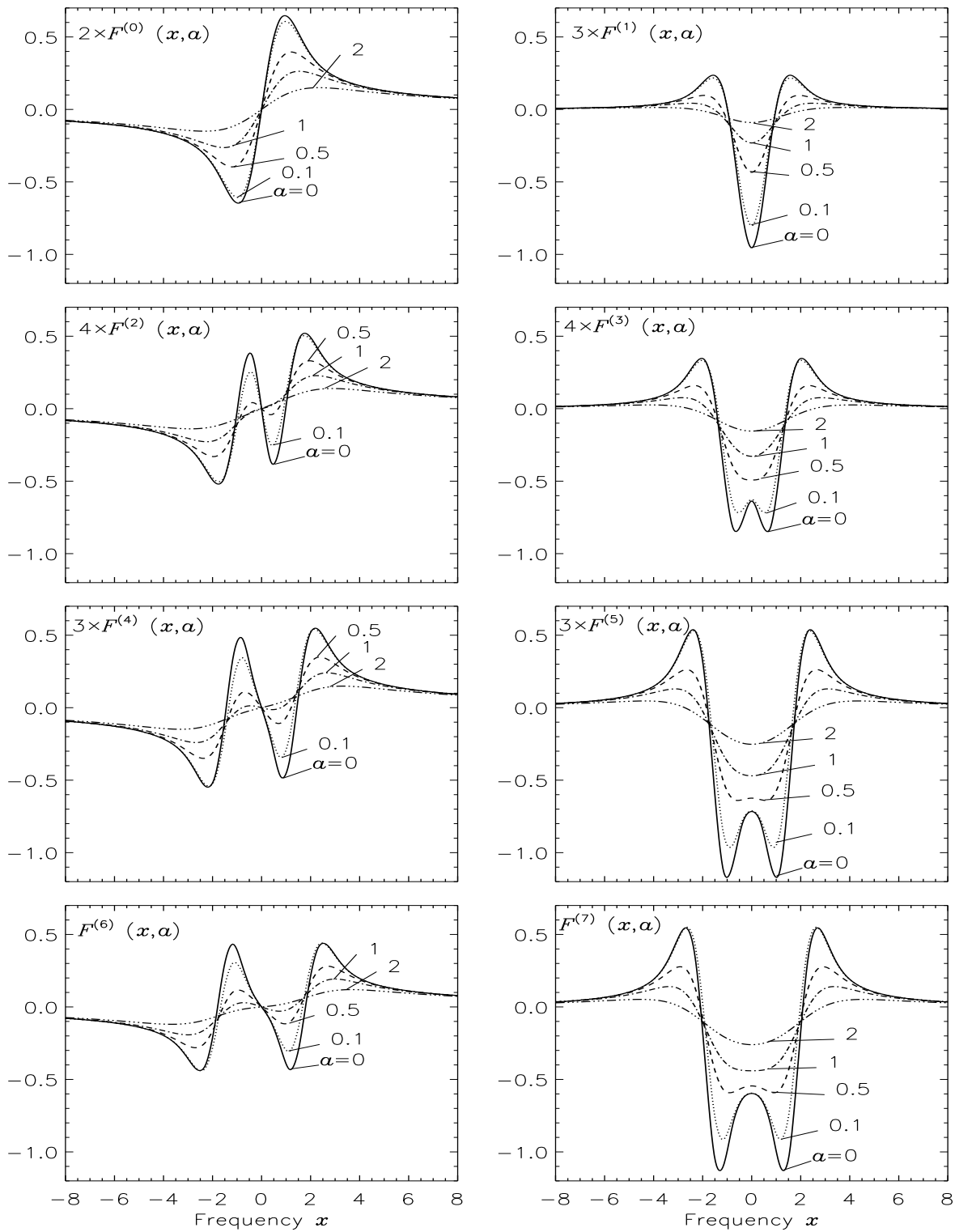


Figure 3.2: Same as Fig. 3.1, but for  $F^{(n)}$  functions. Notice that all the functions have positive and negative values.

observe a flattening of the peaks with increasing values of  $a$  due to the factor  $a^2$  in the denominator of Eq. (3.2).

The  $H^{(n)}$  and  $F^{(n)}$  functions have simple asymptotic behaviors for  $|x|$  and  $a$  going to infinity which can be deduced from Eq. (3.3). In the limit  $z \rightarrow \infty$ , we can write

$$W^{(n)}(z) \simeq \frac{i}{\pi^{3/2}} \frac{1}{z} \int_{-\infty}^{+\infty} u^n e^{-u^2} \left[ 1 + \frac{u}{z} + \text{h.o.t.} \right] du, \quad (3.15)$$

where h.o.t. stands for higher order terms. Thus when  $n$  is even, say  $n = 2k$ , we have to the leading order

$$W^{(2k)}(z) \simeq \frac{i}{\pi} \frac{c^{(2k)}}{z}, \quad (3.16)$$

where  $c^{(2k)}$  is the constant already introduced in Eq. (3.7). Thus, to the leading order,

$$H^{(2k)}(x, a) \simeq \frac{1}{\pi} \frac{a}{x^2 + a^2} c^{(2k)}, \quad a \neq 0, \quad (3.17)$$

$$F^{(2k)}(x, a) \simeq \frac{1}{\pi} \frac{x}{x^2 + a^2} c^{(2k)}. \quad (3.18)$$

When  $n$  is odd, say  $2k + 1$ , the leading term comes from the second term in the square bracket of Eq. (3.15). We thus obtain

$$W^{(2k+1)}(z) \simeq \frac{i}{\pi} \frac{c^{(2k+2)}}{z^2}, \quad (3.19)$$

from which we deduce

$$H^{(2k+1)}(x, a) \simeq \frac{1}{\pi} \frac{2ax}{(x^2 + a^2)^2} c^{(2k+2)}, \quad a \neq 0, \quad (3.20)$$

$$F^{(2k+1)}(x, a) \simeq \frac{1}{\pi} \frac{x^2 - a^2}{(x^2 + a^2)^2} c^{(2k+2)}. \quad (3.21)$$

When  $a = 0$ , the  $H^{(n)}(x, 0)$  decrease exponentially at large  $|x|$  as already pointed out above (see Eq. (3.8)).

For  $|x|$  going to infinity and  $a$  small or order of unity, Eqs. (3.17) - (3.21) simplify to

$$H^{(2k)}(x, a) \simeq \frac{1}{\pi} \frac{a}{x^2} c^{(2k)}; \quad F^{(2k)}(x, a) \simeq \frac{1}{\pi} \frac{1}{x} c^{(2k)}, \quad (3.22)$$

$$H^{(2k+1)}(x, a) \simeq \frac{1}{\pi} \frac{2a}{x^3} c^{(2k+2)}; \quad F^{(2k+1)}(x, a) \simeq \frac{1}{\pi} \frac{1}{x^2} c^{(2k+2)}. \quad (3.23)$$

For  $a$  smaller than unity, this asymptotic behavior holds for  $|x| \gg \sqrt{-\ln a}$ . One can observe in Figs. 3.1 and 3.2 that the  $H^{(n)}$  and  $F^{(n)}$  of odd order have less extended wings

than the corresponding functions of even order. We stress that the asymptotic behavior of  $F^{(n)}$  is independent of  $a$ . Thus, even for  $a = 0$ , the  $F^{(n)}$  have slowly decreasing wings. In Fig. 3.3, we can clearly observe that the wings of the  $F^{(n)}$  functions are independent of  $a$ , for say  $x > 5$ . The asymptotic behavior of the  $F^{(n)}$  can also be deduced from the asymptotic behavior of the Dawson's integral (see Abramowitz & Stegun 1964):

$$D(x) \simeq \frac{1}{2x} \left( 1 + \sum_{k=1}^{\infty} \frac{1 \cdot 3 \dots (2k-1)}{2^k x^{2k}} \right), \quad x \rightarrow \infty. \quad (3.24)$$

When  $|x|$  is small and  $a$  large, Eqs. (3.17) - (3.21) yield

$$H^{(2k)}(x, a) \simeq \frac{1}{\pi} \frac{1}{a} c^{(2k)}; \quad F^{(2k)}(x, a) \simeq \frac{1}{\pi} \frac{x}{a^2} c^{(2k)}; \quad (3.25)$$

$$H^{(2k+1)}(x, a) \simeq \frac{1}{\pi} \frac{2x}{a^3} c^{(2k+2)}; \quad F^{(2k+1)}(x, a) \simeq -\frac{1}{\pi} \frac{1}{a^2} c^{(2k+2)}. \quad (3.26)$$

These asymptotic behaviors can be observed in contour plots shown in Fig. 3.3.

### 3.2.3 Computational aspects of $H^n$ and $F^{(n)}$ functions

In this section we discuss details of computation of the generalized Voigt functions. All the calculations have been performed in double precision. For computing  $H^{(0)}$  and  $F^{(0)}$ , we use algorithm of Matta & Reichel (1971), where  $H^{(0)}$  and  $F^{(0)}$  are represented as a series in terms of an expansion parameter  $h$ . The exact values are recovered when  $h$  goes to zero. The errors due to the finite value of  $h$  can be expressed in terms of a function  $E(h)$  that goes to zero with  $h$ . They vary like  $aE(h)$  for  $H^{(0)}$  and like  $xE(h)$  for  $F^{(0)}$ . Here we use  $h = 0.5$  and 12 terms in the series expansion. For this choice, Matta & Reichel give  $E(h)$  around  $10^{-15}$  and errors around  $10^{-15}$  in the summation due to truncation of the series. The  $H^{(n)}$  and  $F^{(n)}$  functions are computed with the recurrence relations given in Eqs. (3.5) and (3.6). In Figs. 3.1 and 3.2 we have shown these functions up to  $n = 7$  for values of  $a$  and  $x$  typical of LTE (Local Thermodynamic Equilibrium), and non-LTE astrophysical problems. These figures clearly show that an asymptotic regime is reached for  $|x| > 4$ .

In Fig. 3.3 we present  $H^{(0,1,2)}$  and  $F^{(0,1,2)}$ , computed on a logarithmic grid of damping parameters ( $10^{-3} \leq a \leq 10^2$ ) and frequencies ( $10^{-3} \leq |x| \leq 10^4$ ), both with a resolution of 51 points per decade. We have chosen this very wide parameter range as considered in previous works on the numerical calculations of the function  $H^{(0)}$  and its derivative (see Wells 1999) to examine the applicability of our recurrence relations in the asymptotic regime.

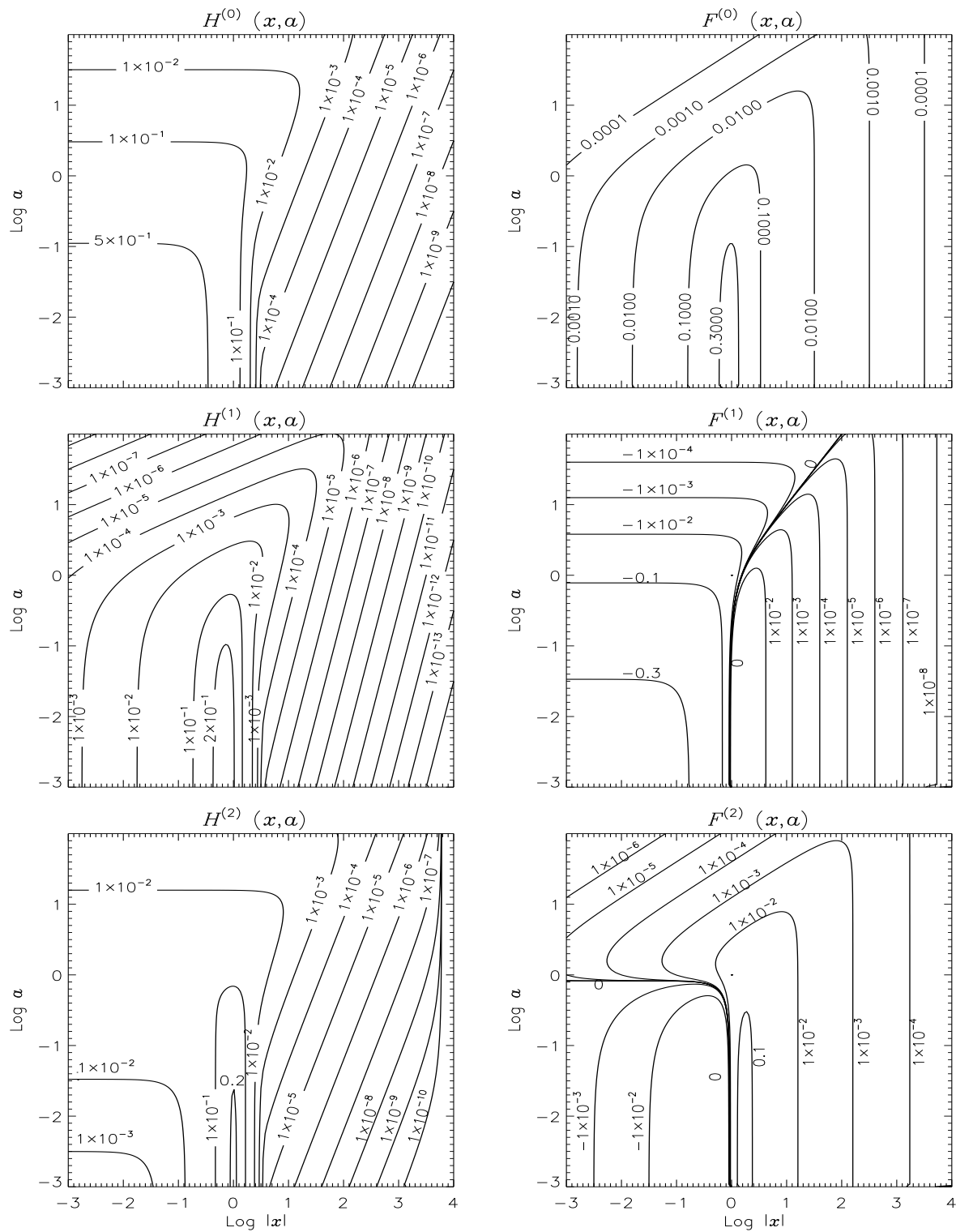


Figure 3.3: Higher order generalized Voigt functions in the  $(|x|, a)$  plane. Notice a departure from the correct asymptotic regime (large  $|x|$  and large  $a$ ) visible through the change of slope in the panel for  $H^{(2)}$ .



Since we are using recurrence relations to calculate the functions  $H^{(n)}$  and  $F^{(n)}$ , errors contained within the initial  $n = 0$  solution will propagate in the generalized Voigt functions of higher order, due to additions and subtractions of terms involved in these relations. The nature of these numerical errors are similar to those discussed by Wells (1999), with reference to the use of recurrence formula. Also, since the functions of order  $(n - 1)$  in the r.h.s. of Eqs. (3.5) and (3.6) are multiplied by factors  $x$  and  $a$ , one can expect the errors to increase with the value of these variables. This phenomenon can indeed be detected in the contour plots shown in Fig. 3.3. In the regime of large  $|x|$  the functions  $H^{(n)}$  and  $F^{(n)}$  become straight lines in the  $(\log |x|, \log a)$  plane since they vary algebraically with  $a$  and  $|x|$  (see the asymptotic behavior given in Eqs. (3.22) and (3.23)). When errors become significant, this asymptotic behavior is destroyed. In Fig. 3.3, panel with  $H^{(2)}$ , we see that the straight lines start bending for large  $|x|$  values (see the contours for function values  $< 10^{-7}$ ). For  $F^{(2)}$ , the asymptotic behavior is preserved, presumably because there are less rounding errors,  $F^{(2)}$  decreasing more slowly than  $H^{(2)}$ . The region of  $(|x|, a)$  plane in which  $H^{(n)}$  and  $F^{(n)}$  functions are computed to acceptable accuracy gradually shrinks as  $n$  increases. Figs. 3.1 and 3.2 are computed for values of  $x$ ,  $a$  and  $n$  ( $x < 20$ ,  $a < 3$ ,  $n \leq 7$ ) for which the recurrence relations yield numerically reliable results. That the recurrence relations may have some problems in the asymptotic regime of large  $|x|$  can be guessed by inserting the leading terms of the asymptotic behaviors of  $H^{(n-1)}$  and  $F^{(n-1)}$  in the r.h.s. of Eqs. (3.5) and (3.6). For  $n$  even, one correctly recovers the leading terms in the asymptotic behaviors of  $H^{(n)}$  and  $F^{(n)}$ , but for odd values of  $n$ , the leading terms cancel each other, and it becomes necessary to go to higher order terms in the asymptotic expansion. In the asymptotic regimes of large  $|x|$  and/or  $a$ , the best strategy is to use asymptotic formulae rather than recurrence relations. This strategy is recommended by Wells (1999) for the calculation of the functions  $H^{(0)}$  and  $F^{(0)}$  and is carried out in § 3.3.4 to calculate the partial derivatives of  $H^{(n)}$  and  $F^{(n)}$ .

### 3.3 Partial derivatives of generalized Voigt functions

Closed form expressions to evaluate partial derivatives of  $H^{(0)}$  and  $F^{(0)}$  are presented in Heinzl (1978). We have adapted Heinzl's approach to obtain the partial derivatives of  $H^{(n)}$  and  $F^{(n)}$  to all orders  $m$ . We first re-express  $W^{(n)}(z)$  in a form more suitable for the construction of recurrence relations for these partial derivatives. Following the same method as for  $H^{(0)}$  (see Mihalas 1978), we set  $z = x + ia$  in Eq. (3.3) and recognize that we can write

$$\frac{i}{x - u + ia} = \int_0^\infty e^{-ay} e^{i(x-u)y} dy. \quad (3.27)$$

The function  $W^{(n)}(x, a)$  can thus be rewritten as

$$W^{(n)}(x, a) = \frac{1}{\pi^{3/2}} \int_{-\infty}^{+\infty} u^n e^{-u^2} \int_0^{\infty} e^{-ay} e^{i(x-u)y} dy du. \quad (3.28)$$

Introducing the  $n^{\text{th}}$  derivative of  $e^{-iuy}$  with respect to  $y$ , and then calculating the integral over  $u$ , we obtain

$$W^{(n)}(t) = \frac{i^n}{\pi} \int_0^{\infty} e^{-ty} \frac{d^n}{dy^n} \left( e^{-y^2/4} \right) dy, \quad (3.29)$$

where  $t = a - ix$ . The function  $W^{(n)}(t)$  is analytic in the right-hand part of the complex plane defined by  $\Re(t) > 0$ .

We remark that for  $a \neq 0$ , it is possible to construct series expansions in powers of  $a$  in the form  $H^{(n)}(x, a) = \sum_k a^k H_k^{(n)}(x)$  with a technique inspired from the method described in Mihalas (1978). This is achieved by expanding  $e^{-ay}$  in Eq. (3.28) in power series of  $a$ . This method is interesting when  $a \ll 1$  and may provide  $H^{(n)}$  with a greater accuracy than the method based on recurrence relations. As recalled in Wells (1999), the calculation of  $H^{(0)}$  for  $a$  very small is a numerical challenge. Similar series expansions can be constructed for the  $F^{(n)}$  and for the partial derivatives of  $H^{(n)}$  and  $F^{(n)}$ .

Differentiating Eq. (3.29)  $m$  times with respect to  $t$ , we obtain

$$\frac{d^m}{dt^m} W^{(n)} = \frac{(-1)^m i^n}{\pi} \int_0^{\infty} y^m e^{-ty} \frac{d^n}{dy^n} \left( e^{-y^2/4} \right) dy. \quad (3.30)$$

For  $n = 0$ , the above equation is the same as Eq. (3.1) in Heinzl (1978). For simplicity we introduce the notations

$$d_t^m W^{(n)} = \frac{d^m}{dt^m} W^{(n)}, \quad \partial_x^m G^{(n)} = \frac{\partial^m G^{(n)}}{\partial x^m}, \quad \partial_a^m G^{(n)} = \frac{\partial^m G^{(n)}}{\partial a^m},$$

where  $G$  stands for any of the functions  $W$ ,  $H$  and  $F$ . The analyticity of  $W^{(n)}$  (see e.g. Eq. (3.30)) yields for any  $m$ , the two important relations:

$$d_t^m W^{(n)} = \partial_a^m W^{(n)} = \partial_a^m H^{(n)} + i \partial_a^m F^{(n)}, \quad (3.31)$$

$$d_t^m W^{(n)} = i^m \partial_x^m W^{(n)} = i^m [\partial_x^m H^{(n)} + i \partial_x^m F^{(n)}], \quad (3.32)$$

which are the consequence of the regularity (differentiability) of  $W^{(n)}$ . Equating the r.h.s. and taking the real and imaginary parts, we obtain Cauchy-Riemann conditions for the partial derivatives of  $H^{(n)}$  and  $F^{(n)}$  with respect to  $x$  and  $a$  (see for e.g. Carrier et al. 1966). For even values of  $m$ , they may be written as:

$$\partial_a^m H^{(n)} = (-1)^{m/2} \partial_x^m H^{(n)}, \quad (3.33)$$

with a similar expression for  $\partial_a^m F^{(n)}$ . For odd values of  $m$ ,

$$\partial_a^m H^{(n)} = (-1)^{(m+1)/2} \partial_x^m F^{(n)}; \quad \partial_a^m F^{(n)} = (-1)^{(m-1)/2} \partial_x^m H^{(n)}. \quad (3.34)$$

In the next section we show how to calculate the partial derivatives with respect to  $x$  of  $H^{(n)}$  and  $F^{(n)}$  of any order  $m$ . Using the Cauchy-Riemann conditions one can then get their partial derivatives with respect to  $a$ .

### 3.3.1 Recurrence relations

To compute  $d_t^m W^{(n)}$  for all possible  $n$  and  $m$ , a direct recurrence formula is most convenient. Such a formula can be derived from Eq. (3.30). Following Heinzl (1978) we integrate Eq. (3.30) by parts and thus obtain

$$d_t^m W^{(n)} = \frac{(-1)^{m+1} i^n}{\pi} \int_0^\infty \frac{y^{(m+1)}}{m+1} e^{-ty} \left[ -t \frac{d^n}{dy^n} + \frac{d^{(n+1)}}{dy^{(n+1)}} \right] (e^{-y^2/4}) dy. \quad (3.35)$$

Changing  $m \rightarrow m-1$  and  $n \rightarrow n-1$  in the above equation, we obtain the recurrence relation

$$d_t^m W^{(n)} = i m d_t^{m-1} W^{(n-1)} + i t d_t^m W^{(n-1)}; \quad (n, m) \geq 1. \quad (3.36)$$

However the above relation holds only for  $n \geq 1$ . To get recurrence relation for  $n = 0$ , we start from Eq. (3.30) with  $n = 0$ . An integration by parts yields

$$d_t^m W^{(0)} = 2 t d_t^{m-1} W^{(0)} + 2 (m-1) d_t^{m-2} W^{(0)}; \quad m \geq 2. \quad (3.37)$$

We note that our symbols  $W^{(0)}$ ,  $t$ , and  $x$  correspond to respectively  $D(w)$ ,  $w$ , and  $u$  of Heinzl (1978) and that our Eq. (3.37) is Heinzl's Eq. (4.1).

Using Eqs. (3.31) and (3.32), we can write the recurrence relations for the partial derivatives of  $W^{(n)}$  as

$$\partial_x^m W^{(n)} = (x + ia) \partial_x^m W^{(n-1)} + m \partial_x^{m-1} W^{(n-1)}, \quad (3.38)$$

$$\partial_a^m W^{(n)} = (x + ia) \partial_a^m W^{(n-1)} + i m \partial_a^{m-1} W^{(n-1)}, \quad (m, n) \geq 1. \quad (3.39)$$

With Eq. (3.38), as we now show, it is possible to construct separate recurrence relations for the partial derivatives of  $H^{(n)}$  and  $F^{(n)}$  with respect to  $x$ . Taking the real and imaginary parts of Eq. (3.38), we obtain

$$\Re [\partial_x^m W^{(n)} - m \partial_x^{m-1} W^{(n-1)} - x \partial_x^m W^{(n-1)}] = -a \Im [\partial_x^m W^{(n-1)}], \quad (3.40)$$

$$\Im [\partial_x^m W^{(n)} - m \partial_x^{m-1} W^{(n-1)} - x \partial_x^m W^{(n-1)}] = a \Re [\partial_x^m W^{(n-1)}]. \quad (3.41)$$

To obtain a recurrence relation for, say,  $\Re [\partial_x^m W^{(n)}] = \partial_x^m H^{(n)}$ , we extract from the r.h.s. of Eq. (3.40) the three terms which appear in the left hand side of Eq. (3.41). For this purpose we write Eq. (3.40) for the three sets  $(m, n)$ ,  $(m, n - 1)$  (Eq. (3.40) itself), and  $(m - 1, n)$ . Exchanging the roles of Eqs. (3.40) and (3.41), we obtain a recurrence relation for  $\Im [\partial_x^m W^{(n)}] = \partial_x^m F^{(n)}$ . It is actually the same as the recurrence relation for  $\partial_x^m H^{(n)}$ . They can be written as

$$\begin{aligned} & \partial_x^m G^{(n)} - 2x \partial_x^m G^{(n-1)} + (x^2 + a^2) \partial_x^m G^{(n-2)} - 2m \partial_x^{m-1} G^{(n-1)} \\ & + 2mx \partial_x^{m-1} G^{(n-2)} + m(m-1) \partial_x^{m-2} G^{(n-2)} = 0; \quad (n, m) \geq 2, \end{aligned} \quad (3.42)$$

where  $G^{(n)}$  stands for  $H^{(n)}$  or  $F^{(n)}$ .

The partial derivatives with respect to  $a$  can be deduced from the partial derivatives with respect to  $x$  by making use of the Cauchy-Riemann conditions written in Eqs. (3.33) and (3.34). We remark here that the procedure applied to Eq. (3.38) to obtain recurrence relations for the partial derivatives with respect to  $x$  does not work with Eq. (3.39). The real and imaginary parts of Eq. (3.39) yield a set of equations similar to (3.40) and (3.41) but they cannot be combined to obtain recurrence relations separately for the partial derivatives of  $H^{(n)}$  and  $F^{(n)}$  with respect to  $a$ .

### 3.3.2 Initialization of the recurrence relations

In order to apply the recurrence formula given in Eq. (3.42) to the computation of the partial derivatives with respect to  $x$ , it is necessary to know all the  $m^{\text{th}}$  derivatives of  $H^{(0)}$ ,  $F^{(0)}$ ,  $H^{(1)}$  and  $F^{(1)}$ , and the first derivatives with respect to  $x$  of all the  $H^{(n)}$  and  $F^{(n)}$ . The  $m^{\text{th}}$  derivatives of  $H^{(0)}$  and  $F^{(0)}$  are given in Heinzl (1978) (see also Eq. (3.59)). The  $m^{\text{th}}$  derivatives of  $H^{(1)}$  and  $F^{(1)}$  can be related to the  $m^{\text{th}}$  derivatives of  $H^{(0)}$  and  $F^{(0)}$ . Starting from the definition of  $H^{(0)}$  and  $F^{(0)}$ , making the change of variable  $x - u = v$ , and using

$$\frac{d^m}{dv^m} \left[ e^{-(x-v)^2} \right] = -2 \frac{d^{m-1}}{dv^{m-1}} \left[ (x-v) e^{-(x-v)^2} \right], \quad (3.43)$$

we immediately obtain

$$\partial_x^m G^{(1)} = -\frac{1}{2} \partial_x^{m+1} G^{(0)}, \quad m \geq 1, \quad (3.44)$$

where  $G$  stands for  $H$  or  $F$ . The first derivative with respect to  $x$  of all the  $H^{(n)}$  and  $F^{(n)}$  can be obtained with the same procedure. Starting from the definition of  $H^{(n)}$  (or  $F^{(n)}$ ), we find

$$\partial_x^1 G^{(n)} = n G^{(n-1)} - 2G^{(n+1)}, \quad (3.45)$$

where, again  $G$  stands for  $H$  or  $F$ .

## 3.3.3 Asymptotic behavior of the partial derivatives

The partial derivatives of  $H^{(n)}$  and  $F^{(n)}$  have simple asymptotic behaviors for  $|x|$  and  $a$  going to infinity which can be deduced from Eq. (3.3). In the limit  $z \rightarrow \infty$ , we can write

$$\frac{d^m W^{(n)}}{dz^m}(z) \simeq (-1)^m \frac{i}{\pi^{3/2}} \frac{m!}{z^{m+1}} \int_{-\infty}^{+\infty} u^n e^{-u^2} \left[ 1 + (m+1) \frac{u}{z} + \text{h.o.t.} \right] du. \quad (3.46)$$

We thus obtain up to the first order sub-leading term

$$\frac{d^m W^{(2k)}}{dz^m}(z) \simeq (-1)^m \frac{i}{\pi} \frac{m!}{z^{m+1}} c^{(2k)} \left[ 1 + \frac{(2k+1)(m+2)(m+1)}{4z^2} \right], \quad (3.47)$$

$$\frac{d^m W^{(2k+1)}}{dz^m}(z) \simeq (-1)^m \frac{i}{\pi} \frac{(m+1)!}{z^{m+2}} c^{(2k+2)} \left[ 1 + \frac{(2k+3)(m+3)(m+2)}{12z^2} \right], \quad (3.48)$$

where  $k$  is a positive integer and the constant  $c^{(n)}$ ,  $n$  even, has been introduced in Eq. (3.7). For example  $c^{(0)} = 1$ ,  $c^{(2)} = 1/2$ ,  $c^{(4)} = 3/4$ . Separating real and imaginary parts, one readily obtains the partial derivatives with respect to  $x$  or  $a$  of  $H^{(n)}$  and  $F^{(n)}$  of any order  $m$ . The asymptotic formulae for the first two partial derivatives of  $H^{(0,1)}$  are :

$$\frac{\partial H^{(0)}}{\partial x} \simeq -\frac{1}{\pi} \frac{2ax}{(x^2 + a^2)^2} \left[ 1 + \frac{3(x^2 - a^2)}{(x^2 + a^2)^2} \right], \quad (3.49)$$

$$\frac{\partial^2 H^{(0)}}{\partial x^2} \simeq \frac{2}{\pi} \frac{a(3x^2 - a^2)}{(x^2 + a^2)^3} \left[ 1 + \frac{3(5x^4 + a^4 - 10x^2a^2)}{(3x^2 - a^2)(x^2 + a^2)^2} \right], \quad (3.50)$$

$$\frac{\partial H^{(1)}}{\partial x} \simeq -\frac{1}{\pi} \frac{a(3x^2 - a^2)}{(x^2 + a^2)^3} \left[ 1 + \frac{3(5x^4 + a^4 - 10x^2a^2)}{(3x^2 - a^2)(x^2 + a^2)^2} \right], \quad (3.51)$$

$$\frac{\partial^2 H^{(1)}}{\partial x^2} \simeq \frac{12}{\pi} \frac{ax(x^2 - a^2)}{(x^2 + a^2)^4} \left[ 1 + \frac{5(3x^4 + 3a^4 - 10x^2a^2)}{2(x^2 - a^2)(x^2 + a^2)^2} \right]. \quad (3.52)$$

The corresponding formulae for  $F^{(0,1)}$  are :

$$\frac{\partial F^{(0)}}{\partial x} \simeq -\frac{1}{\pi} \frac{(x^2 - a^2)}{(x^2 + a^2)^2} \left[ 1 + \frac{3(x^4 + a^4 - 6x^2a^2)}{2(x^2 - a^2)(x^2 + a^2)^2} \right], \quad (3.53)$$

$$\frac{\partial^2 F^{(0)}}{\partial x^2} \simeq \frac{2}{\pi} \frac{x(x^2 - 3a^2)}{(x^2 + a^2)^3} \left[ 1 + \frac{3(x^4 + 5a^4 - 10x^2a^2)}{(x^2 - 3a^2)(x^2 + a^2)^2} \right]; \quad (3.54)$$

$$\frac{\partial F^{(1)}}{\partial x} \simeq -\frac{1}{\pi} \frac{x(x^2 - 3a^2)}{(x^2 + a^2)^3} \left[ 1 + \frac{3(x^4 + 5a^4 - 10x^2a^2)}{(x^2 - 3a^2)(x^2 + a^2)^2} \right], \quad (3.55)$$

$$\frac{\partial^2 F^{(1)}}{\partial x^2} \simeq \frac{3}{\pi} \frac{(x^4 + a^4 - 6x^2a^2)}{(x^2 + a^2)^4} \left\{ 1 + \frac{5[x^6 - a^6 - 15x^2a^2(x^2 - a^2)]}{(x^4 + a^4 - 6x^2a^2)(x^2 + a^2)^2} \right\}. \quad (3.56)$$

The first and second partial derivatives of  $H^{(2)}$  and  $F^{(2)}$  can be easily deduced from the corresponding derivatives of  $H^{(0)}$  and  $F^{(0)}$ . It suffices to multiply the leading terms by

$c^{(2)}/c^{(0)} = 1/2$  and the sub-leading term by  $c^{(4)}/c^{(2)} = 3/2$ . We stress that the asymptotic expansions for the first derivatives of  $H^{(1)}$  and  $F^{(1)}$  satisfy the exact relation in Eq. (3.44) which yields  $\partial_x^m H^{(1)}$  in terms of  $\partial_x^{m+1} H^{(0)}$  and similarly for  $F^{(1)}$ .

For  $|x|$  going to infinity and small  $a$ , the expressions given above simplify. We note that the leading terms can be recovered in a straight forward way by taking partial derivatives with respect to  $x$  of the leading terms of  $H^{(n)}$  and  $F^{(n)}$  given in Eqs. (3.22) and (3.23).

### 3.3.4 Computation of the partial derivatives of $H^{(n)}$ and $F^{(n)}$

We have used the recurrence relations given in Eqs. (3.42), (3.44) and (3.45) to calculate the  $m = 1$  and  $m = 2$  partial derivatives of  $H^{(1,2)}$  and  $F^{(1,2)}$  with respect to  $x$ . All the partial derivatives entering in Eqs. (3.42) and (3.44) have been expressed in terms of  $H^{(n)}$  and  $F^{(n)}$  using the results in Table 3.1. Fig. 3.4 left side panels show  $\partial_x^1 H^{(1)}$ ,  $\partial_x^1 H^{(2)}$ ,  $\partial_x^2 H^{(1)}$ ,  $\partial_x^2 H^{(2)}$  as a function of  $x$  for different values of  $a$  and right side panels show the corresponding quantities for  $F^{(n)}$ . In addition to the obvious symmetries, this figure shows that an asymptotic regime is reached for  $|x| > 4$  and in some cases even for  $|x| > 3$ . For small values of  $a$  (say,  $a < 0.5$ ), the derivatives show a strong frequency dependence in the line center region ( $|x| < 4$ ). For larger values of  $a$ , these derivatives weakly depend on frequency and approach an asymptotic regime with respect to  $a$  also. When  $|x|$  and  $a$  take large values, in the hundreds or thousands, the recurrence relations fail to reproduce the correct asymptotic behavior. We have encountered a similar numerical problems when computing the  $H^{(n)}$  and  $F^{(n)}$  functions for  $n \geq 2$  (see Fig. 3.3). They are due to cancellation effects and rounding errors. The accuracy problem is accentuated for larger  $n$  and larger  $m$ , and also larger values of  $|x|$  and  $a$ . For the partial derivatives considered here ( $m \leq 2$ ,  $n \leq 2$ ) the applicability domain of the recurrence relations is  $|x| \leq 11$ ,  $a \leq 11$ . It will be larger for lower order derivatives and smaller for higher ones. From the asymptotic expansions, it is clear that they are valid if  $|x|$  and/or  $a$  are sufficiently large. We have found by trial and error, comparing values given by the asymptotic expansions and values given by the recurrence relations, that they give identical results in the region  $6 < |x| \leq 11$  and  $6 < a \leq 11$ . To obtain matching solution in this domain, the asymptotic expansion had to be pushed to the first order sub-leading term. Keeping only the leading term was not sufficient. In contrast with the upper bound of the matching domain, the lower bound for the validity of the asymptotic expansion will be essentially independent of the values of  $n$  and  $m$  (see Figs. 3.1 and 3.2 for  $H^{(n)}$  and  $F^{(n)}$ ).

We show in Fig. 3.5 contour plots corresponding to Fig. 3.4. They are computed using

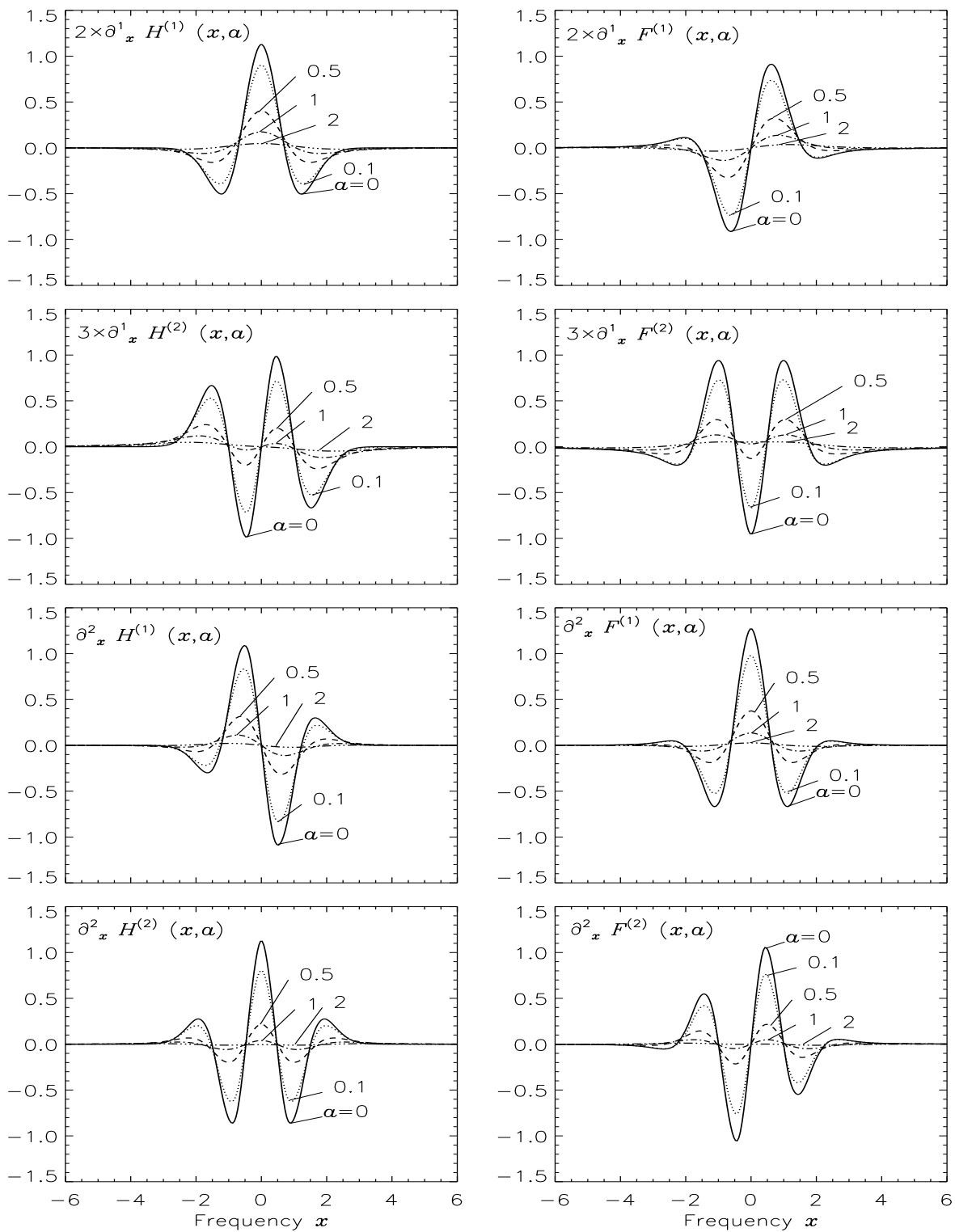


Figure 3.4: Partial derivatives first and second order ( $m \leq 2$ ) generalized Voigt functions. Notice the onset of the asymptotic regime  $|x| \sim 5$  and  $\alpha \geq 2$ .

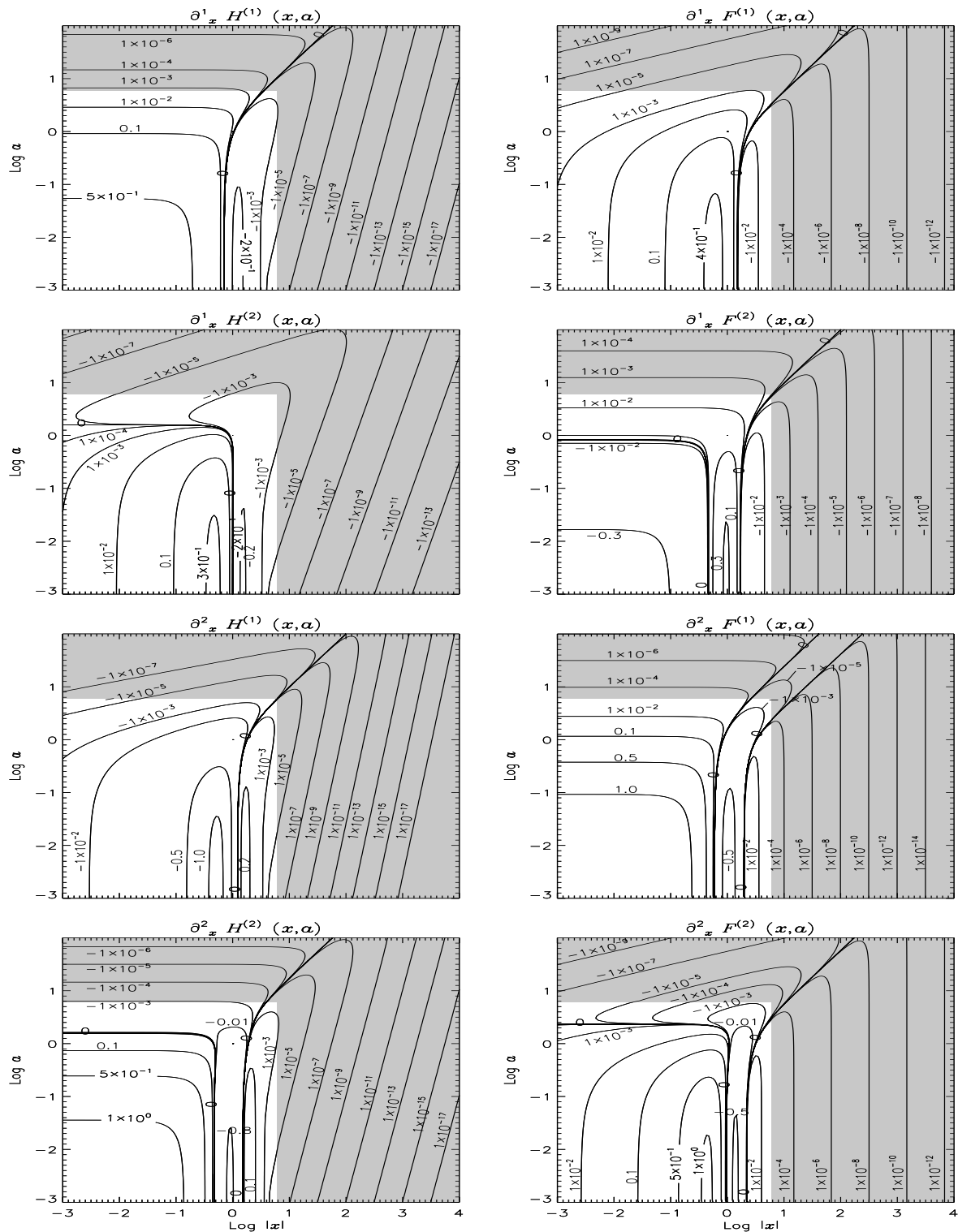


Figure 3.5: Contour plots of partial derivatives of  $H^{(n)}$  and  $F^{(n)}$  functions, in the  $(|x|, a)$  plane. For  $|x| \leq 6$  and  $a \leq 6$  recurrence relations are used. Outside, this domain asymptotic formulae are used, as the recurrence relations become less accurate.



the recurrence relations inside the domain ( $|x|, a \leq 6$ ) and the asymptotic formulae outside this domain. One can note a perfect matching between the two set of values. We stress that the same cut-off between the asymptotic domain and the recurrence relations should be applied to all the functions occurring in the recurrence relation (3.42). In computing Fig. 3.5 we use a grid resolution of 51 points per decade in both  $|x|$  and  $a$  variables. For the practical range of parameters that we encounter in Solar line formation theory, namely  $a$  smaller than unity and  $x$  a few Doppler widths, the recurrence relations are applicable.

**3.4 Partial derivatives of  $H^{(0)}$  and  $F^{(0)}$  in terms of  $H^{(n)}$  and  $F^{(n)}$**

The partial derivatives of  $H^{(0)}$  and  $F^{(0)}$  have been expressed in terms of  $H^{(0)}$  and  $F^{(0)}$  themselves in Heinzel (1978). In this section, we show that it is possible to write the partial derivatives of  $H^{(0)}$  and  $F^{(0)}$  in terms of the  $H^{(n)}$  and  $F^{(n)}$ . Setting  $n = 0$  and  $x - u = v$  in Eqs. (3.1) and (3.2), we see that the calculation of the  $m^{\text{th}}$  partial derivative of  $H^{(0)}$  with respect to  $x$  requires the  $m^{\text{th}}$  derivative of  $e^{-(x-v)^2}$ . As recognized in Luque et al. (2005), they can be expressed in terms of Hermite polynomial  $\mathcal{H}_m$  (see Abramowitz & Stegun 1964, p. 785). Indeed we have

$$\frac{d^m}{dx^m} \left( e^{-x^2} \right) = (-1)^m e^{-x^2} \mathcal{H}_m(x). \tag{3.57}$$

The Hermite polynomial can be written as a power series in  $x$  (see Abramowitz & Stegun 1964, p. 775)

$$\mathcal{H}_m(x) = m! \sum_{k=0}^{[m/2]} \frac{(-1)^k}{k!(m-2k)!} (2x)^{(m-2k)}, \tag{3.58}$$

where  $[m/2]$  means  $m/2$  for even  $m$  and  $(m-1)/2$  for odd  $m$ . Using the definition of  $H^{(n)}$ , we obtain the general formula

$$\partial_x^m H^{(0)} = (-1)^m m! \sum_{k=0}^{[m/2]} \frac{(-1)^k}{k!(m-2k)!} 2^{(m-2k)} H^{(m-2k)}. \tag{3.59}$$

For the  $\partial_x^m F^{(0)}$  we have an expression similar to the above with  $H^{(m-2k)}$  replaced by  $F^{(m-2k)}$ . With this general formula one can determine the partial derivatives of  $H^{(0)}$  for any given  $m$ , in terms of  $H^{(n)}$  functions, which in turn can be easily computed using the recurrence relations (3.5) and (3.6). We note that  $m^{\text{th}}$  partial derivatives of  $H^{(1)}$  and  $F^{(1)}$  with respect to  $x$  can also be expressed in terms of  $H^{(n)}$  and  $F^{(n)}$ , by combining Eqs. (3.44) and (3.59).

Table 3.1: First three partial derivatives of  $H^{(0)}$  and  $F^{(0)}$  in terms of  $H^{(n)}$  and  $F^{(n)}$ . The partial derivatives of  $F^{(0)}$  with respect to  $x$  have the same form as that for  $H^{(0)}$ , but with  $H^{(n)}$  replaced by  $F^{(n)}$ .

$\partial_x^1 H^{(0)} = -2H^{(1)}$	$\partial_a^1 H^{(0)} = 2F^{(1)}$	$\partial_a^1 F^{(0)} = -2H^{(1)}$
$\partial_x^2 H^{(0)} = -2H^{(0)} + 4H^{(2)}$	$\partial_a^2 H^{(0)} = 2H^{(0)} - 4H^{(2)}$	$\partial_a^2 F^{(0)} = 2F^{(0)} - 4F^{(2)}$
$\partial_x^3 H^{(0)} = 12H^{(1)} - 8H^{(3)}$	$\partial_a^3 H^{(0)} = 12F^{(1)} - 8F^{(3)}$	$\partial_a^3 F^{(0)} = -12H^{(1)} + 8H^{(3)}$

The derivatives of  $H^{(0)}$  and  $F^{(0)}$  with respect to the damping parameter  $a$  can also be expressed in terms of  $H^{(n)}$  and  $F^{(n)}$ . Using for  $n = 0$  the Cauchy-Riemann conditions given in Eqs. (3.33) and (3.34), we obtain

$$\partial_a^m H^{(0)} = (-1)^{3m/2} m! \sum_{k=0}^{m/2} \frac{(-1)^k}{k!(m-2k)!} 2^{(m-2k)} H^{(m-2k)}, \quad (3.60)$$

for even values of  $m$ , and a similar expression for  $\partial_a^m F^{(0)}$ . For odd values of  $m$

$$\partial_a^m H^{(0)} = (-1)^{(3m+1)/2} m! \sum_{k=0}^{(m-1)/2} \frac{(-1)^k}{k!(m-2k)!} 2^{(m-2k)} F^{(m-2k)}, \quad (3.61)$$

$$\partial_a^m F^{(0)} = (-1)^{(3m-1)/2} m! \sum_{k=0}^{(m-1)/2} \frac{(-1)^k}{k!(m-2k)!} 2^{(m-2k)} H^{(m-2k)}. \quad (3.62)$$

In Table 3.1 we list the first three partial derivatives of  $H^{(0)}$  with respect to  $x$ , calculated using Eq. (3.59). The partial derivatives of  $F^{(0)}$  satisfy the same relation. We also list  $\partial_a^m H^{(0)}$  and  $\partial_a^m F^{(0)}$ , for  $m = 1, 2, 3$ , calculated using the Eqs. (3.60) - (3.62). If we use the recurrence relations given in Eqs. (3.5) and (3.6) for  $H^{(n)}$  and  $F^{(n)}$ , we recover the expressions given in Table 1 of Heinzel (1978), where the derivatives are expressed in terms of  $H^{(0)}$  and  $F^{(0)}$  and polynomials in  $a$  and  $x$ .

### 3.5 Concluding remarks

In this chapter we have studied in detail a special class of functions called generalized Voigt functions  $H^{(n)}(x, a)$  and  $F^{(n)}(x, a)$  and their partial derivatives, which are useful in the theory of polarized spectral line formation in stochastic media. For  $n = 0$  they reduce

---

to the usual Voigt and Faraday-Voigt functions  $H(x, a)$  and  $F(x, a)$ . Simple recurrence relations are established and used for the calculation of the functions themselves and of their partial derivatives. Asymptotic expansions are given for large values of  $x$  and  $a$ . They are used to examine the range of applicability of the recurrence relations and to construct a numerical algorithm for the calculation of the generalized Voigt functions and of their derivatives valid in a large  $(x, a)$  domain. It is also shown that the partial derivatives of the usual  $H(x, a)$  and  $F(x, a)$  can be expressed in terms of  $H^{(n)}(x, a)$  and  $F^{(n)}(x, a)$ .



## Chapter 4

# Zeeman line radiative transfer in a random magnetic field<sup>1</sup>

### 4.1 Introduction

The Zeeman effect has been used in Astrophysics for more than a century to measure magnetic fields in the Sun, stars and other objects. The very first analysis of the Zeeman effect was carried out with uniform magnetic fields. Together with a higher quality of data, appeared multi-components models (Stenflo 1994), each component having a different but uniform, or slowly varying, magnetic field. For these models, the observable Stokes parameters are given by a conveniently weighted average of the Stokes parameters of each component. Prompted by measurements of asymmetrical Stokes  $V$  profiles, multi-components models of another type were introduced under the name of MISMA (Sánchez Almeida et al. 1996). In this model, each component is optically thin and the Zeeman absorption matrix is replaced by an average over the various components. These two types of models can be made quite sophisticated. With the terminology used for random velocity fields broadening, one can say that the first model is of the macro-turbulent type, since the averaging is over the radiation field, whereas the second type of model is of the micro-turbulent type since the averaging is done locally over the absorption matrix.

These two types of models may be insufficient to encompass the complexity of the solar atmosphere which shows inhomogeneities, undoubtedly related to the magnetic field structure, down to scales at the limit of the resolution power of present day telescopes. For example there is an active discussion on the fine structure of sunspot penumbrae. It

---

<sup>1</sup>This chapter is based on the publication : Frisch, H., Sampoorna, M., & Nagendra, K. N. 2006, *A&A*, 453, 1095-1109

seems accepted that penumbral magnetic fields have a more or less horizontal component in the form of flux tubes embedded in a more vertical background. However the diameter of these flux tubes and their spatial distribution is still a matter of controversy, the number quoted in the literature varying from 1–15km to 100 km (Sánchez Almeida 1998, Martinez Pillet 2000, Borrero et al. 2005). In addition, because of very large kinetic and magnetic Reynolds numbers prevailing in the solar atmosphere (Childress & Gilbert 1995), turbulent magnetic and velocity fields have spectra extending over a wide range of wave-numbers. We were thus strongly motivated to consider the Zeeman effect in a medium where the magnetic field is random with a correlation length, i.e. characteristic scale of variation, comparable to radiative transfer characteristic scales. The importance of this problem has been stressed again recently (Landi Degl’Innocenti 2003, LL04).

The general regime, neither macro nor micro-turbulent, leads to polarized radiative transfer equations with random coefficients. Only a few papers have been devoted to this subject in the past (see however, Faulstich 1980, Landi Degl’Innocenti 1994, henceforth L94). Recently this field seems to be receiving some renewed interest (Carroll and Staude 2003a, 2005a, Silant’ev 2005). Similar problems, somewhat simpler though, have been solved in the seventies for the transfer of unpolarized radiation in the presence of a turbulent velocity with a finite correlation length (see Mihalas 1978 for a list of references). Turbulent velocity field models introduced were less or more sophisticated. The simplest one, is the Kubo-Anderson process (KAP). For radiative transfer problems, it was used in the context of turbulent velocity fields for LTE lines (Auvergne et al. 1973) and non-LTE lines (Frisch & Frisch 1976, Froeschlé & Frisch 1980), and also in the context of random magnetic fields for the Zeeman (L94) and Hanle (Frisch 2006) effects. Actually KAP was introduced for nuclear magnetic resonance (Anderson 1954, Kubo 1954). It was also used to model the electric field in stochastic Stark effect (Brissaud & Frisch 1971, Frisch & Brissaud 1971). The name Kubo-Anderson process was introduced in Auvergne et al. (1973).

The idea of the KAP is to describe the atmosphere in a number of “eddies” having lengths distributed according to a Poisson distribution with given density. It is assumed that in each eddy the magnetic field and other random parameters, such as the velocity or temperature, are constant and their values drawn at random from a probability distribution function (PDF). The mean polarized radiation field is obtained by averaging over this distribution, and the distribution of the length of the eddies. A KAP is thus characterized by a correlation length and a PDF for the values of the random variables. The correlation length and the PDF can be selected independently. This model is fairly simple but has the correct micro and macro-turbulent limits corresponding to a correlation length which

is zero or infinite. As we show here, when associated to a simple atmospheric model like the Milne-Eddington model, it yields a convolution-type integral equation for the mean propagation operator from which one can deduce explicit expressions for the mean and rms fluctuations of the Stokes parameters at the surface of the atmosphere, and also for the cross-correlations between Stokes parameters. In L94, only the mean Stokes parameters at the surface are considered. It is quite clear that having explicit expressions is very useful for exploring finite correlation length effects.

Chapter 2 was devoted to a detailed study on the effects of a micro-turbulent magnetic field. In this chapter the main focus is on the effects of random magnetic fields with a finite correlation length. For a full description of say, turbulent eddies or random distribution of flux tubes in a sunspot penumbrae, it is necessary to incorporate all the other relevant atmospheric parameters which typically should be described by the same type of random process as the magnetic field, in particular the same correlation length. When the magnetic field is described by a KAP, incorporating other random parameters, in particular a velocity field, also described by a KAP with the same correlation length as the magnetic field is no additional work as we explain in the Remark at the end of § 4.2.6.

In § 4.2 we define the random magnetic field model, establish a convolution-type integral equation for the mean propagation operator, solve it exactly for its Laplace transform and give an explicit expression for the mean value of the Stokes parameters at the surface of the atmosphere. The latter is used in § 4.3 to study numerically the sensitivity of the mean Stokes parameters to the correlation length of a random magnetic field with isotropic Gaussian fluctuations. In § 4.4 we establish an explicit expression for the second-order moments of the Stokes parameters and study numerically the dispersion of the Stokes parameters about their mean values. The second-order moments give also access to the mean cross-correlations between Stokes parameters. In § 4.5 we introduce various extensions of the Milne-Eddington and magnetic field model and establish the corresponding integral equations for the mean propagation operator. A summary of the main results is presented in § 4.6.

## 4.2 Analytical calculation of the mean Stokes parameters

### 4.2.1 Expression for the emergent Stokes parameters

We consider a line formed in LTE in semi-infinite one-dimensional medium and assume that the source function is a linear function of depth. The radiative transfer equation for

the Stokes vector  $\mathbf{I} = (I Q U V)^T$  for rays propagating outwards along the normal to the surface may be written as

$$\frac{d}{ds}\mathbf{I}(s) = \mathbf{K}(s)[\mathbf{I}(s) - \mathbf{S}(s)]. \quad (4.1)$$

Here,  $s$  is the ray-path coordinate which varies inside the medium from 0 to  $\infty$ , with the surface at  $s = 0$ ,  $\mathbf{K}$  the  $4 \times 4$  propagation matrix and  $\mathbf{S}(s)$  the vector source function which is of the form

$$\mathbf{S}(s) = (C_0 + C_1 s) \mathbf{U}, \quad (4.2)$$

where  $C_0$  and  $C_1$  are constants and  $\mathbf{U}$  a constant vector. If  $\mathbf{S}(s)$  is of thermal origin, say the Planck function,  $\mathbf{U} = (1000)^T$ . The Stokes vector and the matrix  $\mathbf{K}$  are functions of frequency. We omit the frequency variable since there is no scattering term to couple the frequencies of incident and emergent beams.

Following the usual procedure, we define the evolution operator  $\mathbf{O}(s, s')$ , as the linear operator which transforms  $\mathbf{I}(s')$  into  $\mathbf{I}(s)$  when the source term  $\mathbf{S}$  in Eq. (4.1) vanishes (Landi Degl'Innocenti 1987, see also the Appendix D). Since photons propagate from positive  $s$  (inside) to  $s = 0$  (surface), we always take  $s' > s$ . The formal solution of the transfer equation at  $s = 0$  may be written as

$$\mathbf{I}(0) = \left[ C_0 \mathbf{E} + C_1 \int_0^\infty \mathbf{O}(0, s) ds \right] \mathbf{U}, \quad (4.3)$$

where  $\mathbf{E}$  is the  $4 \times 4$  identity matrix. We are interested in the calculation of  $\langle \mathbf{I}(0) \rangle_{\text{KA}}$ , the mean value of  $\mathbf{I}(0)$  over all the realizations of the random magnetic field, given by

$$\langle \mathbf{I}(0) \rangle_{\text{KA}} = \left[ C_0 \mathbf{E} + C_1 \int_0^\infty \langle \mathbf{O}(0, s) \rangle_{\text{KA}} ds \right] \mathbf{U}. \quad (4.4)$$

The notation  $\langle \dots \rangle_{\text{KA}}$  will always mean an average over all the realizations of the KAP.

### 4.2.2 The random magnetic field model

Assuming that the magnetic field  $\mathbf{B}(s)$  is a KAP implies that  $\mathbf{B}(s)$  is piecewise constant, jumping at randomly chosen points between random values. The jumping point  $s_i$  are uniformly and independently distributed in  $[0, +\infty]$  with a Poisson distribution of density  $\nu$  independent of  $s$ . In each interval  $s_{i-1} < s < s_i$ , the magnetic field takes a constant value  $\mathbf{B}(s) = \mathbf{B}_i$ . The  $\mathbf{B}_i$  are random variables with a PDF  $P(\mathbf{B})$  independent of  $s$ . Hence a KAP is fully characterized by a PDF and a correlation length here defined as  $1/\nu$ . Figure 4.1 shows a typical realization of a KAP. We recall that for a Poisson distribution



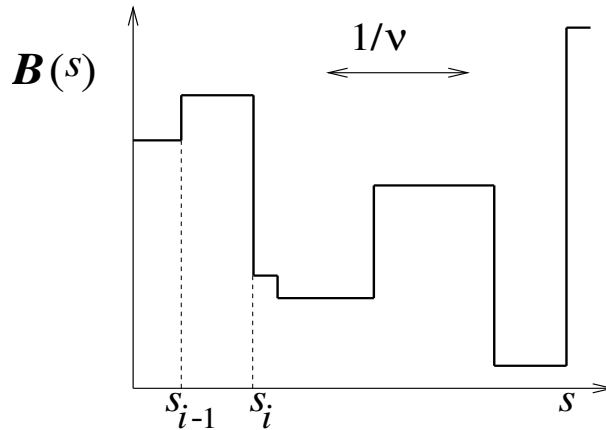


Figure 4.1: A typical realization of Kubo-Anderson process  $\mathbf{B}(s)$  with density  $\nu$  (mean correlation length is  $1/\nu$ ).

of density  $\nu$ , the probability of having  $r$  jumps in an interval of length  $L$  is  $e^{-\nu L}(\nu L)^r/r!$ . Since  $\mathbf{B}(s)$  is a KAP, any element of the Zeeman propagation matrix  $\mathbf{K}$  is also a KAP.

The absence of memory of the Poisson process implies that a KAP is a Markov process (see the definition after Eq. (4.7)). The Markov property and the fact that  $\mathbf{B}(s)$  is piecewise constant are the two properties which allow us to obtain an integral equation for the mean propagation operator. In addition, because  $P(\mathbf{B})$  and  $\nu$  are chosen independent of  $s$ , the KAP is a stationary process (unconditioned statistical properties are invariant under space translations). As a consequence, the integral equation for the mean propagation operator is of the convolution type (see Eq. (4.10)). Examples of integral equations, which are not of the convolution type because the stationarity assumption has been relaxed, are given in § 4.5.

### 4.2.3 The mean propagation operator

The mean value  $\langle \mathbf{O}(0, s) \rangle_{\text{KA}}$  can be calculated by summing the contributions from realizations having  $N=0, N=1, N=2$ , etc. jumping points (e.g. Brissaud & Frisch 1971). This technique yields the mean value as sum of a series. The latter is equivalent to a Neumann series expansion of the convolution-type integral equation (see Eq. (4.10)). Following Brissaud & Frisch (1974) (see also Auvergne et al. 1973) we show how to establish an integral equation for  $\langle \mathbf{O}(0, s) \rangle_{\text{KA}}$  directly. A summation method is used in § 4.4 to calculate the second-order moments of the Stokes parameters.

When the propagation matrix is independent of space, the propagation operator  $\mathbf{O}(s, s')$  is an exponential and depends only on the difference  $s - s'$ . Henceforth referred to as the “static” evolution operator and denoted by  $\mathbf{O}_S$  (S stands for static), it may be written as

$$\mathbf{O}_S(s, s') = e^{-(s'-s)\mathbf{K}}. \quad (4.5)$$

The exponential of the constant matrix  $\mathbf{K}$  is defined in a standard way, e.g. by its power-series expansion. The operator  $\mathbf{O}_S$  will play an important role in the following.

First we consider all the realizations without jumping point between 0 and  $s$ . For each realization  $\mathbf{K}$  is constant in the interval  $[0, s]$  and the propagation operator is given by its static value. The probability that there is no jump in the interval  $[0, s]$  is  $e^{-\nu s}$ . Thus, the contribution to the mean propagation operator from the realizations with no jump is given by:

$$\langle \mathbf{O}(0, s) \rangle_{\text{KA}}^{(\text{no jump})} = e^{-\nu s} \langle e^{-\mathbf{K}s} \rangle = e^{-\nu s} \langle \mathbf{O}_S(s) \rangle, \quad (4.6)$$

where  $\langle \dots \rangle$  denotes an average involving only the PDF  $P(\mathbf{B})$  of the magnetic field.

Next we assume that there are one or several jumping points between 0 and  $s$  and denote by  $t$  the last jumping point before  $s$ . For a Poisson distribution, the probability distribution of  $s - t$  is the same as the probability distribution of the intervals between successive jumps. Hence the probability that  $t$  falls within the small interval  $[s', s' + \delta s']$  is given by the usual Poisson formula  $\nu \delta s' e^{-\nu(s-s')}$ .

The mean of the propagation operator, when there is at least one jump, is obtained by integrating its conditional mean, *knowing* that the last jump falls in the small interval  $\delta s'$ , weighted by the probability of the conditioning event. The integral is over all possible values of  $s'$ , that is from 0 to  $s$ . (Note that the probability that the KAP has its last jump in the small interval  $\delta s'$  is proportional to  $\delta s'$ , but the conditional probability is, to leading order, independent of  $\delta s'$ .) The mean of the propagation operator for the case with at least one jump may thus be written as

$$\langle \mathbf{O}(0, s) \rangle_{\text{KA}}^{(\text{jumps})} = \int_0^s \nu e^{-\nu(s-s')} \langle \mathbf{O}(0, s) \rangle_{\text{KA}, s'} ds', \quad (4.7)$$

where  $\langle \dots \rangle_{\text{KA}, s'}$  denotes the conditional mean, evaluated with the conditional probability.

Two key properties are now used: (i) The Markov property of the KAP, which guarantees that, after conditioning, the “past” ( $0 < t < s'$ ) and the “future” ( $s' < t < s$ ) are independent and (ii) the semi-group property  $\mathbf{O}(0, s) = \mathbf{O}(0, s')\mathbf{O}(s', s)$  (see Appendix D).

Using (i) and (ii), and the fact that the propagation operator in the interval  $[s', s]$  is just the static one, we have

$$\langle \mathbf{O}(0, s) \rangle_{\mathbf{K}_A, s'} = \langle \mathbf{O}(0, s') \rangle_{\mathbf{K}_A, s'} \langle \mathbf{O}_S(s - s') \rangle. \quad (4.8)$$

We claim that

$$\langle \mathbf{O}(0, s') \rangle_{\mathbf{K}_A, s'} = \langle \mathbf{O}(0, s') \rangle_{\mathbf{K}_A}. \quad (4.9)$$

Indeed, the knowledge that a jump occurs at  $s'$ , imposes no constraint on previous jumping points and previous values of  $\mathbf{K}(t)$ . Observe that the r.h.s. is an unconditional average.

Adding the contributions from Eqs. (4.6) and (4.7), we obtain a closed convolution-type integral equation for the mean propagation operator :

$$\langle \mathbf{O}(0, s) \rangle_{\mathbf{K}_A} = e^{-\nu s} \langle \mathbf{O}_S(s) \rangle + \int_0^s \nu e^{-\nu(s-s')} \langle \mathbf{O}(0, s') \rangle_{\mathbf{K}_A} \langle \mathbf{O}_S(s - s') \rangle ds'. \quad (4.10)$$

The stationary property implies that Eq. (4.10), written here for the interval  $[0, s]$ , holds for any interval  $[s_1, s_2]$ , provided the necessary changes are made.

Equation (4.10) can be solved explicitly by introducing the Laplace transforms,

$$\tilde{\mathbf{O}}(0, p) \equiv \int_0^\infty e^{-ps} \mathbf{O}(0, s) ds, \quad (4.11)$$

$$\tilde{\mathbf{O}}_S(p) \equiv \int_0^\infty e^{-ps} \mathbf{O}_S(s) ds, \quad (4.12)$$

where it is assumed that  $\Re(p) \geq 0$  to ensure convergence. The notation  $\equiv$  means that we are introducing a definition. Equation (4.5) implies that

$$\langle \tilde{\mathbf{O}}_S(p) \rangle = \langle (p\mathbf{E} + \mathbf{K})^{-1} \rangle. \quad (4.13)$$

Taking the Laplace transform of Eq. (4.10) and transforming the integral  $\int_0^\infty ds \int_0^s \dots ds'$  into  $\int_0^\infty ds' \int_{s'}^\infty \dots ds$ , we obtain

$$\langle \tilde{\mathbf{O}}(0, p) \rangle_{\mathbf{K}_A} = \langle \tilde{\mathbf{O}}_S(p + \nu) \rangle + \nu \langle \tilde{\mathbf{O}}(0, p) \rangle_{\mathbf{K}_A} \langle \tilde{\mathbf{O}}_S(p + \nu) \rangle, \quad (4.14)$$

which leads to

$$\langle \tilde{\mathbf{O}}(0, p) \rangle_{\mathbf{K}_A} = \langle \tilde{\mathbf{O}}_S(p + \nu) \rangle \left[ \mathbf{E} - \nu \langle \tilde{\mathbf{O}}_S(p + \nu) \rangle \right]^{-1}. \quad (4.15)$$

We note that the two factors in Eq. (4.15) commute, the product being of the form  $\mathbf{A}[\mathbf{E} + \alpha\mathbf{A}]^{-1}$  with  $\alpha$  a scalar. This can be shown by expanding the second factor in powers of  $\mathbf{A}$  or by using  $\mathbf{E} = \mathbf{A}\mathbf{A}^{-1}$ .

In principle, by performing an inverse Laplace transform on the r.h.s. of Eq. (4.15) we can obtain the mean propagation operator  $\langle \mathbf{O}(0, s) \rangle_{\mathbf{K}_A}$ . Actually in our applications, only the Laplace transform is needed.

#### 4.2.4 Mean values of the emergent Stokes parameters

Returning to Eq. (4.4), we see that the integral in the r.h.s. is the Laplace transform of  $\langle O(0, s) \rangle_{\text{KA}}$  for  $p = 0$  (see Eq. (4.11)). The mean value of the Stokes vector at the surface can thus be written as

$$\langle \mathbf{I}(0) \rangle_{\text{KA}} = \left[ C_0 \mathbf{E} + C_1 \langle \tilde{\mathbf{O}}(0, 0) \rangle_{\text{KA}} \right] \mathbf{U}, \quad (4.16)$$

where, according to Eq. (4.15),

$$\langle \tilde{\mathbf{O}}(0, 0) \rangle_{\text{KA}} = \langle \tilde{\mathbf{O}}_S(\nu) \rangle \left[ \mathbf{E} - \nu \langle \tilde{\mathbf{O}}_S(\nu) \rangle \right]^{-1}, \quad (4.17)$$

with  $\langle \tilde{\mathbf{O}}_S(\nu) \rangle$  given by Eq. (4.13) with  $p = \nu$ .

Equation (4.16), combined with Eqs. (4.17) and (4.13), yields an explicit expression for the mean value of the Stokes vector at the surface. The sole averaging which has to be performed is the averaging over  $P(\mathbf{B})$  in Eq. (4.13).

As mentioned above, this expression has first been obtained in L94, with a stochastic magnetic field model identical to ours, even if it is not referred to as a KAP. The proof, which is very elegant, starts from Eq. (4.4). The integral over  $[0, \infty]$  is first replaced by a sum from  $i = 1$  to  $\infty$  over all the intervals  $[s_{i-1}, s_i]$ . Elementary algebra shows that each term in the sum is of the form

$$\left[ \prod_{j=2}^{j=i} \exp(-\Delta s_{j-1} \mathbf{K}_{j-1}) \right] \left[ \mathbf{E} - \exp(-\Delta s_j \mathbf{K}_j) \right] \mathbf{K}_j^{-1}, \quad (4.18)$$

where  $\mathbf{K}_j$  is the constant value of Zeeman propagation matrix in the interval  $\Delta s_j = s_j - s_{j-1}$ . The  $s_i$  are assumed to be distributed according to a Poisson law characterized by a density  $1/s_e$  and the  $\mathbf{K}_i$  to be uncorrelated. The mean value of the Stokes vector is then obtained by averaging over all the possible partitions of the  $s$ -axis and over the PDF of  $\mathbf{K}$ . The expression given in L94 is

$$\langle \mathbf{I}(0) \rangle_{\text{KA}} = C_0 \mathbf{U} + C_1 \left\{ \left[ \mathbf{E} - \langle (1 + s_e \mathbf{K})^{-1} \rangle \right]^{-1} \left[ \langle \mathbf{K}^{-1} \rangle - \langle (1 + s_e \mathbf{K})^{-1} \mathbf{K}^{-1} \rangle \right] \right\} \mathbf{U}. \quad (4.19)$$

Replacing  $s_e$  by  $1/\nu$ , it can be checked that Eq. (4.19) is identical to our result. A more detailed proof can be found in LL04.

#### 4.2.5 The macro and micro-turbulent limits

The macro-turbulent limit corresponds to a correlation length  $1/\nu$  going to infinity. In this case the magnetic field is independent of optical depth but its value is random with a PDF

$P(\mathbf{B})$ . Setting  $\nu = 0$  in Eq. (4.17) we obtain for the macro-turbulent limit,

$$\langle \mathbf{I}(0) \rangle_{\text{macro}} = (C_0 \mathbf{E} + C_1 \langle \mathbf{K}^{-1} \rangle) \mathbf{U}. \quad (4.20)$$

In the micro-turbulent limit, the correlation length  $1/\nu$  goes to zero. Using

$$\langle (\nu \mathbf{E} + \mathbf{K})^{-1} \rangle \simeq \frac{1}{\nu} \langle \mathbf{E} - \frac{1}{\nu} \mathbf{K} \rangle, \quad \nu \rightarrow \infty, \quad (4.21)$$

one obtains

$$\langle \mathbf{I}(0) \rangle_{\text{micro}} = (C_0 \mathbf{E} + C_1 \langle \mathbf{K} \rangle^{-1}) \mathbf{U}. \quad (4.22)$$

The micro and macro-turbulent limits can be constructed with the standard Unno-Rachkovsky solution (e.g. Rees 1987, Jefferies et al. 1989, LL04). It suffices to average  $\mathbf{K}$  over  $P(\mathbf{B})$  in the micro-turbulent limit and the Unno-Rachkovsky solution itself in the macro-turbulent limit. Following L94, we can say that the result given in Eqs. (4.16) and (4.17) is a generalization of the traditional Unno-Rachkovsky solution for random magnetic fields. We can also remark that the macro-turbulent limit is of the same nature as a standard multi-component model whereas the micro-turbulent limit is of the MISMA type. Of course, these models usually incorporate many physical processes in addition to the Zeeman effect.

#### 4.2.6 Emergent residual Stokes vector

The propagation matrix will usually contain a contribution from the background continuum opacity which we assume here to be unpolarized. The propagation matrix is then of the form

$$\mathbf{K} = k_c \mathbf{E} + k_0 \mathbf{\Phi}, \quad (4.23)$$

where  $k_c$  is the continuum opacity, assumed to be independent of frequency,  $k_0$  the frequency integrated line opacity and  $\mathbf{\Phi}$  the spectral line absorption matrix. We assume that the continuum and line source functions are identical and given by the Planck function. We introduce the ratio  $k_0/k_c = \beta$ , with  $\beta$  a constant, and the continuum optical depth  $d\tau_c = k_c ds$  which is now used as the space variable. The radiative transfer equation can then be written as

$$\frac{d\mathbf{I}}{d\tau_c} = (\mathbf{E} + \beta \mathbf{\Phi}) (\mathbf{I} - \mathbf{S}). \quad (4.24)$$

We assume that the Planck function is linear in  $\tau_c$  and write  $\mathbf{S}(\tau_c) = (C_0 + C_1 \tau_c) \mathbf{U}$  with  $\mathbf{U} = (1000)^T$ . The assumptions of a constant  $\beta$  and a linear source function are characteristic of a Milne-Eddington model.

At the surface, the Stokes vector in the continuum is given by

$$\mathbf{I}_c(0) = (C_0 + C_1)\mathbf{U}. \quad (4.25)$$

With our choice for  $\mathbf{U}$ , only the first component of  $\mathbf{I}_c$ , i.e. the intensity component  $I_c$ , is non-zero.

Equation (4.16) shows that the magnetic field effects are contained in  $\langle \tilde{\mathbf{O}}(0, 0) \rangle_{\text{KA}}$ . This suggests to introduce

$$\mathbf{r}(0) \equiv [\mathbf{E} - \tilde{\mathbf{O}}(0, 0)]\mathbf{U} = \frac{1}{C_1}[\mathbf{I}_c(0) - \mathbf{I}(0)], \quad (4.26)$$

with  $\tilde{\mathbf{O}}(0, 0)$  the Laplace transform for  $p = 0$  of the propagation operator (see Eq. (4.11)). For simplicity,  $\mathbf{r}(0)$  will be referred to as the residual Stokes vector, although the usual residual Stokes vector, also called line depression Stokes vector (Stenflo 1994, p. 244), is defined as  $[\mathbf{I}_c(0) - \mathbf{I}(0)]/I_c(0)$ . Equations (4.16) and (4.17) yield

$$\begin{aligned} \langle \mathbf{r}(0) \rangle_{\text{KA}} &= \left\{ \mathbf{E} - \langle \tilde{\mathbf{O}}_S(\nu) \rangle \left[ \mathbf{E} - \nu \langle \tilde{\mathbf{O}}_S(\nu) \rangle \right]^{-1} \right\} \mathbf{U} \\ &= \left[ \mathbf{E} - (1 + \nu) \langle \tilde{\mathbf{O}}_S(\nu) \rangle \right] \left[ \mathbf{E} - \nu \langle \tilde{\mathbf{O}}_S(\nu) \rangle \right]^{-1} \mathbf{U}, \end{aligned} \quad (4.27)$$

where

$$\langle \tilde{\mathbf{O}}_S(\nu) \rangle = \frac{1}{1 + \nu} \left\langle \left( \mathbf{E} + \frac{\beta}{1 + \nu} \Phi \right)^{-1} \right\rangle. \quad (4.28)$$

The expression of  $\langle \tilde{\mathbf{O}}_S(\nu) \rangle$  follows from Eq. (4.13) where we have set  $p = \nu$  and  $\mathbf{K} = \mathbf{E} + \beta\Phi$ .

The mean residual Stokes vector can also be written as

$$\langle \mathbf{r}(0) \rangle_{\text{KA}} = (1 + \nu) \mathbf{R}_{\text{macro}} \left( \frac{\beta}{1 + \nu} \Phi \right) \left[ \mathbf{E} + \nu \mathbf{R}_{\text{macro}} \left( \frac{\beta}{1 + \nu} \Phi \right) \right]^{-1} \mathbf{U}, \quad (4.29)$$

where

$$\mathbf{R}_{\text{macro}}(\lambda\Phi) \equiv \langle \lambda\Phi[\mathbf{E} + \lambda\Phi]^{-1} \rangle, \quad (4.30)$$

with  $\lambda$  a scalar.

In the macro-turbulent and micro-turbulent limits, Eq. (4.29) reduces to

$$\langle \mathbf{r}(0) \rangle_{\text{macro}} = \mathbf{R}_{\text{macro}}(\beta\Phi)\mathbf{U}, \quad (4.31)$$

$$\langle \mathbf{r}(0) \rangle_{\text{micro}} = \beta \langle \Phi \rangle (\mathbf{E} + \beta \langle \Phi \rangle)^{-1} \mathbf{U}. \quad (4.32)$$

The micro-turbulent limit is readily obtained by subtracting  $\mathbf{I}_c(0)$  from Eq. (4.22). The mean value  $\langle \Phi \rangle$  has been investigated in some detail for random magnetic fields with isotropic and anisotropic Gaussian fluctuations in Chapter 2 (see also DP72, DP79, Chapter 5).

The expressions given here for the residual Stokes vector are similar to the expressions given in Auvergne et al. (1973) for the broadening by a turbulent velocity field. The only difference is that the line absorption coefficient is now a matrix instead of a simple scalar. From a numerical point of view, it is more convenient to work with the residual Stokes vector than with the Stokes vector itself because the averaging is done on quantities which go to zero at large frequencies.

### Remark

In the proof given above we have assumed for simplicity that randomness in  $\Phi$ , and thus in  $\mathbf{K}$ , comes only from the magnetic field. If randomness comes from other physical parameters and provided they are described with the same type of random process as the magnetic field, in particular the same correlation length, all the theoretical results given here will still hold, but the averaging over  $P(\mathbf{B})$  must be replaced by an averaging over a joint PDF  $P(\mathbf{B}, \alpha_1, \alpha_2, \dots)$ , where the  $\alpha_i$  are scalar or vector random parameters. This remark holds also for the results in § 4.4 on the second-order moments.

## 4.3 Numerical evaluation of the mean Stokes parameters

In this section we use Eq. (4.29) to study the dependence of  $\langle \mathbf{r}(0) \rangle_{\text{KA}}$  on the correlation length of a random magnetic field with isotropic Gaussian fluctuations. We assume that the velocity field is micro-turbulent. Its effects can thus be incorporated in the definition of the profile  $\Phi$  and of the Doppler width (see Eq. (2.9)). This assumption allows us to clearly identify the effects of the random magnetic field. The function  $P(\mathbf{B})$  is already defined in § 2.4. We present the numerical results in § 4.3.1. We introduce  $f = 1/y_0$  (see Eq. (2.19)) which measures the strength of the turbulent fluctuations, large values corresponding to strong turbulence and small ones to weak turbulence.

### 4.3.1 Numerical results: Effects of a finite correlation length

The numerical method for averaging over  $P(\mathbf{B})$  is described in Chapter 2, where it is applied to the calculation of  $\langle \Phi \rangle$ . Although the expressions here are somewhat more

complicated, the same technique can be applied. The PDF  $P(\mathbf{B})$  in § 2.4 is defined in a reference frame with the  $Z$ -axis along the mean field direction, henceforth referred to as the magnetic reference frame (MRF). Thus, we need to perform the averaging in the MRF. However the Zeeman absorption matrix  $\Phi$  (see Eqs. (2.4) and (2.5) or equivalently Eqs. (2.10) and (2.11)) is written in the LOS reference frame. The corresponding expressions of the elements of  $\Phi$  in the MRF are given in Appendix E. The averaging involves a triple integration over the variables  $y = B/\sqrt{2}\sigma$ ,  $\Theta$  and  $\Psi$ . The  $y$ -integration requires some care. It is performed using a Gauss-Legendre quadrature formula with 10 to 30 points in a range  $[0, 2y_{\max}]$ . We have chosen  $y_{\max} = 1$  for  $y_0 < 1$  and  $y_{\max} = y_0$  for  $y_0 > 1$ . The mean residual Stokes parameters are calculated in a frequency-bandwidth  $[-x_{\max}, +x_{\max}]$  with  $x_{\max} = 4\gamma_B y_{\max}$ . All the calculations reported here are performed with a damping parameter  $a = 0$ . In Chapter 2 it is shown that the elements of  $\langle \Phi \rangle$  are not very sensitive to the value of  $a$ , unless it becomes larger than 0.1.

Equation (4.29) shows that  $\langle \mathbf{r}(0) \rangle_{\text{KA}}$  involves the parameter  $\nu$  and the ratio  $\beta/(1+\nu)$ . When  $\beta$  is small, and a fortiori  $\beta/(1+\nu)$ , Eq. (4.28) (or (4.30)) shows that  $\beta\Phi/(1+\nu)$  can be neglected compared to the identity matrix. Hence, for small values of  $\beta$ ,  $\langle \mathbf{r} \rangle_{\text{micro}} \simeq \langle \mathbf{r} \rangle_{\text{macro}} \simeq \beta\langle \Phi \rangle \mathbf{U}$ . Therefore for weak lines, the Stokes parameters depend only on  $P(\mathbf{B})$  (through  $\langle \Phi \rangle$ ) in the region of the line formation. For lines sensitive to the value of  $\nu$ , the micro-turbulent regime is reached when  $\beta/\nu < 1$ , i.e. when the correlation length has a line optical depth smaller than unity. These remarks are illustrated in Fig. 4.2 which shows  $L(\nu)$ , the full frequency width at half-maximum of  $\langle I(0) \rangle_{\text{KA}}$  (the mean value of Stokes  $I$ ), for different choices of  $\beta$  and  $\nu$ . We have assumed  $\Delta_Z B_0 = 0.1$  and  $\gamma_B = 1$ , in order to have for Stokes  $I$  a single well defined peak allowing for an unambiguous definition of  $L(\nu)$ . Figure 4.2 clearly shows that the dependence on  $\nu$  increases with  $\beta$  and that the micro-turbulent regime, indicated by the fact that  $L(\nu)$  reaches a constant value, sets in at roughly  $\nu \simeq \beta$ .

Numerical results illustrating the  $\nu$  dependence of  $\langle r_{I,Q,V} \rangle$ , the Stokes  $I$ ,  $Q$  and  $V$  components of  $\langle \mathbf{r}(0) \rangle_{\text{KA}}$ , are shown in Figs. 4.3 to 4.9 for different values of  $\beta$  (10 and 100) and different magnetic field parameters. To simplify the notation, without risk of confusion, we have omitted the subscript ‘‘KA’’ and the value  $\tau_c = 0$  for the components of  $\langle \mathbf{r}(0) \rangle_{\text{KA}}$ . In all the figures  $\gamma_B = \Delta_Z \sqrt{2}\sigma = 1$ , which means that the random magnetic field broadening is of the same order as the broadening by combined thermal and turbulent velocities. Hence the strength of the fluctuations is always  $f = 1/\Delta_Z B_0$ . For comparison we also show the Unno-Rachkovsky solution calculated with the mean field  $\mathbf{B}_0$ , henceforth referred to as the mean Unno-Rachkovsky solution and denoted UR. The relative varia-



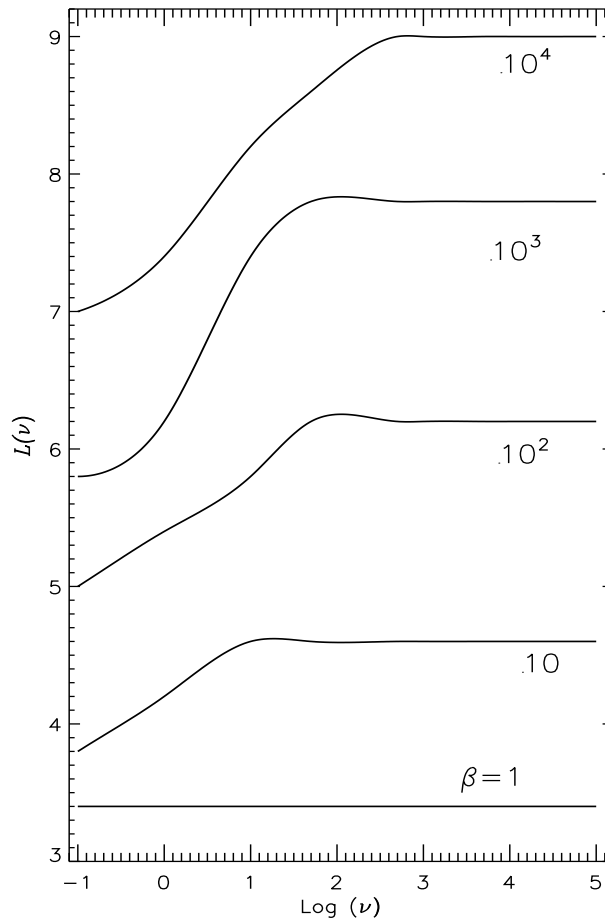


Figure 4.2: Variation of the full width at half maximum  $L(\nu)$  of the emergent Stokes  $I$  profile with the jump frequency  $\nu$  for various values of the line strength  $\beta$ . The model parameters used are  $y_0 = \Delta_Z B_0 = 0.1$ ,  $\gamma_B = 1$ ,  $\theta_0 = 0^\circ$ ,  $\phi_0 = 0^\circ$  and  $a = 0$ .

tion between the micro and macro-turbulent limits are evaluated by considering the ratio  $\delta\langle r_X \rangle = (|\langle r_X \rangle_{\text{micro}} - \langle r_X \rangle_{\text{macro}}|) / |\langle r_X \rangle_{\text{micro}}|$  where the subscript  $X$  stands for  $I$ ,  $Q$  or  $V$ .

(i) Behavior of  $\langle r_I \rangle$ . All the Figs. 4.3 to 4.9 clearly show that the profiles corresponding to a finite value of  $\nu$  lie, as expected, between the micro-turbulent and macro-turbulent limits, with the micro-turbulent profiles being at all frequencies broader than the macro-turbulent ones, especially around the frequencies corresponding to the  $\sigma$ -components. When  $\beta = 10$  (Figs. 4.3 to 4.7), the relative variations, measured with  $\delta\langle r_I \rangle$ , are between 10% and 20% at line center and also in the  $\sigma$ -components, when the latter are well separated. The main trend at line center is an increase of  $\delta\langle r_I \rangle$  with  $\Delta_Z B_0$ . The value of  $f$  seems to be essentially irrelevant. In Fig. 4.6, where the mean field is longitudinal,  $\langle r_I \rangle$  shows an unpolarized  $\pi$ -component created by the angular averaging of the  $\sin^2 \theta$  factor

## Weak Field/ Longitudinal

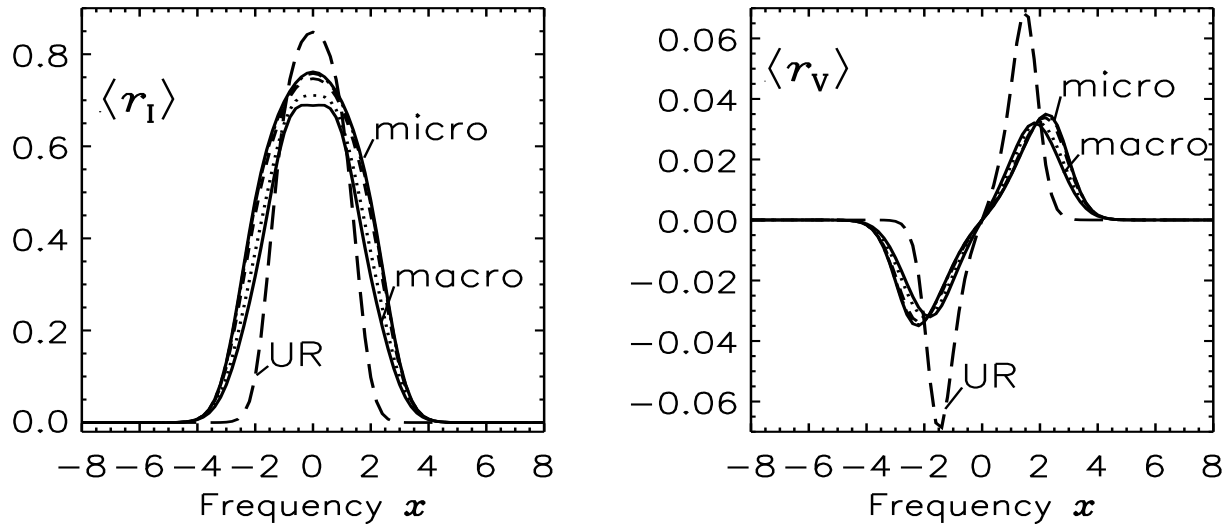


Figure 4.3: Dependence of the mean Stokes parameters on the correlation length  $1/\nu$  for a weak mean magnetic field and strong turbulence ( $f = 10$ ). The model parameters are:  $\beta = 10$ ,  $\Delta_Z B_0 = 0.1$ ,  $\gamma_B = 1$ . The mean field  $\mathbf{B}_0$  is in the direction of LOS. The full lines show the macro ( $\nu = 0$ ) and micro limits. The line types are: dotted ( $\nu = 1$ ); dashed ( $\nu = 10$ ); dot-dashed ( $\nu = 50$ ). The long-dashed lines correspond to the UR solution calculated with  $\mathbf{B}_0$ .

in the  $\pi$ -component of the absorption coefficient (see Chapter 2). The strength of this component is very sensitive to the angular distribution of the magnetic field fluctuations.

When  $\beta = 100$  (Figs. 4.8 and 4.9),  $\langle r_I \rangle$  deviates strongly from the UR solution. When  $\mathbf{B}_0$  is longitudinal (Fig. 4.8), a peak appears at line center and its value is almost independent of the correlation length. As shown by the UR solution the central component behaves essentially as  $\beta \langle \varphi_I \rangle / (1 + \beta \langle \varphi_I \rangle)$ , with  $\langle \varphi_I \rangle$  the mean value of the absorption coefficient. At line center, when the magnetic field is random,  $\langle \varphi_I \rangle$  becomes much larger than its deterministic counterpart calculated with  $\mathbf{B}_0$ . Hence when  $\beta$  is fairly large, the value of the central peak may approach unity (see Chapter 5). When  $\mathbf{B}_0$  is in the transverse direction, one observes drastic changes between the macro-turbulent and micro-turbulent limits which can also be explained in terms of the behavior of  $\langle \varphi_I \rangle$ .

(ii) Behavior of  $\langle r_V \rangle$ . A striking feature (see Figs. 4.3, 4.4, 4.6, and 4.8) is the strong deviation from the UR solution for strong and moderate turbulence (see Figs. 4.3 and 4.4 with  $f = 10$  and  $f = 1$ ) while for weak turbulence,  $\langle r_V \rangle$  stays very close to the UR

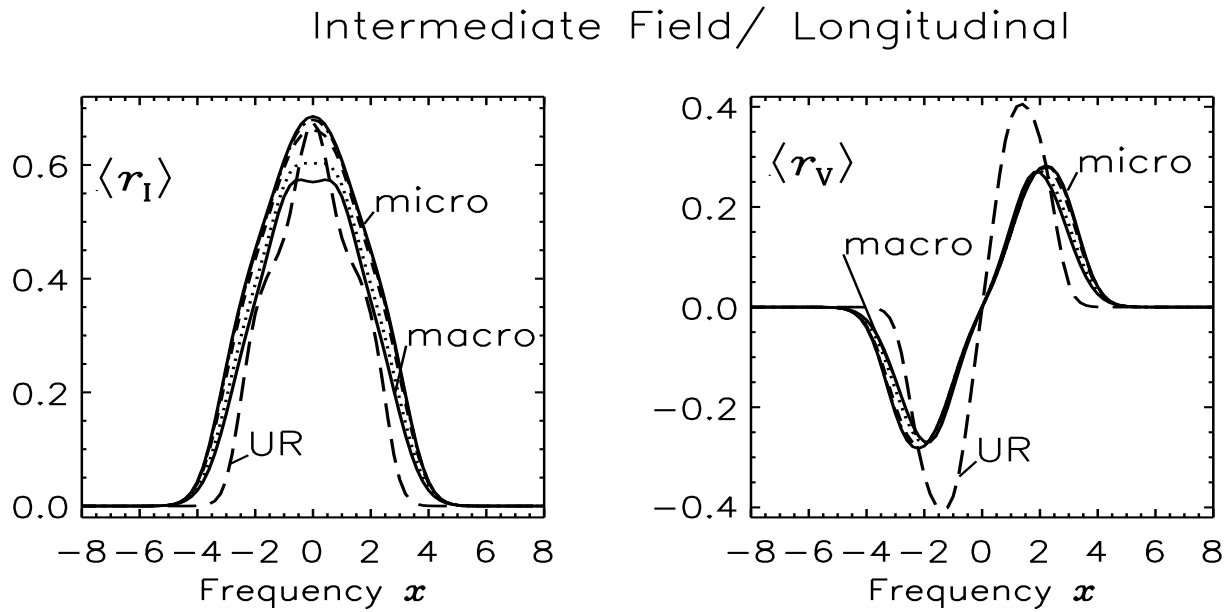


Figure 4.4: Same as Fig. 4.3 but for moderate turbulence ( $f = 1$ ). The model parameters are:  $\beta = 10$ ,  $\Delta_Z B_0 = 1$ ,  $\gamma_B = 1$ .

solution (see Figs. 4.6 and 4.8 with  $f = 1/3$ ). The relative variations between the micro and macro-turbulent limits seems to be largely independent of the value of  $f$ . They are always smaller than 10% and in general smaller than the variation of  $\langle r_I \rangle$  at line center, except for the case of Fig. 4.3 where they are both of the same order and slightly less than 10%. It thus seems that  $\langle r_V \rangle$ , can be calculated with the micro-turbulent limit, with reasonable confidence, ignoring the correlation length of the magnetic field.

(iii) Behavior of  $\langle r_Q \rangle$ . Figures 4.5, 4.7, and 4.9 show a strong deviation from the UR solution which decreases when the strength of the turbulent fluctuations decreases. For  $\beta = 10$ , at line center  $\delta \langle r_Q \rangle$  reaches 75% when  $f = 1$  but decreases to 20% when  $f = 1/3$ . For this value of  $\beta$ , one can observe that the line center is more sensitive to the correlation length than the  $\sigma$ -components. For  $\beta = 100$  and although  $f = 1/3$  only (see Fig. 4.9),  $\langle r_Q \rangle$  is very sensitive to the correlation length, at line center and also in the wings. At line center,  $\langle r_Q \rangle$  is bounded by the macro and micro-turbulent limits, but in the  $\sigma$ -components the behavior is not so simple because the position of the peaks moves away from the line center when  $\nu$  increases. The maximum depth of the  $\sigma$ -components stays however always above the macro-turbulent value. Finally we remark that for weak fluctuations ( $f = 1/3$ ),  $\langle r_Q \rangle$  will depart more from the UR solution than  $\langle r_V \rangle$  (compare Figs. 4.6 and 4.7).

All the figures shown in this section confirm the remark that micro-turbulence is reached

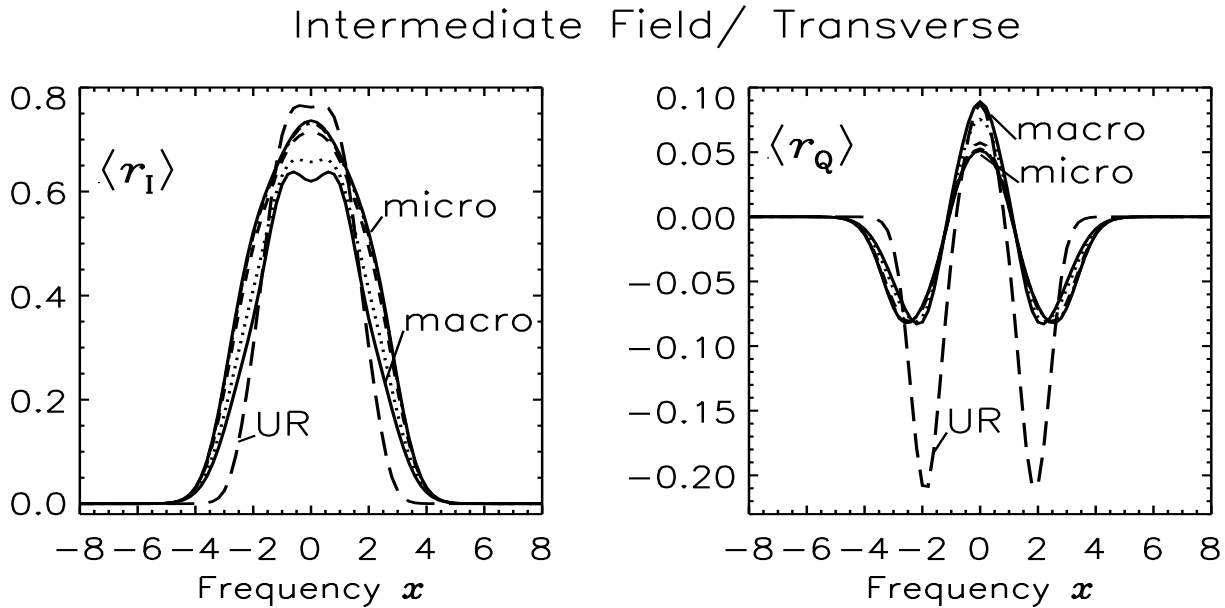


Figure 4.5: Same as Fig. 4.4, but with the mean field  $\mathbf{B}_0$  perpendicular to the direction of the LOS.

when  $\beta/\nu \simeq 1$ .

#### 4.4 Second-order moments and dispersion of the Stokes parameters

We now examine the fluctuations of the Stokes parameters around their mean values. For each Stokes parameter, we consider the square of the dispersion,

$$\sigma_i^2(0) \equiv \langle I_i^2(0) \rangle_{\text{KA}} - \langle I_i(0) \rangle_{\text{KA}}^2, \quad (4.33)$$

where  $I_i$  stands for  $I$ ,  $Q$ ,  $U$  or  $V$ . To calculate these quantities, we must consider second-order moments of the Stokes parameters, i. e. quantities of the form  $\langle I_i(0)I_j(0) \rangle_{\text{KA}}$ .

Second-order moments are investigated in Brissaud & Frisch (1974) for systems of linear stochastic equations, but only for homogeneous systems or systems with a white noise inhomogeneous term. Here we show that explicit expressions for second-order moments can also be obtained for inhomogeneous systems with a constant inhomogeneous term. Our method is inspired by Brissaud & Frisch (1974).

When the source vector  $\mathbf{S}(\tau_c)$  varies linearly with optical depth, one can easily obtain a vector transfer equation with a constant inhomogeneous term. It suffices to introduce

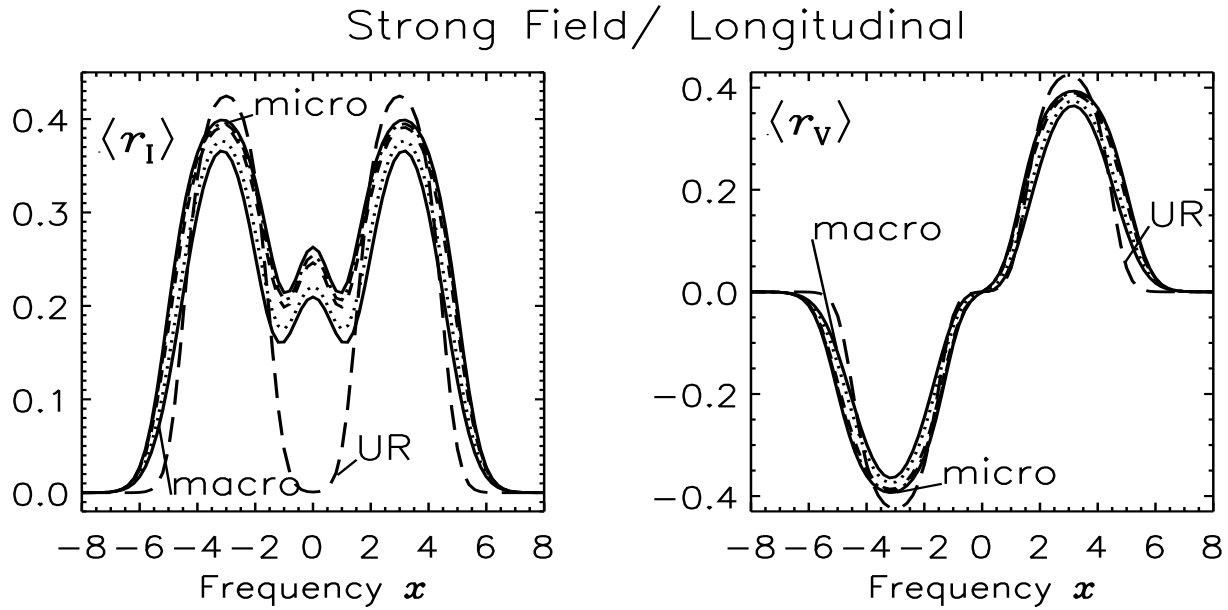


Figure 4.6: Dependence of the mean Stokes parameters on the correlation length  $1/\nu$  of the magnetic field for a strong mean field and weak turbulence ( $f = 1/3$ ). The model parameters are:  $\beta = 10$ ,  $\Delta_Z B_0 = 3$ ,  $\gamma_B = 1$ . The mean field  $\mathbf{B}_0$  is in the direction of the LOS. The line types have the same meaning as in Fig. 4.3.

the new unknown vector

$$\mathbf{Y}(\tau_c) \equiv \mathbf{I}(\tau_c) - \mathbf{S}(\tau_c). \quad (4.34)$$

Since  $\mathbf{S}$  is non-random,  $\mathbf{I}$  and  $\mathbf{Y}$  will have the same dispersion. The vector  $\mathbf{Y}$  satisfies the transfer equation

$$\frac{d\mathbf{Y}}{d\tau_c} = (\mathbf{E} + \beta\Phi)\mathbf{Y} - C_1\mathbf{U} = \mathbf{K}\mathbf{Y} - C_1\mathbf{U}, \quad (4.35)$$

where the inhomogeneous term  $C_1\mathbf{U}$  is a constant vector. In this section, to simplify the notation, we set  $\tau_c = s$ . The solution of Eq. (4.35) can be written as

$$\mathbf{Y}(s) = C_1 \left[ \int_s^\infty \mathbf{O}(s, s') ds' \right] \mathbf{U}, \quad (4.36)$$

where  $\mathbf{O}(s, s')$  has been introduced in § 4.2 as the propagation operator for Eq. (4.1).

In § 4.4.1, we use Eq. (4.36) to establish a transfer equation for the tensor product  $\mathbf{Y}(s) \otimes \mathbf{Y}(s)$  and solve it for  $\mathbf{Y}(0) \otimes \mathbf{Y}(0)$ . In § 4.4.2 we establish an explicit expression for  $\langle \mathbf{Y}(0) \otimes \mathbf{Y}(0) \rangle_{\text{KA}}$  by a summation method and use it in § 4.4.3 to illustrate the dependence of the dispersion on the correlation length and strength of the magnetic field fluctuations.

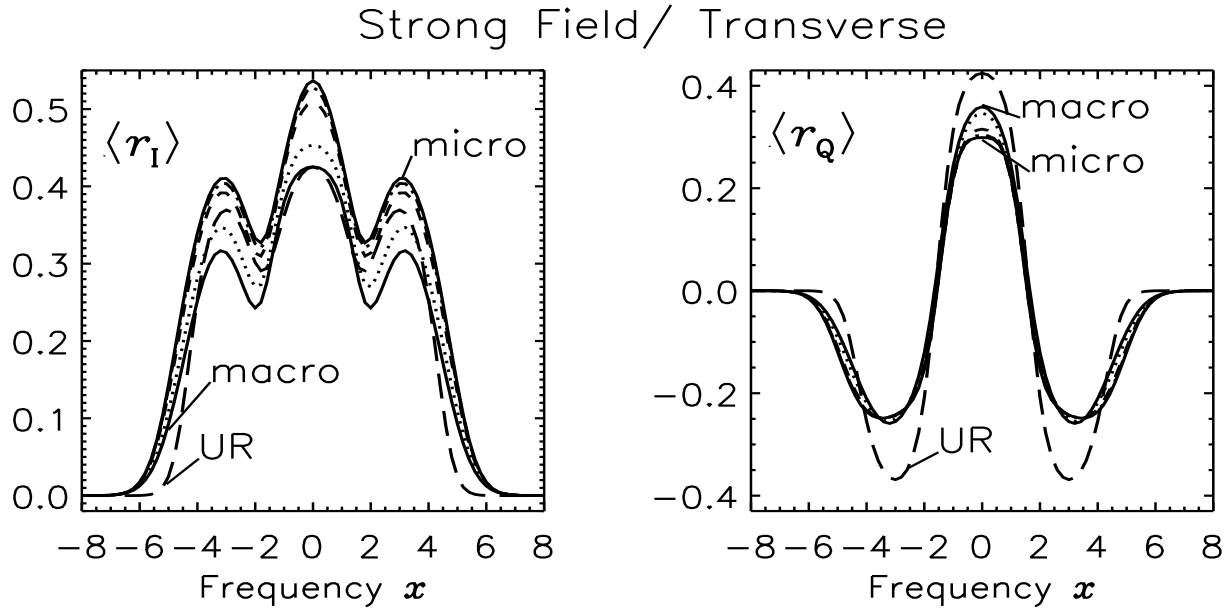


Figure 4.7: Same as Fig. 4.6, but with the mean field  $\mathbf{B}_0$  perpendicular to the direction of the LOS.

#### 4.4.1 Transfer equation for the second-order moment of the Stokes vector

To calculate the dispersions  $\sigma_i^2(0)$ , we need only  $\langle Y_i(0)Y_i(0) \rangle_{\text{KA}}$ , however the latter cannot be calculated independently of the other  $\langle Y_i(0)Y_j(0) \rangle_{\text{KA}}$ . We therefore introduce the tensor product

$$\mathbf{Y}(s) \otimes \mathbf{Y}(s) = Y_i(s)Y_j(s), \quad \text{with } i, j = 1, \dots, 4. \quad (4.37)$$

We associate the indices 1 to 4 to  $I$ ,  $Q$ ,  $U$  and  $V$ , respectively. We consider  $Y_i(s)Y_j(s)$  to be the components of a 16-dimension vector. For symmetry reasons, there is actually only 10 different components. One could also consider  $Y_i(s)Y_j(s)$  to be elements of a  $4 \times 4$  matrix. However there is no real advantage to work with a matrix and furthermore such a description will not hold for third or higher moments.

It follows from Eq. (4.35) that  $\mathbf{Y}(s) \otimes \mathbf{Y}(s)$  satisfies the transfer equation

$$\frac{d}{ds} \left[ \mathbf{Y}(s) \otimes \mathbf{Y}(s) \right] = \mathbf{K}\mathbf{Y} \otimes \mathbf{Y} + \mathbf{Y} \otimes \mathbf{K}\mathbf{Y} - C_1(\mathbf{U} \otimes \mathbf{Y} + \mathbf{Y} \otimes \mathbf{U}). \quad (4.38)$$

We recall that the tensor product, also called Kronecker product (Iyanaga & Kawada 1970, p. 851), of a  $m \times n$  matrix  $\mathbf{C}$  by a  $r \times s$  matrix  $\mathbf{D}$  is a  $mr \times ns$  matrix which can be written

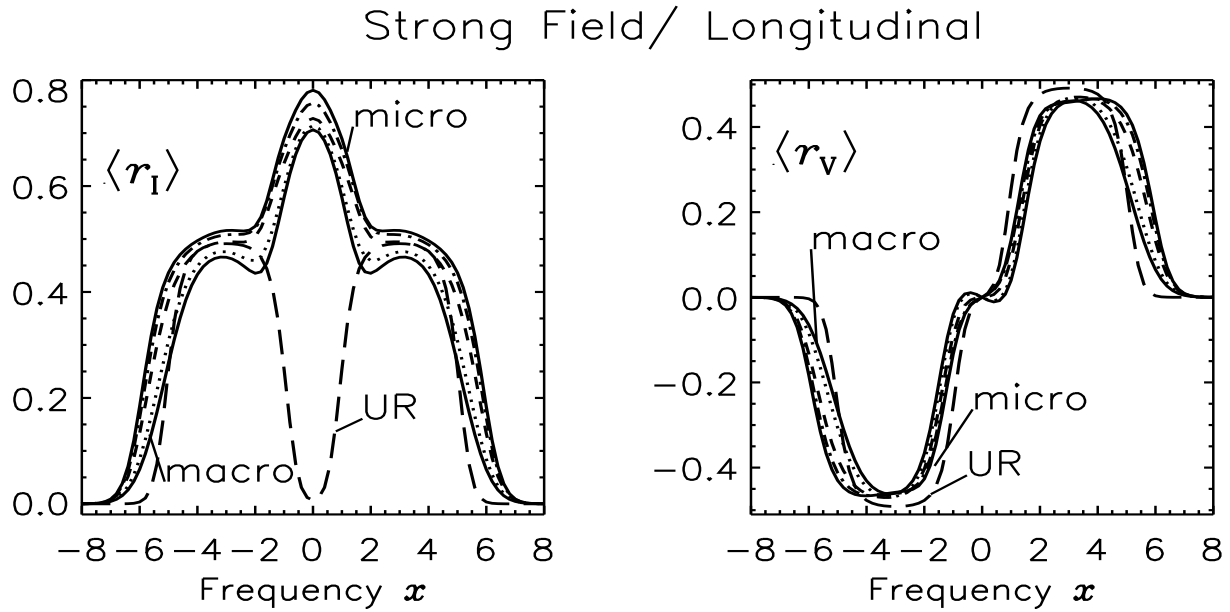


Figure 4.8: Dependence of the mean Stokes parameters on the correlation length  $1/\nu$  of the magnetic field for a strong line:  $\beta = 100$ . The other model parameters are  $\Delta_Z B_0 = 3$  and  $\gamma_B = 1$ . They are the same as in Fig. 4.6 and correspond to a weak turbulence case ( $f = 1/3$ ). The mean field  $\mathbf{B}_0$  is in the direction of the LOS. The line types have the same meaning as in Fig. 4.3.

as

$$\mathbf{C} \otimes \mathbf{D} = \begin{pmatrix} C_{11}\mathbf{D} & \dots & C_{1n}\mathbf{D} \\ \vdots & \ddots & \vdots \\ C_{m1}\mathbf{D} & \dots & C_{mn}\mathbf{D} \end{pmatrix}. \quad (4.39)$$

A useful formula satisfied by tensor products is

$$(\mathbf{C}_1 \otimes \mathbf{D}_1)(\mathbf{C}_2 \otimes \mathbf{D}_2) = \mathbf{C}_1 \mathbf{C}_2 \otimes \mathbf{D}_1 \mathbf{D}_2, \quad (4.40)$$

provided the matrix products can be defined. It is used here several times with one of the matrix, say  $\mathbf{C}_1$ , equal to the identity matrix  $\mathbf{E}$ . In that case,

$$(\mathbf{E} \otimes \mathbf{D}_1)(\mathbf{C}_2 \otimes \mathbf{D}_2) = \mathbf{C}_2 \otimes \mathbf{D}_1 \mathbf{D}_2. \quad (4.41)$$

It follows from Eq. (4.41), that Eq. (4.38) can be rewritten as

$$\frac{d}{ds} [\mathbf{Y}(s) \otimes \mathbf{Y}(s)] = \mathbf{\kappa}(\mathbf{Y} \otimes \mathbf{Y}) - C_1 \mathbf{Y}, \quad (4.42)$$

## Strong Field/ Transverse

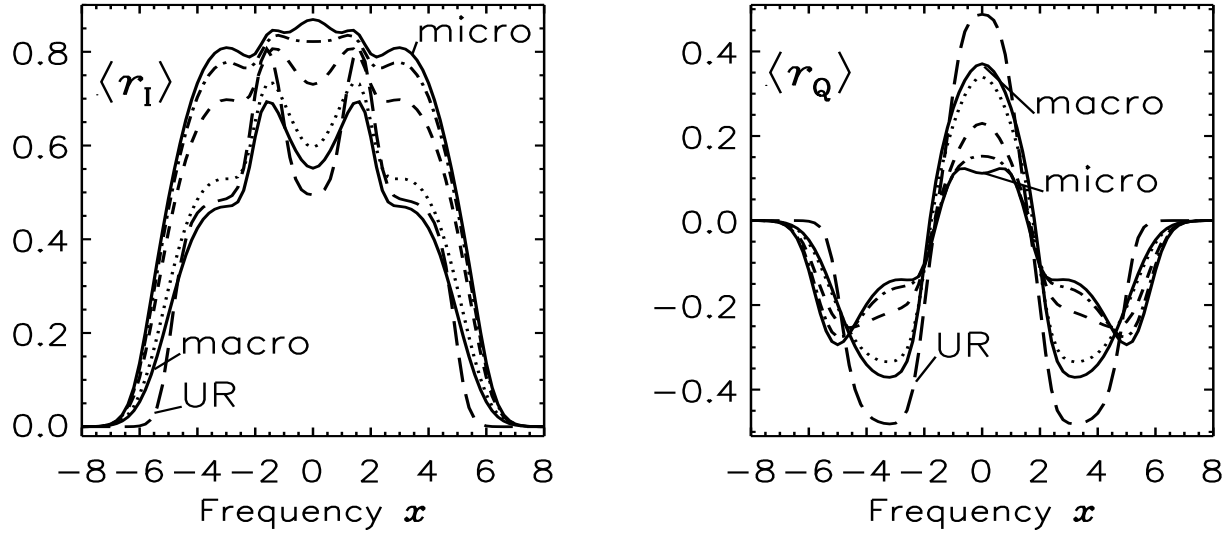


Figure 4.9: Same as Fig. 4.8, but with the mean field  $\mathbf{B}_0$  perpendicular to the direction of the LOS.

where

$$\mathbf{y} \equiv \mathbf{U} \otimes \mathbf{Y} + \mathbf{Y} \otimes \mathbf{U}, \quad (4.43)$$

$$\mathbf{K} \equiv \mathbf{K} \otimes \mathbf{E} + \mathbf{E} \otimes \mathbf{K}, \quad (4.44)$$

with  $\mathbf{y}$  a 16-dimension vector and  $\mathbf{K}$  a  $16 \times 16$  matrix. We use calligraphic letters to denote  $16 \times 16$  matrices and 16-dimension vectors (the indices run from 1 to 16).

The Green's function (or propagation operator)  $\mathcal{G}(s, s')$  associated to Eq. (4.42) satisfies

$$\frac{d}{ds} \mathcal{G}(s, s') = \mathbf{K}(s) \mathcal{G}(s, s'), \quad \text{with } \mathcal{G}(s, s) = \mathcal{E}, \quad (4.45)$$

where  $\mathcal{E}$  is the  $16 \times 16$  identity matrix. The function  $\mathcal{G}(s, s')$  has a static version  $\mathcal{G}_S(s)$  corresponding to  $\mathbf{K}$  (i.e.  $\mathbf{K}$ ) independent of  $s$ . Combining the transfer equation for  $\mathbf{O}(s, s')$  (identical to Eq. (4.45) with  $\mathbf{K}(s)$  replaced by  $\mathbf{K}(s)$ ), Eqs. (4.44) and (4.45), one can show that

$$\mathcal{G}(s, s') = \mathbf{O}(s, s') \otimes \mathbf{O}(s, s'). \quad (4.46)$$

We note that in Brissaud & Frisch (1974),  $\mathcal{G}(s, s')$  is referred to as the double Green's function.

In terms of  $\mathcal{G}(s, s')$ , the solution of Eq. (4.42) at the surface may be written as

$$\mathbf{Y}(0) \otimes \mathbf{Y}(0) = C_1 \int_0^\infty \mathcal{G}(0, s) \mathbf{y}(s) ds. \quad (4.47)$$



Using now Eqs. (4.36), (4.41) and (4.43), we obtain

$$\mathbf{Y}(0) \otimes \mathbf{Y}(0) = C_1^2 \left\{ \int_0^\infty \mathbf{g}(0, s) \int_s^\infty [\mathcal{O}^l(s, s') + \mathcal{O}^r(s, s')] ds' ds \right\} (\mathbf{U} \otimes \mathbf{U}), \quad (4.48)$$

where

$$\mathcal{O}^l(s, s') \equiv \mathbf{E} \otimes \mathbf{O}(s, s'); \quad \mathcal{O}^r(s, s') \equiv \mathbf{O}(s, s') \otimes \mathbf{E}. \quad (4.49)$$

Equation (4.48) is the starting point for the calculation of the mean value of  $\mathbf{Y}(0) \otimes \mathbf{Y}(0)$ .

#### 4.4.2 Averaging the second-order moments

In this section we show that the average of  $\mathbf{Y}(0) \otimes \mathbf{Y}(0)$  over all the realizations of the KAP can be written in the form

$$\langle \mathbf{Y}(0) \otimes \mathbf{Y}(0) \rangle_{\text{KA}} = C_1^2 \mathcal{M} (\mathbf{U} \otimes \mathbf{U}), \quad (4.50)$$

where  $\mathcal{M}$  is a  $16 \times 16$  matrix which can be written as

$$\mathcal{M} = \mathcal{M}^l + \mathcal{M}^r, \quad (4.51)$$

with

$$\mathcal{M}^{lr} = \left[ \boldsymbol{\varepsilon} - \nu \langle \tilde{\mathcal{G}}_s(\nu) \rangle \right]^{-1} \langle \tilde{\mathcal{G}}_s(\nu) \tilde{\mathcal{O}}_s^{lr}(\nu) \rangle \left[ \boldsymbol{\varepsilon} - \nu \langle \tilde{\mathcal{O}}_s^{lr}(\nu) \rangle \right]^{-1}, \quad (4.52)$$

$$\tilde{\mathcal{O}}_s^l(\nu) \equiv \mathbf{E} \otimes \tilde{\mathcal{O}}_s(\nu), \quad \tilde{\mathcal{O}}_s^r(\nu) \equiv \tilde{\mathcal{O}}_s(\nu) \otimes \mathbf{E}, \quad (4.53)$$

and  $\tilde{\mathcal{G}}_s(\nu)$  the Laplace transform of the static double Green's function. We recall that  $\tilde{\mathcal{O}}_s(\nu)$  is the Laplace transform for  $p = \nu$  of the static propagation operator  $\mathbf{O}(s, s')$  (see Eq. (4.12)). The explicit expressions of the Laplace transforms are (see Eq. (4.13))

$$\tilde{\mathcal{O}}_s(\nu) = (\nu \mathbf{E} + \mathbf{K})^{-1}; \quad \tilde{\mathcal{G}}_s(\nu) = (\nu \boldsymbol{\varepsilon} + \boldsymbol{\kappa})^{-1}. \quad (4.54)$$

We now give a proof of Eq. (4.52) based on the summation of a series, the Nth term of the series corresponding to all possible realizations having N jumping points.

#### Proof

Taking the average of Eq. (4.48), we see that

$$\mathcal{M}^l = \left\langle \int_0^\infty \mathbf{g}(0, s) \int_s^\infty \tilde{\mathcal{O}}^l(s, s') ds' ds \right\rangle_{\text{KA}}, \quad (4.55)$$

with a similar definition for  $\mathcal{M}^r$ . To simplify the notation, we drop the superscript l on  $\mathcal{M}^l$  and  $\mathcal{O}^l$ .

We now consider an interval  $[0, s']$ , and examine all the realizations of the KAP. We characterize them by the number of jumping points  $N$  in the interval  $[0, s']$ . We stress that  $s'$  varies from  $s$  to  $\infty$ , while  $s$  varies from  $0$  to  $\infty$ . In § 4.2.3 we have already introduced the elements needed here, namely that the probability to have no jump in an interval of length  $L$  is  $e^{-\nu L}$  and that the probability to have a jump in a small interval  $\delta s_i$  around  $s_i$  is  $\nu \delta s_i$ . The proof is based on the remarks that  $\mathcal{G}(s, s')$  and  $\mathcal{O}(s, s')$  satisfy a semi-group property and that they can be replaced by their static values if there is no jumping points between  $s$  and  $s'$ .

**For  $N=0$**  we have no jump in  $[0, s']$  hence no jump in  $[0, s]$  and  $[s, s']$ , so we can replace  $\mathcal{G}(0, s)$  and  $\mathcal{O}(s, s')$  by  $\mathcal{G}_S(s)$  and  $\mathcal{O}_S(s' - s)$ , respectively. We can thus write

$$\mathcal{M}_0 = \left\langle \int_0^\infty \int_s^\infty e^{-\nu s} \mathcal{G}_S(s) e^{-\nu(s'-s)} \mathcal{O}_S(s' - s) ds' ds \right\rangle, \quad (4.56)$$

where the exponential term is the probability that there is no jump in the intervals  $[0, s]$  and  $[s, s']$  and the averaging is over the random value of the vector magnetic field, i.e. over  $P(\mathbf{B})$ . The r.h.s. can be expressed in terms of the Laplace transforms of the static propagation operators. We thus obtain

$$\mathcal{M}_0 = \langle \tilde{\mathcal{G}}_S(\nu) \tilde{\mathcal{O}}_S(\nu) \rangle, \quad (4.57)$$

where the average in the r.h.s. is over  $P(\mathbf{B})$ .

**For  $N=1$** , we have one jump, say at a point  $s_1$ , within an interval  $\delta s_1$ , which can lie in either one of the intervals  $[0, s]$  or  $[s, s']$ . We consider the two cases separately.

Case (a):  $0 < s_1 < s < s'$

First we use the semi-group property to write

$$\mathcal{G}(0, s) \mathcal{O}(s, s') = \mathcal{G}(0, s_1) \mathcal{G}(s_1, s) \mathcal{O}(s, s'). \quad (4.58)$$

Since there is no jump in each of the intervals  $[0, s_1]$ ,  $[s_1, s]$ ,  $[s, s']$ , we can replace the propagation operators by their static value, which depend only on the random value of the vector magnetic field  $\mathbf{B}$ . Now we remark that with the conditioning at  $s_1$ , the random values of  $\mathbf{B}$  to the left and to the right of  $s_1$  become independent. This implies that we can average separately over  $P(\mathbf{B})$  the factor  $\mathcal{G}_S(s_1)$  and the product  $\mathcal{G}_S(s - s_1) \mathcal{O}_S(s' - s)$ .

After averaging over all the possible values of  $s_1$ , we thus obtain

$$\mathcal{M}_{1,a} = \int_0^\infty \int_0^s \int_s^\infty \nu e^{-\nu s_1} \langle \mathcal{G}_S(s_1) \rangle e^{-\nu(s-s_1)} e^{-\nu(s'-s)} \langle \mathcal{G}_S(s-s_1) \mathcal{O}_S(s'-s) \rangle ds' ds_1 ds, \quad (4.59)$$

where the product of exponential terms, multiplied by  $\nu$ , is the probability of having only one jump at  $s_1$  (within  $\delta s_1$ ).

The integrations over  $s_1$ ,  $s$  and  $s'$  can be carried out explicitly in terms of the Laplace transforms  $\tilde{\mathcal{G}}_S(\nu)$  and  $\tilde{\mathcal{O}}_S(\nu)$ . The integral over  $s'$  is already a Laplace transform. Changing the order of integration, the integral  $\int_0^\infty ds \int_0^s \dots ds_1$  can be transformed into  $\int_0^\infty ds_1 \int_{s_1}^\infty \dots ds$ . We thus obtain

$$\mathcal{M}_{1,a} = \nu \langle \tilde{\mathcal{G}}_S(\nu) \rangle \langle \tilde{\mathcal{G}}_S(\nu) \tilde{\mathcal{O}}_S(\nu) \rangle, \quad (4.60)$$

where the averages are over the distribution  $P(\mathbf{B})$ .

Case (b):  $0 < s < s_1 < s'$

Since  $s_1$  is to the right of  $s$ , we now write

$$\mathcal{G}(0, s) \mathcal{O}(s, s') = \mathcal{G}(0, s) \mathcal{O}(s, s_1) \mathcal{O}(s_1, s'). \quad (4.61)$$

Proceeding exactly as above, we obtain

$$\mathcal{M}_{1,b} = \int_0^\infty \int_s^\infty \int_s^{s'} e^{-\nu s} e^{-\nu(s_1-s)} \langle \mathcal{G}_S(s) \mathcal{O}_S(s_1-s) \rangle \nu e^{-\nu(s'-s_1)} \langle \mathcal{O}_S(s'-s_1) \rangle ds_1 ds' ds. \quad (4.62)$$

Transforming the integral  $\int_s^\infty ds' \int_s^{s'} \dots ds_1$  into  $\int_s^\infty ds_1 \int_{s_1}^\infty \dots ds'$ , integrating over  $s'$ , then over  $s_1$  and finally over  $s$ , we obtain

$$\mathcal{M}_{1,b} = \nu \langle \tilde{\mathcal{G}}_S(\nu) \tilde{\mathcal{O}}_S(\nu) \rangle \langle \tilde{\mathcal{O}}_S(\nu) \rangle. \quad (4.63)$$

**For  $N=2$** , we have three different cases: (a) two jumping points, say  $s_1$  and  $s_2$ , in the interval  $[0, s]$  and zero in the interval  $[s, s']$ ; (b) one jumping point  $s_1$  in  $[0, s]$  and one jumping point  $s_2$  in  $[s, s']$ ; (c) zero jumping points in  $[0, s]$  and two jumping points in  $[s, s']$ . With the same kind of arguments as above, we obtain

$$\begin{aligned} \mathcal{M}_{2,a} &= \nu^2 \langle \tilde{\mathcal{G}}_S(\nu) \rangle^2 \langle \tilde{\mathcal{G}}_S(\nu) \tilde{\mathcal{O}}_S(\nu) \rangle, \\ \mathcal{M}_{2,b} &= \nu^2 \langle \tilde{\mathcal{G}}_S(\nu) \rangle \langle \tilde{\mathcal{G}}_S(\nu) \tilde{\mathcal{O}}_S(\nu) \rangle \langle \tilde{\mathcal{O}}_S(\nu) \rangle, \\ \mathcal{M}_{2,c} &= \nu^2 \langle \tilde{\mathcal{G}}_S(\nu) \tilde{\mathcal{O}}_S(\nu) \rangle \langle \tilde{\mathcal{O}}_S(\nu) \rangle^2. \end{aligned} \quad (4.64)$$

We can now construct the general formula for an arbitrary number of jumps. We denote by  $s_-$  the last jumping point before  $s$  and by  $s_+$  the first jumping point after  $s$  ( $s_- < s < s_+$ ). The two intervals  $[s_-, s]$  and  $[s, s_+]$  will produce a term  $\langle \tilde{\mathcal{G}}_S(\nu) \tilde{\mathcal{O}}_S(\nu) \rangle$ . All the intervals to the right of  $s_+$  will contribute with factors  $\langle \tilde{\mathcal{O}}_S(\nu) \rangle$  and all the intervals to the left of  $s_-$  with factors  $\langle \tilde{\mathcal{G}}_S(\nu) \rangle$ . If the last jumping point  $s_N$  is such that  $s_N < s$ , the term  $\langle \tilde{\mathcal{G}}_S(\nu) \tilde{\mathcal{O}}_S(\nu) \rangle$  comes from the intervals  $[s_N, s]$  and  $[s, \infty]$  and if the first jumping point  $s_1$  is such that  $s < s_1$ , then this term comes from the intervals  $[0, s]$  and  $[s, s_1]$ .

Summing all the contributions from  $N=0$  to infinity, we find the result given in Eq. (4.52) for the matrices  $\mathcal{M}^l$  and  $\mathcal{M}^r$ . The central term corresponds to the interval  $[s_-, s_+]$ , the term to its right contains the contributions of all the intervals to the right of  $s_+$  and the term to its left the contributions of all the intervals between 0 and  $s_-$ .

We can now write an explicit expression for  $\sigma_i^2(0)$ . Since we have assumed that the line and continuum source vectors are unpolarized,  $\mathbf{U} = (1\ 0\ 0\ 0)^T$  and  $\mathbf{u} = (1\ 0\ \dots\ 0)^T$ . Hence, only the first column in the matrix  $\mathcal{M}$  will contribute to  $\langle \mathbf{Y}(0) \otimes \mathbf{Y}(0) \rangle_{\text{KA}}$ . For Stokes  $I$  and  $V$  we thus have

$$\sigma_1^2(0) = C_1^2 \left\{ \mathcal{M}(1, 1) - \left[ \langle \tilde{\mathcal{O}}(0, 0) \rangle_{\text{KA}}(1, 1) \right]^2 \right\}, \quad (4.65)$$

and

$$\sigma_4^2(0) = C_1^2 \left\{ \mathcal{M}(16, 1) - \left[ \langle \tilde{\mathcal{O}}(0, 0) \rangle_{\text{KA}}(4, 1) \right]^2 \right\}, \quad (4.66)$$

where the matrix  $\langle \tilde{\mathcal{O}}(0, 0) \rangle_{\text{KA}}$  is given in Eq. (4.17) and the numbers refer to the matrix elements. We have similar expressions for the dispersion around the mean values of Stokes  $Q$  and  $U$ . We note also that the knowledge of the elements of  $\mathcal{M}$  gives access to the cross-correlations  $[\langle I_i(0) I_j(0) \rangle_{\text{KA}} - \langle I_i(0) \rangle_{\text{KA}} \langle I_j(0) \rangle_{\text{KA}}]$ ,  $i \neq j$ .

In the micro-turbulent and macro-turbulent limits, the expressions for the dispersion of the Stokes parameters are simpler. In the micro-turbulent limit, the dispersion is simply zero since all the coefficients in the transfer equation are replaced by their mean values. One is actually dealing with a deterministic problem. In the macro-turbulent limit the second order moments can be deduced from the UR solution which leads to

$$\mathcal{M}_{\text{macro}} = \langle \mathbf{K}^{-1} \otimes \mathbf{K}^{-1} \rangle. \quad (4.67)$$

One can check that Eq. (4.52) with  $\nu = 0$  is consistent with this expression. The macro-turbulent limit is interesting because it provides an upper limit for the dispersion. This point is illustrated in the next section.

We checked the result given in Eqs. (4.50) to (4.54) by applying our summation method to a scalar transfer equation where the propagation matrix  $\mathbf{K}$  is replaced by an absorption coefficient  $K$ . For this scalar problem, the second-order moment can also be calculated with a method introduced by Bourret et al. (1973) which relies on the introduction of new quadratic dependent variables, chosen in such a way that they satisfy a homogeneous system of linear stochastic equations. This method, restricted to scalar problems, has been applied by Auvergne et al. (1973) for the broadening of spectral lines by a turbulent velocity field.

Once the problem of calculating the second-order moments of  $\langle I_i(0)I_j(0) \rangle_{\text{KA}}$  has been reduced to the calculation of the mean value of the r.h.s. in Eq. (4.48), it is very likely that methods somewhat different from the summation method presented here can be set up. In particular L94 method should work, although it could be algebraically somewhat cumbersome since it does not make direct use of the Laplace transform of the evolution operator.

#### 4.4.3 Numerical evaluation of the dispersion

To calculate the dispersion of the Stokes parameters we must evaluate the elements of the matrix  $\mathcal{M}$ . The averages over  $P(\mathbf{B})$  (see Eq. (4.52)) are performed with Gauss-Legendre quadratures. The integration over the magnetic field strength can be carried out with the same grid points as for the calculation of the mean Stokes parameters (see § 4.3.1). The angular integrations over the polar angles  $\Theta$  and  $\Psi$  require more refined grids. Typically one needs around 30 points to calculate the dispersion while 10 or less are enough for the mean values. We note also that the width  $x_{\text{max}}$  of the frequency domain must be significantly increased.

In the macro-turbulent limit, the calculation of the dispersion is much simpler since

$$\sigma_i^2(0)_{\text{macro}} = \langle I_i^2(0) \rangle - \langle I_i(0) \rangle^2, \quad (4.68)$$

where  $I_i(0)$  is the Unno-Rachkovsky solution for the Stokes parameter  $I_i$ .

We note also that all the results obtained for the second-order moments of the Stokes parameters hold for the residual Stokes parameters, provided we divide them by  $C_1^2$  (see Eq. (4.50)).

Figure 4.10 shows  $\langle r_X \rangle \pm \sigma_X$ , ( $\sigma_X > 0$ ) for the four Stokes parameters and different values of  $\nu$  (we drop the subscript - the same convention as in § 4.3.1). The magnetic field parameters are  $\Delta_Z B_0 = 1$  and  $\gamma_B = 1$  as in Figs. 4.4 and 4.5 and hence correspond to a

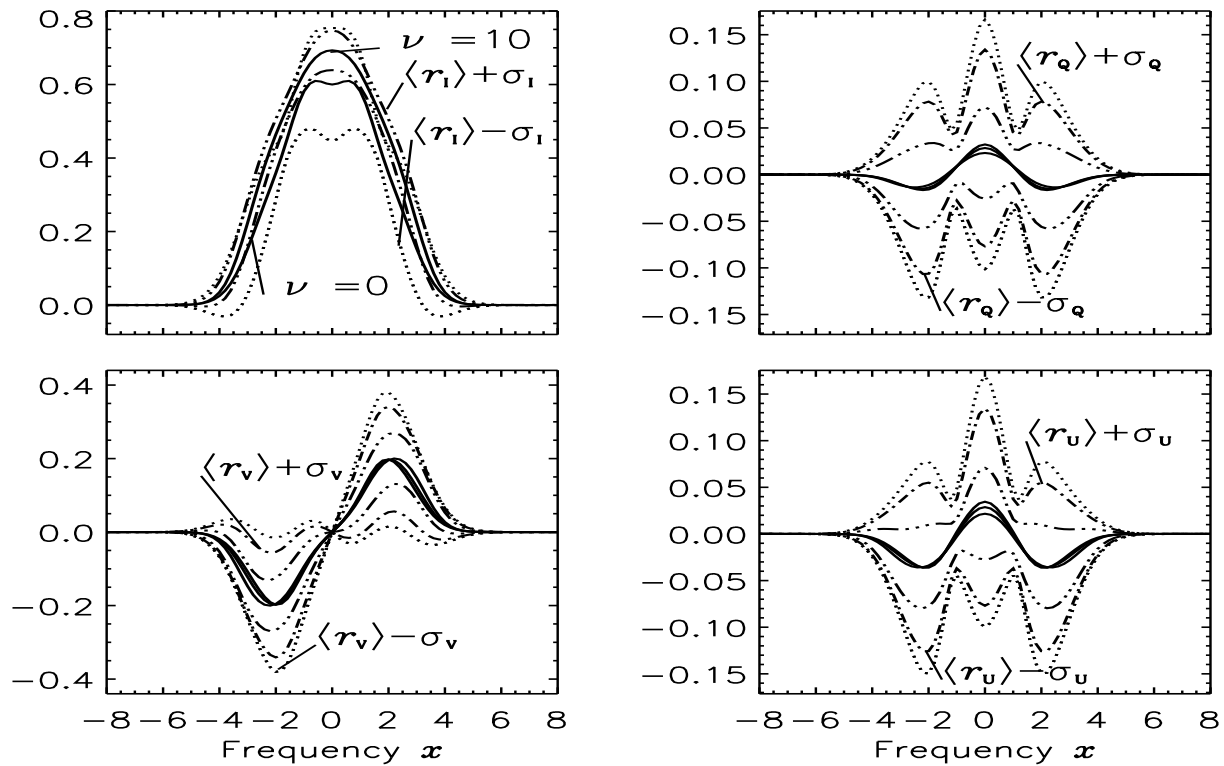


Figure 4.10: Mean Stokes parameters with dispersion for moderately strong fluctuations of the magnetic field. The model parameters are:  $\beta = 10$ ,  $\Delta_Z B_0 = 1$ ,  $\gamma_B = 1$ . The direction of the mean magnetic field  $\mathbf{B}_0$  is defined by  $\theta_0 = 45^\circ$  and  $\phi_0 = 30^\circ$ . The full lines show the mean profiles and the discontinuous lines the mean values plus and minus the square root of the dispersion. The line types are: dotted ( $\nu = 0$ ); dot-dashed ( $\nu = 1$ ); triple-dot-dashed ( $\nu = 10$ ). In this figure  $\langle \dots \rangle$  stands for  $\langle \dots \rangle_{\text{KA}}$ .

case of moderately strong fluctuations ( $f = 1$ ). The direction of the mean field is  $\theta_0 = 45^\circ$  and  $\phi_0 = 30^\circ$ . Comparing with Figs. 4.4 and 4.5 where  $\phi_0 = 0^\circ$  and  $\theta_0 = 0^\circ$  or  $\theta_0 = 90^\circ$ , we see that  $\langle r_Q \rangle$  has become much smaller, as expected, and has become almost insensitive to the value of  $\nu$  (on the scale of Fig. 4.10). Of course,  $\langle r_V \rangle$  has also become somewhat smaller and remains almost independent of  $\nu$ . For  $\langle r_I \rangle$ , the dependence on  $\nu$  does seem to depend on the direction of the mean field.

In contrast with the mean values, we see that the  $\sigma_X$  are very sensitive to the value of  $\nu$ . They have their largest values in the macro-turbulent limit ( $\nu = 0$ ) and go to zero in the micro-turbulent limit. In the macro-turbulent limit, the dispersion is quite large compared to the mean value. For the mean Stokes profiles, we have seen that the micro-turbulent limit is essentially reached when  $\nu \simeq \beta$ . Figure 4.10 shows that the dispersion has still

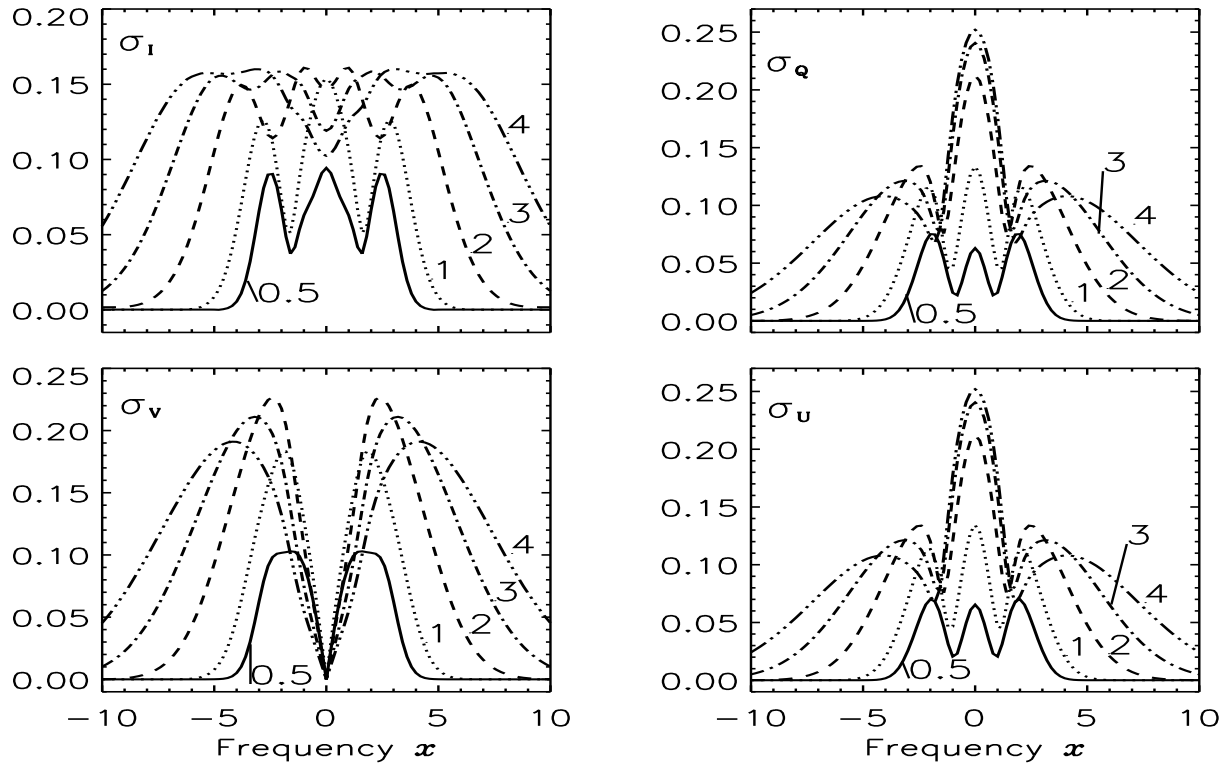


Figure 4.11: Variation of the dispersion with the strength of the magnetic field fluctuations. The dispersion is shown only for the macro-turbulent limit  $\nu = 0$ . The line strength  $\beta$  and the mean magnetic field parameters are the same as in Fig. 4.10. The curves are labeled with the value of  $f$ .

a significant value when  $\nu \simeq \beta$ . This makes the dispersion much more sensitive to the characteristic scale of the random magnetic field.

Figure 4.11 shows the macro-turbulent limit of  $\sigma_X$  calculated with Eq. (4.68) for  $\Delta_Z B_0 = 1$  (as in Fig. 4.10) and different values of  $f$  varying between 0.5 and 4. For Stokes  $I$ ,  $Q$  and  $U$  the dispersion has maxima at line center and at the frequencies corresponding to the inflexion points in the Stokes  $I$  profile. For Stokes  $V$ , the dispersion is zero at line center for symmetry reason, and has its maximum at the inflexion points of  $I$  also. The minima of  $\sigma_Q$  and  $\sigma_U$  correspond to the zero-crossing frequencies in the mean Stokes profiles.

Starting from a case of weak fluctuations ( $f = 0.5$ ), we observe that the dispersion increases with  $f$ , as expected, until say  $f = 2$ . For larger values of  $f$ , we observe a decrease of the peak value in the wings of  $\sigma_Q$ ,  $\sigma_U$  and  $\sigma_V$ , associated to a significant

broadening which reflects the fact that the stronger the fluctuations of the magnetic field, the further out from line center can they be felt. At line center  $\sigma_Q$  and  $\sigma_U$  keep increasing with  $f$ , even beyond  $f = 2$ . Numerical experiments, not presented, here indicate that  $\sigma_Q$  and  $\sigma_U$  saturate to a value around 0.25 but that this phenomenon is related to the choice of  $P(\mathbf{B})$ . When the random magnetic field has a fixed direction and varies in strength only, the values of  $\sigma_Q$  and  $\sigma_U$  at line center will decrease after going through a maximum. For Stokes  $I$ , the dispersion has a fairly complicated behavior, specially around the line center. The initial increase is also followed by some kind of saturation, but again, this is related to the choice of  $P(\mathbf{B})$ . In the wings, the behavior is essentially the same as for the other Stokes parameters.

## 4.5 Various generalizations

When some of the assumptions that were introduced to obtain explicit expressions for the mean Stokes parameters are dropped, it may still be possible to write an integral equation for the mean propagation operator. In some cases this equation can still be solved explicitly by a Laplace transform method, but in general a numerical solution is required. A few examples are given below.

### 4.5.1 Exponential source function

It follows from the solution of Eq. (4.1) (see Eq. (D.11)) that the mean value of the Stokes vector at the surface can be written as

$$\langle \mathbf{I}(0) \rangle_{\text{KA}} = \mathbf{S}(0) + \int_0^\infty \langle \mathbf{O}(0, s) \rangle_{\text{KA}} \left[ \frac{d\mathbf{S}(s)}{ds} \right] ds. \quad (4.69)$$

When  $\mathbf{S}$  is linear in  $s$  one recovers Eq. (4.4). When  $\mathbf{S}$  has an exponential variation  $e^{-\alpha s}$  with  $\alpha$  a constant,  $\langle \mathbf{I}(0) \rangle_{\text{KA}}$  can be expressed in terms of the Laplace transform of  $\langle \mathbf{O}(0, s) \rangle_{\text{KA}}$  for  $p = \alpha$ .

Let us consider an example presented in LL04 (p. 419) in which the continuum and line source functions are different and both have exponential terms. The transfer equation is now of the form

$$\frac{d\mathbf{I}}{d\tau_c} = (\mathbf{E} + \beta\Phi)\mathbf{I} - (\mathbf{E}S_c + \beta\Phi S_l)\mathbf{U}. \quad (4.70)$$

The line and continuum source functions  $S_l$  and  $S_c$  are given by

$$S_c(\tau_c) = C_0 + C_1\tau_c + A_1e^{-\alpha_1\tau_c}, \quad (4.71)$$



$$S_l(\tau_c) = C_0 + C_1\tau_c + A_1e^{-\alpha_1\tau_c} - A_2e^{-\alpha_2\tau_c}. \quad (4.72)$$

The term  $A_1e^{-\alpha_1\tau_c}$  can describe a chromospheric rise of temperature and the term  $A_2e^{-\alpha_2\tau_c}$  allows for a drop of the line source function below the continuum source function at optical depths  $\tau_c \leq 1/\alpha_2$ . Simple algebra (see also LL04) yields for the mean Stokes vector

$$\langle \mathbf{I}(0) \rangle_{\text{KA}} = \left[ S_l(0)\mathbf{E} + C_1\langle \tilde{\mathbf{O}}(0,0) \rangle_{\text{KA}} - \alpha_1 A_1\langle \tilde{\mathbf{O}}(0,\alpha_1) \rangle_{\text{KA}} + A_2(1+\alpha_2)\langle \tilde{\mathbf{O}}(0,\alpha_2) \rangle_{\text{KA}} \right] \mathbf{U}, \quad (4.73)$$

where  $\tilde{\mathbf{O}}(0,p)$  is defined in Eq. (4.11) and its mean value in Eq. (4.15).

When  $\mathbf{S}$  contains an exponential, it does not seem possible to transform the original transfer equation into a new equation with a homogeneous source term and obtain with the method described in § 4.4 an explicit expression for the dispersion around the mean Stokes parameters.

#### 4.5.2 Arbitrary depth-dependence of source function and line strength

We now assume that the line and continuum source functions and the ratio  $\beta = k_0/k_c$  (introduced in § 4.2.6) can vary with optical depth, but not the Zeeman absorption matrix  $\Phi$ . This implies that the Doppler width is taken constant. There is no hope to obtain an exact result for the mean Stokes parameters, however an expression given in Pecker and Schatzman (1959) for the difference  $I_c(0) - I(0)$ , in the case of non-polarized transfer, could be a good starting point for their numerical calculation. For the polarized case, the expression given in the above reference becomes

$$\mathbf{I}_c(0) - \mathbf{I}(0) = \left[ w(0)\mathbf{E} + \int_0^\infty w'(s)\mathbf{O}(0,s) ds \right] \mathbf{U}. \quad (4.74)$$

Here  $s$  is the continuum optical depth along the line of sight,  $w'(s)$  and  $w(0)$  are the derivative and surface value of the function

$$w(s) = \int_s^\infty S_c(s')e^{-s'} ds' - S_l(s)e^{-s}, \quad (4.75)$$

and

$$\mathbf{O}(s,s') = \exp \left[ -\Phi \int_s^{s'} \beta(s'') ds'' \right]. \quad (4.76)$$

The derivation of Eq. (4.74) starts from the solutions of Eq. (4.70) for  $\mathbf{I}_c(0)$  and  $\mathbf{I}(0)$ . The main steps are the following: one combines the two terms containing  $S_c$  and introduces  $dI_c^+(s)/ds$  with  $I_c^+(s) = \int_s^\infty S_c(s')e^{-s'} ds'$ . An integration by parts then yields Eq. (4.74).

The mean value  $\langle \mathbf{O}(0,s) \rangle_{\text{KA}}$  still satisfies Eq. (4.10) but the static propagation operator, as shown by Eq. (4.76), is now a function of  $s$  and  $s'$ .

### 4.5.3 Depth-dependence of correlation length

In the preceding sections, it has been assumed that  $\nu$ , the density of the Poisson distribution, is independent of the optical depth  $s$  along the LOS. If we let  $\nu$  vary with depth, the Poisson process becomes a non-homogeneous Poisson process.<sup>2</sup> The probability that no jumps occur between  $s$  and  $s'$  is  $\exp\left[-\int_s^{s'} \nu(s'') ds''\right]$ . Equation (4.10) becomes

$$\langle \mathbf{O}(0, s) \rangle_{\text{KA}} = \langle \mathbf{O}_S(s) \rangle e^{-\int_0^s \nu(s') ds'} + \int_0^s \nu(s') e^{-\int_s^{s'} \nu(s'') ds''} \langle \mathbf{O}(0, s') \rangle_{\text{KA}} \langle \mathbf{O}_S(s - s') \rangle ds', \quad (4.77)$$

with  $\mathbf{O}_S(s)$  still given by Eq. (4.5). This integral equation can only be solved numerically.

Some other generalizations can still lead to convolution equations for the mean evolution operator. For example, if  $\nu$  depends on the modulus of the random magnetic field or if the random magnetic field consists of several fields with different characteristic scales. Such generalizations have been considered for the statistical Stark effect (Brissaud & Frisch 1971).

### 4.5.4 Arbitrary direction of propagation

The results given in the previous sections hold for an outward directed ray normal to the surface of the atmosphere. They can easily be extended to the case of a ray making an angle  $\vartheta$  with the vertical. It suffices to project on to the LOS the quantities which describe the variations of the model along the normal to the atmosphere, such as the source function, absorption coefficients, and correlation length.

For the example treated in § 4.5.1,  $\langle \mathbf{I}(0, \mu) \rangle_{\text{KA}}$  will be given by Eq. (4.73) with  $C_1$  changed to  $C_1\mu$  and  $\alpha_1$  and  $\alpha_2$  changed to  $\mu\alpha_1$  and  $\mu\alpha_2$ , where  $\mu = \cos\vartheta$ . For the linear source function  $S_l = S_c = C_0 + C_1\tau_c$  treated in § 4.2.6, the usual residual Stokes vector  $(\mathbf{I}_c(0, \mu) - \mathbf{I}(0, \mu))/I_c(0, \mu)$  will be given by Eq. (4.27) multiplied by  $C_1\mu/(C_0 + C_1\mu)$ . For the example treated in § 4.5.2,  $w(s)$  and  $\mathbf{O}(s, s')$  become

$$w(s, \mu) = \int_s^\infty S_c(s') e^{-s'/\mu} \frac{ds'}{\mu} - S_l(s) e^{-s/\mu}, \quad (4.78)$$

and

$$\mathbf{O}(s, s', \mu) = \exp\left[-\Phi \int_s^{s'} \beta(s'') \frac{ds''}{\mu}\right]. \quad (4.79)$$

Here  $s$  denotes the optical depth in continuum in a direction normal to the atmosphere.

<sup>2</sup>[http://en.wikipedia.org/wiki/Non-homogeneous\\_Poisson\\_process](http://en.wikipedia.org/wiki/Non-homogeneous_Poisson_process)

For the calculation of  $\langle \mathbf{O}(s, s', \mu) \rangle$ , the correlation length should also be projected along the LOS, which means transforming  $1/\nu$  into  $1/\mu\nu$ . Thus in Eqs. (4.27) - (4.29),  $\nu$  should be changed to  $\nu\mu$ . This is also the change made in LL04 (see Eq. 9.280, p. 500), where  $t_e$ , the mean length of the eddies measured in the vertical direction, becomes  $t_e/\mu$  along the LOS. As a consequence, the more inclined with respect to the vertical are the rays, the closer is one to a macro-turbulent type of averaging. This is consistent with a picture of random fluctuations organized in turbulent layers. Now, even in a plane parallel atmosphere, one may want to have a more or less isotropic distribution of turbulent eddies. This can be achieved by keeping the same value of  $\nu$  (i.e. same correlation length) in all directions.

## 4.6 Summary and concluding remarks

This chapter presents the first detailed investigation of the Zeeman effect created by a random magnetic field with a finite correlation length. The goal of this work is to overcome usual treatments whereby the correlation length of the magnetic field is either much smaller, or much larger, than a photon mean free path, i.e. the micro-turbulent and macro-turbulent limits. The random magnetic field is described by a Kubo-Anderson process which takes constant but random values on intervals of random length distributed according to a Poisson distribution of density  $\nu$ . The random magnetic field is thus characterized by a mean correlation length defined here as  $1/\nu$  and the probability distribution function  $P(\mathbf{B})$  of the random values taken by the magnetic field. The micro and macro-turbulent limits are recovered when the correlation length goes to zero or infinity.

The Kubo-Anderson process has been associated to a Milne-Eddington atmospheric model with a linear source function. This combination has allowed us to construct explicit expressions that were used to study numerically the mean Stokes parameters and their dispersion at the surface of the atmosphere. The main theoretical results concern the construction of:

- (i) a convolution-type integral equation for the mean propagation operator associated to the Zeeman effect which can be solved explicitly for its Laplace transform;
- (ii) an explicit expression for the mean Stokes parameters at the surface of the atmosphere which corroborates a result obtained by Landi Degl'Innocenti (1994);
- (iii) an explicit expression for the second-order moments of the Stokes parameters which are needed to evaluate the dispersions and cross-correlations of Stokes parameters.

We have also given integral equations for the mean propagation operator when one relaxes some of the assumptions defining a Milne-Eddington model or Kubo-Anderson process, like depth-independent correlation length. These integral equations are not of the convolution type and must be solved numerically.

Numerical investigations have been carried out for a PDF  $P(\mathbf{B})$  describing a random magnetic field with mean value  $\mathbf{B}_0$  and isotropic Gaussian fluctuations with dispersion  $\sqrt{3}\sigma$ . We have assumed a micro-turbulent velocity with a Gaussian distribution which is equivalent to incorporating an additional thermal broadening into the Doppler width of the line. In agreement with the Milne-Eddington model, the ratio  $\beta = k_0/k_c$  of the line to continuum opacity has been taken constant. For weak lines ( $\beta$  order of unity or less), the Stokes parameters are essentially given by the profiles of the absorption coefficients and hence depend only on  $P(\mathbf{B})$ . For stronger lines, sensitive to the correlation length of the magnetic field, the mean Stokes parameters lie between the micro and macro-turbulent limits. This is strictly true for Stokes  $I$ , because it is a positive quantity, and at line center only for Stokes  $Q$  and  $U$ . It is a bit more complicated for Stokes  $V$  and the  $\sigma$ -components of Stokes  $Q$  and  $U$ , because the position of the peaks depend on the correlation length. The micro-turbulent limit is reached when the correlation length is around unity in the line optical depth unit, i.e. when  $\beta/\nu \simeq 1$ .

The numerical calculations have been performed for  $\beta = 10$  (a few cases with  $\beta = 100$  have also been considered), for different values of the mean magnetic field  $\mathbf{B}_0$ , dispersion  $\sigma$  and correlation length  $1/\nu$ . The dispersion and mean field have been combined to construct a dimensionless parameter  $f = \sqrt{2}\sigma/B_0$  which measures the relative strength of the magnetic field fluctuations. The assumption that the magnetic field fluctuations are isotropic influences some of the results but not the general trends which are summarized here.

Concerning the mean values, we have found that :

(i) for Stokes  $I$ , the variation between the micro and macro-turbulent limits is between 10% and 20%. It grows with the strength of the mean field  $\mathbf{B}_0$  but seems fairly insensitive to the value of  $f$ . Departures from the UR solution (calculated with the mean field  $\mathbf{B}_0$ ) can become quite large at line center when the  $\sigma$ -components are well separated, but this is partly due to the isotropy assumption.

(ii) Stokes  $V$  shows very little dependence on the correlation length and hence, with reasonable confidence, may be calculated with the micro-turbulent limit. The departures from

the UR solution are very large, unless  $f$  is significantly smaller than unity.

(iii) for Stokes  $Q$ , the line center is quite sensitive to the correlation length of the magnetic field but only when  $\mathbf{B}_0$  is in the transverse direction with respect to the LOS, or close to it. For a given random magnetic field, the departures from the UR solution are larger for Stokes  $Q$  than for Stokes  $V$ .

In sharp contrast with the mean Stokes parameters, dispersions around mean values are very sensitive to the correlation length and could probably serve as a diagnostic tool to determine the scale of the unresolved features in the solar atmosphere. Dispersions have their maximum values in the macro-turbulent limit, go to zero in the micro-turbulent limit and are very sensitive to the value of  $f$ . In relative value, the dispersion is smaller for Stokes  $I$  than for the polarization components  $Q$ ,  $U$  and  $V$ .

In addition to the magnetic field, a whole set of other atmospheric random parameters (velocities, temperatures, densities, ...) are needed to properly describe a distribution of flux tubes or magnetohydrodynamical turbulence. These additional parameters should typically be described by the same type of random processes as the magnetic field, in particular the same correlation length. In this case all the theoretical results given here will hold, provided  $P(\mathbf{B})$  is replaced by a joint PDF  $P(\mathbf{B}, \alpha_1, \alpha_2, \dots)$ , where  $\alpha_i$  stand for the other random parameters. If the random parameters have different correlation lengths, a KAP-type of modeling can still be set up. An example can be found in the case of the stochastic Stark effect (Brissaud & Frisch 1971). There a composite KAP is introduced to handle simultaneously the ion and electron electric fields with their quite different characteristic lengths due to the large mass difference between the two types of particles.



## Chapter 5

# Unno-Rachkovsky solution for turbulent magnetic fields<sup>1</sup>

### 5.1 Introduction

Quantitative analysis of spectro-polarimetric data entered an active phase with the analytical solution of Unno (1956). This solution considers only the absorption/emission of polarized radiation in a magnetized medium. The extension by Rachkovsky (1962a, 1962b) includes magneto-optical effects due to differential shifts between orthogonal polarization states, which appear during the propagation through the medium. Magneto-optical effects are important when Zeeman shifts are of the order of Doppler widths and affect Stokes parameters mainly around the line center. The analytical solution of the Stokes vector transfer equation known as Unno-Rachkovsky (UR) solution implies a uniform magnetic field and approximations regarding the atmospheric model known as Milne-Eddington approximations - namely that the line strength is independent of the depth in the atmosphere, and that the line source function varies linearly with optical depth. The Milne-Eddington approximation has provided insight into the physical processes taking place in line formation. Its specific analytical character is its most powerful feature. A new area in the analysis of polarization spectra was opened with numerical solutions of the polarized radiative transfer equation for realistic atmospheres involving depth-dependent physical quantities. It started with the work by Beckers (1969a, 1969b), Wittmann (1974), Landi Degl'Innocenti (1976). See Rees (1987) for a historical review.

However the UR solutions continue to be used in astrophysics, in particular in inversion

---

<sup>1</sup>This chapter is based on the publication: Sampoorna, M., Frisch, H., & Nagendra, K. N. 2008, *New Astronomy*, 13, 233-243

codes aimed at the automatic reconstruction of magnetic fields and atmospheric parameters from large sets of polarimetric data (e.g. UNNO-FIT technique - LL04, p. 634 and references cited therein, Bellot Rubio 2006 and references cited therein). It can, as recently shown, provide a systematic approach to evaluate the sensitivity of Stokes profiles to atmospheric and magnetic field parameters (Orozco Suárez & del Toro Iniesta 2007). Let us also mention that a widely used atlas of theoretical Stokes profiles was constructed with the help of UR solution (Arena & Landi Degl'Innocenti 1982). An excellent description of UR solution, extensions and practical applications, are presented in del Toro Iniesta (2003) and Landi Degl'Innocenti & Landolfi (2004).

In this chapter we present a systematic study of the UR solution for random magnetic fields. The UR solution, can be employed for random fields in two limiting regimes: (i) the regime of micro-turbulence in which the characteristic scale of variation of the random magnetic field is much smaller than a typical photon mean free-path, and (ii) the regime of macro-turbulence where one has the opposite situation. The micro-turbulent approach, suggested in Stenflo (1971), has been employed for e.g. in Stenflo & Lindegren (1977), Sánchez et al. (1996). Multi-components models are special versions of the macro-turbulent limit (see e.g. Stenflo 1994 and references cited therein). Here we assume that the magnetic field fluctuations are described by a PDF  $P(\mathbf{B})$ . In the micro-turbulent regime, the coefficients of the polarized transfer equation, in particular the Zeeman absorption matrix can be locally averaged over  $P(\mathbf{B})$ . Dolginov & Pavlov (1972) and Domke & Pavlov (1979) were the first to examine Zeeman line transfer for micro-turbulent magnetic fields and proposed explicit expressions for the mean values of the coefficients of the Zeeman absorption matrix. An up-to-date presentation of their results and some extensions is given in Chapter 2. In the macro-turbulent regime, the magnetic field is uniform over the region where the spectral line is formed but takes random values distributed according to  $P(\mathbf{B})$ . The averaging over  $P(\mathbf{B})$  is performed on the emergent UR solution itself.

The micro and macro-turbulent limits cannot describe situations where the mean free path of photons is of the same order as the characteristic scale of variation of the magnetic field. This more general situation requires the solution of polarized radiative transfer equations with stochastic coefficients (Chapter 4, see also Carroll & Kopf 2007). The corresponding mean Stokes parameters always lie between the micro and macro-turbulent limits. The latter have thus a significant interest for assessing the effects of random magnetic fields.

In this chapter we examine the micro and macro-turbulent limits for isotropic and



anisotropic Gaussian magnetic field distributions. The velocity field is assumed to be micro-turbulent, and uncorrelated to the magnetic field. The results are compared to the UR solution corresponding to the mean magnetic field, henceforth referred to as the mean field solution. The comparison is carried out for lines with different line strength  $\beta = k_0/k_c$  ( $k_0$  the frequency averaged line absorption coefficient,  $k_c$  the continuum absorption coefficient). In a Milne-Eddington atmosphere  $\beta$  is a constant. The UR solution varies linearly with  $\beta$  when  $\beta$  is small or around unity, but non-linearly when  $\beta$  becomes large. We investigate in detail this non-linear behavior for turbulent magnetic fields.

In § 5.2 we consider the micro-turbulent limit and in § 5.3 the macro-turbulent limit for both the longitudinal and transverse propagation. In these sections and all the following ones, the results are shown for a residual Stokes vector  $\mathbf{r} = (r_I, r_Q, r_U, r_V)^T$ , independent of the slope of the source function (see Eq. (4.26)). In § 5.4 we compare micro and macro-turbulence effects for an arbitrary orientation of the mean field and in § 5.5 we discuss mean Stokes profiles calculated with isotropic and anisotropic distributions. In § 5.6 concluding remarks are given. Appendix F describes the basic equations regarding the UR solution.

## 5.2 Micro-turbulence with isotropic Gaussian fluctuations

In the micro-turbulent limit, the Stokes parameters and residual Stokes vector defined in Eq. (4.26) can be calculated with the UR solution given in Eqs. (F.4) - (F.10) where all the absorption and dispersion coefficients are replaced by their averages over the PDF  $P(\mathbf{B})$  of the vector magnetic field. In this chapter we consider PDFs that are cylindrically symmetrical about the direction of a mean field  $\mathbf{B}_0$ . They are defined in a reference frame with the  $Z$ -axis along the mean field direction (see Fig. E.1) and then transformed to the LOS reference frame (see Fig. 2.1) with the  $Z$ -axis along the LOS (see Appendix E).

In this section we consider a random magnetic field with a mean value  $\mathbf{B}_0$  and fluctuations that are Gaussian and isotropic (other angular distributions are considered in § 5.5). The PDF may thus be written as (see also Eq. 2.29)

$$P_I(\mathbf{B}) d\mathbf{B} = \frac{1}{\pi^{3/2}} e^{-(y_0^2 + y^2)} e^{2y_0 y \cos \Theta} y^2 dy \sin \Theta d\Theta d\Psi, \quad (5.1)$$

where  $\Theta$  is the angle between the vector magnetic field  $\mathbf{B}(\theta, \phi)$  and the mean magnetic field  $\mathbf{B}_0(\theta_0, \phi_0)$  and  $\Psi$  the azimuth of  $\mathbf{B}$  in a MRF in which the  $Z$ -axis is taken along  $\mathbf{B}_0$  (see Fig. E.1). The non-dimensional quantities  $y$  and  $y_0$  are defined as  $y = B/(\sqrt{2}\sigma)$ , and  $y_0 = B_0/(\sqrt{2}\sigma)$ , with  $\sigma$  being the rms fluctuation given by  $3\sigma^2 = \langle (\mathbf{B} - \mathbf{B}_0)^2 \rangle$ . Two important parameters of the model are  $\Delta_Z B_0$  and  $\gamma_B = \Delta_Z \sqrt{2}\sigma$ , the Zeeman shifts

due to the mean magnetic field and to the rms fluctuations (measured in Doppler width units). Here  $\Delta_Z = ge/(4\pi m\Delta\nu_D)$ , with  $g$  the Landé factor and  $\Delta\nu_D$  the Doppler width which includes thermal and micro-turbulent velocity broadening (see e.g. Mihalas 1978, also Eq. (2.9)). The ratio  $f = 1/y_0 = \gamma_B/\Delta_Z B_0$  is a measure of the strength of the fluctuations, with large and small values of  $f$  corresponding to strong and weak turbulence respectively.

For a micro-turbulent magnetic field, the Doppler broadening is replaced by a combination of thermal, velocity and magnetic broadening described by the parameter  $\gamma_1 = \sqrt{1 + \gamma_B^2}$ . We shall discuss separately two limiting cases corresponding to  $\gamma_1 > \Delta_Z B_0$  and  $\gamma_1 < \Delta_Z B_0$  (see also Chapter 2). The first corresponds to a *weak mean field* with strong fluctuations and the second one to a *strong mean field* with weak fluctuations. For the numerical calculations we have chosen  $\gamma_B = 1$ , i.e. magnetic broadening equal to Doppler broadening, and  $\Delta_Z B_0 = 0.1$  and  $\Delta_Z B_0 = 3$ , to represent the weak and strong mean field limits. The mean absorption and dispersion coefficients are calculated by numerical averaging over the PDF. In the limiting cases of weak and strong mean field, it is possible to obtain fairly simple analytical expressions for mean opacity and anomalous dispersion coefficients (see Chapter 2, also DP72, DP79). These analytic expressions are used to analyze the numerical results.

In this section we examine in detail the dependence of the mean residual Stokes profiles on the value of line strength  $\beta$ . The results are presented for  $\beta$  in the range 1 to  $10^4$ . Very large values of  $\beta$ , around  $10^4$  can be found in magnetic white dwarfs (see for e.g. Martin & Wickramasinghe 1981, Nagendra & Peraiyah 1985a, 1985b, Wickramasinghe & Ferrario 2000). We assume that the mean magnetic field is in the longitudinal ( $\theta_0 = 0^\circ$ ) or in a transverse direction ( $\theta_0 = 90^\circ$ ,  $\phi_0 = 0^\circ$ ). Because the magnetic field fluctuations are isotropic,  $\langle r_Q \rangle = \langle r_U \rangle = 0$  when  $\theta_0 = 0^\circ$  and  $\langle r_V \rangle = 0$  when  $\theta_0 = 90^\circ$ , for symmetry reason. In addition  $\langle r_U \rangle = 0$  when  $\phi_0 = 0^\circ$ . The notation  $\langle \rangle$  stands for average over  $P(\mathbf{B})$ . All the calculations have been performed with a line damping parameter  $a = 0$ . § 5.2.1 is devoted to the weak mean field limit, §§ 5.2.2 and 5.2.3 to the strong mean field limit.

### 5.2.1 Weak mean field (strong fluctuations) limit

Figure 5.1a shows  $\langle r_I \rangle$ , and  $\langle r_V \rangle$  for  $\theta_0 = 0^\circ$  calculated with Eqs. (F.11) and (F.12). When  $\beta$  is small ( $\beta\langle\varphi_I\rangle \ll 1$  for all  $x$ ), one simply has  $\langle r_{I,V} \rangle \simeq \beta\langle\varphi_{I,V}\rangle$ . For large values of  $\beta$ , the shapes of  $\langle r_I \rangle$  and  $\langle r_V \rangle$  can be explained with the help of approximate expressions for

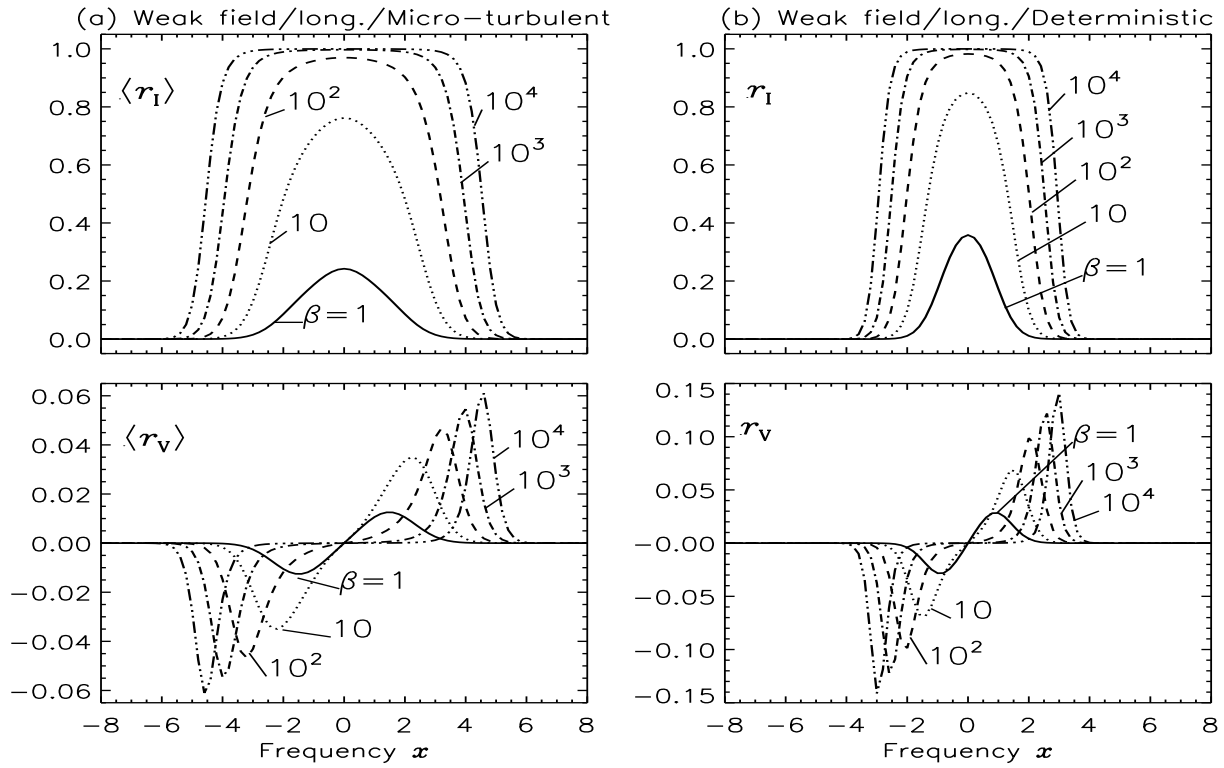


Figure 5.1: Weak mean field limit. Dependence of  $\langle r_I \rangle$ , and  $\langle r_V \rangle$  on line strength  $\beta$  for  $a = 0, \theta_0 = 0^\circ$ . Panel (a): micro-turbulent limit with  $\Delta_Z B_0 = 0.1, \gamma_B = 1$  hence  $y_0 = 0.1$  and  $f = 10$ . Panel (b): deterministic case with  $\Delta_Z B = 0.1$ . Frequency  $x$  in Doppler width units. See § 5.2.1 for discussions.

$\langle \varphi_{I,V} \rangle$ . When  $\gamma_1 > \Delta_Z B_0$ , we have (see Eqs. (2.16), (2.41) - (2.43)),

$$\langle \varphi_I(x) \rangle \simeq \frac{1}{3} h^{(0)}(x) + \frac{2}{3\gamma_1^3} \left[ h^{(0)}\left(\frac{x}{\gamma_1}\right) + 2\gamma_B^2 h^{(2)}\left(\frac{x}{\gamma_1}\right) \right], \quad (5.2)$$

$$\langle \varphi_V(x) \rangle \simeq 2\Delta_Z B_0 \cos \theta_0 \frac{1}{\gamma_1^4} \left[ h^{(1)}\left(\frac{x}{\gamma_1}\right) + \frac{2}{3}\gamma_B^2 h^{(3)}\left(\frac{x}{\gamma_1}\right) \right], \quad (5.3)$$

where  $h^{(n)}(x) = x^n e^{-x^2} / \sqrt{\pi}$ . When  $a$  is not zero, the  $h^{(n)}$  functions become generalized Voigt functions  $H^{(n)}$  (for details see Chapters 2 and 3). We remark that  $\langle \varphi_I \rangle$  is independent of  $\theta_0$  and  $\langle \varphi_V(x) \rangle$  of the order of  $\Delta_Z B_0$ . The mean values  $\langle \varphi_Q(x) \rangle$  and  $\langle \varphi_U(x) \rangle$  are of the order of  $\Delta_Z B_0^2$  (see Chapter 2). The numerical results presented in Fig. 5.1a can be reproduced with an error less than 1%, when the approximations given in Eqs. (5.2) and (5.3) are combined with the expressions of  $\langle r_I \rangle$  and  $\langle r_V \rangle$  for  $\Delta_Z B_0 < 1$  given in Eqs. (F.15) and (F.16).

The over all behavior of  $\langle r_{I,V} \rangle$  (namely, width of  $\langle r_I \rangle$ , and peak position of  $\langle r_V \rangle$ ) can be explained by simple scaling arguments. For  $\langle r_I \rangle$ , the width of the peak (Full width at Half Maximum FWHM) can be defined by the condition  $\beta \langle \varphi_I(x_c) \rangle \simeq 1$  with  $x_c$  the half-width. In Eq. (5.2) the terms with argument  $x/\gamma_1$  are controlling the width of  $\langle r_I \rangle$ , because they are decreasing more slowly with  $x$  than the  $h^{(0)}(x)$  term. Hence  $x_c \sim \gamma_1 \sqrt{\ln \beta}$ . When  $|x| < x_c$ ,  $\langle r_I \rangle \rightarrow 1$  as  $\beta \rightarrow \infty$  and when  $|x| > x_c$ ,  $\langle r_I \rangle$  behaves as  $\beta \langle \varphi_I \rangle$ .

Equation (5.3) shows that the positions of the peaks of  $\langle r_V \rangle$  go like  $\gamma_1 \sqrt{\ln \beta}$  and their height goes as  $\sqrt{\ln \beta}$ . These predicted behaviors are very close to what is observed in the numerical results. For example the peak positions of  $\langle r_V \rangle$  scale as  $1.5\sqrt{\ln \beta}$  whereas for our choice of parameters  $\gamma_1 = 1.4$ .

Comparison between the micro and mean field solution (see Fig. 5.1b), shows that magnetic turbulence produces a broadening of the peaks of  $\langle r_I \rangle$  and  $\langle r_V \rangle$  by a factor  $\gamma_1$  and a decrease in amplitude of the  $\langle r_V \rangle$  peaks due to the factor  $1/\gamma_1^4$  (see Eq. (5.3)).

When  $\theta_0 = 90^\circ$ , the effects of a micro-turbulent magnetic field on  $\langle r_Q \rangle$  and  $\langle r_U \rangle$  are the same as for  $\langle r_V \rangle$ , namely decrease in the amplitude of all three Zeeman components and broadening plus shifts in the positions of the  $\sigma$ -components away from line center.

### 5.2.2 Strong mean field (weak fluctuations) limit: Longitudinal case

Figure 5.2a shows  $\langle r_I \rangle$  and  $\langle r_V \rangle$  and Fig. 5.2b the corresponding curves for the mean field  $B_0$ . It is clear that the profiles are quite different. We stress that the curves with  $\beta = 1$  give a good approximation of the coefficients  $\varphi_I$  and  $\varphi_V$  and of their average values  $\langle \varphi_I \rangle$  and  $\langle \varphi_V \rangle$ . Results presented in Fig. 5.2a can be understood using approximate (asymptotic) expression for  $\langle \varphi_{I,V} \rangle$ . For  $\gamma_1 < \Delta_Z B_0$ , we have (see Eqs. (2.16), (2.38) - (2.40)),

$$\langle \varphi_I \rangle \simeq \bar{\varphi}_0 + \frac{1}{2}(\bar{\varphi}_{+1} + \bar{\varphi}_{-1}) + \frac{1}{2}(\bar{c}_{+1} + \bar{c}_{-1}), \quad (5.4)$$

$$\langle \varphi_V \rangle \simeq \frac{1}{2}(\bar{\varphi}_{+1} - \bar{\varphi}_{-1}), \quad (5.5)$$

with

$$\bar{\varphi}_0 \simeq \frac{1}{2y_0^2} h^{(0)}(x); \quad \bar{\varphi}_{\pm 1}(x) \simeq \frac{1}{\gamma_1} \left( 1 - \frac{1}{2y_0^2} \right) h^{(0)}(\bar{x}_{\pm 1}), \quad (5.6)$$

$$\bar{c}_q(x) \simeq \frac{1}{4y_0^3} \left( \frac{\gamma_1}{y_0 + |xq|\gamma_B} \right) h^{(0)}(\bar{x}_q), \quad (5.7)$$

and  $\bar{x}_q = (x - q\Delta_Z B_0)/\gamma_1$ ,  $q = \pm 1$ . One notices in Eq. (5.4) the appearance of a term  $\bar{\varphi}_0$  at line center which is zero for deterministic case (see Eq. (2.5) for  $\theta = 0^\circ$ ), and is created

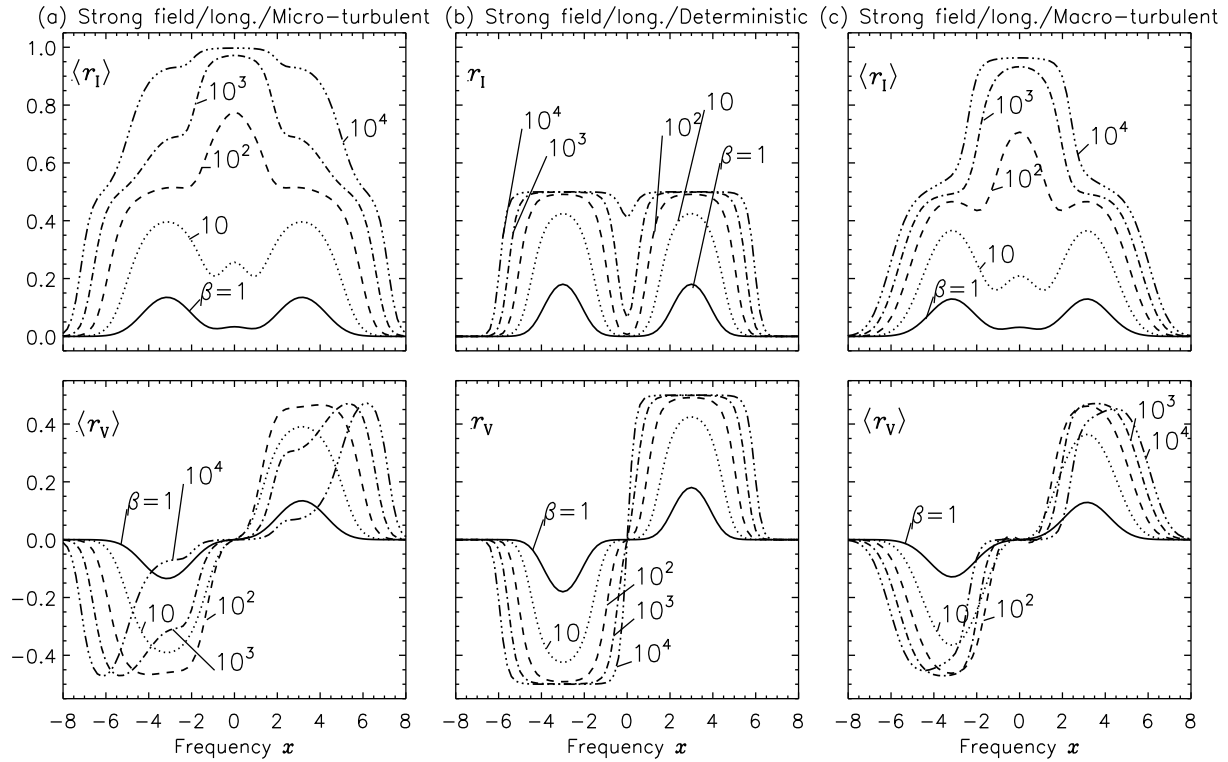


Figure 5.2: Strong mean field limit. Longitudinal mean field case. Dependence of  $\langle r_I \rangle$ , and  $\langle r_V \rangle$  on line strength  $\beta$  for  $a = 0$ ,  $\theta_0 = 0^\circ$ . Panel (a): micro-turbulent limit with  $\Delta_Z B_0 = 3$ ,  $\gamma_B = 1$ , hence  $y_0 = 3$  and  $f = 1/3$ . Panel (b): deterministic case with  $\Delta_Z B = 3$ . Panel (c): macro-turbulent limit with the same model as in panel (a). See §§ 5.2.2 and 5.3 for discussions.

by the averaging of  $\sin^2 \theta$  over the random directions of the magnetic field. Equation (5.6) shows that the  $\sigma$ -components have a smaller amplitude and are broader by a scaling factor  $\gamma_1$ . The terms with  $\bar{c}_q$  were not considered in the strong mean field limit expression for  $\langle \varphi_I \rangle$  in Chapter 2 (see Eqs. (2.40) and (2.44)). This term  $\bar{c}_q$  comes from the factor  $3/(4y_0^2 y)$  in Eq. (2.34). The expression given in Eq. (5.7) is an asymptotic expression for damping parameter  $a = 0$ . For  $q = +1$ , it is valid for  $x$  around  $y_0/\gamma_B$  and for  $q = -1$ , it is valid for  $x$  around  $-y_0/\gamma_B$ . In spite of being small compared to  $\bar{\varphi}_q$ , this term plays an important role around  $x \simeq \pm \Delta_Z B_0$ , when  $\beta$  is large. Using Eqs. (5.4) - (5.7) in Eqs. (F.11) and (F.12), we can reproduce the results presented in Fig. 5.2a to a good approximation.

When  $\beta$  becomes large, the quadratic terms in the denominator of the equations for  $\langle r_I \rangle$  and  $\langle r_V \rangle$  play an important role. For the analysis of the results, it is interesting to

write the denominator as

$$d_1 \simeq 1 + 2\beta \left[ \bar{\varphi}_0 + \frac{1}{2}(\bar{\varphi}_{+1} + \bar{\varphi}_{-1}) \right] + \beta^2 \left\{ \bar{\varphi}_0^2 + \left[ \bar{\varphi}_0 + \frac{1}{2}(\bar{c}_{+1} + \bar{c}_{-1}) \right] (\bar{\varphi}_{+1} + \bar{\varphi}_{-1}) + \bar{\varphi}_{+1}\bar{\varphi}_{-1} \right\}, \quad (5.8)$$

retaining only the leading terms.

In the upper panel of Fig. 5.2a we see that  $\langle r_I \rangle$  approaches unity at line center and that this limiting value is almost reached for  $\beta = 10^3$ . At line center we have the exact relation

$$\langle r_I(0) \rangle = \frac{\beta \langle \varphi_I(0) \rangle}{1 + \beta \langle \varphi_I(0) \rangle}, \quad (5.9)$$

hence  $\langle r_I(0) \rangle$  goes to one when  $\beta \langle \varphi_I(0) \rangle \gg 1$ . Around the line center,  $\langle \varphi_I(x) \rangle \simeq \bar{\varphi}_0(x) \simeq e^{-x^2}/(\sqrt{\pi}2y_0^2)$  (see Eq. (5.6)). Hence,  $\langle r_I(0) \rangle \simeq 1$  when  $\beta \gg \sqrt{\pi}2y_0^2$ . For  $y_0 = 3$ , this condition yields  $\beta \gg 30$ , in agreement with the numerical results. It is the existence of a central component  $\bar{\varphi}_0$  which is responsible for the very large difference between the micro-turbulent and the deterministic profiles.

The  $\sigma$ -components of  $\langle r_I(0) \rangle$  are well separated as long as  $\beta \leq 10$ , and their width is around  $\gamma_1 \sqrt{\ln \beta}$ . For larger values of  $\beta$ , one notices a plateau with a value about 1/2 and then a further increase towards one. This can be understood by considering Eq. (5.8). At frequencies around  $\Delta_Z B_0$ , we have  $\bar{\varphi}_{+1} \gg \bar{\varphi}_0 \gg \bar{\varphi}_{-1}$ , hence

$$\langle r_I(\Delta_Z B_0) \rangle \simeq 1 - \frac{\frac{\beta}{2} \bar{\varphi}_{+1}}{1 + \beta \bar{\varphi}_{+1} + \beta^2 (\bar{\varphi}_0 + \bar{c}_{+1}/2) \bar{\varphi}_{+1}}. \quad (5.10)$$

The plateau around 1/2 is reached when  $\beta \bar{\varphi}_{+1}/2 \gg 1$ , i.e., when  $\beta \gg 2\gamma_1 \sqrt{\pi}$ . Figure 5.2a shows that this plateau is reached for  $10 < \beta < 10^2$ , in agreement with the prediction. The saturation to one will occur when the term quadratic in  $\beta$  becomes larger than the linear term. This condition is satisfied when  $\beta[\bar{\varphi}_0(\Delta_Z B_0) + \bar{c}_{+1}(\Delta_Z B_0)/2] \gg 1$ . For our choice of parameters, this yields  $\beta \gg 10^3$ . Figure 5.2a shows that  $\langle r_I(\Delta_Z B_0) \rangle$  is close to one for  $\beta = 10^4$ . In the deterministic case  $\bar{\varphi}_0 = 0$ , hence the  $\sigma$ -components saturate to 1/2 as shown in Fig. 5.2b, upper panel.

The variations of  $\langle r_V \rangle$  with  $\beta$  are shown in lower panel of Fig. 5.2a. The  $\sigma$ -components tend to 1/2 when  $\beta$  increases, and their width goes as  $\gamma_1 \sqrt{\ln \beta}$ . When the term  $\beta^2[\bar{\varphi}_0 + \bar{c}_{+1}/2]\bar{\varphi}_{+1}$  becomes larger than  $\beta \bar{\varphi}_{+1}$ , a dip appears at frequencies  $x \simeq \pm \Delta_Z B_0$ . It becomes clearly visible when  $\beta = 10^3$ . For frequencies beyond  $\pm \Delta_Z B_0$ , the effect of  $[\bar{\varphi}_0 + \bar{c}_{+1}/2]$  decreases, the term of order  $\beta^2$  becomes small compared to the term of order  $\beta$  and  $\langle r_V \rangle$  goes to 1/2. Finally,  $\langle r_V \rangle$  goes to zero as  $\beta \langle \varphi_V \rangle$  when the frequency is large enough to give

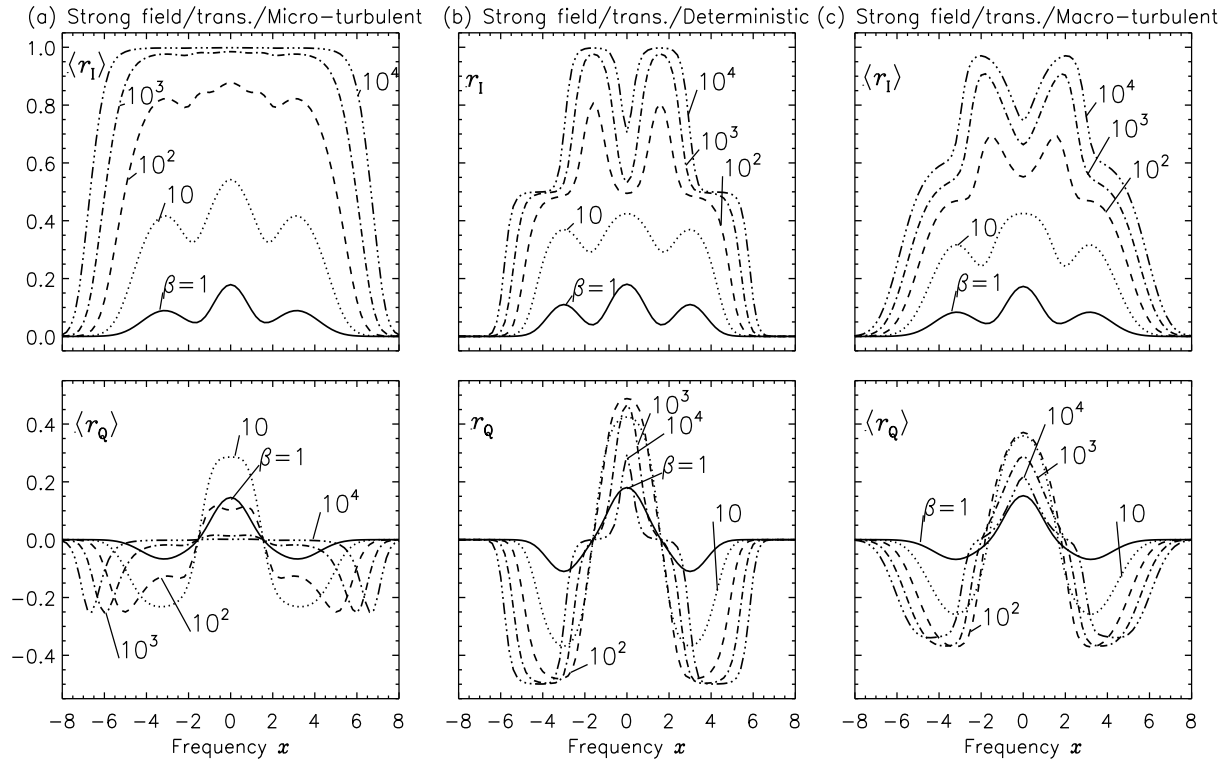


Figure 5.3: Strong mean field limit. Transverse mean field case. Dependence of  $\langle r_1 \rangle$ , and  $\langle r_Q \rangle$  on line strength  $\beta$  for  $a = 0$ ,  $\theta_0 = 90^\circ$ ,  $\phi_0 = 0^\circ$ . Panel (a): micro-turbulent limit with  $\Delta_Z B_0 = 3$ ,  $\gamma_B = 1$ , hence  $y_0 = 3$  and  $f = 1/3$ . Panel (b): deterministic case with  $\Delta_Z B = 3$ . Panel (c): macro-turbulent limit with the same model as in panel (a). See §§ 5.2.3 and 5.3 for discussions.

$d_1 \simeq 1$ . The frequency at the peak, determined by the condition  $\beta \langle \varphi_V \rangle \simeq 1/2$ , is about  $|x| \simeq \Delta_Z B_0 + \gamma_1 \sqrt{\ln \beta}$ . Thus, for  $\beta$  sufficiently large, the peaks of  $\langle r_V \rangle$  lose their box like structure and the position of the maximum is essentially controlled by the parameter  $\beta$  and not by the Zeeman shift  $\Delta_Z B_0$ , unlike in the deterministic case (see Fig. 5.2b lower panel).

### 5.2.3 Strong mean field (weak fluctuations) limit: Transverse case

Figure 5.3a shows  $\langle r_1 \rangle$  and  $\langle r_Q \rangle$  in the strong mean field (weak fluctuations) limit, for a mean field perpendicular to the LOS, i.e.  $\theta_0 = 90^\circ$ . We also assume  $\phi_0 = 0^\circ$ . Hence only  $\langle \varphi_{I,Q} \rangle$  are non-zero. Figure 5.3b shows the corresponding curves calculated with the mean field. Again we observe a large difference between micro-turbulent and deterministic profiles.

To analyze the numerical results presented in Fig. 5.3a, we consider approximate expression for  $\langle\varphi_{I,Q}\rangle$ . At leading order (see Eqs. (2.16), (2.38) - (2.40)),

$$\langle\varphi_I\rangle \simeq \frac{1}{2} \left(1 - \frac{1}{2y_0^2}\right) h^{(0)}(x) + \frac{1}{4\gamma_1} \left(1 + \frac{1}{2y_0^2}\right) [h^{(0)}(\bar{x}_{+1}) + h^{(0)}(\bar{x}_{-1})], \quad (5.11)$$

$$\langle\varphi_Q\rangle \simeq \frac{1}{2} \left(1 - \frac{3}{2y_0^2}\right) h^{(0)}(x) - \frac{1}{4\gamma_1} \left(1 - \frac{3}{2y_0^2}\right) [h^{(0)}(\bar{x}_{+1}) + h^{(0)}(\bar{x}_{-1})]. \quad (5.12)$$

The terms  $\bar{c}_q$  play no role in this case. The terms  $3/2y_0^2$  and  $1/2y_0^2$  are small compared to unity since  $y_0 = 3$ . However, when we consider the difference  $\langle\varphi_I\rangle^2 - \langle\varphi_Q\rangle^2$  in the denominator of Eqs. (F.13) and (F.14) for  $\langle r_I\rangle$  and  $\langle r_Q\rangle$ , these factors cannot be neglected. We thus have

$$d_t \simeq 1 + 2\beta\langle\varphi_I\rangle + \beta^2 \left\{ \frac{1}{2y_0^2} [h^{(0)}(x)]^2 + \frac{1}{4\gamma_1^2 y_0^2} [h^{(0)}(\bar{x}_{+1}) + h^{(0)}(\bar{x}_{-1})]^2 + \frac{1}{2\gamma_1} h^{(0)}(x) [h^{(0)}(\bar{x}_{+1}) + h^{(0)}(\bar{x}_{-1})] \right\}. \quad (5.13)$$

When  $\beta$  is sufficiently small,  $d_t \simeq 1$  and we recover the mean opacity coefficients  $\beta\langle\varphi_I\rangle$  and  $\beta\langle\varphi_Q\rangle$  which are fairly well represented by the curves corresponding to  $\beta = 1$ . We remark that the Eqs. (5.11) and (5.12), when used in Eqs. (F.13) and (F.14) for  $\langle r_I\rangle$  and  $\langle r_Q\rangle$  can reproduce the numerical result in Fig. 5.3a to a very good approximation.

With Eqs. (5.11) to (5.13) we can explain why  $\langle r_I\rangle$  approaches unity at all frequencies fairly rapidly when  $\beta$  increases. For  $x$  around the line center we can write

$$d_t \simeq 1 + \beta h^{(0)}(x) \left[ 1 + \frac{\beta}{2y_0^2} h^{(0)}(x) \right], \quad (5.14)$$

and for  $x$  around the  $\sigma$ -components

$$d_t \simeq 1 + \frac{\beta}{2\gamma_1} h^{(0)}(\bar{x}_{\pm 1}) \left[ 1 + \frac{\beta}{2y_0^2 \gamma_1} h^{(0)}(\bar{x}_{\pm 1}) \right], \quad (5.15)$$

(the third term in the curly bracket in Eq. (5.13) can be neglected). The  $\beta^2$ -terms, which come from the small differences between the  $\pi$  and  $\sigma$ -components of  $\langle\varphi_I\rangle$  and  $\langle\varphi_Q\rangle$ , (see Eqs. (5.11) and (5.12)) become relevant when  $\beta/2y_0^2$  and  $\beta/2y_0^2\gamma_1$  become of order or larger than unity. For our choice of parameters, this means that they play an important role when  $\beta > 50$ . This implies that the second term in Eq. (F.13) becomes small compared to unity because the numerator scales as  $\beta$  and the denominator as  $\beta^2$ . As a consequence  $\langle r_I\rangle$  goes to unity at line center and around the  $\sigma$ -components.



Roughly half-way between the  $\pi$  and  $\sigma$ -components, we have the point where  $\langle\varphi_Q\rangle = 0$ . Around this frequency, denoted  $x_m$ ,

$$\langle r_I(x_m) \rangle \simeq \frac{\beta \langle \varphi_I(x_m) \rangle}{1 + \beta \langle \varphi_I(x_m) \rangle}. \quad (5.16)$$

This expression rapidly approaches unity when  $\beta$  increases. Thus, when the mean field is in the transverse direction,  $\langle r_I \rangle$  approaches unity at line center, in the  $\sigma$ -components and half-way between these two regions. This explains the shape of the  $\langle r_I \rangle$  profiles shown in Fig. 5.3a, upper panel.

For  $\langle r_Q \rangle$ , the micro-turbulent profile has qualitatively the same shape as the mean field profile (see lower panels in Fig. 5.3). There are however quantitative differences also due to the  $\beta^2$ -term in  $d_t$ . At line center, when  $\beta$  is large,  $\langle r_Q \rangle$  is much smaller than the mean field solution. One observes also that the wing minima move away from line center to frequencies such that the  $\beta^2$ -term in  $d_t$  becomes negligible. Their positions vary roughly as  $x \simeq \pm(\Delta_Z B_0 + \gamma_1 \sqrt{\ln \beta})$ . The amplitude of the minima are not very sensitive to the value of  $\beta$  and are approximately given by

$$\langle r_Q \rangle \simeq \frac{\langle \varphi_Q \rangle}{2 \langle \varphi_I \rangle} \simeq -\frac{1 - 3/2y_0^2}{1 + 1/2y_0^2} \simeq -0.4, \quad (5.17)$$

in fairly good agreement with the numerical results which yield  $\langle r_Q \rangle \simeq -0.35$ .

### 5.3 Macro-turbulence with isotropic Gaussian fluctuations

We use the isotropic Gaussian distribution already used to study the micro-turbulent limit (see Eq. (5.1)). We consider only the case of strong mean field with weak fluctuations ( $\gamma_B = 1$ ,  $\Delta_Z B_0 = 3$ ). We show in Figs. 5.2c and 5.3c the residual Stokes parameters for a longitudinal and a transverse mean field respectively. When the mean field is longitudinal, we have for symmetry reasons  $\langle r_Q \rangle = 0$  and  $\langle r_U \rangle = 0$ . It is easy to check that  $Q$  and  $U$  average to zero when they are integrated over the azimuthal angle  $\phi$ . When the mean field is in a transverse direction, i.e. when  $\theta_0 = 90^\circ$ , averaging over an isotropic distribution yields  $\langle r_V \rangle = 0$ . When in addition  $\phi_0 = 0^\circ$ , one also has  $\langle r_U \rangle = 0$ .

In the longitudinal case, as shown by Fig. 5.2c,  $\langle r_I \rangle$  behaves much as in the micro-turbulent case (see Fig. 5.2a, upper panel). A weak central component appears, which is created by the averaging over the angular distribution of the magnetic field. It is already visible when  $\beta = 1$  and its value goes to unity when  $\beta$  increases. In the transverse case (see Fig. 5.3c),  $\langle r_I \rangle$  behaves essentially as in the deterministic case, except that the differ-

ent components are somewhat broader and have a smaller value for the same value of  $\beta$  (compare upper panels of Fig. 5.3b, and 5.3c).

For  $\langle r_V \rangle$  (longitudinal case), the behavior is similar to the micro-turbulent limit, but for very large values of  $\beta$  ( $\beta > 10^3$ ), the profiles are less distorted compared to the micro-turbulent case, and stay closer to the mean field value (see Fig. 5.2, lower panels). One can remark also that the position, height and shape of the peaks are largely independent of the value of  $\beta$  in a wide range of values ( $1 < \beta < 10^3$ ).

For  $\langle r_Q \rangle$  (transverse case), we observe a shift of the positions of the minima away from the line center when  $\beta$  increases. It is stronger than in the deterministic case, but much weaker than in the micro-turbulent case (see Fig. 5.3, lower panels). Note also that the frequency at which  $\langle r_Q \rangle = 0$  depends slightly on  $\beta$ . This comes from the averaging process.

To summarize, for macro-turbulence the mean Stokes profiles of strong lines have a behavior which is similar to the micro-turbulent limit for the longitudinal case and similar to the mean field solution for the transverse case. For weak lines,  $\beta \simeq 1$ , or less,  $\langle \mathbf{r} \rangle_{\text{micro}} \simeq \langle \mathbf{r} \rangle_{\text{macro}} \simeq \beta \langle \Phi \rangle \mathbf{U}$  as shown by Eqs. (4.31) and (4.32). Weak lines are not sensitive to the correlation length of the magnetic field.

## 5.4 Micro and macro-turbulent profiles for arbitrary orientation of $B_0$

In this section we compare micro-turbulent, macro-turbulent and mean field solution Stokes profiles for a mean magnetic field with arbitrary orientation, and isotropic Gaussian fluctuations characterized by  $y_0 = 3$ , and  $\gamma_B = 1$ . This model corresponds to the strong mean field limit with weak fluctuations ( $f = 1/3$ ). We know that for weak lines ( $\beta \leq 1$ ), there are no differences between the micro and macro-turbulent limit and differences start showing up for  $\beta = 10$ , and they become quite large when  $\beta$  is around 100 or more. Hence the comparison is carried out for a spectral line with  $\beta = 100$  and damping parameter  $a = 0$ .

Figure 5.4 shows the micro, macro and mean field Stokes profiles. In Fig. 5.4a we present  $\langle r_{I,Q,U,V} \rangle$  for  $\theta_0 = 60^\circ$ ,  $\phi_0 = 30^\circ$ . The dependence of  $\langle r_I \rangle$  on field inclination  $\theta_0$  is shown in Fig. 5.4b. The behavior of  $\langle r_{Q,U,V} \rangle$  for micro-turbulent limit at  $\pi$  and  $\sigma$ -components is quite similar to that observed for longitudinal and transverse case (see lower panels of Figs. 5.2a and 5.3a). For example appearance of a dip at  $x = 3$  and shifting of the  $\sigma$ -component peak position to a larger  $x$  are due to the dominance of the  $\beta^2$  terms in the denominator of  $\langle r_{Q,U,V} \rangle$  (see Eqs. (F.4) - (F.10)).

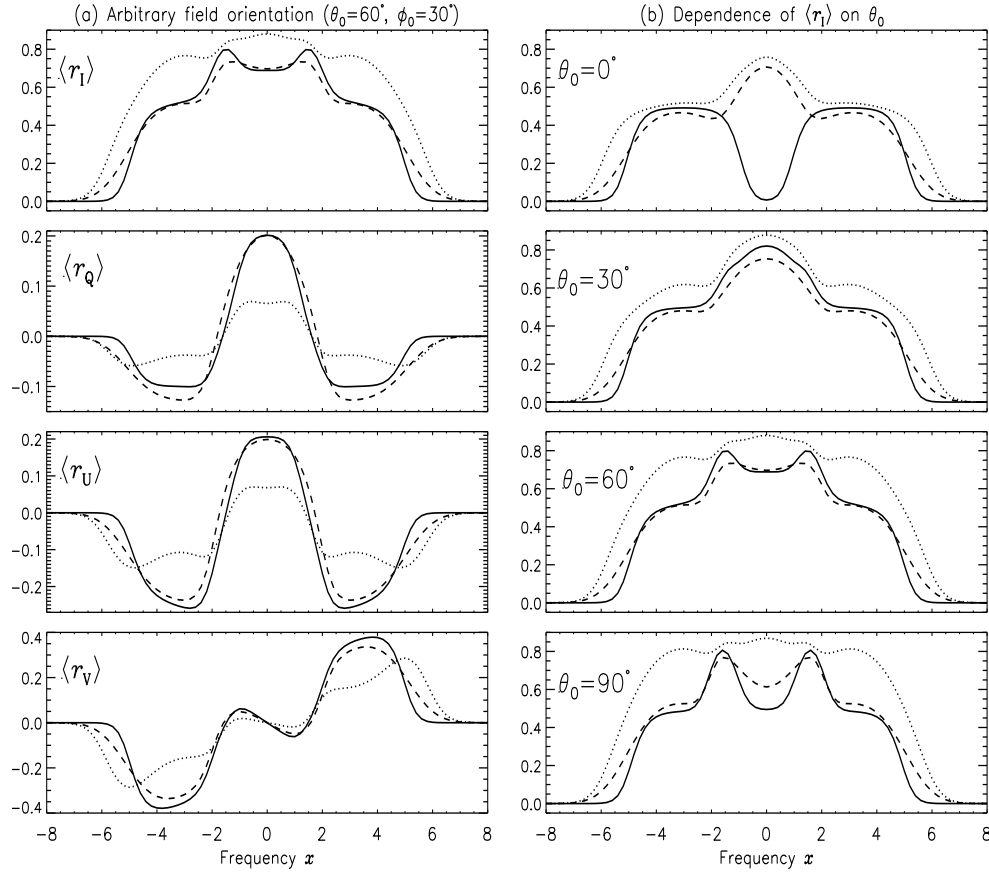


Figure 5.4: UR solution for mean field (solid line), micro (dotted line), and macro (dashed line) limits. The line parameters are  $a = 0$ , and  $\beta = 100$ . Panel (a): Mean magnetic field with parameters  $\theta_0 = 60^\circ$ ,  $\phi_0 = 30^\circ$ ,  $\Delta_Z B_0 = 3$ ; weak magnetic field fluctuations ( $\gamma_B = 1$ ). Panel (b): dependence of  $\langle r_I \rangle$  on  $\theta_0$ . The value of  $\theta_0$  is indicated in each sub-panel. See § 5.4 for discussions.

For all the Stokes components the micro-turbulent profiles are broader than the macro-turbulent and mean field ones, and the difference between the macro and micro-turbulent profiles are large, except for the case  $\theta_0 = 0^\circ$ . This phenomenon is illustrated for  $\langle r_I \rangle$  in the upper panel of Fig. 5.4b. The large difference between the turbulent and mean field profiles for large values of  $\beta$  have already been discussed in §§ 5.2 and 5.3.

For an arbitrary orientation of the mean magnetic field, the exact and approximate expressions for the mean absorption and dispersion coefficients under strong field limit given in Eqs. (2.16), (2.38) - (2.40) give the numerical result presented in Fig. 5.4 (dotted line) to a very good approximation for  $\theta_0 \neq 0^\circ$ . In the case of  $\theta_0$  around  $0^\circ$ , one should

also consider the term  $\bar{c}_{\pm 1}$ .

Another parameter which may affect the difference between the micro and macro-turbulent limits is the value of the damping parameter  $a$ . An increase in  $a$  produces a broadening and a decrease in magnitude of all the Zeeman components of the elements of the matrix  $\Phi$  and as a consequence leads to a broadening and decrease in magnitude of all the Zeeman components of  $r_{Q,U,V}$ , for turbulent as well as non-turbulent fields. For  $r_I$ , the broadening of the Zeeman components may lead to the formation of a single peak.

## 5.5 Anisotropic magnetic field distributions

In the preceding sections we have considered a random magnetic field with isotropic distribution. For simplicity we refer to this model as 3D turbulence. This type of angular distribution can be considered as a reasonable approximation to magneto-hydrodynamic turbulence. Randomness of a quite different nature can be expected in sunspot umbra where thin flux tubes corresponding to umbral dots will probably be more or less oriented in the same direction (Thomas & Weiss 2004). In this case, the magnetic field fluctuates mainly in magnitude. For pure Gaussian fluctuations in field strength Eq. (5.1) reduces to (see also Eq. (2.21))

$$P_L(\mathbf{B}) d\mathbf{B} = \frac{1}{\pi^{1/2}} e^{-(y-y_0)^2} dy, \quad -\infty \leq y \leq +\infty, \quad (5.18)$$

a model which we refer to for simplicity as 1D or longitudinal turbulence. For 1D turbulence, the fluctuations of the magnetic field strength affect the  $\varphi_{\pm 1}$  Zeeman components, but not the central component  $\varphi_0$ . The same is true for the anomalous dispersion coefficients.

Intermediate between isotropic and longitudinal fluctuations, as far as angular distribution is concerned, are fluctuations transverse to the mean field. The corresponding PDF (see Eq. (2.51), also DP79) may be written as

$$P_T(\mathbf{B}) d\mathbf{B} = \frac{1}{\pi} e^{-(y^2-y_0^2)} y dy d\Psi, \quad y_0 \leq y \leq +\infty. \quad (5.19)$$

This case, referred here as 2D turbulence, is typical of Alfvén waves. When the magnitude of the mean field is zero, this distribution can describe a magnetic canopy since the random magnetic field remains in a plane perpendicular to the direction  $(\theta_0, \phi_0)$ .

We show in Fig. 5.5 the mean Stokes parameters for 1D, 2D and 3D turbulence in the micro-turbulent limit for a line with  $\beta = 100$  and the same magnetic field model as in the

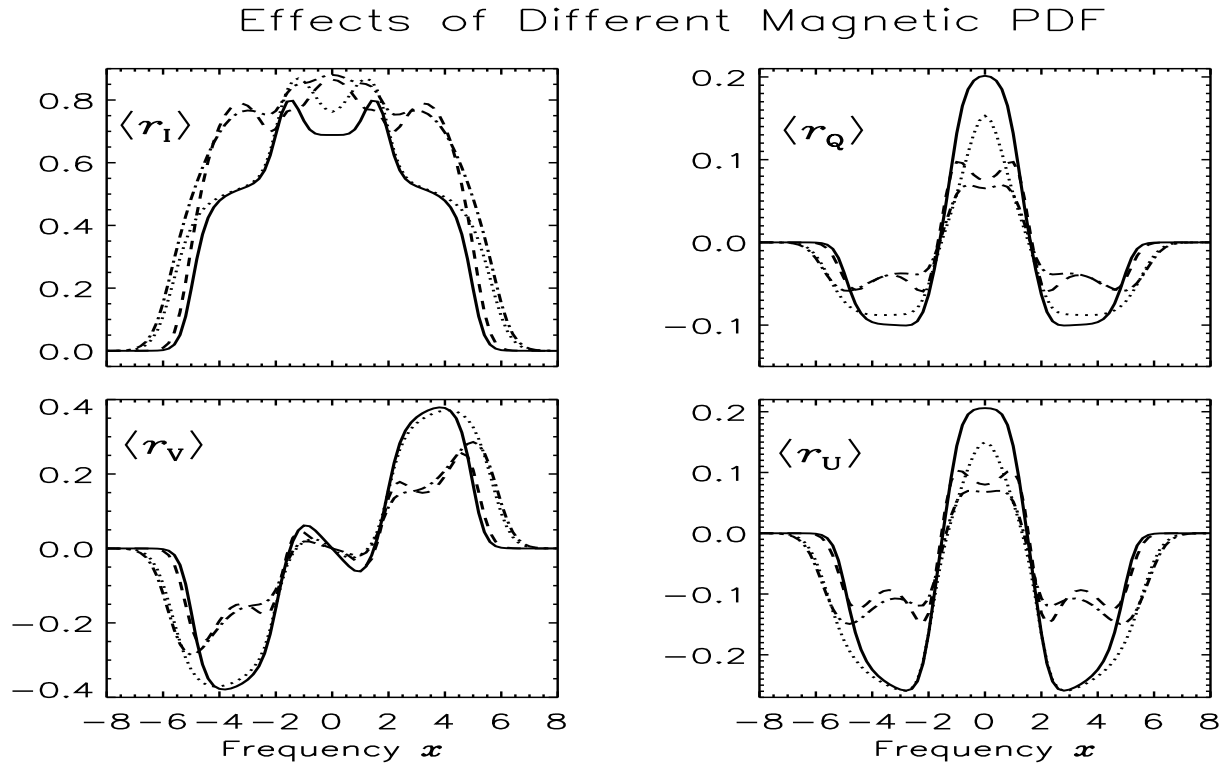


Figure 5.5: Effects of different models of magnetic turbulence under micro turbulent limit. The solutions displayed are: deterministic mean field (solid line); 1D turbulence (dotted line); 2D turbulence (dashed line); 3D turbulence (dot-dashed line). The magnetic field parameters used are the same as in Fig. 5.4. See § 5.5 for discussions.

preceding section ( $\phi_0 = 30^\circ$ ,  $\theta_0 = 60^\circ$ ,  $\Delta_Z B_0 = 3$ ,  $\gamma_B = 1$ ). The mean absorption and dispersion coefficients can be written explicitly in terms of the usual Voigt and Faraday-Voigt functions for 1D turbulence (see Eqs. (2.16) and (2.22)). For 2D turbulence they also have explicit expressions but for  $a = 0$  only (see Eqs. (2.16), (2.55) - (2.60) and also DP79). Other numerical aspects of the calculation are presented in Chapter 4.

The upper left panel of Fig. 5.5 shows that amplitude of  $\langle r_I \rangle$  is fairly sensitive to the anisotropy of the distribution function. At line center, micro-turbulence always produces an increase in amplitude due to the broadening of the  $\sigma$ -components and to the averaging over the magnetic field directions, the latter mechanism being effective in the 2D and 3D cases only. Line center enhancement is present, for any value of  $\theta_0$  (see e.g. dotted lines in Fig. 5.4b). The magnitude of the  $\sigma$ -components is larger for 2D and 3D turbulence when compared to the mean field and 1D case because of the important role played by the  $\beta^2$  terms.

For the polarization components, turbulence always broadens the Zeeman components and reduces their magnitude. For 1D turbulence, the  $\pi$ -component in  $\langle r_{Q,U} \rangle$  is reduced, and the  $\sigma$ -component in  $\langle r_{Q,U,V} \rangle$  are broadened compared to the mean field profiles. For  $\langle r_Q \rangle$  and  $\langle r_U \rangle$ , 2D and 3D turbulence reduce the  $\pi$  and  $\sigma$ -component rather efficiently. For  $\langle r_V \rangle$ , one can observe the same effect as for the  $\sigma$ -components of  $\langle r_{Q,U} \rangle$ . The mean profiles for 2D and 3D turbulence are very similar, except for the width of the  $\sigma$ -components which are smaller for 2D than for 3D or 1D turbulence because the fluctuations are perpendicular to the mean field.

We also investigated the case of macro-turbulence. Compared to micro-turbulence, the averaged profiles stay closer to the mean field solution (see e.g. dashed lines in Fig. 5.4b).

## 5.6 Summary and concluding remarks

In this chapter we take the example of a normal Zeeman triplet to explore the effects of a random magnetic field with mean value  $\mathbf{B}_0$  on polarized line formation. The Unno-Rachkovsky solution which provides an explicit expression for the Stokes parameters at the surface of a Milne-Eddington atmosphere is used to calculate the mean Stokes parameters for random magnetic fields with scales of variations that are much smaller, or much larger than the mean free path of photons. These micro and macro-turbulent limits provide bounds for more general random magnetic fields with finite scales of variation. Thanks to the Unno-Rachkovsky (UR) solution, we could explore a broad range of magnetic field and spectral line parameters. For the spectral line, we varied the line strength  $\beta$  measured as the ratio of the line to continuum opacity.

For the random magnetic field  $\mathbf{B}$ , we have assumed Gaussian fluctuations about  $\mathbf{B}_0$  given by a distribution function  $P(\mathbf{B})$ . Isotropic fluctuations and anisotropic ones (parallel and perpendicular to the mean field) are considered. The distribution is characterized by two Zeeman shifts:  $\Delta_Z B_0$  due to the mean field and  $\gamma_B$  due to the rms fluctuations. The ratio  $f = \gamma_B / \Delta_Z B_0$  provides a measure of the strength of the turbulent fluctuations. Most of the results concern a strong field or weak fluctuations limit ( $\Delta_Z B_0 = 3$ ,  $f = 1/3$ ).

In the micro-turbulent limit (§ 5.2), using explicit approximate expressions for the mean coefficients, we could follow in detail the variations of the Stokes profiles shapes as  $\beta$  increases and explain various saturation stages. These expressions along with the UR solution can predict Stokes profile that matches with the numerical result to a good approximation. For  $\langle r_I \rangle$  we have shown how fluctuations in the strength and direction of

the magnetic field can produce an enhancement of the  $\pi$ -component which can lead, when  $\beta$  is large, to drastic changes in the profile shape as compared to the mean field solution.

In the macro-turbulent regime (see § 5.3) the UR solution is averaged over  $P(\mathbf{B})$ . Hence it is harder to perform a precise quantitative analysis of the mean profiles. Numerical calculations show that the macro-turbulent profiles have the same type of behavior as the micro-turbulent ones, but on the whole stay closer to mean field solutions.

Differences between the micro and macro-turbulent limits (see § 5.4) are sensitive to the values of the damping parameter  $a$  and the line strength  $\beta$ . Non-existent for weak lines, say  $\beta = 1$  or less, they become significant for  $\langle r_{\text{I}} \rangle$  when  $\beta = 10$ , but stay marginal for  $\langle r_{\text{Q,U,V}} \rangle$ . They become really important only when  $\beta$  is around 100.

The sensitivity of the mean profiles to the angular distribution of the magnetic field is examined in § 5.5 for a line with  $\beta = 100$  and  $a = 0$  and weak fluctuations ( $f = 1/3$ ,  $\Delta_Z B_0 = 3$ ). Micro-turbulent profiles are very sensitive to the choice of PDF  $P(\mathbf{B})$ . The macro-turbulent profiles are however less sensitive than the micro-turbulent ones. It is a general feature of macro-turbulence in the case of weak fluctuations except for  $\theta_0 = 0^\circ$ .

All the numerical results presented in this work have been obtained with a Gaussian distribution function. There is evidence for Voigt type distribution functions or stretched exponentials for the magnetic field strength (see e.g. Stenflo & Holzreuter 2003a, Stein & Nordlund 2006). We consider the effect of such distribution functions on the mean residual Stokes profiles in Chapter 6.





## Chapter 6

# Studies with empirical probability distribution functions<sup>1</sup>

### 6.1 Introduction

Magneto-convection on the Sun has a size spectrum that spans several orders of magnitudes and hence develops turbulent elements or eddies the sizes of which are much smaller than the spatial resolution of current spectro-polarimeters (about 0.2 arcsec or 150 km at the photospheric level). Thus the Stokes profiles that we observe are always averages - the averaging being over space, time, and along the line-of-sight. This suggests that it may be sufficient to characterize the magnetic field responsible for spectral line polarization by a probability distribution function (PDF). Attempts have been made to deduce such PDFs from observational data by *inversion* methods (c.f. Domínguez Cerdeña et al. 2006). Here we consider the *forward* method, namely the calculation of the mean Stokes parameters for a given PDF. Our primary goal is to compare Stokes profiles calculated with different types of PDFs. We have used PDFs determined from observations (Stenflo & Holzreuter 2002, 2003a, 2003b) and from numerical simulations of magneto-convection (Vögler et al. 2005, Stein & Nordlund 2006, and the papers cited therein). The observational PDFs have been deduced from magnetograms and describe the vertical magnetic field in the solar photosphere. For simplicity we neglect any depth-dependence of the PDFs inside the atmosphere.

In the solar photosphere the mean free path of optical photons is in the range 50-100 km, corresponding approximately to the middle part of the turbulent spectrum. The

---

<sup>1</sup>This chapter is based on the paper which is under revision : Sampoorana, M., Nagendra, K. N., Frisch, H., & Stenflo, J. O. 2008, A&A, under review

calculation of mean Stokes parameters for this spatial range, sometimes referred to as *meso-turbulence*, has been considered in Chapter 4 (see also Landi Degl’Innocenti 1994, Carroll & Staude 2003b, 2005a, 2005b, 2006, Carroll & Kopf 2007). The mean Stokes parameters for meso-turbulence are always bounded by the micro and macro-turbulent limits. The concept of micro-turbulence is associated to optically thin magnetic eddies while macro-turbulence corresponds to optically thick ones.

In the micro-turbulent limit the Zeeman absorption matrix (containing both absorptive and magneto-optical effects) can be averaged over the PDF and the line transfer equation solved with the averaged absorption matrix. Distributions of optically thin elements and transfer equations with mean coefficients were first considered by Stenflo (1971, and references cited therein). One of the effects of micro-turbulent magnetic field is to produce line broadening. The earliest observational attempt to search for magnetic fields by this broadening mechanism dates back to Unno (1959). Stenflo & Lindegren (1977) performed a statistical analysis of 402 unblended Fe I lines in the optical region and found an upper limit of 100 G for the rms magnetic field fluctuations responsible for the line broadening. Along the same lines, Sánchez Almeida et al. (1996) introduced the MISMA model (Micro Structured Magnetic Atmospheres) consisting of spatially intermittent optically thin structures.

In the macro-turbulent limit, the emergent spectrum may be formed within a single magnetic structure. The averaging over different realizations of the vector magnetic field is now performed on the emergent solution of the transfer equation. Multi-component models representing optically thick unresolved structures were introduced by Stenflo (1971, 1973, 1994), and Stenflo et al. (1984). The special case of a two-component model forms the basis of the line ratio technique (Stenflo 1973).

For our present investigation of the effects of various types of PDF, we consider both the micro and macro-turbulent limits. The case of Gaussian PDFs was studied in Chapters 2, 4, and 5 (see also Dolginov & Pavlov 1972, Domke & Pavlov 1979). In this chapter we use more realistic types of PDFs, namely Voigt type and stretched exponential type distributions for the strength of a magnetic field with a fixed direction. We also consider axially symmetric magnetic fields of constant strength, but with random directions distributed according to a power law. Finally we introduce a heuristic PDF, which combines distributions in strength and direction. The angular distribution is described by a power law and the strength distribution by either a Voigt function or a stretched exponential.

The PDFs that we are adopting can be used in a general numerical solution of the

polarized line transfer equations. However in this chapter, we restrict ourselves to the Unno-Rachkovsky solution (see Unno 1956, Rachkovsky 1962a, 1962b). We believe that the approximation of a Milne-Eddington (ME) atmosphere is adequate for exploratory work on the sensitivity of Stokes profiles to different magnetic field PDFs. In the micro-turbulent limit we average the Zeeman absorption matrix over the PDF before applying the Unno-Rachkovsky solution. In the macro-turbulent limit we average the Unno-Rachkovsky solution over the magnetic field PDF. In these two limits, it is possible within the framework of the ME model to introduce fluctuations of the atmospheric parameters (velocity, temperature, density), the correlations between them and also with the magnetic field. Adequate joint PDFs would have to be introduced for this purpose. Correlations between velocity fields and magnetic fields will produce asymmetric profiles (see eg. Figs. 9.19 and 9.20 in Landi Degl'Innocenti & Landolfi 2004, hereafter LL04). Here we analyze only pure magnetic fields effects.

In §§ 6.2–6.5 we present mean Stokes profiles for a Zeeman triplet computed with different kinds of PDFs, for micro and macro-turbulence. We also consider the dispersion of the Stokes profiles around their mean values. In § 6.6 we generalize our averaging procedures to the anomalous general Zeeman pattern. Conclusions are presented in § 6.7.

## 6.2 Magnetic field strength distribution : Voigt PDF

Recently Stenflo & Holzreuter (2002, 2003a, 2003b) have found from an analysis of high resolution La Palma and MDI solar magnetograms that the PDF for the line-of-sight (LOS) component of the magnetic field is nearly independent of the spatial scale and can be well represented by a simple function which has a Gaussian core and Lorentzian type wings. The Gaussian core is centered around zero field. The PDF wings are generally significantly different for the positive and negative polarities. Stenflo & Holzreuter (2002, 2003a) have proposed a PDF for the LOS field strength that can be represented by a Voigt function depending on a magnetic damping parameter  $a_B$  and a magnetic width  $\Delta_B$ . The parameter  $\Delta_B$  is a measure of the rms fluctuations of the LOS component of the field. It represents the width of the Gaussian core, while the parameter  $a_B$  describes the damping of the Lorentzian wings. These two parameters are not based on any theory but only define a convenient and compact analytical fit function.

If one chooses  $\Delta_B = 6$  G and  $a_B = 1.5$ , it surprisingly well describes the empirical PDF for the LOS magnetic field strength derived from magnetograms. A symmetric Voigt function however has zero net flux, whereas in real magnetograms the magnetic flux is

generally unbalanced locally (although the global ensembles should in general be balanced). Such situations can be well represented by a Voigt PDF that has a symmetric Gaussian core, but with different damping parameters  $a_B$  for the positive and negative polarities.

We examine in § 6.2.1 the effects of a symmetric Voigt PDF on the mean Stokes profiles. Because of the symmetry around zero, the mean magnetic field is zero. In § 6.2.2 we consider asymmetric PDFs with Gaussian core and Lorentzian wings. The corresponding mean fields and mean Stokes  $V$  parameters are now different from zero.

### 6.2.1 Symmetric Voigt PDF

In terms of the parameters  $a_B$  and  $\Delta_B$ , the Voigt PDFs considered in this section have the functional form

$$P_V\left(\frac{B}{\Delta_B}, a_B\right) = \frac{a_B}{\pi^{3/2}} \int_{-\infty}^{+\infty} \frac{e^{-(B_1/\Delta_B)^2}}{[(B - B_1)/\Delta_B]^2 + a_B^2} \frac{dB_1}{\Delta_B}. \quad (6.1)$$

Here  $B$  is the magnetic field component along a given direction. We introduce the non-dimensional parameters

$$y = \frac{B}{\Delta_B}; \quad u = \frac{B_1}{\Delta_B}; \quad \gamma_B = \Delta_Z \Delta_B, \quad (6.2)$$

where the quantity  $\Delta_Z$  is defined in Eq. (2.8).  $\gamma_B$  represents the rms fluctuations  $\Delta_B$  converted to Zeeman shift in Doppler width units. Equation (6.1) then takes the form

$$P_V(y, a_B) = \frac{a_B}{\pi^{3/2}} \int_{-\infty}^{+\infty} \frac{e^{-u^2}}{(y - u)^2 + a_B^2} du. \quad (6.3)$$

For a magnetic damping parameter  $a_B = 0$ , this Voigt PDF reduces to a 1D Gaussian distribution with zero mean field as considered in Chapter 2.

The average Zeeman absorption matrix  $\langle \Phi \rangle$  is given by

$$\langle \Phi \rangle = \int_{-\infty}^{+\infty} \Phi(\mathbf{B}) P_V\left(\frac{B}{\Delta_B}, a_B\right) \frac{dB}{\Delta_B}. \quad (6.4)$$

This integral can be calculated analytically because it involves the convolution of Voigt or Faraday-Voigt functions with a Voigt PDF. Explicit expressions for these convolutions are given in Eq. (5.65) of LL04 (p. 171). For the average absorption coefficients, they yield

$$\begin{aligned} \langle \varphi_I \rangle &= \bar{A}_0 - \frac{1}{3} \bar{A}_2 (3 \cos^2 \theta - 1); & \langle \varphi_V \rangle &= \bar{A}_1 \cos \theta, \\ \langle \varphi_Q \rangle &= \bar{A}_2 \sin^2 \theta \cos 2\phi; & \langle \varphi_U \rangle &= \langle \varphi_Q \rangle \tan 2\phi, \end{aligned} \quad (6.5)$$

where

$$\begin{aligned}
\bar{A}_0 &= \frac{1}{3} \sum_{q=-1}^{q=+1} \frac{1}{\gamma_q} H(\bar{x}_q, \bar{a}_q), \quad q = 0, \pm 1, \\
\bar{A}_1 &= \frac{1}{2} \sum_{q=\pm 1} q \frac{1}{\gamma_q} H(\bar{x}_q, \bar{a}_q), \\
\bar{A}_2 &= \frac{1}{4} \sum_{q=-1}^{q=+1} (2 - 3q^2) \frac{1}{\gamma_q} H(\bar{x}_q, \bar{a}_q), \quad q = 0, \pm 1.
\end{aligned} \tag{6.6}$$

The non-dimensional quantities  $\gamma_q$ ,  $\bar{x}_q$ , and  $\bar{a}_q$  in Eqs. (6.6) are

$$\gamma_q = \sqrt{1 + q^2 \gamma_B^2}, \quad q = 0, \pm 1, \tag{6.7}$$

and

$$\bar{x}_q = \frac{x}{\gamma_q}, \quad \bar{a}_q = \frac{(a + q^2 \gamma_B a_B)}{\gamma_q}. \tag{6.8}$$

In Eq. (6.8),  $x = (\nu_0 - \nu)/\Delta\nu_D$  is the frequency measured from the line center in units of the Doppler width  $\Delta\nu_D$ , while  $a$  is the damping parameter. In the set of Eqs. (6.5) and (6.6),  $(\theta, \phi)$  define the orientation of the random magnetic field with respect to the LOS and  $H(\bar{x}_q, \bar{a}_q)$  is the Voigt function. Because  $\bar{x}_q$  and  $\bar{a}_q$  only depend on  $q^2$ , we have  $\bar{A}_1 = 0$  and hence  $\langle \varphi_V \rangle = 0$ . For the magneto-optical coefficients  $\langle \chi_{Q,U,V} \rangle$  one has similar expressions, but with Faraday-Voigt functions  $F(\bar{x}_q, \bar{a}_q)$ .

It is important to note that in practical computations with Eq. (6.4) one should restrict the integration to the range  $[-B_{\max}, +B_{\max}]$ , where  $B_{\max}$  is approximately 1500 G. Small-scale photospheric fields with strengths larger than about 1500 G would not be expected to occur, since stronger fields cannot be contained by the ambient gas pressure that prevails in the photosphere. As mentioned above, high resolution La Palma magnetogram data can be represented well with a Voigt like PDF with a magnetic width  $\Delta_B = 6$  G. Using this as the standard magnetic width, the limits of integration in non-dimensional units are  $[-y_{\max}, +y_{\max}] = [-250, +250]$ . We have verified that for such a large value of the cut-off, the average absorption matrix (obtained by numerical averaging) does not differ significantly from the corresponding analytical result (see Eq. (6.5)) derived with  $[-y_{\max}, +y_{\max}] = [-\infty, +\infty]$ . We have also verified numerically that the part of the PDF that affects the mean absorption coefficient is from  $y \approx -50$  to  $y \approx +50$ . Thus Eq. (6.5) may indeed be used to analyze the numerical results, to a good approximation. To perform the  $y$  integral numerically we use a Gauss-Legendre quadrature with approximately 300 quadrature points, otherwise one would get oscillations in the wings of the emergent

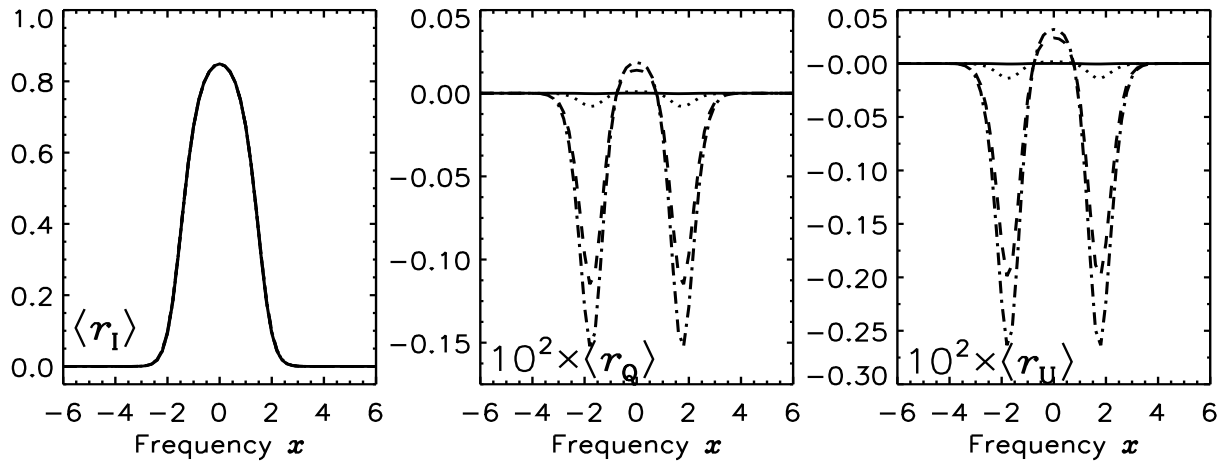


Figure 6.1: Effect of the magnetic damping parameter  $a_B$  on the mean residual Stokes parameters  $\langle r_{I,Q,U} \rangle$ . The average is taken over the Voigt type PDF with zero mean field defined in Eq. (6.1), assuming micro-turbulent limit. Different line types correspond to different values of the magnetic damping parameter:  $a_B = 0$  (solid), 0.1 (dotted), 1.5 (dashed), and 2 (dash-dotted). Notice the increase of polarization throughout the line profile, with an increase in  $a_B$ .

solutions. It has been shown that the maximum frequency band width should be chosen for consistency to satisfy the condition  $x_{\max} = 4\gamma_B y_{\max}$  (see Chapter 2).

We have calculated the averaged emergent residual Stokes parameters  $\langle r_{I,Q,U} \rangle$  for the Voigt type PDF defined in Eq. (6.1), in the micro- and macro-turbulent limits. The random field has a fixed orientation with respect to the LOS defined by the polar angles  $\theta = 60^\circ$  and  $\phi = 30^\circ$ . The emergent residual Stokes parameters  $r_X$  with the symbol  $X$  denoting  $I$ ,  $Q$ ,  $U$ , or  $V$  are defined in Eq. (4.26). The model used has damping parameter  $a = 0$ , line strength parameter  $\beta = k_0/k_c = 10$  (ratio of line to the continuous absorption coefficient). We also assume that the spectral line has a wavelength around  $5000 \text{ \AA}$ , a Landé factor of 2 and a Doppler width of  $1.5 \text{ km s}^{-1}$ . For this typical line,  $1/\Delta_Z = 1.07 \times 10^3 \text{ G}$ . Hence the value of  $\gamma_B$  corresponding to rms magnetic field fluctuations  $\Delta_B = 6 \text{ G}$  is  $\gamma_B = 0.0056$ . This means that we will be dealing here with very small Zeeman shifts. As a result the  $\langle r_I \rangle$  profiles in all the figures in this chapter remain insensitive to the parameters of the PDFs.

The results presented in Fig. 6.1 correspond to the micro-turbulent limit. They are calculated with  $\gamma_B = 0.0056$  and  $a = 0$ . The magnetic damping parameter  $a_B$  is taken as a free parameter. Because of the symmetry of the PDF  $\langle \varphi_V \rangle = 0$  and hence  $\langle r_V \rangle = 0$ .

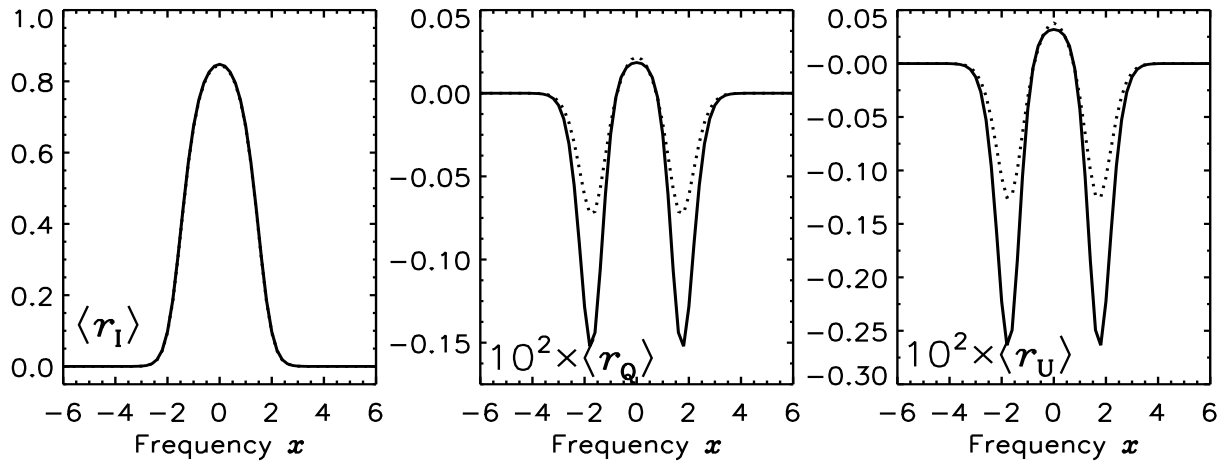


Figure 6.2: Comparison of lines formed for micro-turbulent (solid line) and macro-turbulent (dotted line) limits. The model parameters are the same as in Fig. 6.1, but with  $a_B = 1.5$ .

The  $\langle r_I \rangle$  profile is insensitive to the value of  $a_B$  for the reason given above. The  $\langle r_{Q,U} \rangle$  can be understood from Eqs. (6.5) – (6.8). Since  $\gamma_B \ll 1$ , we have  $\gamma_q \simeq 1$ ,  $x_q \simeq x$  and  $\bar{a}_1 \simeq \gamma_B a_B \ll 1$  ( $a_B$  is zero or of the order of unity). For  $a_B \neq 0$ , we can expand  $H(x_q, \bar{a}_1)$  in powers of  $\bar{a}_1$  (see Mihalas 1978, p. 280). We find  $\bar{A}_2 \simeq -(1/\pi)\gamma_B a_B [2xD(x) - 1]$ , where  $D(x)$  is the Dawson function of real argument. This expression explains the order of magnitude of  $\langle r_{Q,U} \rangle$  and the increase with  $a_B$ , i.e. with the broadening of the magnetic field PDF. For  $a_B = 0$ , an expansion of  $\bar{A}_2$  for small  $\gamma_B$  yields  $\bar{A}_2 \simeq (1/4\sqrt{\pi})\gamma_B^2(1 - 2x^2)\exp(-x^2)$ . The  $\langle r_{Q,U} \rangle$  are thus of the order of  $10^{-6}$ .

In Fig. 6.2 we compare the mean residual Stokes vector corresponding to the micro-turbulent (solid line), and macro-turbulent (dotted line) limits. The model is the same as in Fig. 6.1, but with a fixed magnetic damping parameter  $a_B = 1.5$ . As the value of  $\gamma_B$  is very small, the  $\langle r_I \rangle$  profile for both the cases are nearly identical. Significant differences are observed in the wing peaks of  $\langle r_{Q,U} \rangle$ , the polarization being much larger in the micro-turbulent limit than the macro-turbulent limit.

### 6.2.2 Asymmetric Voigt PDF

Asymmetric Voigt PDFs can be constructed by choosing different values of the magnetic damping parameter  $a_B$  for different parts of the PDF while the Gaussian core is kept symmetrical. Figure 6.3a shows examples of asymmetric PDFs. The three lines are constructed as follows :

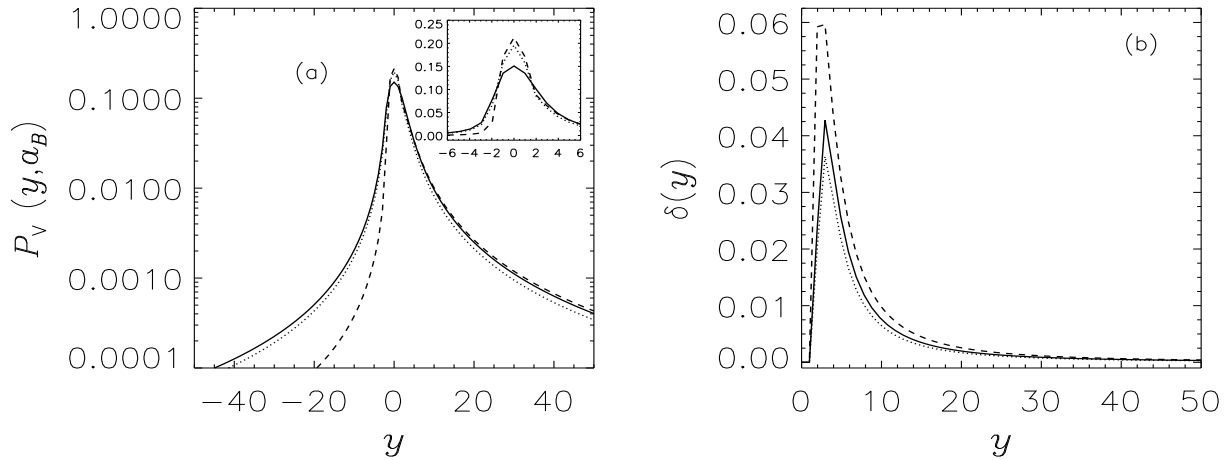


Figure 6.3: (a) Asymmetric Voigt PDFs defined in § 6.2. A multiplication of the non-dimensional unit  $y$  by  $\Delta_B$  yields the magnetic field strength in Gauss. According to Stenflo & Holzreuter (2002)  $\Delta_B = 6$  G in the solar atmosphere. The PDFs are shown in log-scale to resolve the wing region and in linear scale to resolve the core region. (b) The asymmetry  $\delta(y)$  for the PDFs shown in panel (a). In both panels, solid line:  $y_0 = 3.4$ ; dotted line:  $y_0 = 2.9$ ; dashed line:  $y_0 = 4.5$ .

- solid line: For  $y < -1$ ,  $a_B = 0.5$ ; for  $y \geq -1$ ,  $a_B = 2.5$
- dotted line: For  $y < -1$ ,  $a_B = 0.5$ ; for  $-1 \leq y \leq +1$ ,  $a_B = 1.5$ ; for  $y > 1$ ,  $a_B = 2.5$
- dashed line: For  $y < -1$ ,  $a_B = 0.1$ ; for  $-1 \leq y \leq +1$ ,  $a_B = 1.5$ ; for  $y > 1$ ,  $a_B = 2.9$

All of them have been normalized to unity and more or less resemble the PDF for the La Palma magnetogram in Fig. 2 of Stenflo & Holzreuter (2002).

The asymmetry in  $P_V(y, a_B)$  can be measured by the difference  $\delta(y) = P_V(y > 0) - P_V(y < 0)$  shown in Fig. 6.3b. The mean magnetic field is the average of  $y$  over  $\delta(y)$ . Here we denote it by  $y_0$ . The values corresponding to the examples in Fig. 6.3a are: (solid line)  $y_0 = 3.4$ ; (dotted line)  $y_0 = 2.9$ ; (dashed line)  $y_0 = 4.5$ .

Figure 6.4 shows the mean residual emergent solutions for the three PDFs in Fig. 6.3a in the micro-turbulent limit. The other model parameters are the same as in Figs. 6.1 and 6.2. The  $\langle r_{Q,U} \rangle$  profiles show a very small sensitivity to the asymmetry of the PDFs and the  $\langle r_I \rangle$  profiles remain insensitive to the PDF asymmetry for reasons explained above. For all three PDFs  $\langle r_V \rangle$  peaks around  $x \approx 1.5$ . The amplitude of the peaks increases with the mean field. For the two first cases of asymmetry (solid and dotted lines in Fig. 6.3), the values of  $\langle r_V \rangle$  do not differ significantly as the  $y_0$  have similar values.



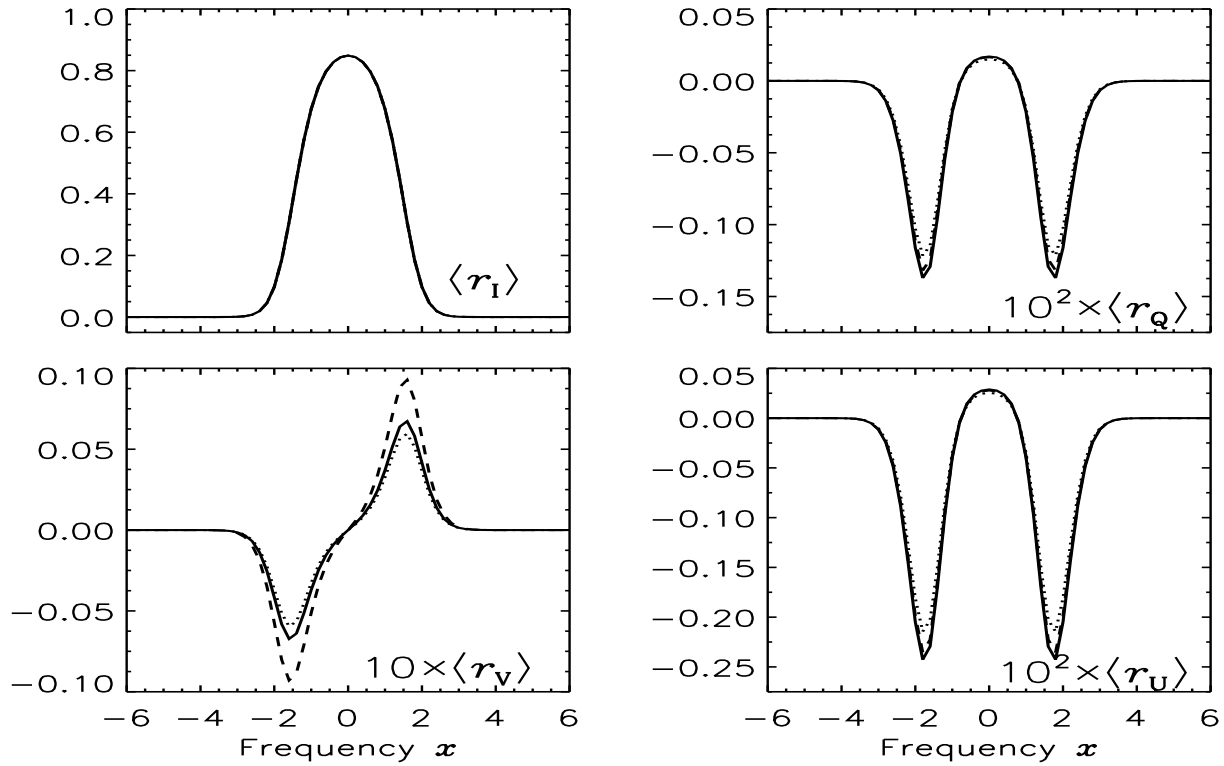


Figure 6.4:  $\langle r_{I,Q,U,V} \rangle$  computed with the asymmetric Voigt PDFs in Fig. 6.3a. The relation between line type and PDF is the same as in Fig. 6.3a, namely, solid line :  $y_0 = 3.4$ ; dotted line :  $y_0 = 2.9$ ; dashed line :  $y_0 = 4.5$ .

We have computed also the mean Stokes profiles for the macro-turbulent limit using the same three asymmetric PDFs. For  $\langle r_{I,Q,U} \rangle$ , the differences between the micro- and macro-turbulent limit solutions are essentially similar to those shown in Fig. 6.2. For  $\langle r_V \rangle$  the differences are minimal. This confirms our previous conclusion (Chapter 4) that  $\langle r_V \rangle$  shows little dependence on the correlation length and may be calculated using the micro-turbulent limit with reasonable confidence.

In a random magnetic field, the Stokes profiles fluctuate around their mean values. The order of magnitude of the fluctuations is given by the dispersion (square root of the variance)  $\sigma_X$ , ( $X = I, Q, U, V$ ). For the reduced Stokes profiles,

$$\sigma_X^2 = \langle r_X^2 \rangle - \langle r_X \rangle^2, \quad (6.9)$$

where the average  $\langle \rangle$  is over all the realizations of the random field. In the micro-turbulent limit,  $\sigma_X$  is zero since  $r_X$  is equal to its mean value. The dispersion has its maximum value in the macro-turbulent limit. Then  $\langle \rangle$  stands for the average over the Unno-Rachkovsky

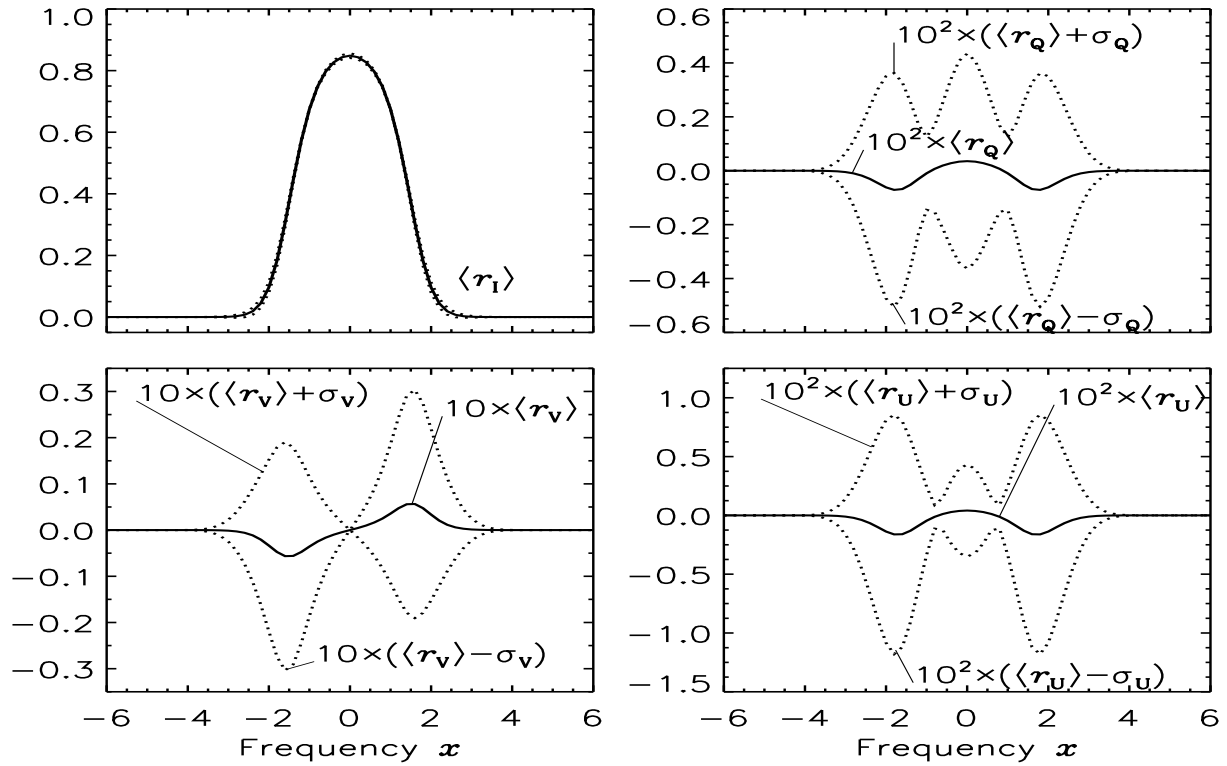


Figure 6.5: Dispersion around the mean  $\langle r_{I,Q,U,V} \rangle$  in the macro-turbulent limit. The calculations have been performed with the asymmetric Voigt PDF corresponding to the mean field  $y_0 = 3.4$  (see Fig. 6.3). Notice the fairly large dispersion for  $\langle r_{Q,U,V} \rangle$ .

solution. Examples of the variation of  $\sigma_X$  with the characteristic scale of the magnetic field can be found in Chapter 4. Details on the numerical work required to calculate the dispersion in the macro-turbulent limit can be found also in the same chapter.

It is interesting to consider the dispersion  $\sigma_X$  for a given value of the mean field  $y_0$ , and to compare it with the spread introduced in  $\langle r_X \rangle$  by varying  $y_0$  (see Fig. 6.4). In Fig. 6.5 we show  $\langle r_X \rangle \pm \sigma_X$ , with  $X = I, Q, U, V$  for  $y_0 = 3.4$ . The other values of  $y_0$  (2.9 and 4.5) yield very similar results. The dispersion is very small for  $\langle r_I \rangle$  but for  $\langle r_{Q,U,V} \rangle$  much larger than the spread introduced by different choice of  $y_0$ . One should not forget that the values shown in Fig. 6.5 are upper bounds.

### 6.3 Magnetic field strength distribution : Stretched exponential PDF

Numerical simulations of magneto-convection near the solar surface by Stein & Nordlund (2006) show that the magnetic field is intermittent with a stretched exponential distribution. We will now consider the effect of such a distribution function on the emergent mean residual Stokes profiles. The functional form of a stretched exponential (abbreviated “se”) may be written as <sup>2</sup>

$$P_{\text{se}}(y)dy = C e^{-|y|^k} dy. \quad (6.10)$$

Here  $y$  is the magnetic field strength, in non-dimensional units, defined as in Eq. (6.2). We let  $y$  vary from  $-y_{\text{max}}$  to  $+y_{\text{max}}$ . The frequency shifts due to the Zeeman effect (measured in Doppler width units) are  $\pm y\gamma_B$  where  $\gamma_B$  is defined in Eq. (6.2). As in the case of Voigt PDFs, we choose  $y_{\text{max}} = 250$ ,  $\Delta_B = 6$  G and  $\gamma_B = 0.0056$ . The quantity  $k$  is a parameter that can range between 0 and 1 and is referred to as the stretching parameter.  $C$  is the normalization constant that is determined numerically by normalization. For  $y_{\text{max}} = \infty$ ,  $C = k/[2\Gamma(1/k)]$ , where  $\Gamma(1/k)$  is the Gamma function. We find numerically that for  $y_{\text{max}} = 250$ , we have  $C \approx k/[2\Gamma(1/k)]$ . The part of the PDF that affects the mean absorption coefficient is from  $y \approx -50$  to  $y \approx +50$ , as above. For accurate evaluation of the  $y$  integral we use Gauss-Legendre quadrature with approximately 300 points.

In Fig. 6.6 we show stretched exponentials and a Voigt PDF with a damping parameter  $a_B = 1.5$  as suggested by the solar data. The stretched exponentials for  $k \leq 0.5$  decrease slower than the Voigt PDF, while for  $k > 0.5$  they decrease faster. It is clear that the transition at  $k_{\text{crit}} = 0.5$  depends on the value  $a_B$ . Stenflo & Holzreuter (2002) mention that Voigt PDFs cannot fit the PDFs derived by magneto-convection simulations. The main problem is the core region, which is much more peaked with stretched exponentials than a Gaussian.

In Fig. 6.7 we compare the mean residual Stokes vector for micro-turbulent limit computed with the stretched exponential PDFs and the Voigt PDF shown in Fig. 6.6. The Voigt PDF produces the largest degree of linear polarization (c.f.  $\langle r_Q \rangle$  and  $\langle r_U \rangle$ ). As the stretching parameter  $k$  increases, the profiles  $\langle r_{Q,U} \rangle$  decrease at all frequencies because of the disappearance of the strong field tails of  $P_{\text{se}}(y)$  (see Fig. 6.6). The  $\langle r_I \rangle$  profile as before remains insensitive to the different PDFs.

We find that for a stretched exponential the dispersion and the differences between

---

<sup>2</sup>[http://en.wikipedia.org/wiki/Stretched\\_exponential](http://en.wikipedia.org/wiki/Stretched_exponential)

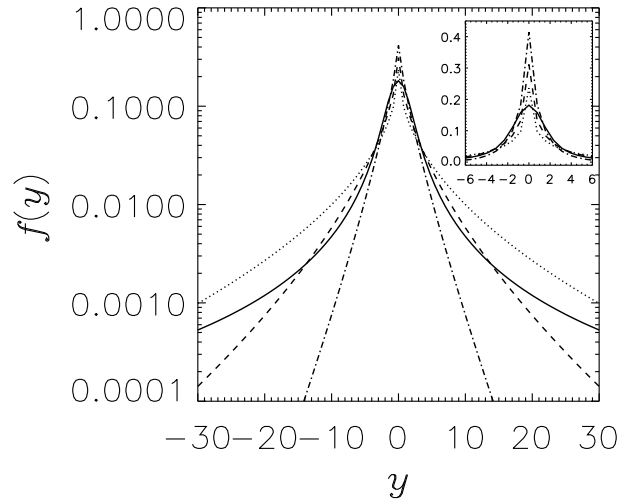


Figure 6.6: Stretched exponentials and Voigt PDFs. The non-dimensional  $y$ -scale is related to the  $B$ -scale through a multiplying factor  $\Delta_B$  equal to 6 G according to Stenflo & Holzreuter (2002). The solid line corresponds to  $f(y) = P_V(y, a_B = 1.5)$ , while the dotted, dashed and dash-dotted lines correspond respectively to stretched exponentials  $f(y) = P_{se}(y)$  with the stretching parameter  $k = 0.5, 0.6, \text{ and } 0.8$ , respectively. The inset figure shows a magnified view of the core region in linear scale.

the micro- and macro-turbulent limit solutions are small, much smaller than for the Voigt PDF case, unless the stretching parameter  $k$  is chosen to be small ( $< 0.5$ ). Dispersion and differences between the micro- and macro-turbulent limits are zero when the magnetic field has a fixed value and orientation. They will remain small as long as the magnetic field PDF shows no extended tails. They will appear with Voigt PDFs or when  $k$  is small.

Asymmetric PDFs with non-zero mean field can be constructed with stretched exponentials. It suffices to choose different  $k$  values for positive and negative polarities. Figure 6.8a shows three examples constructed as follows:

- solid line: For  $y < -1$ ,  $k = 0.8$ ; for  $-1 \leq y \leq +1$ ,  $k = 0.7$ ; for  $y > 1$ ,  $k = 0.6$
- dotted line: For  $y < -1$ ,  $k = 0.9$ ; for  $-1 \leq y \leq +1$ ,  $k = 0.7$ ; for  $y > 1$ ,  $k = 0.5$
- dashed line: For  $y < -1$ ,  $k = 0.8$ ; for  $-1 \leq y \leq +1$ ,  $k = 0.6$ ; for  $y > 1$ ,  $k = 0.4$

All these profiles have been normalized to unity. The asymmetries  $\delta(y) = P_{se}(y > 0) - P_{se}(y < 0)$  are shown in Fig. 6.8b. The values of the mean field  $y_0$  are: solid line ( $y_0 = 1$ ), dotted line ( $y_0 = 3.2$ ), dashed line ( $y_0 = 11.6$ ).

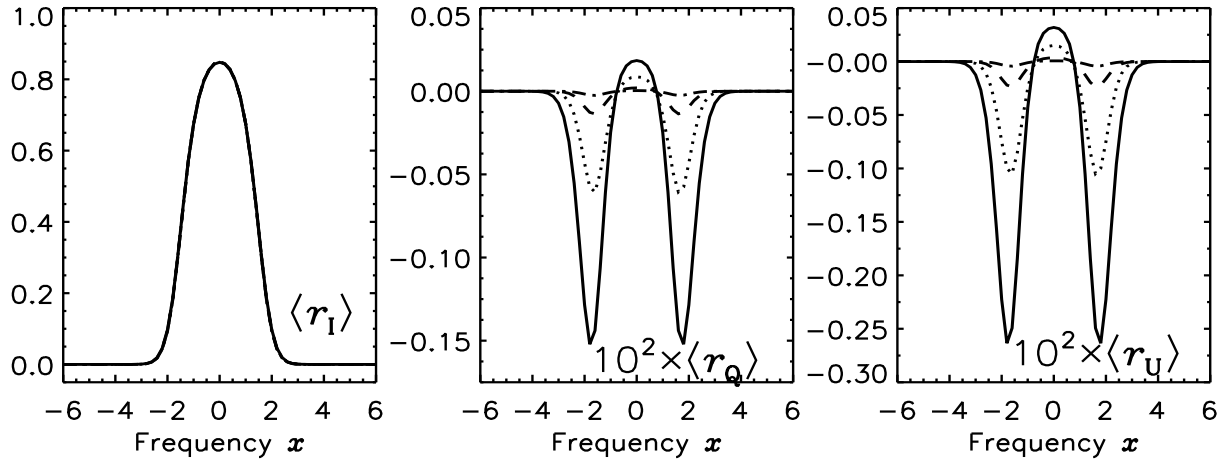


Figure 6.7: Mean Stokes profiles  $\langle r_{I,Q,U} \rangle$  for micro-turbulent limit computed using three stretched exponential PDFs with different values of  $k$  and one Voigt PDF. The model parameters are the same as in Fig. 6.2. Line types: solid (Voigt with  $a_B = 1.5$ ), dotted ( $k = 0.5$ ), dashed ( $k = 0.6$ ), and dash-dotted ( $k = 0.8$ ).

We have calculated the mean residual Stokes profiles for these three PDFs in the regime of micro- and macro-turbulent limits. Now  $\langle r_V \rangle$  is not zero. Figure 6.9 shows the results of our calculations for the micro-turbulent limit and one case of macro-turbulent limit corresponding to  $y_0 = 11.6$ . When  $y_0 = 1$  and  $y_0 = 3.2$  there are no significant differences between the micro- and macro-turbulent limit solutions because of the rapid drop of the PDF tails.

In the micro-turbulent limit, we observe a clear increase in the peak amplitudes of  $\langle r_{Q,U,V} \rangle$  when the mean field  $y_0$  increases. The positions of the peaks are however essentially insensitive to the mean field value. The  $\langle r_I \rangle$  profiles show no splitting and remain insensitive to the changes in the asymmetries. The differences between the micro- and macro-turbulent limits that appear when  $y_0 = 11.6$  are due to the extended tail of the PDF for positive polarities. They are significant for Stokes  $Q$  and  $U$  but remain small for Stokes  $V$ . The relative insensitivity of Stokes  $V$  to the scale of the magnetic field fluctuations seems pretty general. We have already observed it for Voigt and Gaussian PDFs (see § 6.2.2).

We have calculated the dispersion around the mean Stokes parameters (for the macro-turbulent limit). In Fig. 6.10, we show the dependence of  $\sigma_V$  on the value of  $y_0$ . For  $y_0 = 11.6$ , it can become as large as the dispersion for a Voigt PDF shown in Fig. 6.5. The dependence of  $\sigma_{I,Q,U}$  on  $y_0$  is similar to that of  $\sigma_V$ , and hence we do not present them here.

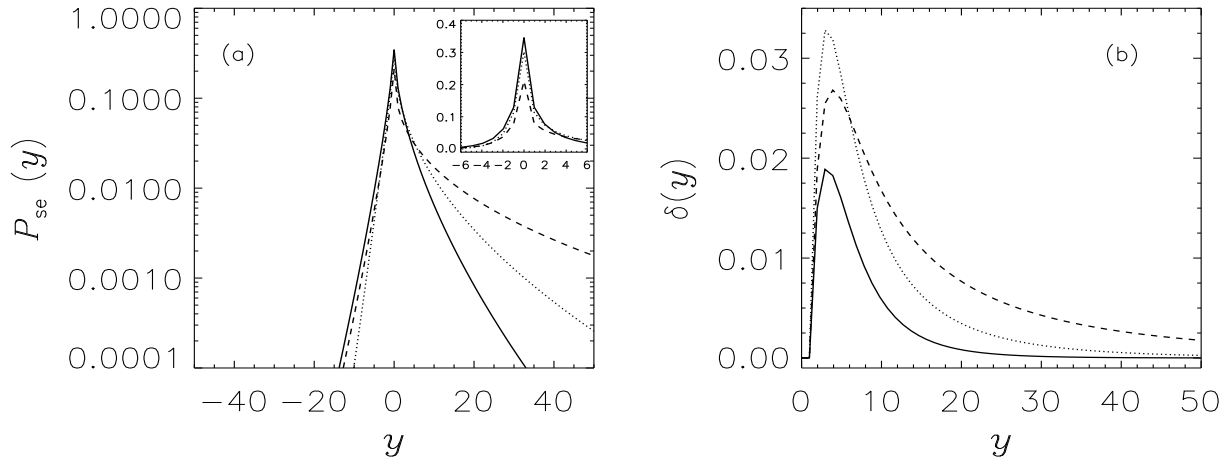


Figure 6.8: (a) Asymmetric stretched exponential PDFs defined in § 6.3. (b) The asymmetry  $\delta(y)$  of  $P_{se}(y)$  for the PDFs shown in panel (a). In panels (a) and (b) the line types are solid line:  $y_0 = 1$ , dotted line:  $y_0 = 3.2$ , dashed line:  $y_0 = 11.6$ . To convert to the field strength scale, multiply  $y$  by  $\Delta_B = 6$  G.

#### 6.4 Magnetic field angular distribution : Power law PDF

A large fraction of the solar atmosphere is filled with mixed polarity fields, and the intergranular lanes contain fields directed upward or downward. To represent this scenario, we consider magnetic fields that have a fixed value of the strength  $B$  but random orientations. For such a random field, the following angular distribution has been suggested by Stenflo (1987) :

$$P_{pl}(\mu_B) = \frac{(p+1)}{4\pi} |\mu_B|^p, \quad -1 \leq \mu_B \leq +1. \quad (6.11)$$

Here,  $\mu_B = \cos \vartheta_B$ , with  $\vartheta_B$  the field orientation with respect to the vertical direction, chosen as the normal to the atmosphere. The abbreviation “pl” stands for “power law”. In Stenflo (1987) the same expression as above is given without modulus on  $\mu_B$ , but it is actually Eq. (6.11) which is meant.

The power law index  $p$  can take any value. The  $p = 0$  case corresponds to an isotropic distribution. As  $p$  increases the distribution becomes more and more peaked in the vertical direction (see Fig. 6.11). One can verify that the power law  $P_{pl}(\mu_B)$  is normalized to unity i.e.,

$$\int_0^{2\pi} \int_{-1}^{+1} P_{pl}(\mu_B) d\mu_B d\varphi_B = 1, \quad (6.12)$$

where  $\varphi_B$  is the azimuth of the random field. In Eq. (6.11)  $P_{pl}(\mu_B)$  is expressed in the at-

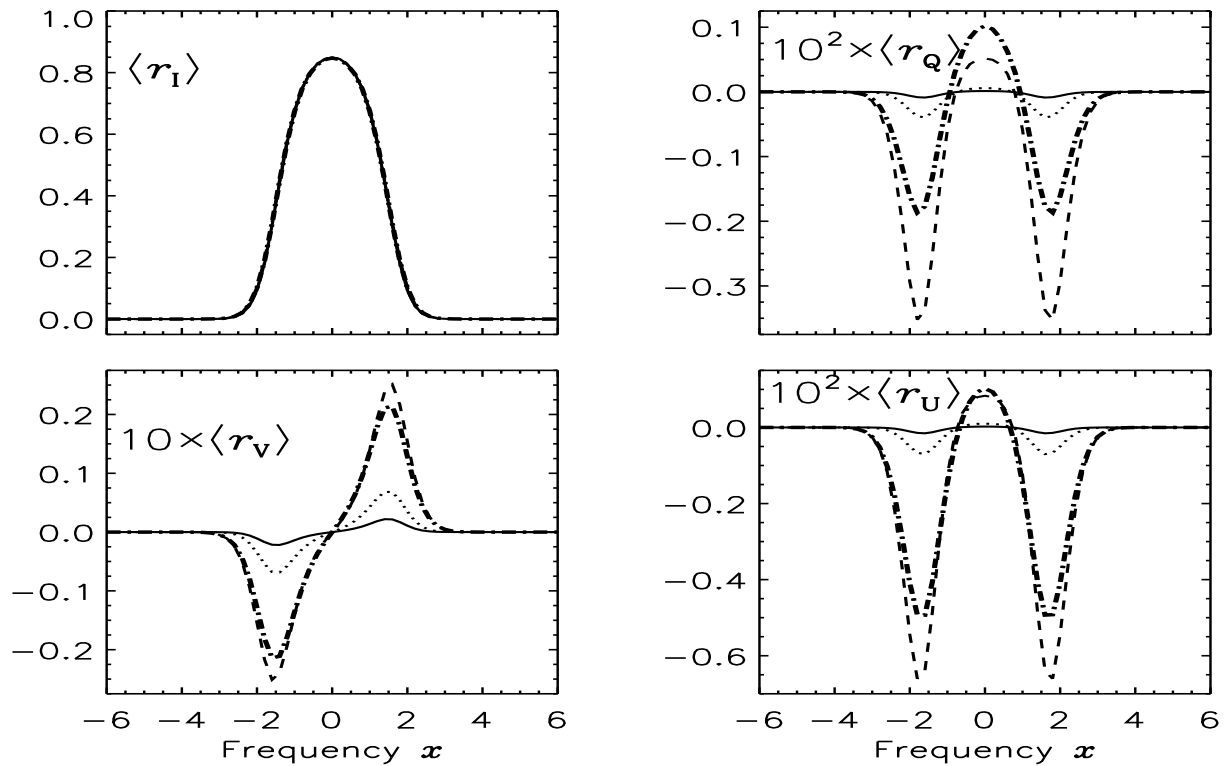


Figure 6.9: Mean Stokes profiles  $\langle r_{I,Q,U,V} \rangle$  computed using asymmetric stretched exponential PDFs. The solid, dotted and dashed lines are micro-turbulent limit calculations, the line types referring to the corresponding PDFs in Fig. 6.8a. The heavy dot-dashed line is a macro-turbulent limit calculation for  $y_0 = 11.6$ .

mospheric reference frame (ARF). Therefore the Zeeman absorption matrix usually formulated in the LOS frame needs to be transformed to the ARF. The required transformation is given by (c.f. Varshalovich et al. 1988):

$$\begin{pmatrix} \sin \theta \cos \phi \\ \sin \theta \sin \phi \\ \cos \theta \end{pmatrix} = \begin{pmatrix} \cos \vartheta \cos \varphi & \cos \vartheta \sin \varphi & -\sin \vartheta \\ -\sin \varphi & \cos \varphi & 0 \\ \sin \vartheta \cos \varphi & \sin \vartheta \sin \varphi & \cos \vartheta \end{pmatrix} \begin{pmatrix} \sin \vartheta_B \cos \varphi_B \\ \sin \vartheta_B \sin \varphi_B \\ \cos \vartheta_B \end{pmatrix}, \quad (6.13)$$

where  $(\vartheta, \varphi)$  defines the orientation of the LOS with respect to the ARF,  $(\theta, \phi)$  the field orientation with respect to the LOS, and  $(\vartheta_B, \varphi_B)$  the field orientation with respect to the ARF.

The average Zeeman absorption matrix  $\langle \Phi \rangle$  is given by

$$\langle \Phi \rangle = \int_0^{2\pi} d\varphi_B \int_{-1}^1 \Phi(\mathbf{B}) P_{\text{pl}}(\mu_B) d\mu_B. \quad (6.14)$$

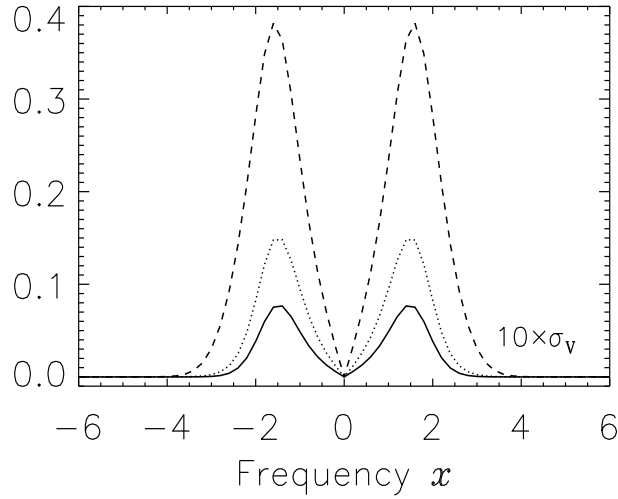


Figure 6.10: Dispersion  $\sigma_V$  in the macro-turbulent limit for the model of Fig. 6.9. Different line types are solid line:  $y_0 = 1$ , dotted line:  $y_0 = 3.2$ , dashed line:  $y_0 = 11.6$ .

Using the transformation formula of Eq. (6.13), it can be shown that

$$\langle \varphi_I \rangle = A_0 - \frac{1}{3} A_2 \frac{p}{p+3} (3\mu^2 - 1), \quad (6.15)$$

$$\langle \varphi_Q \rangle = A_2 \frac{p}{p+3} (1 - \mu^2), \quad (6.16)$$

where  $\mu = \cos \vartheta$ . The coefficients  $A_{0,2}$  are given by

$$\begin{aligned} A_0 &= \frac{1}{3} \sum_{q=-1}^{q=+1} H(x_q, a), \quad q = 0, \pm 1 \\ A_2 &= \frac{1}{4} \sum_{q=-1}^{q=+1} (2 - 3q^2) H(x_q, a), \quad q = 0, \pm 1, \end{aligned} \quad (6.17)$$

where  $x_q = x - q\Delta_Z B$ . We note that  $\langle \varphi_{I,Q} \rangle$  depend on the orientation  $\vartheta$  of the LOS but are independent of azimuth  $\varphi$ . When we use the transformation formula (6.13), we obtain terms proportional to  $\cos(\varphi - \varphi_B)$ ,  $\sin(\varphi - \varphi_B)$ ,  $\cos 2(\varphi - \varphi_B)$ , or  $\sin 2(\varphi - \varphi_B)$ , which vanish when averaged over  $\varphi_B$ . As a result  $\langle \varphi_U \rangle = 0$ . Further,  $\langle \varphi_V \rangle = 0$  for symmetry reasons. As for the anomalous dispersion coefficients, the only non-zero coefficient is  $\langle \chi_Q \rangle$ . It has the same expression as  $\langle \varphi_Q \rangle$  with the Voigt function replaced by the Faraday-Voigt function. From Eqs. (6.15) and (6.16) we see that when  $p = 0$  (isotropic turbulence case), or when  $\mu = \cos \vartheta = 1$  (disk center observation),  $\langle \varphi_Q \rangle = 0$ .



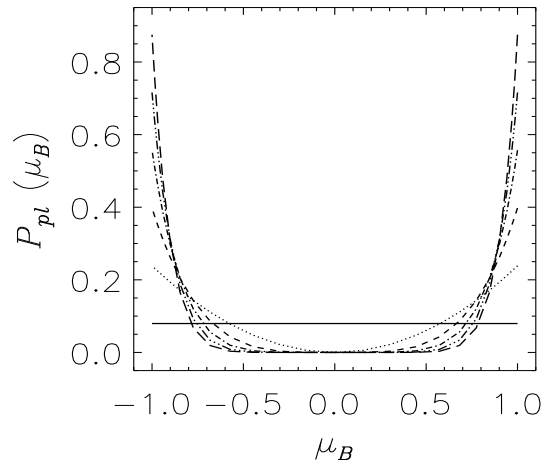


Figure 6.11: Power law PDFs as a function of the cosine of the random field orientation  $\vartheta_B$  (defined with respect to the vertical). The line types correspond to  $p = 0$  (solid), 2 (dotted), 4 (dashed), 6 (dash-dotted), 8 (dash-triple-dotted), and 10 (long-dashed). As  $p$  increases the PDF becomes more and more peaked in the forward and backward directions.

The mean profiles  $\langle r_{I,Q} \rangle$  have been calculated in the micro- and macro-turbulent limits. The average absorption matrix elements given by Eqs. (6.15) and (6.16) have been used for the micro-turbulent limit. The model parameters are magnetic field strength  $\Delta_Z B = 0.1$ , line strength  $\beta = 10$ , damping parameter  $a = 0$ . The index  $p$  of the power law PDF is taken as a free parameter.

Figure 6.12 shows  $\langle r_{I,Q} \rangle$  for the micro-turbulent limit at the limb ( $\mu = 0.1$ ). The results are fairly simple to explain. Since the magnetic field is weak ( $\Delta_Z B = 0.1$ ),  $x_q \simeq x$ . As a consequence  $A_2$  is very small. This implies  $\langle \varphi_I \rangle \approx H(x, a)$  (see Eq. (6.15)). Hence  $\langle \varphi_I \rangle$  is independent of  $p$ . The small value of  $A_2$  also implies  $\langle \varphi_Q \rangle \ll \langle \varphi_I \rangle$  and thus  $\langle r_Q \rangle \ll \langle r_I \rangle$ . As already mentioned,  $\langle \varphi_Q \rangle = 0$  when  $p = 0$ , hence  $\langle r_Q \rangle$  is also zero. As  $p$  gets larger, the factor  $p/(p+3)$  in Eq. (6.16) tends to unity. Therefore  $\langle \varphi_Q \rangle$  first increases with  $p$  and then saturates. A similar behavior is exhibited by  $\langle r_Q \rangle$ . The saturation is reached for  $p \simeq 100$  as can be observed in Fig. 6.12.

The mean profiles  $\langle r_{I,Q} \rangle$  for the macro-turbulent limit do not differ significantly from the micro-turbulent limit solutions because the absolute value of the magnetic field along the LOS is bounded by the condition  $\Delta_Z B = 0.1$ . The dispersion around the mean value (for the macro-turbulent limit) decreases with an increase in the value of  $p$ . This was expected because as  $p$  increases the field becomes more and more unidirectional and confined to the two values  $\pm 0.1$ .

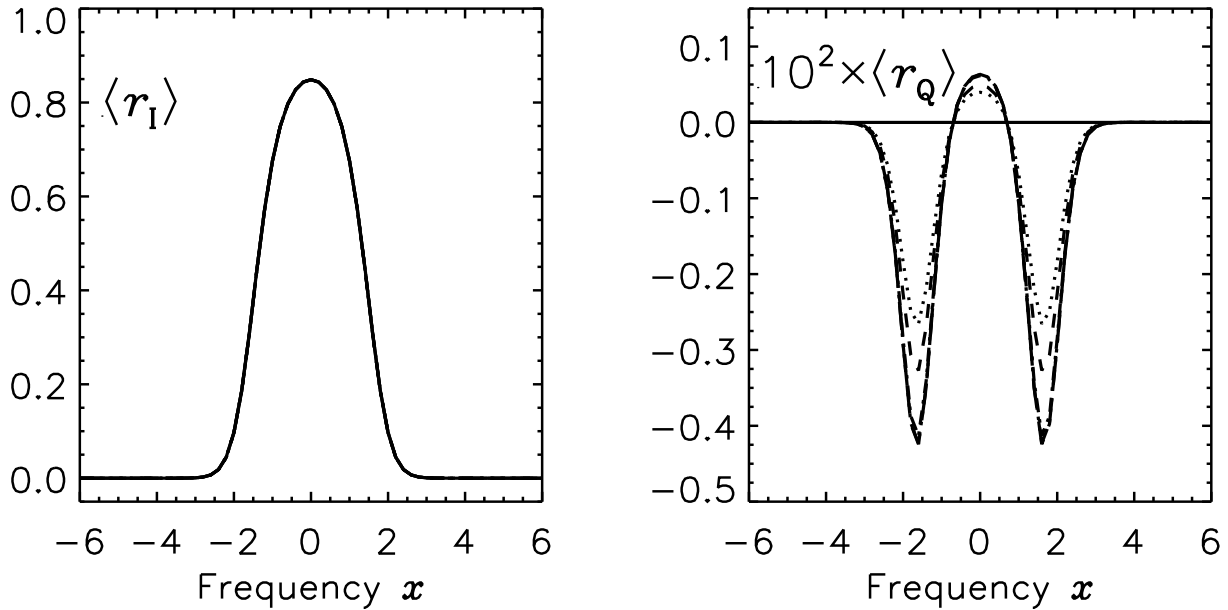


Figure 6.12: Residual mean Stokes profiles  $\langle r_{I,Q} \rangle$  at  $\mu = 0.1$  (limb observation) for the micro-turbulent limit and the angular power law PDF defined in Eq. (6.11). Line types:  $p = 0$  (solid), 5 (dotted), 10 (dashed), 100 (dot-dashed), 500 (dash-triple-dotted), and 1000 (long dashed). In this case  $\langle r_{U,V} \rangle = 0$ .

## 6.5 PDFs to represent the random vector magnetic fields

For a complete description of turbulent vector magnetic fields one needs a PDF that combines the strength and angular distributions. The strength distributions have been determined empirically (Stenflo & Holzreuter 2002, 2003a, 2003b) and by simulation (Stein & Nordlund 2006). Little is known from observations about the angular distribution. A very recent analysis of Hinode data suggests a predominance of very inclined hG fields in the internetwork (Orozco Suárez et al. 2007, Lites et al. 2007, 2008). From physical considerations one can argue that the angular distribution should be strongly field-strength dependent. For the strongest fields the distribution should be peaked around the vertical direction, as the strong fields would tend to have an intermittent flux tube morphology, and the powerful buoyancy forces would push the flux tubes to stand upright (like the stems of lotus flowers that are anchored to the bottom of the lake but float on top). The weakest fields on the other hand would be passively moved and bent by the turbulent fluid motions and get so tangled up that their distribution would be nearly isotropic. The transition between the isotropic and peaked distributions would probably be gradual (possibly around 50 G).

Based on this scenario we propose here PDFs, that are combinations of two PDFs, one for the angular distribution and one for the field strength distribution. For the angular part we use the power law distribution introduced in § 6.4, while for the field strength part we consider either a Voigt function (see § 6.2) or a stretched exponential (see § 6.3).

### 6.5.1 Stretched exponential \* Power law PDF

The functional form of the vector magnetic PDF when we combine a stretched exponential with a power law distribution may be written as

$$P(y, \mu_B, \varphi_B) d\mu_B d\varphi_B dy = P_{se}(y) P_{pl}(\mu_B) d\mu_B d\varphi_B dy, \quad (6.18)$$

where the power law is given by Eq. (6.11), but now used only for the range  $[0 \leq \mu_B \leq 1]$ . If we choose the symmetric stretched exponential introduced in Eq. (6.10) we can write

$$P(y, \mu_B, \varphi_B) d\mu_B d\varphi_B dy = \frac{k}{2\Gamma(1/k)} \frac{(p+1)}{2\pi} e^{-|y|^k} \mu_B^p dy d\mu_B d\varphi_B. \quad (6.19)$$

Here  $y$  varies in the range  $[-y_{\max}, +y_{\max}]$ ,  $\mu_B$  in the range  $[0, 1]$ , and  $\varphi_B$  in the range  $[0, 2\pi]$ . The angular and strength distributions are coupled by letting the power law index  $p$  depend on  $y$ . We have chosen  $p = |y|/y_t$  with  $y_t = B_t/\Delta_B$ , where  $B_t$  represents the field strength around which the transition between isotropic and peaked distribution occurs. We refer to  $y_t$  as the transition field strength. We note that  $y_t = \infty$  corresponds to fully isotropic distribution for all field strengths. Gauss-Legendre quadrature is used to perform the integration over  $y$ ,  $\vartheta_B$  and  $\varphi_B$ . For the  $y$  integration we use 300 quadrature points, and for the  $\vartheta_B$  and  $\varphi_B$  integrations we use 30 and 10 points, respectively.

The average Zeeman absorption matrix  $\langle \Phi \rangle$  is obtained by averaging  $\Phi(\mathbf{B})$  over the PDF defined in Eq. (6.19). The integration over  $\mu_B$  and  $\varphi_B$  can be performed analytically to obtain

$$\langle \varphi_I \rangle = \langle A_0 \rangle - \frac{1}{3} \langle A_2 \rangle (3\mu^2 - 1), \quad (6.20)$$

$$\langle \varphi_Q \rangle = \langle A_2 \rangle (1 - \mu^2). \quad (6.21)$$

After averaging,  $\langle \varphi_U \rangle = 0$  and  $\langle \varphi_V \rangle = 0$ . The mean coefficients in the above equations are given by

$$\langle A_0 \rangle = \frac{k}{2\Gamma(1/k)} \int_{-y_{\max}}^{+y_{\max}} A_0(y) e^{-|y|^k} dy, \quad (6.22)$$

$$\langle A_2 \rangle = \frac{k}{2\Gamma(1/k)} \int_{-y_{\max}}^{+y_{\max}} \frac{|y|}{|y| + 3y_t} A_2(y) e^{-|y|^k} dy, \quad (6.23)$$

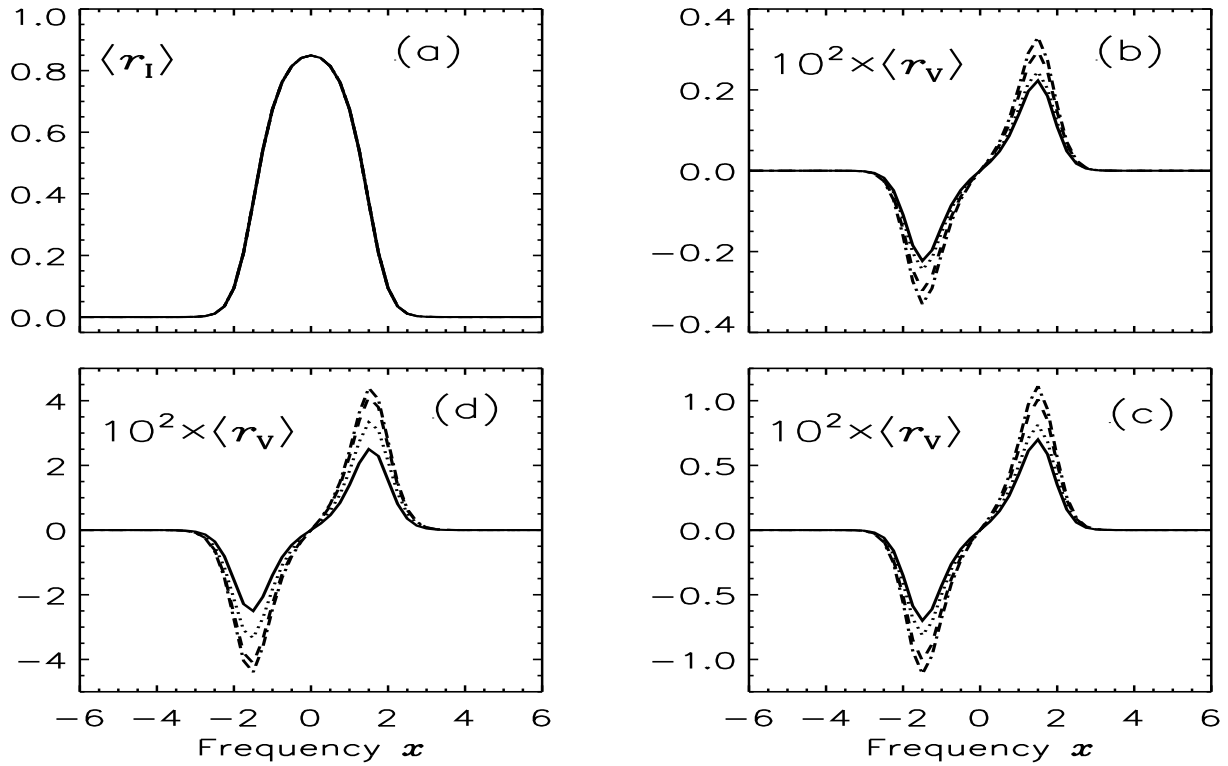


Figure 6.13:  $\langle r_{I,V} \rangle$  in the micro-turbulent limit computed using the composite PDF given in Eq. (6.18) with asymmetric stretched exponential PDFs shown in Fig. 6.8a. Disk center observation ( $\mu = 1$ ). Line types refer to  $y_t = \infty$  (solid),  $y_t = 50$  (dotted),  $y_t = 10$  (dashed), and  $y_t = 5$  (dash-dotted). Panels (a) and (b) correspond to a mean field  $y_0 = 1$ , panel (c) to  $y_0 = 3.2$  and panel (d) to  $y_0 = 11.6$

where  $A_0(y)$  and  $A_2(y)$  are given by Eq. (6.17) with  $x_q = x - q\gamma_B y$  and  $\gamma_B y = \Delta_Z B$  (see in Eq. (2.8) the definition of  $\Delta_Z$ ). Notice that  $\langle A_2 \rangle = 0$  and hence  $\langle \varphi_Q \rangle = 0$ , for  $y_t = \infty$ .

We can also use in Eq. (6.18) asymmetric stretched exponentials. In that case  $\langle \varphi_V \rangle$  is not zero nor is  $\langle r_V \rangle$ . We have calculated the mean profiles in the micro- and macro-turbulent limits for the distributions shown in Fig. 6.8a. The model parameters are  $(a, \beta, \gamma_B) = (0, 10, 0.0056)$ , LOS perpendicular to the atmosphere ( $\mu = 1$ ). For this LOS,  $\langle r_{Q,U} \rangle = 0$  due to symmetry. Figure 6.13 shows  $\langle r_I \rangle$  and  $\langle r_V \rangle$  in the micro-turbulent limit. As already observed (see Fig. 6.9),  $\langle r_I \rangle$  is insensitive to the asymmetry of  $P_{se}(y)$  because of the very weak value of  $\gamma_B$ . Figures 6.13b,c,d show that the magnitude of  $\langle r_V \rangle$  increases with the value of the mean field  $y_0$  as in Fig. 6.9. As  $y_t$  increases,  $\langle r_V \rangle$  profiles approach the isotropic case (solid lines in Figs. 6.13b,c,d). As the asymmetry increases we need larger and larger values of  $y_t$  to uniformly approach the isotropic limit.

The  $\langle r_V \rangle$  profiles for the macro-turbulent limit differ from micro-turbulent limit solutions for  $y_0 = 11.6$  only, and the differences remain small (as between the thin dashed and thick dot-dashed lines in Fig. 6.9).

We have calculated the dispersion  $\sigma_V$  around  $\langle r_V \rangle$  for several values of the mean field  $y_0$  and of the transition field strength  $y_t$ . For a given value of  $y_t$ , the dispersion increases in magnitude with  $y_0$  as shown in Fig. 6.10. For a given value of  $y_0$ , there is an increase in  $\sigma_V$  as the angular distribution becomes more and more anisotropic (decreasing  $y_t$ ). Actually the increase of  $\sigma_V$  follows that of  $\langle r_V \rangle$  (see Fig. 6.13d) and the ratio  $\sigma_V/|\langle r_V \rangle|$  remains essentially independent of  $y_t$ . We stress again that the amplitude of  $\sigma_V$  will decrease with decreasing sizes of the magnetic structures.

### 6.5.2 Voigt \* Power law PDF

Next we consider a composite PDF constructed with a Voigt PDF instead of an stretched exponential. We can use symmetric or asymmetric PDFs. With the symmetric PDF defined in Eq. (6.1), we have

$$P(y, \mu_B, \varphi_B) dy d\mu_B d\varphi_B = \frac{(p+1)}{2\pi} P_V(y, a_B) \mu_B^p dy d\mu_B d\varphi_B. \quad (6.24)$$

The power law index is chosen as  $p = |y|/y_t$  as in § 6.5.1. The range of variations of  $y$ ,  $\mu_B$ , and  $\varphi_B$  and the numerical integration scheme are also the same as in § 6.5.1. The mean coefficients are also given by Eqs. (6.20) – (6.23), but with  $[k/2\Gamma(1/k)]e^{-|y|^k}$  replaced by  $P_V(y, a_B)$ .

We have calculated the mean residual Stokes parameters for the asymmetric PDF with mean field  $y_0 = 4.5$  (dashed line in Fig. 6.3a) for the micro- and macro-turbulent limits. The model parameters are  $(a, \beta, \gamma_B) = (0, 10, 0.0056)$ , the LOS nearly parallel to the limb ( $\mu = 0.1$ ). Figure 6.14 shows the solutions for micro-turbulent limit. The different line types correspond to different values of the transition field strength  $y_t$ . As discussed earlier  $\langle r_I \rangle$  is essentially insensitive to the asymmetry of the Voigt PDF and to the variation of  $y_t$ . When  $y_t \rightarrow \infty$ , the mean coefficient  $\langle \varphi_Q \rangle \rightarrow 0$  since  $\langle A_2 \rangle \rightarrow 0$  (see Eq. (6.23)), and hence  $\langle r_Q \rangle \rightarrow 0$ . As  $y_t$  decreases, the PDF becomes more and more peaked and hence  $\langle r_Q \rangle$  as well as  $\langle r_V \rangle$  increase in magnitude. For symmetry reason, as in § 6.5.1,  $\langle \varphi_U \rangle = 0$ . However some amount of  $\langle r_U \rangle$  is created due to the presence of magneto-optical effects. Therefore  $\langle r_U \rangle$  is very small with a behavior similar to  $\langle r_Q \rangle$ . The differences between the micro- and macro-turbulent limit solutions are similar to the one noted in Fig. 6.2 for  $\langle r_{I,Q,U} \rangle$  and in Fig. 6.9 for  $\langle r_V \rangle$ .

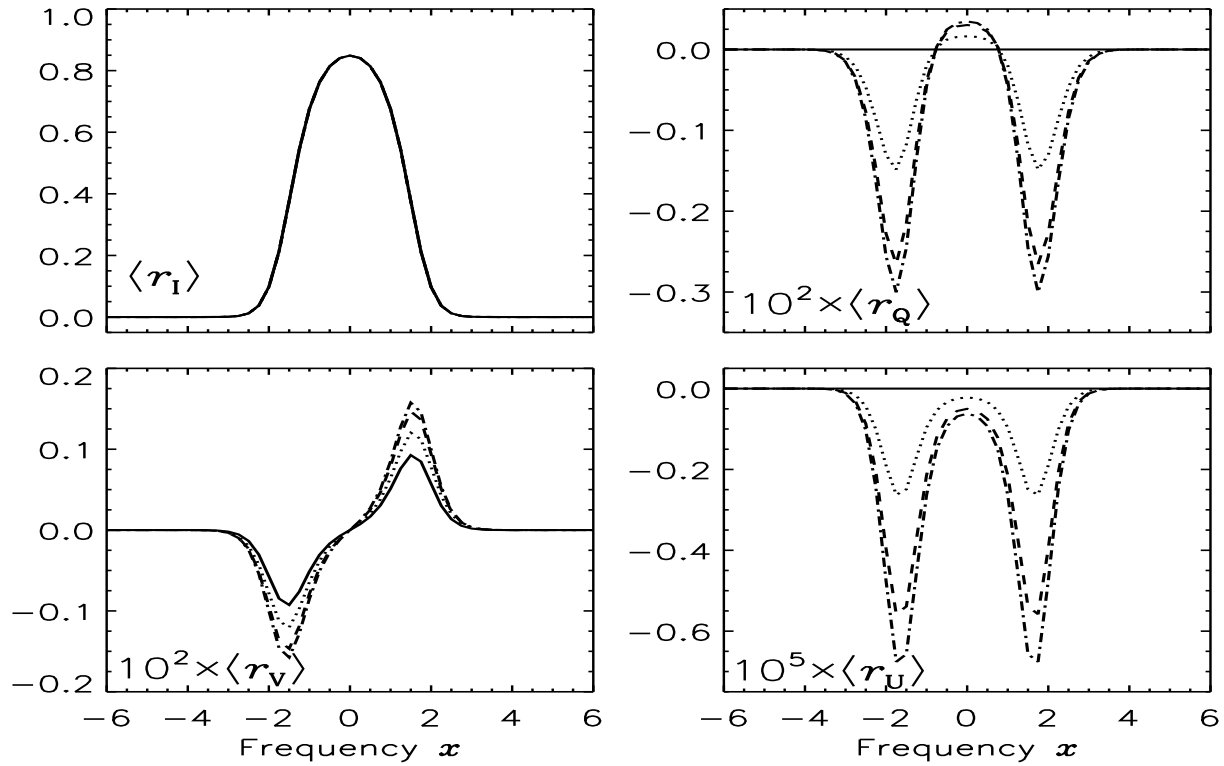


Figure 6.14:  $\langle r_{I,Q,U,V} \rangle$  micro-turbulent profiles for limb observation ( $\mu = 0.1$ ). Composite PDF with asymmetric Voigt function corresponding to a mean field  $y_0 = 4.5$  (dashed line of Fig. 6.3). The line types correspond to  $y_t = \infty$  (solid),  $y_t = 50$  (dotted),  $y_t = 10$  (dashed), and  $y_t = 5$  (dash-dotted).

## 6.6 Turbulent line formation for anomalous Zeeman splitting

For a general Zeeman pattern, the elements of the absorption matrix have contributions from each individual Zeeman component. The relative strengths of these various components is thus needed to calculate the absorption matrix. Under local thermodynamic equilibrium (LTE) the line strengths are proportional to the matrix elements  $|\langle l s j m | \mathbf{D} | l' s' j' m' \rangle|^2$ , where  $\mathbf{D}$  is the dipole operator, and are given by the quantities (see Stenflo 1994, p. 107-111)

$$S_q(M_l, M_u) \equiv \frac{\tilde{S}_q(M_l, M_u)}{\sum_{M_l, M_u} \tilde{S}_q(M_l, M_u)}, \quad q = 0, \pm 1, \quad (6.25)$$

where  $M_{l,u}$  are the magnetic quantum numbers of the lower and upper levels respectively, and  $q = M_l - M_u$ . The unnormalized strengths  $\tilde{S}_q(M_l, M_u)$  are listed in Table 6.1 of Stenflo (1994).

The Zeeman splitting of the individual components can be written in compact form as

$$x_q = x - [qg_u - M_l(g_u - g_l)]\Delta'_Z B,$$

where  $g_{u,l}$  are the Landé factors of the upper and lower level respectively, and  $\Delta'_Z = e/(4\pi m\Delta\nu_D)$ . The elements of the Zeeman absorption matrix formally remain the same, but the normalized profiles  $\varphi_q$  and  $f_q$  are now given by (see also § 2.6)

$$\bar{\varphi}_q = \sum_{M_u} S_q(M_l, M_u) H(x_q, a), \quad \text{and} \quad \bar{f}_q = \sum_{M_u} S_q(M_l, M_u) F(x_q, a), \quad (6.26)$$

respectively, subject to the constraint  $M_l = M_u + q$ . The equations required for computing transition strengths for Zeeman multiplets and their absorption coefficients are also presented in del Toro Iniesta (2003, p. 136-145). The shapes of the Zeeman absorption matrix elements for the multiplet case are also shown in this reference.

Equations (6.26) are valid for a deterministic magnetic field. To use the same equations for a random field, we just need to replace  $\Delta'_Z B$  by  $\gamma'_B y$ , where  $y$  is defined in Eq. (6.2), and  $\gamma'_B = \Delta'_Z \Delta_B$ .

Figure 6.15 shows  $\langle r_{I,Q,U,V} \rangle$  for a  ${}^4P_{1/2} - {}^4F_{3/2}$  transition. For this particular transition there are two  $\pi$  components and four  $\sigma$  components. Keeping the same kind of spectral line as in the preceding sections (wavelength 5000 Å, Doppler width 1.5 km s<sup>-1</sup>), we find  $\gamma'_B = \gamma_B/2 = 0.0028$ . Our model parameters are now:  $(a, \beta, \gamma'_B) = (0, 10, 0.0028)$ . For the magnetic field, we assume a fixed orientation  $(\theta, \phi) = (60^\circ, 30^\circ)$  and random strength. We use an asymmetric Voigt PDF and an asymmetric stretched exponential. They yield mean profiles  $\langle r_{Q,U,V} \rangle$  with similar shapes. As always  $\langle r_I \rangle$  remains insensitive to the choice of the PDF.  $\langle r_{Q,U} \rangle$  are larger for the asymmetric Voigt PDF (solid lines), than for the asymmetric stretched exponential (dotted lines) for nearly the same values of the mean magnetic fields (3.4 and 3.2, respectively). This is because  $\langle r_{Q,U} \rangle$  are sensitive to the type of PDF used, as already shown in Fig. 6.7 (for symmetric PDFs).  $\langle r_V \rangle$  is generated purely by the asymmetry in the PDF, and hence it is more sensitive to the value of the mean field  $y_0$  than to the exact shape of the PDF. For this figure we have chosen nearly the same mean value  $y_0$  for both PDFs, with the consequence that the solid and dotted curves for  $\langle r_V \rangle$  do not differ.

We also have calculated mean Stokes profiles for macro-turbulent limit. The only difference appears to be that the micro-turbulent limit produce  $\langle r_{Q,U} \rangle$  of slightly larger magnitude than the macro-turbulent ones.

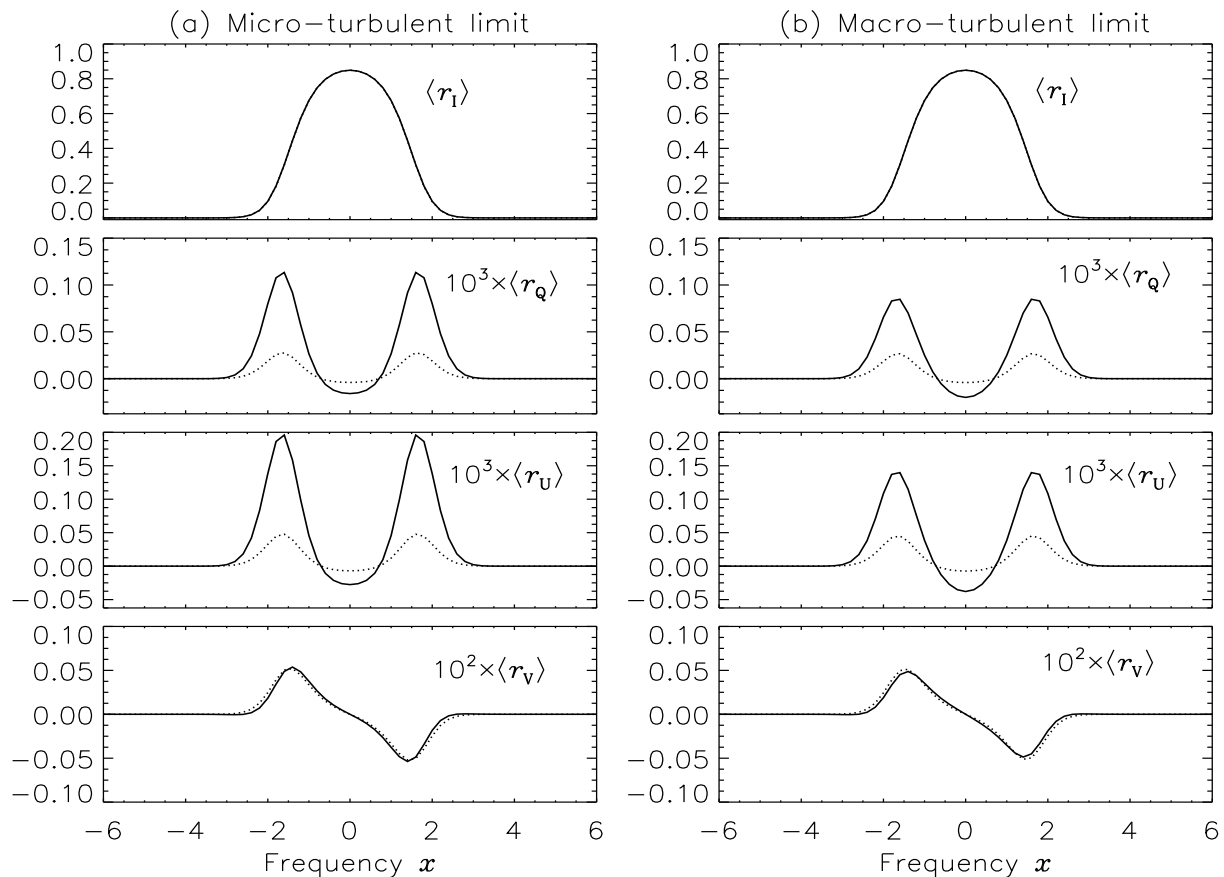


Figure 6.15: Effect of turbulence on a Zeeman multiplet. Two types of PDFs are used. Solid lines: asymmetric Voigt with mean field  $y_0 = 3.4$  presented as solid line in Fig. 6.3a. Dotted lines: asymmetric stretched exponential with mean field  $y_0 = 3.2$  presented as dotted line in Fig. 6.8a.

## 6.7 Concluding remarks

We have presented mean Stokes profiles formed in media with spatially unresolved magnetic structures. We have considered the cases of micro- and macro-turbulent limits which involve the computation of mean absorption matrices or mean emergent Stokes profiles, respectively. We have also calculated the dispersion around the mean Stokes profiles in the macro-turbulent limit (it is zero in the micro-turbulent limit). The dispersion provides an upper bound for the order of magnitude of the fluctuations of the Stokes profiles around their mean values. To perform such averaging we use a probability distribution function (PDF) that describes the fluctuations of the ambient field. A Gaussian PDF with isotropic or anisotropic fluctuations has been considered in detail in Chapter 2. Here we have



experimented with other types of PDFs and show the difference between the emergent Stokes profiles computed from them. We consider very weak fluctuations of the magnetic field: The Zeeman shift from the magnetic field rms fluctuations in Doppler width units, denoted here  $\gamma_B$ , equals 0.0056. As a consequence the  $\langle r_I \rangle$  profiles are insensitive to the shape of the magnetic field PDF. In contrast, the other mean Stokes profiles and the dispersion are quite sensitive to the PDF shapes. For stronger fluctuations (say  $\gamma_B = 1$ ),  $\langle r_I \rangle$  would also get significantly modified.

In § 6.2 we consider a Voigt type PDF for the magnetic field strength derived from observations by Stenflo & Holzreuter (2002, 2003a, 2003b). The Voigt PDF is characterized by two parameters, the magnetic width  $\Delta_B$  and the magnetic damping parameter  $a_B$ . For  $a_B = 0$ , we recover the results of the 1D Gaussian distribution considered in Chapter 2. The effect of a non-zero  $a_B$  on the average Stokes profiles  $\langle r_{Q,U} \rangle$  is to enhance core and wing polarization. We have introduced asymmetric Voigt PDFs which provide a non-zero net magnetic flux, thereby generating an  $\langle r_V \rangle$  profile. They are constructed by taking different magnetic damping parameters for the opposite polarities of the random field.

Stretched exponentials for the magnetic field strength derived from magneto-convection simulations by Stein & Nordlund (2006) are considered in § 6.3. These PDFs are characterized by a single parameter, the stretching parameter  $k$ , which takes values between 0 and 1. A decrease of the stretching parameter  $k$  enhances the contribution from strong fields and thus induces an increase in the values of  $\langle r_{Q,U} \rangle$  (see Fig. 6.7). In this case also we construct asymmetric PDFs by using different values of the stretching parameter  $k$  for the opposite polarities of the magnetic field.

In § 6.4 we have examined an angular power law distribution proposed by Stenflo (1987). The only parameter for this PDF is the power law index  $p$ . For  $p = 0$ , the distribution is isotropic. As  $p$  increases the random field becomes more and more oriented in both the forward and backward directions. Because of the axial symmetry,  $\langle r_U \rangle = 0$  for this PDF.

For a complete description of the turbulent vector magnetic field one needs PDFs which describe both the angular and the strength distribution of the magnetic field vector. In § 6.5 we have constructed empirical PDFs of this kind by combining a power law for the angular distribution with a Voigt function or stretched exponential for the field strength. The PDFs for the angular and strength distributions are coupled by letting the power law index explicitly depend on the field strength. We have introduced a cut-off in the magnetic field strength below which the random magnetic field is essentially isotropic and above which it is dominantly vertical. Construction and application of these composite PDFs

represent the main result of the present chapter. They could be used to represent the conditions prevailing in the solar photosphere. Finally, in § 6.6, we show how to generalize the averaging technique to the case of anomalous Zeeman splitting patterns.

This chapter highlights the need to consider fluctuations in the field orientation besides the field strength. We have experimented with a few composite PDF of this type. However, we would like observations to provide us with empirical PDFs not only for the field strength, but also for the angular distribution, but unfortunately such empirical angular PDFs are not yet available.

We compute the mean Stokes profiles for a given line-of-sight using a PDF that is independent of depth. In reality the mean Stokes profiles are the result of space and/or time averages. Further, we have not considered realistic temperature and density stratifications, and we also ignore the velocity turbulence (except for the micro-turbulent line broadening included in the Doppler width). For these reasons our mean Stokes profiles are not yet suited for model fitting of observed Stokes profiles.

Another aspect that we need to keep in mind is the relation between the complete PDF used in our pure theoretical profiles, and the sampling that occurs in an actual observation. In our computations we use ‘complete’ PDFs which cover the entire range in field strength and orientation. In contrast, high spatial resolution observations may only sample different fractions of a PDF in terms of strength and orientation because magnetic structures have finite sizes. A complete PDF would be obtained (asymptotically) if we add samples of many resolution elements, or if we deliberately perform a low spatial resolution measurement. Thus the observed high spatial resolution Stokes profiles represent fluctuations about a mean profile. These fluctuations will in general be of the order of the dispersion around the mean profile. The dispersion is zero in the limit of infinitely thin magnetic structures and in this limit the sampling is necessarily complete.

Stenflo & Holzreuter (2003a) suggest that the magnetic pattern is fractal with a high degree of self-similarity over several orders of magnitude. If this coexistence of weak and strong fields continues far below the current spatial resolution limit, then the PDF sampling will be more complete than in the non-fractal case, and the sampling of the PDF may be substantial even for very high spatial resolution observations.

## **Part-II**

**Polarized line formation in scattering  
media : Theory and numerical  
methods**



## Chapter 7

# Classical theory of Hanle-Zeeman redistribution matrix<sup>1</sup>

### 7.1 Introduction

The discovery of the extremely rich structuring of the Second Solar Spectrum (Stenflo & Keller 1996, 1997) opened the window to a new, previously unexplored territory with great diagnostic potential. This linearly polarized spectrum, which is formed by coherent scattering processes, has been mapped with high spectral resolution from the UV at 3160 Å to the red at 6995 Å (Gandorfer 2000, 2002, 2005), providing us with a wealth of new information both about the Sun and about the physics of spectral line formation in magnetized stellar atmospheres. The Second Solar Spectrum is modified by magnetic fields through the Hanle and Zeeman effects. The Hanle effect represents the magnetic modification of the scattering polarization (c.f. § 1.3.3). It is a coherency phenomenon and responds to weak fields, when the Zeeman splitting is comparable to the small damping width of line transitions. The usual Zeeman effect polarization (c.f. § 1.3.1), on the other hand, is produced by stronger fields, when the Zeeman splitting gets comparable to the much larger Doppler width of the line. A further difference between the two effects is that the Hanle effect is sensitive to spatially unresolved turbulent fields with zero net magnetic flux, while the Zeeman effect is blind to such fields (due to its different symmetry properties). The two effects therefore nicely complement each other (see Stenflo 1994).

Many of the strongest and most conspicuous lines in the Second Solar Spectrum are strong lines that are formed rather high, often in the chromosphere above the tempera-

---

<sup>1</sup>This chapter is based on the publication: Sampoorana, M., Nagendra, K. N., & Stenflo, J. O. 2007a, ApJ, 663, 625-642

ture minimum. From standard, unpolarized and non-magnetic line-formation theory such lines are known to be formed under conditions that are very far from local thermodynamic equilibrium. They are characterized by broad damping wings surrounding a Doppler core. Doppler shifts in combination with collisions cause photons that are absorbed at a given frequency to be redistributed in frequency across the line profile in a complex way during the scattering process. Two idealized, limiting cases to describe this redistribution are “frequency coherence” and “complete redistribution” (CRD), but the general theory that properly combines these two limiting cases goes under the name “partial frequency redistribution” (PRD). Strong lines can only be properly modeled when PRD is taken into account.

The complexity of the redistribution problem escalates when we include polarization and magnetic fields, since the previously unpolarized scalar ‘redistribution function’ becomes a  $4 \times 4$  ‘redistribution matrix’ that describes how the Stokes 4-vector is redistributed in both frequency and angle. In the absence of magnetic fields the frequency redistribution factorizes out from the polarization properties, which can be described by a frequency-independent  $4 \times 4$  ‘phase matrix’. Such non-magnetic but polarized PRD has been applied to describe the polarized line profile of Ca II K and Ca I 4227 Å (Saliba 1985, Faurobert-Scholl 1992) and later to model other strong lines in the Second Solar Spectrum (Fluri et al. 2003a, Holzreuter et al. 2005, 2006, Fluri et al. 2006, Holzreuter & Stenflo 2007a, 2007b), like Na I D<sub>2</sub> 5890 Å, and other important lines such as Sr II 4078 Å, and Cr I 3594 Å.

To exploit these strong lines for magnetic-field diagnostics we need however to go one step further, namely to develop the theory for PRD in the presence of magnetic fields of ‘arbitrary strengths’. This is the aim of the present chapter. In the presence of magnetic fields we can no longer factorize the polarization and frequency redistribution problem, instead they get deeply intertwined. This naturally increases the complexity of the problem, but this complexity also has a rich structure with many symmetries.

The general concepts of theory of PRD were first developed for the scalar problem of non-polarized scattering (see Mihalas 1978). The theory of PRD from a classical perspective was originally introduced by Zanstra (1941a, 1941b), who addressed the issue of collisions on non-magnetic frequency redistribution in resonance lines. Stenflo (1994, 1996, 1998) has developed a modern approach to the classical oscillator theory and applied it to atomic line transitions. His method can handle light scattering on atomic energy levels in the presence of arbitrary magnetic fields and various kinds of collisions (treated approximately). This classical framework was further extended by Bommier & Stenflo (1999,

hereafter called BS99) to handle PRD effects in the presence of arbitrary magnetic fields and collisions. Recently, Lin et al. (1998) have proposed a classical theory of the Hanle effect (similar to that of Stenflo 1994), to explain the polarization of He I 10830 Å line observed in a solar filament. This classical theory has been extended by Lin & Casini (2000) to derive the polarization properties of the coronal forbidden emission lines, which arise from magnetic dipole (M1) transitions.

The quantum mechanical framework for the problem of atomic line scattering was developed by Weisskopf (1933), Wooley (1938), Henyey (1940), Hummer (1962), Lamb & ter Haar (1971), House (1971), Omont et al. (1972, 1973), Heinzel (1981), Cooper et al. (1982), Landi Degl’Innocenti (1983a, 1984), Domke & Hubeny (1988), Streater et al. (1988), Landi Degl’Innocenti et al. (1997), Bommier (1997a, 1997b, 1999, 2003), Casini & Manso Sainz (2005). See the reviews by Hubeny (1985), Nagendra (2003a) for a historical development of the PRD formulations, and Trujillo Bueno (2003a), Uitenbroek (2003) for applications in Astrophysical line formation theory, and Nagendra et al. (2002, 2003, and papers cited therein), and Fluri et al. (2003b) for powerful numerical methods of solving the relevant line transfer problem of varying complexity.

The theory developed in BS99 solved the time-dependent oscillator equation in combination with a classical model for collisions (see Stenflo 1994, ch. 10). This gives self-consistent and non-perturbative expressions for the polarized PRD redistribution matrix, in the presence of magnetic fields of arbitrary strength and direction in the atomic frame. The explicit form of the redistribution matrix in the laboratory frame (LF) was not given. BS99 hints at the way to arrive at such expressions, which are needed, when the generalized Hanle-Zeeman redistribution matrix is to be used in a radiative line transfer code.

When we here use the term “Hanle-Zeeman”, we mean the full field strength regime, from zero field to completely split lines. This general case contains many sub-regimes, which only become distinct from each other if one makes idealizations, to deal with each separately. We do not do any such idealizations here, so in this general case, the sub-regimes partially overlap or gradually flow into each other. The Hanle effect has three sub-regimes: (i) Very weak fields, when the field dependence can be disregarded, and the scattering behaves like the non-magnetic case. (ii) Weak to intermediate fields, when the scattering polarization depends on both the strength and direction of the field. This is what is most often referred to as the “Hanle regime”. (iii) Saturated Hanle regime, when the fields are so strong that the scattering polarization becomes insensitive to the field strength, but still depends on the field direction. This saturated Hanle regime is what applies to the

coronal forbidden lines. The saturation occurs when the Zeeman splitting becomes much larger than the damping width. Even in this saturated regime the Zeeman splitting can remain much smaller than the Doppler width, as it does in the case of the coronal forbidden lines. When the Zeeman splitting is no longer too small in comparison with the Doppler width, then ordinary Zeeman effect polarization starts to show up. The field strengths for which this occurs depend on the relative prominence of scattering polarization and the polarimetric sensitivity of the instrument. While the Hanle and Zeeman effects show relative dominance in different regimes, they fundamentally overlap over the whole field strength regime.

In this chapter we derive an explicit form of the Hanle-Zeeman redistribution matrix in the LF, for the special case of a normal Zeeman triplet, in a coordinate system in which the polar  $Z$ -axis is oriented along the magnetic field (see Fig. 7.1). This choice of geometry does not limit the applicability of the theory, since the redistribution matrix for an arbitrary field direction can be obtained by first choosing a system with the  $Z$ -axis along the magnetic field, and then applying Mueller rotation matrices to obtain the redistribution matrix for any other system with an arbitrary orientation of its  $Z$ -axis (see Appendix K).

In § 7.2, starting from the atomic frame expression for the ensemble averaged coherency matrix (c.f. § 1.2.2) given in BS99, we derive the corresponding expression in the LF. In § 7.3 we present the analytical form of the Hanle-Zeeman redistribution matrix. The magnetic redistribution basis functions that we encounter in § 7.2 (see also Bommier 1997b) are numerically studied in § 7.4, because the total scattering probability essentially depends on their angular and frequency dependence. The scattered Stokes vector can be interpreted using the properties of these basis functions. The extension of the classical theory presented in §§ 7.2 and 7.3, to treat atomic and molecular scattering for any combination of quantum numbers is discussed in § 7.5. Concluding remarks are given in § 7.6.

## 7.2 Coherency matrix

The time dependent solution  $r_q(t, \xi')$ , of the oscillator equation (c.f. Eq. (1.16)), which describes the motion of a particle with charge  $-e$  and mass  $m$  in a central Coulomb potential, subject to an external magnetic field  $\mathbf{B}$  and an external oscillating electric field  $\mathbf{E}'$ , is given by (see Eqs. (16) - (18) of BS99)

$$r_q(t, \xi') = r_{q, \text{stat}}(t, \xi') + Cr_{q, \text{trans}}(t, \xi') e^{i\delta}, \quad (7.1)$$



where

$$r_{q, \text{stat}}(t, \xi') = \frac{1}{\pi} \frac{e^{-2\pi i \xi' t}}{\xi' - (\nu_0 - qg\nu_L - i\gamma/4\pi)}, \quad (7.2)$$

represents the stationary solution, and

$$r_{q, \text{trans}}(t, \xi') = \frac{1}{\pi} \frac{e^{-2\pi i(\nu_0 - qg\nu_L - i\gamma/4\pi)t}}{\xi' - (\nu_0 - qg\nu_L - i\gamma/4\pi)}, \quad (7.3)$$

represents the transitory solution for a free, damped oscillator.  $C$  and  $\delta$  represent the amplitude and phase of the oscillator.  $\xi'$  is the frequency of the incident radiation in the atomic frame.  $\nu_0$ ,  $\nu_L$  are the frame independent line center frequency and Larmor frequency, respectively.  $g$  is the Landé factor (which is unity in classical theory, however we retain it for the sake of comparison with quantum theory).

The spectral properties of the scattered radiation are obtained by taking the Fourier transform of  $r_q(t, \xi')$ , defined as

$$\tilde{r}_q(\xi, \xi') = \int_{-\infty}^{+\infty} r_q(t, \xi') e^{2\pi i \xi t} dt, \quad (7.4)$$

where  $\xi$  is the frequency of the scattered radiation in the atomic frame. The ensemble average of bilinear products, also called the coherency matrix, is denoted by  $\langle \tilde{r}_q \tilde{r}_{q'}^* \rangle$  and contains all the frequency information, including the PRD effects that correlate the incident and scattered frequencies with each other. The ensemble average is performed to include the random phase shifts that arise due to random phase destroying collisions.

### 7.2.1 Redistribution in the atomic frame

The expression for the ensemble averaged coherency matrix  $\langle \tilde{r}_q \tilde{r}_{q'}^* \rangle$  is given in BS99, in the atomic frame (see Eqs. (27), (35) and (39) of BS99) as

$$\begin{aligned} \langle \tilde{r}_q \tilde{r}_{q'}^* \rangle &\sim A \cos \beta_{q-q'} e^{i\beta_{q-q'}} \Phi_{qq'}^{\gamma+\gamma_c}(\xi') \delta(\xi - \xi') + \mathcal{B} \cos \beta_{q-q'} \cos \alpha_{q-q'} e^{i(\beta_{q-q'} + \alpha_{q-q'})} \\ &\times \Phi_{qq'}^{\gamma+\gamma_c}(\xi') \Phi_{qq'}^{\gamma+\gamma_c}(\xi), \end{aligned} \quad (7.5)$$

where  $\beta_{q-q'}$  and  $\alpha_{q-q'}$  are Hanle angles defined as

$$\tan \beta_{q-q'} = \frac{(q - q')2\pi g\nu_L}{\gamma + \gamma_c}, \quad (7.6)$$

$$\tan \alpha_{q-q'} = \frac{(q - q')2\pi g\nu_L}{\gamma + \gamma_c/2}, \quad (7.7)$$

with  $\gamma$  being a sum of radiative and inelastic collisional damping constants and  $\gamma_c$  the elastic collisional damping rate.  $q, q'$  take values  $0, \pm 1$ . The effect of Hanle angle  $\beta_{q-q'}$  vanishes in the line core due to cancellation between contributions from stationary and transitory solutions. Thereby only the Hanle angle  $\alpha_{q-q'}$  remains operative in the line core, and causes depolarization via the  $\cos \alpha_{q-q'}$  factor, and rotation of the plane of polarization through the  $e^{i\alpha_{q-q'}}$  factor. In the line wings the Hanle effect from both  $\alpha_{q-q'}$  and  $\beta_{q-q'}$  vanishes as shown in Stenflo (1998).

The generalized profile function is defined as

$$\Phi_{qq'}^{\gamma+\gamma_c}(\xi) = \frac{1}{2} [\Phi_{\gamma+\gamma_c}(\nu_q - \xi) + \Phi_{\gamma+\gamma_c}^*(\nu_{q'} - \xi)], \quad (7.8)$$

with the profile function given by

$$\Phi_{\gamma+\gamma_c}(\nu_q - \xi) = \frac{1/\pi i}{\nu_0 - qq\nu_L - \xi - i(\gamma + \gamma_c)/4\pi}, \quad (7.9)$$

where  $\nu_q = \nu_0 - qq\nu_L$ . We can rewrite Eq. (7.9) as

$$\Phi_{\gamma+\gamma_c}(\nu_q - \xi) = \frac{1}{\pi} \frac{\delta_w - i(\nu_0 - qq\nu_L - \xi)}{\delta_w^2 + (\nu_0 - qq\nu_L - \xi)^2}, \quad (7.10)$$

where  $\delta_w = (\gamma + \gamma_c)/4\pi$ .

$A$  and  $\mathcal{B}$  in Eq. (7.5) are branching ratios between stationary and transitory solutions, determined by probability arguments and normalization. The stationary solution is the source of frequency-coherent scattering. The branching ratio  $A$  for frequency-coherent process is (see Eq. (40) of BS99)

$$A = \frac{\Gamma_R}{\Gamma_R + \Gamma_I + \Gamma_E}, \quad (7.11)$$

where  $\Gamma_R$  is radiative rate, while  $\Gamma_I$  and  $\Gamma_E$  are inelastic and elastic collision rates, respectively.

The transitory solution is the source of CRD. Thus branching ratio  $\mathcal{B}$  represents the fraction of the scattering processes for which the atom is subject to elastic collisions that destroy the frequency-coherence but not the atomic polarization (the  $2K$ -multipole). Hence  $\mathcal{B}$  is given by (see Eq. (41) of BS99)

$$\mathcal{B} = \frac{\Gamma_E - D^{(K)}}{\Gamma_R + \Gamma_I + \Gamma_E} \frac{\Gamma_R}{\Gamma_R + \Gamma_I + D^{(K)}}, \quad (7.12)$$

where  $D^{(K)}$  is the rate of destruction of the  $2K$ -multipole, with  $K = 0, 1, 2$  (note that  $D^{(0)} = 0$ ). We note that  $\Gamma_R + \Gamma_I = \gamma$ ,  $\Gamma_E = \gamma_c$ , and  $D^{(K)} = \gamma_c/2$  in the classical theory (see Eqs. (31)-(33) of BS99).

Substituting Eq. (7.8) into Eq. (7.5), we obtain

$$\begin{aligned}
\langle \tilde{r}_q \tilde{r}_{q'}^* \rangle \sim & A \cos \beta_{q-q'} e^{i\beta_{q-q'}} \frac{1}{2} [\Phi'_{\gamma+\gamma_c}(\nu_q - \xi') \delta(\xi - \xi') + \Phi'^*_{\gamma+\gamma_c}(\nu_{q'} - \xi') \delta(\xi - \xi')] \\
& + \mathcal{B} \cos \beta_{q-q'} \cos \alpha_{q-q'} e^{i(\beta_{q-q'} + \alpha_{q-q'})} \frac{1}{4} [\Phi'_{\gamma+\gamma_c}(\nu_q - \xi') \Phi_{\gamma+\gamma_c}(\nu_q - \xi) \\
& + \Phi'^*_{\gamma+\gamma_c}(\nu_{q'} - \xi') \Phi_{\gamma+\gamma_c}(\nu_q - \xi) + \Phi'_{\gamma+\gamma_c}(\nu_q - \xi') \Phi'^*_{\gamma+\gamma_c}(\nu_{q'} - \xi) \\
& + \Phi'^*_{\gamma+\gamma_c}(\nu_{q'} - \xi') \Phi'^*_{\gamma+\gamma_c}(\nu_{q'} - \xi)]. \tag{7.13}
\end{aligned}$$

Clearly, terms in the square brackets represent the well known type II (in first square bracket) and III (in second square bracket) atomic frame redistribution functions of Hummer (1962). However, the essential difference is that we now have magnetically shifted frequencies (for both incoming and outgoing photons), and the profile functions are complex Lorentzian's. The complex profile functions automatically take into account the magneto-optical effects (imaginary part) and the absorption or emission effects (real part). The radiative transfer equation is always formulated in the LF. Therefore the redistribution matrices that appear in the scattering integral should refer to the LF. Hence there is a need to transform them from the atomic frame to the LF.

### 7.2.2 Redistribution in the laboratory frame: Doppler effect

The effect of the Doppler shifts (introduced by the motion of scattering atoms relative to the fixed LF) is taken into account by convolving the atomic frame redistribution function with a velocity distribution of the scattering atoms, which is conventionally assumed to be Maxwellian (see Mihalas 1978, Eq. (13.13), p. 417). Thus when going from the atomic frame to the LF, we first have to replace  $\xi'$  and  $\xi$  by their Doppler shifted values, related through

$$\begin{aligned}
\xi &= \nu - \nu_0(\mathbf{v} \cdot \mathbf{n})/c, \\
\xi' &= \nu' - \nu_0(\mathbf{v} \cdot \mathbf{n}')/c, \tag{7.14}
\end{aligned}$$

where  $\mathbf{v}$  is the velocity vector, and  $c$  is the speed of light.  $\nu$  and  $\nu'$  are outgoing and incoming frequencies relative to the LF, and  $\mathbf{n}$  and  $\mathbf{n}'$  are the directions of the outgoing and incoming radiation. We introduce the dimensionless quantities

$$x = \frac{\nu_0 - \nu}{\Delta\nu_D}; \quad v_q = x - \frac{qg\nu_L}{\Delta\nu_D}; \quad a = \frac{\delta_w}{\Delta\nu_D}, \tag{7.15}$$

which are respectively, the emission frequency, magnetic shift, and damping parameter.  $\Delta\nu_D$  is the Doppler width.

From Eq. (7.13) it is clear that each term in the square bracket can be independently transformed to the LF. Following Mihalas (1978, ch. 13), one can easily obtain (after some algebra) the ensemble averaged coherency matrix in the LF as

$$\begin{aligned} \langle \tilde{r}_q \tilde{r}_{q'}^* \rangle \sim & A \cos \beta_{q-q'} e^{i\beta_{q-q'}} \frac{1}{2} [R_{\text{II}}^q(x, \mathbf{n}; x', \mathbf{n}'; B) + R_{\text{II}}^{q'*}(x, \mathbf{n}; x', \mathbf{n}'; B)] + \mathcal{B} \cos \beta_{q-q'} \\ & \times \cos \alpha_{q-q'} e^{i(\beta_{q-q'} + \alpha_{q-q'})} \frac{1}{4} [R_{\text{III}}^{qq'}(x, \mathbf{n}; x', \mathbf{n}'; B) + R_{\text{III}}^{q'*q}(x, \mathbf{n}; x', \mathbf{n}'; B) \\ & + R_{\text{III}}^{qq'*}(x, \mathbf{n}; x', \mathbf{n}'; B) + R_{\text{III}}^{q'q'*}(x, \mathbf{n}; x', \mathbf{n}'; B)], \end{aligned} \quad (7.16)$$

where

$$R_{\text{II}}^q(x, \mathbf{n}; x', \mathbf{n}'; B) = \frac{1}{\pi \sin \Theta} \exp \left\{ - \left[ \frac{x - x'}{2 \sin(\Theta/2)} \right]^2 \right\} \mathcal{H} \left( \frac{v_q + v_{q'}}{2 \cos(\Theta/2)}, \frac{a}{\cos(\Theta/2)} \right), \quad (7.17)$$

and

$$R_{\text{III}}^{qq'}(x, \mathbf{n}; x', \mathbf{n}'; B) = \frac{1}{\pi^2 \sin \Theta} \int_{-\infty}^{+\infty} du e^{-u^2} \left[ \frac{a - i(v_{q'} - u)}{a^2 + (v_{q'} - u)^2} \right] \mathcal{H} \left( \frac{v_{q'} - u \cos \Theta}{\sin \Theta}, \frac{a}{\sin \Theta} \right). \quad (7.18)$$

The symbol  $R_{\text{III}}^{q'*q}(x, \mathbf{n}; x', \mathbf{n}'; B)$  stands for complex conjugation only on the incoming profile (i.e., on the complex Lorentzian in Eq. (7.18) - the term in the square bracket), while the symbol  $R_{\text{III}}^{q'q'*}(x, \mathbf{n}; x', \mathbf{n}'; B)$  stands for complex conjugation on both the incoming and outgoing profiles<sup>2</sup>. In Eqs. (7.17) and (7.18),  $\Theta$  is the scattering angle (the angle between incident and scattered ray - see Fig. 7.1), and we have introduced the complex function

$$\mathcal{H}(x, a) = H(x, a) - iF(x, a), \quad (7.19)$$

with the Voigt and Faraday-Voigt functions defined as<sup>3</sup>

$$\begin{aligned} H(x, a) &= \frac{a}{\pi} \int_{-\infty}^{+\infty} \frac{e^{-y^2} dy}{(x - y)^2 + a^2}, \\ F(x, a) &= \frac{1}{\pi} \int_{-\infty}^{+\infty} \frac{(x - y)e^{-y^2} dy}{(x - y)^2 + a^2}. \end{aligned} \quad (7.20)$$

<sup>2</sup>Note: a prime on  $v$  means incoming radiation, while the absence of a prime on  $v$  means outgoing radiation. This convention does not hold for indices  $q$  and  $q'$ .

<sup>3</sup>In part I of the thesis we worked with Voigt and Faraday-Voigt functions that are normalized to unity and zero respectively. In part II of the thesis we use unnormalized  $H(x, a)$  and  $F(x, a)$  functions in conformity with the standard convention in scattering theory. The normalizations are taken care later in the redistribution functions.

From Eqs. (7.17) and (7.18) we can construct the real valued mathematical basis functions, which we call the magnetic redistribution functions (hereafter magnetic RF). They are given by

$$R_{\text{II,H}}^q(x, x', \Theta; B) = \frac{1}{\pi \sin \Theta} \exp \left\{ - \left[ \frac{x - x'}{2 \sin(\Theta/2)} \right]^2 \right\} H \left( \frac{v_q + v'_q}{2 \cos(\Theta/2)}, \frac{a}{\cos(\Theta/2)} \right), \quad (7.21)$$

$$R_{\text{II,F}}^q(x, x', \Theta; B) = \frac{1}{\pi \sin \Theta} \exp \left\{ - \left[ \frac{x - x'}{2 \sin(\Theta/2)} \right]^2 \right\} F \left( \frac{v_q + v'_q}{2 \cos(\Theta/2)}, \frac{a}{\cos(\Theta/2)} \right), \quad (7.22)$$

for redistribution of type II, which depends only on  $q$  and

$$R_{\text{III,HH}}^{qq'}(x, x', \Theta; B) = \frac{1}{\pi^2 \sin \Theta} \int_{-\infty}^{+\infty} du e^{-u^2} \left[ \frac{a}{a^2 + (v'_q - u)^2} \right] H \left( \frac{v_{q'} - u \cos \Theta}{\sin \Theta}, \frac{a}{\sin \Theta} \right), \quad (7.23)$$

$$R_{\text{III,HF}}^{qq'}(x, x', \Theta; B) = \frac{1}{\pi^2 \sin \Theta} \int_{-\infty}^{+\infty} du e^{-u^2} \left[ \frac{a}{a^2 + (v'_q - u)^2} \right] F \left( \frac{v_{q'} - u \cos \Theta}{\sin \Theta}, \frac{a}{\sin \Theta} \right), \quad (7.24)$$

$$R_{\text{III,FH}}^{qq'}(x, x', \Theta; B) = \frac{1}{\pi^2 \sin \Theta} \int_{-\infty}^{+\infty} du e^{-u^2} \left[ \frac{(v'_q - u)}{a^2 + (v'_q - u)^2} \right] H \left( \frac{v_{q'} - u \cos \Theta}{\sin \Theta}, \frac{a}{\sin \Theta} \right), \quad (7.25)$$

and

$$R_{\text{III,FF}}^{qq'}(x, x', \Theta; B) = \frac{1}{\pi^2 \sin \Theta} \int_{-\infty}^{+\infty} du e^{-u^2} \left[ \frac{(v'_q - u)}{a^2 + (v'_q - u)^2} \right] F \left( \frac{v_{q'} - u \cos \Theta}{\sin \Theta}, \frac{a}{\sin \Theta} \right), \quad (7.26)$$

for redistribution of type III, which depends on both  $q$  and  $q'$ . We note that  $R_{\text{II,H}}^0$  and  $R_{\text{III,HH}}^{00}$  (dropping the arguments for brevity), are nothing but the well known  $R_{\text{II}}$  and  $R_{\text{III}}$  scalar redistribution functions of Hummer (1962) in the LF. It will be shown in § 7.4, that the overall behavior of the magnetic RF is similar to the non-magnetic RF of Hummer, except for changes caused by Zeeman frequency shifts (appearance of several magnetic components:  $(2 \times 3)$  in  $R_{\text{II}}$  type scattering;  $(4 \times 9)$  in  $R_{\text{III}}$  type scattering).

For notational simplification, we now introduce the following auxiliary functions (which are linear combination of magnetic RF introduced above),

$$h_{qq'}^{\text{II}} = \frac{1}{2} \left( R_{\text{II,H}}^q + R_{\text{II,H}}^{q'} \right), \quad (7.27)$$

$$f_{qq'}^{\text{II}} = \frac{1}{2} \left( R_{\text{II,F}}^{q'} - R_{\text{II,F}}^q \right), \quad (7.28)$$

for type II functions. For type III functions, we define a complex  $h$ -function :

$$h_{qq'}^{\text{III}} = \Re\left(h_{qq'}^{\text{III}}\right) + i\Im\left(h_{qq'}^{\text{III}}\right), \quad (7.29)$$

where the real ( $\Re$ ) and imaginary ( $\Im$ ) parts are defined through

$$\Re\left(h_{qq'}^{\text{III}}\right) = \frac{1}{4} \left( R_{\text{III,HH}}^{q'q'} + R_{\text{III,HH}}^{q'q} + R_{\text{III,HH}}^{qq'} + R_{\text{III,HH}}^{qq} \right), \quad (7.30)$$

$$\Im\left(h_{qq'}^{\text{III}}\right) = \frac{1}{4} \left( R_{\text{III,FH}}^{q'q'} + R_{\text{III,FH}}^{q'q} - R_{\text{III,FH}}^{qq'} - R_{\text{III,FH}}^{qq} \right), \quad (7.31)$$

which are expressed in terms of HH and FH type of basis functions respectively. An analogous expression can be written for the complex  $f$ -function :

$$f_{qq'}^{\text{III}} = \Re\left(f_{qq'}^{\text{III}}\right) + i\Im\left(f_{qq'}^{\text{III}}\right), \quad (7.32)$$

where the real and imaginary parts are now defined through

$$\Re\left(f_{qq'}^{\text{III}}\right) = \frac{1}{4} \left( R_{\text{III,HF}}^{q'q'} - R_{\text{III,HF}}^{q'q} + R_{\text{III,HF}}^{qq'} - R_{\text{III,HF}}^{qq} \right), \quad (7.33)$$

$$\Im\left(f_{qq'}^{\text{III}}\right) = \frac{1}{4} \left( R_{\text{III,FF}}^{q'q'} - R_{\text{III,FF}}^{q'q} - R_{\text{III,FF}}^{qq'} + R_{\text{III,FF}}^{qq} \right). \quad (7.34)$$

We note that  $f_{qq'}^{\text{II}}$ ,  $\Im\left(h_{qq'}^{\text{III}}\right)$ ,  $f_{qq'}^{\text{III}}$  are non-zero only when  $q \neq q'$ . The auxiliary quantities defined above satisfy the following symmetry relations :

$$h_{qq'}^{\text{II}} = h_{q'q}^{\text{II}}; \quad f_{qq'}^{\text{II}} = -f_{q'q}^{\text{II}}; \quad h_{qq'}^{\text{III}} = h_{q'q}^{\text{III}*}; \quad f_{qq'}^{\text{III}} = -f_{q'q}^{\text{III}*}. \quad (7.35)$$

Using Eqs. (7.27) - (7.34), we can rewrite Eq. (7.16) as

$$\begin{aligned} \langle \tilde{r}_q \tilde{r}_{q'}^* \rangle &\sim A \cos \beta_{q-q'} e^{i\beta_{q-q'}} \left( h_{qq'}^{\text{II}} + i f_{qq'}^{\text{II}} \right) + \mathcal{B} \cos \beta_{q-q'} \cos \alpha_{q-q'} e^{i(\beta_{q-q'} + \alpha_{q-q'})} \\ &\times \left\{ \Re\left(h_{qq'}^{\text{III}}\right) - \Im\left(f_{qq'}^{\text{III}}\right) + i \left[ \Im\left(h_{qq'}^{\text{III}}\right) + \Re\left(f_{qq'}^{\text{III}}\right) \right] \right\}. \end{aligned} \quad (7.36)$$

### 7.3 Analytical form of the Hanle-Zeeman redistribution matrix

For clarity and compactness we have derived analytical expression for the Hanle-Zeeman redistribution matrix for the simpler case of a normal Zeeman triplet ( $J = 0 \rightarrow 1 \rightarrow 0$  scattering transition), and for a coordinate system in which the polar axis is along the magnetic field. Fig. 7.1 shows the corresponding scattering geometry. The incident ray

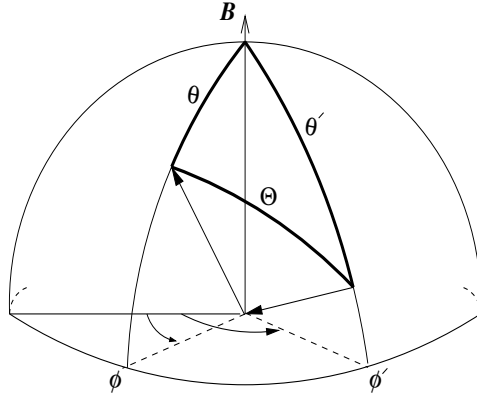


Figure 7.1: The geometry showing the scattering process in a coordinate system where the polar  $Z$ -axis is oriented along the magnetic field.  $(\theta', \phi')$  refer to the incident ray,  $(\theta, \phi)$  to the scattered ray.  $\Theta$  is the scattering angle.

makes an angle  $\theta'$  and azimuth  $\phi'$  with respect to field direction, while outgoing ray makes an angle  $\theta$  and azimuth  $\phi$ . It is however possible to compute the redistribution matrix for arbitrary orientations of vector magnetic fields by using transformation matrices (see Appendix K).

The Mueller scattering matrix  $\mathbf{M}$  that describes scattering of the Stokes vector is readily obtained from the coherency matrix (see Eq. (10) of BS99), using the expression (c.f. Eqs. (1.11) and (1.12))

$$\mathbf{M} = \mathbf{T} (\mathbf{w} \otimes \mathbf{w}^*) \mathbf{T}^{-1}, \quad (7.37)$$

where  $\mathbf{w}$  is the Jones scattering matrix. Explicit expressions of  $(\mathbf{w} \otimes \mathbf{w}^*)$  and the purely mathematical transformation matrices  $\mathbf{T}$  and  $\mathbf{T}^{-1}$  are given in Eqs. (1.12) and (1.13).

The elements of the Jones scattering matrix are given by (see Eq. (8) of BS99)

$$w_{\alpha\beta} \sim \sum_q \left[ \frac{r_q(t, \omega')}{E'_{q,0}} \right] \varepsilon_q^{\alpha*} \varepsilon_q^\beta, \quad (7.38)$$

where  $E'_{q,0}$  is the amplitude of the  $q^{\text{th}}$  spherical component of incoming monochromatic plane wave, and  $\varepsilon_q^{\alpha,\beta}$  are geometrical factors for the outgoing ( $\alpha$ ) and incoming ( $\beta$ ) radiation, respectively. These geometrical factors are given by

$$\varepsilon_0^1 = -\sin \theta; \quad \varepsilon_\pm^1 = \mp \frac{\mu}{\sqrt{2}} e^{\pm i\phi}; \quad \varepsilon_0^2 = 0; \quad \varepsilon_\pm^2 = -\frac{i}{\sqrt{2}} e^{\pm i\phi}, \quad (7.39)$$

for the outgoing radiation, with  $\mu = \cos \theta$  (see Stenflo 1994, p. 57). For the incoming radiation we simply replace  $(\theta, \phi)$  by  $(\theta', \phi')$ , in the above equations.

The tensor product  $(\mathbf{w} \otimes \mathbf{w}^*)$ , requires the construction of bilinear products  $w_{\alpha\beta} w_{\alpha'\beta'}^*$ , given by

$$w_{\alpha\beta} w_{\alpha'\beta'}^* = \sum_{qq'} \left[ \frac{r_q(t, \omega') r_{q'}^*(t, \omega')}{E'_{q,0} E'_{q',0}} \right] \varepsilon_q^{\alpha*} \varepsilon_{q'}^{\alpha'} \varepsilon_q^\beta \varepsilon_{q'}^{\beta'*}. \quad (7.40)$$

Next we replace the term in the square bracket by the ensemble average  $\langle \tilde{r}_q \tilde{r}_{q'}^* \rangle$ , in order to take into account the collisions (see § 7.2). Thus Eq. (7.40) becomes

$$w_{\alpha\beta} w_{\alpha'\beta'}^* = \sum_{qq'} \langle \tilde{r}_q \tilde{r}_{q'}^* \rangle \varepsilon_q^{\alpha*} \varepsilon_{q'}^{\alpha'} \varepsilon_q^\beta \varepsilon_{q'}^{\beta'*}. \quad (7.41)$$

Therefore the Mueller matrix  $\mathbf{M}$  can be calculated using Eqs. (7.36), (7.37), (7.39), and (7.41). The Hanle-Zeeman redistribution matrix is then given by

$$\mathbf{R}(x, \mathbf{n}; x', \mathbf{n}'; \mathbf{B}) = \frac{3}{2} \mathbf{M}, \quad (7.42)$$

where 3/2 is the normalization constant (see Eq. (8.38) of Stenflo 1994).

We can now write the final expression for the Hanle-Zeeman grand redistribution matrix as

$$\mathbf{R}(x, \mathbf{n}; x', \mathbf{n}'; \mathbf{B}) = \mathbf{R}^{\text{II}}(x, \mathbf{n}; x', \mathbf{n}'; \mathbf{B}) + \mathbf{R}^{\text{III}}(x, \mathbf{n}; x', \mathbf{n}'; \mathbf{B}), \quad (7.43)$$

where

$$\mathbf{R}^{\text{II}}(x, \mathbf{n}; x', \mathbf{n}'; \mathbf{B}) = A \mathbf{M}_{\text{II}}, \quad (7.44)$$

$$\mathbf{R}^{\text{III}}(x, \mathbf{n}; x', \mathbf{n}'; \mathbf{B}) = B \mathbf{M}_{\text{III}}, \quad (7.45)$$

with

$$\begin{aligned} \mathbf{M}_{\text{II}} = & \frac{3}{4} \left[ c_{00}^{\text{II}} \mathbf{C}_0^0 + \frac{1}{2} (c_{11}^{\text{II}} + c_{-1-1}^{\text{II}}) \mathbf{C}_+^0 + \frac{1}{2} (c_{11}^{\text{II}} - c_{-1-1}^{\text{II}}) \mathbf{C}_-^0 + c_{1-1}^{\text{II}} \mathbf{C}_+^2 + s_{1-1}^{\text{II}} \mathbf{S}_+^2 \right] + \frac{3}{4} \sin \theta \\ & \times \sin \theta' \left[ (c_{01}^{\text{II}} + c_{0-1}^{\text{II}}) \mathbf{C}_+^1 + (c_{01}^{\text{II}} - c_{0-1}^{\text{II}}) \mathbf{C}_-^1 + (s_{0-1}^{\text{II}} - s_{01}^{\text{II}}) \mathbf{S}_+^1 + (-s_{01}^{\text{II}} - s_{0-1}^{\text{II}}) \mathbf{S}_-^1 \right], \quad (7.46) \end{aligned}$$

with a similar expression for  $\mathbf{M}_{\text{III}}$ , when all  $c^{\text{II}}$  and  $s^{\text{II}}$  coefficients (see Eqs. (G.1) and (G.2)) are replaced by the  $c^{\text{III}}$  and  $s^{\text{III}}$  coefficients (see Eqs. (G.3) and (G.4)), respectively. Various auxiliary coefficients and matrices appearing in Eq. (7.46) are given in Appendix G. Notice that Eq. (7.46) has a form similar to Eq. (49) of Stenflo (1998). Also note that



the  $3/2$  factor of Eq. (7.42) has already been included in the definition of  $\mathbf{M}_{\text{II}}$  and  $\mathbf{M}_{\text{III}}$  in Eq. (7.46). The Hanle-Zeeman PRD grand redistribution matrix is strongly angle-dependent, and needs special care in numerical evaluation. This matrix appears inside the scattering integral of the line radiative transfer equation. A sufficiently general form of this matrix is presented in Eq. (7.43), which takes care of the radiative and collisional contributions in a neatly factorized manner (see Nagendra 1994, Nagendra et al. 1999).

## 7.4 A study of magnetic redistribution functions

The magnetic RF defined in Eqs. (7.21) – (7.26) form the basis for the frequency dependence of magnetic redistribution matrices, which are expressed as a combination of different types of “angular phase matrices” ( $\mathbf{C}$  and  $\mathbf{S}$ ), and the  $c$  and  $s$  coefficients. A good knowledge about the nature of these basis functions would be useful to understand the physics of Hanle-Zeeman scattering. We will now explore the magnetic RF in some detail. In § 7.4.1 we discuss the dependence of RF on the scattering angle and incoming frequency for a fixed value of the field strength. The field strength dependence is considered in § 7.4.2.

### 7.4.1 Dependence of the magnetic redistribution functions on scattering angle and incoming frequency

We will here consider the magnetic RF of Hummer’s type II and III for three scattering angles  $\Theta = 30^\circ$ ,  $90^\circ$ , and  $150^\circ$  and incoming frequencies  $x' = 0$ ,  $2$ , and  $4$ . The damping parameter is chosen to be  $a = 10^{-3}$ , and the field strength is chosen such that  $v_B = g\nu_L/\Delta\nu_D = 1$ . We introduce the notion of ‘frequency-coherence’ ( $x \simeq x'$ ) and ‘magnetic-coherence’ ( $x \simeq v_B$ ), in order to interpret the results.

#### RF of type II

The magnetic RF of Hummer’s type II are shown in Fig. 7.2. The solid lines refer to incoming frequency  $x' = 0$ , the dotted lines to  $x' = 2$  and the dashed lines to  $x' = 4$ . All the thin lines correspond to magnetic quantum number  $q = -1$ , medium lines to  $q = 0$ , and thick lines to  $q = +1$ . The  $q = 0$  case represents the non-magnetic scalar RF of Hummer (1962).

The function  $R_{\text{II,H}}^q(x, x', \Theta; B)$  is shown in Fig. 7.2a. For forward ( $\Theta = 0$ ) scattering, the function  $R_{\text{II,H}}^q$  exhibits exact frequency-coherence ( $x = x'$ ) at all the absorption frequencies  $x'$ , while for backward scattering ( $\Theta = \pi$ ), the function peaks at  $x = -x'$  (see

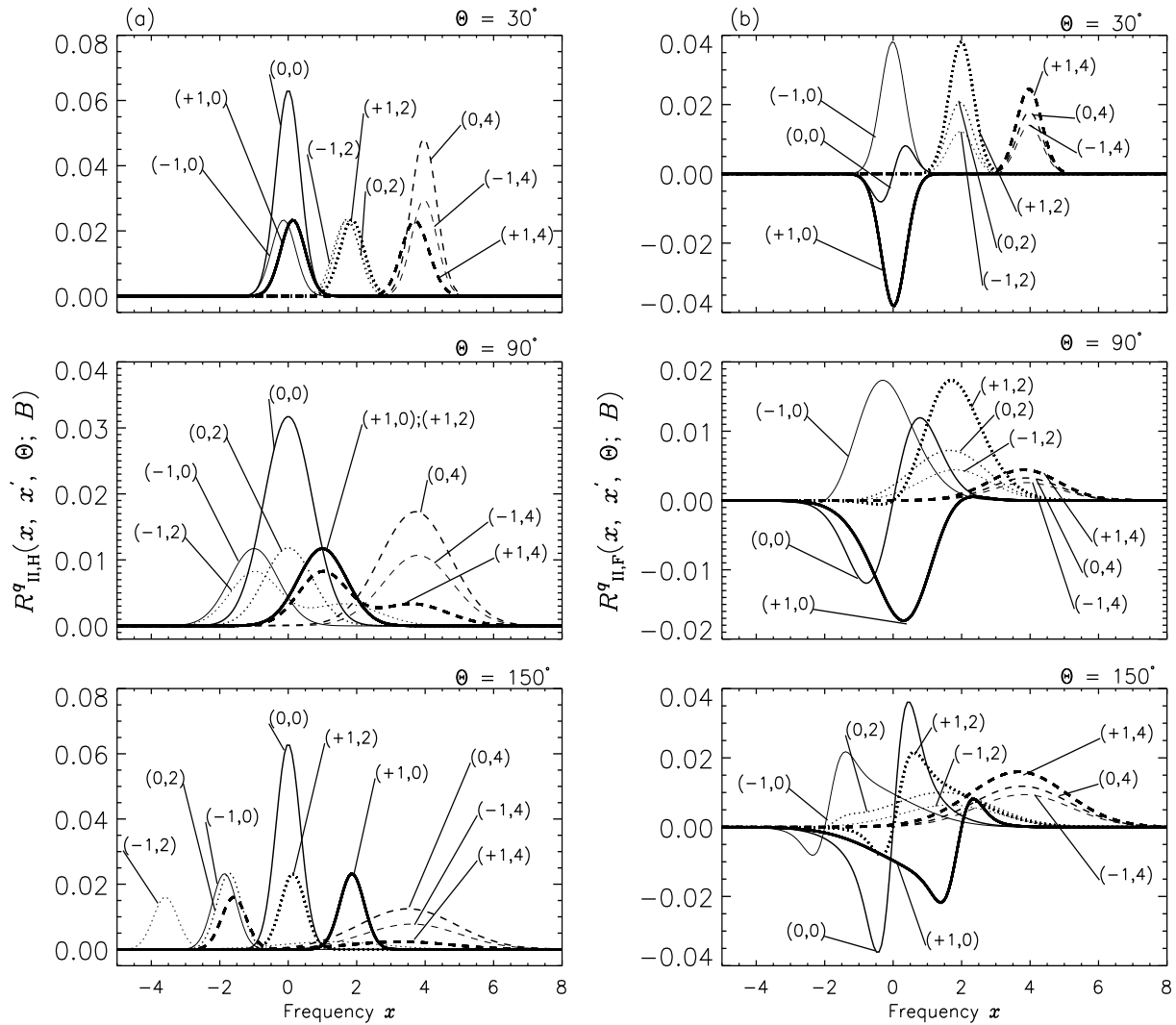


Figure 7.2: The magnetic RF of Hummer's type II. (a)  $R_{II,H}^q$  and (b)  $R_{II,F}^q$  for different values of the scattering angle. The redistribution function  $R_{II,F}^q$  can take negative values. The different line types are labeled with a pair of parameters  $(q, x')$ . In all the three panels of (a), the thin dotted  $(-1, 2)$  and thick dashed  $(+1, 4)$  lines are multiplied by  $2 \times 10^3$ , the thin dashed  $(-1, 4)$  and medium dashed  $(0, 4)$  lines are multiplied by  $2 \times 10^4$ , and the medium dotted  $(0, 2)$  line by 20, to be able to present them in the same panel. In (b) all the dashed lines of the  $\Theta = 30^\circ$  case are multiplied by a factor of 2, and of the  $\Theta = 150^\circ$  case by 5, in order to show the details clearly. The thin dotted line  $(-1, 2)$  and medium dotted line  $(0, 2)$  of the  $\Theta = 150^\circ$  case in (b) are multiplied by 2. See § 7.4.1 for discussions.

e.g. Henyey 1940, Cannon 1985, Wallace & Yelle 1989). This strong coherence is retained for small scattering angles. This can be clearly seen for  $\Theta = 30^\circ$ . For  $|x - qv_B| \leq 3$ , the peak position of the RF varies approximately as  $x_{\max} = x' \cos \Theta + 2qv_B \sin^2 \Theta/2$  (see also Wallace & Yelle 1989, for the non-magnetic  $R_{\text{II,H}}^0$  case). In the non-magnetic  $R_{\text{II,H}}^0$  case, it is well known that for arbitrary scattering angles the frequency-coherence behaves in a very unique way, namely with the appearance of a double peak in the transition frequencies ( $2 < x' < 4$ ) — one coherent peak at  $x \sim x'$ , with the frequency position of the second non-coherent peak depending strongly on scattering angle  $\Theta$  (see Fig. 7.4 of Cannon 1985). This behavior is also preserved by the RF for  $q = \pm 1$ . For example,  $(q, x') = (-1, 2)$  (thin solid line) and  $(+1, 4)$  (thick dashed line) show this double peak profile for both  $\Theta = 90^\circ$  and  $150^\circ$  scattering angles. Also the RF becomes narrow as the scattering angle changes from  $90^\circ$  to  $150^\circ$  or  $30^\circ$ , which implies a lack of diffusion in frequency space in each scattering event. We note that for the  $\Theta = 90^\circ$  case the  $(+1, 0)$  (thick solid line) and  $(+1, 2)$  (thick dotted line) coincide. Broad coherent emission profiles are observed about  $x \sim x'$  for all the components  $q = 0, \pm 1$ , when (a) the incoming frequencies ( $x'$ ) are large ( $x' > 3$ ), and (b) the scattering angles are large ( $\Theta \geq 90^\circ$ ) (see the thin, medium, and thick dashed lines for  $\Theta = 90^\circ$  and  $150^\circ$  scattering). In addition the  $q = +1$  case, as already described, produces double peaks. The  $q = +1$  case would show broad peaks about  $x \sim x'$ , without a non-coherent component, if we chose still larger values for the incoming frequency  $x'$ .

In Fig. 7.2b we show the function  $R_{\text{II,F}}^q(x, x', \Theta; B)$ . For  $(q, x') = (0, 0)$  (medium solid line), regardless of the scattering angle,  $R_{\text{II,F}}^0$  exhibits an emission component similar to the anti-symmetric Faraday-Voigt function. The magnitude of this function increases as we go from  $\Theta = 30^\circ$  to  $150^\circ$ . For  $\Theta = 30^\circ$  and  $90^\circ$  scattering, the magnetic components  $(-1, 0)$  (thin solid lines) are entirely positive and  $(+1, 0)$  (thick solid lines) entirely negative. The magnetic components  $(\pm 1, 0)$  are highly coherent and nearly symmetric, peaking about  $x = 0$  in the  $\Theta = 30^\circ$  case. For  $\Theta = 90^\circ$  scattering they peak slightly away from line center and are much broader compared to the corresponding small angle scattering case. In the  $\Theta = 30^\circ$  case all the components  $q = 0, \pm 1$ , show highly coherent symmetric peaks at  $x = x'$  for both the incoming frequencies  $x' = 2$  and  $4$ . Corresponding cases for  $\Theta = 90^\circ$  show broad and slightly asymmetric peaks about  $x \sim x'$ . The profiles corresponding to  $\Theta = 150^\circ$  and  $x' = 0, 2$  show a complex behavior for scattering via all the magnetic substates ( $q = 0, \pm 1$ ). All the three magnetic components for  $x' = 4$  (dashed lines) show broad emission profiles peaking at about  $x \sim 4$ . We further note that as the scattering angle decreases,  $R_{\text{II,F}}^q$  become increasingly coherent, except for the  $(0, 0)$  case, where it is non-coherent.

In type II magnetic RF two competing processes are at work. They are, the frequency-coherent effect (controlled by the Gaussian of Eqs. (7.21) and (7.22)), and the magnetic-coherent effect for  $R_{\text{II,H}}^q$  (controlled by the Voigt function of Eq. (7.21)), and sign reversal property for  $R_{\text{II,F}}^q$  (controlled by Faraday-Voigt function of Eq. (7.22)). For small scattering angles ( $\Theta \leq 30^\circ$ ), it is the frequency-coherent effect that dominates (see Fig. 7.2 – top two panels). As the scattering angle increases, which of these two effects dominate is determined by values of  $x'$ ,  $q$  and  $v_B$  (see Fig. 7.2; see also Fig. 7.7), taken together.

### RF of type III

The magnetic redistribution functions of Hummer's type III are shown in Figs. 7.3 - 7.6, for the same set of parameters as in Fig. 7.2. Unlike the case of the magnetic RF of Hummer's type II, the type III functions depend on the pair of magnetic quantum numbers ( $q, q'$ ) simultaneously. They in fact refer to the interference between the upper level magnetic sub-states. Thus there are 9 combinations of ( $q, q'$ ), which are distinguished as different line types of different line thickness. The thin lines refer to the ( $q, q'$ ) pairs as follows: solid  $(-1, -1)$ ; dotted  $(0, -1)$ ; dashed  $(+1, -1)$ . Medium thickness lines refer as follows: solid  $(-1, 0)$ ; dotted  $(0, 0)$ ; dashed  $(+1, 0)$ . Thick lines refer as follows: solid  $(-1, +1)$ ; dotted  $(0, +1)$ ; dashed  $(+1, +1)$ . Note that the HH type profiles with ( $q, q'$ ) =  $(0, 0)$  are nothing but the well known Hummer's non-magnetic RF of type III.

### Basis Functions of type HH

In Fig. 7.3 we show  $R_{\text{III,HH}}^{qq'}(x, x', \Theta; B)$  as a function of outgoing frequency  $x$ . All profiles shown for the  $x' = 4$  case (see Fig. 7.3c) are 3 orders of magnitude smaller than those shown in Fig. 7.3a.  $R_{\text{III,HH}}^{qq'}$  is always positive. Unlike the RF of Hummer's type II, which shows perfect coherence for  $\Theta = 0^\circ$ , the RF of Hummer's type III is completely non-coherent, CRD like (for  $\Theta = 90^\circ$ ) and does not show coherence even for  $\Theta = 0^\circ$ . For the  $\Theta = 90^\circ$  case, the set of thin ( $q, -1$ ) and the set of thick ( $q, +1$ ) line profiles are shifted symmetrically about  $x = 0$  and peak at the shifted frequencies  $x = \pm 1$ . The ( $q, 0$ ) components (the set of medium lines) are unshifted and peak at  $x = 0$ . This behavior can be easily understood from Eq. (7.23), which for  $\Theta = 90^\circ$  reduces to

$$R_{\text{III,HH}}^{qq'}(x, x', 90^\circ; B) = \frac{1}{\pi} H(v'_q, a)H(v_{q'}, a), \quad (7.47)$$

i.e., it behaves like CRD (complete non-coherence). For  $x' = 0$  in particular the functional values of  $H(v'_{+1} = -1, a)$  and  $H(v'_{-1} = +1, a)$  are the same, because the Voigt function is a symmetric function. As a result the function  $R_{\text{III,HH}}^{qq'}(x, x', 90^\circ; B) = \text{const} \times H(v_{q'}, a)$  for

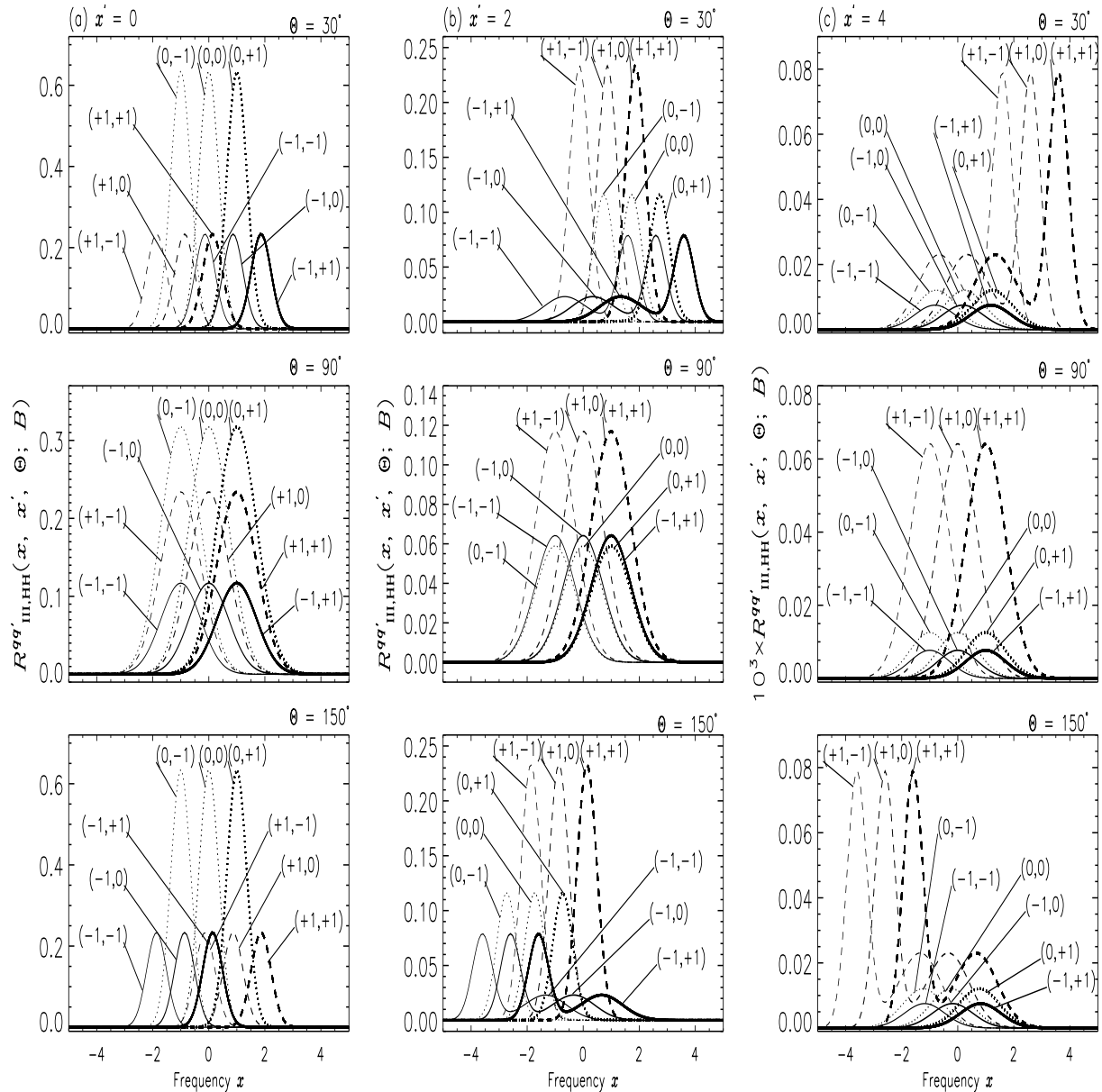


Figure 7.3: Magnetic RF of Hummer's type III. The basis function of type HH is shown. The model parameters are the same as in Fig. 7.2. In (a), in the panel for  $\Theta = 90^\circ$ , all the dashed lines are multiplied by a factor of 2, since they would otherwise overlap exactly on the solid lines. The different line types are labeled with  $(q, q')$  as described in the text. The set of panels exhibit the angular dependence for a given value of  $x'$ . The pair  $(q, q')$  describes either self-interaction ( $q = q'$ ) or  $m$ -state interference ( $q \neq q'$ ). In all three panels of (b) the solid lines are multiplied by  $10^3$  and the dotted lines by 10. See § 7.4.1 for discussions.

$q = \pm 1$  and  $x' = 0$ . This implies that all solid lines  $(-1, q')$  coincide with the corresponding dashed lines  $(+1, q')$ . However, to make all the dashed lines visible in Fig. 7.3a, they have been multiplied by 2. The triplet-like structure centered around  $x = 0$  is conserved by the dotted lines  $(0, q')$  for  $x' = 0$  and all the scattering angles (see Fig. 7.3a). A similar behavior is exhibited by the set of lines for  $(+1, q')$  (dashed lines) and  $(-1, q')$  (solid lines) magnetic substates also, except that they are centered around frequencies  $x = \pm 1$  for  $\Theta = 30^\circ$  and  $150^\circ$  scattering. For the  $x' = 0$  case (see Fig. 7.3a), all the magnetic components of HH type RF show narrow profiles for  $\Theta = 30^\circ$  and  $150^\circ$  scattering as compared with the  $90^\circ$  scattering case.

From Eqs. (7.23) - (7.26) one can easily verify that the following reflection symmetry about  $x = 0$  is obeyed by the RF :

$$R_{\text{III, XH}}^{qq'}(-x, x', \pi - \Theta; B) = R_{\text{III, XH}}^{q-q'}(x, x', \Theta; B), \quad (7.48)$$

$$R_{\text{III, XF}}^{qq'}(-x, x', \pi - \Theta; B) = -R_{\text{III, XF}}^{q-q'}(x, x', \Theta; B), \quad (7.49)$$

where the symbol X stands for H or F. The above expressions are generalizations of the original non-magnetic symmetry relations described in Cannon (1985) to cover the magnetic scattering case. This reflection symmetry represents a combined symmetry involving both frequencies and angles. In Fig. 7.3 the panels for  $\Theta = 30^\circ$  and  $150^\circ$  clearly show this reflection symmetry for  $x' = 0, 2,$  and  $4$  and  $X = H$  in Eq. (7.48).

### Basis Functions of types HF, FH, and FF

Figure 7.4 shows  $R_{\text{III, HF}}^{qq'}(x, x', \Theta; B)$  as a function of scattering angle  $\Theta$  ( $= 30^\circ, 90^\circ,$  and  $150^\circ$ ) and scattered frequency  $x$ , for three incoming frequencies ( $x' = 0, 2,$  and  $4$ ).  $R_{\text{III, HF}}^{qq'}$  obviously assumes both positive and negative values. The reflection symmetry of  $R_{\text{III, HF}}^{qq'}$  given in Eq. (7.49) with  $X = H$  can be clearly seen in Fig. 7.4 for  $\Theta = 30^\circ$  and  $150^\circ$ . All the magnetic components for the  $\Theta = 90^\circ$  scattering case show a similar behavior for  $x' = 0, 2,$  and  $4$ : all thin lines  $(q, -1)$  have a positive peak around  $x = 0$  (and a negative peak around  $x = -2$ ); all medium lines  $(q, 0)$  peak at  $|x| = 1$ ; all thick lines  $(q, +1)$  exhibit a positive peak at  $x = 2$  (and a negative peak at  $x = 0$ ). Such a behavior can be understood from Eq. (7.24), which for  $\Theta = 90^\circ$  reduces to

$$R_{\text{III, HF}}^{qq'}(x, x', 90^\circ; B) = \frac{1}{\pi} H(v'_q, a) F(v_{q'}, a). \quad (7.50)$$

From Eq. (7.50) we note that  $R_{\text{III, HF}}^{qq'}(x, x', 90^\circ; B)$  has a zero crossing at  $x = q'v_B$ , regardless of the value of  $q$  (see Fig. 7.4). In Fig. 7.4a, the dashed lines for  $\Theta = 90^\circ$  have been

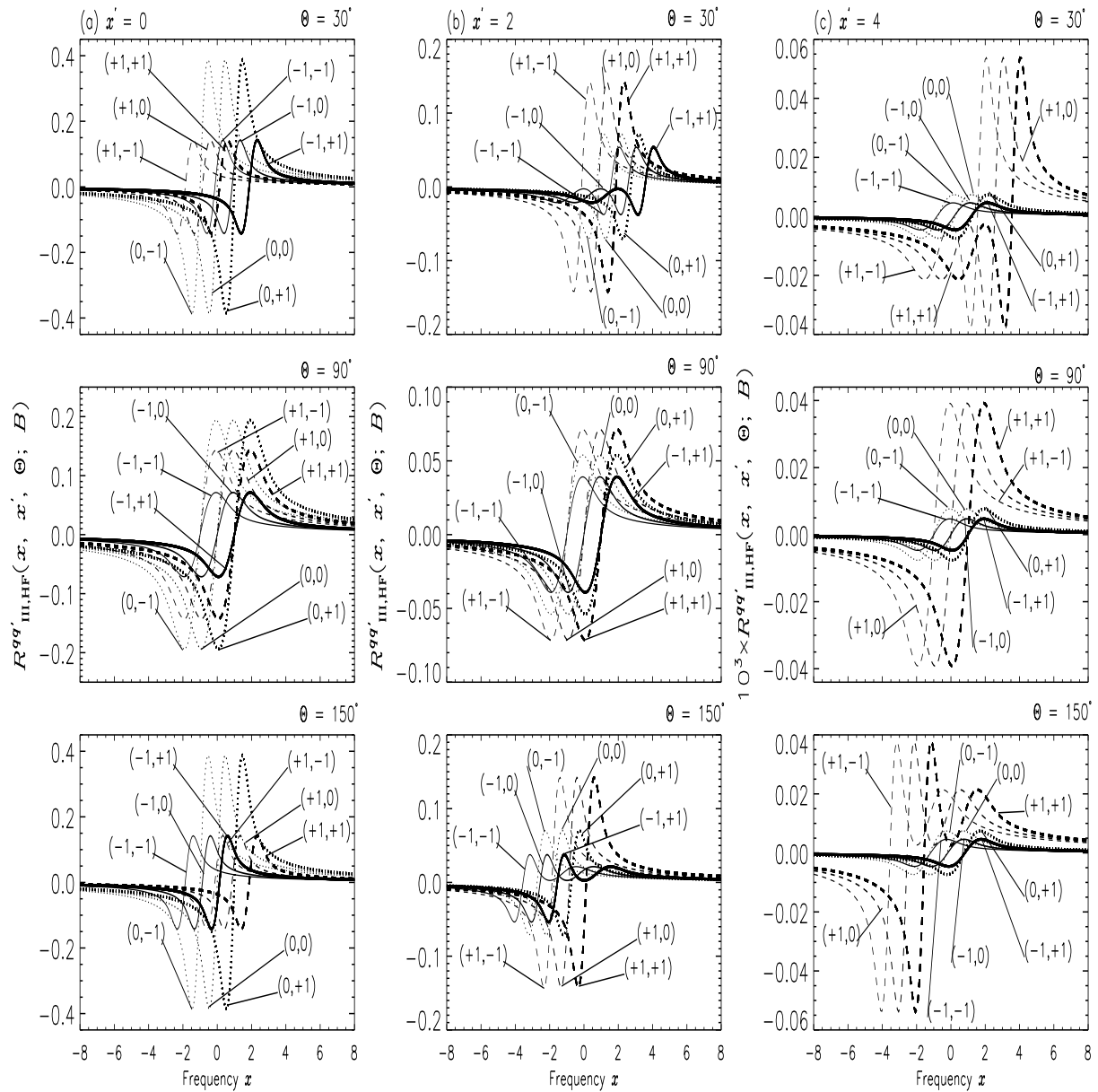


Figure 7.4: Magnetic RF of Hummer's type III. The basis function of type HF (absorption and dispersion) is shown. This function can have negative values and exhibit the typical behavior of the  $F$  function (zero crossing at certain  $x$  values, with very slowly decreasing wings for large  $x$ ). The model parameters are the same as in Fig. 7.3. In (b) the solid lines in all three panels are multiplied by  $10^3$ , while all the dotted lines for the  $\Theta = 30^\circ$  and  $150^\circ$  cases are multiplied by 10, and for the  $\Theta = 90^\circ$  case by 15. See § 7.4.1 for discussions.

multiplied by 2, as they would otherwise superimpose on the corresponding solid lines (see the discussion following Eq. (7.47)). The magnetic components  $(+1, q')$  (the dashed lines) for  $x' = 4$  and  $\Theta = 30^\circ$  ( $150^\circ$ ) show double negative (positive) peaks.

The function  $R_{\text{III, FH}}^{qq'}(x, x', \Theta; B)$  is shown in Fig. 7.5 for the same set of parameters as in Fig. 7.4. Like  $R_{\text{III, HF}}^{qq'}$ , the function  $R_{\text{III, FH}}^{qq'}$  takes both positive and negative values. For  $\Theta = 90^\circ$  the nature of all the components of RF can be understood in terms of the Eq. (7.25), which for this particular case simplifies to

$$R_{\text{III, FH}}^{qq'}(x, x', 90^\circ; B) = \frac{1}{\pi} F(v'_q, a) H(v_{q'}, a). \quad (7.51)$$

From Eq. (7.51) we note that  $R_{\text{III, FH}}^{qq'}(x, x', 90^\circ; B)$  vanishes when  $x' = qv_B$ , since then  $F(v'_q = 0, a)$  is zero. Thus all dotted lines  $(0, q')$  are zero (see Fig. 7.5a). At line center  $x' = 0$ , the function  $F(v'_{-1} = 1, a)$  assumes a positive fixed value, while  $F(v'_{+1} = -1, a)$  takes a negative fixed value. Therefore all the solid lines  $(-1, q')$  in Fig. 7.5a are modified Voigt functions  $H(v_{q'}, a)$ , while the dashed lines  $(+1, q')$  are modified inverted Voigt functions  $-H(v_{q'}, a)$ . The peak positions of both the solid  $(-1, q')$  and dashed  $(+1, q')$  lines are given by  $x = q'$ , since we have chosen  $v_B = 1$ . The behavior of  $R_{\text{III, FH}}^{qq'}(x, x', 90^\circ; B)$  for  $x' = 2$ , and 4 can also be easily explained in terms of Eq. (7.51). We note that in Figs. 7.5b and 7.5c, the function  $R_{\text{III, FH}}^{qq'}(x, x', 90^\circ; B)$  is entirely positive, since  $F(2 - q, a)$  and  $F(4 - q, a)$  are positive for all  $q$ . For  $x' = -2$  or  $x' = -4$ ,  $F(-2 - q, a)$  and  $F(-4 - q, a)$  are negative, which leads to inverted profiles compared to the ones shown in Figs. 7.5b and 7.5c for the  $\Theta = 90^\circ$  case. The reflection symmetry of  $R_{\text{III, FH}}^{qq'}$  as given in Eq. (7.48) with  $X = F$  can be seen in Fig. 7.5 for  $\Theta = 30^\circ$  and  $150^\circ$ . In Fig. 7.5c for the wing frequency  $x' = 4$ , the  $\Theta = 30^\circ$  and  $150^\circ$  redistribution profiles show behavior similar to that exhibited by  $\Theta = 90^\circ$ , with a very slight difference in magnitude (angular isotropy of the scattering probability).

The function  $R_{\text{III, FF}}^{qq'}(x, x', \Theta; B)$  given in Eq. (7.26) is plotted in Fig. 7.6. Like the HF and FH type redistribution,  $R_{\text{III, FF}}^{qq'}$  also has both positive and negative values. To understand the  $\Theta = 90^\circ$  case, we can write Eq. (7.26) for this particular case as

$$R_{\text{III, FF}}^{qq'}(x, x', 90^\circ; B) = \frac{1}{\pi} F(v'_q, a) F(v_{q'}, a). \quad (7.52)$$

From Eq. (7.52) we note that  $R_{\text{III, FF}}^{qq'}(x, x', 90^\circ; B)$  vanishes when  $x' = qv_B$  (see Fig. 7.6a), like the FH type RF, and has a zero crossing at  $x = q'v_B$  (see Fig. 7.6), like the HF type RF. In Fig. 7.6a for  $90^\circ$  scattering the dotted lines  $(0, q')$  are zero, the solid lines  $(-1, q')$  are modified Faraday-Voigt functions  $F(v_{q'}, a)$ , while the dashed lines  $(+1, q')$  are modified



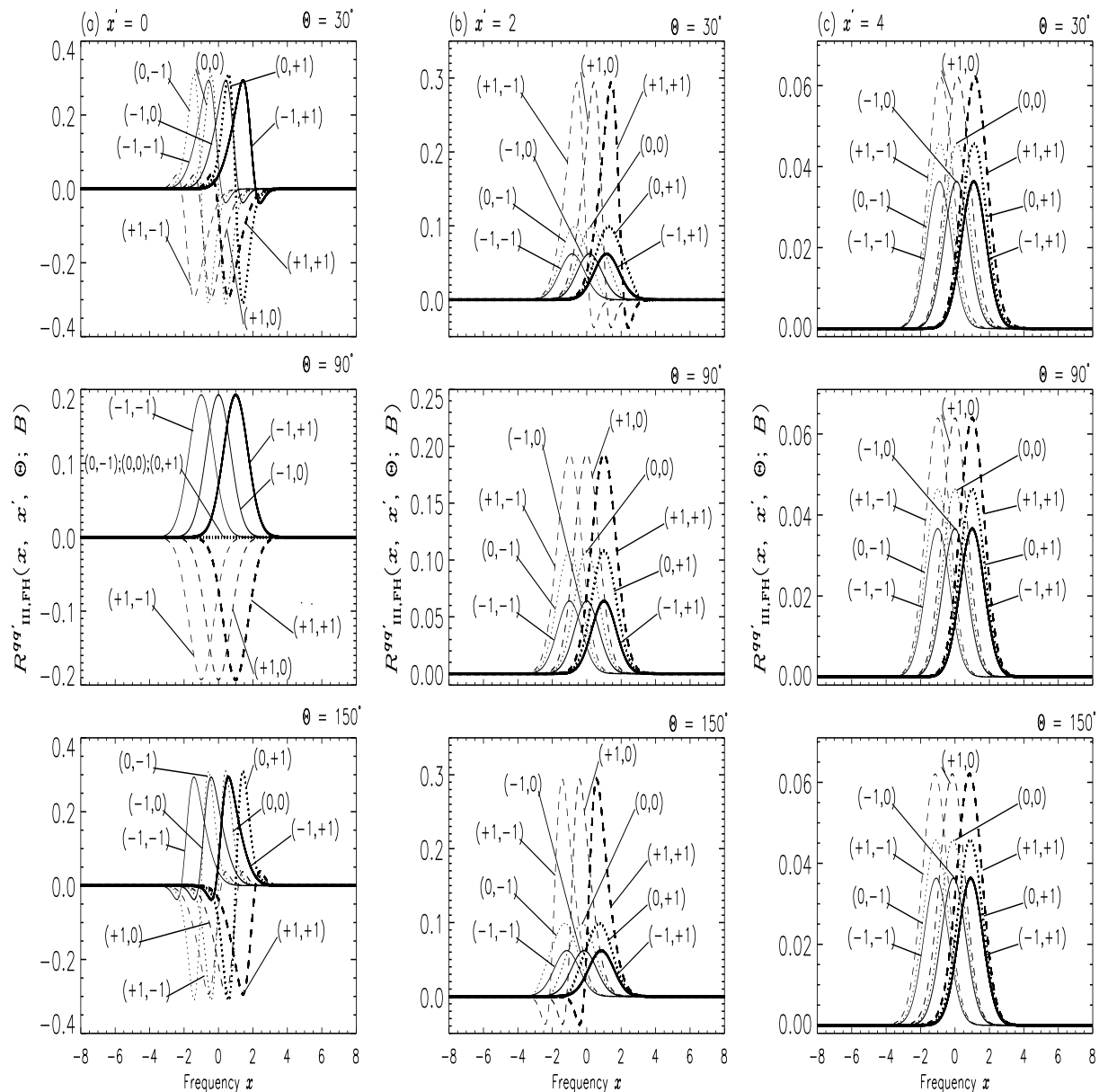


Figure 7.5: Magnetic RF of Hummer's type III. The basis function of type FH is shown. Note that the nature of the FH function is very different from that of HF (displayed in Fig. 7.4). The function is rather confined to the line core, in contrast to the HF type function, which exhibits very broad wings. The model parameters are the same as in Fig. 7.3. See § 7.4.1 for discussions.

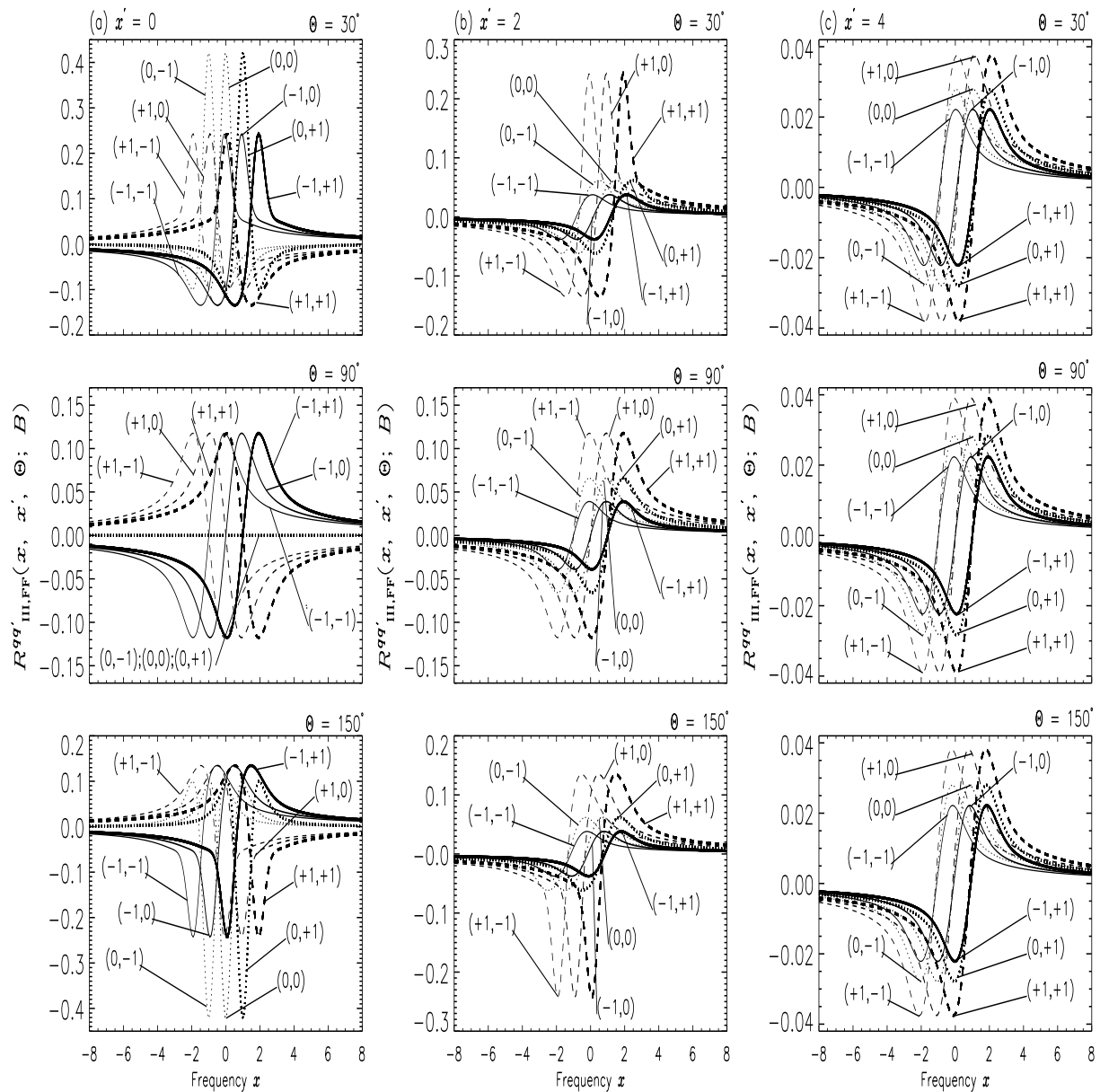


Figure 7.6: Magnetic RF of Hummer's type III. The basis function of type FF is shown. Note the very slow decrease of the function (high level of non-coherence) even in comparison with the HF or FH type functions. The model parameters are the same as in Fig. 7.3. See § 7.4.1 for details.

inverted Faraday-Voigt functions  $-F(v_{q'}, a)$ , for the same reason as noted below Eq. (7.51). The behavior of  $R_{\text{III,FF}}^{qq'}(x, x', 90^\circ; B)$  for  $x' = 2$ , and 4 (see Figs. 7.6b and 7.6c) can also be easily understood through Eq. (7.52). The reflection symmetry of  $R_{\text{III,FF}}^{qq'}$  as given in Eq. (7.49) with  $X = F$  is clearly seen in Fig. 7.6 for the scattering angles  $\Theta = 30^\circ$  and  $150^\circ$ . Again, when  $x' = 4$  and  $\Theta = 30^\circ$  or  $150^\circ$ ,  $R_{\text{III,FF}}^{qq'}$  exhibits a similar behavior as  $R_{\text{III,FH}}^{qq'}$  (nearly isotropic angular scattering).

The HF redistribution function is not always similar to the FH type, except for  $90^\circ$  scattering, and in particular, when  $q = q'$  (self-interference of  $m$ -states). The FH type redistribution is similar to FF for  $\Theta = 90^\circ$  scattering, except for the shape of the redistribution function, which for FH resembles a modified Voigt and for FF a modified Faraday-Voigt function. Same arguments hold good for mutual comparison of HH and HF type functions.

#### 7.4.2 Dependence of the magnetic redistribution functions on field strength

To study the dependence of the magnetic RF on  $v_B$  (field strength), we chose a scattering geometry that produces maximum linear polarization, namely  $90^\circ$  scattering, assuming a photon with incoming frequency  $x' = 3$ . The damping parameter is chosen as  $a = 10^{-3}$ . The field strength parameter  $v_B$  is varied as follows:  $v_B = 0.0008$  (solid line), 0.004 (dotted line), 0.02 (dashed line), 0.1 (dash-dotted line), 0.5 (dash-triple-dotted line), 2.5 (long-dashed line), and 5 (thick dotted line). This range for  $v_B$  covers the weakest fields through intermediate to quite strong fields, with reference to the Doppler width of an optical line (see Stenflo 1998).

#### Type II RF

Figure 7.7 shows the  $R_{\text{II,H}}^q$  and  $R_{\text{II,F}}^q$  functions of Eqs. (7.21) and (7.22). We first discuss  $R_{\text{II,H}}^q$  (see Fig. 7.7a). The  $q = 0$  case is non-magnetic and hence all the lines merge, showing a typical double peaked behavior as discussed with regard to Fig.7.2a. This double peaked behavior is retained for weak magnetic fields ( $v_B \leq 0.1$ ) for both  $q = \pm 1$ . The peak amplitudes at  $(q, x) = (-1, 0/3)$  diminish as the field strength increases. For  $v_B > 0.1$ , the  $q = -1$  profiles exhibit a single peak at  $x \sim x' \sim 3$ , which is typical non-magnetic coherence in the case of  $R_{\text{II,H}}^q$ . In contrast the  $q = +1$  profiles exhibit magnetic-coherence ( $x \simeq v_B$ ), and the magnitude of  $R_{\text{II,H}}^q$  increases with increasing  $v_B$ , since magnetic-coherence dominates as compared with the  $q = -1$  case, for which frequency-coherence dominates. We have found that for small angles ( $\Theta \leq 30^\circ$ ) the highly frequency-coherent behavior of

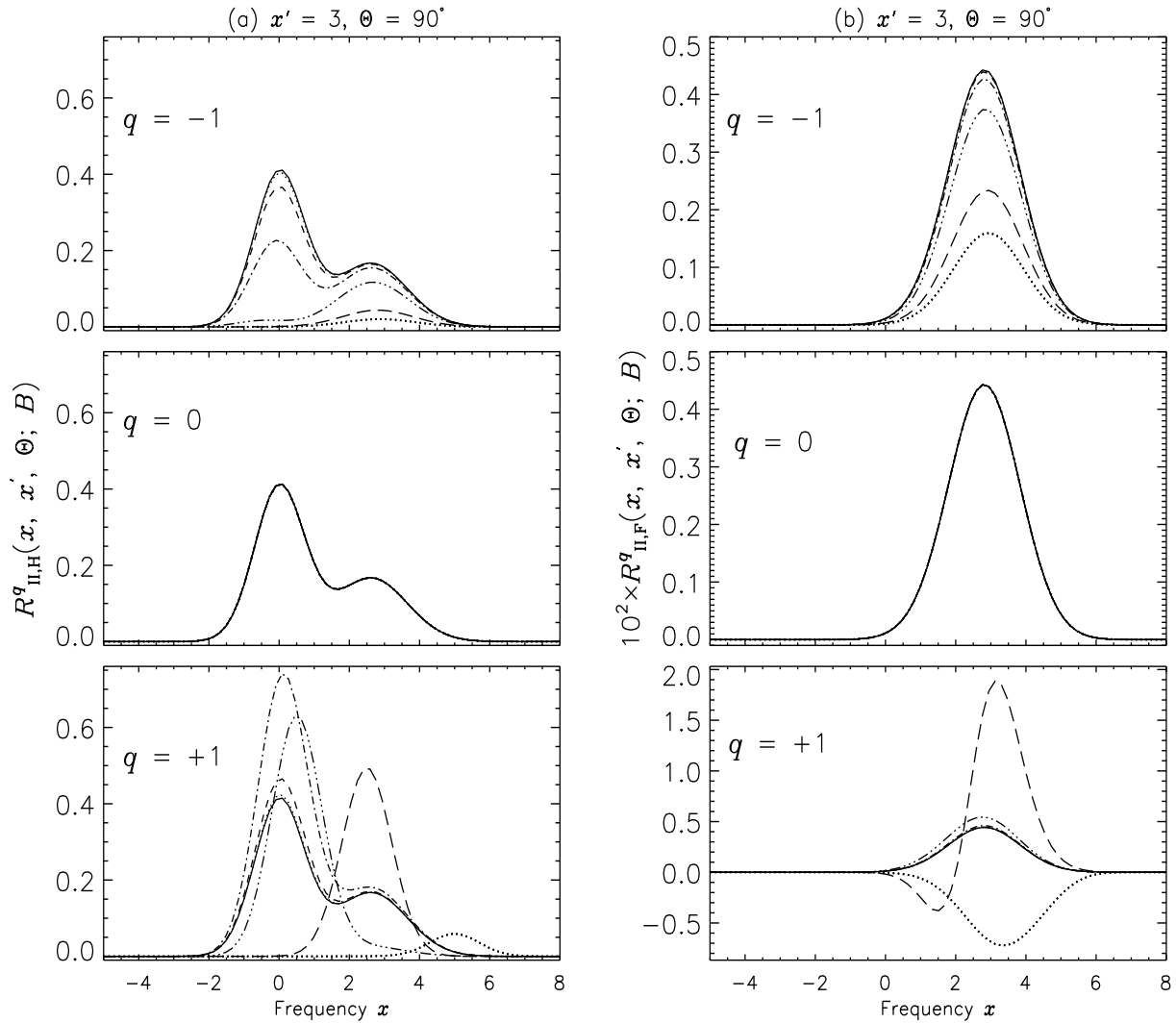


Figure 7.7: Effect of field strength on the Hanle-Zeeman redistribution. The magnetic RF of Hummer's type II is shown. (a)  $R_{II,H}^q(x, x', \Theta; B)$  and (b)  $R_{II,F}^q(x, x', \Theta; B)$  for different values of the field strength, parameterized through  $v_B$ . The model parameters and line types are given in § 7.4.2. We note that all lines for  $q = -1, 0$  of  $R_{II,H}^q$  (in (a)) are multiplied by a factor of  $10^5$ . For  $q = +1$ , the solid to the dash-dotted lines (four of the lines) are multiplied by  $10^5$ , the dash-triple dotted line by  $10^4$ , the long-dashed line by 20, and the thick dotted line by  $10^2$ , to be able to have them displayed in the same panel. See § 7.4.2 for discussions.

$R_{\text{II,H}}^q$  is preserved, even if the field strength is as high as  $v_B = 5$ . For large angle scattering ( $\Theta > 30^\circ$ ), the peak positions of  $R_{\text{II,H}}^q$  depend on  $x'$ ,  $q$  and  $v_B$  as noted in § 7.4.1. For example, when  $x' = 6$  and  $v_B = 2.5$ , it is the frequency-coherence that dominates and magnetic-coherent peak appears just as a bump (illustration not shown for brevity).

Figure 7.7b shows  $R_{\text{II,F}}^q$ . For the  $q = 0$  case we have a single positive peak at  $x \simeq x' \simeq 3$ , as in this case the (non-magnetic) frequency-coherent part (the Gaussian) completely dominates and erases the negative part of Faraday-Voigt function (see Eq. (7.22)). This dominance of frequency-coherence over the dispersive effects remains valid for  $q = -1$ , but the peak amplitude decreases with increasing  $v_B$ . For  $q = +1$  this behavior is observed only for weak fields ( $v_B \leq 0.5$ ). For fields with  $v_B = 2.5$  the profile shows both positive and negative peaks, as dispersive effects slowly start dominating over the frequency-coherence. For  $v_B = 5$  the dispersive effects completely dominate over frequency-coherence effects, resulting in an entirely negative peak at  $x \simeq x' \simeq 3$ . For  $x' = 3$ , the  $\Theta = 30^\circ$  and  $\Theta = 150^\circ$  cases (not illustrated here) largely resemble the  $\Theta = 90^\circ$  case, differing only in the magnitude of  $R_{\text{II,F}}^q$ .

### RF of type III, HH

In Fig. 7.8 we show  $R_{\text{III,HH}}^{qq'}(x, x' = 3, \Theta = 90^\circ; B)$  for the same values of the field strength parameter as in Fig. 7.7. The behavior of  $R_{\text{III,HH}}^{qq'}(x, 3, 90^\circ; B)$  can be easily understood through Eq. (7.47). For the case  $(q, q') = (q, 0)$  the function  $R_{\text{III,HH}}^{q0}(x, 3, 90^\circ; B) = (1/\pi)H(3 - qv_B, a)H(x, a)$ . Thus the shape of  $R_{\text{III,HH}}^{q0}$  is given by  $H(x, a)$ , irrespective of the value of  $v_B$ . The effect of  $v_B$  is only to scale  $H(x, a)$  up or down, as can be seen from Fig. 7.8b, where the peak amplitude decreases with increasing  $v_B$  for  $q = -1$ , while for  $q = +1$  the peak amplitude increases with  $v_B$ , reaching a maximum for  $v_B = 2.5$  (since then  $H(3 - qv_B, a)$  becomes  $H(0.5, a)$ ), and then decreases for  $v_B > 2.5$ . In other words, for the  $(q, q') = (+1, 0)$  case the largest peak amplitude corresponds to the case when  $x' = v_B$ .

For the case  $(-1, q')$  (the top panels of Figs. 7.8a-c) the function  $R_{\text{III,HH}}^{-1q'}(x, 3, 90^\circ; B) = (1/\pi)H(3 + v_B, a)H(x - q'v_B, a)$ . Thus  $R_{\text{III,HH}}^{-1q'}$  peaks at  $x = q'v_B$ . However, as  $v_B$  increases, the peak amplitude decreases, since the scaling factor  $H(3 + v_B, a)$  decreases with  $v_B$ . In the case of  $(0, q')$  (the middle panels of Figs. 7.8a-c) the function  $R_{\text{III,HH}}^{0q'}(x, 3, 90^\circ; B) = (1/\pi)H(3, a)H(x - q'v_B, a)$ . Again the peak position is governed by  $H(x - q'v_B, a)$ , but now the scaling factor is independent of  $v_B$ . Therefore the peak amplitude of the  $q' = -1$  and  $q' = +1$  lines and the different  $v_B$  lines are identical. In the case of  $(+1, q')$  (the bottom panels of Figs. 7.8a-c) the function  $R_{\text{III,HH}}^{+1q'}(x, 3, 90^\circ; B) = (1/\pi)H(3 - v_B, a)H(x - q'v_B, a)$ .

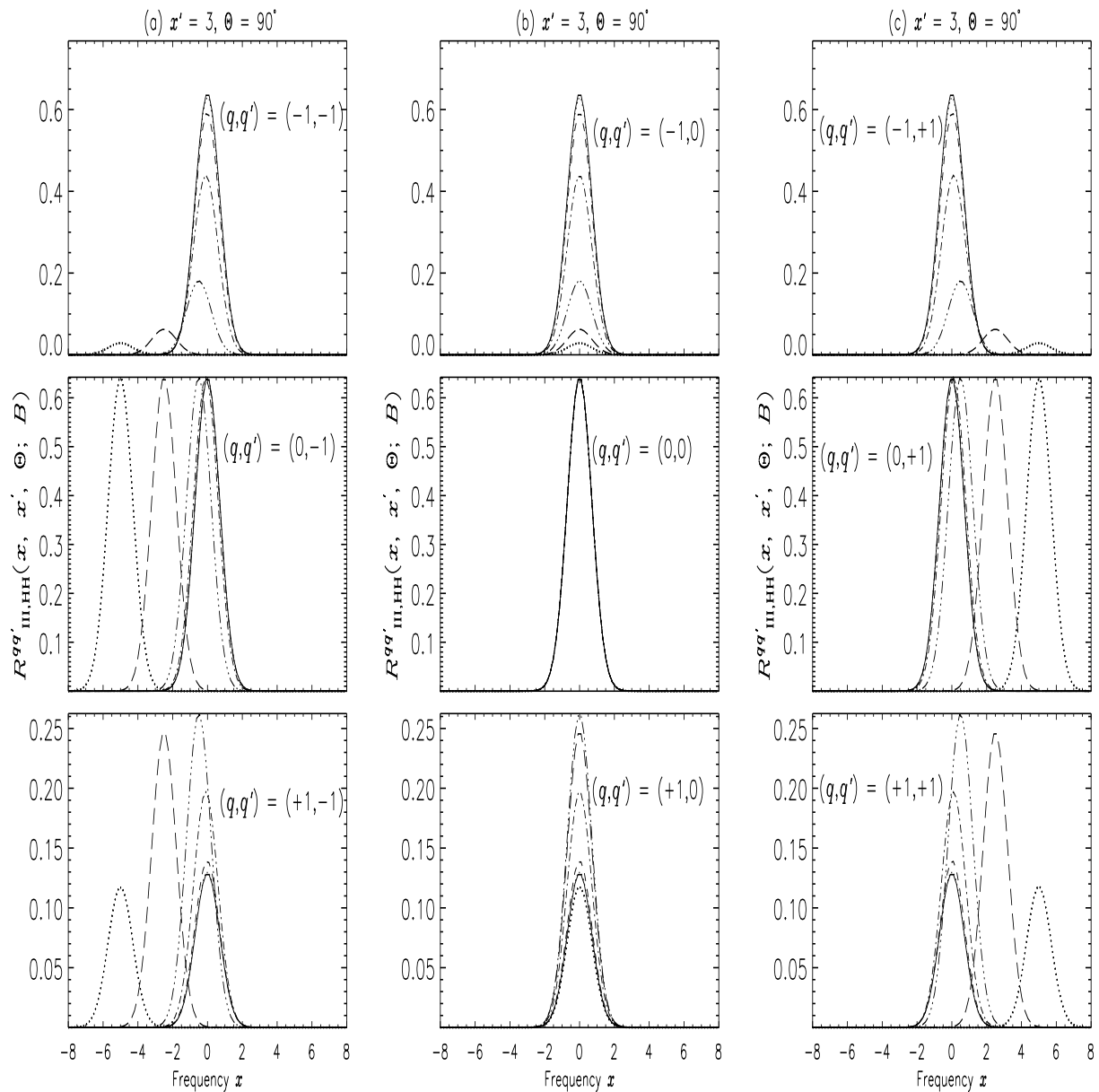


Figure 7.8: Effect of field strength on the magnetic redistribution function  $R_{\text{III,HH}}^{qq'}$ . The different line types and model parameters are the same as in Fig. 7.7. All the lines in the two top panels of Figs. 7.8a-c are multiplied by  $10^4$ . In the bottom panels, the solid to the dash-dotted lines (four lines) are multiplied by  $2 \times 10^3$ , the dash-triple-dotted line by 400, and the thick dotted line by 20. See § 7.4.2 for details.

The shape and peak position are governed by  $H(x - q'v_B, a)$ , while the scaling factor increases until  $v_B = 3$  and then decreases for  $v_B > 3$ .

For scattering angles  $\Theta = 30^\circ$  and  $\Theta = 150^\circ$  (not illustrated here),  $R_{\text{III,HH}}^{qq'}$  shows basically the similar type of behavior as for  $\Theta = 90^\circ$ , except that the shape of  $R_{\text{III,HH}}^{00}$  is rather similar to  $(-1, 0)$  (medium solid line in Fig. 7.3b), and the peak positions and shapes of the other components are now determined not only by  $v_B$  but also by the scattering angle  $\Theta$ .

### RF of type III, HF

The function  $R_{\text{III,HF}}^{qq'}(x, x', 90^\circ; B)$  is given by Eq. (7.50). Clearly the dependence of  $R_{\text{III,HF}}^{qq'}$  on  $v_B$  will be the same as that of  $R_{\text{III,HH}}^{qq'}$ , except that the shape of  $R_{\text{III,HF}}^{qq'}$  is now determined by the dispersion profile  $F(x - q'v_B, a)$  instead of the absorption profile  $H(x - q'v_B, a)$ . Therefore we do not present these profiles here.

### RF of type III, FF

The redistribution functions  $R_{\text{III,FF}}^{qq'}(x, x' = 3, \Theta = 90^\circ; B)$  for the same range of the field strength parameter  $v_B$  as in Figs. 7.7 and 7.8 are shown in Fig. 7.9. The form of the FF type RF for  $\Theta = 90^\circ$  is given in Eq. (7.52). Clearly the shape and peak position are determined by the function  $F(x - q'v_B, a)$ . For  $q' = 0$  it follows from Eq. (7.52) that  $R_{\text{III,FF}}^{q0}(x, 3, 90^\circ; B) = (1/\pi)F(3 - qv_B, a)F(x, a)$ . Hence the shape is basically governed by  $F(x, a)$ , which is scaled up or down by  $F(3 - qv_B, a)$ . For  $q = -1$  the scaling factor  $F(3 + v_B, a)$  is positive and decreases as  $v_B$  increases. Therefore the peak amplitude of  $R_{\text{III,FF}}^{-10}$  decreases with increasing  $v_B$ . In contrast, for  $q = +1$ , the scaling factor  $F(3 - v_B, a)$  is positive as long as  $v_B < 3$  and becomes negative for  $v_B > 3$ . Thus, as clearly shown in Fig. 7.9,  $R_{\text{III,FF}}^{+10}$  reverses sign for  $v_B = 3$ . Further, since  $F(3 - v_B, a)$  increases with  $v_B$  until  $v_B < 3$  and then starts decreasing for  $v_B > 3$ , the function  $R_{\text{III,FF}}^{+10}$  also exhibits the same behavior.

The zero crossing of  $R_{\text{III,FF}}^{qq'}(x, 3, 90^\circ; B)$  is at  $x = q'v_B$ , as noted below Eq. (7.52). When  $(q, q') = (-1, q')$  (the top panels of Figs. 7.9a-c) we have  $R_{\text{III,FF}}^{-1q'}(x, 3, 90^\circ; B) = (1/\pi)F(3 + v_B, a)F(x - q'v_B, a)$ . As already noted,  $F(3 + v_B, a)$  decreases with  $v_B$  and hence  $R_{\text{III,FF}}^{-1q'}$  also decreases with  $v_B$ . For  $(0, q')$  the scaling factor is independent of  $v_B$  (as it equals  $F(3, a)$ ). Thus all the lines in the middle panels of Figs. 7.9a-c have the same value for their peak amplitude. For  $(+1, q')$  the same behavior as noted for  $(+1, 0)$  is observed (see bottom panels of Figs. 7.9a-c).

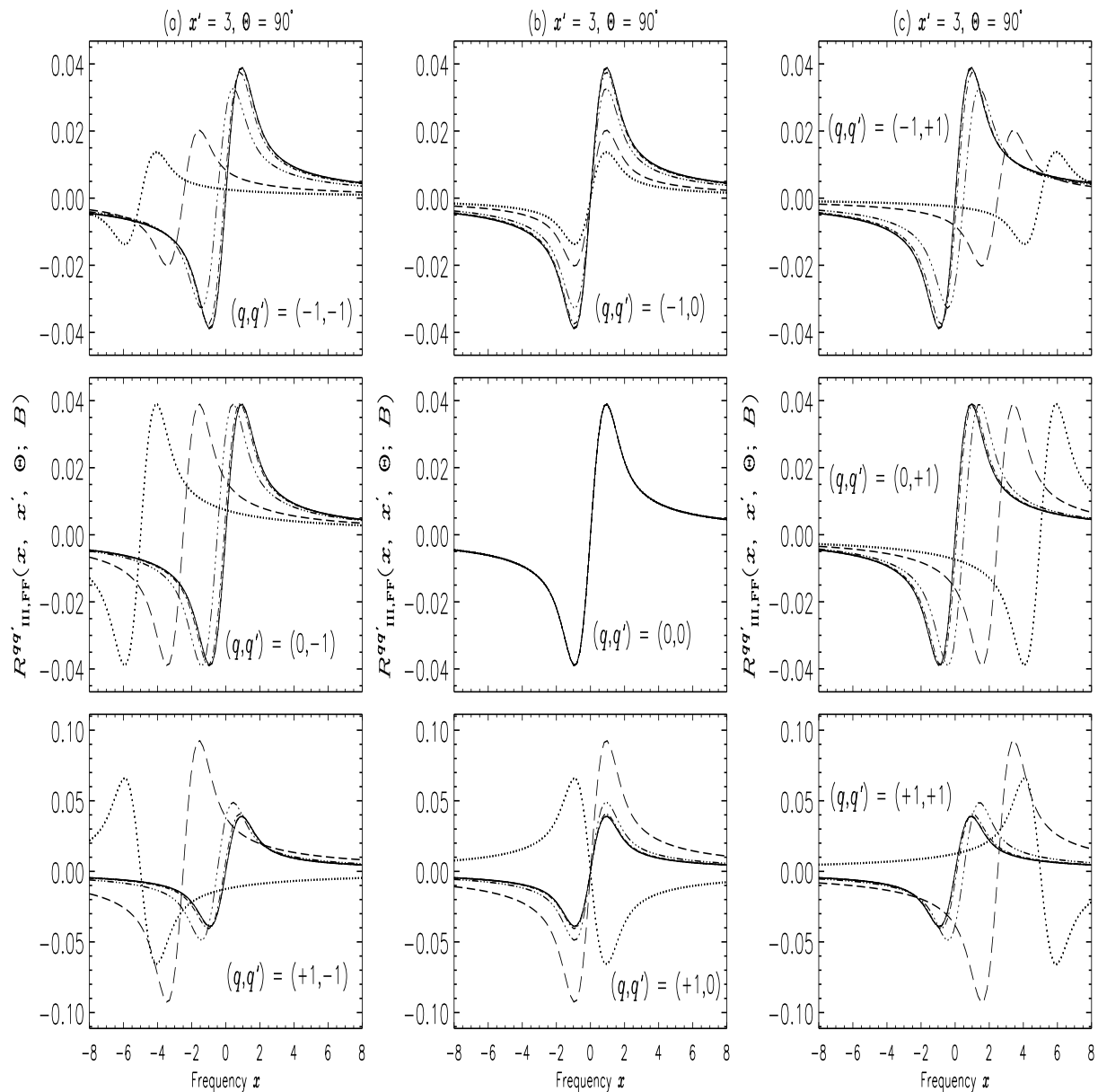


Figure 7.9: Effect of field strength on the magnetic redistribution function  $R^{qq'}_{III,FF}$ . The different line types and model parameters are the same as in Fig. 7.7. In all the panels the zero crossing occurs at  $x = q'v_B$ . See § 7.4.2 for discussions.



The above discussion on the dependence of  $R_{\text{III,FF}}^{qq'}$  on  $v_B$  is also qualitatively valid for scattering angles other than  $\Theta = 90^\circ$ .

### RF of type III, FH

The dependence of  $R_{\text{III,FH}}^{qq'}$  on field strength for  $90^\circ$  scattering is basically the same as that discussed for  $R_{\text{III,FF}}^{qq'}$ , the only difference being the shape and peak position of  $R_{\text{III,FH}}^{qq'}$ , which are determined by  $H(x - q'v_B, a)$  (see Eq. (7.51)). Hence we do not illustrate these functions here.

## 7.5 Extension to the general quantum mechanical scattering case

Our treatment so far has been limited to the special case of a  $J = 0 \rightarrow 1 \rightarrow 0$  scattering transition, since this case can be dealt with in terms of classical time-dependent oscillator theory and is sufficiently simple to allow a comprehensive and explicit analytical treatment of the full and general polarized redistribution problem in the presence of arbitrary magnetic fields. With this foundation we can now address the issue of how to extend our polarized PRD theory for the restricted case of triplet to more general case of atomic and molecular transitions involving arbitrary quantum numbers. Here we indicate how such an extension is possible and conceptually already understood, although it is outside the scope of this chapter to present this extension in explicit form.

The extension proceeds in a phenomenological way, on the direct analogy between the Kramers-Heisenberg scattering amplitude in quantum mechanics and the Jones matrix for classical scattering. The Jones scattering matrix for the classical case can be written (see Eq. (8.116) of Stenflo 1994) as

$$w_{\alpha\beta} \sim \sum_q \Phi_{-q} \varepsilon_q^{\alpha*} \varepsilon_q^\beta, \quad (7.53)$$

while the Kramers-Heisenberg version for general combinations of quantum numbers (see Eq. (1) in Stenflo 1998) is

$$w_{\alpha\beta} \sim \sum_b \frac{\langle f | \hat{\mathbf{r}} \cdot \mathbf{e}_\alpha | b \rangle \langle b | \hat{\mathbf{r}} \cdot \mathbf{e}_\beta | a \rangle}{\omega_{bf} - \omega - i\gamma/2}. \quad (7.54)$$

where  $\hat{\mathbf{r}}$  is the position operator (which is proportional to the dipole moment operator),  $\mathbf{e}_{\alpha,\beta}$  are the linear unit polarization vectors for the outgoing and incoming radiation, respectively,  $a$  represents the set of quantum numbers (including the magnetic substates) for the initial state,  $b$  the corresponding set for the intermediate state, and  $f$  for the final state.

$\omega_{bf}$  is the resonant frequency for a transition between the magnetic substates with upper magnetic quantum number  $m_b$  and lower magnetic quantum number  $m_f$ . Equation (7.54) may be rewritten as

$$w_{\alpha\beta} \sim \sum_b t_{ab} t_{bf} \Phi_{-q} \varepsilon_q^{\alpha*} \varepsilon_{q'}^\beta. \quad (7.55)$$

Here

$$q = m_f - m_b; \quad q' = m_a - m_b, \quad (7.56)$$

and  $t_{ab}$  and  $t_{bf}$  are, respectively, the two transition amplitudes (including sign) for the transitions between the intermediate state  $b$  and the initial and final states  $a$  and  $f$ , given by the matrix elements in Eq. (7.54).  $\Phi_{-q}$  is the normalized profile function that has the same form as the one in Eq. (7.54) with  $\omega_{bf}$  given by  $(\omega_0 - qg\omega_L)$  in the classical case. In the quantum case  $-qg\omega_L$  is replaced by  $(g_b m_b - g_f m_f)\omega_L$ , where  $\omega_L$  is the Larmor frequency and  $g_{b,f}$  are the Landé factors of the intermediate and final states.

When comparing the classical Eq. (7.53) with the quantum Eq. (7.55) we see that they are the same, with two differences: (1) The transition amplitudes  $t$  between the magnetic substates involved in the scattering transition appear as weights. They are not needed in the classical or  $J = 0 \rightarrow 1 \rightarrow 0$  case, since in this case the three amplitudes involved are identical. (2) In one of the geometric  $\varepsilon$  factors a  $q'$  appears instead of a  $q$ .

These two differences between the classical and quantum case however do not influence the frequency redistribution for an individual  $m$  state scattering transition. The product of the transition amplitudes provides a global, frequency-independent scaling factor for the strength of the scattering transition. The frequency-independent  $\varepsilon$  factors represent pure geometric projections, and also have nothing to do with the frequency redistribution problem. All the frequency redistribution physics is contained in the only frequency dependent factor, namely  $\Phi_{-q}$ , the profile function, which is the same in the classical and quantum case.

Now it needs to be remembered that the profile function given in the usual version (Eq. (7.54)) of the Kramers-Heisenberg dispersion formula, refers to the atomic frame without Doppler motions or collisions. This is the frequency-coherent case. The whole problem of frequency redistribution arises exclusively due to the presence of collisions in the atomic frame, and in addition due to Doppler shifts in the observer's frame, and to the circumstance that the Doppler and collisional redistributions get coupled in an intricate way. Once we have specified the collisional redistribution in the atomic frame, the transformation to the observer's frame, while being mathematically complicated, merely

involves the introduction of Doppler redistribution, which has nothing to do with the question of whether the atomic-frame redistribution has been treated with quantum or classical physics.

The whole question of redistribution therefore boils down to the question on how to treat the collisional redistribution in the general quantum mechanical case. The way that we did it in the classical case was to solve the time-dependent equation for an oscillating electron. When the oscillator equation was decomposed in complex spherical vectors, it decoupled into independent component equations, one for each  $q$ . The solution could then be expressed with two terms, one for the static and one for the transitory solution in the atomic frame. The frequency-coherent part  $R_{\text{II}}$  of the redistribution has its source in the stationary solution, while the complete redistribution part  $R_{\text{III}}$  has its source in the transitory solution.

In the classical collision theory of Stenflo (1994) and BS99 the effect of elastic collisions is to destroy the phase coherence by truncating the damped oscillation of the transitory solution (the stationary solution is not affected by the collisions, since it is driven by the incident electromagnetic field). This leads to both collisional broadening and to collisional depolarization ( $D^{(K)}$ ), with a depolarization rate that is half the broadening rate ( $\gamma_c$ ).

An immediate and natural phenomenological extension of the classical collision theory to general quantum transitions is to treat each radiative emission transition between magnetic substates  $m_b$  and  $m_f$ , which represents a given value of  $q$  in the quantum Eq. (7.55), as a damped oscillation that gets truncated by collisions. The subsequent Fourier transformation of this truncated oscillation then leads to the broadening and depolarization in exactly the same way as in the classical case. Therefore, when considering the scattering transitions for each individual combination of  $m$  states separately, the classical frequency redistribution theory can be carried over to be used directly.

In this way we have fully defined how the present theory can be generalized to any quantum scattering transitions. Although the classical and quantum cases behave the same for transitions between the individual  $m$  states, the two cases will differ considerably when the individual  $m$  state transitions are added together due to the different transition strengths and due to the different  $m_a \rightarrow m_f$  combinations in the geometric factors. These differences will be enhanced and convolved when the bilinear products between the Jones matrix elements are formed (see Eq. (8) of Stenflo 1998), which contain the various interference terms that describe the Hanle effect.

A further extension can be done to the case when the ground state acquires atomic polarization due to optical pumping. This is done by attaching the weight  $\rho_{m_a m_{a'}}$  to the bilinear products  $w_{\alpha\beta} w_{\alpha'\beta'}^*$  before summing over all the initial  $m$  states  $m_a$  and  $m_{a'}$ . Here  $\rho_{m_a m_{a'}}$  is a density matrix element of the initial state. When  $m_a$  equals  $m_{a'}$ , then  $\rho$  describes the  $m$  state population, when they are different it describes the  $m$  state coherences.  $\rho$  has to be found by solving the statistical equilibrium problem.

Although a full generalization of our polarized redistribution theory for arbitrary magnetic fields is thus rather straightforward, it does not easily lend itself to a comprehensive presentation in such an explicit analytical form, as we could do here for the special  $J = 0 \rightarrow 1 \rightarrow 0$  case. The various magnetic redistribution basis functions with their intrinsic symmetries that we have described for the special case, continue to be ingredients in any general quantum redistribution theory, although these basis functions will be combined and weighted differently from case to case, depending on the particular combination of quantum numbers. Nevertheless, the present work provides insight into the mathematical structure of the general case while elucidating the underlying physics.

## 7.6 Concluding remarks

The discovery of the wealth of structures in the Second Solar Spectrum has created an urgent need for new theoretical tools, which were not available before, since there had not been a concrete demand for them. Still the theory is severely lagging behind the observational developments. The full Second Solar Spectrum has been mapped with high spectral resolution and polarimetric sensitivity from 3100 – 7000 Å. The spatial and temporal variations of the scattering polarization in selected portions of the Second Solar Spectrum are being explored in various magnetic regions on the Sun, and narrow-band filter systems are being introduced to map the Hanle-Zeeman effect in different spectral lines (Feller et al. 2006). Many of these lines are strong chromospheric lines with both Doppler core and damping wings, and they offer great promise for diagnosing the magnetic field in the solar chromosphere via the Hanle effect. This promise can only be fulfilled if we have the right tools for a quantitative analysis of the observations. For chromospheric lines these tools need to account for partial frequency redistribution (PRD) of polarized radiation in the presence of magnetic fields of arbitrary strength and orientation. In the present chapter we have developed this theory in the form of the Hanle-Zeeman redistribution matrix, and we have explored its mathematical structure in detail.

Our PRD theory is based on a classical approach, via the solution of the time-dependent

classical oscillator equation. This might seem as a limited approach, and that a correct treatment should instead be in terms of quantum physics. However, as we will show explicitly in Chapter 8, our classical approach produces a Hanle-Zeeman redistribution matrix that is identical to that obtained with a perturbative quantum field theory for a  $J = 0 \rightarrow 1 \rightarrow 0$  scattering transition. All the mathematical functions that we have described in the present chapter, including all their intricate relations and symmetries, are obtained exactly via QED. This equivalence is far from obvious and instead rather miraculous, hinting at a deeper meaning, since the two formalisms are vastly different. Here we have used the classical approach, since it is (in our opinion) much more transparent and lends itself to a more intuitive understanding of the physics involved.

Several chromospheric spectral lines are of the type  $J = 0 \rightarrow 1 \rightarrow 0$ , that we have treated here. Examples are the well-studied Ca I 4227 Å line and the Cr I 3594 Å line, which is found (for still unknown reasons) to be the most polarizing line in the whole spectrum (from 3100 – 7000 Å) (Stenflo 2006). Most other lines have different quantum number structures, which means that the present PRD theory needs to be extended to cover these other cases. In the preceding section we have outlined how a straightforward extension can be done, and how the mathematical framework of the present chapter can be used as an ingredient of such a generalized theory. Since the theory can be discussed in a comprehensive way for the special  $J = 0 \rightarrow 1 \rightarrow 0$  case, we have limited our explicit treatment to this particular case, while showing how it may be generalized.

While we now have a well formulated and understood theory for the general Hanle-Zeeman redistribution matrix, its practical implementation within a polarized radiative-transfer framework will be a major challenge, in particular the development of numerical computer codes that can solve the polarized transfer problem with PRD for realistic magnetized atmospheres. The present chapter lays a foundation for progress toward this goal.



## Chapter 8

# Equivalence of classical and quantum redistribution matrix<sup>1</sup>

### 8.1 Introduction

Information about magnetic fields on the Sun and stars can be obtained through spectropolarimetric observations interpreted with polarized radiative transfer theory. A key component of this theory is the proper treatment of the scattering process, which leads to a complex coupling described through redistribution of the radiation in frequency, angle, and polarization. A general formulation of this scattering theory is not yet available, although it is urgently needed for all magnetic field diagnostics that make use of spectral lines for which scattering plays a role. In this part II of the thesis we aim at laying a foundation for this theory, which is centered around the Hanle-Zeeman redistribution matrix that is valid for the general case of partial frequency redistribution (PRD) in the presence of magnetic fields of arbitrary strength and direction. The term “Hanle-Zeeman” indicates that all field strengths are covered, from the weak (in the “Hanle regime”) to intermediate and strong (“Zeeman regime”) fields.

A quantum electrodynamic (QED) theory of Hanle-Zeeman redistribution matrices is developed in Bommier (1997a, 1997b, hereafter VB97a and VB97b respectively). The formulation presented in VB97a and VB97b includes the effects of PRD in line scattering for a two-level atom. In VB97b the laboratory frame (LF) expressions for the angle-dependent, as well as angle-averaged PRD matrices are already presented (see also Bommier 1999, 2003). The theory begins with a perturbative development for the atom-radiation interac-

---

<sup>1</sup>This chapter is based on the publication: Sampoorna, M., Nagendra, K. N., & Stenflo, J. O. 2007b, *ApJ*, 670, 1485-1503

tion. The PRD effects (introduced through the well known  $R_{\text{II}}$  and  $R_{\text{III}}$  LF redistribution functions of Hummer) appear in the fourth order. The perturbation development is then extended to infinite orders, leading to a series which when summed, converges to a result that agrees with the classical non-perturbative theory (Bommier & Stenflo 1999). The perturbation development of the atom-radiation interaction can be restricted to the second order in the case of complete frequency redistribution (CRD). Landi Degl’Innocenti & co-workers (see the book by Landi Degl’Innocenti & Landolfi 2004, and references cited therein) have developed such a CRD theory. Recently a quantum mechanical approach to derive the Hanle-Zeeman phase matrix only for ‘frequency coherent scattering in the LF’, in the presence of a uniform magnetic field and quadrupolar electric fields, has been presented in Yee Yee Oo et al. (2007, see also Yee Yee Oo 2004).

A classical theory of PRD in line scattering for the Hanle-Zeeman effect has been formulated by Bommier & Stenflo (1999, hereafter BS99). This non-perturbative theory, which is based on a time-dependent classical oscillator, describes the scattering process in a transparent way. The classical theory for Hanle-Zeeman scattering developed by Stenflo (1998) considered only coherent scattering in the LF. In BS99 the redistribution matrices were derived in the atomic rest frame. The corresponding LF redistribution matrices have been derived in Chapter 7. The historical developments and the modern perspectives on the theory of PRD in light scattering on atoms, in the presence of magnetic fields, have also been presented in Chapter 7. Therefore we do not repeat them here.

In the present chapter we establish the equivalence between the classical and QED redistribution matrices for the Zeeman triplet case. This equivalence is far from obvious, since the formalisms of the two theories are vastly different.

We start from the atomic frame expressions given in VB97b and derive the corresponding LF expressions in § 8.2. The equivalence between the classical and QED redistribution matrices for the triplet case is established in § 8.3. In § 8.4 we numerically validate both the classical (see Chapter 7) and the QED expressions derived in § 8.2, by comparing them with the redistribution scattering diagrams (which we call hereafter PRD diagrams) presented in VB97b. In § 8.5 we present Stokes  $I$  and the fractional polarization  $Q/I$ ,  $U/I$ , and  $V/I$  profiles for a singly scattered beam, which is incident on an atom immersed in a magnetic field of arbitrary strength. The dependence of polarization on field strength, and the influence of elastic collisions on the frequency redistribution are examined. The chapter ends with a brief summary with concluding remarks in § 8.6.



## 8.2 Quantum electrodynamic redistribution matrix in the lab frame

In order to establish the equivalence between classical and QED redistribution theories, we give an explicit analytic form of the LF QED redistribution matrices in terms of the magnetic redistribution functions introduced in Chapter 7. We start from Eqs. (49) and (52) of VB97b for  $\mathbf{R}^{\text{III}}$  and  $\mathbf{R}^{\text{II}}$  type matrices, respectively. For the simpler case of a triplet ( $J = 0 \rightarrow J' = 1$ ), with an infinitely sharp lower level, the total redistribution matrix can be written as

$$\mathbf{R}_{ij}(\xi, \mathbf{n}; \xi', \mathbf{n}'; \mathbf{B}) = \mathbf{R}_{ij}^{\text{II}}(\xi, \mathbf{n}; \xi', \mathbf{n}'; \mathbf{B}) + \mathbf{R}_{ij}^{\text{III}}(\xi, \mathbf{n}; \xi', \mathbf{n}'; \mathbf{B}), \quad (8.1)$$

where the  $(i, j)$ th element of the  $\mathbf{R}^{\text{II}}$  type matrix is given by

$$\begin{aligned} \mathbf{R}_{ij}^{\text{II}}(\xi, \mathbf{n}; \xi', \mathbf{n}'; \mathbf{B}) &= \sum_{K'K''Q} \frac{\Gamma_{\text{R}}}{\Gamma_{\text{R}} + \Gamma_{\text{I}} + \Gamma_{\text{E}} + i\omega_{\text{L}}g_{J'}Q} (-1)^Q \mathcal{T}_Q^{K''}(i, \mathbf{n}) \mathcal{T}_{-Q}^{K'}(j, \mathbf{n}') \\ &\times \delta(\xi - \xi') w_{J'J}^{(K'')} \Phi_Q^{K'',K'}(J, J'; \xi'), \end{aligned} \quad (8.2)$$

while the  $(i, j)$ th element of the  $\mathbf{R}^{\text{III}}$  type matrix is given by

$$\begin{aligned} \mathbf{R}_{ij}^{\text{III}}(\xi, \mathbf{n}; \xi', \mathbf{n}'; \mathbf{B}) &= \sum_{KK'K''Q} \frac{\Gamma_{\text{R}}}{\Gamma_{\text{R}} + \Gamma_{\text{I}} + D^{(K)} + i\omega_{\text{L}}g_{J'}Q} \frac{\Gamma_{\text{E}} - D^{(K)}}{\Gamma_{\text{R}} + \Gamma_{\text{I}} + \Gamma_{\text{E}} + i\omega_{\text{L}}g_{J'}Q} \\ &\times (-1)^Q \mathcal{T}_Q^{K''}(i, \mathbf{n}) \mathcal{T}_{-Q}^{K'}(j, \mathbf{n}') \Phi_Q^{K,K''}(J, J'; \xi) \Phi_Q^{K,K'}(J, J'; \xi'). \end{aligned} \quad (8.3)$$

In the above expressions  $g_{J'}$  is the Landé factor of the upper level  $J'$ ,  $\Gamma_{\text{R}}$  is the radiative deexcitation rate,  $\Gamma_{\text{I}}$  the inelastic collisional deexcitation rate, and  $\Gamma_{\text{E}}$  the elastic collisional rate, which is related to the  $2K$ -multipole destruction rate  $D^{(K)}$ . The index  $K$  takes values 0, 1, and 2, while  $Q$  varies in the range  $-K \leq Q \leq +K$ . The irreducible spherical tensors for polarimetry  $\mathcal{T}_Q^K(i, \mathbf{n})$  have been given by Landi Degl'Innocenti (1984, Appendix 1, Eq. (A6)). The generalized profile functions  $\Phi_Q^{K,K'}(J, J', \xi)$  have been defined in Landi Degl'Innocenti et al. (1991a). The incoming and outgoing radiation frequencies in the atomic rest frame are given by  $\xi'$  and  $\xi$ , respectively. The Larmor frequency  $\omega_{\text{L}} = 2\pi\nu_{\text{L}}$ . The quantity  $w_{J'J}^{(K'')}$  appearing in Eq. (8.2) is  $(-1)^{K''}$  for the triplet case.<sup>2</sup> To simplify the notation we denote  $g_{J'}$  by  $g$  as in Chapter 7.

---

<sup>2</sup>We note that below Eq. (24) of VB97b it is incorrectly stated that  $w_{J',J}^{K''} = 1$  for a normal Zeeman triplet.

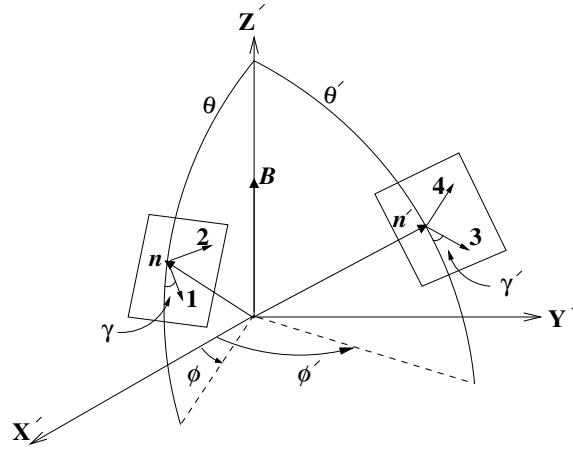


Figure 8.1: Magnetic reference frame (MRF) with magnetic field vector  $\mathbf{B}$  along the  $Z'$ -axis. The incoming ray  $\mathbf{n}'$  is characterized by  $(\theta', \phi', \gamma')$ , while the outgoing ray  $\mathbf{n}$  by  $(\theta, \phi, \gamma)$ . The symbols  $\mathbf{1}$  and  $\mathbf{2}$  are unit vectors in a plane perpendicular to  $\mathbf{n}$ , and  $\mathbf{3}$  and  $\mathbf{4}$  are corresponding unit vectors defined for  $\mathbf{n}'$ .

### 8.2.1 $\mathbf{R}^{\text{II}}$ type redistribution matrix in the lab frame

We derive analytical expressions for the LF  $\mathbf{R}^{\text{II}}$  type redistribution matrix, starting from Eq. (8.2). The irreducible tensors  $\mathcal{T}_Q^K(i, \mathbf{n})$  take a particularly simple form in a coordinate system in which the magnetic field is oriented along the polar axis  $Z'$ . It is preferable to work in such a coordinate system. We refer to it as magnetic reference frame (MRF). Figure 8.1 shows the scattering geometry in MRF. The incoming ray  $\mathbf{n}'$  is characterized by polar angles  $\theta'$  and  $\phi'$  with respect to MRF. Further to define the positive Stokes  $Q$  direction, we introduce two real unit vectors  $\mathbf{3}$  and  $\mathbf{4}$  in the plane perpendicular to  $\mathbf{n}'$ , in such a way that  $\mathbf{3}$  forms an angle  $\gamma'$  with the meridian plane that contains  $\mathbf{n}'$  and the  $Z'$ -axis (see Landi Degl'Innocenti 1983a). Similarly the outgoing ray  $\mathbf{n}$  is characterized by  $(\theta, \phi, \gamma)$ . Following Landi Degl'Innocenti & Landolfi (2004, hereafter LL04) we choose  $\gamma = \gamma' = 0$ , which means that the positive Stokes  $Q$  direction for both the incoming and scattered radiation coincide with the meridian plane of the MRF. Thus in the MRF the irreducible tensors are given by (see LL04, p. 208)

$$\mathcal{T}_Q^K(i, \mathbf{n}) = \sum_P t_P^K(i) \mathcal{D}_{PQ}^K(R), \quad (8.4)$$

where the elements  $t_P^K(i)$  are given in Table 5.5 of LL04,  $\mathcal{D}$  are rotation matrices and  $R \equiv (0, -\theta, -\phi)$ . The  $\mathcal{T}_Q^K(i, \mathbf{n})$  in the MRF are also listed in LL04 (p. 211).

The generalized profile function at frequency  $\xi$  of a line connecting the lower level  $J = 0$

to the upper level  $J' = 1$  is given by (see Landi Degl'Innocenti et al. 1991a)

$$\begin{aligned} \Phi_Q^{K,K'}(0, 1; \xi) &= \sum_{MM'} (-1)^{M+M'+Q} \sqrt{(2K+1)(2K'+1)} \begin{pmatrix} 1 & K & 1 \\ -M & Q & M' \end{pmatrix} \\ &\times \begin{pmatrix} 1 & 1 & K' \\ -M & M' & Q \end{pmatrix} \frac{1}{2} [\phi(\nu_{1M'00} - \xi) + \phi^*(\nu_{1M00} - \xi)]. \end{aligned} \quad (8.5)$$

The profile function  $\phi(\nu_{1M00} - \xi)$  is given by (see Eq. (2) of VB97b)

$$\phi(\nu_{1M00} - \xi) = \frac{1}{\pi} \frac{\delta_w + i(\nu_0 - \xi + g\nu_L M)}{\delta_w^2 + (\nu_0 - \xi + g\nu_L M)^2}, \quad (8.6)$$

where  $\nu_0$  is the line center frequency, and  $\delta_w = (\Gamma_R + \Gamma_I + \Gamma_E)/4\pi$ . The frequency redistribution part appearing in Eq. (8.2) is still in the atomic rest frame (see Eqs. (8.5) and (8.6)). It can be transformed to the LF as described in § 3.3 of VB97b (or as described in § 7.2.2). In the LF we define the following:

$$x = \frac{\nu_0 - \nu}{\Delta\nu_D}; \quad x_M = \frac{g\nu_L M}{\Delta\nu_D}, \quad (8.7)$$

where  $\nu$  is the scattered frequency in the LF and  $\Delta\nu_D$  the Doppler width. The damping parameter  $a$  is defined as

$$a = \frac{1}{4\pi} \frac{\Gamma_R + \Gamma_I + \Gamma_E}{\Delta\nu_D}. \quad (8.8)$$

Thus the function  $\delta(\xi - \xi')\phi(\nu_{1M00} - \xi)$  in the atomic frame transforms to  $R_{\text{II,H}}^{-q}(x, x', \Theta; B) + iR_{\text{II,F}}^{-q}(x, x', \Theta; B)$  in the LF, where  $\Theta$  is the scattering angle between the incident and scattered ray (see Fig. 8.2). The magnetic redistribution functions  $R_{\text{II,H}}^q$  and  $R_{\text{II,F}}^q$  (dropping the arguments for brevity) are defined in Eqs. (7.21) and (7.22), with  $q = -M$  taking values  $0, \pm 1$ . We denote the quantity  $\delta(\xi - \xi')\Phi_Q^{K'',K'}(0, 1; \xi')$ , after transforming it to the LF, as  $\Phi_{Q,\text{II}}^{K'',K'}(x, x', \Theta; B)$ , which we refer to as ‘composite redistribution functions’ because they are linear combination of magnetic redistribution basis functions. Thus, the  $\mathbf{R}^{\text{II}}$  type redistribution matrix in the LF may be written as

$$\mathbf{R}_{ij}^{\text{II}}(x, \mathbf{n}; x', \mathbf{n}'; \mathbf{B}) = \sum_{K''K'Q} \frac{A}{1 + iQ\Gamma''} (-1)^Q \mathcal{T}_Q^{K''}(i, \mathbf{n}) \mathcal{T}_{-Q}^{K'}(j, \mathbf{n}') w_{J'J}^{(K'')} \Phi_{Q,\text{II}}^{K'',K'}(x, x', \Theta; B). \quad (8.9)$$

The composite redistribution function of type II, namely  $\Phi_{Q,\text{II}}^{K'',K'}$  (dropping the arguments for brevity), are listed in Appendix H. In the above equation (see also Eqs. (88) and (89) of VB97b),

$$A = \frac{\Gamma_R}{\Gamma_R + \Gamma_I + \Gamma_E}; \quad \Gamma'' = \frac{g\omega_L}{\Gamma_R + \Gamma_I + \Gamma_E} = A\Gamma_B, \quad (8.10)$$

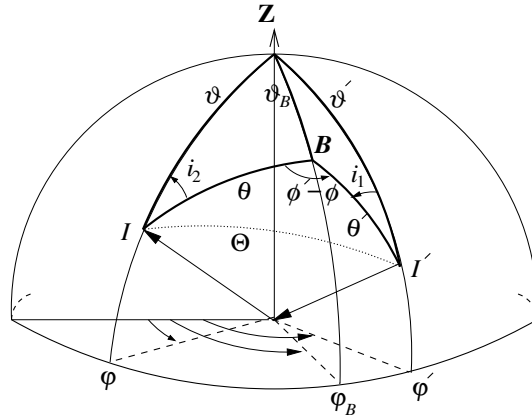


Figure 8.2: The geometry showing the scattering process in a coordinate system where the magnetic field makes an angle  $\vartheta_B$  with respect to the polar  $Z$ -axis taken as perpendicular to the planar slab atmosphere, and has an azimuth of  $\varphi_B$ . We refer to this coordinate system as the atmospheric reference frame (ARF).  $(\vartheta', \varphi')$  refer to the incident ray, and  $(\vartheta, \varphi)$  to the scattered ray in ARF.  $\Theta$  is the scattering angle.  $(\theta', \phi')$  refer to the incident ray, and  $(\theta, \phi)$  to the scattered ray in the MRF shown in Fig. 8.1.

where the Hanle  $\Gamma_B$  parameter is written as  $\Gamma_B = g\omega_L/\Gamma_R$ . To establish correspondence with the classical theory, we can now define the so called Hanle angles

$$\tan \beta_1 = \Gamma''; \quad \tan \beta_2 = 2\Gamma'', \quad (8.11)$$

which characterize the Hanle effect in the case of pure  $\mathbf{R}^{\text{II}}$  type redistribution.

Using the set of Eqs. (H.1)-(H.3), and expressions for  $\mathcal{T}_Q^K(i, \mathbf{n})$  as given in LL04 (p. 211) with a choice  $\gamma = \gamma' = 0$ , one can calculate all the elements of the  $\mathbf{R}^{\text{II}}$  type redistribution matrix, by performing the summations in Eq. (8.9). After elaborate algebra we find that the analytical expressions for the  $\mathbf{R}^{\text{II}}$  type redistribution obtained from the quantum electrodynamic and classical theories are identical.

### 8.2.2 $\mathbf{R}^{\text{III}}$ type redistribution matrix in the lab frame

The analytical expressions for the LF  $\mathbf{R}^{\text{III}}$  are derived starting from Eq. (8.3). The derivation is carried out in the MRF (see Fig. 8.1) for simplicity. Again the positive Stokes  $Q$  direction is defined by  $\gamma = \gamma' = 0$ . In Eq. (8.3) the product of two generalized profile functions appears. The generalized profile functions are calculated using Eq. (8.5). They are then transformed to the LF, as described in § 3.3 of VB97b (or as described in § 7.2.2).

We denote the product of two generalized profile functions  $\Phi_Q^{K,K''}(0, 1; \xi)\Phi_Q^{K,K'}(0, 1; \xi')$ , after transforming them to the LF, as  $\Phi_{Q,III}^{K,K'',K'}(x, x', \Theta; B)$ . This function is expressed in terms of the magnetic redistribution basis functions defined in Eqs. (7.23) - (7.26). For example  $\phi(\nu_{1M'00} - \xi)\phi(\nu_{1M00} - \xi')$  in the atomic rest frame transforms to

$$R_{III,HH}^{-q-q'} - R_{III,FF}^{-q-q'} + i\left(R_{III,HF}^{-q-q'} + R_{III, FH}^{-q-q'}\right)$$

in the LF, and  $\phi(\nu_{1M'00} - \xi)\phi^*(\nu_{1M00} - \xi')$  transforms to

$$R_{III,HH}^{-q-q'} + R_{III,FF}^{-q-q'} + i\left(R_{III,HF}^{-q-q'} - R_{III, FH}^{-q-q'}\right),$$

where  $R_{III,XY}^{qq'}$  with X and Y denoting the H and/ or F are defined in Eqs. (7.23) - (7.26). Thus, the  $\mathbf{R}^{III}$  type redistribution matrix in the LF may be written as

$$\begin{aligned} \mathbf{R}_{ij}^{III}(x, \mathbf{n}; x', \mathbf{n}'; B) &= \sum_{KK'K''Q} \frac{B^{(K)}}{(1+iQ\Gamma^{(K)})(1+iQ\Gamma^{(K'')})} (-1)^Q \mathcal{T}_Q^{K''}(i, \mathbf{n}) \mathcal{T}_{-Q}^{K'}(j, \mathbf{n}') \\ &\times \Phi_{Q,III}^{K,K'',K'}(x, x', \Theta; B). \end{aligned} \quad (8.12)$$

The composite redistribution functions of type III, namely  $\Phi_{Q,III}^{K,K'',K'}$  (dropping the arguments), are listed in Appendix H. In Eq. (8.12)

$$B^{(K)} = \frac{\Gamma_R}{\Gamma_R + \Gamma_I + D^{(K)}} \frac{\Gamma_E - D^{(K)}}{\Gamma_R + \Gamma_I + \Gamma_E}; \quad \Gamma^{(K)} = \frac{g\omega_L}{\Gamma_R + \Gamma_I + D^{(K)}} = r^{(K)}\Gamma_B, \quad (8.13)$$

where

$$r^{(K)} = \frac{\Gamma_R}{\Gamma_R + \Gamma_I + D^{(K)}}. \quad (8.14)$$

In this case, we obtain another set of Hanle angles

$$\tan \alpha_1^{(K)} = \Gamma^{(K)}; \quad \tan \alpha_2^{(K)} = 2\Gamma^{(K)}, \quad (8.15)$$

which give rise to Hanle rotation and depolarization in the case of pure  $\mathbf{R}^{III}$  type redistribution.

Using Eqs. (H.7) - (H.29) for  $\Phi_{Q,III}^{K,K'',K'}$  and the expressions for  $\mathcal{T}_Q^K(i, \mathbf{n})$  of LL04 (given in p. 211, with  $\gamma = \gamma' = 0$ ), one can calculate all the elements of the  $\mathbf{R}^{III}$  type redistribution matrix by performing the summations in Eq. (8.12). After tedious algebra, the final expression for the  $\mathbf{R}^{III}$  type Hanle-Zeeman redistribution matrix can be written as

$$\mathbf{R}^{III} = B^{(0)}\mathbf{M}_{III}^{(0)} + B^{(1)}\mathbf{M}_{III}^{(1)} + B^{(2)}\mathbf{M}_{III}^{(2)}, \quad (8.16)$$

where

$$\begin{aligned}
 \mathbf{M}_{\text{III}}^{(0)} = & \frac{1}{4} \left\{ (hh)_{00}^{\text{III}+} \mathbf{C}_0^0 + (hh)_{01}^{\text{III}+} \mathbf{D}_{01}^+ + (hh)_{10}^{\text{III}+} \mathbf{D}_{10}^+ + \frac{1}{2} \left[ (hh)_{11}^{\text{III}+} + (hh)_{1-1}^{\text{III}+} \right] \mathbf{D}_{11}^+ \right. \\
 & + \frac{1}{2} \left[ (hh)_{11}^{\text{III}+} - (hh)_{1-1}^{\text{III}+} \right] \mathbf{D}_{1-1}^+ + (hh)_{01}^{\text{III}-} \mathbf{D}_{01}^- + (hh)_{10}^{\text{III}-} \mathbf{D}_{10}^- + (hh)_{11}^{\text{III}-} \mathbf{D}_{11}^- \\
 & \left. + (hh)_{1-1}^{\text{III}-} \mathbf{D}_{1-1}^- \right\}, \tag{8.17}
 \end{aligned}$$

$$\begin{aligned}
 \mathbf{M}_{\text{III}}^{(1)} = & \frac{3}{8} \left\{ (hh)_{11}^{\text{III}-} \mathbf{D}_{11}^- - (hh)_{1-1}^{\text{III}-} \mathbf{D}_{1-1}^- + \frac{1}{2} \left[ (hh)_{11}^{\text{III}+} + (hh)_{1-1}^{\text{III}+} \right] \mathbf{D}_{1-1}^+ \right. \\
 & \left. + \frac{1}{2} \left[ (hh)_{11}^{\text{III}+} - (hh)_{1-1}^{\text{III}+} \right] \mathbf{D}_{11}^+ \right\} + \frac{3}{4} \sin \theta \sin \theta' \left[ c_1^{(1)\text{III}} \mathbf{F}_1^{(1)} + c_2^{(1)\text{III}} \mathbf{F}_2^{(1)} \right. \\
 & \left. + c_3^{(1)\text{III}} \mathbf{F}_3^{(1)} + c_4^{(1)\text{III}} \mathbf{F}_4^{(1)} + s_1^{(1)\text{III}} \mathbf{S}_1^{(1)} - s_3^{(1)\text{III}} \mathbf{S}_3^{(1)} - s_4^{(1)\text{III}} \mathbf{S}_4^{(1)} \right], \tag{8.18}
 \end{aligned}$$

$$\begin{aligned}
 \mathbf{M}_{\text{III}}^{(2)} = & \frac{1}{4} \left\{ 2(hh)_{00}^{\text{III}+} \mathbf{C}_0^0 - (hh)_{01}^{\text{III}+} \mathbf{D}_{01}^+ - (hh)_{10}^{\text{III}+} \mathbf{D}_{10}^+ + \frac{1}{4} \left[ (hh)_{11}^{\text{III}+} + (hh)_{1-1}^{\text{III}+} \right] \mathbf{D}_{11}^+ \right. \\
 & + \frac{1}{4} \left[ (hh)_{11}^{\text{III}+} - (hh)_{1-1}^{\text{III}+} \right] \mathbf{D}_{1-1}^+ - (hh)_{01}^{\text{III}-} \mathbf{D}_{01}^- - (hh)_{10}^{\text{III}-} \mathbf{D}_{10}^- + \frac{1}{2} (hh)_{11}^{\text{III}-} \mathbf{D}_{11}^- \\
 & \left. + \frac{1}{2} (hh)_{1-1}^{\text{III}-} \mathbf{D}_{1-1}^- \right\} + \frac{3}{4} \left[ c_{1-1}^{\text{III}} \mathbf{C}_+^2 + s_{1-1}^{\text{III}} \mathbf{S}_+^2 \right] + \frac{3}{4} \sin \theta \sin \theta' \left[ c_2^{(2)\text{III}} \mathbf{F}_1^{(1)} \right. \\
 & \left. + c_1^{(2)\text{III}} \mathbf{F}_2^{(1)} - c_4^{(2)\text{III}} \mathbf{F}_3^{(1)} - c_3^{(2)\text{III}} \mathbf{F}_4^{(1)} - s_2^{(2)\text{III}} \mathbf{S}_1^{(1)} - s_4^{(2)\text{III}} \mathbf{S}_3^{(1)} - s_3^{(2)\text{III}} \mathbf{S}_4^{(1)} \right]. \tag{8.19}
 \end{aligned}$$

The expressions for  $c_{1-1}^{\text{III}}$  and  $s_{1-1}^{\text{III}}$  that appear in Eq. (8.19) are given in Eqs. (G.3) and (G.4), also with  $\alpha_2$  appearing there now replaced by  $\alpha_2^{(2)}$ . The various auxiliary coefficients and matrices appearing in Eqs. (8.17) - (8.19) are listed in Appendix I.

The analytic expression for  $\mathbf{R}^{\text{III}}$  (Eqs. (8.16) - (8.19)) derived from QED is very different from the corresponding classical theory expression (see Eq. (7.46) with II replaced by III). The reason is that the branching ratios (that are phenomenologically imported from quantum theory) are not properly incorporated in the classical theory. The multipole index  $K$  on  $B^{(K)}$  was wrongly identified as  $|q - q'|$  in Stenflo (1994, p. 213). In Chapter 7, the  $B^{(K)}$ s are assumed to be indistinguishable (see Eq. (7.12)). In other words in Chapter 7 we have used  $D^{(0)} = D^{(1)} = D^{(2)}$ . This is not correct, since  $D^{(0)}$  is not equal to  $D^{(1)}$  or  $D^{(2)}$ , and in fact it is close to zero (since it relates to the inelastic collision rate, which is much smaller than the elastic collision rate that governs  $D^{(1)}$  and  $D^{(2)}$ ). This fact, that  $D^{(K)}$  is non-zero only for  $K = 1, 2$  and is always close to zero for  $K = 0$ , is also clearly stated in

BS99. However the index  $K$  is missing on symbol  $\mathcal{B}$  in BS99 (see their Eq. (41)), where it should read  $B^{(K)}$ . Thus, one has to distinguish between  $B^{(0)}$ ,  $B^{(1)}$ , and  $B^{(2)}$ . Therefore in Chapter 7, Eq. (7.45) and the first statement following Eq. (7.46), are valid only in the very restricted case of  $D^{(0)} = D^{(1)} = D^{(2)} = 0$ , namely complete neglect of the depolarizing elastic collisions. In section 8.3 we show the correct way of including  $B^{(K)}$ s in the classical theory and then establish the equivalence between the classical and quantum theories.

### 8.3 Equivalence of the classical and quantum expressions for $\mathbf{R}$

In order to establish the equivalence between the classical and quantum expressions for the redistribution matrix, particularly in the case of  $\mathbf{R}^{\text{III}}$  type redistribution, we need to properly include the branching ratios  $B^{(K)}$  into the classical theory. The only way to do this is to expand the redistribution matrix  $\mathbf{R}$  as a sum of its multipole components  $\mathbf{R}^{(K)}$  (see eg. Eq. (5.137) of LL04 for the weak field case). Then we can properly assign the correct depolarization factor with  $D^{(K)}$  (and thereby branching ratios  $B^{(K)}$ ) to the corresponding  $\mathbf{R}^{(K)}$  components. This expansion of  $\mathbf{R}$  in terms of multipole components is for a  $J = 0$  to 1 transition a matter of pure geometry. Therefore the multipole expansion can be seen simply as an extension of the classical theory, not a take-over or borrowing from quantum mechanics. It is only the actual expressions for the branching ratios  $B^{(K)}$  for the various multipoles that are phenomenologically imported from quantum mechanics.

The way to achieve the multipole expansion is to introduce the irreducible spherical tensors  $\mathcal{T}_Q^K$  as described in the book by Landi Degl'Innocenti & Landolfi (2004), into the classical formalism of Stenflo (1994, hereafter S94) for the weak field Hanle case, and BS99 (see also Chapter 7) for the intermediate field Hanle-Zeeman case. In Appendix J we take the example of weak field, and describe the procedure to include irreducible spherical tensors into the classical theory of S94.

We can extend the procedure described in Appendix J to the classical theory of BS99 (see also Chapter 7) for the Hanle-Zeeman case. Substituting Eq. (J.1) in Eqs. (7) and (8) of BS99, we get

$$E_\mu \sim \sum_{\rho q} \frac{r_q(t, \xi')}{E'_{q,0}} (e_\mu(\mathbf{n}))_q^* (e_\rho(\mathbf{n}'))_q E'_\rho, \quad (8.20)$$

where  $r_q(t, \xi')$  is the time-dependent solution of the classical oscillator (see Eqs. (7.1) - (7.3)), and  $E'_{q,0}$  is the amplitude of the  $q$ th spherical component of the incoming monochromatic plane wave. Now the elements of the coherency matrix may be written in the atomic

frame as

$$I_{\mu\nu}^S = \sum_{\rho\sigma} T_{\mu\nu,\rho\sigma}^S(\xi, \mathbf{n}, \xi', \mathbf{n}', \mathbf{B}) I_{\rho\sigma}^{S'} \quad (8.21)$$

where

$$T_{\mu\nu,\rho\sigma}^S(\xi, \mathbf{n}, \xi', \mathbf{n}', \mathbf{B}) = \sum_{qq'} \left[ \frac{r_q(t, \xi') r_{q'}^*(t, \xi)}{E'_{q,0} E_{q',0}^*} \right] (e_\mu(\mathbf{n}))_q^* (e_\nu(\mathbf{n}))_{q'} (e_\rho(\mathbf{n}'))_q (e_\sigma(\mathbf{n}'))_{q'}^*. \quad (8.22)$$

Following BS99 and Chapter 7, we replace the term in the square bracket by  $\langle \tilde{r}_q \tilde{r}_{q'}^* \rangle$ , and using the reducible tensor  $\mathcal{E}_{qq'}^S$  defined in Eq. (J.6), we may re-write Eq. (8.22) as

$$T_{\mu\nu,\rho\sigma}^S(\xi, \mathbf{n}, \xi', \mathbf{n}', \mathbf{B}) = \frac{3}{2} \sum_{qq'} \langle \tilde{r}_q \tilde{r}_{q'}^* \rangle \mathcal{E}_{qq'}^S(\mu, \nu, \mathbf{n}) \mathcal{E}_{q'q}^S(\sigma, \rho, \mathbf{n}'). \quad (8.23)$$

The expression for  $\langle \tilde{r}_q \tilde{r}_{q'}^* \rangle$  in the atomic and laboratory frames are given in Eqs. (7.5) and (7.36) respectively.

Following the procedure described in Appendix J, we may obtain an expression for the Hanle-Zeeman redistribution matrix in terms of irreducible spherical tensors. The total redistribution matrix is then given by Eq. (8.1), with the type II and III redistribution in the atomic frame given respectively by

$$\begin{aligned} \mathbf{R}_{ij}^{\text{II}}(\xi, \mathbf{n}; \xi', \mathbf{n}'; \mathbf{B}) &= \sum_{K'K''Q} A \cos \beta_Q e^{i\beta_Q} (-1)^Q \left[ \mathcal{T}_Q^{K''}(i, \mathbf{n}) \right]^S \left[ \mathcal{T}_{-Q}^{K'}(j, \mathbf{n}') \right]^S \\ &\times \left[ \sum_{qq'} \sqrt{(2K'+1)(2K''+1)} \begin{pmatrix} 1 & 1 & K'' \\ q & -q' & -Q \end{pmatrix} \begin{pmatrix} 1 & 1 & K' \\ q' & -q & Q \end{pmatrix} \delta(\xi - \xi') \Phi_{qq'}^{\gamma+\gamma_c}(\xi') \right], \quad (8.24) \end{aligned}$$

$$\begin{aligned} \mathbf{R}_{ij}^{\text{III}}(\xi, \mathbf{n}; \xi', \mathbf{n}'; \mathbf{B}) &= \sum_{K'K''Q} \mathcal{B} \cos \beta_Q \cos \alpha_Q e^{i(\beta_Q + \alpha_Q)} (-1)^Q \left[ \mathcal{T}_Q^{K''}(i, \mathbf{n}) \right]^S \left[ \mathcal{T}_{-Q}^{K'}(j, \mathbf{n}') \right]^S \\ &\times \left[ \sum_{qq'} \sqrt{(2K'+1)(2K''+1)} \begin{pmatrix} 1 & 1 & K'' \\ q & -q' & -Q \end{pmatrix} \begin{pmatrix} 1 & 1 & K' \\ q' & -q & Q \end{pmatrix} \Phi_{qq'}^{\gamma+\gamma_c}(\xi') \Phi_{qq'}^{\gamma+\gamma_c}(\xi) \right], \quad (8.25) \end{aligned}$$

where  $A$  and  $\mathcal{B}$  are branching ratios (see Eqs. (7.11) and (7.12)). The classical Hanle angles  $\beta_Q$  and  $\alpha_Q$  with  $Q = q - q'$  appearing in the above equations are defined in Eqs. (7.6) and (7.7). Also the generalized profile function  $\Phi_{qq'}^{\gamma+\gamma_c}(\xi)$  is defined in Eqs. (7.8) - (7.10). To avoid ambiguity we call  $\Phi_{qq'}^{\gamma+\gamma_c}(\xi)$  the classical generalized profile function.



### 8.3.1 The type III redistribution

We first consider the redistribution of type III in order to show the equivalence between the classical and QED expressions (of VB97b). To achieve this we need to carry out the multipole expansion of the classical generalized profile function. This is done as explained below.

Comparing Eqs. (7.10) and (8.6), we see that  $M = -q$ , and

$$\Phi_{\gamma+\gamma_c}(\nu_q - \xi) = \phi^*(\nu_{1-q00} - \xi). \quad (8.26)$$

The above equation gives the relation between the profile functions defined in BS99 and VB97b. Using Eqs. (7.8) and (8.26), we may re-write the term in the bottom square bracket of Eq. (8.25), as

$$\begin{aligned} & \sum_{qq'} \sqrt{(2K'+1)(2K''+1)} \begin{pmatrix} 1 & 1 & K'' \\ q & -q' & -Q \end{pmatrix} \begin{pmatrix} 1 & 1 & K' \\ q' & -q & Q \end{pmatrix} \\ & \times \frac{1}{2} [\phi(\nu_{1-q'00} - \xi) + \phi^*(\nu_{1-q00} - \xi)] \frac{1}{2} [\phi(\nu_{1-q'00} - \xi') + \phi^*(\nu_{1-q00} - \xi')]. \end{aligned} \quad (8.27)$$

Now replacing  $-q$  by  $M$  and  $-q'$  by  $M'$ , as well as  $Q$  by  $-Q$  (since  $Q = q - q'$ ), in the above equation we obtain

$$\begin{aligned} & \sum_{MM'} \sqrt{(2K'+1)(2K''+1)} \begin{pmatrix} 1 & 1 & K'' \\ -M & M' & Q \end{pmatrix} \begin{pmatrix} 1 & 1 & K' \\ -M & M' & Q \end{pmatrix} \\ & \times \frac{1}{2} [\phi(\nu_{1M'00} - \xi) + \phi^*(\nu_{1M00} - \xi)] \frac{1}{2} [\phi(\nu_{1M'00} - \xi') + \phi^*(\nu_{1M00} - \xi')], \end{aligned} \quad (8.28)$$

where we have made use of properties of 3- $j$  symbols that involve sign changes and permutations.

The Eq. (22) of VB97b, for the particular case of a triplet ( $0 \rightarrow 1 \rightarrow 0$  transition) may be written as

$$\begin{aligned} & \sum_K \Phi_Q^{K,K''}(0, 1; \xi) \Phi_Q^{K,K'}(0, 1; \xi') = \sum_{MM'} \sqrt{(2K'+1)(2K''+1)} \begin{pmatrix} 1 & 1 & K'' \\ -M & M' & Q \end{pmatrix} \\ & \times \begin{pmatrix} 1 & 1 & K' \\ -M & M' & Q \end{pmatrix} \frac{1}{2} [\phi(\nu_{1M'00} - \xi) + \phi^*(\nu_{1M00} - \xi)] \frac{1}{2} [\phi(\nu_{1M'00} - \xi') + \phi^*(\nu_{1M00} - \xi')]. \end{aligned} \quad (8.29)$$

Comparing Eq. (8.28) with the r.h.s. of Eq. (8.29), we see that they are the same. Hence Eq. (8.25) may be re-written as (remembering that we have to change  $Q$  to  $-Q$ , see the

sentence following Eq. (8.27)),

$$\begin{aligned} \mathbf{R}_{ij}^{\text{III}}(\xi, \mathbf{n}; \xi', \mathbf{n}'; \mathbf{B}) &= \sum_{KK'K''Q} B^{(K)} \cos \beta_Q \cos \alpha_Q^{(K)} e^{-i(\beta_Q + \alpha_Q^{(K)})} \\ &\times (-1)^Q \left[ \mathcal{T}_{-Q}^{K''}(i, \mathbf{n}) \right]^S \left[ \mathcal{T}_Q^{K'}(j, \mathbf{n}') \right]^S \Phi_Q^{K, K''}(0, 1; \xi) \Phi_Q^{K, K'}(0, 1; \xi'). \end{aligned} \quad (8.30)$$

Thus the multipole index  $K$  now properly gets assigned to the classical branching ratio  $\mathcal{B}$ . Note that the multipole index  $K$  is included in the classical Hanle angle  $\alpha_Q$  also, following the identification done in BS99, namely  $D^{(K)} = \Gamma_E/2$  for  $K = 1, 2$ . This identification ensures that the classical Hanle angles  $\alpha$  for the emission process also depend on the multipole index  $K$ , unlike in BS99 and Chapter 7. Using Eq. (J.22), we may re-write Eq. (8.30) in terms of irreducible tensors of LL04 (dropping the ‘L’ on irreducible tensor) as

$$\begin{aligned} \mathbf{R}_{ij}^{\text{III}}(\xi, \mathbf{n}; \xi', \mathbf{n}'; \mathbf{B}) &= \sum_{KK'K''Q} B^{(K)} \cos \beta_Q \cos \alpha_Q^{(K)} e^{-i(\beta_Q + \alpha_Q^{(K)})} (-1)^Q \mathcal{T}_Q^{K''}(i, \mathbf{n}) \mathcal{T}_{-Q}^{K'}(j, \mathbf{n}') \\ &\times \Phi_Q^{K, K''}(0, 1; \xi) \Phi_Q^{K, K'}(0, 1; \xi'). \end{aligned} \quad (8.31)$$

The above equation is the same as Eq. (8.3), which thereby establishes the equivalence between the classical and quantum expressions in the case of type III redistribution. In Eq. (8.3), the Hanle angles are implicitly contained inside the branching ratios (see Eqs. (8.10), (8.11), (8.13), (8.14), and (8.15)).

### 8.3.2 The type II redistribution

We now consider the redistribution of type II in order to show the equivalence between the classical and QED expressions in the atomic frame. Using Eq. (8.26), we may re-write the term in the bottom square bracket of Eq. (8.24), as

$$\begin{aligned} \sum_{qq'} \sqrt{(2K'+1)(2K''+1)} \begin{pmatrix} 1 & 1 & K'' \\ q & -q' & -Q \end{pmatrix} \begin{pmatrix} 1 & 1 & K' \\ q' & -q & Q \end{pmatrix} \\ \times \delta(\xi - \xi')^{\frac{1}{2}} [\phi(\nu_{1-q'00} - \xi') + \phi^*(\nu_{1-q00} - \xi')]. \end{aligned} \quad (8.32)$$

Again in the above equation, we replace  $-q$  by  $M$ ,  $-q'$  by  $M'$ , as well as  $Q$  by  $-Q$  (since  $Q = q - q'$ ), and use the properties of 3- $j$  symbols (see LL04, p. 38). The resulting equation is then compared with the r.h.s. of Eq. (8.5), so that we may re-write Eq. (8.32) as

$$w_{j', j}^{(K'')} \delta(\xi - \xi') \Phi_Q^{K'', K'}(0, 1; \xi'). \quad (8.33)$$

We note that the factor  $(-1)^{M+M'+Q}$  appearing in Eq. (8.5) is unity, since  $Q = M - M'$  (and  $M, M'$  are always integers for the triplet case). As mentioned before,  $w_{J'J}^{(K'')} = (-1)^{K''}$  in the triplet case. Thus we may re-write Eq. (8.24) in terms of the irreducible tensors of LL04 (dropping the 'L' on irreducible tensor, and remembering that  $Q$  should be changed to  $-Q$ ) as

$$\begin{aligned} \mathbf{R}_{ij}^{\text{II}}(\xi, \mathbf{n}; \xi', \mathbf{n}'; \mathbf{B}) &= \sum_{K'K''Q} A \cos \beta_Q e^{-i\beta_Q} (-1)^Q \mathcal{T}_Q^{K''}(i, \mathbf{n}) \mathcal{T}_{-Q}^{K'}(j, \mathbf{n}') \\ &\times w_{J',J}^{(K'')} \delta(\xi - \xi') \Phi_Q^{K'',K'}(0, 1; \xi'). \end{aligned} \quad (8.34)$$

The above equation is exactly the same as Eq. (8.2), which thereby establishes the equivalence between the classical and quantum expressions in the case of type II redistribution. Once again it is necessary to remember that in Eq. (8.2) the Hanle angles are implicitly built into the branching ratios (see Eqs. (8.10) and (8.11)).

## 8.4 Numerical evidence for the equivalence of classical and quantum R

In the previous sections we established the analytical correspondence between the classical and QED expressions. In the present section we demonstrate numerically the equivalence by making PRD diagrams which are similar to those presented in VB97b. For this purpose we use the same input parameters as in VB97b. Note that the explicit expressions for the redistribution matrix derived in Chapter 7 (from classical theory) as well as in the present chapter (from QED theory of VB97b) refer to scattering in the MRF (see Fig. 8.1). However for comparison with observations, the Stokes profiles need to be presented in an atmospheric reference frame (see Fig. 8.2). In the present chapter the single scattered Stokes profiles are computed for an arbitrary orientation of the magnetic field with respect to the polar  $Z$ -axis, which is chosen along the vertical direction in the atmosphere. We refer to such a geometry as atmospheric reference frame (ARF, see Fig. 8.2). The transformation between the MRF and ARF is described in Appendix K.

The magnetic field is characterized by the Hanle  $\Gamma_B$  parameter in the quantum calculations, while in the classical calculations it is characterized by the parameter  $v_B$  (i.e., the magnetic shift from the line center in Doppler width units). The two parameters are related through

$$v_B = 2\Gamma_B a_R, \quad (8.35)$$

where  $a_R = \Gamma_R / (4\pi\Delta\nu_D)$ , which is related to the total damping parameter  $a$  of Eq. (8.8)

through

$$a_{\text{R}} = \frac{a}{1 + (\Gamma_{\text{I}} + \Gamma_{\text{E}})/\Gamma_{\text{R}}}. \quad (8.36)$$

The classical analogue of Eq. (8.8) is

$$a_{\text{cl}} = \frac{\gamma + \gamma_c}{4\pi\Delta\nu_{\text{D}}}. \quad (8.37)$$

Comparing Eqs. (8.8) and (8.37), we see that  $\gamma = \Gamma_{\text{R}} + \Gamma_{\text{I}}$  and  $\gamma_c = \Gamma_{\text{E}}$ . In the numerical computation we give as input model parameters the ratios  $\Gamma_{\text{E}}/\Gamma_{\text{R}}$ ,  $D^{(K)}/\Gamma_{\text{R}}$  and scattering parameter  $\epsilon (= \Gamma_{\text{I}}/(\Gamma_{\text{I}} + \Gamma_{\text{R}}))$ . The branching ratios  $A$  and  $B^{(K)}$  can be expressed in terms of  $\epsilon$  and the ratios of the collision rates mentioned above.

Most of the figures presented in VB97b have been computed for the absence of inelastic collisions (i.e.,  $\Gamma_{\text{I}} = 0$ , which implies  $\epsilon = 0$ ), and depolarizing collision rate  $D^{(K)} = 0$ , while the elastic collision rate  $\Gamma_{\text{E}} = \gamma_c$  is chosen as a free parameter. Even though this choice is physically inconsistent (since  $\Gamma_{\text{E}}$  is always proportional to  $D^{(K)}$  for  $K = 1, 2$ ), we employ it for the purpose of mathematical comparison with PRD benchmark diagrams presented in VB97b. Unless otherwise stated we present our results for the same choice of branching ratios as in VB97b. Thus  $\Gamma_{\text{R}} = \gamma$  and

$$A = \frac{1}{1 + \gamma_c/\gamma}, \quad (8.38)$$

$$\mathcal{B} = B^{(K)} = \frac{\gamma_c/\gamma}{1 + \gamma_c/\gamma} = 1 - A. \quad (8.39)$$

In the absence of inelastic collisions the classical Hanle angles can be computed using (see Eqs. (7.6) and (7.7)),

$$\tan \beta_{q-q'} = \frac{(q - q')v_{\text{B}}}{2a}, \quad (8.40)$$

$$\tan \alpha_{q-q'} = \frac{(q - q')v_{\text{B}}}{2a_{\text{R}} \left[ 1 + \gamma_c/(2\gamma) \right]}. \quad (8.41)$$

For the  $D^{(K)} = \gamma_c/2 = 0$  case, Eq. (8.41) reduces to

$$\tan \alpha_{q-q'} = \frac{(q - q')v_{\text{B}}}{2a_{\text{R}}} = (q - q')\Gamma_{\text{B}}. \quad (8.42)$$

In Eq. (8.42) one can clearly see the correspondence between the classical ‘Hanle angle  $\alpha_{q-q'}$ ’ and the quantum ‘Hanle parameter  $\Gamma_{\text{B}}$ ’, both of which are related to the field strength.

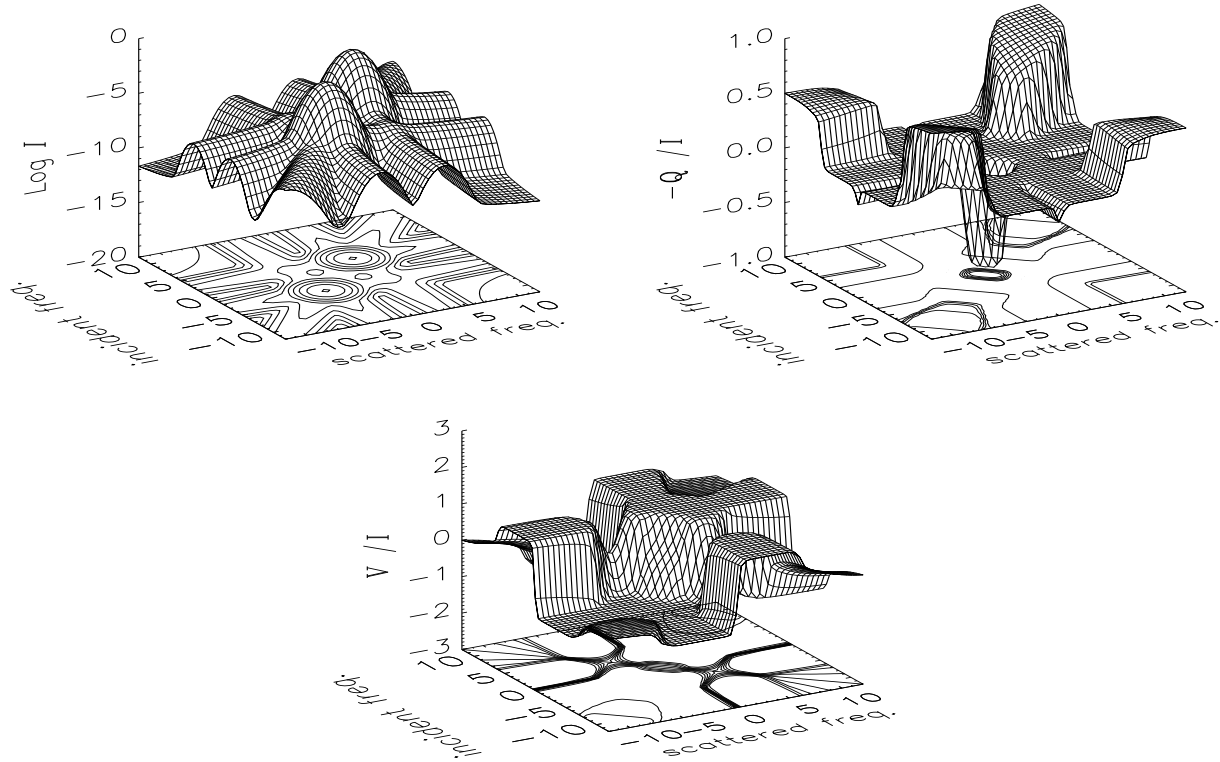


Figure 8.3: Stokes parameters vs. incident frequency  $x'$  and scattered frequency  $x$ , as produced in a  $90^\circ$  single scattering event involving a pencil of unpolarized incident radiation. The model parameters are  $[a, v_B, \Theta; \epsilon, \Gamma_E/\Gamma_R, D^{(K)}/\Gamma_R] = [10^{-3}, 3, 90^\circ; 0, 1, 0]$ . This combination of parameters corresponds to an equal mix of both  $\mathbf{R}^{\text{III}}$  and  $\mathbf{R}^{\text{II}}$  type redistribution (since  $A = 0.5$ ).  $U/I$  is zero for the geometry chosen by us.  $V/I$  stays within the range  $(-1, +1)$ , although we use a z-scale  $(-3, +3)$  in order to avoid overlapping of surface and contour plots. The magnetic field is along the line-of-sight.

In order to numerically prove the equivalence between our classical theory expressions with those of QED, we have reproduced Figs. 1 - 7 of VB97b, which refer to angle-dependent PRD. The classical PRD diagrams are found to agree in all details with those obtained from QED. Here we choose to illustrate only the reproduction of Fig. 14 in VB97b, which refers to the interesting case of Rayleigh scattering in strong fields (see § 6 of VB97b), with the field strength given by  $v_B = 3$ . The following is the set of standard model parameters chosen to compute the results shown in Fig. 8.3: damping parameter  $a = 10^{-3}$ , Hanle parameter  $\Gamma_B = 1$ , inelastic collision rate  $\Gamma_I = 0$  (purely scattering medium), depolarizing collision rate  $D^{(K)} = 0$ , scattering parameter  $\epsilon = 0$  (as follows from  $\Gamma_I = 0$ ). The magnetic field is chosen to be oriented along the scattered ray. This choice ( $\vartheta_B = \vartheta$ ,  $\varphi_B = \varphi$ ) corresponds

to the maximum impact of the Hanle effect on line scattering. The Stokes parameters for a single scattering event are simply given by the first column of the redistribution matrix.

In the geometry considered for all the illustrations in VB97b (magnetic field along the line-of-sight),  $V/I$  is very small (nearly zero) as long as the magnetic field is very weak, but for a longitudinal field as strong as  $v_B = 3$ , the ratio  $V/I$  is very large. However, the  $V/I$  profile for this particular case is not presented in VB97b. In Fig. 8.3 we reproduce Fig. 14 of VB97b and in addition present the  $V/I$  profile. The surface plots of  $[\log I, -Q/I, V/I]$  in Fig. 8.3 show the  $(x, x')$  dependence of the first column of the actual redistribution matrix. The contour plot below each surface plot depicts the so-called two-dimensional ‘domain structure’ in the  $(x, x')$  space. These contours are expected to be lines of constant values of  $[\log I, -Q/I, V/I]$  at selected contour levels. We would like to recall that our definition of ‘positive Q direction’ differs from that of VB97b whose  $(Q/I, U/I)$  plots differ from our plots only in the sign and not in magnitude. This simply arises due to our particular choice for the definition of the angles  $\gamma$  and  $\gamma'$  in the MRF (see § 8.2.1 and Fig. 8.1).

## 8.5 Hanle-Zeeman scattering of an unpolarized incident flat spectrum

In the present section we discuss how an atom immersed in a radiation field that is frequency independent across the spectral line produces line polarization through Hanle-Zeeman line scattering. We choose the magnitude of the incident intensity to be unity. Integration over  $x'$  can then readily be done. Branching ratios are chosen in such a way that we cover both the regimes of ‘purely coherent’ and the ‘completely non-coherent’ scattering. In contrast to VB97b, who gives the total damping parameter  $a$  as input, we prefer to give the radiative damping parameter  $a_R$  as input. It is indeed advantageous to keep  $a_R$  fixed for a given line, whose total damping width then changes depending on the rate of elastic collisions, given by the ratio  $\Gamma_E/\Gamma_R$ . As in VB97b, we assume the inelastic collision rate to be zero (i.e., a pure scattering medium). The elastic collisions only change the correlations between the incident and scattered photons, but do not induce a transition.

In Fig. 8.4 we show the  $x'$  - integrated Stokes  $I$  and fractional polarizations  $Q/I$ ,  $U/I$ , and  $V/I$ . The model parameters used are:  $[a_R, \vartheta_B, \varphi_B, \Theta; \epsilon, D^{(K)}/\Gamma_R] = [0.004, 90^\circ, 45^\circ, 90^\circ; 0, 0]$ . We present the scattered Stokes profiles for several values of the field strength parameter  $v_B$ . The parameters chosen are the same as in Fig. 3 of Stenflo (1998). The Hanle  $\Gamma_B$  parameter corresponding to various values of  $v_B$  are:  $[0.1, 0.5, 2.5, 12.5, 62.5, 125, 312.5]$ , spanning a dynamic range of 3125, between the highest and lowest field strengths. Fig-

ure 8.4a corresponds to a pure  $\mathbf{R}^{\text{II}}$  type scattering ( $\Gamma_{\text{E}}/\Gamma_{\text{R}} = 0$ ), and Fig. 8.4b to an equally mixed  $\mathbf{R}^{\text{II}}$  and  $\mathbf{R}^{\text{III}}$  type scattering ( $\Gamma_{\text{E}}/\Gamma_{\text{R}} = 1$ ). Figure 8.4c corresponds to the case of  $\Gamma_{\text{E}}/\Gamma_{\text{R}} = 999$ , i.e., the almost pure  $\mathbf{R}^{\text{III}}$  type scattering. Since the effect of collisions is more clearly visible in the fractional polarization profiles, we present them instead of the Stokes parameters themselves.

The scattered polarization profiles in Fig. 8.4a (for  $A = 1$ ) resemble the corresponding profiles of Fig. 3 of Stenflo (1998). Indeed the  $(Q/I, U/I, V/I)$  profiles closely agree with his results throughout the line profiles. This is not surprising, because Stenflo (1998, Fig. 3) assumed pure coherent scattering in the LF, which is a good approximation to the pure  $\mathbf{R}^{\text{II}}$  type scattering especially in the line wings.

Figure 8.4b refers to the case of an equal mix of  $\mathbf{R}^{\text{II}}$  and  $\mathbf{R}^{\text{III}}$  type scattering. We note that the  $I$  and  $V/I$  profiles do not differ from those of pure  $\mathbf{R}^{\text{II}}$  type scattering. The fractional polarizations  $Q/I$  and  $U/I$  in the line core region  $|x| \leq 2$  resemble the corresponding profiles of the pure  $\mathbf{R}^{\text{II}}$  case. However, in the line wing there is a substantial difference as compared with Fig. 8.4a. Clearly  $Q/I$  does not approach unity, and  $U/I$  is non-zero in the wing (showing that the scattering does not approach the Rayleigh limit for which  $Q/I = -1$  and  $U/I = 0$ ). We refer to this  $Q/I \neq -1$  and  $U/I \neq 0$  in the wings of a pure line case (without the presence of continuum absorption and scattering), as wing Hanle-effect – arising due to an elastic collision transferring the Hanle rotation from the line core to the line wing, before an inelastic polarization destroying collision intervenes. This transfer of coherence is most effective when  $\Gamma_{\text{E}}/\Gamma_{\text{R}} = 1$  (see Fig. 7 of Nagendra et al. 2002). In other words, in the presence of a small number of elastic collisions, the Hanle effect does not vanish in the line wings contrary to the standard assumption (employing a Rayleigh phase matrix for  $|x| > 3$ ) used in Hanle scattering computations. The VB97b theory for the Hanle effect in domain based form was included by Nagendra et al. (2002, see also Nagendra et al. 2003) in line transfer computations, which showed how the wing Hanle effect arises due to the presence of elastic collisions, in combination with PRD in Hanle scattering. The present single scattering calculations based on a more general Hanle-Zeeman scattering matrix confirm this prediction.

Figure 8.4c refers to the case of almost pure  $\mathbf{R}^{\text{III}}$  type scattering ( $\Gamma_{\text{E}}/\Gamma_{\text{R}} = 999$ ). The total damping parameter corresponding to this case is  $a = 4$  (see Eq. (8.36)). Clearly this corresponds to a regime of extremely large line broadening, which shows up in all the Stokes profiles. As a result the triplet structure is no longer visible even when  $v_B = 2.5$  (see the thin long-dashed line in Fig. 8.4c). For the same reason the magnitude of  $I$  is

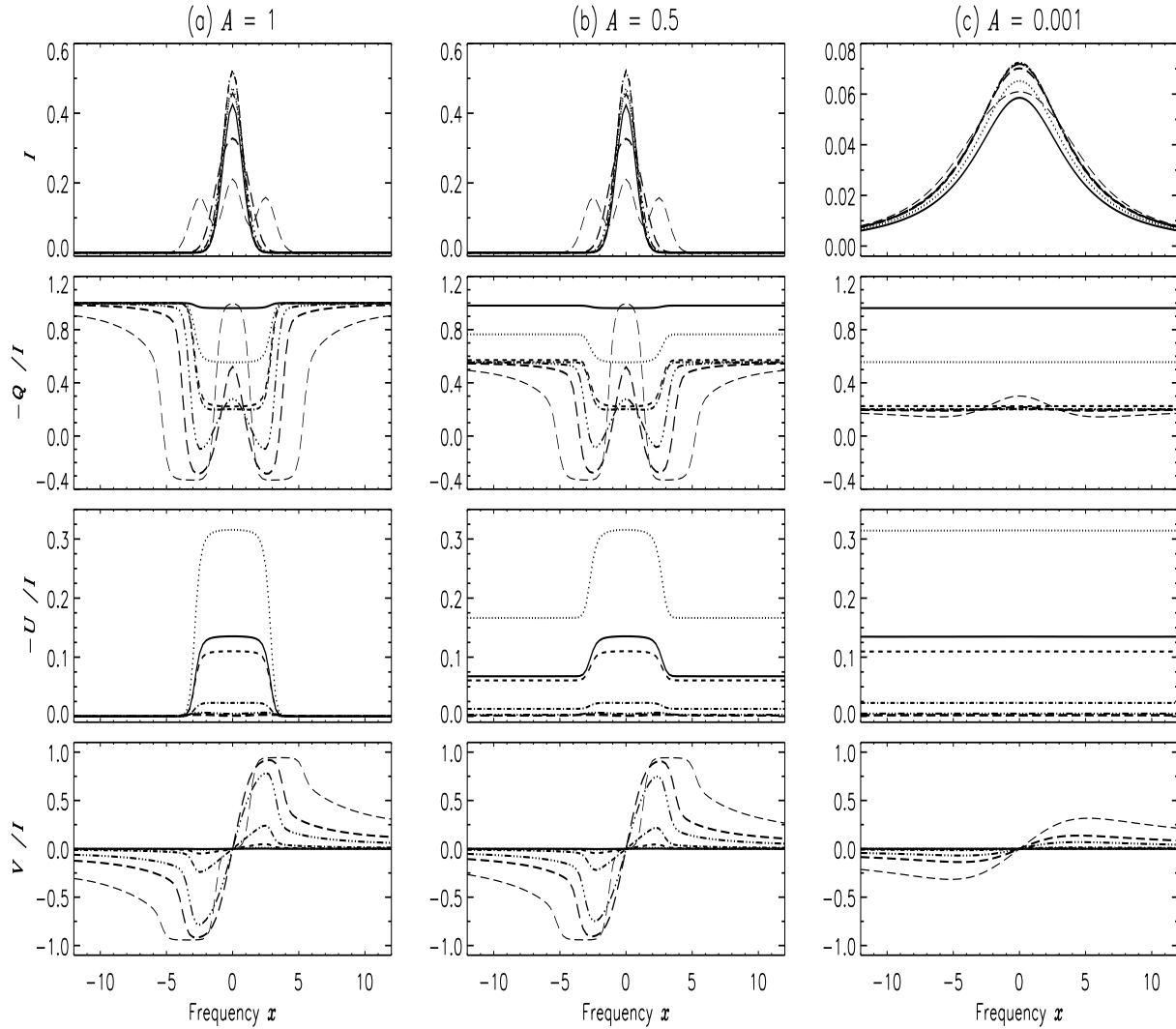


Figure 8.4: Stokes profile  $I$  and the fractional polarization profiles  $Q/I$ ,  $U/I$ , and  $V/I$  after integration over the incoming frequencies ( $x'$ ). The model parameters are:  $[a_R, \vartheta_B, \varphi_B, \Theta; \epsilon, D^{(K)}/\Gamma_R] = [0.004, 90^\circ, 45^\circ, 90^\circ; 0, 0]$ . Different line types correspond to  $v_B = 0.0008$  (solid), 0.004 (dotted), 0.02 (dashed), 0.1 (dot-dashed), 0.5 (dash-triple-dotted), 1.0 (long-dashed), 2.5 (thin long-dashed). (a) and (b) correspond to  $\Gamma_E/\Gamma_R = 0$ , and 1 (pure  $\mathbf{R}^{\text{II}}$ ; and equally mixed  $\mathbf{R}^{\text{II}}$  and  $\mathbf{R}^{\text{III}}$  respectively), while (c) corresponds to  $\Gamma_E/\Gamma_R = 999$  — the case of almost pure  $\mathbf{R}^{\text{III}}$  type scattering. See § 8.5 for discussions.



an order of magnitude smaller than in Figs. 8.4a,b. The magnitudes of the fractional linear polarizations (of both  $Q/I$  and  $U/I$ ) remain nearly constant through the entire line profile. This occurs due to the extreme dominance of collisional line broadening (principally through  $\mathbf{R}^{\text{III}}$ ), which produces similarly shaped ( $I$ ,  $Q$ ,  $U$ ) scattered profiles, except for different scaling factors.  $V/I$  is strongly reduced once again due to the line broadening.

## 8.6 Concluding remarks

In the present chapter we have explicitly demonstrated (for a  $J = 0 \rightarrow 1 \rightarrow 0$  transition) the equivalence between the Hanle-Zeeman redistribution matrices that are derived through QED and those derived through classical, time-dependent oscillator theory. To establish this equivalence, we have appropriately extended the classical scattering theory developed in Stenflo (1994) and Bommier & Stenflo (1999). This generalization involves an expansion of the redistribution matrix  $\mathbf{R}$  in terms of its multipole components  $\mathbf{R}^{(K)}$ . It requires the use of irreducible spherical tensors  $\mathcal{T}_Q^K$  as described in Landi Degl’Innocenti & Landolfi (2004). The equivalence includes all the intricately coupled PRD correlations in frequency, angle, and polarization between the incoming and outgoing wave packets of the scattering process, and it holds for all strengths and directions of the magnetic field. In view of the rich symmetries and complex mathematical behavior of the general redistribution matrix, this equivalence is remarkable and may have a deeper meaning.

The Hanle-Zeeman redistribution matrix refers to scattering in magnetic fields of arbitrary strength and orientation. For simplicity, we consider a pure scattering medium ( $\Gamma_{\text{I}} = 0$ ), although the formulation can handle both elastic and inelastic collisions. We have explored the dependence of the line polarization on field strength and on the relative rate of elastic collisions  $\Gamma_{\text{E}}/\Gamma_{\text{R}}$ . Usually the efficiency of the Hanle effect is confined to the line core. However, under the natural conditions of a mix of  $\mathbf{R}^{\text{II}}$  and  $\mathbf{R}^{\text{III}}$  type redistributions, the coherence (caused by the anisotropy of the radiation field) is transferred from the line core to the line wings due to the elastic collisions. This results in enhanced linear polarization ( $Q/I$ ,  $U/I$ ) in the line wings. We call it the “wing Hanle effect”. It is particularly pronounced in the case of angle-dependent PRD (Nagendra et al. 2002, 2003).

We have now formulated and explored the detailed behavior of the Hanle-Zeeman redistribution matrix for single scattering processes. Our next step is to integrate it into a radiative transfer formalism, to be able to deal with polarized multiple scattering in opaque magnetized media, which is the topic of Chapter 9. This is the tool we need for making use of the rich diagnostic potential of the Second Solar Spectrum (see Stenflo 2004) and

for determinations of chromospheric magnetic fields.

## Chapter 9

# Solution of the Hanle-Zeeman line formation problem<sup>1</sup>

### 9.1 Introduction

The linearly polarized spectrum of the Sun, known as the “second solar spectrum”, contains a wealth of information about the physics of light scattering on atoms. The recent series of “Solar Polarization Workshops” (SPWs, and their proceedings: Stenflo & Nagendra 1996, Nagendra & Stenflo 1999, Trujillo Bueno & Sánchez Almeida 2003, Casini & Lites 2006, Berdyugina et al. 2008) and important polarimetry workshop proceedings (Sigwarth 2001, Trujillo Bueno et al. 2002) highlight the growing body of research directed towards a deeper understanding of the physical processes used to diagnose solar magnetic fields. The solution of the polarized line transfer equation is used to interpret the shapes of observed Stokes line profiles. The physics of anisotropic absorption and scattering has developed hand in hand with sophisticated numerical methods to solve these complex radiative transfer equations.

Reviews on the methods of solving the polarized transfer equation (Trujillo Bueno 2003a, Nagendra 2003a, 2003b, Nagendra & Sampoorna 2008) list several exact and approximate numerical methods. Novel iterative schemes have been developed by Trujillo Bueno and co-workers (see Trujillo Bueno 2003a, and references therein to their previous works) to solve the polarized non-local thermodynamic equilibrium (NLTE) radiative transfer equation together with the statistical equilibrium equation in multilevel atoms, including multi-dimensional geometries. Here we limit our attention to the vector version of the standard two-level atom NLTE line transfer equation (Mihalas 1978, Stenflo 1994).

---

<sup>1</sup>This chapter is based on the paper which is accepted for publication: Sampoorna, M., Nagendra, K. N., & Stenflo, J. O. 2008, ApJ (in press)

The new aspect of our treatment is that it allows us to solve the line transfer problem for the general case of arbitrary magnetic fields with full account of partial frequency redistribution (PRD).

The solar atmosphere with its magnetically active regions harbor a whole range of field strengths (milligauss to kilogauss fields). Hence a general form of the radiative transfer equation that is valid in this entire range has to be formulated and tested. Such a transfer equation has been formulated by Stenflo (1994, see also § 9.2 of the present chapter). It is also briefly discussed in the review of Trujillo Bueno (2003a).

Polarized PRD scattering in the presence of magnetic fields of arbitrary strength and direction is called Hanle-Zeeman scattering. In this chapter, we use a perturbation approach to solve the Hanle-Zeeman line transfer problem. Perturbation methods have often been applied in polarized line transfer (Rees 1978, Rees & Murphy 1987, Faurobert 1987, Nagendra et al. 2002). It is a practical approach, which works for any type of scattering redistribution matrix in the polarized source vector.

Efficient numerical methods to solve the polarized radiative transfer equation in the presence of magnetic fields have been developed in the past. In the weak field limit of the Hanle effect, techniques like Polarized Approximate Lambda Iteration (PALI) taking into account both complete frequency redistribution (Nagendra et al. 1998) and PRD (Nagendra et al. 1999, Fluri et al. 2003b, see also Chapter 10) have been developed. However, in the weak field limit a scalar isotropic absorption coefficient is often assumed instead of the Zeeman absorption matrix, even when the magnetic field is non-zero. At the other extreme, for the strong field Zeeman effect, techniques like the Feautrier method (Auer et al. 1977), the Diagonal Element Lambda Operator (DELO) method (Rees et al. 1989), and DELOPAR (Trujillo Bueno 2003a) have been developed. In this strong field limit one assumes local thermodynamic equilibrium (LTE), where scattering effects are either neglected or are taken into account through a complete redistribution (CRD) line source function, which is then solved using the polarization free approximation of Trujillo Bueno & Landi Degl'Innocenti (1996). However, scattering included in this way does not account for coherent scattering in the presence of strong magnetic fields.

In a correct treatment of NLTE line formation in the presence of a magnetic field of arbitrary strength, one has to take into account both the Zeeman absorption matrix and PRD effects. Such a treatment requires a redistribution matrix which is valid in all field strength regimes. Clearly the weak field Hanle phase matrix (Landi Degl'Innocenti & Landi Degl'Innocenti 1988, Stenflo 1994) does not suit these requirements. A quantum electro-

dynamic (QED) and classical theory of PRD line scattering in the presence of magnetic fields of arbitrary strength, and including collisions have been formulated respectively by Bommier (1997a, 1997b) and Bommier & Stenflo (1999). The classical theory describes the scattering process in a transparent way. In Bommier & Stenflo (1999) the redistribution matrices have been derived in the atomic rest frame. The corresponding laboratory frame redistribution matrices are given in Chapter 7. The equivalence between the classical (Chapter 7) and QED approach of Bommier (1997b) for the Zeeman triplet case has been established in Chapter 8. Following Stenflo (1998) we refer to this as the ‘Hanle-Zeeman redistribution matrix’, since it covers the entire field strength regime. In the present chapter we incorporate the Hanle-Zeeman redistribution matrix derived in Chapters 7 and 8 into the polarized line transfer equation.

In § 9.2 we present the governing equations, a description of the general line radiative transfer equation and its various limiting forms. In § 9.3 we introduce a numerical method to solve the polarized transfer equation including ‘both the Zeeman absorption matrix and the Hanle-Zeeman redistribution matrix’. § 9.4 is devoted to the results and discussions, and § 9.5 to the concluding remarks.

## 9.2 Governing equations of the Hanle-Zeeman scattering theory

In the formulation that we are using here, the full Zeeman absorption matrix and the Hanle-Zeeman redistribution matrix (see Chapters 7 and 8) are simultaneously and self-consistently incorporated (assuming an unpolarized ground state). We remark that the Hanle-Zeeman line transfer theory presented in this chapter is valid for a normal Zeeman triplet ( $J = 0 \rightarrow 1 \rightarrow 0$ ) case only.

### 9.2.1 Formulation of the relevant radiative transfer equation

In the presence of a magnetic field, the vector radiative transfer equation for the Stokes vector  $\mathbf{I}(\tau, x, \mathbf{n}) = (I Q U V)^T$  may be written as (see Stenflo 1994)

$$\mu \frac{\partial}{\partial \tau} \mathbf{I}(\tau, x, \mathbf{n}) = \mathbf{K} \mathbf{I}(\tau, x, \mathbf{n}) - \mathbf{S}(\tau, x, \mathbf{n}), \quad (9.1)$$

where the source vector  $\mathbf{S}(\tau, x, \mathbf{n}) = \mathbf{j}(\tau, x, \mathbf{n})/k_0$ , with  $\tau$  being the line-center optical depth and  $x$  the frequency separation from line center in Doppler width units. The vector  $\mathbf{n}(\vartheta, \varphi)$  is the propagation direction of the ray (where  $\vartheta$  is the co-latitude and  $\varphi$  the azimuth), and  $\mu = \cos \vartheta$ . The quantity  $k_0 = (N_l B_{lu} - N_u B_{ul}) h \nu_0 / 4\pi$  is the line center opacity.  $N_l, N_u$  are the populations of lower and upper states,  $B_{lu}$  and  $B_{ul}$  are the Einstein’s

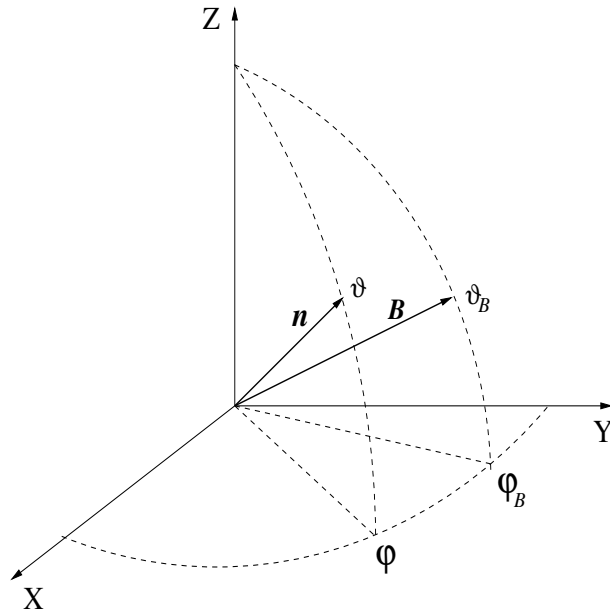


Figure 9.1: Geometry specifying the direction of the magnetic field  $\mathbf{B}$  and of the line-of-sight  $\mathbf{n}$ . The  $Z$ -axis is along the normal to the atmosphere. Angles  $\vartheta$  and  $\vartheta_B$  are the co-latitudes of  $\mathbf{n}$  and  $\mathbf{B}$ , respectively. The azimuthal angles  $\varphi$  and  $\varphi_B$  are measured from the  $X$ -axis in the anti-clockwise direction in the  $XY$ -plane.

$B$  coefficients,  $h$  is the Planck constant, and  $\nu_0$  is the line center frequency. Positive optical depth is measured in the direction opposite to the vertical  $Z$ -axis (see Fig. 9.1). We use the convention that positive  $Q$  direction corresponds to the linear polarization perpendicular to the solar limb.

In Eq. (9.1)  $\mathbf{K}$  is the total absorption matrix

$$\mathbf{K} = \mathbf{\Phi} + r\mathbf{E}, \quad (9.2)$$

where  $\mathbf{\Phi}$  is the  $4 \times 4$  Zeeman line absorption matrix (see Eq. (2.4)),  $\mathbf{E}$  the  $4 \times 4$  unity matrix, and  $r$  the ratio of continuous to line center opacity. The total emission vector  $\mathbf{j}(\tau, x, \mathbf{n})$  has contributions both from line and continuum :

$$\mathbf{j}(\tau, x, \mathbf{n}) = \mathbf{j}_L(\tau, x, \mathbf{n}) + \mathbf{j}_c(\tau, x, \mathbf{n}). \quad (9.3)$$

Assuming unpolarized continuum with emission occurring in LTE,  $\mathbf{j}_c(\tau, x, \mathbf{n}) = rk_0 B_{\nu_0} \mathbf{U}$ , where  $\mathbf{U} = (1000)^T$  and  $B_{\nu_0}$  is the Planck function. The line emission vector has contributions from coherent scattering (undisturbed by collisions), incoherent scattering (collisionally disturbed), and non-scattering emission (see Stenflo 1994, for details), and may

be written as

$$\mathbf{j}_L(\tau, x, \mathbf{n}) = \mathbf{j}_{\text{scat}}(\tau, x, \mathbf{n}) + \mathbf{j}_{\text{ns}}(\tau, x, \mathbf{n}). \quad (9.4)$$

### 9.2.2 The scattering part of the emission vector

The scattering emission vector  $\mathbf{j}_{\text{scat}}$  has contributions from both coherent and incoherent scattering. The term coherent scattering refers to all scattering processes that are purely due to radiative excitation, followed by spontaneous emission which is undisturbed by collisions. The term incoherent scattering refers to all those scattering processes that are disturbed by collisions. The scattering emission vector for this case may be written as

$$\mathbf{j}_{\text{scat}}(\tau, x, \mathbf{n}) = k_0 \oint \frac{d\mathbf{n}'}{4\pi} \int_{-\infty}^{+\infty} dx' \mathbf{R}(x, \mathbf{n}; x', \mathbf{n}'; \mathbf{B}) \mathbf{I}(\tau, x', \mathbf{n}'). \quad (9.5)$$

The redistribution matrix  $\mathbf{R}(x, \mathbf{n}; x', \mathbf{n}'; \mathbf{B})$  accounts for the correlations in frequency, angle and polarization between the incident radiation field at frequency  $x'$  and direction  $\mathbf{n}'$  and the re-emitted radiation at frequency  $x$  and direction  $\mathbf{n}$ . The quantity  $d\mathbf{n}'$  is an element of solid angle around  $\mathbf{n}'$ . For lines formed with PRD the analytic form of  $\mathbf{R}$  is given in Chapters 7 and 8 (see Eqs. (7.43), (7.44), (7.46), and (8.16) - (8.19)). The explicit form of  $\mathbf{R}$  is presented in a frame where the  $Z$ -axis is along the magnetic field (see Figs. 7.1 and 8.1) rather than along the normal to the atmosphere. The required transformation to a frame in which the magnetic field has an arbitrary orientation with respect to the normal to the atmosphere (see Fig. 8.2) is described in Appendix K.

When the atom is in the excited state, collisions cause shifts of the emitted frequency, change of phase, destruction of alignment, orientation etc., depending on the nature of the collisions (quenching, elastic, or inelastic). All these processes are contained in a general redistribution matrix (see Eqs. (7.43), (7.44), (7.46), and (8.16) - (8.19)), through a combination of collisional branching ratios and magnetically modified redistribution functions (type II and III of Hummer 1962), which we have called ‘magnetic redistribution functions’ (see Chapter 7). The theoretical study and applications of such collisional redistributions for the non-magnetic case have been described in Domke & Hubeny (1988), Faurobert-Scholl (1992, 1993b), Nagendra (1994), Stenflo (1994), and for the arbitrary field strength in Bommier (1997a, 1997b), Bommier & Stenflo (1999).

### 9.2.3 The non-scattering part of the emission vector

We refer to a process as non-scattering, if the atom has no memory of how it has been excited when it emits the photon. In other words, the upper state has been populated by

a process different from radiative absorption from the lower state. If the population has been by isotropic collisions, then we get purely thermal emission. If radiative transitions are involved (other than from our initial atomic state) which contribute to populating the excited state then, since they are unspecified, we have assumed that the memory of the population process has been erased. In this case we also get thermal emission as in the collisionally excited case (see the discussion in § 5.3 of Stenflo 1998). Therefore we can lump all these unspecified processes together, since they all contribute with the same form of the emission vector. The non-scattering emission vector is given by (see Stenflo 1994)

$$\mathbf{j}_{\text{ns}}(\tau, x, \mathbf{n}) = k_0 \epsilon B_{\nu_0} \Phi \mathbf{U}. \quad (9.6)$$

Here  $\epsilon = \Gamma_{\text{I}}/(\Gamma_{\text{I}} + \Gamma_{\text{R}})$  denotes the photon destruction probability per scattering, where  $\Gamma_{\text{R}}$  is the radiative rate and  $\Gamma_{\text{I}}$  is the inelastic collision rate.

#### 9.2.4 The Hanle-Zeeman line transfer equation

Combining Eqs. (9.2) - (9.6), we can rewrite the polarized transfer Eq. (9.1) as

$$\mu \frac{\partial}{\partial \tau} \mathbf{I}(\tau, x, \mathbf{n}) = (\Phi + r\mathbf{E}) \mathbf{I}(\tau, x, \mathbf{n}) - [(r\mathbf{E} + \epsilon\Phi) B_{\nu_0} \mathbf{U} + \mathbf{S}_{\text{scat}}(\tau, x, \mathbf{n})], \quad (9.7)$$

where

$$\mathbf{S}_{\text{scat}}(\tau, x, \mathbf{n}) = \oint \frac{d\mathbf{n}'}{4\pi} \int_{-\infty}^{+\infty} dx' \mathbf{R}(x, \mathbf{n}; x', \mathbf{n}'; \mathbf{B}) \mathbf{I}(\tau, x', \mathbf{n}'). \quad (9.8)$$

Note that the factor  $(1 - \epsilon)$  is implicitly contained in  $\mathbf{R}$  through the branching ratios. We refer to Eq. (9.7) as the Hanle-Zeeman line transfer equation, as it includes both the Zeeman absorption matrix ( $\Phi$ ) and the Hanle-Zeeman redistribution matrix ( $\mathbf{R}$ ).

Three limiting forms of Eq. (9.7) may be considered: (i) True absorption, or LTE: We may set  $\epsilon = 1$  and thereby recover the LTE Zeeman line transfer equation, for which rapid solutions are available. (ii) NLTE strong field limit: In the presence of strong fields, if we neglect the coherent scattering (PRD) contribution and retain only completely incoherent scattering, then Eq. (9.7) takes the form given in Trujillo Bueno & Landi Degl'Innocenti (1996). In this case scattering effects are taken into account through a CRD like line source function, and the radiative transfer equation is solved by using the polarization free approximation of Trujillo Bueno & Landi Degl'Innocenti (1996). (iii) NLTE weak field limit: In the weak field limit the line absorption matrix can be approximated by a diagonal matrix with a single absorption coefficient profile  $\phi(x)$ , and the redistribution matrix can be approximated by a scalar redistribution function (CRD or PRD) times a weak field frequency independent Hanle phase matrix. This is the conventionally employed



Hanle scattering line transfer problem that has been solved in various papers in the past (eg. Faurobert-Scholl 1991, Nagendra et al. 1998, 1999).

Bommier (1997b) proposed three kinds of Approximations (I, II, III, in order of decreasing complexity) for weak field Hanle scattering. In Approximation I, the redistribution functions are not factorized and retain their couplings to the angular phase matrix. Approximations II and III are based on asymptotic expansion of the generalized profiles (see Eqs. (86) and (87) of Bommier 1997b). These expansions in the line center and in the line wings lead to a decomposition of frequency space into several domains. In each domain the frequency redistribution function is decoupled from the angular phase matrix. Approximation II uses the angle-dependent (AD) redistribution functions, Approximation III the corresponding angle-averaged (AA) functions. Approximations II and III have been applied and tested in line transfer calculations by Nagendra et al. (2002) using a computationally expensive perturbation approach. Approximation III was later integrated into a high speed PALI method by Fluri et al. (2003b). Both these papers use a domain based treatment of polarized PRD. In Chapter 10 we develop a PALI method based on non-domain based treatment of PRD, namely adopting the AA version of Approximation I of Bommier (1997b). The present chapter deals with the more general problem that fully includes the Zeeman absorption matrix when solving the full Hanle-Zeeman scattering problem with PRD. We use a perturbation technique similar to the one proposed by Nagendra et al. (2002), with appropriate generalizations.

### 9.3 Numerical method of solution for the transfer equation

Here we present a perturbation method to solve the Hanle-Zeeman PRD line transfer problem. There are two stages in the perturbation method that we use. In stage 1 we solve the Hanle-Zeeman scattering problem neglecting Zeeman absorption (see § 9.3.1). In stage 2 the full problem including both Zeeman absorption and the Hanle-Zeeman redistribution matrix is solved (see § 9.3.2).

#### 9.3.1 Stage 1: Initializing $\mathbf{S}_{\text{scat}}(\tau, x, \mathbf{n})$

If we replace  $\Phi$  by  $\phi(x)$  in Eq. (9.7), we obtain the transfer equation traditionally used for solving the weak field Hanle effect (e.g. Faurobert-Scholl 1991, Nagendra et al. 1998, 1999, 2002)

$$\mu \frac{\partial}{\partial \tau} \mathbf{I}(\tau, x, \mathbf{n}) = [\phi(x) + r] \mathbf{I}(\tau, x, \mathbf{n}) - \{[r + \epsilon \phi(x)] B_{\nu_0} \mathbf{U} + \mathbf{S}_{\text{scat}}(\tau, x, \mathbf{n})\}. \quad (9.9)$$

However, the difference is that we now use the newly derived Hanle-Zeeman redistribution matrix instead of the weak field Hanle redistribution matrix.

Equation (9.9) is solved using a perturbation technique presented in Nagendra et al. (2002). We first calculate the scalar PRD intensity using an ALI method, which is used to compute a first estimate  $\mathbf{S}_{\text{scalar}}(\tau, x, \mathbf{n}) = (S(\tau, x) \ 0 \ 0 \ 0)^T$ . In the 2nd step the polarized transfer equation is solved using a short characteristic formal solver (FS) of Auer & Paletou (1994), for which  $\mathbf{S}_{\text{scalar}}$  is used as input. In this step we use the AA version of the magnetic redistribution functions (see § 9.3.5 for details). This procedure is repeated until the relative variations of the polarization rate at the surface between two successive perturbations is less than 1% (see § 9.3.4 for details). The converged source vector  $\mathbf{S}_{\text{pol,AA}}$  becomes the input to step 3. The 3rd step is exactly the same as step 2, except for the use of AD magnetic redistribution functions (see Eqs. (7.21) - (7.26)) in the explicit computation of the scattering integral. In this way we obtain a good initial estimate of  $\mathbf{S}_{\text{scat}}$ , which we call  $\mathbf{S}_{\text{pol,AD}}$ .

### 9.3.2 Stage 2: Full solution by perturbation

The Hanle-Zeeman line transfer equation (9.7) is now solved in three steps described below :

1. The initial values  $\mathbf{S}_{\text{pol,AD}}$  obtained from stage 1 are used as input to a FS, which finds the solution of Eq. (9.7). For this purpose we use DELOPAR introduced by Trujillo Bueno (2003a, see § 9.3.3 of this chapter for details).
2. The Stokes vector obtained from the FS is used to compute the new value of  $\mathbf{S}_{\text{scat}}$  from Eq. (9.8).
3. The perturbation sequence is tested for convergence (see § 9.3.4) and returned to step 1 if the convergence is not yet reached.

### 9.3.3 Formal solution using DELOPAR

A numerical method for the formal solution of NLTE Zeeman line transfer equations was first given by Auer et al. (1977). It is a Feautrier type method which involves writing the equations in second-order form and solving them by a finite-difference technique. However,

the Feautrier method involves handling large matrices, and hence it is slow. A much faster method was developed by Rees et al. (1989), which they call DELO method. Trujillo Bueno (2003a) clearly showed that the DELO method, as a FS, is less accurate when compared with his new FS, which is a generalization of the scalar short characteristic method of Kunasz & Auer (1988) to the polarized case. The reason for the inaccuracies of the DELO method when solving hard problems of NLTE polarization transfer is that it is based on a linear interpolation approximation to the source vector in optical depth segments.

Trujillo Bueno (2003a) overcame this problem by developing an improved DELO method, which is based on using a parabolic interpolation for the total source vector. This method is called DELOPAR.

In the present work, we apply the DELOPAR method. Let us define a total optical depth  $d\tau^{\text{tot}} = d\tau(\varphi_{\text{I}} + r)/\mu$ , where  $\varphi_{\text{I}}$  is the diagonal element of the Zeeman absorption matrix  $\Phi$ . For notational simplification we will here call  $d\tau^{\text{tot}} = d\tau$ . Equation (9.7) can be rewritten as

$$\frac{\partial}{\partial \tau} \mathbf{I}(\tau, x, \mathbf{n}) = \mathbf{I}(\tau, x, \mathbf{n}) - \mathbf{S}_{\text{eff}}(\tau, x, \mathbf{n}). \quad (9.10)$$

Here the effective source vector is

$$\mathbf{S}_{\text{eff}}(\tau, x, \mathbf{n}) = \mathbf{S}_{\text{tot}}(\tau, x, \mathbf{n}) - \mathbf{K}' \mathbf{I}(\tau, x, \mathbf{n}), \quad (9.11)$$

where we have redefined the total absorption matrix of Eq. (9.2) as

$$\mathbf{K}' = \frac{\mathbf{K}}{(\varphi_{\text{I}} + r)} - \mathbf{E}. \quad (9.12)$$

The total source vector is defined as

$$\mathbf{S}_{\text{tot}}(\tau, x, \mathbf{n}) = \frac{1}{(\varphi_{\text{I}} + r)} [(\epsilon \Phi + r \mathbf{E}) B_{\nu_0} \mathbf{U} + \mathbf{S}_{\text{scat}}(\tau, x, \mathbf{n})]. \quad (9.13)$$

On the interval  $(\tau_k, \tau_{k+1})$ , the solution of Eq. (9.10) is

$$\mathbf{I}_k = E_k \mathbf{I}_{k+1} + \int_{\tau_k}^{\tau_{k+1}} e^{\tau_k - t} [\mathbf{S}(t) - \mathbf{K}'(t) \mathbf{I}(t)] dt, \quad (9.14)$$

where  $\mathbf{I}_k = \mathbf{I}(\tau_k)$ , and  $E_k = e^{-\tilde{\delta}_k}$ , with  $\tilde{\delta}_k = \tau_{k+1} - \tau_k$ . Note that we have dropped the other two arguments of  $\mathbf{I}$  and  $\mathbf{S}$ , and also the subscript on  $\mathbf{S}_{\text{tot}}$ . Changing the variable ( $p = t - \tau_k$ ), Eq. (9.14) can be rewritten as

$$\mathbf{I}_k = E_k \mathbf{I}_{k+1} + \int_0^{\tilde{\delta}_k} e^{-p} [\mathbf{S}(p) - \mathbf{K}'(p) \mathbf{I}(p)] dp. \quad (9.15)$$

We assume that  $\mathbf{S}$  varies parabolically,

$$\mathbf{S}(p) = \mathbf{S}_k + \mathbf{C}_1 p + \mathbf{C}_2 p^2, \quad (9.16)$$

where the coefficients are

$$\begin{aligned} \mathbf{C}_1 &= \frac{(\mathbf{S}_{k+1} - \mathbf{S}_k) \bar{\delta}_{k-1}}{\bar{\delta}_k (\bar{\delta}_k + \bar{\delta}_{k-1})} + \frac{(\mathbf{S}_k - \mathbf{S}_{k-1}) \bar{\delta}_k}{\bar{\delta}_{k-1} (\bar{\delta}_k + \bar{\delta}_{k-1})}, \\ \mathbf{C}_2 &= \frac{(\mathbf{S}_{k+1} - \mathbf{S}_k)}{\bar{\delta}_k (\bar{\delta}_k + \bar{\delta}_{k-1})} - \frac{(\mathbf{S}_k - \mathbf{S}_{k-1})}{\bar{\delta}_{k-1} (\bar{\delta}_k + \bar{\delta}_{k-1})}. \end{aligned} \quad (9.17)$$

Further we assume that  $\mathbf{K}'\mathbf{I}$  varies linearly,

$$\mathbf{K}'(p)\mathbf{I}(p) = \mathbf{K}'_k \mathbf{I}_k + [\mathbf{K}'_{k+1} \mathbf{I}_{k+1} - \mathbf{K}'_k \mathbf{I}_k] \frac{p}{\bar{\delta}_k}. \quad (9.18)$$

If we insert expressions (9.16) and (9.18) into Eq. (9.15), it can be integrated analytically. After some algebra, we obtain

$$\mathbf{I}_k = \mathbf{P}_k + \mathbf{Q}_k \mathbf{I}_{k+1}, \quad (9.19)$$

where

$$\begin{aligned} \mathbf{P}_k &= \left[ \mathbf{E} + \left( F_k - \frac{G_k}{\bar{\delta}_k} \right) \mathbf{K}'_k \right]^{-1} [F_k \mathbf{S}_k + G_k \mathbf{C}_1 + H_k \mathbf{C}_2], \\ \mathbf{Q}_k &= \left[ \mathbf{E} + \left( F_k - \frac{G_k}{\bar{\delta}_k} \right) \mathbf{K}'_k \right]^{-1} \left[ E_k \mathbf{E} - \frac{G_k}{\bar{\delta}_k} \mathbf{K}'_{k+1} \right], \end{aligned} \quad (9.20)$$

and

$$F_k = 1 - E_k; \quad G_k = 1 - (1 + \bar{\delta}_k) E_k; \quad H_k = 2G_k - \bar{\delta}_k^2 E_k. \quad (9.21)$$

At the lower boundary we specify a boundary condition (either 0 or 1). Then Eq. (9.19) can be applied recursively to derive the emergent Stokes vector at the surface.

### 9.3.4 The convergence criteria

The formal solver DELOPAR computes the Stokes vector at all depth, frequency and angle points, provided a known source vector is given. To initialize the perturbation loop, the starting values  $\mathbf{S}_{\text{pol,AD}}$  for  $\mathbf{S}_{\text{scat}}$  (see § 9.3.1) are given as input to DELOPAR, which delivers new values of the Stokes vector. These new values are then used to compute a new  $\mathbf{S}_{\text{scat}}$  using the defining Eq. (9.8).

This procedure is repeated until the maximum relative variations of polarization rate at the surface between two successive iterations is less than 1%. The maximum relative

variations of polarization rate denoted by  $p_{\text{surf}}$ , is defined as

$$p_{\text{surf}} = \max_{x, \mu, \varphi} \left[ \frac{|P^{(n)}(x, \mu, \varphi) - P^{(n-1)}(x, \mu, \varphi)|}{\bar{P}^{(n)}(x, \mu, \varphi)} \right]. \quad (9.22)$$

Here  $P^{(n)} = \sqrt{Q^2 + U^2 + V^2}/I$  is the degree of polarization at the surface for the  $n$ th iterate, and  $\bar{P}^{(n)} = [P^{(n)} + P^{(n-1)}]/2$ . The same convergence criteria is used for step 2 and 3 of stage 1 of the perturbation method.

### 9.3.5 Computational details

The memory and CPU time requirements of the perturbation method is discussed in detail in Nagendra et al. (2002). In the Hanle-Zeeman scattering theory, the redistribution matrix contains the magnetic redistribution functions (see Eqs. (7.21) - (7.26)). The type II and III magnetic redistribution functions are denoted as  $R_{\text{II},X}^q(x, x', \Theta; B)$  and  $R_{\text{III},XY}^{qq'}(x, x', \Theta; B)$ , where X and Y stand for the symbols H and/or F,  $\Theta$  the scattering angle, and  $q, q' = 0, \pm 1$ . Clearly, there are 6 type II and 36 type III magnetic redistribution functions. In contrast, in the limit of weak field domain based Hanle scattering theory, we need to compute only one each of the scalar type II and III redistribution functions of Hummer (1962). Therefore there is a much larger demand on the CPU time and memory in the Hanle-Zeeman case. For this reason, we restrict ourselves to slabs of optical depth 20 and 200 in this chapter, for which a smaller frequency band width is sufficient.

It is well known that  $(I, Q, U)$  are symmetric about  $x = 0$  and  $V$  is anti-symmetric about  $x = 0$ . Thus the frequency integral in Eq. (9.8) can be written as follows:

$$\begin{aligned} & \int_{-\infty}^{+\infty} dx' \sum_{i=1}^4 \sum_{j=1}^3 R_{ij}(x, \mathbf{n}; x', \mathbf{n}'; \mathbf{B}) Z_j(\tau, x', \mathbf{n}') \\ &= \int_0^{+\infty} dx' \sum_{i=1}^4 \sum_{j=1}^3 [R_{ij}(x, \mathbf{n}; +x', \mathbf{n}'; \mathbf{B}) + R_{ij}(x, \mathbf{n}; -x', \mathbf{n}'; \mathbf{B})] Z_j(\tau, x', \mathbf{n}'), \end{aligned} \quad (9.23)$$

for  $Z_j(\tau, x', \mathbf{n}') = I, Q, U$ , when  $j = 1, 2, 3$ . The corresponding equation for  $V(\tau, x', \mathbf{n}')$  is

$$\begin{aligned} & \int_{-\infty}^{+\infty} dx' \sum_{i=1}^4 R_{i4}(x, \mathbf{n}; x', \mathbf{n}'; \mathbf{B}) V(\tau, x', \mathbf{n}') \\ &= \int_0^{+\infty} dx' \sum_{i=1}^4 [R_{i4}(x, \mathbf{n}; +x', \mathbf{n}'; \mathbf{B}) - R_{i4}(x, \mathbf{n}; -x', \mathbf{n}'; \mathbf{B})] V(\tau, x', \mathbf{n}'). \end{aligned} \quad (9.24)$$

Thus the magnetic redistribution functions entering individual elements of redistribution matrix  $\mathbf{R}$  are now computed in the range  $(0, x_{\text{max}})$  and  $(-x'_{\text{max}}, +x'_{\text{max}})$ , which are then

folded as shown in the square bracket of Eqs. (9.23) and (9.24). This reduces the computing time by a factor of two. Further, the memory is also reduced, as we store the concerned quantities over the range  $(0, x_{\max})$  and  $(0, x'_{\max})$  only.

We recall that in the 2nd step of the stage 1 of the perturbation method (see § 9.3.1), we use AA version of the individual AD magnetic redistribution functions appearing in the Hanle-Zeeman redistribution matrix. We call this the AA approximation. The AA functions can be computed from AD functions by numerically integrating over the scattering angle  $\Theta$  as follows:

$$\bar{R}_{\text{II},X}^q(x, x'; B) = \frac{1}{2} \int_0^\pi R_{\text{II},X}^q(x, x', \Theta; B) \sin \Theta d\Theta, \quad (9.25)$$

(see also Bommier 1997b), and

$$\bar{R}_{\text{III},XY}^{qq'}(x, x'; B) = \frac{1}{2} \int_0^\pi R_{\text{III},XY}^{qq'}(x, x', \Theta; B) \sin \Theta d\Theta. \quad (9.26)$$

The AA functions still contain the physics of frequency redistribution and are very economical to compute compared to corresponding AD functions. We use a Gauss-Legendre quadrature with 31 angle points to numerically compute Eqs. (9.25) and (9.26). We remark that to obtain only the AA solution we skip step 3 of stage 1 and directly go to the stage 2 of the perturbation method, when  $\mathbf{S}_{\text{pol,AA}}$  becomes the initial guess for  $\mathbf{S}_{\text{scat}}$ .

Such a replacement of AD functions by their AA counterparts is not new (see e.g. Rees & Saliba 1982). Although approximate, it gives very reasonable results. In line formation computations, it is therefore reasonable to use AA functions in preliminary work. Faurobert (1987) has shown that in the non-magnetic resonance scattering problem the use of AA type II redistributions instead of AD functions give nearly the same overall behavior of the linear polarization profile, but it may lead to an overestimate in the near wing maximum by about 50% when the optical thickness is larger than 10. Nagendra et al. (2002) have shown for the case of weak field ‘domain-based Hanle redistribution matrix’ (Approximations II and III of Bommier 1997b) that there are large differences in particular for the  $U$  Stokes parameter, between solutions that are obtained using AA and AD functions. We briefly examine this important question again, but now for the Hanle-Zeeman regime (see § 9.4.4).

## 9.4 Results and discussions

Line transfer computations involving the Hanle effect traditionally use only a scalar absorption coefficient. Here, we explicitly include the full Zeeman absorption matrix, as we consider intermediate and strong fields, where the Zeeman effect is important.

The atmospheric model parameters are represented by  $(T, a, \epsilon, r, \Gamma_E/\Gamma_R)$ , where  $T$  is the optical thickness of the slab, and  $a$  is the damping parameter. The Planck function  $B_{\nu_0}$  is taken as unity for all the results presented here. The magnetic field parameters are  $(\Gamma_B, v_B, \vartheta_B, \varphi_B)$ , where  $\Gamma_B = g\omega_L/\Gamma_R$  with  $g$  being the Landé factor and  $\omega_L = 2\pi\nu_L$  is the Larmor frequency,  $v_B = g\nu_L/\Delta\nu_D$  is the magnetic splitting in Doppler units ( $\Delta\nu_D$ ), and angles  $(\vartheta_B, \varphi_B)$  define the field orientation with respect to the slab normal (see Fig. 8.2). The magnetic splitting parameter  $v_B$  is related to the Hanle parameter  $\Gamma_B$  through the relation  $v_B = 2\Gamma_B a/[1+(\Gamma_I+\Gamma_E)/\Gamma_R]$ , where  $\Gamma_I/\Gamma_R = \epsilon/(1-\epsilon)$  and  $\Gamma_E$  is the elastic collision rate. The depolarizing elastic collision parameter is assumed to be  $D^{(1)} = D^{(2)} = 0.5\Gamma_E$ , while  $D^{(0)} = 0$ . The details of parameterizing the collisional rates are given in Nagendra et al. (2002, see also Chapter 8).

The grid resolution in the physical variables is given by the values of  $(N_d, N_x, N_\mu, N_\varphi)$ . The quantity  $N_d$  represents the number of points per decade in a logarithmically spaced  $\tau$ -grid with the first depth point  $\tau_{\min} = 10^{-2}$ , unless stated otherwise. The frequency points are equally spaced in the line core, with a gradual switch over to logarithmic spacing in the wings, and satisfy the condition  $\phi(x_{\max})T \ll 1$  in the far wings (the atmosphere becomes so thin at these far wing frequencies that the radiative transfer effects gradually become insignificant).  $N_x$  represents the number of frequency points from 0 to  $x_{\max}$ . We use a Gauss-Legendre quadrature for co-latitude  $\vartheta$  ( $\mu \in [0, 1]$ ) with  $N_\mu$  points, and trapezoidal quadrature for the azimuthal angles  $\varphi \in [0, 2\pi]$  with  $N_\varphi$  points. Unless stated otherwise, we use  $N_d = 5$  points per decade on a logarithmic scale,  $N_x = 45$  (with  $x_{\max} = 17$ ),  $N_\mu = 7$ , and  $N_\varphi = 8$ . Such a grid resolution requires about 3 GB of main memory and half an hour to one hour of computing time to obtain AA solutions. To obtain the corresponding AD solutions, we require about 8 GB of main memory and about 65 to 75 hours of computing time. Figures 9.2, 9.3 and 9.6 are computed using the AD magnetic redistribution functions, while Figs. 9.4 and 9.6 are computed using the AA magnetic redistribution functions.

#### 9.4.1 Scattering at optically thin slabs

The classical theory for Hanle-Zeeman scattering developed by Stenflo (1998) considered only coherent scattering in the laboratory frame. Stenflo (1998, Fig. 3) presents the scattered Stokes line profiles for Hanle-Zeeman coherent scattering in a  $90^\circ$  single scattering event. To mimic such single scattering event from a Hanle-Zeeman line transfer problem with PRD (described in § 9.2 and solved by a perturbation method discussed in § 9.3), we consider an optically thin slab illuminated at the lower boundary by a unidirectional unpolarized beam of radiation, namely  $\mathbf{I}(\tau = T, x', \mu' = 0.95, \varphi' = 0^\circ) = \mathbf{U}$ . Observation

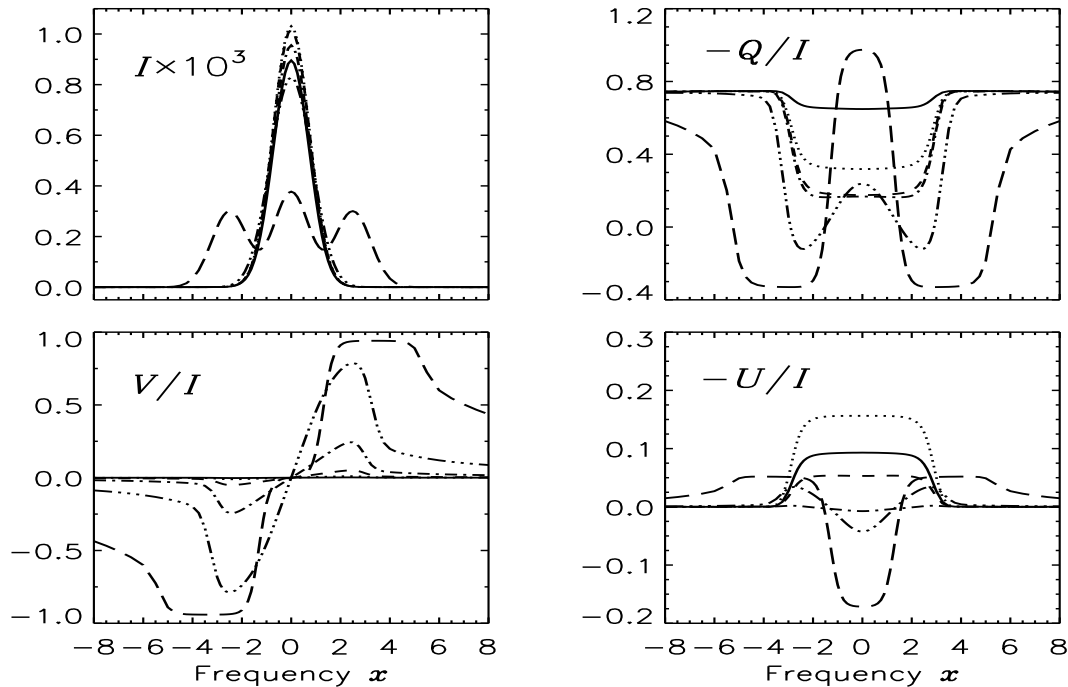


Figure 9.2: Emergent Stokes  $I$  and ratios  $(-Q/I)$ ,  $(-U/I)$  and  $(V/I)$  profiles formed in an optically thin medium, are shown as a function of frequency  $x$  for  $(\mu = 0.11, \varphi = 0^\circ)$ . The model parameters are:  $(T, a, \epsilon, r, \Gamma_E/\Gamma_R) = (0.02, 4 \times 10^{-3}, 0, 10^{-9}, 0)$ . A nearly vertical  $(\mu' = 0.95, \varphi' = 0^\circ)$  beam of radiation is used as lower boundary condition. The magnetic field orientation is:  $(\vartheta_B, \varphi_B) = (90^\circ, 45^\circ)$ . Line types are: solid ( $\Gamma_B = 0.1, v_B = 0.0008$ ); dotted (0.5, 0.004); short-dashed (2.5, 0.02); dash-dotted (12.5, 0.1); dash-triple-dotted (62.5, 0.5); and long-dashed (312.5, 2.5). This figure is to be compared with Fig. 3 of Stenflo (1998), which corresponds to single scattering.

of radiation from the upper boundary, along a nearly tangential direction ( $\mu = 0.11$  and  $\varphi = 0^\circ$ ) mimics extreme limb observations. For our present studies we consider a solar chromospheric canopy like magnetic field (fields parallel to the surface of the slab medium) with  $\vartheta_B = 90^\circ$  and  $\varphi_B = 45^\circ$ . The Zeeman splitting parameter  $v_B$  is chosen as a free parameter. The other parameters used are  $(T, a, \epsilon, r, \Gamma_E/\Gamma_R) = (0.02, 4 \times 10^{-3}, 0, 10^{-9}, 0)$ . The optical depth is chosen very small so that the emergent diffuse radiation field is ‘dominated’ by single scattered photons. The first depth point is  $\tau_{\min} = 10^{-4}$ ,  $N_d = 3$  points per decade, and  $N_\mu = 5$ .

The scattering parameter  $\epsilon = 0$  and  $r = 10^{-9}$  together represent a highly scattering medium with negligible continuum absorption. The choice of  $\Gamma_E/\Gamma_R = 0$  corresponds to the



pure  $\mathbf{R}^{\text{II}}$  case and somewhat mimics the Fig. 3 of Stenflo (1998) which describes coherent scattering in the laboratory frame. A comparison with Fig. 3 of Stenflo (1998) shows that the shape of these profiles are very similar to the ‘single scattered profiles’ presented there, except for  $U/I$  (which slightly differs because we do not have perfect  $90^\circ$  scattering now, and  $U$  is indeed very angle sensitive). In addition, an admixture of multiply scattered photons is also responsible for the differences with respect to the single scattering results.

For an optical line  $\lambda_0 = 5000 \text{ \AA}$  with photospheric like Doppler width  $\Delta\lambda_D = 30 \text{ m\AA}$  and Landé factor of unity, the field strength  $v_B$  variation that is used here covers magnetic field strengths in the range 2 to 6000 Gauss, approximately. In the case of very weak fields (solid line), the  $(-Q/I)$  profile is nearly frequency independent with a value of  $\simeq 80\%$  throughout the profile instead of  $100\%$  as in the single scattering case, because of multiple scattering contributions as already mentioned.

The  $(-U/I)$  profile shows Hanle rotation of the polarization plane (the generation of Stokes  $U$ ) in the line core  $|x| < 3.5$  (see the solid, dotted and short-dashed lines in Fig. 9.2), but approaches zero in the line wings  $|x| > 3.5$ . This is in agreement with the traditionally used assumption that, in the case of weak fields, it is sufficient to consider the combination of using the weak field Hanle phase matrix (see e.g. Landi Degl’Innocenti & Landi Degl’Innocenti 1988, Stenflo 1994) in the line core, the Rayleigh phase matrix in the wings.

In the strong field limit ( $v_B = 0.5$  (1285 G) and  $v_B = 2.5$  (6424 G)), Stokes  $Q/I$ ,  $U/I$  and  $V/I$  appear very similar to the true Zeeman absorption profiles. For  $v_B = 2.5$  the intensity profile is clearly split into a Zeeman triplet.

It is well known that Stokes  $V$  gets completely decoupled from  $(IQU)^T$  and transfers independently both in the non-magnetic Rayleigh limit (Chandrasekhar 1950) and in the weak field Hanle limit (Landi Degl’Innocenti & Landi Degl’Innocenti 1988). Thus, unless a Stokes  $V$  parameter is given as input, or generated internally through a thermal emission coefficient, Stokes  $V$  is not generated at all. However, in the Hanle-Zeeman scattering problem, the  $V$  parameter is naturally coupled to  $(IQU)^T$  and is generated even if no input  $V$  is given or the anisotropic Zeeman absorption matrix is not considered explicitly. The coupling of  $V$  to  $(IQU)^T$  is weak in the weak field case and thus the  $V/I$  signal is small (see the solid, dotted, and short-dashed lines in Fig. 9.2). This coupling increases as the field strength increases, and hence  $V/I$  also becomes large (see the dot-dashed, dash-triple dotted, and long dashed lines in Fig. 9.2).

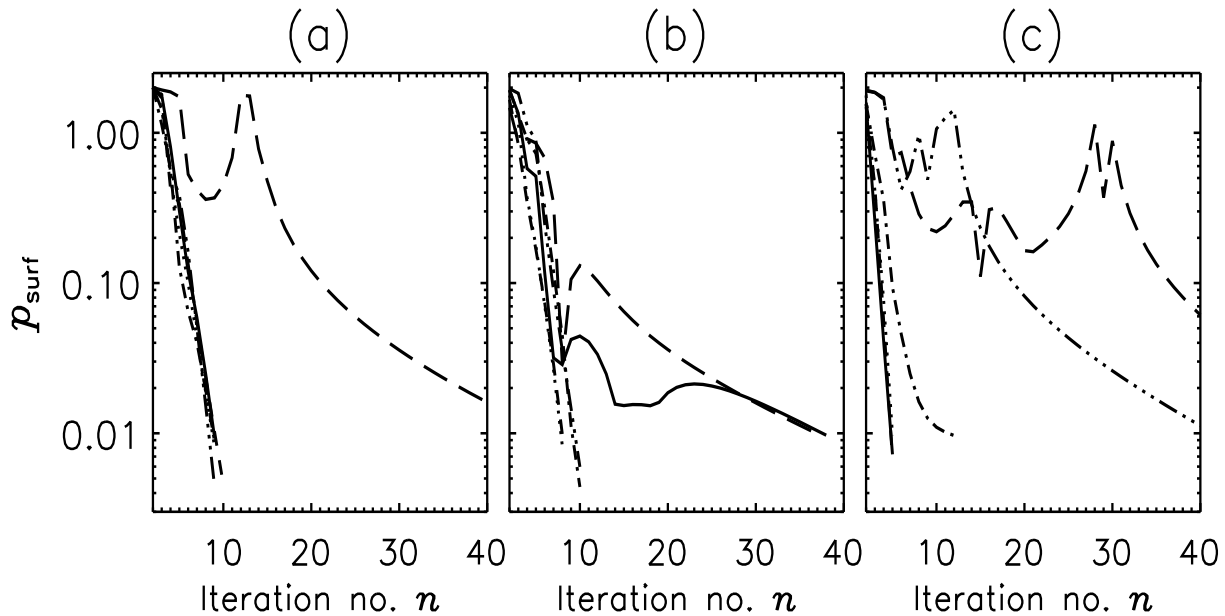


Figure 9.3: Convergence behavior. Panels (a) and (b) correspond to steps 2 and 3 of stage 1 in the perturbation method (see § 9.3.1), panel (c) to stage 2 (see § 9.3.2). Isothermal self-emitting slab with model parameters:  $(T, a, \epsilon, r, \Gamma_E/\Gamma_R) = (20, 10^{-3}, 10^{-4}, 10^{-9}, 1)$  and field orientation  $(\vartheta_B, \varphi_B) = (30^\circ, 0^\circ)$ . Different line types are: solid ( $\Gamma_B = 1, v_B = 0.001$ ); dotted (3, 0.003); short-dashed (10, 0.01); dash-dotted (50, 0.05); dash-triple-dotted (100, 0.1); and long-dashed (200, 0.2). Notice rapid convergence for  $(\Gamma_B \leq 10, v_B \leq 0.01)$  and slow convergence for  $(\Gamma_B > 10, v_B > 0.01)$  in panel (c). The  $(\Gamma_B = 200, v_B = 0.2)$  case converges at  $n = 47$  in panel (a) and at  $n = 60$  in panel (c).

#### 9.4.2 Convergence behavior of the perturbation method

A plot of  $p_{\text{surf}}$  (defined in Eq. (9.22)) versus iteration number  $n$  is presented in Fig. 9.3. The model parameters are  $(T, a, \epsilon, r, \Gamma_E/\Gamma_R) = (20, 10^{-3}, 10^{-4}, 10^{-9}, 1)$  and field orientation  $(\vartheta_B, \varphi_B) = (30^\circ, 0^\circ)$ . The Hanle  $\Gamma_B$  parameter is chosen as a free parameter. Panels (a) and (b) correspond respectively to step 2 and 3 of stage 1 of the perturbation method, while panel (c) corresponds to the stage 2 in the perturbation method. We note that for  $(\Gamma_B \leq 10, v_B \leq 0.01)$ , the convergence is reached within 10 iterations in both panels (a) and (b) (except for  $(\Gamma_B = 1, v_B = 0.001)$  in panel (b)). Further, from panel (c) we see that for  $(\Gamma_B \leq 10, v_B \leq 0.01)$ , the convergence is reached within 5 to 6 iterations. This clearly shows that the contribution from Zeeman absorption is quite small as expected.

For  $(\Gamma_B > 10, v_B > 0.01)$ , the increasing contribution from the Zeeman absorption

matrix slows down the convergence (see dash-dotted, dash-triple-dotted, and long-dashed lines in Fig. 9.3c). The numerical method fails to converge for ( $\Gamma_B > 200$ ,  $v_B > 0.2$ ). This is because the perturbation method is based on the assumption that the source vectors corresponding to  $Q$ ,  $U$  and  $V$  serve as perturbation to that of  $I$ . For ( $\Gamma_B > 200$ ,  $v_B > 0.2$ ) this condition is no longer satisfied. In this chapter we have applied the perturbation method to solve hard problems and used it as far as it gives a stable and converged solution.

However, for optically thin slabs (for eg. see Fig. 9.2) where the single scattering dominates the line radiation field, the polarization at every frequency is produced in the very first scattering and has a small probability of undergoing modifications by subsequent scattering events (within the slab). For this reason, the perturbation convergence is rapid (3 to 5 iterations), with hardly any difference from first iteration to the second, and so on, irrespective of the field strength. Therefore for thin slabs the final solution is extremely close to the 1st iteration solution. For the same reason, in optically thin slabs, irrespective of whether one uses a scalar absorption coefficient, or matrix absorption, the convergence rate is nearly the same.

### 9.4.3 Hanle saturation of the line polarization

In Figure 9.4 we present the emergent Stokes parameters for a range of field strengths, varying from very weak to the Hanle saturation regime. The model used is same as that of Fig. 9.3, but for  $T = 200$ . The Hanle  $\Gamma_B$  parameter is chosen as a free parameter and varied from 0.1 to 100. The choice of  $\Gamma_E/\Gamma_R = 1$  corresponds to a nearly equal mix of  $\mathbf{R}^{\text{II}}$  and  $\mathbf{R}^{\text{III}}$ . The results in the left panels are computed using the PALI method of Fluri et al. (2003b), while the results in the right panels are obtained by solving Eq. (9.7), using the perturbation technique described in the present chapter with AA Hanle-Zeeman redistribution matrix. We also show in Fig. 9.5 the convergence behavior of the perturbation method for the model considered in this section. The convergence rate in the AA case is somewhat larger than the AD case (presented in Fig. 9.3). Also, the convergence is more uniform in the AA case, compared to the AD case.

Domain based Hanle PRD theories show a saturation behavior as we go from weak fields to the intermediate field regime ( $\Gamma_B$  going from 0.1 to 100, see Fig. 9.4a). The  $Q$  values initially decrease (depolarization) and then approach a saturation limit for all frequencies. The  $U$  values initially increase (Hanle rotation of the polarization plane), then decrease and approach zero at all the line frequencies. Such a saturation behavior is not exhibited

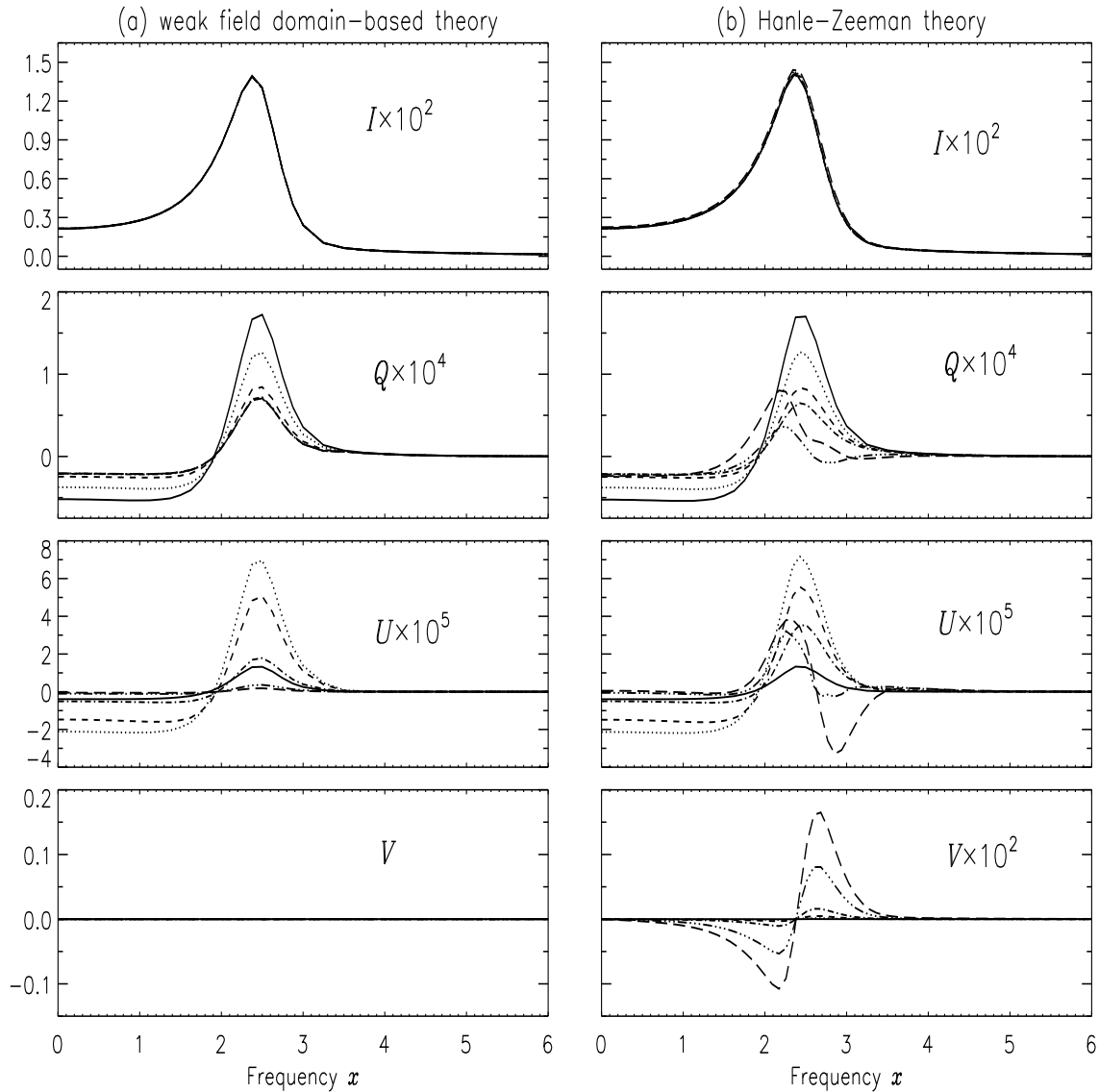


Figure 9.4: Comparison of domain based weak field theory with the full Hanle-Zeeman theory, for a range of field strengths varying from very weak to the Hanle saturation regime, for  $\mu = 0.11$  and  $\varphi = 0^\circ$ . Model parameters:  $(T, a, \epsilon, r, \Gamma_E/\Gamma_R) = (200, 10^{-3}, 10^{-4}, 10^{-9}, 1)$ . Magnetic field orientations:  $(\vartheta_B, \varphi_B) = (30^\circ, 0^\circ)$ . Isothermal, self-emitting slab. The Hanle  $\Gamma_B$  parameter is: 0.1 (solid), 1 (dotted), 3 (dashed), 10 (dot-dashed), 50 (dash-triple-dotted), and 100 (long-dashed). We note that in the  $U$  panel of Fig. 9.4b the long-dashed line has been rescaled by the factor  $2 \times 10^4$  and not by  $10^5$  that has been applied to the other lines in the panel.

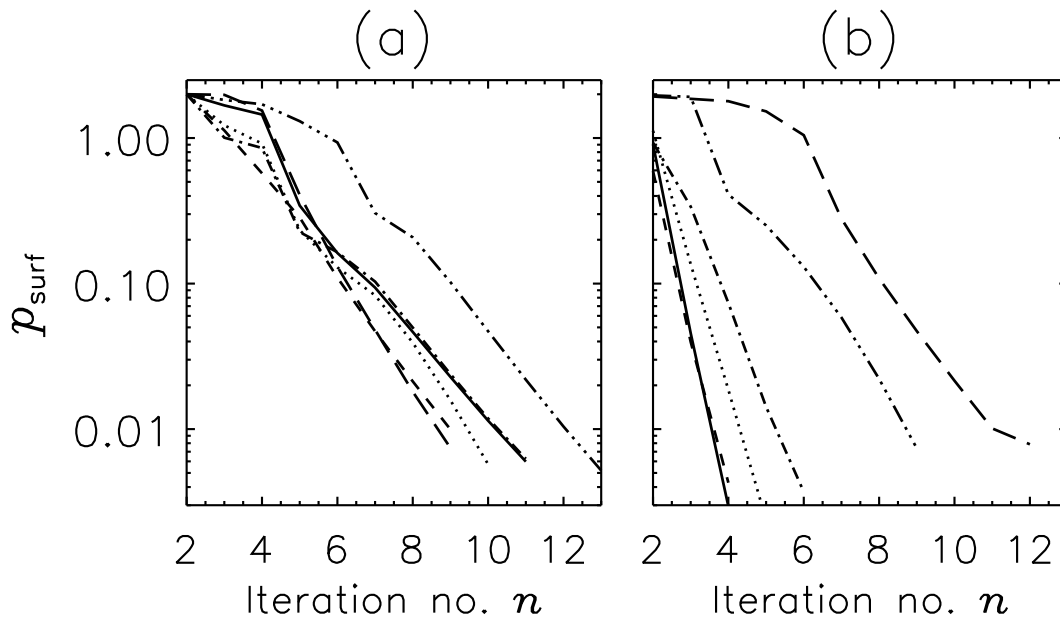


Figure 9.5: Convergence behavior of the perturbation method for the model considered in Fig. 9.4. Panel (a) corresponds to step 2 of the stage 1 in the perturbation method (scalar absorption coefficient), and panel (b) to the stage 2 of the perturbation method (matrix absorption). We recall that to obtain the AA solution we skip the step 3 (AD computation) of stage 1 in the perturbation method. Line types have the same meaning as in Fig. 9.4.

in the Hanle-Zeeman theory (see Fig. 9.4b). For  $\Gamma_B > 10$ , the Zeeman absorption matrix plays a significant role, and we get a smooth transition from the scattering dominated weak field Hanle effect to the Hanle-Zeeman effect for arbitrary fields. The contribution from the Zeeman absorption is responsible for larger values of Stokes  $U$ . For example Stokes  $U$  in the  $\Gamma_B = 100$  case (see long-dashed line in Fig. 9.4b) is 5 times larger when compared to the Stokes  $U$  profiles computed using smaller values of  $\Gamma_B$ .

From Fig. 9.4a we can define various field strength regimes for the Hanle effect. The Hanle effect becomes operative when the Zeeman splitting ( $g\nu_L$ ) is comparable to the small damping width ( $\Gamma_R$ ) of the line transition. Thus the different field regimes for the Hanle effect can be defined in terms of the parameter  $\Gamma_B$ . The value of  $\Gamma_B$  in the range  $0 < \Gamma_B \leq 0.2$  may be considered as weak field regime for the Hanle effect, since the scattering polarization in this regime is close to the Rayleigh scattering polarization. The intermediate field regime of the Hanle effect corresponds to the range  $0.2 < \Gamma_B < 5$  (see also Stenflo 1994, p. 228), with  $\Gamma_B = 1$  representing the optimum field strength for which the Hanle effect is most significant. The Hanle effect finally saturates for  $\Gamma_B > 5$  and hence

$\Gamma_B > 5$  may be considered as the strong field limit for the Hanle effect.

Similarly we may define the weak, intermediate and strong field regimes for the Zeeman effect. The Zeeman effect becomes operative when the Zeeman splitting ( $g\nu_L$ ) is comparable to the much larger Doppler width ( $\Delta\nu_D$ ) of the line. Thus we define the different field regimes for the Zeeman effect in terms of the parameter  $v_B$ . Weak field regime of the Zeeman effect corresponds to  $v_B \leq 0.3$ . The intermediate and strong field regimes are respectively  $0.3 < v_B < 1.2$  and  $v_B > 1.2$  (see Stenflo 1994, p. 299). Clearly, the Hanle and Zeeman effects are two different physical effects. Further, it is important to note that the intermediate Hanle regime and the intermediate Zeeman regime are very different, with little overlap between the two.

The new aspect of the Hanle-Zeeman line transfer theory is that it covers all the field strength regimes defined above, hence the name Hanle-Zeeman regime. The polarized PRD scattering for all field strengths (from zero field to completely split lines) is described by the Hanle-Zeeman redistribution matrix, while the absorption effects are accounted for by the Zeeman absorption matrix. Both the parameters  $\Gamma_B$  and  $v_B$  enter the calculations, but in different ways. The Hanle parameter  $\Gamma_B$  appears in the scattering part, while the parameter  $v_B$  appears both in the absorption part (through  $\Phi$ ) and in the scattering part (through the magnetic redistribution functions, see Chapter 7).  $\Gamma_B$  and  $v_B$  are related, but the relation is model dependent. For the model chosen here, the Zeeman absorption effects become significant for ( $\Gamma_B > 10$ ,  $v_B > 0.01$ ). In this regime the scattering effects can only be correctly included through the Hanle-Zeeman redistribution matrix. To obtain a self-consistent solution one therefore has to solve the full Hanle-Zeeman line transfer problem.

#### 9.4.4 Comparison of angle-dependent and angle-averaged solutions

In Fig. 9.6 we compare the AD (solid lines) and AA (dotted lines) solutions for the Hanle and Hanle-Zeeman regimes. The model used is the same as that of Fig. 9.3. A detailed comparison of AA and AD solutions for the weak field Hanle effect are presented in Nagendra et al. (2002). They show that for the effectively thin slabs ( $\epsilon T \ll 1$ ) the AA and AD solutions show quite a large difference in  $Q$  and  $U$  (which decreases for effectively thick case). We re-confirm their result for the Hanle regime from the present computations. Our numerical experiments show that as we increase  $\Gamma_B$ , the differences between the AA and AD solution decreases and vanishes for  $\Gamma_B = 200$ . This behavior can be attributed to the progressive dominance of the Zeeman absorption effect (which is blind to the choice of

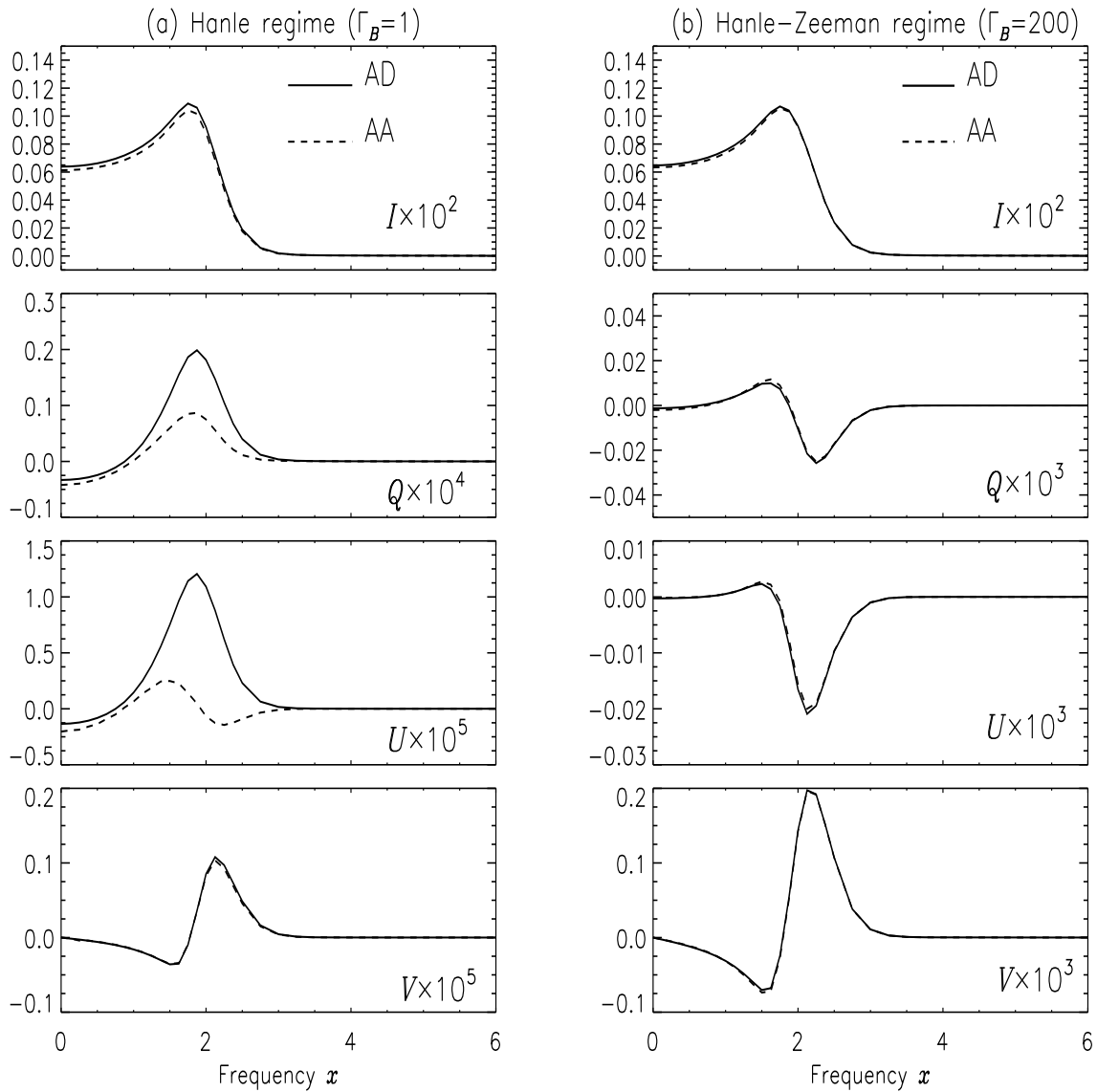


Figure 9.6: Comparison of AA and AD solutions. The model used is the same as that of Fig. 9.3. Notice that as the field strength increases, the differences between the AA and AD solutions become insignificant (panel (b)).

AA or AD functions in the scattering part), over the scattering effects. It is interesting to note that the Stokes  $V$  parameter is also insensitive to the choice of AA or AD functions irrespective of the field strength as shown in Fig. 9.6.

## 9.5 Concluding remarks

A general form of the line radiative transfer equation applicable for a two-level atom ( $J = 0 \rightarrow 1$ ) in arbitrary field strengths is presented and solved. We use a standard perturbation method, extended appropriately to include both the Zeeman absorption matrix and the Hanle-Zeeman scattering redistribution matrix.

To reduce the complexity of the PRD treatment in the Hanle scattering problem it has been common to use domain based redistribution matrices. We show that such approaches are indeed valid for weak fields. For intermediate fields, it is necessary to apply the Hanle-Zeeman PRD line transfer problem presented in this chapter.

The scattering as well as absorption mechanisms in intermediate fields are self-consistently included in the transfer equation. In the Hanle-Zeeman line transfer problem the Stokes  $V$  parameter is coupled to  $(I, Q, U)$  and is generated not only by Zeeman absorption but also by scattering. We have discussed the weak, intermediate, and strong field regimes for both Hanle and Zeeman effects independently. The Hanle-Zeeman line transfer theory covers all these regimes, from zero field to the completely split line. For the model used to present the numerical results in this chapter, we conclude that one has to solve the Hanle-Zeeman line transfer problem to obtain self-consistent solution for  $(\Gamma_B > 10, v_B > 0.01)$ .

In the solar atmosphere one encounters fields of all magnitudes (milligauss to kilogauss). The method developed here addresses this complex problem of Hanle-Zeeman line transfer in the presence of arbitrary field strengths. The weakness of the perturbation method is its great demand for computer memory and CPU time (because it solves the non-axisymmetric Stokes vector transfer equation explicitly). We use the perturbation method, because the axisymmetric form (the so called reduced form) of the concerned transfer equation is yet to be derived. A more elegant and powerful approach would have been to develop a PALI (Polarized Approximate Lambda Iteration) method, which uses the more simple axisymmetric form of the transfer equation. As a first step in this direction we develop such a method in Chapter 10 to solve the transfer problem with weak field Hanle scattering.



## Chapter 10

# A PALI method for Hanle effect with partial redistribution<sup>1</sup>

### 10.1 Introduction

Hanle effect refers to the line polarization caused by resonance scattering of radiation in the presence of an external weak magnetic field. Resonance scattering in non-magnetic media itself produces polarization of the scattered radiation. It is caused by an unequal population of degenerate (non-split) Zeeman substates. Such unequal population naturally arises in solar atmospheric conditions – because the radiation field that illuminates the atom is anisotropic (limb darkened/ brightened), excepting in the deepest layers. In this way the atom gets ‘polarized’ (temporary phase coherences are established between the degenerate substates). In a scattering event, the ‘atomic polarization’ is transferred to the outgoing photon. This ‘resonance polarization’ mechanism with the relevant scattering phase matrix, and radiative transfer equation are described in Chandrasekhar (1950), Stenflo (1994), Landi Degl’Innocenti & Landolfi (2004). The presence of a weak magnetic field (such that the electron Larmor frequency is of the same order as the upper state life-time) causes two important modifications to the non-magnetic resonance scattering polarization – (a) the plane of polarization is rotated with respect to the non-magnetic value, (b) the degree of linear polarization is changed with respect to the corresponding non-magnetic case (Stenflo 1978, and references cited therein).

The Hanle effect has a good diagnostic potential to measure weak directed fields, as in the case of prominences, or canopy like chromospheric structures, and turbulent magnetic

---

<sup>1</sup>This chapter is based on the paper which is under review : Sampoorna, M., Nagendra, K. N., & Frisch, H. 2008, JQSRT (under review)

fields (see e.g. Trujillo Bueno 2003b, and references cited therein). The analysis of Hanle scattering polarization in the polarized line spectrum of Sun usually requires the solution of a radiative transfer equation in which the scattering term involves a redistribution matrix that describes the correlation in frequency, angle and polarization between the incoming and outgoing radiation.

In the case of subordinate lines (which also happen to be generally weak) the assumption of complete redistribution (CRD) is reasonable. It allows one to decouple the polarization from frequency redistribution effects which are described by a scalar redistribution function independent of the scattering angle. When such a decoupling exists, the Stokes parameters can be expanded in cylindrically symmetric irreducible components (Faurobert-Scholl 1991, Frisch 2007). The decomposition method of Faurobert-Scholl (1991) is based on azimuthal Fourier expansions of the radiation field and of the “weak field Hanle phase matrix” (Landi Degl’Innocenti & Landi Degl’Innocenti 1988, Stenflo 1994). In Frisch (2007), it is shown that the Stokes vector decomposition is readily obtained when the Hanle phase matrix is expressed in terms of the irreducible tensors for polarimetry  $\mathcal{T}_Q^K(i, \mathbf{n})$  introduced by Landi Degl’Innocenti (1984, 1985; see also Landi Degl’Innocenti & Landolfi 2004, p. 208).<sup>2</sup> In previous works, the Stokes vector decomposition into irreducible components has been employed to develop PALI (Polarized Approximate Lambda Iteration) methods for CRD and a poor man’s version of partial frequency redistribution (PRD) in which frequency redistribution is angle-averaged and decoupled from polarization (see Nagendra et al. 1998, 1999, Fluri et al. 2003b). Reviews can be found in Nagendra (2003a) and Nagendra & Sampoorna (2008). The decoupling between frequency redistribution and polarization was first suggested in Rees & Saliba (1982) for resonance scattering. A PALI method for resonance scattering with PRD is developed in Paletou & Faurobert-Scholl (1997).

Taking properly into account PRD effects is of fundamental importance to interpret the polarization of resonance lines (which happen to be generally strong). Examples of such lines are: Ca I 4227 Å line, Ca II H and K lines. An exact theory of polarized scattering with PRD in the presence of a magnetic field of arbitrary strength was developed by Bommier (1997b, hereafter VB97b). It is based on a QED approach, holds for a two-level atom with unpolarized ground level and takes into account elastic and inelastic collisions. Explicit form of the redistribution matrix elements in the laboratory frame have been derived in Chapters 7 and 8, for a normal Zeeman triplet ( $J_l = 0$ ,  $J_u = 1$ ). This is referred to as the Hanle-Zeeman redistribution matrix since it covers the full field strength

---

<sup>2</sup>The variable  $i$  ( $i = 0, \dots, 3$ ) refers to the Stokes parameter and  $\mathbf{n}$  to a ray direction.

regime from zero field to the completely split lines. VB97b has also presented useful approximations in the limit of weak field Hanle scattering for practical applications, namely Approximations I, II and III. In Approximation I, the Stokes  $V$  gets decoupled from the other Stokes parameters, but the generalized profiles  $\Phi_Q^{K,K}(J_l, J_u, \xi)$  remain coupled to the irreducible spherical tensor  $\mathcal{T}_Q^K(i, \mathbf{n})$ , the Hanle rotation angle, and the branching ratios (see Eqs. (80) and (81) of VB97b), so that the redistribution matrix continues to couple frequency redistribution and polarization. Approximations II and III are based on asymptotic expansion of the generalized profiles  $\Phi_Q^{K,K}$  at line center and in the wings, and lead to a decomposition of the frequency space into several domains. In each domain frequency redistribution is decoupled from polarization. Approximation II uses the angle-dependent (AD) redistribution functions, and Approximation III the corresponding angle-averaged (AA) functions.

A PALI method for the Hanle effect with frequency domain decomposition is developed in Fluri et al. (2003b, hereafter PALI6) for Approximation III. Here we generalize the redistribution matrix of Approximation III to investigate quantitatively the consequences of the asymptotic expansions of the generalized profiles. We start from Approximation I of VB97b describing the weak field Hanle effect, and angle-average the Doppler broadened generalized profiles. In this new approximation, referred to as Approximation I-a, frequency redistribution is angle-averaged as in Approximation III, but remains coupled to polarization. Also there is no frequency domain decomposition. A decomposition of the Stokes vector in azimuthally symmetric components is still possible (Frisch 2007) and is used to construct a PALI method, hereafter referred to as PALI7. Stokes parameters calculated with the PALI7 method are compared to results obtained with PALI6 in order to evaluate possible inaccuracies due to the asymptotic expansions.

In § 10.2 we present the redistribution matrix in the laboratory frame, under the Approximation I-a. In § 10.3 we write the radiative transfer equation for the real irreducible components of the Stokes parameters. The PALI7 method is presented in § 10.4. Its numerical implementation and comparisons with other methods are presented in § 10.5. We compare with the PALI6 method, and also with a perturbation based numerical method developed to solve the polarized line transfer equation including both Zeeman absorption matrix and the Hanle-Zeeman redistribution matrix (Chapter 9). We consider effectively thin and effectively thick self-emitting slabs, and the interesting and a more difficult case of conservative scattering in an irradiated slab. In § 10.6 we discuss the role of elastic collisions on Hanle scattering. Conclusions are presented in § 10.7. In the Appendix L, we list the elements of a magnetic kernel directly related to the redistribution matrix elements.

## 10.2 The weak field Hanle redistribution matrix

Following VB97b, we write the redistribution matrix as

$$\mathbf{R}_{ij}(x, \mathbf{n}; x', \mathbf{n}'; \mathbf{B}) = \mathbf{R}_{ij}^{\text{II}}(x, \mathbf{n}; x', \mathbf{n}'; \mathbf{B}) + \mathbf{R}_{ij}^{\text{III}}(x, \mathbf{n}; x', \mathbf{n}'; \mathbf{B}). \quad (10.1)$$

The indices  $i, j = 0, 1, 2$ , and 3 correspond to the four Stokes parameters,  $\mathbf{B}$  is the magnetic field,  $(x, x')$  are respectively the outgoing and incoming frequency in Doppler width units with zero at line center (see Eq. (7.15)), and  $(\mathbf{n}, \mathbf{n}')$  the outgoing and incoming ray directions. The indices II and III refer to Hummer (1962) type II and III PRD mechanisms. The scattering angle between  $\mathbf{n}$  and  $\mathbf{n}'$  is denoted as  $\Theta$  (see Fig. 8.2). Approximation I-a is constructed by averaging the Doppler broadened generalized profile over the scattering angle.

The elements of the redistribution matrix for Approximation I-a can be expanded as in VB97b and Frisch (2007). For a normal Zeeman triplet, in the reference frame where quantization axis is parallel to the magnetic field (which we call magnetic reference frame), they may be written as

$$\mathbf{R}_{ij}^{\text{II,III}} = \sum_{KQ} \mathcal{T}_Q^K(i, \mathbf{n}) Z_{KQ}^{\text{II,III}}(x, x'; B) (-1)^Q \mathcal{T}_{-Q}^K(j, \mathbf{n}'), \quad (10.2)$$

with

$$Z_{KQ}^{\text{II}}(x, x'; B) = \frac{\Gamma_{\text{R}}}{\Gamma_{\text{R}} + \Gamma_{\text{I}} + \Gamma_{\text{E}} + i\omega_{\text{L}}gQ} (-1)^K \overline{\Phi}_{Q,\text{II}}^{K,K}(x, x', B), \quad (10.3)$$

and

$$Z_{KQ}^{\text{III}}(x, x'; B) = \frac{\Gamma_{\text{R}}}{\Gamma_{\text{R}} + \Gamma_{\text{I}} + D^{(K)} + i\omega_{\text{L}}gQ} \frac{\Gamma_{\text{E}} - D^{(K)}}{\Gamma_{\text{R}} + \Gamma_{\text{I}} + \Gamma_{\text{E}} + i\omega_{\text{L}}gQ} \overline{\Phi}_{Q,\text{III}}^{K,K,K}(x, x', B). \quad (10.4)$$

The indices  $K$  and  $Q$  are integers coming from the multipolar decomposition of the density matrix elements into irreducible spherical tensors. The index  $K$  takes the value  $K = 0, 1, 2$ , and for each value of  $K$ , the range in  $Q$  is  $-K \leq Q \leq K$ . In the above expressions  $\overline{\Phi}_{Q,\text{II}}^{K,K}(x, x', B)$  denotes the AA version of the AD composite redistribution function  $\Phi_{Q,\text{II}}^{K,K}(x, x', \Theta; B)$  introduced in § 8.2.1 (see Eq. (8.9)). Similarly  $\overline{\Phi}_{Q,\text{III}}^{K,K,K}(x, x', B)$  is the AA version of the corresponding AD composite redistribution function  $\Phi_{Q,\text{III}}^{K,K,K}(x, x', \Theta; B)$  introduced in § 8.2.2 (see Eq. (8.12)). The explicit expressions for the angle-dependent  $\Phi_{Q,\text{II}}^{K,K}$  and  $\Phi_{Q,\text{III}}^{K,K,K}$  are given in Appendix H. They can be expressed in terms of the magnetic redistribution functions introduced in Chapter 7.

We recall that in Eqs. (10.3) and (10.4),  $\Gamma_{\text{R}}$  is the radiative rate,  $\Gamma_{\text{I}}$  and  $\Gamma_{\text{E}}$  are inelastic and elastic collision rates respectively.  $D^{(K)}$  represents the rate of destruction of the  $2K$  -

multipole by elastic collisions (note that  $D^{(0)} = 0$ ).  $\omega_L$  is the Larmor frequency and  $g$  is the Landé factor of the upper level.

In the atmospheric reference frame (ARF), defined with the  $Z$ -axis along the normal to the atmosphere (see Fig. 8.2), the elements of the redistribution matrix may be written (see e.g. Frisch 2007, LL04) as

$$\mathbf{R}_{ij}^{\text{II,III}} = \sum_{KQQ'} \mathcal{T}_Q^K(i, \mathbf{n}) \mathcal{N}_{QQ'}^{K,\text{II,III}}(x, x'; \mathbf{B}) (-1)^{Q'} \mathcal{T}_{-Q'}^K(j, \mathbf{n}'). \quad (10.5)$$

In this chapter the direction of the positive  $Q$  corresponds to linear polarization perpendicular to the limb (reference angle  $\gamma = 0^\circ$ ). The magnetic kernel is of the form

$$\mathcal{N}_{QQ'}^{K,\text{II,III}}(x, x'; \mathbf{B}) = e^{i(Q'-Q)\varphi_B} \sum_{Q''} d_{QQ''}^K(\vartheta_B) d_{Q''Q'}^{K'}(-\vartheta_B) Z_{KQ''}^{\text{II,III}}(x, x'; B), \quad (10.6)$$

where  $\vartheta_B$  and  $\varphi_B$  define the orientation of the magnetic field in the ARF. Explicit expressions for the reduced rotation matrices  $d_{MM'}^J$  can be found in Landi Degl'Innocenti & Landolfi (2004, Table 2.1, p. 57).

### 10.3 Transfer equation for the real irreducible Stokes vector components

For redistribution matrices of the type written in Eq. (10.5), it is shown in Frisch (2007, § 6), that the Stokes vector has an expansion in terms of the spherical tensor  $\mathcal{T}_Q^K(i, \mathbf{n})$ , which has the form

$$I_i(\tau, x, \mathbf{n}) = \sum_{KQ} \mathcal{T}_Q^K(i, \mathbf{n}) I_Q^K(\tau, x, \mu). \quad (10.7)$$

Here  $\mathbf{n}$  is defined by its polar angle  $\vartheta$  and  $\varphi$  with respect to the ARF (see Fig. 8.2) and  $\mu = \cos \vartheta$ . If we only consider linear polarization, the index  $K$  takes the values 0 and 2. Hence only 6-components are needed to represent the Stokes parameters  $I$ ,  $Q$ , and  $U$ . The components  $I_Q^K$  are complex, and satisfy the same conjugation relation as the  $\mathcal{T}_Q^K$ , namely

$$(I_Q^K)^* = (-1)^Q I_{-Q}^K. \quad (10.8)$$

Here we work with the real functions  $I_Q^{xK} = \Re(I_Q^K)$  and  $I_Q^{yK} = \Im(I_Q^K)$ . Note that  $I_Q^K$  are real for  $Q = 0$ .

In matrix notation the transfer equation for the real components may be written as

$$\mu \frac{\partial \mathcal{R}(\tau, x, \mu)}{\partial \tau} = [\phi(x) + r] [\mathcal{R}(\tau, x, \mu) - \mathcal{S}(\tau, x)], \quad (10.9)$$

where  $\mathcal{R} = (I_0^0 I_0^2 I_1^{x2} I_1^{y2} I_2^{x2} I_2^{y2})^T$ , and  $\tau$  is the line-center optical depth. The absorption profile  $\phi(x)$  is a normalized Voigt profile function.  $r$  is the ratio of continuum to integrated line absorption coefficient. The Stokes parameters  $I$ ,  $Q$  and  $U$  and the components of  $\mathcal{R}$  are related through the following expressions (see Frisch 2007)

$$\begin{aligned} I(\tau, x, \mathbf{n}) &= I_0^0 + \frac{1}{2\sqrt{2}}(3 \cos^2 \vartheta - 1) I_0^2 - \sqrt{3} \cos \vartheta \sin \vartheta (I_1^{x2} \cos \varphi - I_1^{y2} \sin \varphi) \\ &\quad + \frac{\sqrt{3}}{2}(1 - \cos^2 \vartheta)(I_2^{x2} \cos 2\varphi - I_2^{y2} \sin 2\varphi), \end{aligned} \quad (10.10)$$

$$\begin{aligned} Q(\tau, x, \mathbf{n}) &= -\frac{3}{2\sqrt{2}}(1 - \cos^2 \vartheta) I_0^2 - \sqrt{3} \cos \vartheta \sin \vartheta (I_1^{x2} \cos \varphi - I_1^{y2} \sin \varphi) \\ &\quad - \frac{\sqrt{3}}{2}(1 + \cos^2 \vartheta)(I_2^{x2} \cos 2\varphi - I_2^{y2} \sin 2\varphi), \end{aligned} \quad (10.11)$$

$$U(\tau, x, \mathbf{n}) = \sqrt{3} \sin \vartheta (I_1^{x2} \sin \varphi + I_1^{y2} \cos \varphi) + \sqrt{3} \cos \vartheta (I_2^{x2} \sin 2\varphi + I_2^{y2} \cos 2\varphi). \quad (10.12)$$

To simplify the notation the dependence on  $\tau$ ,  $x$ ,  $\mu$  of the functions  $I_0^K$ ,  $I_Q^{xK}$  and  $I_Q^{yK}$  is not explicitly indicated. We remark that Stokes  $I$  is controlled by  $I_0^0$ , Stokes  $Q$  by  $I_0^2$  and Stokes  $U$  by  $I_Q^{x2}$  and  $I_Q^{y2}$  for  $Q \neq 0$ .

The 6-component source vector in Eq. (10.9) is of the form

$$\mathcal{S}(\tau, x) = \frac{\phi(x) \mathcal{S}_l(\tau, x) + r \mathcal{G}(\tau)}{\phi(x) + r}. \quad (10.13)$$

Here  $\mathcal{G}(\tau) = (B_{\nu_0} 0 0 0 0 0)^T$  is the primary source vector with  $B_{\nu_0}$  the Planck function and the line source vector is given by

$$\mathcal{S}_l(\tau, x) = \epsilon \mathcal{G}(\tau) + \int_{-\infty}^{+\infty} \frac{\mathbf{N}^r(x, x', \mathbf{B})}{\phi(x)} \mathcal{J}(\tau, x') dx', \quad (10.14)$$

where  $\epsilon = \Gamma_I / (\Gamma_R + \Gamma_I)$  is the destruction probability per scattering. In the above integral  $\mathbf{N}^r(x, x', \mathbf{B})$  is a  $6 \times 6$  matrix constructed with the elements of the magnetic kernels ( $\mathcal{N}_{QQ'}^{K,II} + \mathcal{N}_{QQ'}^{K,III}$ ) and  $\mathcal{J}(\tau, x')$  is the 6-component mean intensity vector defined by

$$\mathcal{J}(\tau, x') = \frac{1}{2} \int_{-1}^{+1} \Psi(\mu') \mathcal{R}(\tau, x', \mu') d\mu'. \quad (10.15)$$

The elements of  $6 \times 6$  matrix  $\Psi(\mu)$  are given in Landi Degl'Innocenti & Landolfi (2004, Appendix A20, see also Frisch 2007). The elements of the magnetic kernel  $\mathbf{N}^r(x, x', \mathbf{B})$  are given in Appendix L. For the brevity of notation, we specify the functional dependence from now on only when necessary and as subscripts.

## 10.4 The PALI7 iterative method

In this section we describe the basic equations of PALI7 method used to solve the line transfer equation (10.9) iteratively. The main difference between the domain based PALI6 and the present method is in the definition of the magnetic kernel  $\mathbf{N}^r(x, x', \mathbf{B})$ . In PALI6, the  $(x, x')$  frequency space is divided in different regions (domains) with constant value of  $\mathbf{N}^r$  in each region. In PALI7 the magnetic kernel  $\mathbf{N}^r$  varies continuously with  $x$  and  $x'$ . Several equations in the method are already presented in Nagendra et al. (1999) and Fluri et al. (2003b). We recall the main ones for the sake of clarity.

### 10.4.1 The details of the iteration scheme

The formal solution of the Hanle transfer equation may be stated in terms of the full Lambda operator as

$$\mathcal{J}_x = \Lambda_x[\mathcal{S}_x], \quad (10.16)$$

where  $\Lambda_x$  operates on the quantity within  $[ ]$ . By defining a local, monochromatic approximate Lambda operator  $\Lambda_x^*$  as

$$\Lambda_x = \Lambda_x^* + \delta\Lambda_x = \Lambda_x^* + (\Lambda_x - \Lambda_x^*), \quad (10.17)$$

we can set up an iterative scheme to compute the source vectors, namely

$$\mathcal{S}_x^{(n+1)} = \mathcal{S}_x^{(n)} + \delta\mathcal{S}_x^{(n)}, \quad (10.18)$$

$$\mathcal{S}_{l,x}^{(n+1)} = \mathcal{S}_{l,x}^{(n)} + \delta\mathcal{S}_{l,x}^{(n)}, \quad (10.19)$$

where the superscript  $(n)$  refers to the  $n$ th iteration step. From Eqs. (10.17) and (10.18) it follows, by keeping only terms up to first order, that

$$\mathcal{J}_x^{(n+1)} \approx \mathcal{J}_x^{(n)} + \Lambda_x^* [\delta\mathcal{S}_x^{(n)}]. \quad (10.20)$$

Inserting Eqs. (10.14) and (10.20) into Eq. (10.19) we obtain an equation for the corrections to the line source vector  $\delta\mathcal{S}_{l,x}^{(n)}$ :

$$\delta\mathcal{S}_{l,x}^{(n)} - \int_{-\infty}^{+\infty} \frac{\mathbf{N}_{x,x',\mathbf{B}}^r}{\phi_x} p_{x'} \Lambda_{x'}^* [\delta\mathcal{S}_{l,x'}^{(n)}] dx' = \mathbf{r}_x^{(n)}. \quad (10.21)$$

In deriving the above equation we have used the relation

$$\Lambda_x^* [p_x \delta\mathcal{S}_{l,x}] = p_x \Lambda_x^* [\delta\mathcal{S}_{l,x}]. \quad (10.22)$$

It holds because  $p_x = \phi_x/(\phi_x + r)$  is a scalar quantity, and  $\Lambda_x^*$  is a linear operator. In Eq. (10.21), the frequency dependent residual vector is given by

$$\mathbf{r}_x^{(n)} = \mathbf{S}_{\text{FS},l,x}^{(n)} - \mathbf{S}_{l,x}^{(n)}. \quad (10.23)$$

The formal line source vector is obtained from

$$\mathbf{S}_{\text{FS},l,x}^{(n)} = \epsilon \mathcal{G}(\tau) + \int_{-\infty}^{+\infty} \frac{\mathbf{N}_{x,x',\mathbf{B}}^r}{\phi_x} \mathcal{J}_{x'}^{(n)} dx', \quad (10.24)$$

where the mean intensity  $\mathcal{J}_x^{(n)} = \Lambda_x \left[ \mathbf{S}_x^{(n)} \right]$  is computed using a short characteristic formal solver (FS). The iteration algorithm is a standard one, described for e.g. in Fluri et al. (2003b, § 3.1).

### 10.4.2 Calculation of source vector corrections

The crucial step of the iterative method is the calculation of the source vector corrections  $\delta \mathbf{S}_{l,x}^{(n)}$ . Here we use the frequency by frequency (FBF) method developed in Paletou & Auer (1995) to compute these corrections. They are found from the system of linear Eqs. (10.21) which can be organized as the formal expression

$$\mathbf{A} \delta \mathbf{S}_l = \mathbf{r}, \quad (10.25)$$

where the vector  $\mathbf{r}$  is the right hand side of Eq. (10.21). At each depth point  $\mathbf{A}$  is a  $6N_x \times 6N_x$  matrix with  $N_x$  the number of frequency points, and  $\mathbf{r}$  has a length  $6N_x$ . Each element of  $\mathbf{A}$  corresponding to a given value of  $x$  and  $x'$  is a  $6 \times 6$  block denoted by  $\mathbf{A}^6$  and given by the expression

$$\mathbf{A}_{ij}^6 = \delta_{ij} \mathbf{E} - \frac{\mathbf{N}_{ij}^r}{\phi_i} p_j \Lambda_j^*; \quad i, j = 1, 2, \dots, N_x. \quad (10.26)$$

Here  $\mathbf{E}$  is the  $6 \times 6$  identity matrix.  $\delta_{ij}$  is the Kronecker's symbol. The indices  $(i, j)$  now refer to the discretized values of  $(x, x')$  respectively. The matrix  $\mathbf{A}$  is computed only once as it does not change during the iteration.

### 10.4.3 Angle-averaged magnetic redistribution functions

The elements of the magnetic kernel  $\mathbf{N}^r(x, x', \mathbf{B})$ , given in Appendix L, contain frequency redistribution functions denoted as  $\overline{R}_{\text{II},X}^q$  and  $\overline{R}_{\text{III},XY}^{qq'}$  with X and Y standing for the Voigt or Faraday–Voigt functions, and  $q, q' = 0, \pm 1$ . They are defined in Eqs. (L.13) and (L.45) and are calculated by numerical integration. For this purpose we use a Gauss–Legendre



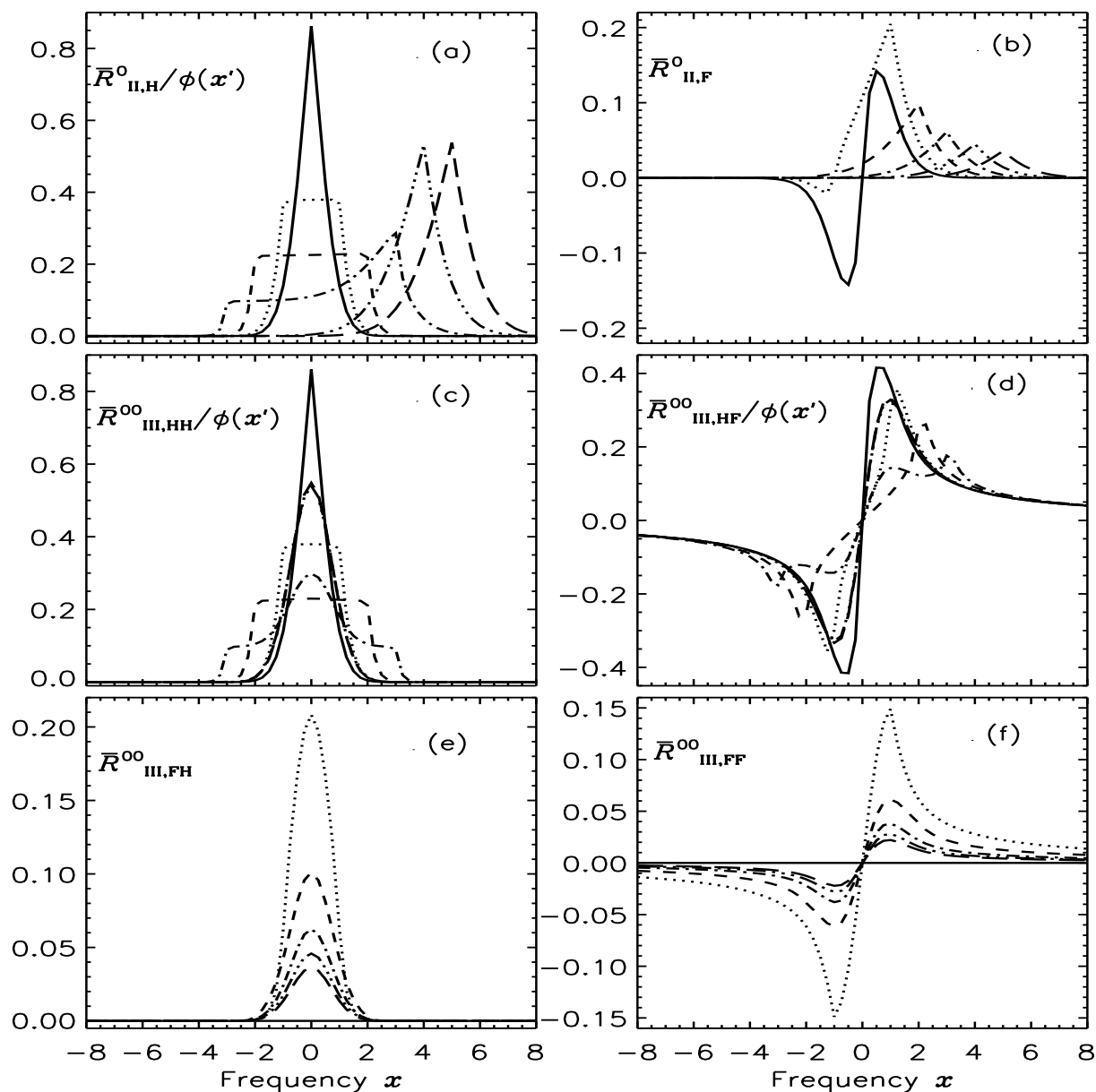


Figure 10.1: Angle-averaged magnetic redistribution functions of Hummer's type II (panels (a) and (b)) and type III (panels (c) – (f)) for  $q = q' = 0$ . Damping parameter  $a = 10^{-3}$ . Different line types correspond to the incoming frequencies:  $x' = 0$  (solid), 1 (dotted), 2 (dashed), 3 (dash-dotted), 4 (dash-triple-dotted) and 5 (long-dashed).

quadrature with 31 angle points. There are 6 components of the type II and 36 of the type III. We now present their main properties.

It is well known that the Hanle effect has its largest sensitivity for  $\Gamma_B = 1$ , where  $\Gamma_B$  is the Hanle efficiency factor defined by  $\Gamma_B = g\omega_L/\Gamma_R$ . In the solar atmosphere,  $\Gamma_B = 1$  corresponds to a field strength of a few Gauss for a electric-dipole transition. For such weak fields the different  $q$  components of  $\bar{R}_{II,X}^q$ , and  $(q, q')$  components of  $\bar{R}_{III,XY}^{qq'}$  differ very little (in the 4th digit after the decimal). However, the differences between components with different  $q, q'$  are significant when we form quantities like  $\bar{f}_{qq'}^{II}$  (see Eq. (L.12)), which ensure of a smooth transition from Hanle effect in the line core to Rayleigh scattering in the wings.

In Fig. 10.1 we present the components corresponding to  $q = q' = 0$ , the other components being graphically identical. The damping parameter  $a$  of the Voigt absorption profile  $\phi(x) = H(x, a)/\sqrt{\pi}$  is taken equal to  $10^{-3}$ . The function  $\bar{R}_{II,H}^0$  shown in Fig. 10.1a is the usual angle-averaged Hummer redistribution function of type II (see e.g. Jefferies 1968, Mihalas 1978). The new type II redistribution function,  $\bar{R}_{II,F}^0$  has the shape of a typical Faraday-Voigt function for  $x' = 0$ . As  $x'$  increases,  $\bar{R}_{II,F}^0$  also exhibits a frequency-coherent behavior with decreasing peak value, quite similar to that of  $\bar{R}_{II,H}^0$ . However for  $x' > 2$ ,  $\bar{R}_{II,F}^0$  is larger than  $\bar{R}_{II,H}^0$  (compare in Fig. 10.1 the panels (a) and (b) where we show  $\bar{R}_{II,H}^0/\phi(x')$  and  $\bar{R}_{II,F}^0$ ). This can be ascribed to the fact that Faraday-Voigt function decreases slowly compared to the Voigt function.

The AA magnetic redistribution functions of type III are presented in Figs. 10.1c - f. In Fig. 10.1c,  $\bar{R}_{III,HH}^{00}$  is the usual angle-averaged Hummer redistribution function. The AA redistribution functions of type III are very similar to the corresponding AD functions for a scattering angle of  $90^\circ$ . We now use this analogy to analyze them. For a  $90^\circ$  scattering angle, the AD type III functions are of the CRD type and may be written as  $R_{III,XY}^{00} = X(x', a)Y(x, a)/\pi$  (see Eqs. (7.47), (7.50) - (7.52)). This expression shows that the variations with  $x$  are determined by  $Y(x, a)$ , and the overall amplitudes by  $X(x', a)$ . For this reason, to show the  $x$ -dependence of the functions  $\bar{R}_{III,HY}^{00}$  for different values of  $x'$  in the same panel we rescaled them by  $\phi(x') = H(x', a)/\sqrt{\pi}$ . For  $\bar{R}_{III,FY}^{00}$  (panels (e) and (f)) this rescaling is not needed because  $F(x', a)$  decreases slowly for large  $x'$ . With the simple approximation given above, it is easy to understand that the shapes of  $\bar{R}_{III,HH}^{00}$  and  $\bar{R}_{III,FH}^{00}$  are Voigt like and the shapes of  $\bar{R}_{III,HF}^{00}$  and  $\bar{R}_{III,FF}^{00}$  are Faraday-Voigt like. We note that for  $x' = 0$ , the functions  $\bar{R}_{III,FY}^{00}$  are zero because  $F(0, a) = 0$ .

It can be seen in Fig. 10.1f that the  $\bar{R}_{III,FF}^{00}$  fall very slowly and hence that a large

frequency bandwidth is needed in the radiative transfer calculations to correctly handle this function. Also these functions should be calculated with a great numerical accuracy since they enter as differences in the magnetic kernels elements (see Eqs. (L.12), (L.39) - (L.42)).

## 10.5 Numerical results and tests of the PALI7 method

In this section we calculate the emergent Stokes parameters from a plane parallel slab characterized by a set of input parameters  $(T, a, \epsilon, r, \Gamma_E/\Gamma_R)$ , where  $T$  is the optical thickness of the slab. The other parameters have been introduced above. The magnetic field is characterized by a set of three parameters  $(\Gamma_B, \vartheta_B, \varphi_B)$ . We consider isothermal self-emitting slabs of thickness  $T = 200$  and  $T = 2 \times 10^6$  (in §§ 10.5.1 and 10.5.2 respectively), and also an irradiated slab with conservative scattering of thickness  $T = 200$  (in § 10.5.3). In §§ 10.5.1 and 10.5.2 we assume pure  $R_{II}$ , i.e.  $\Gamma_E/\Gamma_R = 0$ . Other values of this ratio are considered in § 10.6. In § 10.5.3, we assume  $\Gamma_E/\Gamma_R = 0.1$ , i.e. a mixture of  $R_{II}$  and  $R_{III}$ . In all computations shown in this chapter the Planck function  $B_{\nu_0}$  is set to unity and depolarizing collision rate  $D^{(2)}$  to  $0.5\Gamma_E$ .

The PALI7 method is tested for numerical performance and accuracy by comparing the results obtained with PALI7 to those obtained with PALI6 (Fluri et al. 2003b) and an independent perturbation method for Hanle-Zeeman scattering (Chapter 9).

In our previous PALI methods for the Hanle effect with PRD (namely, Nagendra et al. 1999, Fluri et al. 2003b), the redistribution matrix is factorized into a product of angular phase matrices of Hanle or Rayleigh type and of scalar frequency redistribution functions of Hummer type II and III. Since the magnetic kernel remains outside the integral in Eq. (10.21) within each frequency domain, it was possible to apply the “core-wing separation” method introduced by Paletou & Auer (1995), also called the CRD-CS method. This method amounts to calculate the integral over frequency separately in the core and in the wings. It is very efficient. In the present problem we are dealing with a set of magnetic redistribution functions which are not only of Hummer’s standard type II and III, but also of a new type involving plasma dispersion functions (see Fig. 10.1, and also Chapter 7). It is not clear how to apply the existing core-wing separation techniques to these new magnetic redistribution functions. For this reason, we restrict ourselves to a FBF method which is however computationally more expensive than a CRD-CS method as discussed below. The convergence properties of the FBF iterative method are very similar to that of the CRD-CS method used in Nagendra et al. (1998, 1999) for polarized

problems. Therefore we do not elaborate on this point in the present chapter.

The perturbation method for Hanle-Zeeman scattering has been set up to handle resonance scattering in magnetic fields of any strength. It is based on the Hanle-Zeeman redistribution matrix (see Bommier 1997b, Bommier & Stenflo 1999, Chapters 7 and 8). Here we are using this method with the AA version of the magnetic redistribution functions. This method has been described in detail in § 9.3. It must be said that this method works only when the Stokes parameters  $Q$ ,  $U$ , and  $V$  are small in magnitude compared to Stokes  $I$ . In this sense it can be called a weak polarization method (only several percents in the degree of polarization) but can work up to  $\Gamma_B \simeq 200$ . For this value of  $\Gamma_B$ , the magnetic field is around a thousand Gauss for a typical solar line, but Stokes  $V$  remains a few percent of Stokes  $I$ .

### 10.5.1 Thin slab model

Figure 10.2a is devoted to the "thin" slab ( $T = 200$ ) atmosphere. In such a medium, the  $I$  profile is a self-absorbed emission line because the optical depth in the wings become smaller than unity. The model parameters are  $(T, a, \epsilon, r, \Gamma_E/\Gamma_R) = (200, 10^{-3}, 10^{-4}, 0, 0)$  with the magnetic field parameters  $(\Gamma_B, \vartheta_B, \varphi_B) = (1, 30^\circ, 0^\circ)$ . For accurate computation of Stokes vector, we have used an optical depth resolution of 9 points per decade in a logarithmic scale, covering the range  $10^{-2} \leq \tau \leq 200$ , a Gaussian quadrature with 7 colatitudes [ $0 < \mu < 1$ ], and a 45 point non-uniform frequency grid with the last frequency point  $x_{\max} = 17$ . In the case of the perturbation method an integration over azimuth angle  $\varphi$  is also involved as we solve the non-axisymmetric Stokes vector transfer equation. For azimuthal integration, we use 8 point trapezoidal grid in the range [ $0 \leq \varphi \leq 2\pi$ ].

Figure 10.2a shows that our PALI7 method gives results that are quite similar to the perturbation method and to PALI6. Only small differences are observed for Stokes  $U$ . This good agreement implies that for thin slabs and weak magnetic fields, PALI7 is a good approximation for the more general perturbation method and also that Approximation III of VB97b with the domain decomposition implemented in PALI6 is a good approximation for the more general Approximation I-a implemented in PALI7. For thick slabs, large differences between PALI6 and PALI7 are observed for Stokes  $U$  (see Fig. 10.2b).

In Table 10.1 we compare the CPU time and memory requirements of the above mentioned three methods for the model corresponding to Fig. 10.2a. The main differences in memory requirement and CPU time between the PALI7 and PALI6 is due to the following reasons: (i) In PALI7 we need to compute 6 type II and 36 type III angle-averaged

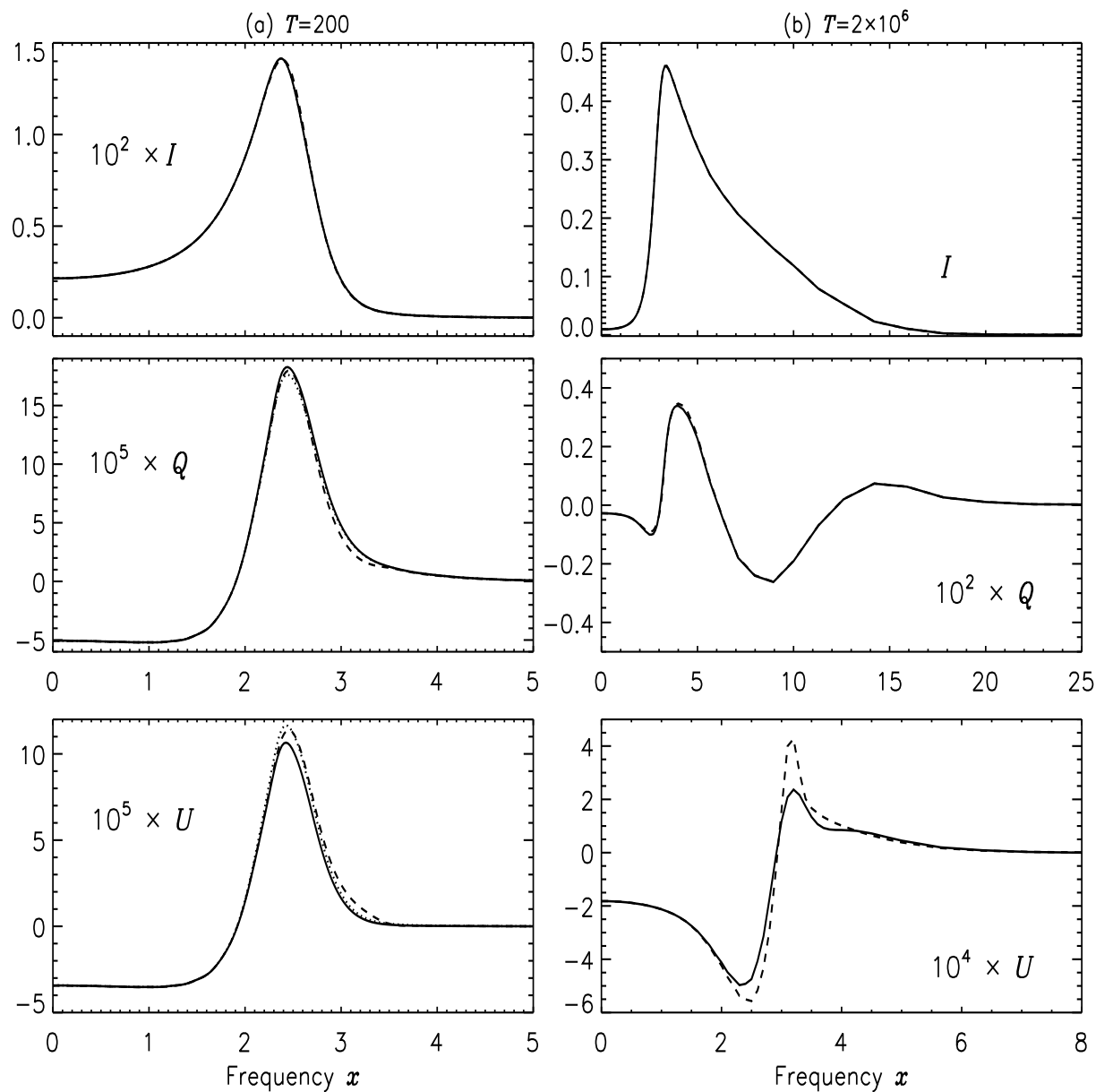


Figure 10.2: Emergent Stokes parameters for the direction  $\mu = 0.11$  and  $\varphi = 0^\circ$  computed with different numerical methods. Isothermal self-emitting slab with the model parameters  $(a, \epsilon, r, \Gamma_E/\Gamma_R) = (10^{-3}, 10^{-4}, 0, 0)$ , and the magnetic field parameters  $(\Gamma_B, \vartheta_B, \varphi_B) = (1, 30^\circ, 0^\circ)$ . Panel (a) “thin” slab with  $T = 200$ . Panel (b) “thick” slab with  $T = 2 \times 10^6$ . Solid line: PALI7 method, dashed line: PALI6 method, dotted line: perturbation method for  $T = 200$ .

Table 10.1: CPU time and memory requirements for PALI7, the PALI6 and perturbation methods. The model parameters are the same as those used for Fig. 10.2a. The computations are performed on Sun Fire V20z Server, 2385 MHz with a Single-core AMD Opteron processor.

Method	CPU time (second)	Memory (MB)
PALI6	16	6
PALI7	292	77
Perturbation	2141	3000

magnetic redistribution functions, compared to one for each type II and III in PALI6. (ii) Further we need to invert and store a  $6N_x \times 6N_x$  matrix for  $N_T$  depth points because we are using a FBF method instead of a core-wing separation method (see §§ 10.4.2 and 10.5). The perturbation method is significantly more demanding in both CPU time and memory requirements than either PALI6 or PALI7 because we are solving the transfer equation for the non-axisymmetric Stokes vector.

### 10.5.2 Thick slab model

Figure 10.2b is devoted to the “thick” slab model with  $T = 2 \times 10^6$ . The other model parameters are the same as that of Fig. 10.2a. The calculations are performed with a logarithmic optical depth scale having a resolution of 5 points per decade, 7 point Gaussian quadrature for  $[0 < \mu < 1]$ , and a 71 point non-uniform frequency grid with  $x_{\max} = 100$ .

Figure 10.2b shows the emergent Stokes parameters computed with PALI7 (solid line) and PALI6 (dashed line) methods for  $\mu = 0.11$  and  $\varphi = 0^\circ$ . For the moment we have not been able to apply the perturbation method to very thick slabs. The profiles of Stokes  $I$  and  $Q$  show a good match. Unlike the effectively thin case ( $\epsilon T \ll 1$  shown in Fig. 10.2a), there are some considerable differences in Stokes  $U$  profile. Differences in  $U$  are mainly in the peak amplitude at the transition between core and wings, which corresponds to a cut-off frequency in the PALI6 method.

We show in Fig. 10.3 the frequency and angle dependence of the real and imaginary parts of  $I_Q^K$  corresponding to the model used in Fig. 10.2b. We observe limb darkening in the case of  $I_0^0$  (which controls Stokes  $I$ ) and limb brightening in case of  $I_0^2$  (which controls Stokes  $Q$ ). The 2nd harmonic components  $I_1^{x2}$ ,  $I_1^{y2}$  show limb darkening and the  $I_2^{x2}$ ,  $I_2^{y2}$  limb brightening. Together these four components contribute to the shape of the  $U$  profile

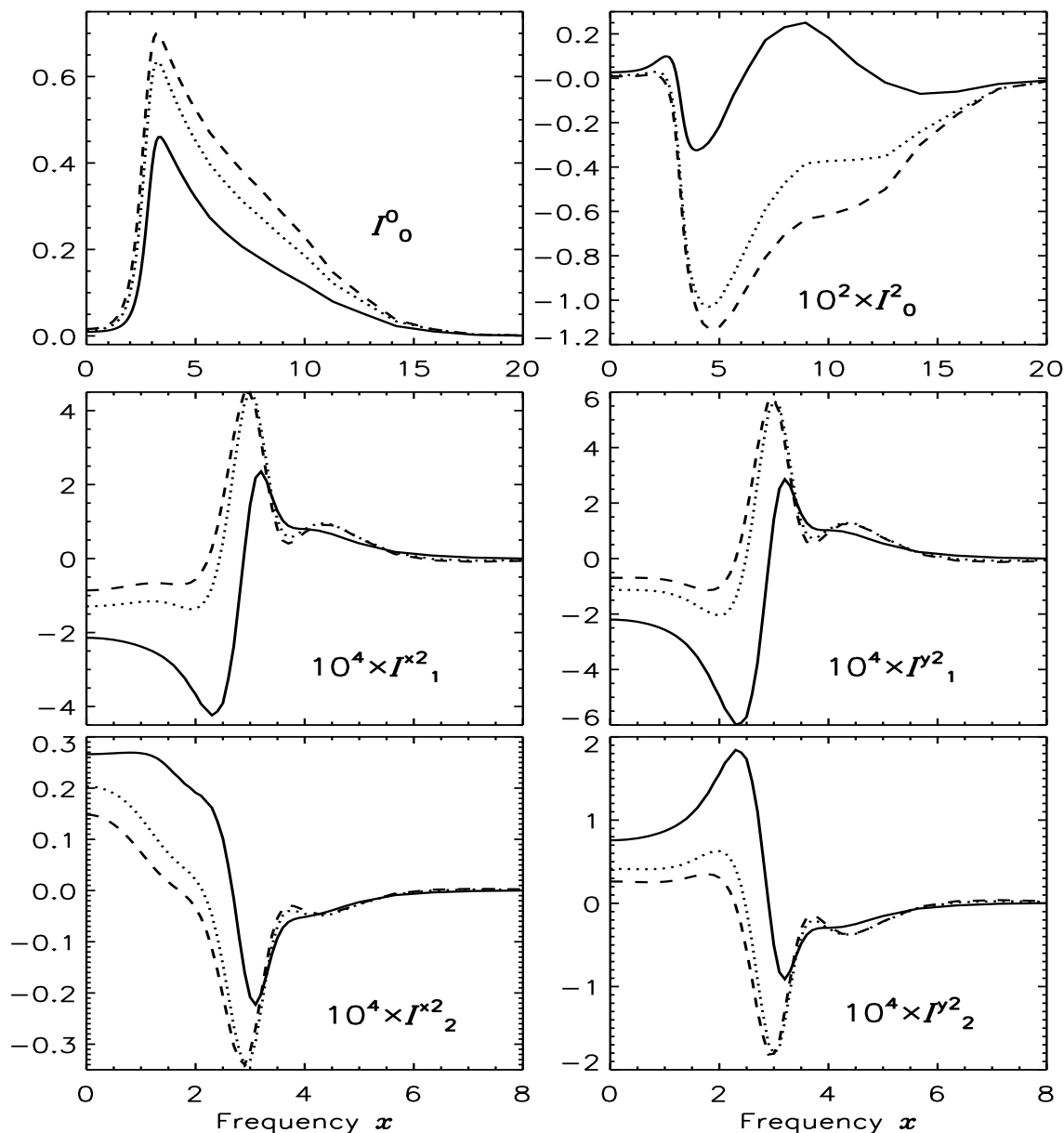


Figure 10.3: Real irreducible components for the model of Fig. 10.2b. Different line types are: solid line ( $\mu = 0.11$ ), dotted line ( $\mu = 0.5$ ) and dashed line ( $\mu = 0.89$ ). We show  $I_0^K$  for a larger frequency bandwidth to show the far wing behavior. Notice that  $I_0^0$  and  $I_0^2$  for  $\mu = 0.11$  have nearly same shape as the Stokes  $I$  and  $Q$  of Fig. 10.2b.

in Fig. 10.2b.

To study the relative difference between the solution obtained from PALI6 and PALI7, we plot the difference  $|{}^7I_Q^K - {}^6I_Q^K|$  for the real and imaginary parts of  $I_Q^K$ , with 7 and 6 denoting PALI7 and PALI6 respectively. Figure 10.4 shows this difference for a self-emitting slab solution presented in Fig. 10.3. The relative difference between the domain based and non-domain based solutions is largest around the cut-off frequency  $x \sim 3$ . For  $I_0^K$ , the relative difference is of the order 1%, while for other components it can be as large as 100%. Clearly the non-domain based PRD is a better choice for uniform accuracy all through the Stokes  $U$  profile. In Stokes  $I$  and  $Q$  the simple domain based PRD still provides a correct solution to a reasonable accuracy of few percent.

### 10.5.3 Irradiated slab model

In this section we present a benchmark which is interesting from both the physical and numerical viewpoint – namely conservative scattering ( $\epsilon = 0$ ,  $r = 0$ ) in a medium irradiated by an unpolarized incident radiation  $\mathcal{R}(\tau = T, x, \mu) = B_{\nu_0} \mathbf{U}$ , with  $\mathbf{U} = (1\ 0\ 0\ 0\ 0)^T$ , on its lower boundary. The numerical errors (arising due to poor normalization of the redistribution and profile functions, or due to the accumulated round off errors that build up after a large number of scatterings if the medium is very thick) can easily be quantified in this set up. This is done by checking “flux conservation”, namely that the sum of the emergent fluxes at both the boundaries remains equal to the incident flux. In the case of PALI7 flux conservation is satisfied to an accuracy of  $10^{-8}$ .

Any scattering problem with given boundary conditions can be converted into a problem with primary sources inside the medium and no incident radiation. For the problem at hand, this transformation will help us to understand the creation of the polarization inside the slab. First we decompose the radiation field into primary and diffuse fields: we write

$$\mathcal{R}(\tau, x, \mu) = \mathcal{R}^p(\tau, x, \mu) + \mathcal{R}^d(\tau, x, \mu), \quad (10.27)$$

where the intensity  $\mathcal{R}^p$  of the directly transmitted radiation is given by

$$\mathcal{R}^p(\tau, x, \mu) = B_{\nu_0} e^{-(T-\tau)\phi(x)/\mu} \mathbf{U}, \quad \text{for } \mu > 0. \quad (10.28)$$

Substituting Eq. (10.27) into Eq. (10.9) with  $\epsilon = 0$  and  $r = 0$ , we obtain for the diffuse



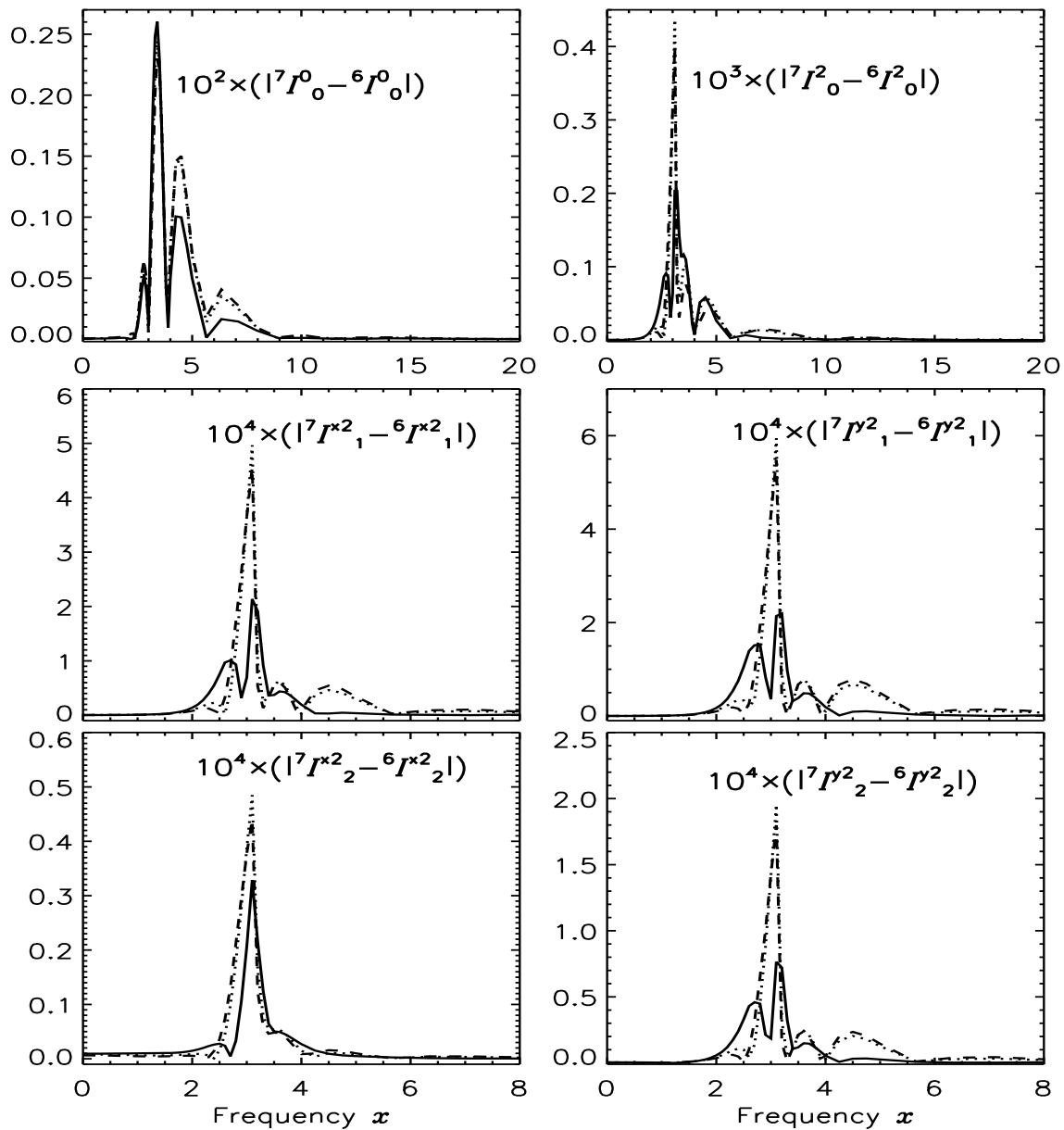


Figure 10.4: Difference between the solution obtained from PALI6 and PALI7. The model and different line types are the same as that of Fig. 10.3. The relative difference is largest around the cut-off frequency  $x \sim 3$ .

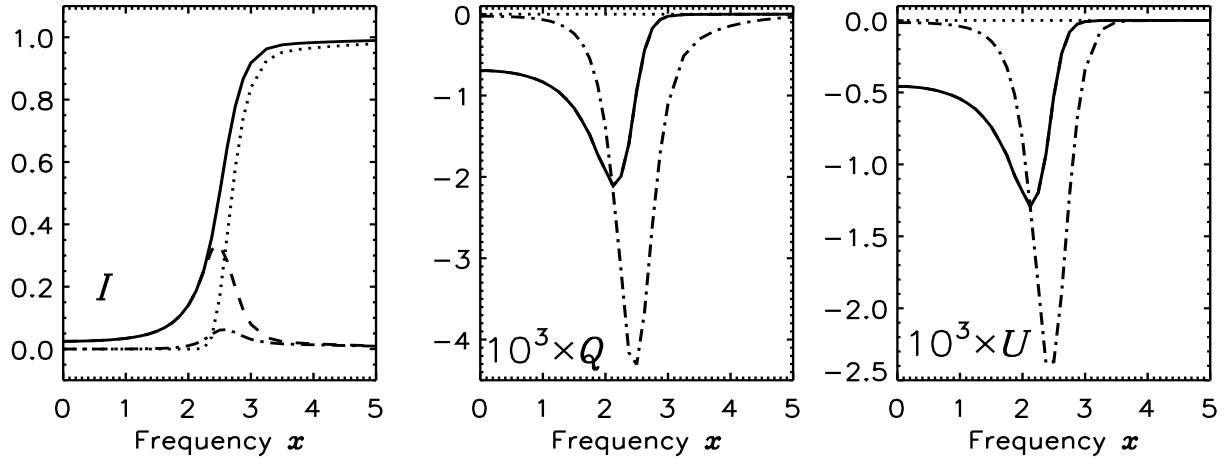


Figure 10.5: Line polarization in a conservatively scattering medium. Model parameters and line types are listed in § 10.5.3.

field  $\mathcal{R}^d$  the transfer equation

$$\begin{aligned} \mu \frac{\partial \mathcal{R}^d(\tau, x, \mu)}{\partial \tau} = & \phi(x) \left[ \mathcal{R}^d(\tau, x, \mu) - \int_{-\infty}^{+\infty} \frac{1}{2} \int_{-1}^{+1} \frac{\mathbf{N}^r(x, x', \mathbf{B})}{\phi(x)} \right. \\ & \left. \times \Psi(\mu') \mathcal{R}^d(\tau, x', \mu') d\mu' dx' - \mathcal{S}^p(\tau, x) \right], \end{aligned} \quad (10.29)$$

where  $\mathcal{S}^p$  plays the role of the primary source. It is given by

$$\mathcal{S}^p(\tau, x) = \frac{B_{\nu 0}}{2} \int_{-\infty}^{+\infty} \int_0^{+1} e^{-(T-\tau)\phi(x')/\mu'} \frac{\mathbf{U}^p(x, x', \mu', B)}{\phi(x)} d\mu' dx', \quad (10.30)$$

with

$$\mathbf{U}^p = N_{11}^r \mathbf{u} + \frac{1}{2\sqrt{2}} (3\mu'^2 - 1) (0, N_{22}^r, N_{32}^r, N_{42}^r, N_{52}^r, N_{62}^r)^T. \quad (10.31)$$

The elements  $N_{k2}^r$ , with  $k = 2, \dots, 6$  are the elements of the second column of the matrix  $\mathbf{N}^r$  (see Appendix L).

In Fig. 10.5 we show the Stokes parameters at the surface  $\tau = 0$  for  $\mu = 0.13$  calculated with PALI7. The slab model is defined by  $(T, a, \epsilon, r, \Gamma_E/\Gamma_R) = (200, 10^{-3}, 0, 0, 0.1)$  and  $(\Gamma_B, \vartheta_B, \varphi_B) = (1, 30^\circ, 0^\circ)$ . The PALI6 and perturbation methods yield essentially the same results, differences being similar to those shown in Fig. 10.2a. The memory requirements for PALI7, PALI6 and the perturbation methods are the same as those given in Table 10.1. The CPU time needed are 326 s for PALI7, 23 s for PALI6 and 3297 s for perturbation method. The increases in memory and CPU time requirements between PALI6 and PALI7 and the perturbation method are explained in § 10.5.1.

The solid line is the solution of the initial problem. The dotted line represents the unpolarized directly transmitted radiation computed using Eq. (10.28). The dashed line is the diffuse field. For  $Q$  and  $U$  the dashed lines are identical to the solid lines since the direct field is unpolarized. The total field, shown by the solid curves, is the sum of the dotted and dashed curves. We also show, dot-dashed line, the emergent Stokes profiles due to the primary source  $\mathcal{S}^p$  when the scattering term in Eq. (10.29) is ignored.

The results displayed in Fig. 10.5 clearly show the contributions from the direct and diffuse fields. In the wings, say for  $x > 3$ , the slab becomes optically thin and it is the direct field which controls the Stokes profiles. This implies that Stokes  $Q$  and  $U$  are zero, and that Stokes  $I$  goes to  $B_{\nu_0} = 1$ . All the polarization is created by multiple scattering of the polarized primary photons contained in  $\mathcal{S}^p$ . In the near wings this multiple scattering decreases the magnitude of the polarization created by  $\mathcal{S}^p$  (dot-dashed line) but around the line center they have an opposite effect.

## 10.6 The effect of elastic collisions on the Stokes profiles

For strong resonance lines formed with PRD, elastic collisions have an important effect on the shapes and values of Stokes  $I$ ,  $Q$ , and  $U$ . The sensitivity to elastic collisions has already been examined in Nagendra et al. (2002) for a slab with a thickness  $2 \times 10^4$ . We return to this topic with an example that emphasizes even further the role of elastic collisions and their effect on the anisotropy of the radiation. We recall that for  $\Gamma_E/\Gamma_R = 0$ , frequency redistribution is described by  $R_{II}$ , i.e. by coherent scattering. When  $\Gamma_E/\Gamma_R \neq 0$ , redistribution becomes a mixture of coherent scattering (the  $R_{II}$  term) and incoherent scattering (the  $R_{III}$  term). Although  $R_{II}$  redistribution has a larger weightage than  $R_{III}$  redistribution through branching ratio, the latter controls the wings of the Stokes profiles for lines with very large optical depth as explained below. The effects of elastic collisions are illustrated in Fig. 10.6.

The Stokes parameters have been calculated with PALI6 and PALI7 for thin ( $T = 200$ ) and thick ( $T = 2 \times 10^6$ ) self-emitting slabs and different choices of the ratio  $\Gamma_E/\Gamma_R$ . For the thin slab case, differences between the PALI6 and PALI7 results are independent of the value of  $\Gamma_E/\Gamma_R$ . They remain as shown in Fig. 10.2a. For the thick slab, differences in Stokes  $U$ , between PALI6 and PALI7 are also independent of  $\Gamma_E/\Gamma_R$ . They are similar to those shown in Fig. 10.2b and can be ascribed to the frequency domain decomposition in PALI6. For Stokes  $I$  and  $Q$ , we have observed small differences when  $|x| > 5$  and the ratio  $\Gamma_E/\Gamma_R$  is about unity (maximum relative differences are of the order of 5%). They

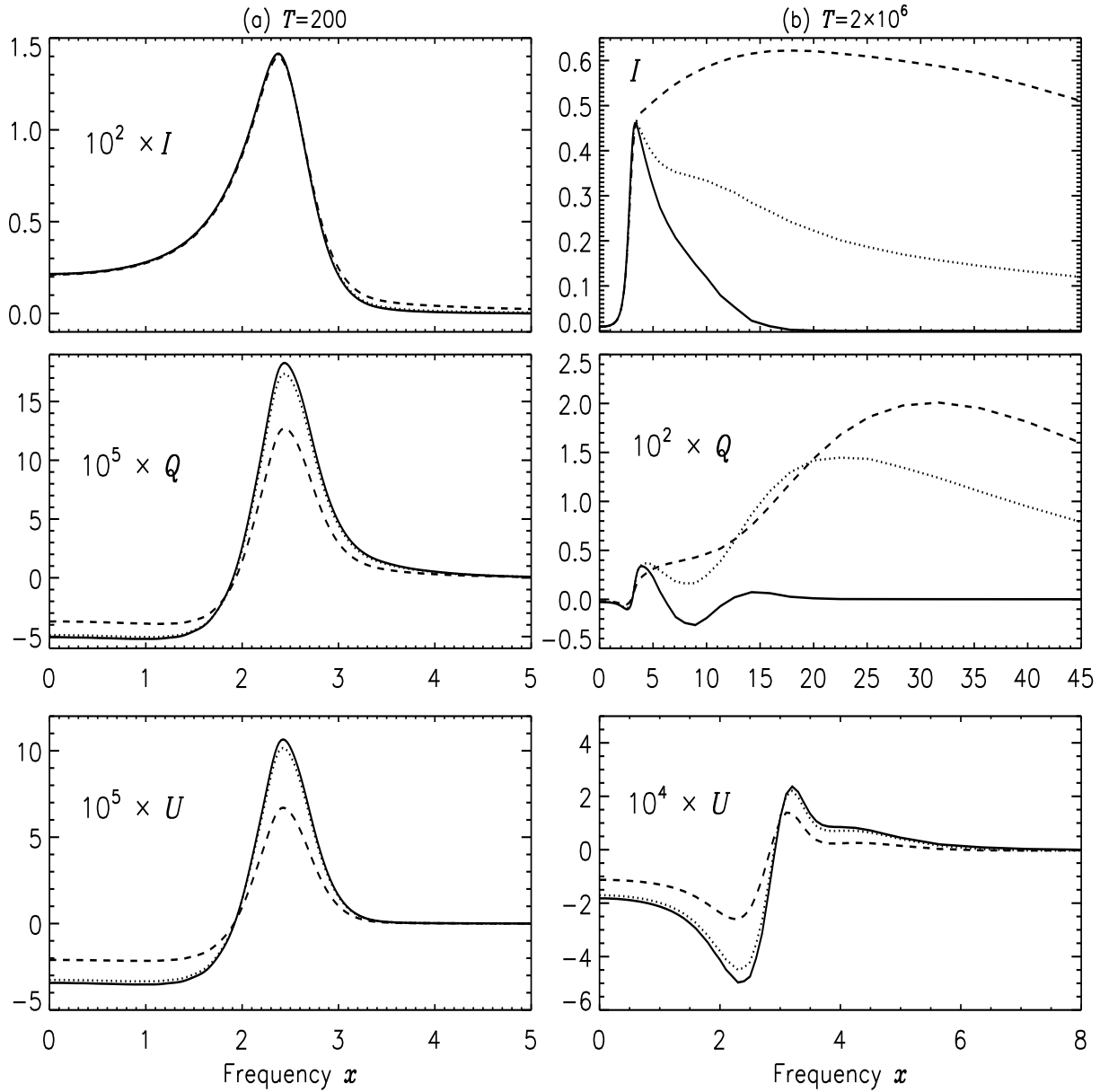


Figure 10.6: Effect of elastic collisions on the emergent Stokes parameters for the direction  $\mu = 0.11$  and  $\varphi = 0^\circ$  computed using the PALI7 method. The model used is the same as Fig. 10.2, except for  $\Gamma_E/\Gamma_R$  which is taken as a free parameter. Different line types are: solid line  $\Gamma_E/\Gamma_R = 0$ , dotted line  $\Gamma_E/\Gamma_R = 0.1$ , and dashed line  $\Gamma_E/\Gamma_R = 1$ .

are probably due to some approximations made to set up the CRD-CS method used in PALI6 but a detailed investigation on their origin is beyond the scope of this chapter.

For lines with small or moderate optical depths, the transfer effects are confined to the line core and the near wings ( $x < 4$ ). Elastic collisions have essentially no effect on Stokes  $I$  and have a simple depolarizing effect on Stokes  $Q$  and  $U$  (see Fig. 10.6a).

For very strong lines, the dependence of Stokes profiles on the ratio  $\Gamma_E/\Gamma_R$  is illustrated in Fig. 10.6b for the self-emitting slab model with  $T = 2 \times 10^6$ . Already for  $\Gamma_E/\Gamma_R = 0.1$ , Stokes  $I$  and  $Q$  strongly depart from the  $\Gamma_E/\Gamma_R = 0$  case. For pure  $R_{II}$ , in spite of Doppler broadening, scattering in the distant wings remains almost coherent in frequency and wing photons can suffer a larger number of scatterings before being destroyed or escaping the medium. As a result Stokes  $I$  is almost isotropic (Frisch & Bardos 1981) and the polarization zero (see middle panel of Fig. 10.6b). The profiles of Stokes  $I$  and  $Q$  change drastically as soon as a small percentage of incoherent scattering (through the elastic collisions) is introduced. For large frequencies,  $R_{III}$  behaves essentially as CRD. In this case, as well known, there is a strong coupling between core and wing photons and the latter cannot be trapped in the wings. Since photons are created in the line core, the strong core-wing coupling leads to a Stokes  $I$  profile with very extended wings (see upper panel of Fig. 10.6b). This phenomenon has been known for quite a while (see e.g. Mihalas 1978). Since photons cannot remain in the wings, the radiation field away from line center is anisotropic (Frisch & Frisch 1977, Frisch 1980) and induces in Stokes  $Q$  the formation of a broad maximum. For  $\Gamma_E/\Gamma_R = 0.1$  its peak value is around  $x \sim 20$ . For  $\Gamma_E/\Gamma_R = 1$ , the  $Q$  maximum shifts further to  $x \sim 30$ . This trend does not continue for  $\Gamma_E/\Gamma_R > 1$ , as the non-monotonic behavior of the composite branching ratios ensure an overall decrease of the polarization. For more detail on this regime see Nagendra et al. (2002).

For Stokes  $U$ , an increase in  $\Gamma_E/\Gamma_R$  simply results in a decrease in  $U$  because the Stokes  $U$ , which is directly linked to the Hanle rotation, is more or less confined to the line core. This situation may change if the magnetic field becomes strong enough to produce some Zeeman splitting (Hanle–Zeeman effect).

## 10.7 Concluding remarks

In previous PALI methods devoted to the weak field Hanle effect with partial frequency redistribution, the frequency space is separated in several domains in which frequency redistribution is decoupled from polarization. In this chapter we introduce an approximate

redistribution matrix referred to as Approximation I-a. It is constructed by angle-averaging the Doppler broadened generalized profile functions entering in the weak field Hanle redistribution matrix (Approximation I in VB97b). Coupling between frequency redistribution and polarization is preserved and the magnetic field effects vary continuously along the line profile. This Approximation I-a is a generalized version of Approximation III in VB97b in the sense that there is no frequency domain decomposition while frequency redistribution remains angle-averaged. For this new redistribution matrix a PALI method (referred to as PALI7) has been developed. Its philosophy is identical to previous PALI methods which rely on the decomposition of the Stokes vector into a finite number of cylindrically symmetrical components  $I_Q^K$  ( $K = 0, 1, 2; -K \leq Q \leq +K$ ) which satisfy standard transfer problems with the source vector independent of the ray direction.

The PALI7 method has been used to examine the consequence of the frequency space decomposition. For a few atmospheric models, we have compared the Stokes parameters calculated with PALI7 and PALI6 (the method introduced in Fluri et al. 2003b to treat Approximation III of VB97b). It is found that a frequency domain decomposition leads to somewhat incorrect evaluations of the components  $I_Q^K$  for  $Q \neq 0$ . The largest errors may reach 100% and occur at the border between core and the wings. This implies errors of the same order for Stokes  $U$  (assuming that positive  $Q$  refers to polarization plane perpendicular to the limb). Frequency domain decomposition barely affects Stokes  $I$  and Stokes  $Q$  which are controlled by  $I_0^0$  and  $I_0^2$ . Our calculations with PALI7 thus confirm the merits of the asymptotic expansions of the generalized profiles at line center and in the wings introduced in VB97b. They also vindicate the usefulness of PALI6, which is numerically much less expensive than PALI7. However only PALI7 can treat the more general problem of non-domain based Hanle PRD.

In its present form, the numerical method employs a frequency by frequency (FBF) approach which is not very economical computationally because it requires matrix inversions. The computational work could be reduced if a core-wing method, as employed in PALI6, could be set up. The difficulty is that the redistribution matrix involves Faraday-Voigt dispersion functions (which change sign) with slow fall-off at large frequencies, hence demanding very large frequency bandwidths to correctly compute the scattering integral. In previous PALI methods, because of domain decomposition, only Voigt functions enter in the redistribution matrices.

For the moment, PALI methods require angle-averaged (AA) frequency redistribution. The next step should be to devise a PALI method for angle-dependent (AD) frequency

---

redistribution. Calculations performed in Nagendra et al. (2002, see also Chapter 9) with a perturbation method for Approximation II of VB97b and its angle-averaged version Approximation III, clearly show the need to take angle-dependence of frequency redistribution into account for the calculation of the Hanle scattering polarization. The introduction of Fourier expansions to handle azimuthal variations of the redistribution functions, in addition to the spherical tensor expansion for the redistribution matrix seems to be a promising approach to generalize the PALI methods to solve angle-dependent PRD problems (see Firsch 2008).





## Chapter 11

### Outlook : Future developments

In this thesis we have touched upon two very interesting front-line topics in the field of solar spectro-polarimetry. First one concerns the polarized line formation in stochastic media. The second one concerns the partial redistribution (PRD) scattering theory for applications in the polarized radiation transfer in the presence of arbitrary magnetic fields. We addressed some fundamental ideas under these two topics, basically by formulating the necessary theoretical framework in this thesis. What remains to be done in the near future, for example, is the sophisticated modeling of the polarimetric observations using these frameworks in the ‘line transfer theory’.

#### 11.1 Stochastic atmospheres for solar polarimetric studies

Due to the solar convection, photospheric plasma has a rather complicated structure in terms of its temperature and velocity distribution. This dynamic behavior also influences the magnetic field, in particular in a region where the gas pressure is comparable to or larger than the magnetic pressure. Thus the photospheric magnetic fields are certainly turbulent with a wide range of wave-numbers.

The theory developed for the stochastic Zeeman line formation is based on a simple Milne-Eddington atmosphere, although various possible generalizations are outlined (see Chapter 4). However, for modeling the actual observations, the theory developed here needs to be used in a code that can handle realistic atmospheres taking full account of the temperature-density stratification. Such an effort is worth trying, since the photospheric magnetic fields seem to comprise a broad range of structures which span from micro to meso to macro scales (see for eg. Stenflo & Holzreuter 2002, Khomenko et al. 2003, Domínguez Cerdeña et al. 2003a). Some efforts in this direction have already been made by Carroll

& Kopf (2007). However there is scope for more detailed investigations.

The Hanle effect is a powerful diagnostic tool for the measurement of weak magnetic field, deterministic or turbulent (see Stenflo 1994, Trujillo Bueno et al. 2004, Bommier et al. 2005). Thus it is necessary to develop the theory and numerics for the Hanle effect produced by a turbulent magnetic field with finite correlation length. Such a theory has been developed by Frisch (2006) by assuming a KAP (Kubo-Anderson process) model for the magnetic field fluctuations along each incident photon path. She gives explicit expressions for the mean Stokes parameters with a two-scattering approximation. This theory needs to be implemented in a numerical code to investigate the effect of correlation length and of the different PDFs (probability distribution functions considered in Chapters 2 and 6) on the Hanle polarization profiles.

The solar atmosphere with its magnetically active regions harbor a whole range of field strengths (milligauss to kilogauss fields). The most ambitious project would be to develop the theory for ‘stochastic Hanle-Zeeman line formation’ in random magnetic fields.

## 11.2 Matter-radiation interaction including partial redistribution effects

The basic theoretical tool required to model the “second solar spectrum” (Stenflo & Keller 1996, 1997) is the polarized radiation transfer equation. First one has to formulate the theory of polarized radiation transfer for a multi-level atom in the presence of arbitrary field strengths taking account of all the relevant physical processes like PRD, quantum interferences, hyperfine structure etc. The solution of the transfer equation so derived requires developing fast iterative algorithms. These basic theoretical tools are already available to model only those spectral lines for which PRD effects are not important (see Landi Degl’Innocenti 2003). However for strong lines PRD effects are important. But the required theory of polarized scattering with PRD line formation is still at its beginning. This theory is developed only recently for a two-level atom with unpolarized ground level (see Bommier 1997b, Bommier & Stenflo 1999, Chapters 7 and 8 in this thesis). A fully consistent formalism capable of handling the PRD in polarized radiation scattering in multi-level atomic models is yet to be developed.

One of the major goals in theory is the development of fast algorithms for solving the Hanle-Zeeman line transfer problems (see Chapter 9). So far, the fast iterative methods like PALI (Polarized Approximate Lambda Iteration) have been developed only for weak

field Hanle scattering problem using angle-averaged PRD functions (see Chapter 10). It will be a numerical challenge to develop a PALI method for (i) angle-dependent PRD function (still in the weak field limit) and (ii) the full Hanle-Zeeman line transfer problems in arbitrary fields. Some efforts have been made on the former (see Frisch 2008), while no attempt is yet made on the latter.

There are many open questions and unsolved problems in the field of solar spectropolarimetry, that deserve an intensive theoretical effort in the near future. It is exactly these unanswered questions that form a source of inspiration for those who like to specialize in ‘scattering physics’ and apply it to solar magnetic field diagnostics!



## Appendix A

### Some properties of Wigner rotation matrices $D_{mm'}^{(l)}$ and spherical harmonics $Y_{lm}$

The properties that are needed here can be found in Brink & Satchler (1968, Appendix IV), Varshalovich et al. (1988), Dolginov et al. (1995) or in LL04. We reproduce them here for convenience. The Wigner matrices  $D_{mm'}^{(l)}(\alpha, \beta, \gamma)$  ( $l \geq 0$ ,  $-l \leq m, m' \leq +l$ ) are the transformation matrices for irreducible tensors of rank  $l$  in rotations of the reference frame. The Euler angles of the rotation are  $\alpha, \beta, \gamma$ . The  $D_{mm'}^{(l)}$  have an explicit representation :

$$D_{mm'}^{(l)} = e^{-im\alpha} d_{mm'}^{(l)}(\beta) e^{-im'\gamma}, \quad (\text{A.1})$$

where  $d_{mm'}^{(l)}(\beta)$  is real. Tables of  $d_{mm'}^{(l)}$  can be found in the above references. The  $Y_{lm}$  are special cases of  $D_{mm'}^{(l)}$  corresponding to  $m' = 0$  (or  $m = 0$ ) :

$$D_{m0}^{(l)}(\phi, \theta, \gamma) = \sqrt{\frac{4\pi}{2l+1}} Y_{lm}^*(\theta, \phi) = \sqrt{\frac{4\pi}{2l+1}} d_{m0}^{(l)}(\theta) e^{im\phi}. \quad (\text{A.2})$$

The Legendre polynomial  $P_l(\theta)$  are special cases of Wigner matrices corresponding to  $m = 0$  and  $m' = 0$ , or in other words, special cases of  $Y_{lm}$  corresponding to  $m = 0$  :

$$P_l(\cos \theta) = D_{00}^{(l)}(\phi, \theta, \gamma) = \sqrt{\frac{4\pi}{2l+1}} Y_{l0}^*(\theta, \phi). \quad (\text{A.3})$$

The first Legendre polynomials are

$$P_0(\theta) = 1; \quad P_1(\theta) = \cos \theta; \quad P_2(\theta) = \frac{1}{2}(3 \cos^2 \theta - 1). \quad (\text{A.4})$$

The  $Y_{lm}$  for  $l = 2$  and  $m = \pm 2$  are

$$Y_{2,\pm 2} = \left(\frac{15}{32\pi}\right)^{1/2} \sin^2 \theta e^{\pm 2i\phi}. \quad (\text{A.5})$$

The angular dependence of  $\varphi_{\text{I,Q,U,V}}$  can thus be expressed in terms of the  $Y_{lm}$  (see Eq. (2.10)). This property is used to calculate their average values over the magnetic field distribution.

## Appendix B

# Integration over Gaussian probability distribution functions

The mean values  $\bar{A}_i$  are given by the averages, over the magnetic field distributions, of Voigt or Faraday-Voigt functions, multiplied by some polynomials (see Eq. (2.17)). Explicit expressions for the average values are given in Eq. (2.22) for 1D turbulence, in Eqs. (2.38) - (2.43), for 3D turbulence. We show here how to obtain these expressions which for 3D turbulence involve the generalized  $H^{(n)}$  (and  $F^{(n)}$ ) functions introduced in § 2.4.1 and discussed in Chapter 3. Several methods are available to carry out the integration. One can consider the Fourier transforms of the quantities to be averaged. One can write the functions  $H^{(0)}$  and  $F^{(0)}$  as real and imaginary parts of the function  $W^{(0)}(z)$ , with  $z$  complex (see Chapter 3) and then do contour integrations in the complex plane. Here we describe a direct method based on simple change of variables.

The integrals we want to transform are of the form

$$G_q = \frac{a}{\pi^{3/2}} \frac{1}{\sqrt{\pi}} \int_{-\infty}^{+\infty} \int_{-\infty}^{+\infty} \frac{e^{-u^2}}{(x - u - q\gamma_B y)^2 + a^2} e^{-(y_0 - y)^2} P(y) dy du, \quad (\text{B.1})$$

where  $P(y)$  is a polynomial in  $y$ . For 1D turbulence,  $P(y) = 1$  (see § 2.3). The weak field limit corresponds to  $y_0 = 0$ .

First we transform the integral over  $u$ . We write

$$x - u - q\gamma_B y = t - s, \quad (\text{B.2})$$

with  $t$  and  $s$  defined by

$$t = x - q\gamma_B y_0; \quad s = u + q\gamma_B (y - y_0). \quad (\text{B.3})$$

Note that  $t = 0$  gives the positions of the  $\sigma$ -components corresponding to the mean magnetic field  $B_0$ . We thus get

$$G_q = \frac{a}{\pi^{3/2}} \frac{1}{\sqrt{\pi}} \int_{-\infty}^{+\infty} \int_{-\infty}^{+\infty} \frac{e^{-[s-q\gamma_B(y-y_0)]^2}}{(t-s)^2 + a^2} e^{-(y_0-y)^2} P(y) dy ds. \quad (\text{B.4})$$

Regrouping the two exponentials, we rewrite

$$[s - q\gamma_B(y - y_0)]^2 + (y_0 - y)^2 = s^2 + (y - y_0)^2 \gamma_1^2 - 2sq\gamma_B(y - y_0) = \frac{s^2}{\gamma_q^2} + \frac{\zeta^2}{\gamma_q^2}, \quad (\text{B.5})$$

with

$$\zeta = \gamma_q^2 \left[ (y - y_0) - q \frac{\gamma_B}{\gamma_q^2} s \right]. \quad (\text{B.6})$$

Thus Eq. (B.4) becomes

$$G_q = \frac{a}{\pi^{3/2}} \frac{1}{\sqrt{\pi}} \int_{-\infty}^{+\infty} \int_{-\infty}^{+\infty} \frac{e^{-s^2/\gamma_q^2}}{(t-s)^2 + a^2} e^{-\zeta^2/\gamma_q^2} \frac{1}{\gamma_q^2} P \left( y_0 + \frac{\zeta}{\gamma_q^2} + q \frac{\gamma_B}{\gamma_q^2} s \right) d\zeta ds. \quad (\text{B.7})$$

Since  $P$  is a polynomial in  $\zeta$ , the Gaussian integral over  $\zeta$  can be calculated explicitly and one obtains a polynomial in  $s$ . It is easy to see that the integral over  $s$  can be expressed as a combination of  $H^{(n)}$  functions. When  $P(y) = 1$ , the integral over  $\zeta$ , divided by  $\sqrt{\pi}$ , gives a factor  $\gamma_q$  and one obtains  $G_q = H(\bar{x}_q, \bar{a}_q)/\gamma_q$ , where  $\bar{x}_q$ ,  $\bar{a}_q$  and  $\gamma_q$  are defined in Eqs. (2.23) and (2.24).

## Appendix C

### Modified spherical Bessel functions

The functions of order 0, 1 and 2 introduced in Eqs. (2.45), (2.46) and (2.47) can be obtained by performing the integration over  $\mu$  in Eq. (2.30) (see also Abramowitz & Stegun 1964, p. 443). They may be written as

$$\sqrt{\frac{\pi}{2z}} I_{1/2}(z) = \frac{1}{z} \sinh z, \quad (\text{C.1})$$

$$\sqrt{\frac{\pi}{2z}} I_{3/2}(z) = -\frac{1}{z^2} \sinh z + \frac{1}{z} \cosh z, \quad (\text{C.2})$$

$$\sqrt{\frac{\pi}{2z}} I_{5/2}(z) = \left( \frac{3}{z^3} + \frac{1}{z} \right) \sinh z - \frac{3}{z^2} \cosh z. \quad (\text{C.3})$$

For small values of  $z$ , one has at leading order,

$$\sqrt{\frac{\pi}{2z}} I_{1/2}(z) \simeq 1; \quad \sqrt{\frac{\pi}{2z}} I_{3/2}(z) \simeq \frac{z}{3}, \quad (\text{C.4})$$

$$\sqrt{\frac{\pi}{2z}} I_{5/2}(z) \simeq \frac{z^2}{15}. \quad (\text{C.5})$$

All the functions  $\sqrt{\pi/2z} I_{l+1/2}(z)$ , for  $z$  real and positive, have positive values and go to  $\infty$  as  $z \rightarrow \infty$ .



## Appendix D

### Some properties of the transport operator

For the benefit of the reader we recall here some of the main properties of the radiative transport operator for polarized transfer (Landi Degl'Innocenti 1987). The homogeneous transfer equation associated to Eq. (4.1) of the text may be written as

$$\frac{d}{ds}\mathbf{I}(s) = \mathbf{K}(s)\mathbf{I}(s), \quad (\text{D.1})$$

where  $s$  is the ray-path coordinate which varies from 0 at the surface to  $\infty$  in the interior,  $\mathbf{K}$  the  $4 \times 4$  propagation matrix and  $\mathbf{I}$  the 4-dimensional Stokes vector. We consider rays propagating from infinity to the surface in the direction normal to the surface.

The Green's function, also called evolution or transport or propagation operator, is here defined by

$$\mathbf{I}(s) = \mathbf{O}(s, s')\mathbf{I}(s'), \quad (\text{D.2})$$

with  $s' > s$  because photons propagate from the interior (positive values of  $s$ ) to the surface at  $s = 0$ . In Landi Degl'Innocenti (1987) and LL04, photons propagate from  $-\infty$  to 0, hence  $\mathbf{O}(s, s')$  is defined with  $s' < s$  (as in time-dependent problems). The evolution operator obeys the limiting condition,

$$\mathbf{O}(s, s) = \mathbf{E}, \quad (\text{D.3})$$

where  $\mathbf{E}$  is the identity operator, and the semi-group property, which can be written as

$$\mathbf{O}(s, s') = \mathbf{O}(s, s'')\mathbf{O}(s'', s'), \quad s \leq s'' \leq s'. \quad (\text{D.4})$$

The evolution operator further satisfies two differential equations,

$$\frac{d}{ds}\mathbf{O}(s, s') = \mathbf{K}(s)\mathbf{O}(s, s'), \quad (\text{D.5})$$

and

$$\frac{d}{ds'} \mathbf{O}(s, s') = -\mathbf{O}(s, s') \mathbf{K}(s'), \quad (\text{D.6})$$

which can be derived from Eqs. (D.1) and (D.2) by taking the derivatives of Eq. (D.2) with respect to  $s$  and  $s'$ .

When the propagation matrix is a constant, the evolution operator is given by

$$\mathbf{O}(s, s') = \exp[-(s' - s)\mathbf{K}]. \quad (\text{D.7})$$

Using Eqs. (D.3) and (D.5) one can verify that the expression

$$\mathbf{I}(s) = -\int_{s_0}^s \mathbf{O}(s, s') \mathbf{K}(s') \mathbf{S}(s') ds' + \mathbf{O}(s, s_0) \mathbf{I}(s_0), \quad (\text{D.8})$$

where  $\mathbf{I}(s_0)$  is the prescribed value of  $\mathbf{I}$  at  $s_0$ , satisfies Eq. (4.1) of the text. Assuming that the source function increases less rapidly than an exponential at infinity, we obtain for the Stokes vector at the surface of a semi-infinite atmosphere,

$$\mathbf{I}(0) = \int_0^\infty \mathbf{O}(0, s) \mathbf{K}(s) \mathbf{S}(s) ds. \quad (\text{D.9})$$

Using Eq. (D.6) we can rewrite this equation as

$$\mathbf{I}(0) = -\int_0^\infty \left[ \frac{d}{ds} \mathbf{O}(0, s) \right] \mathbf{S}(s) ds, \quad (\text{D.10})$$

and after integrating by parts,

$$\mathbf{I}(0) = \mathbf{S}(0) + \int_0^\infty \mathbf{O}(0, s) \left[ \frac{d}{ds} \mathbf{S}(s) \right] ds. \quad (\text{D.11})$$

When  $\mathbf{S}(s) = (C_0 + C_1 s)\mathbf{U}$ , we immediately obtain the result given in Eq. (4.3) of the text.

## Appendix E

### Zeeman absorption matrix in the magnetic reference frame

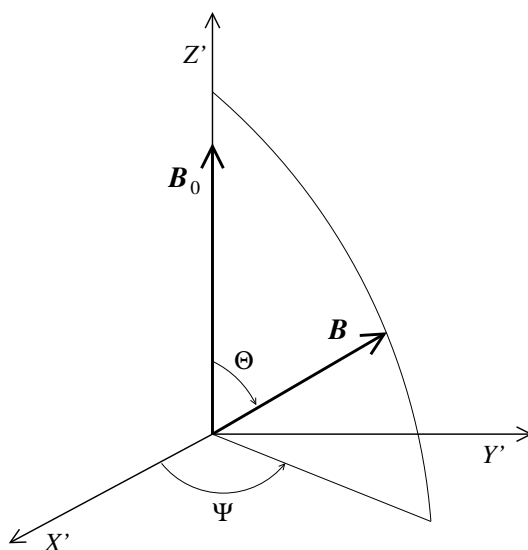


Figure E.1: Right-handed magnetic reference frame (MRF)  $X'Y'Z'$ . The random vector magnetic field  $\mathbf{B}$  is defined by the polar angles  $\Theta$  and  $\Psi$ . The MRF is obtained by an Eulerian rotation of the LOS reference frame (see Fig. 2.1) through  $(\alpha, \beta, \gamma) = (\phi_0, \theta_0, 0)$ .

We now write the coefficients of the Zeeman absorption matrix in the MRF (see Fig. E.1). The Euler angles  $(\alpha, \beta, \gamma)$  of the rotation which brings the LOS reference frame to the MRF are  $\alpha = \phi_0$ ,  $\beta = \theta_0$ ,  $\gamma = 0$ , where  $\theta_0$  and  $\phi_0$  are defined in Fig. 2.1. In this rotation, the spherical harmonics transform according to (Varshalovich et al. 1988, p. 141):

$$Y_{lm}(\theta, \phi) = \sum_{m'} Y_{lm'}(\Theta, \Psi) D_{m'm}^{(l)}(0, -\theta_0, -\phi_0), \quad (\text{E.1})$$

where  $\Theta$  and  $\Psi$  are the polar angles of the field  $\mathbf{B}$  in the MRF (see Fig. E.1). Combining Eq. (E.1) with Eq. (2.10), and using the explicit forms of the  $Y_{lm}$  and  $D_{m'm}^{(l)}$  (see e.g. Brink & Satchler 1968, Varshalovich et al. 1988, LL04), we find

$$\varphi_{\text{I}} = A_0 - \frac{2}{3}A_2 \left[ P_2(\cos \theta_0)P_2(\cos \Theta) - \frac{3}{4}\sin 2\theta_0 \sin 2\Theta \cos \Psi + \frac{3}{4}\sin^2 \theta_0 \sin^2 \Theta \cos 2\Psi \right], \quad (\text{E.2})$$

$$\varphi_{\text{V}} = A_1 [P_1(\cos \theta_0)P_1(\cos \Theta) - \sin \theta_0 \sin \Theta \cos \Psi], \quad (\text{E.3})$$

$$\varphi_{\text{Q}} = A_2 [\cos 2\phi_0 [1] - \sin 2\phi_0 [2]], \quad (\text{E.4})$$

$$\varphi_{\text{U}} = A_2 [\sin 2\phi_0 [1] + \cos 2\phi_0 [2]], \quad (\text{E.5})$$

with

$$[1] = \sin^2 \theta_0 P_2(\cos \Theta) + \frac{1}{2}\sin 2\theta_0 \sin 2\Theta \cos \Psi + \frac{1}{2}(1 + \cos^2 \theta_0) \sin^2 \Theta \cos 2\Psi, \quad (\text{E.6})$$

$$[2] = \sin \theta_0 \sin 2\Theta \sin \Psi + \cos \theta_0 \sin^2 \Theta \sin 2\Psi. \quad (\text{E.7})$$

The anomalous dispersion coefficients are given by Eqs. (E.3) to (E.5) but with the Voigt functions in  $A_1$  and  $A_2$  replaced by Faraday–Voigt functions.

## Appendix F

# Unno-Rachkovsky solution for the deterministic fields

According to the Unno-Rachkovsky (UR) solution (see for e.g. Landi Degl'Innocenti 1976, Jefferies et al. 1989, Rees 1987) the surface value of the Stokes vector may be written as

$$\mathbf{I}(0) = [C_0 + C_1 \mathbf{K}^{-1}] \mathbf{U}, \quad (\text{F.1})$$

where  $\mathbf{K} = \mathbf{E} + \beta \Phi$ . We introduce the vector

$$\mathbf{r}(0) = \frac{1}{C_1} [\mathbf{I}_c(0) - \mathbf{I}(0)], \quad (\text{F.2})$$

where

$$\mathbf{I}_c(0) = (C_0 + C_1) \mathbf{U}, \quad (\text{F.3})$$

is the continuum intensity at the surface. For simplicity we call  $\mathbf{r}(0)$  the residual Stokes vector, although the usual residual Stokes vector, also called line depression Stokes vector (Stenflo 1994, p. 244), is defined by Eq. (F.2) with the intensity of the continuum  $I_c(0)$  in place of  $C_1$ .

The UR solution yields

$$r_I = 1 - [\kappa_I(\kappa_I^2 + \rho_Q^2 + \rho_U^2 + \rho_V^2)]/D, \quad (\text{F.4})$$

$$r_Q = [\kappa_I^2 \eta_Q + \kappa_I(\eta_V \rho_U - \eta_U \rho_V) + \rho_Q W]/D, \quad (\text{F.5})$$

$$r_U = [\kappa_I^2 \eta_U + \kappa_I(\eta_Q \rho_V - \eta_V \rho_Q) + \rho_U W]/D, \quad (\text{F.6})$$

$$r_V = [\kappa_I^2 \eta_V + \rho_V W]/D, \quad (\text{F.7})$$

where

$$\kappa_I = 1 + \beta \varphi_I; \quad \eta_{Q,U,V} = \beta \varphi_{Q,U,V}; \quad \rho_{Q,U,V} = \beta \chi_{Q,U,V}, \quad (\text{F.8})$$

$$W = \eta_Q \rho_Q + \eta_U \rho_U + \eta_V \rho_V, \quad (\text{F.9})$$

$$D = \kappa_I^2 [\kappa_I^2 - \eta_Q^2 - \eta_U^2 - \eta_V^2 + \rho_Q^2 + \rho_U^2 + \rho_V^2] - W^2. \quad (\text{F.10})$$

The absorption and anomalous dispersion coefficients respectively  $\varphi_{I,Q,U,V}$  and  $\chi_{Q,U,V}$  are given in Eq. 2.5. We stress that  $W$ ,  $D$ ,  $(\varphi_Q^2 + \varphi_U^2)$  and  $(\chi_Q^2 + \chi_U^2)$  are independent of the azimuthal angle  $\phi$ . Hence  $r_I$  and  $r_V$  are independent of  $\phi$  whereas  $r_Q$  and  $r_U$  are  $\phi$ -dependent. For  $r_Q$ , the first and third term in the square bracket of Eq. (F.5) vary like  $\cos 2\phi$  and the second term like  $\sin 2\phi$ . For  $r_U$ , it is the first and third term which vary like  $\sin 2\phi$  and the second term like  $\cos 2\phi$ .

UR solution takes a simpler form for longitudinal and transverse fields. When the magnetic field is aligned with the LOS (longitudinal), the UR solution reduces to  $r_Q = r_U = 0$  and

$$r_I = 1 - \frac{1 + \beta\varphi_I}{(1 + \beta\varphi_I)^2 - \beta^2\varphi_V^2}, \quad (\text{F.11})$$

$$r_V = \frac{\beta\varphi_V}{(1 + \beta\varphi_I)^2 - \beta^2\varphi_V^2}, \quad (\text{F.12})$$

with  $\varphi_I = (\varphi_{+1} + \varphi_{-1})/2$ ,  $\varphi_V = (\varphi_{+1} - \varphi_{-1})/2$ .

When the magnetic field is in a transverse direction, the UR solution yields  $r_V = 0$ , and

$$r_I = 1 - \frac{1 + \beta\varphi_I}{(1 + \beta\varphi_I)^2 - \beta^2(\varphi_Q^2 + \varphi_U^2)}, \quad (\text{F.13})$$

$$r_{Q,U} = \frac{\beta\varphi_{Q,U}}{(1 + \beta\varphi_I)^2 - \beta^2(\varphi_Q^2 + \varphi_U^2)}, \quad (\text{F.14})$$

where  $\varphi_I = [\varphi_0 + (\varphi_{+1} + \varphi_{-1})/2]/2$ , and  $\varphi_Q^2 + \varphi_U^2 = [\varphi_0 - (\varphi_{+1} + \varphi_{-1})/2]^2/4$ . The zero-crossing points of  $r_U$  and  $r_Q$  correspond to  $\varphi_Q = \varphi_U = 0$ . They have frequencies  $x = \pm x_m$  with  $x_m$  defined by  $\varphi_0(x_m) = [\varphi_{+1}(x_m) + \varphi_{-1}(x_m)]/2$ . The value of  $x_m$  is independent of  $\beta$ .

When  $\Delta_z B \ll 1$ , one can take  $\varphi_I \simeq \varphi_0 \simeq \varphi_{-1} \simeq \varphi_{+1}$ . Equations (F.11) and (F.13) for  $r_I$ , and Eqs. (F.12) and (F.14) for  $r_V$  and  $r_Q$  become

$$r_I \simeq \frac{\beta\varphi_I}{1 + \beta\varphi_I}, \quad (\text{F.15})$$

$$r_V \simeq \frac{\beta\varphi_V}{(1 + \beta\varphi_I)^2}; \quad r_{Q,U} \simeq \frac{\beta\varphi_{Q,U}}{(1 + \beta\varphi_I)^2}, \quad (\text{F.16})$$

with

$$\varphi_V \simeq -\Delta_z B \frac{d\varphi_I}{dx}; \quad \varphi_Q \simeq -\frac{1}{4} \Delta_z B^2 \frac{d^2\varphi_I}{dx^2}. \quad (\text{F.17})$$

## Appendix G

# Auxiliary coefficients and phase matrices related to R

Here we list the various auxiliary coefficients and matrices appearing in Eq. (7.46). Following Stenflo (1998) we introduce the auxiliary coefficients:

$$c_{qq'}^{\text{II}} = \cos \beta_{q-q'} \left\{ \cos [(q-q')(\phi-\phi')] (h_{qq'}^{\text{II}} \cos \beta_{q-q'} - f_{qq'}^{\text{II}} \sin \beta_{q-q'}) + \sin [(q-q')(\phi-\phi')] (h_{qq'}^{\text{II}} \sin \beta_{q-q'} + f_{qq'}^{\text{II}} \cos \beta_{q-q'}) \right\}, \quad (\text{G.1})$$

$$s_{qq'}^{\text{II}} = \cos \beta_{q-q'} \left\{ \sin [(q-q')(\phi-\phi')] (h_{qq'}^{\text{II}} \cos \beta_{q-q'} - f_{qq'}^{\text{II}} \sin \beta_{q-q'}) - \cos [(q-q')(\phi-\phi')] (h_{qq'}^{\text{II}} \sin \beta_{q-q'} + f_{qq'}^{\text{II}} \cos \beta_{q-q'}) \right\}, \quad (\text{G.2})$$

for type II functions, and

$$c_{qq'}^{\text{III}} = \cos \beta_{q-q'} \cos \alpha_{q-q'} \left( \cos [(q-q')(\phi-\phi')] \left\{ \left[ \Re(h_{qq'}^{\text{III}}) - \Im(f_{qq'}^{\text{III}}) \right] \cos(\beta_{q-q'} + \alpha_{q-q'}) - \left[ \Im(h_{qq'}^{\text{III}}) + \Re(f_{qq'}^{\text{III}}) \right] \sin(\beta_{q-q'} + \alpha_{q-q'}) \right\} + \sin [(q-q')(\phi-\phi')] \left\{ \left[ \Im(h_{qq'}^{\text{III}}) + \Re(f_{qq'}^{\text{III}}) \right] \cos(\beta_{q-q'} + \alpha_{q-q'}) + \left[ \Re(h_{qq'}^{\text{III}}) - \Im(f_{qq'}^{\text{III}}) \right] \sin(\beta_{q-q'} + \alpha_{q-q'}) \right\} \right), \quad (\text{G.3})$$

$$s_{qq'}^{\text{III}} = \cos \beta_{q-q'} \cos \alpha_{q-q'} \left( \sin [(q-q')(\phi-\phi')] \left\{ \left[ \Re(h_{qq'}^{\text{III}}) - \Im(f_{qq'}^{\text{III}}) \right] \cos(\beta_{q-q'} + \alpha_{q-q'}) - \left[ \Im(h_{qq'}^{\text{III}}) + \Re(f_{qq'}^{\text{III}}) \right] \sin(\beta_{q-q'} + \alpha_{q-q'}) \right\} - \cos [(q-q')(\phi-\phi')] \left\{ \left[ \Im(h_{qq'}^{\text{III}}) + \Re(f_{qq'}^{\text{III}}) \right] \cos(\beta_{q-q'} + \alpha_{q-q'}) + \left[ \Re(h_{qq'}^{\text{III}}) - \Im(f_{qq'}^{\text{III}}) \right] \sin(\beta_{q-q'} + \alpha_{q-q'}) \right\} \right), \quad (\text{G.4})$$

for type III functions. The angular phase matrices appearing in Eq. (7.46) are listed below :

$$\mathbf{C}_0^0 = (1 - \mu^2)(1 - \mu'^2) \begin{bmatrix} 1 & 1 & 0 & 0 \\ 1 & 1 & 0 & 0 \\ 0 & 0 & 0 & 0 \\ 0 & 0 & 0 & 0 \end{bmatrix}, \quad (\text{G.5})$$

$$\mathbf{C}_+^0 = \frac{1}{2} \begin{bmatrix} (1 + \mu^2)(1 + \mu'^2) & -(1 + \mu^2)(1 - \mu'^2) & 0 & 0 \\ -(1 - \mu^2)(1 + \mu'^2) & (1 - \mu^2)(1 - \mu'^2) & 0 & 0 \\ 0 & 0 & 0 & 0 \\ 0 & 0 & 0 & 4\mu\mu' \end{bmatrix}, \quad (\text{G.6})$$

$$\mathbf{C}_-^0 = \begin{bmatrix} 0 & 0 & 0 & (1 + \mu^2)\mu' \\ 0 & 0 & 0 & -(1 - \mu^2)\mu' \\ 0 & 0 & 0 & 0 \\ \mu(1 + \mu'^2) & -\mu(1 - \mu'^2) & 0 & 0 \end{bmatrix}, \quad (\text{G.7})$$

$$\mathbf{C}_+^2 = \frac{1}{2} \begin{bmatrix} (1 - \mu^2)(1 - \mu'^2) & -(1 - \mu^2)(1 + \mu'^2) & 0 & 0 \\ -(1 + \mu^2)(1 - \mu'^2) & (1 + \mu^2)(1 + \mu'^2) & 0 & 0 \\ 0 & 0 & 4\mu\mu' & 0 \\ 0 & 0 & 0 & 0 \end{bmatrix}, \quad (\text{G.8})$$

$$\mathbf{S}_+^2 = \begin{bmatrix} 0 & 0 & -(1 - \mu^2)\mu' & 0 \\ 0 & 0 & (1 + \mu^2)\mu' & 0 \\ \mu(1 - \mu'^2) & -\mu(1 + \mu'^2) & 0 & 0 \\ 0 & 0 & 0 & 0 \end{bmatrix}, \quad (\text{G.9})$$

$$\mathbf{C}_+^1 = \mu\mu' \begin{bmatrix} 1 & 1 & 0 & 0 \\ 1 & 1 & 0 & 0 \\ 0 & 0 & 0 & 0 \\ 0 & 0 & 0 & 0 \end{bmatrix} + \mathbf{E}_{33} + \mathbf{E}_{44}; \quad \mathbf{C}_-^1 = \begin{bmatrix} 0 & 0 & 0 & \mu \\ 0 & 0 & 0 & \mu \\ 0 & 0 & 0 & 0 \\ \mu' & \mu' & 0 & 0 \end{bmatrix}, \quad (\text{G.10})$$

$$\mathbf{S}_+^1 = \begin{bmatrix} 0 & 0 & \mu & 0 \\ 0 & 0 & \mu & 0 \\ -\mu' & -\mu' & 0 & 0 \\ 0 & 0 & 0 & 0 \end{bmatrix}; \quad \mathbf{S}_-^1 = \mathbf{E}_{43} - \mathbf{E}_{34}. \quad (\text{G.11})$$



Here  $\mathbf{E}_{ij}$  denotes a matrix that has a single element  $E_{ij} = 1$ , while all the remaining elements are zero. We note that the above matrices are identical to those introduced in Stenflo (1998).

## Appendix H

# Laboratory frame composite redistribution functions

For type II redistribution, to facilitate comparison with the classical equations (derived in Chapter 7), we express  $\Phi_{Q,\text{II}}^{K'',K'}(x, x', \Theta; B)$  in terms of auxiliary functions  $h_{qq'}^{\text{II}}$  and  $f_{qq'}^{\text{II}}$  introduced in Eqs. (7.27) and (7.28). We list below  $\Phi_{Q,\text{II}}^{K'',K'}$  (dropping the arguments) for different combinations of  $K''$ ,  $K'$ , and  $Q$ :

$$\begin{aligned}
\Phi_{0,\text{II}}^{0,0} &= \frac{1}{3} (h_{00}^{\text{II}} + h_{11}^{\text{II}} + h_{-1-1}^{\text{II}}); & \Phi_{0,\text{II}}^{0,1} &= \frac{1}{\sqrt{6}} (h_{11}^{\text{II}} - h_{-1-1}^{\text{II}}), \\
\Phi_{0,\text{II}}^{0,2} &= -\frac{\sqrt{2}}{3} h_{00}^{\text{II}} + \frac{1}{3\sqrt{2}} (h_{11}^{\text{II}} + h_{-1-1}^{\text{II}}); & \Phi_{0,\text{II}}^{1,1} &= -\frac{1}{2} (h_{11}^{\text{II}} + h_{-1-1}^{\text{II}}), \\
\Phi_{1,\text{II}}^{1,1} &= -\frac{1}{2} (h_{10}^{\text{II}} - i f_{10}^{\text{II}} + h_{0-1}^{\text{II}} - i f_{0-1}^{\text{II}}); & \Phi_{0,\text{II}}^{1,2} &= -\frac{1}{2\sqrt{3}} (h_{11}^{\text{II}} - h_{-1-1}^{\text{II}}), \\
\Phi_{1,\text{II}}^{1,2} &= -\frac{1}{2} (h_{10}^{\text{II}} - i f_{10}^{\text{II}} - h_{0-1}^{\text{II}} + i f_{0-1}^{\text{II}}); & \Phi_{0,\text{II}}^{2,2} &= \frac{2}{3} h_{00}^{\text{II}} + \frac{1}{6} (h_{11}^{\text{II}} + h_{-1-1}^{\text{II}}), \\
\Phi_{1,\text{II}}^{2,2} &= -\Phi_{1,\text{II}}^{1,1}; & \Phi_{2,\text{II}}^{2,2} &= h_{1-1}^{\text{II}} - i f_{1-1}^{\text{II}}.
\end{aligned} \tag{H.1}$$

We further note that

$$\Phi_{Q,\text{II}}^{K'',K'} = (-1)^{K''+K'} \Phi_{Q,\text{II}}^{K',K''}. \tag{H.2}$$

The  $\Phi_{-Q,\text{II}}^{K'',K'}$  are obtained using the conjugation property

$$\Phi_{-Q,\text{II}}^{K'',K'} = \left( \Phi_{Q,\text{II}}^{K'',K'} \right)^*. \tag{H.3}$$

For type III redistribution, to simplify the notation, we introduce the following new functions:

$$(hh)_{qq'}^{\text{III}\pm} = \frac{1}{2} \left( R_{\text{III,HH}}^{qq'} \pm R_{\text{III,HH}}^{-q-q'} \right); \quad (ff)_{qq'}^{\text{III}\pm} = \frac{1}{2} \left( R_{\text{III,FF}}^{qq'} \pm R_{\text{III,FF}}^{-q-q'} \right), \tag{H.4}$$

expressed in terms of HH and FF type magnetic redistribution functions respectively, and

$$(hf)_{qq'}^{\text{III}\pm} = \frac{1}{2} \left( R_{\text{III,HF}}^{qq'} \pm R_{\text{III,HF}}^{-q-q'} \right); \quad (fh)_{qq'}^{\text{III}\pm} = \frac{1}{2} \left( R_{\text{III,FH}}^{qq'} \pm R_{\text{III,FH}}^{-q-q'} \right), \tag{H.5}$$

expressed in terms of the corresponding HF and FH type magnetic redistribution functions. Various combinations of these functions are used in the following quantities:

$$\begin{aligned}
d_1 &= 2 [(hh)_{11}^{\text{III}+} - (hh)_{1-1}^{\text{III}+} - (ff)_{11}^{\text{III}+} - (ff)_{1-1}^{\text{III}+}] + 4 [-(ff)_{00}^{\text{III}+} + (ff)_{01}^{\text{III}+} + (ff)_{10}^{\text{III}+}], \\
d_2 &= 2 [(hf)_{11}^{\text{III}-} + (fh)_{11}^{\text{III}-} + (hf)_{1-1}^{\text{III}-} - (fh)_{1-1}^{\text{III}-}] - 4 [(fh)_{01}^{\text{III}-} + (hf)_{10}^{\text{III}-}], \\
d_3 &= 2 [(hh)_{11}^{\text{III}+} + (hh)_{1-1}^{\text{III}+} - (ff)_{11}^{\text{III}+} + (ff)_{1-1}^{\text{III}+}] + 4 [(hh)_{00}^{\text{III}+} + (hh)_{01}^{\text{III}+} + (hh)_{10}^{\text{III}+}], \\
d_4 &= 2 [(hf)_{11}^{\text{III}-} + (fh)_{11}^{\text{III}-} - (hf)_{1-1}^{\text{III}-} + (fh)_{1-1}^{\text{III}-}] + 4 [(hf)_{01}^{\text{III}-} + (fh)_{10}^{\text{III}-}], \\
d_5 &= 2 [(hh)_{11}^{\text{III}-} - (ff)_{11}^{\text{III}-} + (hh)_{1-1}^{\text{III}-} + (ff)_{1-1}^{\text{III}-}] + 4 [(ff)_{01}^{\text{III}-} + (hh)_{10}^{\text{III}-}], \\
d_6 &= 2 [(hf)_{11}^{\text{III}+} + (fh)_{11}^{\text{III}+} - (hf)_{1-1}^{\text{III}+} + (fh)_{1-1}^{\text{III}+}] - 4 [(fh)_{00}^{\text{III}+} + (fh)_{01}^{\text{III}+} - (fh)_{10}^{\text{III}+}], \\
d_7 &= 2 [(hh)_{1-1}^{\text{III}-} + (ff)_{1-1}^{\text{III}-} - (hh)_{11}^{\text{III}-} + (ff)_{11}^{\text{III}-}] - 4 [(hh)_{01}^{\text{III}-} + (ff)_{10}^{\text{III}-}], \\
d_8 &= 2 [(fh)_{1-1}^{\text{III}+} - (hf)_{1-1}^{\text{III}+} - (hf)_{11}^{\text{III}+} - (fh)_{11}^{\text{III}+}] + 4 [(hf)_{00}^{\text{III}+} - (hf)_{01}^{\text{III}+} + (hf)_{10}^{\text{III}+}].
\end{aligned} \tag{H.6}$$

We now list below the functions  $\Phi_{0,\text{III}}^{K,K'',K'}(x, x', \Theta; B)$  for different combinations of  $K$ ,  $K'$ ,  $K''$  and  $Q$  (dropping the arguments):

$$\Phi_{0,\text{III}}^{0,0,0} = \frac{2}{9} \left[ \frac{1}{2} (hh)_{00}^{\text{III}+} + (hh)_{01}^{\text{III}+} + (hh)_{10}^{\text{III}+} + (hh)_{11}^{\text{III}+} + (hh)_{1-1}^{\text{III}+} \right], \tag{H.7}$$

$$\Phi_{0,\text{III}}^{1,0,0} = \frac{1}{3} [(hh)_{11}^{\text{III}+} - (hh)_{1-1}^{\text{III}+}] = \Phi_{0,\text{III}}^{0,1,1}, \tag{H.8}$$

$$\Phi_{0,\text{III}}^{2,0,0} = \frac{1}{9} [2(hh)_{00}^{\text{III}+} - 2(hh)_{01}^{\text{III}+} - 2(hh)_{10}^{\text{III}+} + (hh)_{11}^{\text{III}+} + (hh)_{1-1}^{\text{III}+}] = \Phi_{0,\text{III}}^{0,2,2}, \tag{H.9}$$

$$\Phi_{0,\text{III}}^{0,0,2} = \frac{\sqrt{2}}{9} [-(hh)_{00}^{\text{III}+} - 2(hh)_{01}^{\text{III}+} + (hh)_{10}^{\text{III}+} + (hh)_{11}^{\text{III}+} + (hh)_{1-1}^{\text{III}+}], \tag{H.10}$$

$$\Phi_{0,\text{III}}^{1,0,2} = \Phi_{0,\text{III}}^{1,2,0} = \frac{1}{\sqrt{2}} \Phi_{0,\text{III}}^{1,0,0}; \quad \Phi_{0,\text{III}}^{1,2,2} = \Phi_{0,\text{III}}^{2,1,1} = \frac{1}{2} \Phi_{0,\text{III}}^{1,0,0}, \tag{H.11}$$

$$\Phi_{1,\text{III}}^{1,2,2} = \frac{1}{16} (d_1 + id_2); \quad \Phi_{1,\text{III}}^{2,2,2} = \frac{1}{16} (d_3 + id_4), \tag{H.12}$$

$$\Phi_{0,\text{III}}^{2,0,2} = \frac{1}{9\sqrt{2}} [-4(hh)_{00}^{\text{III}+} + 4(hh)_{01}^{\text{III}+} - 2(hh)_{10}^{\text{III}+} + (hh)_{11}^{\text{III}+} + (hh)_{1-1}^{\text{III}+}], \tag{H.13}$$

$$\Phi_{0,\text{III}}^{2,2,2} = \frac{1}{18} [8(hh)_{00}^{\text{III}+} + 4(hh)_{01}^{\text{III}+} + 4(hh)_{10}^{\text{III}+} + (hh)_{11}^{\text{III}+} + (hh)_{1-1}^{\text{III}+}], \tag{H.14}$$

$$\Phi_{2,\text{III}}^{2,2,2} = \Re(h_{1-1}^{\text{III}}) - \Im(f_{1-1}^{\text{III}}) - i [\Im(h_{1-1}^{\text{III}}) + \Re(f_{1-1}^{\text{III}})], \tag{H.15}$$

$$\Phi_{0,\text{III}}^{2,2,0} = \frac{1}{9\sqrt{2}} [-4(hh)_{00}^{\text{III}+} - 2(hh)_{01}^{\text{III}+} + 4(hh)_{10}^{\text{III}+} + (hh)_{11}^{\text{III}+} + (hh)_{1-1}^{\text{III}+}], \tag{H.16}$$

$$\Phi_{0,\text{III}}^{0,2,0} = \frac{\sqrt{2}}{9} [-(hh)_{00}^{\text{III}+} + (hh)_{01}^{\text{III}+} - 2(hh)_{10}^{\text{III}+} + (hh)_{11}^{\text{III}+} + (hh)_{1-1}^{\text{III}+}], \quad (\text{H.17})$$

$$\Phi_{0,\text{III}}^{0,1,0} = \frac{\sqrt{2}}{3\sqrt{3}} [(hh)_{01}^{\text{III}-} - (hh)_{1-1}^{\text{III}-} + (hh)_{11}^{\text{III}-}], \quad (\text{H.18})$$

$$\Phi_{0,\text{III}}^{0,1,2} = \frac{1}{3\sqrt{3}} [-2(hh)_{01}^{\text{III}-} - (hh)_{1-1}^{\text{III}-} + (hh)_{11}^{\text{III}-}] = \sqrt{2}\Phi_{0,\text{III}}^{2,1,0}, \quad (\text{H.19})$$

$$\Phi_{0,\text{III}}^{1,1,0} = \frac{1}{\sqrt{6}} [(hh)_{11}^{\text{III}-} + (hh)_{1-1}^{\text{III}-}] = \sqrt{2}\Phi_{0,\text{III}}^{1,1,2}, \quad (\text{H.20})$$

$$\Phi_{1,\text{III}}^{1,1,2} = \frac{1}{16} (d_5 + id_6); \quad \Phi_{1,\text{III}}^{2,1,2} = -\frac{1}{16} (d_7 + id_8), \quad (\text{H.21})$$

$$\Phi_{0,\text{III}}^{2,1,2} = \frac{1}{6\sqrt{3}} [4(hh)_{01}^{\text{III}-} - (hh)_{1-1}^{\text{III}-} + (hh)_{11}^{\text{III}-}], \quad (\text{H.22})$$

$$\Phi_{0,\text{III}}^{1,1,1} = \frac{1}{2} [(hh)_{11}^{\text{III}+} + (hh)_{1-1}^{\text{III}+}], \quad (\text{H.23})$$

$$\Phi_{1,\text{III}}^{1,1,1} = \Phi_{1,\text{III}}^{2,2,2}; \quad \Phi_{1,\text{III}}^{2,1,1} = \Phi_{1,\text{III}}^{1,2,2}; \quad \Phi_{1,\text{III}}^{1,2,1} = \Phi_{1,\text{III}}^{2,1,2}; \quad \Phi_{1,\text{III}}^{2,2,1} = \Phi_{1,\text{III}}^{1,1,2}, \quad (\text{H.24})$$

$$\Phi_{0,\text{III}}^{0,2,1} = \frac{1}{3\sqrt{3}} [-2(hh)_{10}^{\text{III}-} + (hh)_{1-1}^{\text{III}-} + (hh)_{11}^{\text{III}-}] = \sqrt{2}\Phi_{0,\text{III}}^{2,0,1}, \quad (\text{H.25})$$

$$\Phi_{0,\text{III}}^{1,2,1} = \frac{1}{2\sqrt{3}} [(hh)_{11}^{\text{III}-} - (hh)_{1-1}^{\text{III}-}] = \frac{1}{\sqrt{2}}\Phi_{0,\text{III}}^{1,0,1}, \quad (\text{H.26})$$

$$\Phi_{0,\text{III}}^{2,2,1} = \frac{1}{6\sqrt{3}} [4(hh)_{10}^{\text{III}-} + (hh)_{1-1}^{\text{III}-} + (hh)_{11}^{\text{III}-}], \quad (\text{H.27})$$

$$\Phi_{0,\text{III}}^{0,0,1} = \frac{\sqrt{2}}{3\sqrt{3}} [(hh)_{10}^{\text{III}-} + (hh)_{1-1}^{\text{III}-} + (hh)_{11}^{\text{III}-}], \quad (\text{H.28})$$

$$\Phi_{-Q,\text{III}}^{K,K'',K'} = \left( \Phi_{Q,\text{III}}^{K,K'',K'} \right)^*. \quad (\text{H.29})$$

The auxiliary functions  $h_{1-1}^{\text{III}}$  and  $f_{1-1}^{\text{III}}$  appearing in Eq. (H.15) are defined in Eqs. (7.29) - (7.34).

## Appendix I

# Auxiliary coefficients and phase matrices related to $\mathbf{R}^{\text{III}}$

Here we list the various auxiliary coefficients and matrices appearing in Eqs. (8.17) - (8.19). We first introduce some intermediate phase matrices with angular factors:

$$\mathbf{C}_0^0 = (1 - \mu^2)(1 - \mu'^2) \begin{bmatrix} 1 & 1 & 0 & 0 \\ 1 & 1 & 0 & 0 \\ 0 & 0 & 0 & 0 \\ 0 & 0 & 0 & 0 \end{bmatrix}, \quad (\text{I.1})$$

$$\mathbf{D}_{01}^+ = \begin{bmatrix} (1 + \mu^2)(1 - \mu'^2) & (1 + \mu^2)(1 - \mu'^2) & 0 & 0 \\ -(1 - \mu^2)(1 - \mu'^2) & -(1 - \mu^2)(1 - \mu'^2) & 0 & 0 \\ 0 & 0 & 0 & 0 \\ 0 & 0 & 0 & 0 \end{bmatrix}, \quad (\text{I.2})$$

$$\mathbf{D}_{10}^+ = \begin{bmatrix} (1 - \mu^2)(1 + \mu'^2) & -(1 - \mu^2)(1 - \mu'^2) & 0 & 0 \\ (1 - \mu^2)(1 + \mu'^2) & -(1 - \mu^2)(1 - \mu'^2) & 0 & 0 \\ 0 & 0 & 0 & 0 \\ 0 & 0 & 0 & 0 \end{bmatrix}, \quad (\text{I.3})$$

$$\mathbf{D}_{11}^+ = \begin{bmatrix} (1 + \mu^2)(1 + \mu'^2) & -(1 + \mu^2)(1 - \mu'^2) & 0 & 0 \\ -(1 - \mu^2)(1 + \mu'^2) & (1 - \mu^2)(1 - \mu'^2) & 0 & 0 \\ 0 & 0 & 0 & 0 \\ 0 & 0 & 0 & 0 \end{bmatrix}, \quad (\text{I.4})$$

$$\mathbf{D}_{1-1}^+ = 4\mu\mu'\mathbf{E}_{44}, \quad (\text{I.5})$$

$$\mathbf{D}_{01}^- = 2\mu(1 - \mu'^2) \begin{bmatrix} 0 & 0 & 0 & 0 \\ 0 & 0 & 0 & 0 \\ 0 & 0 & 0 & 0 \\ 1 & 1 & 0 & 0 \end{bmatrix}; \quad \mathbf{D}_{10}^- = 2(1 - \mu^2)\mu' \begin{bmatrix} 0 & 0 & 0 & 1 \\ 0 & 0 & 0 & 1 \\ 0 & 0 & 0 & 0 \\ 0 & 0 & 0 & 0 \end{bmatrix}, \quad (\text{I.6})$$

$$\mathbf{D}_{11}^- = \begin{bmatrix} 0 & 0 & 0 & (1 + \mu^2)\mu' \\ 0 & 0 & 0 & -(1 - \mu^2)\mu' \\ 0 & 0 & 0 & 0 \\ \mu(1 + \mu'^2) & -\mu(1 - \mu'^2) & 0 & 0 \end{bmatrix}, \quad (\text{I.7})$$

$$\mathbf{D}_{1-1}^- = \begin{bmatrix} 0 & 0 & 0 & (1 + \mu^2)\mu' \\ 0 & 0 & 0 & -(1 - \mu^2)\mu' \\ 0 & 0 & 0 & 0 \\ -\mu(1 + \mu'^2) & \mu(1 - \mu'^2) & 0 & 0 \end{bmatrix}, \quad (\text{I.8})$$

$$\mathbf{F}_1^{(1)} = \mu\mu' \begin{bmatrix} 1 & 1 & 0 & 0 \\ 1 & 1 & 0 & 0 \\ 0 & 0 & 0 & 0 \\ 0 & 0 & 0 & 0 \end{bmatrix} + \mathbf{E}_{33}; \quad \mathbf{F}_2^{(1)} = \mathbf{E}_{44}, \quad (\text{I.9})$$

$$\mathbf{F}_3^{(1)} = \mu' \begin{bmatrix} 0 & 0 & 0 & 0 \\ 0 & 0 & 0 & 0 \\ 0 & 0 & 0 & 0 \\ 1 & 1 & 0 & 0 \end{bmatrix}; \quad \mathbf{F}_4^{(1)} = -\mu \begin{bmatrix} 0 & 0 & 0 & 1 \\ 0 & 0 & 0 & 1 \\ 0 & 0 & 0 & 0 \\ 0 & 0 & 0 & 0 \end{bmatrix}, \quad (\text{I.10})$$

$$\mathbf{S}_1^{(1)} = \begin{bmatrix} 0 & 0 & -\mu & 0 \\ 0 & 0 & -\mu & 0 \\ \mu' & \mu' & 0 & 0 \\ 0 & 0 & 0 & 0 \end{bmatrix}; \quad \mathbf{S}_3^{(1)} = \mathbf{E}_{43}; \quad \mathbf{S}_4^{(1)} = \mathbf{E}_{34}, \quad (\text{I.11})$$

$$\mathbf{C}_+^2 = \frac{1}{2} \begin{bmatrix} (1 - \mu^2)(1 - \mu'^2) & -(1 - \mu^2)(1 + \mu'^2) & 0 & 0 \\ -(1 + \mu^2)(1 - \mu'^2) & (1 + \mu^2)(1 + \mu'^2) & 0 & 0 \\ 0 & 0 & 4\mu\mu' & 0 \\ 0 & 0 & 0 & 0 \end{bmatrix}, \quad (\text{I.12})$$

$$\mathbf{S}_+^2 = \begin{bmatrix} 0 & 0 & -(1 - \mu^2)\mu' & 0 \\ 0 & 0 & (1 + \mu^2)\mu' & 0 \\ \mu(1 - \mu'^2) & -\mu(1 + \mu'^2) & 0 & 0 \\ 0 & 0 & 0 & 0 \end{bmatrix}. \quad (\text{I.13})$$

Here  $\mathbf{E}_{ij}$  denotes a matrix that has a single element  $E_{ij} = 1$ , while all the remaining elements are zero. Notice that the matrices  $\mathbf{C}_0^0$ ,  $\mathbf{C}_+^2$ , and  $\mathbf{S}_+^2$  are the same as those introduced in Stenflo (1998), and were also used in Chapter 7.

Using the various quantities defined in Eq. (H.6), we can define the following coefficients:

$$\begin{aligned}
c_1^{(K)\text{III}} &= \frac{1}{8} \cos \alpha_1^{(K)} \cos \beta_1 \left\{ \cos(\phi - \phi') \left[ d_1 \cos(\alpha_1^{(K)} + \beta_1) + d_2 \sin(\alpha_1^{(K)} + \beta_1) \right] \right. \\
&\quad \left. + \sin(\phi - \phi') \left[ d_1 \sin(\alpha_1^{(K)} + \beta_1) - d_2 \cos(\alpha_1^{(K)} + \beta_1) \right] \right\}, \\
c_2^{(K)\text{III}} &= \frac{1}{8} \cos \alpha_1^{(K)} \cos \beta_1 \left\{ \cos(\phi - \phi') \left[ d_3 \cos(\alpha_1^{(K)} + \beta_1) + d_4 \sin(\alpha_1^{(K)} + \beta_1) \right] \right. \\
&\quad \left. + \sin(\phi - \phi') \left[ d_3 \sin(\alpha_1^{(K)} + \beta_1) - d_4 \cos(\alpha_1^{(K)} + \beta_1) \right] \right\}, \\
c_3^{(K)\text{III}} &= \frac{1}{8} \cos \alpha_1^{(K)} \cos \beta_1 \left\{ \cos(\phi - \phi') \left[ d_5 \cos(\alpha_1^{(K)} + \beta_1) + d_6 \sin(\alpha_1^{(K)} + \beta_1) \right] \right. \\
&\quad \left. + \sin(\phi - \phi') \left[ d_5 \sin(\alpha_1^{(K)} + \beta_1) - d_6 \cos(\alpha_1^{(K)} + \beta_1) \right] \right\}, \\
c_4^{(K)\text{III}} &= \frac{1}{8} \cos \alpha_1^{(K)} \cos \beta_1 \left\{ \cos(\phi - \phi') \left[ d_7 \cos(\alpha_1^{(K)} + \beta_1) + d_8 \sin(\alpha_1^{(K)} + \beta_1) \right] \right. \\
&\quad \left. + \sin(\phi - \phi') \left[ d_7 \sin(\alpha_1^{(K)} + \beta_1) - d_8 \cos(\alpha_1^{(K)} + \beta_1) \right] \right\}. \tag{I.14}
\end{aligned}$$

Similarly, we can define another set of coefficients:

$$\begin{aligned}
s_1^{(K)\text{III}} &= \frac{1}{8} (-1)^K \cos \alpha_1^{(K)} \cos \beta_1 \left\{ \sin(\phi - \phi') \left[ d_1 \cos(\alpha_1^{(K)} + \beta_1) + d_2 \sin(\alpha_1^{(K)} + \beta_1) \right] \right. \\
&\quad \left. - \cos(\phi - \phi') \left[ d_1 \sin(\alpha_1^{(K)} + \beta_1) - d_2 \cos(\alpha_1^{(K)} + \beta_1) \right] \right\}, \\
s_2^{(K)\text{III}} &= \frac{1}{8} (-1)^K \cos \alpha_1^{(K)} \cos \beta_1 \left\{ \sin(\phi - \phi') \left[ d_3 \cos(\alpha_1^{(K)} + \beta_1) + d_4 \sin(\alpha_1^{(K)} + \beta_1) \right] \right. \\
&\quad \left. - \cos(\phi - \phi') \left[ d_3 \sin(\alpha_1^{(K)} + \beta_1) - d_4 \cos(\alpha_1^{(K)} + \beta_1) \right] \right\}, \\
s_3^{(K)\text{III}} &= \frac{1}{8} (-1)^K \cos \alpha_1^{(K)} \cos \beta_1 \left\{ \sin(\phi - \phi') \left[ d_5 \cos(\alpha_1^{(K)} + \beta_1) + d_6 \sin(\alpha_1^{(K)} + \beta_1) \right] \right. \\
&\quad \left. - \cos(\phi - \phi') \left[ d_5 \sin(\alpha_1^{(K)} + \beta_1) - d_6 \cos(\alpha_1^{(K)} + \beta_1) \right] \right\}, \\
s_4^{(K)\text{III}} &= \frac{1}{8} (-1)^K \cos \alpha_1^{(K)} \cos \beta_1 \left\{ \sin(\phi - \phi') \left[ d_7 \cos(\alpha_1^{(K)} + \beta_1) + d_8 \sin(\alpha_1^{(K)} + \beta_1) \right] \right. \\
&\quad \left. - \cos(\phi - \phi') \left[ d_7 \sin(\alpha_1^{(K)} + \beta_1) - d_8 \cos(\alpha_1^{(K)} + \beta_1) \right] \right\}. \tag{I.15}
\end{aligned}$$

## Appendix J

# Hanle scattering matrix of Stenflo (1994) in terms of $\mathcal{T}_Q^K$

In this Appendix we describe how to expand the classical expressions in Stenflo (1994, hereafter S94) in terms of the irreducible spherical tensors of Landi Degl'Innocenti (1984, see also LL04), and show this explicitly for the special case of the weak field Hanle effect.

We note the following similarities or differences between the classical formalism of S94 and that of LL04: The elements of the coherency matrix of S94 (see his Eq. (2.33)) are equivalent to the complex conjugate of the polarization tensor ( $E_i^* E_j$ ) of LL04 (see their Eq. (1.14)), where  $E$  is the electric field. In both cases the starting point is the classical oscillator equation, from which the electric vector of the scattered radiation is derived. LL04 determines the polarization tensor, which is then converted to the Stokes representation. In contrast, S94 finds the Jones matrix, from which the Mueller scattering matrix is obtained. Both approaches use geometric factors (as referred to by S94) or direction cosines (as referred to by LL04). LL04 names them  $C_{\alpha i} = \mathbf{u}_\alpha \cdot \mathbf{e}_i^*$ , where  $\mathbf{u}_\alpha$  are complex spherical unit vectors corresponding to the unit vectors that are parallel to the components of the vector magnetic field, and  $\mathbf{e}_i$  are reference directions for the ray. S94 names these geometric factors  $\varepsilon_q^\alpha = \mathbf{e}_\alpha \cdot \mathbf{e}_q$ , where  $\mathbf{e}_q$  are complex spherical unit vectors corresponding to the unit vectors that are parallel to the magnetic field, while  $\mathbf{e}_\alpha$  are linear unit polarization vectors.

For a magnetic field oriented along the polar  $Z'$ -axis, the expression for the geometric factors or direction cosines are given in Eq. (3.86) of S94 and unnumbered equations above Eq. (5.96) of LL04 (p. 187). Clearly  $C_{\alpha i}$  and  $\varepsilon_q^\alpha$  differ simply by a complex conjugation.

In order to introduce an irreducible tensor  $\mathcal{T}_Q^K$  similar to that introduced by LL04 in



the classical formalism of S94, we need to first introduce the reducible spherical tensors  $\mathcal{E}_{qq'}$  and  $\mathcal{T}_{qq'}$ , following LL04 (see their Eqs. (5.115) and (5.131), respectively). To achieve this we have to write  $\varepsilon_q^\alpha$  of S94 in a form similar to that given in Eq. (5.113) of LL04. Following Eq. (5.113) of LL04, we may write

$$\varepsilon_q^\alpha = \sum_{q'} (e_\alpha)_{q'} (e_q)_{q'}^* = \sum_{q'} (e_\alpha)_{q'} \delta_{qq'} = (e_\alpha)_q. \quad (\text{J.1})$$

Thus we can re-write the electric field of the scattered radiation given in Eq. (3.84) of S94 as (dropping the constants)

$$E_\mu \sim \sum_{\rho q} (n_q - 1) (e_\mu(\mathbf{n}))_q^* (e_\rho(\mathbf{n}'))_q E'_\rho, \quad (\text{J.2})$$

where  $n_q$  denotes the refractive index induced by the vector component  $q$  of the vibration, and  $\mathbf{E}'$  is the electric field of the incident radiation. For the linear polarization unit vectors, LL04 choose

$$\begin{aligned} \mathbf{e}_1 &= \frac{1}{\sqrt{2}} [e_a(\mathbf{n}) + i e_b(\mathbf{n})] \equiv \mathbf{e}_{-1}(\mathbf{n}); & \mathbf{e}_2 &= \frac{1}{\sqrt{2}} [-e_a(\mathbf{n}) + i e_b(\mathbf{n})] \equiv \mathbf{e}_{+1}(\mathbf{n}), \\ \mathbf{e}'_1 &= \frac{1}{\sqrt{2}} [e'_a(\mathbf{n}') + i e'_b(\mathbf{n}')] \equiv \mathbf{e}'_{-1}(\mathbf{n}'); & \mathbf{e}'_2 &= \frac{1}{\sqrt{2}} [-e'_a(\mathbf{n}') + i e'_b(\mathbf{n}')] \equiv \mathbf{e}'_{+1}(\mathbf{n}'), \end{aligned} \quad (\text{J.3})$$

where  $(\mathbf{e}_a(\mathbf{n}), \mathbf{e}_b(\mathbf{n}), \mathbf{n})$  form a right handed coordinate system about the outgoing ray and similarly a primed system for the incoming ray. We note that the Eq. (J.2) is written in the basis defined in Eq. (J.3), so that the indices  $\mu, \rho$  take values  $\pm 1$ . Now, the elements of the coherency matrix may be written as

$$I_{\mu\nu}^S = \sum_{\rho\sigma} T_{\mu\nu,\rho\sigma}^S(\mathbf{n}, \mathbf{n}', \mathbf{B}) I_{\rho\sigma}^{\prime S}, \quad (\text{J.4})$$

where  $I_{\mu\nu}^S = E_\mu E_\nu^*$ , which differs from corresponding polarization tensor of LL04 (distinguished through a symbol ‘L’ from our notations distinguished through ‘S’) by a complex conjugation, and

$$T_{\mu\nu,\rho\sigma}^S(\mathbf{n}, \mathbf{n}'; \mathbf{B}) = \sum_{qq'} (n_q - 1) (n_{q'}^* - 1) [e_\mu(\mathbf{n})]_q^* [e_\nu(\mathbf{n})]_{q'} [e_\rho(\mathbf{n}')]_q [e_\sigma(\mathbf{n}')]_{q'}^*. \quad (\text{J.5})$$

Following LL04 we define the ‘reducible spherical tensor’

$$\mathcal{E}_{qq'}^S(\alpha, \beta, \mathbf{n}) = [e_\alpha(\mathbf{n})]_q^* [e_\beta(\mathbf{n})]_{q'}. \quad (\text{J.6})$$

Note that our definition of  $\mathcal{E}_{qq'}^S(\alpha, \beta, \mathbf{n})$  differs from that of LL04, again by a complex conjugation (see their Eq. (5.115)). Following S94, we may replace  $(n_q - 1)(n_{q'}^* - 1)$  in

Eq. (J.5) by  $\cos \bar{\alpha}_{q-q'} e^{i\bar{\alpha}_{q-q'}}$  (see Eq. (5.54) of S94), where  $\bar{\alpha}_{q-q'}$  is the weak field Hanle angle defined in Eq. (5.53) of S94 (where it is referred to as  $\alpha$ ). Thus Eq. (J.5), may be re-written as

$$T_{\mu\nu,\rho\sigma}^S(\mathbf{n}, \mathbf{n}'; \mathbf{B}) = \frac{3}{2} \sum_{qq'} \cos \bar{\alpha}_{q-q'} e^{i\bar{\alpha}_{q-q'}} \mathcal{E}_{qq'}^S(\mu, \nu, \mathbf{n}) \mathcal{E}_{q'q}^S(\sigma, \rho, \mathbf{n}'). \quad (\text{J.7})$$

In the above equation the factor  $3/2$  is the normalization constant (see S94).

To deduce the scattering phase matrix  $\mathbf{P}$  for the Stokes parameters we need the relation between the Stokes parameters  $S_i$ , with  $i = 0, 1, 2, 3$  and the coherency matrix corresponding to the unit vectors (J.3). This relation can be obtained using the equality

$$E_1 \mathbf{e}_a + E_2 \mathbf{e}_b = E_{+1} \mathbf{e}_{+1} + E_{-1} \mathbf{e}_{-1}, \quad (\text{J.8})$$

because the total electric vector should remain the same in both the basis. Using the above equation, we obtain the following expressions for the Stokes vector in terms of the coherency matrix elements, in the new basis as

$$\begin{aligned} I &= I_{-1-1} + I_{+1+1}; & Q &= -[I_{-1+1} + I_{+1-1}], \\ U &= i[I_{+1-1} - I_{-1+1}]; & V &= I_{+1+1} - I_{-1-1}. \end{aligned} \quad (\text{J.9})$$

In other words, we may write

$$S_i = \sum_{\mu\nu} (\boldsymbol{\sigma}_i)_{\nu\mu} I_{\mu\nu}^S, \quad (\text{J.10})$$

and the inverse relation

$$I_{\mu\nu}^S = \frac{1}{2} \sum_{i=0}^3 (\boldsymbol{\sigma}_i)_{\mu\nu} S_i, \quad (\text{J.11})$$

where  $\boldsymbol{\sigma}_i$  are given by

$$\boldsymbol{\sigma}_0 = \begin{pmatrix} 1 & 0 \\ 0 & 1 \end{pmatrix}; \quad \boldsymbol{\sigma}_1 = \begin{pmatrix} 0 & -1 \\ -1 & 0 \end{pmatrix}; \quad \boldsymbol{\sigma}_2 = \begin{pmatrix} 0 & i \\ -i & 0 \end{pmatrix}; \quad \boldsymbol{\sigma}_3 = \begin{pmatrix} -1 & 0 \\ 0 & 1 \end{pmatrix}. \quad (\text{J.12})$$

The  $\boldsymbol{\sigma}_i$  given in the above equation differ from corresponding matrices given in LL04 (see their Eq. (5.128)) by a complex conjugation. Using the Eqs. (J.10) and (J.12), we may write, the scattered Stokes vector as

$$S_i = \sum_{j=0}^3 \mathbf{P}_{ij}(\mathbf{n}, \mathbf{n}'; \mathbf{B}) S'_j, \quad (\text{J.13})$$

where,

$$\mathbf{P}_{ij}(\mathbf{n}, \mathbf{n}'; \mathbf{B}) = \frac{3}{4} \sum_{\mu\nu\rho\sigma qq'} \cos \bar{\alpha}_{q-q'} e^{i\bar{\alpha}_{q-q'}} (\boldsymbol{\sigma}_i)_{\nu\mu} (\boldsymbol{\sigma}_j)_{\rho\sigma} \mathcal{E}_{qq'}^S(\mu, \nu, \mathbf{n}) \mathcal{E}_{q'q}^S(\sigma, \rho, \mathbf{n}'). \quad (\text{J.14})$$

Following LL04, we define (see their Eq. (5.131))

$$\mathcal{T}_{qq'}^S(i, \mathbf{n}) = \sum_{\alpha\beta} \frac{1}{2} (\boldsymbol{\sigma}_i)_{\alpha\beta} \mathcal{E}_{qq'}^S(\beta, \alpha, \mathbf{n}). \quad (\text{J.15})$$

Clearly Eq. (J.14) may be re-written as

$$\mathbf{P}_{ij}(\mathbf{n}, \mathbf{n}'; \mathbf{B}) = 3 \sum_{qq'} \cos \bar{\alpha}_{q-q'} e^{i\bar{\alpha}_{q-q'}} \mathcal{T}_{qq'}^S(i, \mathbf{n}) \mathcal{T}_{q'q}^S(j, \mathbf{n}'). \quad (\text{J.16})$$

From the reducible spherical tensor  $\mathcal{T}_{qq'}^S$ , it is possible to construct an ‘irreducible spherical tensor’ (see Eq. (5.132) of LL04)

$$[\mathcal{T}_Q^K(i, \mathbf{n})]^S = \sum_{qq'} (-1)^{1+q} \sqrt{3(2K+1)} \begin{pmatrix} 1 & 1 & K \\ q & -q' & -Q \end{pmatrix} \mathcal{T}_{qq'}^S(i, \mathbf{n}), \quad (\text{J.17})$$

with the inverse relation given by

$$\mathcal{T}_{qq'}^S(i, \mathbf{n}) = \sum_{KQ} (-1)^{1+q} \sqrt{\frac{2K+1}{3}} \begin{pmatrix} 1 & 1 & K \\ q & -q' & -Q \end{pmatrix} [\mathcal{T}_Q^K(i, \mathbf{n})]^S. \quad (\text{J.18})$$

Substituting for  $\mathcal{T}_{qq'}^S$  from Eq. (J.18) in Eq. (J.16), and using Eq. (2.23a) of LL04, we obtain

$$\mathbf{P}_{ij}(\mathbf{n}, \mathbf{n}'; \mathbf{B}) = \sum_{KQ} \cos \bar{\alpha}_Q e^{i\bar{\alpha}_Q} (-1)^Q [\mathcal{T}_Q^K(i, \mathbf{n})]^S [\mathcal{T}_{-Q}^K(j, \mathbf{n}')^S], \quad (\text{J.19})$$

where  $Q = q - q'$ . In order to evaluate the above expression, we need to first calculate the  $[\mathcal{T}_Q^K]^S$ . Following LL04 (see their Eq. (5.117)), we may write  $\mathcal{E}_{qq'}^S(\alpha, \beta, \mathbf{n}) = \mathcal{D}_{\alpha q}^1(R)^* \mathcal{D}_{\beta q'}^1(R)$ , where  $R \equiv (0, -\theta, -\phi)$  is a rotation that brings the system  $(\mathbf{e}_a(\mathbf{n}), \mathbf{e}_b(\mathbf{n}), \mathbf{n})$  into the system, where the magnetic field is along the polar  $Z'$ -axis. Substituting for  $\mathcal{E}_{qq'}^S$  in Eq. (J.15), which in turn is used in Eq. (J.17), gives

$$[\mathcal{T}_Q^K(i, \mathbf{n})]^S = (-1)^Q \sum_{Q'} [t_{Q'}^K(i)]^S \mathcal{D}_{Q'-Q}^K(R), \quad (\text{J.20})$$

where

$$[t_{Q'}^K(i)]^S = \sum_{\alpha\beta} \frac{1}{2} (\boldsymbol{\sigma}_i)_{\alpha\beta} \sqrt{3(2K+1)} \begin{pmatrix} 1 & 1 & K \\ \alpha & -\beta & -Q' \end{pmatrix}. \quad (\text{J.21})$$

By explicitly determining  $[\mathcal{T}_Q^K]^S$ , making use of the table of rotation matrices given in Table 2.1 of LL04 (p. 57), we find that our new irreducible tensor ( $[\mathcal{T}_Q^K]^S$ ) is just the complex conjugate of the corresponding irreducible tensors ( $[\mathcal{T}_Q^K]^L$ ) listed in Table 5.6 of LL04 (p. 211). In other words,

$$[\mathcal{T}_Q^K]^S = [\mathcal{T}_Q^{K*}]^L. \quad (\text{J.22})$$

Substituting for the newly defined  $[\mathcal{T}_Q^K]^S$  in Eq. (J.19), one can easily verify that we obtain Eq. (5.139) of LL04, which is the Hanle phase matrix in the weak field limit.

## Appendix K

# Transformation between magnetic and atmospheric frames

Here we give the transformation equations for going from magnetic reference frame (MRF) to the atmospheric reference frame (ARF). While it is natural and easy to derive the redistribution matrix in the MRF, its actual use in the radiative transfer equation requires it to be given in the ARF. The geometry of the MRF is shown in Fig. 8.1. In Fig. 8.2 we show the scattering geometry that refers to the ARF. The redistribution matrix in the ARF is given by Eq. (5.66) of Stenflo (1994):

$$\mathbf{R}(x, \vartheta, \varphi; x', \vartheta', \varphi'; v_B, \vartheta_B, \varphi_B) = \mathbf{L}(i_2)\mathbf{R}(x, \theta, \phi; x', \theta', \phi'; v_B)\mathbf{L}(i_1). \quad (\text{K.1})$$

The explicit expressions for  $\mathbf{R}(x, \theta, \phi; x', \theta', \phi'; v_B)$  are given in Eq. (7.46) (classical theory). The corresponding QED expressions are given in Eq. (8.16) (and the discussion at the end of § 8.2.1). The geometry and angles are described in Fig. 8.2. In radiative transfer theory the incoming rays (represented by  $\vartheta', \varphi'$ ) and the outgoing rays (represented by  $\vartheta, \varphi$ ) are given as inputs in the computation of the source vector. To compute the MRF angles  $(\theta, \phi; \theta', \phi')$  we need to perform a transformation of the ARF angles  $(\vartheta, \varphi; \vartheta', \varphi')$ . This is achieved by using the rotation matrix:

$$\mathbf{R}_{\text{rot}}(0, -\vartheta_B, -\varphi_B) = \begin{bmatrix} \cos \vartheta_B \cos \varphi_B & \cos \vartheta_B \sin \varphi_B & -\sin \vartheta_B \\ -\sin \varphi_B & \cos \varphi_B & 0 \\ \sin \vartheta_B \cos \varphi_B & \sin \vartheta_B \sin \varphi_B & \cos \vartheta_B \end{bmatrix}, \quad (\text{K.2})$$

(see Jefferies et al. 1989, LL04, p. 197)

Consider a unit vector  $\mathbf{n}$  along the outgoing ray. The components of  $\mathbf{n}$  in the ARF are:

$$n_x^{\text{ARF}} = \sin \vartheta \cos \varphi; \quad n_y^{\text{ARF}} = \sin \vartheta \sin \varphi; \quad n_z^{\text{ARF}} = \cos \vartheta. \quad (\text{K.3})$$

The respective components in the MRF are given by:

$$n_x^{\text{MRF}} = \sin \theta \cos \phi ; \quad n_y^{\text{MRF}} = \sin \theta \sin \phi ; \quad n_z^{\text{MRF}} = \cos \theta. \quad (\text{K.4})$$

These two sets of components are related through the expression:

$$\mathbf{n}^{\text{MRF}} = \mathbf{R}_{\text{rot}}(0, -\vartheta_B, -\varphi_B) \mathbf{n}^{\text{ARF}}, \quad (\text{K.5})$$

where  $\mathbf{n}^{\text{MRF}} = (n_x^{\text{MRF}} n_y^{\text{MRF}} n_z^{\text{MRF}})^{\text{T}}$  and  $\mathbf{n}^{\text{ARF}} = (n_x^{\text{ARF}} n_y^{\text{ARF}} n_z^{\text{ARF}})^{\text{T}}$ . From these equations we obtain the following simple trigonometric relations:

$$\begin{aligned} \sin \theta \cos \phi &= \cos \vartheta_B \cos \varphi_B \sin \vartheta \cos \varphi + \cos \vartheta_B \sin \varphi_B \sin \vartheta \sin \varphi - \sin \vartheta_B \cos \vartheta, \\ \sin \theta \sin \phi &= -\sin \varphi_B \sin \vartheta \cos \varphi + \cos \varphi_B \sin \vartheta \sin \varphi, \\ \cos \theta &= \sin \vartheta_B \cos \varphi_B \sin \vartheta \cos \varphi + \sin \vartheta_B \sin \varphi_B \sin \vartheta \sin \varphi + \cos \vartheta_B \cos \vartheta. \end{aligned} \quad (\text{K.6})$$

Analogous relations are valid for the incoming ray, but with  $(\theta, \phi)$  changed to  $(\theta', \phi')$  and  $(\vartheta, \varphi)$  changed to  $(\vartheta', \varphi')$ . From these equations one can easily obtain  $\cos \theta, \cos \theta', \sin \theta, \sin \theta', \cos \phi, \cos \phi', \sin \phi, \sin \phi'$ , as required for the construction of the  $c, s$  coefficients and  $\mathbf{C}, \mathbf{S}$  matrices (see Eqs. (G.1) - (G.11) or equivalently Eqs. (I.1) - (I.15)). Further, the angles  $i_1$  and  $i_2$  are given by (see Faurobert-Scholl 1993b)

$$\cos i_1 = \frac{\cos \vartheta_B \sin \vartheta' - \sin \vartheta_B \cos \vartheta' \cos(\varphi' - \varphi_B)}{\sin \theta'}, \quad (\text{K.7})$$

$$\sin i_1 = \frac{\sin \vartheta_B \sin(\varphi' - \varphi_B)}{\sin \theta'}, \quad (\text{K.8})$$

$$\cos i_2 = \frac{\cos \vartheta_B \sin \vartheta - \sin \vartheta_B \cos \vartheta \cos(\varphi - \varphi_B)}{\sin \theta}, \quad (\text{K.9})$$

$$\sin i_2 = \frac{\sin \vartheta_B \sin(\varphi_B - \varphi)}{\sin \theta}. \quad (\text{K.10})$$

Simple trigonometry then gives  $\cos 2i_1, \cos 2i_2, \sin 2i_1, \sin 2i_2$ , which are required for constructing the Mueller rotation matrices  $\mathbf{L}(i_1)$ , and  $\mathbf{L}(i_2)$  (see Eq. (5.65) of Stenflo 1994).

## Appendix L

### Elements of the magnetic kernel $\mathbf{N}^r(x, x', \mathbf{B})$

The magnetic kernel  $\mathbf{N}^r(x, x', \mathbf{B})$  is given by

$$\mathbf{N}^r(x, x', \mathbf{B}) = \mathbf{U}^r(\varphi_B) \mathbf{M}(x, x', \vartheta_B, B) \mathbf{U}^r(-\varphi_B). \quad (\text{L.1})$$

The  $6 \times 6$  matrix  $\mathbf{U}^r(\varphi_B)$  has the form (see also Frisch 2007)

$$\mathbf{U}^r = \begin{pmatrix} 1 & 0 & 0 & 0 & 0 & 0 \\ 0 & 1 & 0 & 0 & 0 & 0 \\ 0 & 0 & \cos \varphi_B & \sin \varphi_B & 0 & 0 \\ 0 & 0 & -\sin \varphi_B & \cos \varphi_B & 0 & 0 \\ 0 & 0 & 0 & 0 & \cos 2\varphi_B & \sin 2\varphi_B \\ 0 & 0 & 0 & 0 & -\sin 2\varphi_B & \cos 2\varphi_B \end{pmatrix}. \quad (\text{L.2})$$

We express the matrix  $\mathbf{M}$  as

$$\mathbf{M}(x, x', \vartheta_B, B) = \mathbf{M}^{\text{II}}(x, x', \vartheta_B, B) + \mathbf{M}^{\text{III}}(x, x', \vartheta_B, B). \quad (\text{L.3})$$

Matrix  $\mathbf{M}^{\text{II}}$  and  $\mathbf{M}^{\text{III}}$  are of the form

$$\mathbf{M} = \begin{pmatrix} b_{11} & 0 & 0 & 0 & 0 & 0 \\ 0 & b_{22} & b_{23} & b_{24} & b_{25} & b_{26} \\ 0 & 2b_{23} & b_{33} & b_{34} & b_{35} & b_{36} \\ 0 & -2b_{24} & -b_{34} & b_{44} & b_{45} & b_{46} \\ 0 & 2b_{25} & b_{35} & -b_{45} & b_{55} & b_{56} \\ 0 & -2b_{26} & -b_{36} & b_{46} & -b_{56} & b_{66} \end{pmatrix}. \quad (\text{L.4})$$

The elements of the matrices  $\mathbf{M}^{\text{II}}$  and  $\mathbf{M}^{\text{III}}$  explicitly contain branching ratios  $A$  and  $B^{(K)}$  given by

$$A = \frac{\Gamma_{\text{R}}}{\Gamma_{\text{R}} + \Gamma_{\text{I}} + \Gamma_{\text{E}}}; \quad B^{(K)} = \frac{\Gamma_{\text{R}}}{\Gamma_{\text{R}} + \Gamma_{\text{I}} + D^{(K)}} \frac{\Gamma_{\text{E}} - D^{(K)}}{\Gamma_{\text{R}} + \Gamma_{\text{I}} + \Gamma_{\text{E}}}. \quad (\text{L.5})$$

We also define  $C_B = \cos \vartheta_B$  and  $S_B = \sin \vartheta_B$ , for notational simplification.

We first consider the elements of the  $\mathbf{M}^{\text{II}}$  matrix. To simplify the notation, we introduce the functions  $r_i^{\text{II}}(x, x', B)$ , with  $i = 1, \dots, 5$ . We note that the subscript  $i$  on  $r_i^{\text{II}}$  do not have any physical meaning. These functions are given by

$$r_0^{\text{II}} = \frac{1}{3} \left( \bar{h}_{00}^{\text{II}} + \bar{h}_{11}^{\text{II}} + \bar{h}_{-1-1}^{\text{II}} \right), \quad (\text{L.6})$$

$$r_1^{\text{II}} = \frac{2}{3} \bar{h}_{00}^{\text{II}} + \frac{1}{6} \left( \bar{h}_{11}^{\text{II}} + \bar{h}_{-1-1}^{\text{II}} \right), \quad (\text{L.7})$$

$$r_2^{\text{II}} = \cos \beta_1 \left[ \left( \bar{h}_{10}^{\text{II}} + \bar{h}_{0-1}^{\text{II}} \right) \cos \beta_1 - \left( \bar{f}_{10}^{\text{II}} + \bar{f}_{0-1}^{\text{II}} \right) \sin \beta_1 \right], \quad (\text{L.8})$$

$$r_3^{\text{II}} = \cos \beta_1 \left[ \left( \bar{h}_{10}^{\text{II}} + \bar{h}_{0-1}^{\text{II}} \right) \sin \beta_1 + \left( \bar{f}_{10}^{\text{II}} + \bar{f}_{0-1}^{\text{II}} \right) \cos \beta_1 \right], \quad (\text{L.9})$$

$$r_4^{\text{II}} = \cos \beta_2 \left( \bar{h}_{1-1}^{\text{II}} \cos \beta_2 - \bar{f}_{1-1}^{\text{II}} \sin \beta_2 \right), \quad (\text{L.10})$$

$$r_5^{\text{II}} = \cos \beta_2 \left( \bar{h}_{1-1}^{\text{II}} \sin \beta_2 + \bar{f}_{1-1}^{\text{II}} \cos \beta_2 \right). \quad (\text{L.11})$$

The auxiliary functions  $\bar{h}_{qq'}^{\text{II}}(x, x', B)$  and  $\bar{f}_{qq'}^{\text{II}}(x, x', B)$  with  $q, q' = 0, \pm 1$  are given by

$$\bar{h}_{qq'}^{\text{II}} = \frac{1}{2} \left( \bar{R}_{\text{II,H}}^q + \bar{R}_{\text{II,H}}^{q'} \right); \quad \bar{f}_{qq'}^{\text{II}} = \frac{1}{2} \left( \bar{R}_{\text{II,F}}^{q'} - \bar{R}_{\text{II,F}}^q \right). \quad (\text{L.12})$$

The functions  $\bar{R}_{\text{II,X}}^q(x, x', B)$ , with X denoting H or F, are given by

$$\bar{R}_{\text{II,X}}^q(x, x', B) = \frac{1}{2} \int_0^\pi R_{\text{II,X}}^q(x, x', \Theta; B) \sin \Theta d\Theta, \quad (\text{L.13})$$

where  $R_{\text{II,X}}^q(x, x', \Theta; B)$  are the AD magnetic redistribution functions of type II introduced in Eqs. (7.21) and (7.22). We refer to  $\bar{R}_{\text{II,X}}^q(x, x', B)$  as the AA magnetic redistribution functions of type II. The indices  $q$  or  $q'$  denote the magnetic substates of the upper level. The smooth transition from Hanle effect in the line core to Rayleigh in the wings is controlled by the function  $\bar{f}_{qq'}^{\text{II}}$  for  $q \neq q'$ . For  $q = q'$ ,  $\bar{f}_{qq'}^{\text{II}}$  are zero. We also introduce Hanle angles  $\beta_1$  and  $\beta_2$ , which are defined as

$$\tan \beta_1 = A\Gamma_B; \quad \tan \beta_2 = 2A\Gamma_B, \quad (\text{L.14})$$

where the Hanle  $\Gamma_B$  parameter is written as  $\Gamma_B = g\omega_L/\Gamma_R$ . We now list the elements of  $\mathbf{M}^{\text{II}}$  matrix below :

$$b_{11}^{\text{II}} = Ar_0^{\text{II}}, \quad (\text{L.15})$$

$$b_{22}^{\text{II}} = A \frac{1}{2} \left[ \frac{1}{2} (3C_B^2 - 1)^2 r_1^{\text{II}} + 3S_B^2 C_B^2 r_2^{\text{II}} + \frac{3}{2} S_B^4 r_4^{\text{II}} \right], \quad (\text{L.16})$$



$$b_{23}^{\text{II}} = A\sqrt{\frac{3}{2}}S_B C_B \left[ -\frac{1}{2}(3C_B^2 - 1)r_1^{\text{II}} + \left(C_B^2 - \frac{1}{2}\right)r_2^{\text{II}} + \frac{1}{2}S_B^2 r_4^{\text{II}} \right], \quad (\text{L.17})$$

$$b_{24}^{\text{II}} = A\sqrt{\frac{3}{8}}S_B (C_B^2 r_3^{\text{II}} + S_B^2 r_5^{\text{II}}), \quad (\text{L.18})$$

$$b_{25}^{\text{II}} = A\sqrt{\frac{3}{8}}S_B^2 \left[ \frac{1}{2}(3C_B^2 - 1)r_1^{\text{II}} - C_B^2 r_2^{\text{II}} + \frac{1}{2}(1 + C_B^2)r_4^{\text{II}} \right], \quad (\text{L.19})$$

$$b_{26}^{\text{II}} = A\sqrt{\frac{3}{8}}S_B^2 C_B (r_5^{\text{II}} - r_3^{\text{II}}), \quad (\text{L.20})$$

$$b_{33}^{\text{II}} = A \left[ 3S_B^2 C_B^2 r_1^{\text{II}} + 2 \left(C_B^2 - \frac{1}{2}\right)^2 r_2^{\text{II}} + S_B^2 C_B^2 r_4^{\text{II}} \right], \quad (\text{L.21})$$

$$b_{34}^{\text{II}} = AC_B \left[ \left(C_B^2 - \frac{1}{2}\right)r_3^{\text{II}} + S_B^2 r_5^{\text{II}} \right], \quad (\text{L.22})$$

$$b_{35}^{\text{II}} = A\frac{1}{2}S_B C_B \left[ -3S_B^2 r_1^{\text{II}} - (C_B^2 - S_B^2)r_2^{\text{II}} + (1 + C_B^2)r_4^{\text{II}} \right], \quad (\text{L.23})$$

$$b_{36}^{\text{II}} = AS_B \left[ \frac{1}{2}(1 - 2C_B^2)r_3^{\text{II}} + C_B^2 r_5^{\text{II}} \right], \quad (\text{L.24})$$

$$b_{44}^{\text{II}} = A \left[ \frac{1}{2}C_B^2 r_2^{\text{II}} + S_B^2 r_4^{\text{II}} \right], \quad (\text{L.25})$$

$$b_{45}^{\text{II}} = A\frac{1}{2}S_B \left[ C_B^2 r_3^{\text{II}} - (1 + C_B^2)r_5^{\text{II}} \right], \quad (\text{L.26})$$

$$b_{46}^{\text{II}} = AS_B C_B \left( r_4^{\text{II}} - \frac{1}{2}r_2^{\text{II}} \right), \quad (\text{L.27})$$

$$b_{55}^{\text{II}} = A\frac{1}{2} \left[ \frac{3}{2}S_B^4 r_1^{\text{II}} + S_B^2 C_B^2 r_2^{\text{II}} + \frac{1}{2}(1 + C_B^2)^2 r_4^{\text{II}} \right], \quad (\text{L.28})$$

$$b_{56}^{\text{II}} = A\frac{1}{2}C_B \left[ S_B^3 r_3^{\text{II}} + (1 + C_B^2)r_5^{\text{II}} \right], \quad (\text{L.29})$$

$$b_{66}^{\text{II}} = A \left( \frac{1}{2}S_B^2 r_2^{\text{II}} + C_B^2 r_4^{\text{II}} \right). \quad (\text{L.30})$$

Next we consider the elements of the  $\mathbf{M}^{\text{III}}$  matrix. Again to simplify the notation, we introduce the functions  $r_i^{\text{III}}(x, x', B)$ , with  $i = 1, \dots, 5$  and they are given by

$$r_0^{\text{III}} = \frac{2}{9} \left[ \frac{1}{2} \overline{(hh)}_{00}^{\text{III}+} + \overline{(hh)}_{01}^{\text{III}+} + \overline{(hh)}_{10}^{\text{III}+} + \overline{(hh)}_{11}^{\text{III}+} + \overline{(hh)}_{1-1}^{\text{III}+} \right], \quad (\text{L.31})$$

$$r_1^{\text{III}} = \frac{1}{18} \left[ 8 \overline{(hh)}_{00}^{\text{III}+} + 4 \overline{(hh)}_{01}^{\text{III}+} + 4 \overline{(hh)}_{10}^{\text{III}+} + \overline{(hh)}_{11}^{\text{III}+} + \overline{(hh)}_{1-1}^{\text{III}+} \right], \quad (\text{L.32})$$

$$r_2^{\text{III}} = \frac{1}{8} \cos \beta_1 \cos \alpha_1^{(2)} \left[ \bar{d}_3 \cos \left( \alpha_1^{(2)} + \beta_1 \right) + \bar{d}_4 \sin \left( \alpha_1^{(2)} + \beta_1 \right) \right], \quad (\text{L.33})$$

$$r_3^{\text{III}} = \frac{1}{8} \cos \beta_1 \cos \alpha_1^{(2)} \times \left[ \bar{d}_4 \cos \left( \alpha_1^{(2)} + \beta_1 \right) - \bar{d}_3 \sin \left( \alpha_1^{(2)} + \beta_1 \right) \right], \quad (\text{L.34})$$

$$r_4^{\text{III}} = \cos \beta_2 \cos \alpha_2^{(2)} \left\{ \left[ \Re \left( \bar{h}_{1-1}^{\text{III}} \right) - \Im \left( \bar{f}_{1-1}^{\text{III}} \right) \right] \cos \left( \alpha_2^{(2)} + \beta_2 \right) - \left[ \Im \left( \bar{h}_{1-1}^{\text{III}} \right) + \Re \left( \bar{f}_{1-1}^{\text{III}} \right) \right] \sin \left( \alpha_2^{(2)} + \beta_2 \right) \right\}, \quad (\text{L.35})$$

$$r_5^{\text{III}} = \cos \beta_2 \cos \alpha_2^{(2)} \left\{ \left[ \Re \left( \bar{h}_{1-1}^{\text{III}} \right) - \Im \left( \bar{f}_{1-1}^{\text{III}} \right) \right] \sin \left( \alpha_2^{(2)} + \beta_2 \right) + \left[ \Im \left( \bar{h}_{1-1}^{\text{III}} \right) + \Re \left( \bar{f}_{1-1}^{\text{III}} \right) \right] \cos \left( \alpha_2^{(2)} + \beta_2 \right) \right\}. \quad (\text{L.36})$$

The various auxiliary functions appearing in the above set of equations depend on  $x$ ,  $x'$  and field strength  $B$ , and are listed below

$$\Re \left( \bar{h}_{qq'}^{\text{III}} \right) = \frac{1}{4} \left( \bar{R}_{\text{III,HH}}^{q'q'} + \bar{R}_{\text{III,HH}}^{q'q} + \bar{R}_{\text{III,HH}}^{qq'} + \bar{R}_{\text{III,HH}}^{qq} \right), \quad (\text{L.37})$$

$$\Im \left( \bar{h}_{qq'}^{\text{III}} \right) = \frac{1}{4} \left( \bar{R}_{\text{III, FH}}^{q'q'} + \bar{R}_{\text{III, FH}}^{q'q} - \bar{R}_{\text{III, FH}}^{qq'} - \bar{R}_{\text{III, FH}}^{qq} \right), \quad (\text{L.38})$$

$$\overline{(hh)}_{qq'}^{\text{III}\pm} = \frac{1}{2} \left( \bar{R}_{\text{III,HH}}^{qq'} \pm \bar{R}_{\text{III,HH}}^{-q-q'} \right), \quad (\text{L.39})$$

$$\overline{(ff)}_{qq'}^{\text{III}\pm} = \frac{1}{2} \left( \bar{R}_{\text{III,FF}}^{qq'} \pm \bar{R}_{\text{III,FF}}^{-q-q'} \right), \quad (\text{L.40})$$

$$\overline{(hf)}_{qq'}^{\text{III}\pm} = \frac{1}{2} \left( \bar{R}_{\text{III, HF}}^{qq'} \pm \bar{R}_{\text{III, HF}}^{-q-q'} \right), \quad (\text{L.41})$$

$$\overline{(fh)}_{qq'}^{\text{III}\pm} = \frac{1}{2} \left( \bar{R}_{\text{III, FH}}^{qq'} \pm \bar{R}_{\text{III, FH}}^{-q-q'} \right), \quad (\text{L.42})$$

$$\bar{d}_3 = 2 \left[ \overline{(hh)}_{11}^{\text{III}+} + \overline{(hh)}_{1-1}^{\text{III}+} - \overline{(ff)}_{11}^{\text{III}+} + \overline{(ff)}_{1-1}^{\text{III}+} \right] + 4 \left[ \overline{(hh)}_{00}^{\text{III}+} + \overline{(hh)}_{01}^{\text{III}+} + \overline{(hh)}_{10}^{\text{III}+} \right], \quad (\text{L.43})$$

$$\bar{d}_4 = 2 \left[ \overline{(hf)}_{11}^{\text{III}-} + \overline{(fh)}_{11}^{\text{III}-} - \overline{(hf)}_{1-1}^{\text{III}-} + \overline{(fh)}_{1-1}^{\text{III}-} \right] + 4 \left[ \overline{(hf)}_{01}^{\text{III}-} + \overline{(fh)}_{10}^{\text{III}-} \right]. \quad (\text{L.44})$$

We note that  $xy$  in the auxiliary function  $\overline{(xy)}_{qq'}^{\text{III}\pm}$  is simply a notation and is not product of  $x$  and  $y$ . The functions  $\bar{R}_{\text{III,XY}}^{qq'}(x, x', B)$ , with X and Y denoting H and/or F, are given by

$$\bar{R}_{\text{III,XY}}^{qq'}(x, x', B) = \frac{1}{2} \int_0^\pi R_{\text{III,XY}}^{qq'}(x, x', \Theta; B) \sin \Theta d\Theta, \quad (\text{L.45})$$

where  $R_{\text{III},XY}^{qq'}(x, x', \Theta; B)$  are the AD magnetic redistribution functions of type III introduced in Eqs. (7.23)-(7.26). We refer to  $\bar{R}_{\text{III},XY}^{qq'}(x, x', B)$  as the AA magnetic redistribution functions of type III. The Hanle angles  $\alpha_1^{(K)}$  and  $\alpha_2^{(K)}$  are defined through

$$\tan \alpha_1^{(K)} = \frac{\Gamma_R}{\Gamma_R + \Gamma_E + D^{(K)}} \Gamma_B, \quad (\text{L.46})$$

$$\tan \alpha_2^{(K)} = 2 \frac{\Gamma_R}{\Gamma_R + \Gamma_E + D^{(K)}} \Gamma_B. \quad (\text{L.47})$$

We now list the elements of  $\mathbf{M}^{\text{III}}$  below :

$$b_{11}^{\text{III}} = B^{(0)} r_0^{\text{III}}, \quad (\text{L.48})$$

$$b_{22}^{\text{III}} = B^{(2)} \frac{1}{2} \left[ \frac{1}{2} (3C_B^2 - 1)^2 r_1^{\text{III}} + 3S_B^2 C_B^2 r_2^{\text{III}} + \frac{3}{2} S_B^4 r_4^{\text{III}} \right], \quad (\text{L.49})$$

$$b_{23}^{\text{III}} = B^{(2)} \sqrt{\frac{3}{2}} S_B C_B \left[ -\frac{1}{2} (3C_B^2 - 1) r_1^{\text{III}} + \left( C_B^2 - \frac{1}{2} \right) r_2^{\text{III}} + \frac{1}{2} S_B^2 r_4^{\text{III}} \right], \quad (\text{L.50})$$

$$b_{24}^{\text{III}} = B^{(2)} \sqrt{\frac{3}{8}} S_B (S_B^2 r_5^{\text{III}} - C_B^2 r_3^{\text{III}}), \quad (\text{L.51})$$

$$b_{25}^{\text{III}} = B^{(2)} \sqrt{\frac{3}{8}} S_B^2 \left[ \frac{1}{2} (3C_B^2 - 1) r_1^{\text{III}} - C_B^2 r_2^{\text{III}} + \frac{1}{2} (1 + C_B^2) r_4^{\text{III}} \right], \quad (\text{L.52})$$

$$b_{26}^{\text{III}} = B^{(2)} \sqrt{\frac{3}{8}} S_B^2 C_B (r_3^{\text{III}} + r_5^{\text{III}}), \quad (\text{L.53})$$

$$b_{33}^{\text{III}} = B^{(2)} \left[ 3S_B^2 C_B^2 r_1^{\text{III}} + 2 \left( C_B^2 - \frac{1}{2} \right)^2 r_2^{\text{III}} + S_B^2 C_B^2 r_4^{\text{III}} \right], \quad (\text{L.54})$$

$$b_{34}^{\text{III}} = B^{(2)} C_B \left[ S_B^2 r_5^{\text{III}} - \left( C_B^2 - \frac{1}{2} \right) r_3^{\text{III}} \right], \quad (\text{L.55})$$

$$b_{35}^{\text{III}} = B^{(2)} \frac{1}{2} S_B C_B \left[ -3S_B^2 r_1^{\text{III}} - (C_B^2 - S_B^2) r_2^{\text{III}} + (1 + C_B^2) r_4^{\text{III}} \right], \quad (\text{L.56})$$

$$b_{36}^{\text{III}} = B^{(2)} S_B \left[ -\frac{1}{2} (1 - 2C_B^2) r_3^{\text{III}} + C_B^2 r_5^{\text{III}} \right], \quad (\text{L.57})$$

$$b_{44}^{\text{III}} = B^{(2)} \left( \frac{1}{2} C_B^2 r_2^{\text{III}} + S_B^2 r_4^{\text{III}} \right), \quad (\text{L.58})$$

$$b_{45}^{\text{III}} = -B^{(2)} \frac{1}{2} S_B \left[ C_B^2 r_3^{\text{III}} + (1 + C_B^2) r_5^{\text{III}} \right], \quad (\text{L.59})$$

$$b_{46}^{\text{III}} = B^{(2)} S_B C_B \left( r_4^{\text{III}} - \frac{1}{2} r_2^{\text{III}} \right), \quad (\text{L.60})$$

$$b_{55}^{\text{III}} = B^{(2)} \frac{1}{2} \left[ \frac{3}{2} S_B^4 r_1^{\text{III}} + S_B^2 C_B^2 r_2^{\text{III}} + \frac{1}{2} (1 + C_B^2)^2 r_4^{\text{III}} \right], \quad (\text{L.61})$$

$$b_{56}^{\text{III}} = B^{(2)} \frac{1}{2} C_B \left[ -S_B^3 r_3^{\text{III}} + (1 + C_B^2) r_5^{\text{III}} \right], \quad (\text{L.62})$$

$$b_{66}^{\text{III}} = B^{(2)} \left( \frac{1}{2} S_B^2 r_2^{\text{III}} + C_B^2 r_4^{\text{III}} \right). \quad (\text{L.63})$$

Even though the expressions for the elements of the matrices  $\mathbf{M}^{\text{II}}$  and  $\mathbf{M}^{\text{III}}$  are cumbersome, one needs to use them for a correct and exact treatment of PRD in Hanle scattering.

## References

- Abramowitz, M., & Stegun, I. A. 1964, “*Handbook of mathematical functions*”, Applied Mathematics Series **55**, National Bureau of Standards (New York: Dover)
- Anderson, P. W. 1954, “*A Mathematical model for the narrowing of spectral lines by exchange or motion*”, J. Phys. Soc. Japan, **9**, 316
- Arena, P., & Landi Degl’Innocenti, E. 1982, “*An atlas of theoretical Stokes profiles for solar disk observations*”, A&AS, **48**, 81
- Auer, L. H., Heasley, J. N., & House, L. L. 1977, “*Non-LTE line formation in the presence of magnetic fields*”, ApJ, **216**, 531
- Auer, L. H., & Paletou, F. 1994, “*Two-dimensional radiative transfer with partial frequency redistribution I. General method*”, A&A, **285**, 675
- Auvergne, M., Frisch, H., Frisch, U., Froeschlé, Ch., & Pouquet, A. 1973, “*Spectral line formation in a turbulent atmosphere*”, A&A, **29**, 93
- Beckers, J. M. 1969a, “*The profiles of Fraunhofer lines in the presence of Zeeman splitting. I: The Zeeman triplet*”, Solar Physics, **9**, 372
- Beckers, J. M. 1969b, “*The profiles of Fraunhofer lines in the presence of Zeeman splitting. II: Zeeman multiplets for dipole and quadrupole radiation*”, Solar Physics, **10**, 262
- Bellot Rubio, L. R. 2006, “*Stokes inversion techniques: Recent advances and new challenges*”, in ASP Conf. Ser. **358**, “*Solar polarization 4*” (SPW4), eds. R. Casini, & B. W. Lites (San Francisco: ASP), 107
- Berdyugina, S. V., Nagendra, K. N., & Ramelli, R. eds. 2008, “*Solar polarization*” (SPW5), ASP Conf. Ser. ... (San Francisco: ASP)

- Bohr, N. 1924, “*Zur Polarisation des Fluoreszenzlichtes*”, *Naturwissenschaften*, **12**, 1115
- Bommier, V. 1977, “*Étude théorique de l’effet Hanle; traitement du cas de la raie  $D_3$  de l’Hélium en vue de la détermination du champ magnétique des protubérances solaires*”, Thèse de 3<sup>ème</sup> cycle, Paris VI University
- Bommier, V. 1996, “*Atomic coherences and level-crossings Physics*”, in “*Solar polarization*” (SPW1), eds. J. O. Stenflo, & K. N. Nagendra (Dordrecht: Kluwer), also *Solar Physics*, **164**, 29
- Bommier, V. 1997a, “*Master equation theory applied to the redistribution of polarized radiation, in the weak radiation field limit I. Zero magnetic field case*”, *A&A*, **328**, 706 (VB97a)
- Bommier, V. 1997b, “*Master equation theory applied to the redistribution of polarized radiation, in the weak radiation field limit II. Arbitrary magnetic field case*”, *A&A*, **328**, 726 (VB97b)
- Bommier, V. 1999, “*The density matrix theory for polarized radiation redistribution: Extensions for multilevel atom model and quantum Doppler effect*”, in *ASSL 243*, “*Solar polarization*” (SPW2), eds. K. N. Nagendra, & J. O. Stenflo (Boston: Kluwer), 43
- Bommier, V. 2003, “*The partial redistribution in the atomic density matrix formalism*”, in *ASP Conf. Ser. 307*, “*Solar polarization*” (SPW3), eds. J. Trujillo Bueno, & J. Sánchez Almeida (San Francisco: ASP), 213
- Bommier, V., Derouich, M., Landi Degl’Innocenti, E., Molodij, G., & Sahal-Bréchet, S. 2005, “*Interpretation of second solar spectrum observations of the Sr I 4607 Å line in a quiet region: Turbulent magnetic field strength determination*”, *A&A*, **432**, 295
- Bommier, V., & Landi Degl’Innocenti, E. 1996, “*Non-LTE polarized radiative transfer in intermediate magnetic fields: Numerical problems and results*”, in “*Solar polarization*” (SPW1), eds. J. O. Stenflo, & K. N. Nagendra (Dordrecht: Kluwer), also *Solar Physics*, **164**, 117
- Bommier, V., Landi Degl’Innocenti, E., & Sahal-Bréchet, S. 1991, “*Resonance line polarization and the Hanle effect in optically thick media. II - Case of a plane-parallel atmosphere*”, *A&A*, **244**, 383

- Bommier, V., & Sahal-Bréchet, S. 1978, “*Quantum theory of the Hanle effect - Calculations of the Stokes parameters of the D $\beta$  helium line for quiescent prominences*”, A&A, **69**, 57
- Bommier, V., & Stenflo, J. O. 1999, “*Partial frequency redistribution with Hanle and Zeeman effects. Non-perturbative classical theory*”, A&A, **350**, 327 (BS99)
- Borrero, J. M., Lagg, A., Solanki, S. K., & Collados, M. 2005, “*On the fine structure of sunspot penumbrae. II. The nature of the Evershed flow*”, A&A, **436**, 333
- Bourret, R. C., Frisch, U., & Pouquet, A. 1973, “*Brownian motion of harmonic oscillator with stochastic frequency*”, Physica, **65**, 303
- Brink, D. M., & Satchler, G. R. 1968, “*Angular momentum*” (2nd ed.; Oxford: Clarendon Press)
- Brissaud, A., & Frisch, U. 1971, “*Theory of Stark broadening - II. Exact line profile with model microfield*”, J. Quant. Spec. Radiat. Transf., **11**, 1767
- Brissaud, A., & Frisch, U. 1974, “*Solving linear stochastic differential equations*”, J. Math. Phys., **15**, 524
- Bruls, J. H. M. J., & Trujillo Bueno, J. 1996, “*The polarization-free approximation applied to multi-level non-LTE radiative transfer*”, in “*Solar polarization*” (SPW1), eds. J. O. Stenflo, & K. N. Nagendra (Dordrecht: Kluwer), also Solar Physics, **164**, 155
- Cannon, C. J. 1985, “*The transfer of spectral line radiation*” (Cambridge: Cambridge University Press)
- Carrier, G. F., Krook, M., & Pearson, C. E. 1966, “*Functions of a complex variable*” (New York: McGraw-Hill)
- Carroll, T. A., & Kopf, M. 2007, “*The meso-structured magnetic atmosphere. A stochastic polarized radiative transfer approach*”, A&A, **468**, 323
- Carroll, T. A., & Staude, J. 2003a, “*Diagnostics of magnetic field mesostructuring*”, in ASP Conf. Ser. **307**, “*Solar polarization*” (SPW3), eds. J. Trujillo Bueno, & J. Sánchez Almeida (San Francisco: ASP), 125

- Carroll, T. A., & Staude, J. 2003b, “*Meso-structured magnetic atmospheres: Stochastic polarized radiative transfer and Stokes profile inversion*”, *Astron. Nachr.*, **324**, 392
- Carroll, T. A., & Staude, J. 2005a, “*Line formation in turbulent magnetic atmospheres*”, *Astron. Nachr.*, **326**, 296
- Carroll, T. A., & Staude, J. 2005b, “*Line formation in inhomogeneous atmospheres and the magnetic structure of the internetwork*”, in ESA SP-596, “*Chromospheric and coronal magnetic fields*”, eds. D. E. Innes, A. Lagg, & S. K. Solanki (Katlenburg-Lindau, Germany: published on CDROM), p. 9.1
- Carroll, T. A., & Staude, J. 2006, “*The characteristic length scale of the magnetic fluctuation in a sunspot penumbra: A stochastic polarized radiative transfer approach*”, in ASP Conf. Ser. **358**, “*Solar polarization 4*” (SPW4), eds. R. Casini, & B. W. Lites (San Francisco: ASP), 137
- Casini, R., & Lites, B. W. eds. 2006, “*Solar polarization 4*” (SPW4), ASP Conf. Ser. **358** (San Francisco: ASP)
- Casini, R., & Manso Sainz, R. 2005, “*Line formation theory for the multiterm atom with hyperfine structure in a magnetic field*”, *ApJ*, **624**, 1025
- Cattaneo, F. 1999, “*On the origin of magnetic fields in the quiet photosphere*”, *ApJ*, **515**, L39
- Cattaneo, F., Emmonet, T., & Weiss, N. 2003, “*On the interaction between convection and magnetic fields*”, *ApJ*, **588**, 1183
- Chandrasekhar, S. 1950, “*Radiative transfer*” (Oxford: Clarendon Press)
- Chiarella, C., & Reichel, A. 1968, “*On the evaluation of integrals related to the Error function*”, *Mathematics of Computation*, **22**, 137
- Childress, S., & Gilbert A. D. 1995, “*Stretch, Twist, Fold: The fast dynamo*” (Springer-Verlag), Lecture Notes in Physics, 37
- Collett, E. 1993, “*Polarized light: Fundamentals and applications*” (New York: Marcel Dekker, Inc.)



- Cooper, J., Ballagh, R. J., Burnett, K., & Hummer, D. G. 1982, “*On redistribution and the equations for radiative transfer*”, ApJ, **260**, 299
- de Wijn, A. G., Rutten, R. J., Haverkamp, E. M. W. P., & Sütterlin, P. 2005, “*DOT tomography of the solar atmosphere. IV. Magnetic patches in internetwork areas*”, A&A, **441**, 1183
- del Toro Iniesta, J. C. 2003, “*Introduction to spectro polarimetry*” (Cambridge: Cambridge University Press)
- Dolginov, A. Z., & Pavlov, G. G. 1972, “*Influence of a random magnetic field on the properties of stellar absorption lines*”, Soviet Ast., **16**, 450 (transl. from Astron. Zhurnal, **49**, 555, 1972) (DP72)
- Dolginov, A. Z., & Pavlov, G. G. 1973, “*Transfer equations for spectral lines in a magnetic field*”, Astron. Zhurnal, **50**, 762
- Dolginov, A. Z., & Pavlov, G. G. 1974, “*Transfer equations for spectral lines in a magnetic field*”, Soviet Astron., **17**, 485
- Dolginov, A. Z., Gnedin, Yu. N., & Silant’ev, N. A. 1995, “*Propagation and polarization of radiation in cosmic media*” (Gordon and Breach Publishers)
- Domínguez Cerdeña, I., Kneer, F., & Sánchez Almeida, J. 2003a, “*Quiet-Sun magnetic fields at high spatial resolution*”, ApJ, **582**, L55
- Domínguez Cerdeña, I., Sánchez Almeida, J., & Kneer, F. 2003b, “*Inter-network magnetic fields observed with sub-arcsec resolution*”, A&A, **407**, 741
- Domínguez Cerdeña, I., Sánchez Almeida, J., & Kneer, F. 2006, “*The distribution of quiet Sun magnetic field strengths from 0 to 1800 G*”, ApJ, **636**, 496
- Domke, H., & Hubeny, I. 1988, “*Scattering of polarized light in spectral lines with partial frequency redistribution - General redistribution matrix*”, ApJ, **334**, 527
- Domke, H., & Pavlov, G. G. 1979, “*Line formation in micro-turbulent magnetic fields*”, Ap&SS, **66**, 47 (DP79)
- Domke, H., & Staude, J. 1973a, “*Non-LTE line formation in a magnetic field. I: Non-coherent scattering and true absorption*”, Solar Physics, **31**, 279

- Domke, H., & Staude, J. 1973b, “*Non-LTE line formation in a magnetic field. II: The influence of non-coherent scattering on line contours*”, *Solar Physics*, **31**, 291
- Dumont, S., Omont, A., Pecker, J. C., & Rees, D. E. 1977, “*Resonance line polarization: The line core*”, *A&A*, **54**, 675
- Fabiani Bendicho, P., & Trujillo Bueno, J. 1999, “*Three-dimensional radiative transfer with multilevel atoms*”, in *ASSL 243, “Solar polarization” (SPW2)*, eds. K. N. Nagendra, & J. O. Stenflo (Boston: Kluwer), 219
- Faddeeva, V. N., & Teren'tev, N. M. 1961, “*Tables of value of the function  $W(z) = e^{-z^2} \left(1 + \frac{2i}{\sqrt{\pi}} \int_0^z e^{t^2} dt\right)$  for complex argument*” (New York: Pergamon Press)
- Faulstich, R. 1980, “*On the transfer of line radiation in random magnetic fields*”, *J. Quant. Spec. Radiat. Transf.*, **24**, 229
- Faurobert, M. 1987, “*Linear polarization of resonance lines in the absence of magnetic fields. I - Slabs of finite optical thickness*”, *A&A*, **178**, 269
- Faurobert, M. 1988, “*Linear polarization of resonance lines in the absence of magnetic fields. II - Semi-infinite atmospheres*”, *A&A*, **194**, 268
- Faurobert, M., Arnaud, J., Vigneau, J., & Frisch, H. 2001, “*Investigation of weak solar magnetic fields. New observational results for the Sr I 460.7 nm linear polarization and radiative transfer modeling*”, *A&A*, **378**, 627
- Faurobert-Scholl, M. 1991, “*Hanle effect with partial frequency redistribution. I - Numerical methods and first applications*”, *A&A*, **246**, 469
- Faurobert-Scholl, M. 1992, “*Hanle effect with partial frequency redistribution. II - Linear polarization of the solar Ca I 4227 Å line*”, *A&A*, **258**, 521
- Faurobert-Scholl, M. 1993a, “*Investigation of micro-turbulent magnetic fields in the solar photosphere by their Hanle effect in the Sr I 4607 Å line*”, *A&A*, **268**, 765
- Faurobert-Scholl, M. 1993b, “*Polarization de resonance des raies spectrales et effet Hanle*” (Nice: Obs. Côte d’Azur)
- Faurobert-Scholl, M. 1996, “*Diagnostics with the Hanle effect*”, in “*Solar polarization*” (SPW1), eds. J. O. Stenflo, & K. N. Nagendra (Dordrecht: Kluwer), also *Solar Physics*, **164**, 79

- Faurobert-Scholl, M., Feautrier, N., Machefert, F., Petrovay, K., & Spielfiedel, A. 1995, “*Turbulent magnetic fields in the solar photosphere: diagnostics and interpretation*”, A&A, **298**, 289
- Faurobert-Scholl, M., Frisch, H., & Nagendra, K. N. 1997, “*An operator perturbation method for polarized line transfer. I. Non-magnetic regime in 1D media*”, A&A, **322**, 896
- Faurobert-Scholl, M., Paletou, F., & Bommier, V. 1999, “*Polarized redistribution matrix for Hanle effect: Numerical tests*”, in ASSL **243**, “*Solar polarization*” (SPW2), eds. K. N. Nagendra, & J. O. Stenflo (Boston: Kluwer), 115
- Feautrier, P. 1964, “*Sur la resolution numerique de l’equation de transfert*”, C. R. Acad. Sci. Paris, **258**, 3189
- Feller, A., Boller, A., & Stenflo, J. O. 2006, “*Tunable narrow-band filter for imaging polarimetry*”, in ASP Conf. Ser. **358**, “*Solar polarization 4*” (SPW4), eds. R. Casini, & B. W. Lites (San Francisco: ASP), 155
- Fluri, D. M., Holzreuter, R., Klement, J., & Stenflo, J. O. 2003a, “*Radiative transfer in Na I  $D_2$  and  $D_1$* ”, in ASP Conf. Ser. **307**, “*Solar polarization*” (SPW3), eds. J. Trujillo Bueno, & J. Sánchez Almeida (San Francisco: ASP), 263
- Fluri, D. M., Holzreuter, R., & Stenflo, J. O. 2006, “*Polarized scattering in strong chromospheric lines: Theory and its confrontation with observations*”, in ASP Conf. Ser. **358**, “*Solar polarization 4*” (SPW4), eds. R. Casini, & B. W. Lites (San Francisco: ASP), 237
- Fluri, D. M., Nagendra, K. N., & Frisch, H. 2003b, “*An operator perturbation method for polarized line transfer VI. Generalized PALI method for Hanle effect with partial frequency redistribution and collisions*”, A&A, **400**, 303 (PALI6)
- Frisch, H. 1980, “*Non-LTE transfer V. The asymptotics of partial redistribution*”, A&A, **83**, 166
- Frisch, H. 1988, “*Radiative transfer with frequency redistribution: Asymptotic methods, scaling laws and approximate solutions*”, in “*Radiation in moving gaseous media*”, eds. Y. Chmielewski, & T. Lanz (Switzerland: Geneva Observatory), 337

- Frisch, H. 1996, “*Partial frequency redistribution of polarized radiation*”, in “*Solar polarization*” (SPW1), eds. J. O. Stenflo, & K. N. Nagendra (Dordrecht: Kluwer), also *Solar Physics*, **164**, 49
- Frisch, H. 1998, “*The Hanle effect. The density matrix and scattering approaches to the  $\sqrt{\epsilon}$ -law*”, *A&A*, **338**, 683
- Frisch, H. 1999, “*Resonance polarization and Hanle effect: The integral equation formulation and some applications*”, in *ASSL 243*, “*Solar polarization*” (SPW2), eds. K. N. Nagendra, & J. O. Stenflo (Boston: Kluwer), 97
- Frisch, H. 2006, “*The Hanle effect in a random medium*”, *A&A*, **446**, 403
- Frisch, H. 2007, “*The Hanle effect. Decomposition of the Stokes parameters into irreducible components*”, *A&A*, **476**, 665
- Frisch, H. 2008, “*The Hanle effect. Angle-dependent frequency redistribution function. Decomposition of the Stokes parameters in irreducible components*”, in *ASP Conf. Ser. ...*, “*Solar polarization*” (SPW5), eds. S. V. Berdyugina, K. N. Nagendra, & R. Ramelli (San Francisco: ASP), Submitted
- Frisch, H., & Bardos, C. 1981, “*Diffusion approximations for the scattering of resonance-line photons: Interior and boundary layer solutions*”, *J. Quant. Spec. Radiat. Transf.*, **26**, 119
- Frisch, H., Faurobert, M., & Nagendra, K. N. 2001, “*The Hanle effect with angle-dependent redistribution functions*”, in *ASP Conf. Ser. 236*, “*Advanced solar polarimetry: Theory, Observation, and Instrumentation*”, ed. M. Sigwarth (San Francisco: ASP), 197
- Frisch, H., & Frisch, U. 1975, “*LTE and non-LTE line formation with turbulent velocity fields*”, in “*Physique des mouvements dans les atmosphères stellaires*”, eds. R. Cayrel, & M. Steinberg (Nice: Obs. Côte d’Azur)
- Frisch, H., & Frisch, U. 1976, “*Non-LTE transfer-II. Two-level atoms with stochastic velocity field*”, *MNRAS*, **175**, 157
- Frisch, U. 1995, “*Turbulence - The legacy of A. N. Kolmogorov*” (Cambridge: Cambridge University Press)

- Frisch, U., & Brissaud, A. 1971, “*Theory of Stark broadening - I. Soluble scalar model as a test*”, J. Quant. Spec. Radiat. Transf., **11**, 1753
- Frisch, U., & Frisch, H. 1977, “*Non-LTE transfer. III - Asymptotic expansion for small epsilon*”, MNRAS, **181**, 273
- Froeschlé, Ch., & Frisch, H. 1980, “*Broadening of non-LTE lines by a turbulent velocity field with a finite correlation length*”, A&A, **91**, 202
- Gandorfer, A. 2000, “*The second solar spectrum*”, Vol I: 4625 Å to 6995 Å line (Zürich: vdf Hochschulverlag), ISBN No. 3 7281 2764 7
- Gandorfer, A. 2002, “*The second solar spectrum*”, Vol II: 3910 Å to 4630 Å line (Zürich: vdf Hochschulverlag), ISBN No. 3 7281 2844 4
- Gandorfer, A. 2005, “*The second solar spectrum*”, Vol III: 3160 Å to 3915 Å line (Zürich: vdf Hochschulverlag), ISBN No. 3 7281 3018 4
- Hale, G. E. 1908, “*Solar vortices (contributions from the Mt. Wilson Solar Observatory, No. 26)*”, ApJ, **28**, 100
- Hamilton, D. R. 1947, “*The resonance radiation induced by elliptically polarized light*”, ApJ, **106**, 457
- Hanle, W. 1923, “*Über den Zeemaneffekt bei der Resonanzfluoreszenz*”, Naturwissenschaften, **11**, 690
- Hanle, W. 1924, “*Über magnetische Beeinflussung der Polarisation der Resonanzfluoreszenz*”, Z. Phys., **30**, 93
- Hanle, W. 1925, “*Die magnetische beeinflussung der resonanzfluoreszenz*”, Ergebnisse der exakten Naturwissenschaften, **4**, 214
- Heinzel, P. 1978, “*Derivatives of the Voigt functions*”, Bull. Astron. Inst. Czechosl, **29**, 159
- Heinzel, P. 1981, “*Non-coherent scattering in subordinate lines: A unified approach to redistribution functions*”, J. Quant. Spec. Radiat. Transf., **25**, 483
- Heisenberg, W. 1925, “*An application of the correspondence principle to the question of the polarization of the fluorescent light*”, Z. Phys., **31**, 617

- Henyey, L. G. 1940, “*The Doppler effect in resonance lines*”, Proc. Natl. Acad. Sci., **26**, 50
- Holzreuter, R., Fluri, D. M., & Stenflo, J. O. 2005, “*Scattering polarization in strong chromospheric lines. I. Explanation of the triplet peak structure*”, A&A, **434**, 713
- Holzreuter, R., Fluri, D. M., & Stenflo, J. O. 2006, “*Ca II K polarization as a diagnostic of temperature bifurcation*”, A&A, **449**, L41
- Holzreuter, R., & Stenflo, J. O. 2007a, “*Scattering polarization in strong chromospheric lines II. Influence of the temperature curve on the Ca II K line*”, A&A, **467**, 695
- Holzreuter, R., & Stenflo, J. O. 2007b, “*Scattering polarization in strong chromospheric lines III. Spatial fluctuations of the polarized Ca II K line profiles*”, A&A, **472**, 919
- House, L. L. 1971, “*Coherence properties of polarized radiation in weak magnetic fields*”, in IAU Symp. **43**, “*Solar magnetic fields*”, ed. R. Howard (Dordrecht: Reidel), 130
- House, L. L., & Steinitz, R. 1975, “*The non-LTE transport equation for polarized radiation in the presence of magnetic fields. I - Formulation*”, ApJ, **195**, 235
- Hubeny, I. 1982, “*Non-coherent scattering in subordinate lines: III. Generalized redistribution functions*”, J. Quant. Spec. Radiat. Transf., **27**, 593
- Hubeny, I. 1985, “*General aspects of partial redistribution and its astrophysical importance*”, in “*Progress in stellar spectral line formation theory*”, eds. J. E. Beckman & L. Crivellari (Dordrecht: Reidel), 27
- Hubeny, I. 1992, “*Accelerated lambda iteration (review)*”, in Lecture Notes in Phys. **401**, “*The atmospheres of early-type stars*”, eds. U. Heber, & C. J. Jeffery (Berlin: Springer), 377
- Hubeny, I. 2003, “*Accelerated lambda iteration: An overview*”, in ASP Conf. Ser. **288**, “*Stellar atmosphere modeling*”, eds. I. Hubeny, D. Mihalas & K. Werner, (San Francisco: ASP), 17
- Hubeny, I., & Cooper, J. 1986, “*Redistribution of radiation in the presence of velocity-changing collisions*”, ApJ, **305**, 852

- Hubeny, I., & Lites, B. W. 1995, “*Partial redistribution in multilevel atoms. I. Method and application to the solar hydrogen line formation*”, ApJ, **455**, 376
- Hubeny, I., Mihalas, D., & K. Werner eds. 2003, “*Stellar atmosphere modeling*”, ASP Conf. Ser. **288** (San Francisco: ASP)
- Hubeny, I., Oxenius, J., & Simonneau, E. 1983a, “*Absorption and emission line profile coefficients of multilevel atoms I. Atomic profile coefficients*”, J. Quant. Spec. Radiat. Transf., **29**, 477
- Hubeny, I., Oxenius, J., & Simonneau, E. 1983b, “*Absorption and emission line profile coefficients of multilevel atoms II. Velocity-averaged profile coefficients*”, J. Quant. Spec. Radiat. Transf., **29**, 495
- Hui, A. K., Armstrong, B. H., & Wray, A. A. 1978, “*Rapid computation of the Voigt and complex error functions*”, J. Quant. Spec. Radiat. Transf., **19**, 509
- Humlíček, J. 1982, “*Optimized computation of the Voigt and complex probability functions*”, J. Quant. Spec. Radiat. Transf., **27**, 437
- Hummer, D. G. 1962, “*Non-coherent scattering: I. The redistribution function with Doppler broadening*”, MNRAS, **125**, 21
- Ignace, R. 2001, “*The Hanle effect as a diagnostic of magnetic fields in stellar envelopes. III. Including the finite star depolarization effect*”, ApJ, **547**, 393
- Ignace, R., Cassinelli, J. P., & Nordsieck, K. H. 1999, “*The Hanle effect as a diagnostic of magnetic fields in stellar envelopes. II. Some theoretical results for resolved line profiles*”, ApJ, **520**, 335
- Ignace, R., Nordsieck, K. H., & Cassinelli, J. P. 1997, “*The Hanle effect as a diagnostic of magnetic fields in stellar envelopes. I. Theoretical results for integrated line profiles*”, ApJ, **486**, 550
- Ivanov, V. V. 1991, “*Analytical methods of line formation theory - Are they still alive*”, in NATO ASI Ser. **C341**, “*Stellar atmospheres: Beyond classical models*”, eds. L. Crivellari, I. Hubeny, & D. G. Hummer (Dordrecht: Reidel), 81
- Ivanov, V. V., Grachev, S. I., & Loskutov, V. M. 1997, “*Polarized line formation by resonance scattering. II. Conservative case*”, A&A, **321**, 968

- Iyanaga, S., & Kawada, Y. 1970, “*Encyclopedic Dictionary of Mathematics*” (Cambridge, Massachusetts: The MIT Press)
- Janßen, K., Vögler, A., & Kneer, F. 2003, “*On the fractal dimension of small-scale magnetic structures in the Sun*”, A&A, **409**, 1127
- Jefferies, J. T. 1968, “*Spectral line formation*” (Waltham: Blaisdell)
- Jefferies, J., Lites, B. W., & Skumanich, A. 1989, “*Transfer of line radiation in a magnetic field*”, ApJ, **343**, 920
- Khomenko, E. 2006, “*Diagnostics of quiet-Sun magnetism*”, in ASP Conf. Ser. **354**, “*Solar MHD theory and observations: A high spatial resolution perspective*”, eds. J. Leibacher, R. F. Stein, & H. Uitenbroek (San Francisco: ASP), 63
- Khomenko, E. V., Collados, M., Solanki, S. K., Lagg, A., & Trujillo Bueno, J. 2003, “*Quiet-Sun inter-network magnetic fields observed in the infrared*”, A&A, **408**, 1115
- Khomenko, E. V., Shelyag, S., Solanki, S. K., & Vögler, A. 2005, “*Stokes diagnostics of simulations of magnetoconvection of mixed-polarity quiet-Sun regions*”, A&A, **442**, 1059
- Kolmogorov, A. N. 1941, “*Dissipation of energy in locally isotropic turbulence*”, Dokl. Akad. Nauk SSSR, **32**, 16 (reprinted in Proc. R. Soc. Lond. A, 1991, **434**, 15)
- Kubo, R. 1954, “*Note on the stochastic theory of resonance absorption*”, J. Phys. Soc. Japan, **9**, 935
- Kunasz, P., & Auer, L. H. 1988, “*Short characteristic integration of radiative transfer problems: Formal solution in two-dimensional slabs*”, J. Quant. Spec. Radiat. Transf., **39**, 67
- Lamb, F. K., & ter Haar, D. 1971, “*The interaction of atoms with polarized light*”, Phys. Rep., **2**, 253
- Landi Degl’Innocenti, E. 1976, “*MALIP - a program to calculate the Stokes parameters profiles of magnetoactive Fraunhofer lines*”, A&AS, **25**, 379
- Landi Degl’Innocenti, E. 1982, “*The determination of vector magnetic fields in prominences from the observations of the Stokes profiles in the D $\beta$  line of helium*”, Solar Physics, **79**, 291



- Landi Degl'Innocenti, E. 1983a, "*Polarization in spectral lines I. A unifying theoretical approach*", Solar Physics, **85**, 3
- Landi Degl'Innocenti, E. 1983b, "*Polarization in spectral lines II. A classification scheme for solar observations*", Solar Physics, **85**, 33
- Landi Degl'Innocenti, E. 1984, "*Polarization in spectral lines III. Resonance polarization in the non-magnetic, collisionless regime*", Solar Physics, **91**, 1
- Landi Degl'Innocenti, E. 1985, "*Polarization in spectral lines IV. Resonance polarization in the Hanle effect, collisionless regime*", Solar Physics, **102**, 1
- Landi Degl'Innocenti, E. 1987, "*Transfer of polarized radiation, using  $4 \times 4$  matrices*", in "*Numerical radiative transfer*", ed. W. Kalkofen (Cambridge University Press), 265
- Landi Degl'Innocenti, E. 1994, "*Recipes for solar polarimetry*", in "*Solar surface magnetism*", eds. R. J. Rutten & C. J. Schrijver (Dordrecht: Kluwer) 29 (L94)
- Landi Degl'Innocenti, E. 1996, "*The density matrix approach to polarized radiative transfer*", in "*Solar polarization*" (SPW1), eds. J. O. Stenflo, & K. N. Nagendra (Dordrecht: Kluwer), also Solar Physics, **164**, 21
- Landi Degl'Innocenti, E. 2002, "*The Physics of polarization*", in "*Astrophysical spectropolarimetry*", eds. J. Trujillo Bueno, F. Moreno Inertis, & F. Sánchez (Cambridge: Cambridge University Press), 1
- Landi Degl'Innocenti, E. 2003, "*Theory of polarization: What's next?*", in ASP Conf. Ser. **307**, "*Solar polarization*" (SPW3), eds. J. Trujillo Bueno, & J. Sánchez Almeida (San Francisco: ASP), 593
- Landi Degl'Innocenti, E., Bommier, V., & Sahal-Bréchet, S. 1987, "*Linear polarization of hydrogen Balmer lines in optically thick quiescent prominences*", A&A, **186**, 335
- Landi Degl'Innocenti, E., Bommier, V., & Sahal-Bréchet, S. 1990, "*Resonance line polarization and the Hanle effect in optically thick media. I - Formulation for the two-level atom*", A&A, **235**, 459

- Landi Degl'Innocenti, E., Bommier, V., & Sahal-Bréchet, S. 1991a, “*Resonance line polarization for arbitrary magnetic fields in optically thick media I. Basic formalism for a 3-dimensional medium*”, A&A, **244**, 391
- Landi Degl'Innocenti, E., Bommier, V., & Sahal-Bréchet, S. 1991b, “*Resonance line polarization for arbitrary magnetic fields in optically thick media II. Case of a plane-parallel atmosphere and absence of Zeeman coherences*”, A&A, **244**, 401
- Landi Degl'Innocenti, E., & Landi Degl'Innocenti, M. 1972, “*Quantum theory of line formation in a magnetic field*”, Solar Physics, **27**, 319
- Landi Degl'Innocenti, E., & Landi Degl'Innocenti, M. 1975, “*Transfer equations for polarized light*”, II Nuovo Cimento B, **27**, 134
- Landi Degl'Innocenti, E., Landi Degl'Innocenti, M., & Landolfi, M. 1997, “*Density matrix and polarized radiative transfer: A heuristic approach to the problem of frequency redistribution*”, in Proc. Forum THÉMIS, “*Science with THÉMIS*”, eds. N. Mein, & S. Sahal-Bréchet (Paris: Obs. Paris-Meudon), 59
- Landi Degl'Innocenti, E., & Landolfi, M. 2004, “*Polarization in spectral lines*” (Dordrecht: Kluwer) (LL04)
- Landi Degl'Innocenti, M., & Landi Degl'Innocenti, E. 1988, “*An analytical expression for the Hanle-effect scattering phase matrix*”, A&A, **192**, 374
- Landi Degl'Innocenti, M., Landolfi, M., & Landi Degl'Innocenti, E. 1976, “*Statistical equilibrium equations in a polarized radiation field*”, II Nuovo Cimento B, **35**, 117
- Lin, H., & Casini, R. 2000, “*A classical theory of coronal emission line polarization*”, ApJ, **542**, 528
- Lin, H., Penn, M. J., & Kuhn, J. R. 1998, “*He I 10830 Å line polarimetry: A new tool to probe the filament magnetic fields*”, ApJ, **493**, 978
- Lites, B. W., Kubo, M., Socas-Navarro, H., Berger, T., Frank, Z., Shine, R., Tarbell, T., Title, A., Ichimoto, K., Katsukawa, Y., Tsuneta, S., Suematsu, Y., Shimizu, T., & Nagata, S. 2008, “*The horizontal magnetic flux of the quiet-Sun internetwork as observed with the Hinode spectro-polarimeter*”, ApJ, **672**, 1237
- Lites, B. W., & Socas-Navarro, H. 2004, “*Characterization of magnetic flux in the quiet Sun. II. The internetwork fields at high angular resolution*”, ApJ, **613**, 600

- Lites, B. W., Socas-Navarro, H., Kubo, M., Berger, T. E., Frank, Z., Shine, R. A., Tarbell, T. D., Title, A. M., Ichimoto, K., Katsukawa, Y., Tsuneta, S., Suematsu, Y., Shimizu, T., & Nagata, S. 2007, “*Hinode observations of horizontal quiet Sun magnetic flux and the hidden turbulent magnetic flux*”, Publ. Astron. Soc. Japan, **59**, S571
- Luque, J. M., Calzada, M. D., & Saez, M. 2005, “*A new procedure for obtaining the Voigt function dependent upon the complex error function*”, J. Quant. Spec. Radiat. Transf., **94**, 151
- Manso Sainz, R. 2002, “*Scattering line polarization and the Hanle effect in weakly magnetized stellar atmospheres*”, PhD Thesis (Tenerife: Universidad de La Laguna)
- Manso Sainz, R., & Trujillo Bueno, J. 1999, “*The Hanle effect in 1D, 2D and 3D*”, in ASSL **243**, “*Solar polarization*” (SPW2), eds. K. N. Nagendra, & J. O. Stenflo (Boston: Kluwer), 143
- Manso Sainz, R., & Trujillo Bueno, J. 2003, “*A multilevel radiative transfer program for modeling scattering line polarization and the Hanle effect in stellar atmospheres*”, in ASP Conf. Ser. **307**, “*Solar polarization*” (SPW3), eds. J. Trujillo Bueno, & J. Sánchez Almeida (San Francisco: ASP), 251
- Martin, B., & Wickramasinghe, D. T. 1981, “*Magneto-optical effects in magnetic white dwarfs. I The line spectra*”, MNRAS, **196**, 23
- Martinez Pillet, V. 2000, “*Spectral signature of uncombed penumbral magnetic fields*”, A&A, **361**, 734
- Matta, F., & Reichel, A. 1971, “*Uniform computation of the error function and other related functions*”, Mathematics of Computation, **25**, 339
- McKenna, S. J. 1984a, “*The transfer of polarized radiation in spectral lines: Solar-type stellar atmospheres*”, Ap&SS, **106**, 283
- McKenna, S. J. 1984b, “*Emergent polarization structure in spectral lines from rotating stars of spectral type B*”, Ap&SS, **107**, 61
- McKenna, S. J. 1985, “*The transfer of polarized radiation in spectral lines: Formalism and solutions in simple cases*”, Ap&SS, **108**, 31
- Mihalas, D. 1978, “*Stellar atmosphere*” (2nd ed.; San Francisco: Freeman)

- Mitchell, A. C. G., & Zemansky, M. W. 1934, "*Resonance radiation and excited atoms*" (Cambridge: Cambridge University Press)
- Moruzzi, G., & Strumia, F. eds. 1991, "*The Hanle effect and level-crossing spectroscopy*" (New York: Plenum Press)
- Nagendra, K. N. 1986, "*Radiative transfer with Stokes vector*", PhD Thesis (Bangalore: Bangalore University)
- Nagendra, K. N. 1988, "*Resonance line polarization in spherical atmospheres*", *ApJ*, **335**, 269
- Nagendra, K. N. 1989, "*Polarization of resonance lines formed in extended spherical atmospheres*", *Ap&SS*, **154**, 119
- Nagendra, K. N. 1994, "*Resonance line polarization in spherical atmospheres: Partial redistribution effects studied with the Domke-Hubeny redistribution matrix*", *ApJ*, **432**, 274
- Nagendra, K. N. 1995, "*Collisional redistribution effects on line polarization in spherical atmospheres*", *Ap&SS*, **274**, 523
- Nagendra, K. N. 2003a, "*Numerical solutions of polarized line transfer equations*", in ASP Conf. Ser. **288**, "*Stellar atmosphere modeling*", eds. I. Hubeny, D. Mihalas, & K. Werner (San Francisco: ASP), 583
- Nagendra, K. N. 2003b, "*Some equations of discrete space method (DSM) for polarized line transfer*", in ASP Conf. Ser. **288**, "*Stellar atmosphere modeling*", eds. I. Hubeny, D. Mihalas, & K. Werner (San Francisco: ASP), 611
- Nagendra, K. N., Frisch, H., & Faurobert-Scholl, M. 1998, "*An operator perturbation method for polarized line transfer. III. Applications to the Hanle effect in 1D media*", *A&A*, **332**, 610
- Nagendra, K. N., Frisch, H., Faurobert-Scholl, M., & Paletou, F. 2000, "*An operator perturbation method of polarized line transfer V. Diagnosis of solar weak magnetic fields*", *JAA*, **21**, 255
- Nagendra, K. N., Frisch, H., & Faurobert, M. 2002, "*Hanle effect with angle-dependent partial redistribution*", *A&A*, **395**, 305

- Nagendra, K. N., Frisch, H., & Fluri, D. M. 2003, “*Numerical methods for solving the polarized line transfer equations with partial frequency redistribution*”, in ASP Conf. Ser. **307**, “*Solar polarization*” (SPW3), eds. J. Trujillo Bueno, & J. Sánchez Almeida (San Francisco: ASP), 227
- Nagendra, K. N., Paletou, F., Frisch, H., & Faurobert-Scholl, M. 1999, “*An operator perturbation method for polarized line transfer IV: Applications to the Hanle effect with partial frequency redistribution*”, in ASSL **243**, “*Solar polarization*” (SPW2), eds. K. N. Nagendra, & J. O. Stenflo (Boston: Kluwer), 127
- Nagendra, K. N., & Peraiah, A. 1985a, “*Numerical solution of the radiative transfer equation in a magnetized medium*”, MNRAS, **214**, 203
- Nagendra, K. N., & Peraiah, A. 1985b, “*Some aspects of the solution of vector transfer equation in a magnetized medium*”, Ap&SS, **117**, 121
- Nagendra, K. N., & Sampoorna, M. 2008, “*Numerical methods in polarized line formation theory*”, in ASP Conf. Ser. ..., “*Solar polarization*” (SPW5), eds. S. V. Berdyugina, K. N. Nagendra, & R. Ramelli (San Francisco: ASP), Submitted
- Nagendra, K. N., & Stenflo, J. O. eds. 1999, “*Solar polarization*” (SPW2), ASSL **243** (Boston: Kluwer)
- Olson, G. L., Auer, L. H., & Buchler, J. R. 1986, “*A rapidly convergent iterative solution of the non-LTE radiation transfer problem*”, J. Quant. Spec. Radiat. Transf., **35**, 431
- Omont, A., Smith, E. W., & Cooper, J. 1972, “*Redistribution of resonance radiation I. The effect of collisions*”, ApJ, **175**, 185
- Omont, A., Smith, E. W., & Cooper, J. 1973, “*Redistribution of resonance radiation II. The effect of magnetic fields*”, ApJ, **182**, 283
- Orozco Suárez, D., Bellot Rubio, L. R., del Toro Iniesta, J. C., Tsuneta, S., Lites, B. W., Ichimoto, K., Katsukawa, Y., Nagata, S., Shimizu, T., Shine, R. A., Suematsu, Y., Tarbell, T. D., & Title, A. M. 2007, “*Quiet-Sun internetwork magnetic fields from the inversion of Hinode measurements*”, ApJ, **670**, L61
- Orozco Suárez, D., & del Toro Iniesta, J. C. 2007, “*The usefulness of analytic response functions*”, A&A, **462**, 1137

- Oxenius, J. 1965, "*Emission and absorption profiles in a scattering atmosphere*", J. Quant. Spec. Radiat. Transf., **5**, 771
- Paletou, F., & Auer, L. H. 1995, "*A new approximate operator method for partial frequency redistribution problems*", A&A, **297**, 771
- Paletou, F., & Faurobert-Scholl, M. 1997, "*An operator perturbation method for polarized line transfer II. Resonance polarization with partial frequency redistribution effects*", A&A, **328**, 343
- Pecker, J. C., & Schatzman, E. 1959, "*Astrophysique Générale*" (Paris: Masson & Cie)
- Povel, H. 1995, "*Imaging Stokes polarimetry with piezoelectric modulators and charge-coupled-device image sensors*", Opt. Eng., **34**, 1870
- Povel, H., Aebbersold, H., & Stenflo, J. O. 1990, "*Charge-coupled device image sensor as a demodulator in a 2-D polarimeter with a piezoelectric modulator*", Appl. Opt., **29**, 1186
- Rachkovsky, D. N. 1962a, "*Magneto-optical effects in spectral lines of sunspots*" (in Russian), Izv. Krymsk. Astrofiz. Obs., **27**, 148
- Rachkovsky, D. N. 1962b, "*Magnetic rotation effects in spectral lines*" (in Russian), Izv. Krymsk. Astrofiz. Obs., **28**, 259
- Rachkovsky, D. N. 1963, "*The development of absorption lines in sunspots, taking into account scattering and absorption*" (in Russian), Izv. Krymsk. Astrofiz. Obs., **29**, 97
- Rachkovsky, D. N. 1967, "*The reduction for anomalous dispersion in the theory of the absorption line formation in a magnetic field*" (in Russian), Izv. Krymsk. Astrofiz. Obs., **37**, 56
- Rees, D. E. 1969, "*Line formation in a magnetic field*", Solar Physics, **10**, 268
- Rees, D. E. 1978, "*Non-LTE resonance line polarization in the absence of magnetic fields*", Publ. Astron. Soc. Japan, **30**, 455
- Rees, D. E. 1987, "*A gentle introduction to polarized radiative transfer*", in "*Numerical radiative transfer*", ed. W. Kalkofen (Cambridge: Cambridge University Press), 213

- Rees, D. E., & Murphy, G. A. 1987, “*Non-LTE polarized radiative transfer in spectral lines*”, in “*Numerical radiative transfer*”, ed. W. Kalkofen (Cambridge: Cambridge University Press), 241
- Rees, D. E., Murphy, G. A., & Durrant, C. J. 1989, “*Stokes profile analysis and vector magnetic fields II. Formal numerical solutions of the Stokes transfer equations*”, *ApJ*, **339**, 1093
- Rees, D. E., & Saliba, G. J. 1982, “*Non-LTE resonance line polarization with partial redistribution effects*”, *A&A*, **115**, 1
- Rybicki, G. B., & Lightman, A. P. 1979, “*Radiative processes in astrophysics*” (New York: Wiley-Interscience)
- Saliba, G. J. 1985, “*Non-LTE resonance line polarization with partial redistribution: The solar Ca II K line*”, *Solar Physics*, **98**, 1
- Saliba, G. J. 1986, “*Non-LTE scattering resonance polarization in solar spectral lines*”, PhD Thesis (University of Sidney)
- Sánchez Almeida, J. 1997, “*Physical properties of the solar magnetic photosphere under the MISMA hypothesis I. Description of the inversion procedure*”, *ApJ*, **491**, 993
- Sánchez Almeida, J. 1998, “*Optically thin irregularities in the penumbrae of sunspots*”, *ApJ*, **497**, 967
- Sánchez Almeida, J. 2004, “*The magnetism of the very quiet Sun*”, in ASP Conf. Ser. **325**, “*The solar-B mission and the forefront of solar physics*”, eds. T. Sakurai & T. Sekii (San Francisco: ASP), 115
- Sánchez Almeida, J., Emonet, T., & Cattaneo, F. 2003a, “*Polarization of photospheric lines from turbulent dynamo simulations*”, *ApJ*, **585**, 536
- Sánchez Almeida, J., Domínguez Cerdeña, I., & Kneer, F. 2003b, “*Simultaneous visible and infrared spectropolarimetry of a solar internetwork region*”, *ApJ*, **597**, L177
- Sánchez Almeida, J., Landi Degl’Innocenti, E., Martinez Pillet, V., & Lites, B. W. 1996, “*Line asymmetries and the microstructure of photospheric magnetic fields*”, *ApJ*, **466**, 537

- Sánchez Almeida, J., & Lites, B. W. 2000, “*Physical properties of the solar magnetic photosphere under the MISMA hypothesis II. Network and internetwork fields at the disk center*”, ApJ, **532**, 1215
- Sánchez Almeida, J., Márquez, I., Bonet, J. A., Domínguez Cerdeña, I., & Muller, R. 2004, “*Bright points in the internetwork quiet Sun*”, ApJ, **609**, L91
- Schreier, F. 1992, “*The Voigt and complex error function: A comparison of computational methods*”, J. Quant. Spec. Radiat. Transf., **48**, 743
- Šidlichovský, M. 1974, “*The formulation of basic equations for spectral line formation in the presence of a magnetic field: A Non-LTE problem*”, Bull. Astron. Inst. Czech., **25**, 198
- Sigwarth, M. ed. 2001, “*Advanced solar polarimetry: Theory, Observation, and Instrumentation: The 20th NSO/Sacramento Peak Summer Workshop*”, ASP Conf. Ser. **236** (San Francisco: ASP)
- Silant'ev, N. A. 2005, “*Radiative transfer and Faraday effect in turbulent atmospheres*”, A&A, **433**, 1117
- Socas-Navarro, H., & Lites, B. W. 2004, “*Observational evidence for small-scale mixture of weak and strong fields in the quiet Sun*”, ApJ, **616**, 587
- Socas-Navarro, H., & Sánchez Almeida J. 2003, “*Magnetic fields in the quiet Sun: Observational discrepancies and unresolved structure*”, ApJ, **593**, 581
- Stein, R. F., & Nordlund, Å. 2006, “*Solar small-scale magnetoconvection*”, ApJ, **642**, 1246
- Stenflo, J. O. 1971, “*The interpretation of magnetograph results: The formation of absorption lines in a magnetic field*”, in IAU Symp. **43**, “*Solar magnetic fields. Polarized radiation diagnostics*”, ed. R. Howard (Dordrecht: Reidel), 101
- Stenflo, J. O. 1973, “*Magnetic-field structure of the photospheric network*”, Solar Physics, **32**, 41
- Stenflo, J. O. 1976, “*Resonance-line polarization I. A non-LTE theory for the transport of polarized radiation in spectral lines in the case of zero magnetic field*”, A&A, **46**, 61



- Stenflo, J. O. 1978, “*Resonance-line polarization III. The Hanle effect in a compact non-LTE radiative transfer formulation*”, A&A, **66**, 241
- Stenflo, J. O. 1982, “*The Hanle effect and the diagnostics of turbulent magnetic fields in the solar atmosphere*”, Solar Physics, **80**, 209
- Stenflo, J. O. 1987, “*Observational constraints on a ‘hidden’, turbulent magnetic field of the sun*”, Solar Physics, **114**, 1
- Stenflo, J. O. 1989, “*Small-scale magnetic structures on the sun*”, A&ARv, **1**, 3
- Stenflo, J. O. 1994, “*Solar magnetic fields - Polarized radiation diagnostics*” (Dordrecht: Kluwer) (S94)
- Stenflo, J. O. 1996, “*Scattering physics*”, in “*Solar polarization*” (SPW1), eds. J. O. Stenflo, & K. N. Nagendra, also Solar Physics, **164**, 1
- Stenflo, J. O. 1998, “*Hanle-Zeeman scattering matrix*”, A&A, **338**, 301
- Stenflo, J. O. 2001, “*Observation of scattering polarization and the diagnostics of solar magnetic fields*”, in ASP Conf. Ser. **236**, “*Advanced solar polarimetry: Theory, Observations, and Instrumentation*”, ed. M. Sigwarth (San Francisco: ASP), 97
- Stenflo, J. O. 2002, “*Polarization radiation diagnostics of solar magnetic fields*”, in “*Astrophysical spectropolarimetry*”, eds. J. Trujillo Bueno, F. Moreno Inertis, & F. Sánchez (Cambridge: Cambridge University Press), 55
- Stenflo, J. O. 2003, “*Scattering polarization in magnetic fields: Anomalies, surprises and enigmas*”, in ASP Conf. Ser. **307**, “*Solar polarization*” (SPW3), eds. J. Trujillo Bueno, & J. Sánchez Almeida (San Francisco: ASP), 385
- Stenflo, J. O. 2004, “*The new world of scattering physics seen by high-precision imaging polarimetry*”, Rev. Mod. Astron., **17**, 269
- Stenflo, J. O. 2006, “*Second solar spectrum: A brief overview*”, in ASP Conf. Ser. **358**, “*Solar polarization 4*” (SPW4), eds. R. Casini, & B. W. Lites (San Francisco: ASP), 215
- Stenflo, J. O., Gandorfer, A., Wenzler, T., & Keller, C. U. 2001, “*Influence of magnetic fields on the coherence effects in the Na I  $D_1$  and  $D_2$  lines*”, A&A, **367**, 1033

- Stenflo, J. O., Harvey, J. W., Brault, J. W., & Solanki, S. 1984, “*Diagnostics of solar magnetic fluxtubes using a Fourier transform spectrometer*”, *A&A*, **131**, 333
- Stenflo, J. O., & Holzreuter, R. 2002, “*Empirical view of magnetoconvection*”, in ESA SP-505, “*Magnetic coupling of the solar atmosphere*”, ed. H. Sawaya-Lacoste, 101
- Stenflo, J. O., & Holzreuter, R. 2003a, “*Distribution of magnetic fields at scales beyond the spatial resolution limit*”, in ASP Conf. Ser. **286**, “*Current theoretical models and future high resolution solar observations: Preparing for ATST*”, eds. A. A. Pevtsov, & H. Uitenbroek (San Francisco: ASP), 169
- Stenflo, J. O., & Holzreuter, R. 2003b, “*Flux tubes or fractal distributions: On the nature of photospheric magnetic fields*”, *Astron. Nachr.*, **324**, No. 4, 397
- Stenflo, J. O., & Keller, C. U. 1996, “*New window for spectroscopy*”, *Nature*, **382**, 588
- Stenflo, J. O., & Keller, C. U. 1997, “*The second solar spectrum: A new window for diagnostics of the Sun*”, *A&A*, **321**, 927
- Stenflo, J. O., & Lindegren, L. 1977, “*Statistical analysis of solar FeI lines: Magnetic line broadening*”, *A&A*, **59**, 367
- Stenflo, J. O., & Nagendra, K. N. eds. 1996, “*Solar polarization*” (SPW1), (Dordrecht: Kluwer), also *Solar Physics*, **164**
- Stenflo, J. O., & Stenholm, L. G. 1976, “*Resonance-line polarization II. Calculations of linear polarization in solar UV emission lines*”, *A&A*, **46**, 69
- Stenflo, J. O., Twerenbold, D., & Harvey, J. W. 1983a, “*Coherent scattering in the solar spectrum: Survey of linear polarization in the range 3165-4230 Å*”, *A&AS*, **52**, 161
- Stenflo, J. O., Twerenbold, D., Harvey, J. W., & Brault, J. W. 1983b, “*Coherent scattering in the solar spectrum: Survey of linear polarization in the range 4200-9950 Å*”, *A&AS*, **54**, 505
- Stenholm, L. G., & Stenflo, J. O. 1978, “*Multi-dimensional non-LTE transfer of polarized radiation in magnetic fluxtubes*”, *A&A*, **67**, 33

- Stepanov, V. E. 1958a, “*The absorption coefficient of atoms in the case of reverse Zeeman effect for an arbitrary directed magnetic field*” (in Russian), *Izv. Krymsk. Astrofiz. Obs.*, **18**, 136
- Stepanov, V. E. 1958b, “*On the theory of the formation of absorption lines in a magnetic field and the profile of Fe  $\lambda$  6173 Å in the solar sunspot spectrum*” (in Russian), *Izv. Krymsk. Astrofiz. Obs.*, **19**, 20
- Streater, A., Cooper, J., & Rees, D. E. 1988, “*Transfer and redistribution of polarized light in resonance lines I. Quantum formulation with collisions*”, *ApJ*, **335**, 503
- Takeda, Y. 1991, “*Numerical approach to Zeeman line radiative transfer*”, *Publ. Astron. Soc. Japan*, **43**, 719
- Thomas, J. H., & Weiss, N. O. 2004, “*Fine structure in sunspots*”, *ARA&A*, **42**, 517
- Trujillo Bueno, J. 1998, “*The iterative solution of polarization transfer problems formulated with the density-matrix theory*”, in “*Radiative transfer and inversion codes*”, ed. C. Briand (Paris: Obs. Paris-Meudon), 27
- Trujillo Bueno, J. 1999, “*Towards the modeling of the second solar spectrum*”, in *ASSL 243, “Solar polarization” (SPW2)*, eds. K. N. Nagendra, & J. O. Stenflo (Boston: Kluwer), 73
- Trujillo Bueno, J. 2001, “*Atomic polarization and the Hanle effect*”, in *ASP Conf. Ser. 236, “Advanced solar polarimetry: Theory, Observations, and Instrumentation*”, ed. M. Sigwarth (San Francisco: ASP), 161
- Trujillo Bueno, J. 2003a, “*The generation and transfer of polarized radiation in stellar atmospheres*”, in *ASP Conf. Ser. 288, “Stellar atmosphere modeling*”, eds. I. Hubeny, D. Mihalas, & K. Werner (San Francisco: ASP), 551
- Trujillo Bueno, J. 2003b, “*New diagnostic windows on the weak magnetism of the solar atmosphere*”, in *ASP Conf. Ser. 307, “Solar polarization” (SPW3)*, eds. J. Trujillo Bueno, & J. Sánchez Almeida (San Francisco: ASP), 407
- Trujillo Bueno, J. 2005, “*Quantum spectropolarimetry and the Sun’s hidden magnetism*”, in *ESA SP-600, “The dynamic Sun: Challenges for theory and observations*”, eds. D. Danesy, S. Poedts, A. De Groof & J. Andries, (Leuven, Belgium: published on CDROM), p. 7.1

- Trujillo Bueno, J., Asensio Ramos, A., & Shchukina, N. 2006, “*The Hanle effect in atomic and molecular lines: A new look at the Sun’s hidden magnetism*”, in ASP Conf. Ser. **358**, “*Solar polarization 4*” (SPW4), eds. R. Casini, & B. W. Lites (San Francisco: ASP), 269
- Trujillo Bueno, J., & Fabiani Bendicho, P. 1995, “*A novel iterative scheme for the very fast and accurate solution of non-LTE radiative transfer problems*”, ApJ, **455**, 646
- Trujillo Bueno, J., & Landi Degl’Innocenti, E. 1996, “*The polarization-free approximation*”, in “*Solar polarization*” (SPW1), eds. J. O. Stenflo, & K. N. Nagendra (Dordrecht: Kluwer), also Solar Physics, **164**, 135
- Trujillo Bueno, J., & Landi Degl’Innocenti, E. 1997, “*Linear polarization due to lower level depopulation pumping in stellar atmospheres*”, ApJ, **482**, L183
- Trujillo Bueno, J., & Manso Sainz, R. 1999, “*Iterative methods for the non-LTE transfer of polarized radiation: Resonance line polarization in one-dimensional atmospheres*”, ApJ, **516**, 436
- Trujillo Bueno, J., Moreno-Inseris, F., & Sanchez, F. eds. 2002, “*Astrophysical spectropolarimetry*” (Cambridge: Cambridge University Press)
- Trujillo Bueno, J., & Sánchez Almeida, J. eds. 2003, “*Solar polarization*” (SPW3), ASP Conf. Ser. **307** (San Francisco: ASP)
- Trujillo Bueno, J., Shchukina, N., & Asensio Ramos, A. 2004, “*A substantial amount of hidden magnetic energy in the quiet Sun*”, Nature, **430**, 326
- Uitenbroek, H. 2003, “*Multi-level accelerated lambda iteration with partial redistribution*”, in ASP Conf. Ser. **288**, “*Stellar atmosphere modeling*”, eds. I. Hubeny, D. Mihalas, & K. Werner (San Francisco: ASP), 597
- Unno, W. 1956, “*Line formation of a normal Zeeman triplet*”, Publ. Astron. Soc. Japan, **8**, 108
- Unno, W. 1959, “*Turbulent motion in the solar atmosphere I. Doppler widths of photospheric lines*”, ApJ, **129**, 375
- Varshalovich, D. A., Moskalev, A. N., & Khersonskii, V. K. 1988, “*Quantum theory of angular momentum*” (World Scientific)

- Vögler, A. 2003, “*Three-dimensional simulations of magneto-convection in the solar photosphere*”, PhD thesis (Göttingen: Göttingen University)
- Vögler, A., Shelyag, S., Schüssler, M., Cattaneo, F., Emonet, T., & Linde, T. 2005, “*Simulations of magneto-convection in the solar photosphere: Equations, methods, and results of the MURaM code*”, A&A, **429**, 335
- Wallace, L., & Yelle, R. V. 1989, “*Resonance line transfer calculations by doubling thin layers II. The use of the  $R_{II}$  redistribution function*”, ApJ, **346**, 489
- Weisskopf, V. F. I. 1933, “*The intensity and structure of spectral lines*”, The Observatory, **56**, 291
- Wells, R. J. 1999, “*Rapid approximation to the Voigt/Faddeeva function and its derivatives*”, J. Quant. Spec. Radiat. Transf., **62**, 29
- Wickramasinghe, D. T., & Ferrario, L. 2000, “*Magnetism in isolated and binary white dwarfs*”, PASP, **112**, 873
- Wittmann, A. 1974, “*Computation and observation of Zeeman multiplet polarization in Fraunhofer lines II. Computation of Stokes parameter profiles*”, Solar Physics, **35**, 11
- Wood, R. W., & Ellett, A. 1923, “*On the influence of magnetic fields on the polarization of resonance radiation*”, Proc. R. Soc., **103**, 396
- Wooley, R. V. D. R. 1938, “*Non-coherent formation of absorption lines*”, MNRAS, **98**, 624
- Yee Yee Oo 2004, “*Studies in astrophysical line formation theory*”, PhD Thesis (Bangalore: Bangalore University)
- Yee Yee Oo, Sampoorna, M., Nagendra, K. N., Ananthamurthy, S., & Ramachandran, G. 2007, “*Scattering polarization in the presence of magnetic and electric fields*”, J. Quant. Spec. Radiat. Transf., **108**, 161
- Zanstra, H. 1941a, “*Theory of a polarization effect in Fraunhofer lines due to oscillator scattering*”, MNRAS, **101**, 250
- Zanstra, H. 1941b, “*On the weakening of the polarization effect by collision damping*”, MNRAS, **101**, 273

Zeeman, P. 1897, "*On the influence of magnetism on the nature of the light emitted by a substance*", *Phil. Mag.*, **43**, 226

# Curriculum Vitae

## 1 Personal information

Name : Ms. M. Sampurna  
Date of birth : 23rd December 1981

## 2 Academic Record

Exam	Institute	Year	Percentage	Class
X	VVS School, Bangalore	1996	81.7	Distinction
PUC (PCMB)	VVS College, Bangalore	1998	82	Distinction
BSc (PCM)	VVSFGCW, Bangalore	2001	88.8	Distinction
MSc (Physics)	Bangalore University	2003	84.3	Distinction
CSIR-UGC (Physics)	Bangalore Center	2002 December	Qualified	
PhD (Astrophysics)	Indian Institute of Science	2003 - 2004	6.7 (CGPA)	B Grade
PhD (Astrophysics)	Indian Institute of Astrophysics	Aug 2004 - March 2008		Thesis submitted in April 2008

## 3 Awards and Achievements

### 3.1 Graduate and Post-graduate level :

Seventh Rank in BSc in the state level examination (Bangalore University). Second Rank in MSc (Physics), in the state level examination (Bangalore University).

### **3.2 Lecture competition :**

Received 3rd Prize in Bondade Lecture Competition (topic: Line Broadening Mechanisms), held by the Indian Physics Association at Bangalore in 2002.

### **3.3 Selection for PhD Programs :**

Selected as Junior Research Fellow for PhD at Raman Research Institute (RRI), Indian Institute of Astrophysics (IIA), and Indian Institute of Science (IISc), Bangalore in 2003.

### **3.4 Sandwich Thesis Scholarship :**

Selected by the Embassy of France in India, under the Sandwich Thesis Scholarship Program. I was one among the 6 doctoral students who got this fellowship on an all India selection, for the year 2004. Scholarship period was for one year. However I utilized the opportunity only for a fractional period. Worked at Observatoire de la Côte d'Azur (OCA), Nice, France during the three visits sponsored by this program, under the guidance of Prof. Hélène Frisch.

## **4 Summer Project**

Project entitled "Theory and Applications of Hanle Effect in Astrophysics" as a requirement for Summer Project-2002 conducted at IIA under the guidance of Prof. K. N. Nagendra, Indian institute of Astrophysics, Bangalore - 560 034.

## **5 Visits to Institutions for Scientific Collaboration**

### **5.1 Visits within India :**

Visited several Research Institutes like: BARC, and TIFR, Bombay; PRL, Ahmadabad; and NCRA, Pune for basic level training in Observational techniques, and data analysis, in a month long Program.



## 5.2 Visits Abroad :

- (1) Visited (a) the Observatoire de la Côte d'Azur (OCA) at Nice, France for 2 months to work with Prof. H. Frisch; (b) Instituto Ricerche Solari Locarno (IRSOL) at Locarno, Switzerland for three weeks to work with Prof. M. Bianda; and (c) Institute of Astronomy at Zurich, Switzerland for a week to work with Prof. J. O. Stenflo; during August - November 2004.
- (2) Visited (a) OCA at Nice, France for 2 months to work with Prof. H. Frisch; and (b) IRSOL at Locarno, Switzerland for three weeks to work with Prof. M. Bianda; during September - November 2005. During the same period also visited La Specola Solare Ticinese, and MET-SVIZERA, the Meteorological Observatory at Locarno, Switzerland.
- (3) Visited (a) OCA at Nice, France for 2 months to work with Prof. H. Frisch; and (b) IRSOL at Locarno, Switzerland for three weeks to work with Prof. M. Bianda; during August - November 2007. In the same period visited the technical university SUPSI at Lugano, Switzerland.

## 6 Popular Lectures given

- (1) As part of centenary celebrations of Einstein's birthday and World year of Physics 2005, I presented a talk on "Einstein as a Humanist" on March 13th 2005.
- (2) Presented two public lectures at Nehru Planetarium, Bangalore, on the topic "Second Solar Spectrum – a new window to the Sun" on June 8th 2006.

## 7 Talks presented

- (1) Presented a talk on "Effect of a turbulent magnetic field on spectral lines polarization", at the 10th Young Astronomers' Meet held at Indian Institute of Astrophysics, Bangalore, India, during January 3 – 5, 2007.

- (2) Participated and presented a contributed talk on “Scattering Polarization in Moderately Strong Solar Magnetic Field: *The Theory of Hanle-Zeeman Scattering*”, at the 5th Solar Polarization Workshop held in Ascona, Switzerland, during September 17 – 21, 2007.

## 8 Meetings/Workshops Attended

- (1) Participated in the second UN/NASA Workshop on “The International Heliophysical Year and Basic Science” held at Indian Institute of Astrophysics, Bangalore, India, during November 27 – December 1, 2006.
- (2) Participated in the Kodai Winter School on “Solar Physics”, held at Kodaikanal Solar Observatory, Indian Institute of Astrophysics, during December 10 – 22, 2006.